ADVANCES IN AFRICAN EARTH SCIENCES

EDITED BY: Islam Fadel, Folarin Kolawole, Mohamed Sobh, D. Sarah Stamps, Tolulope Morayo Olugboji and Musa Manzi

PUBLISHED IN: Frontiers in Earth Science

frontiers Research Topics

ISSN 1664-8714
ISBN 978-2-83250-505-2
DOI 10.3389/978-2-83250-505-2

About Frontiers

Frontiers is more than just an open-access publisher of scholarly articles: it is a pioneering approach to the world of academia, radically improving the way scholarly research is managed. The grand vision of Frontiers is a world where all people have an equal opportunity to seek, share and generate knowledge. Frontiers provides immediate and permanent online open access to all its publications, but this alone is not enough to realize our grand goals.

Frontiers Journal Series

The Frontiers Journal Series is a multi-tier and interdisciplinary set of open-access, online journals, promising a paradigm shift from the current review, selection and dissemination processes in academic publishing. All Frontiers journals are driven by researchers for researchers; therefore, they constitute a service to the scholarly community. At the same time, the Frontiers Journal Series operates on a revolutionary invention, the tiered publishing system, initially addressing specific communities of scholars, and gradually climbing up to broader public understanding, thus serving the interests of the lay society, too.

Dedication to Quality

Each Frontiers article is a landmark of the highest quality, thanks to genuinely collaborative interactions between authors and review editors, who include some of the world's best academicians. Research must be certified by peers before entering a stream of knowledge that may eventually reach the public - and shape society; therefore, Frontiers only applies the most rigorous and unbiased reviews.
Frontiers revolutionizes research publishing by freely delivering the most outstanding research, evaluated with no bias from both the academic and social point of view. By applying the most advanced information technologies, Frontiers is catapulting scholarly publishing into a new generation.

What are Frontiers Research Topics?

Frontiers Research Topics are very popular trademarks of the Frontiers Journals Series: they are collections of at least ten articles, all centered on a particular subject. With their unique mix of varied contributions from Original Research to Review Articles, Frontiers Research Topics unify the most influential researchers, the latest key findings and historical advances in a hot research area! Find out more on how to host your own Frontiers Research Topic or contribute to one as an author by contacting the Frontiers Editorial Office: frontiersin.org/about/contact

ADVANCES IN AFRICAN EARTH SCIENCES

Topic Editors:
Islam Fadel, University of Twente, Netherlands
Folarin Kolawole, Columbia University, United States
Mohamed Sobh, Freiberg University of Mining and Technology, Germany
D. Sarah Stamps, Virginia Tech, United States
Tolulope Morayo Olugboji, University of Rochester, United States
Musa Manzi, University of the Witwatersrand, South Africa

Citation: Fadel, I., Kolawole, F., Sobh, M., Stamps, D. S., Olugboji, T. M., Manzi, M., eds. (2022). Advances in African Earth Sciences. Lausanne: Frontiers Media SA. doi: 10.3389/978-2-83250-505-2

Table of Contents

frontiers in Earth Science

ORIGINAL RESEARCH
published: 07 June 2021
doi: 10.3389/feart.2021.674953

Archaeological Investigation and Hazard Assessment Using Magnetic, Ground-Penetrating Radar, and GPS Tools at Dahshour Area, Giza, Egypt

A. E. El Emam[1], *A. Lethy*[1], *Ali M. Radwan*[2]* *and A. Awad*[1]

[1]Department of Geomagnetic and Geoelectric, National Research Institute of Astronomy and Geophysics (NRIAG), Helwan, Egypt, [2]Department of Geodynamics, National Research Institute of Astronomy and Geophysics (NRIAG), Helwan, Egypt

An archeological study using magnetic and ground-penetrating radar methods has been performed at the Dahshour region (Giza, Egypt), where various covered structures have not been found because of the long coercion of the zone under the military specialists. Dahshour is the southern extension of the Saqqara and Giza Pyramids plateau, around 25 km south of Cairo. The area is known for its colored pyramids—the white, red, and black pyramids, and the famous Bent Pyramid. Four investigation sites were chosen around the Bent Pyramid complex. The geophysical investigation has revealed the presence of some buried structures made up of mud bricks such as tombs, mud-brick walls, causeway, and remains of an ancient temple. Numerous limestone blocks were also detected. The study indicates the possible existence of an older valley temple made up of mud bricks and confirms the existence of another causeway that led to the Nile Valley. To protect the Egyptian heritage around this vital area, a detailed computation of the current crustal stress/strain state has been performed by taking into account all the available GPS observations. Achieved results indicated that the southern and the southeastern sectors of the investigated area are currently accumulating strain, and this means that there is a possibility for future earthquakes to occur around this vital archaeological area. Buried structures are preserved by confinement in the burial materials like a large mold. However, external load or stress can still cause damage. Therefore, during excavation, the stress should be reduced to avoid wall collapsing and structure damage. Therefore, it is recommended to start excavation from the stress direction from the southern side.

Keywords: magnetic, GPR, earthquakes, GPS, Dahshour area

OPEN ACCESS

Edited by:
Mohamed Sobh,
Freiberg University of Mining and Technology, Germany

Reviewed by:
Svetlana Kovacikova,
Institute of Geophysics (ASCR), Czechia
Awad Omran,
Assiut University, Egypt
Giovanni Leucci,
the National Research Council (CNR), Italy

***Correspondence:**
Ali M. Radwan
amradwaneg@yahoo.com

Specialty section:
This article was submitted to Solid Earth Geophysics, a section of the journal Frontiers in Earth Science

Received: *02 March 2021*
Accepted: *17 May 2021*
Published: *07 June 2021*

Citation:
El Emam AE, Lethy A, Radwan AM and Awad A (2021) Archaeological Investigation and Hazard Assessment Using Magnetic, Ground-Penetrating Radar, and GPS Tools at Dahshour Area, Giza, Egypt. Front. Earth Sci. 9:674953. doi: 10.3389/feart.2021.674953

INTRODUCTION

Dahshour area is located southwest of Cairo (**Figure 1A**) within the Giza governorate, which is acclaimed for one of the seven world marvels, the pyramids of Giza. Dahshour is the southern extension of the Saqqara, and Giza Pyramids plateau is around 8 km south of Saqqara.

The current study is conducted in the vast area between the scan locations of both Mekkawi et al. (2013) and Abdallatif et al. (2010). The study area belongs to the Bent Pyramid complex structure area (the selected survey sites are within the expected locations of these pyramid complex structures,

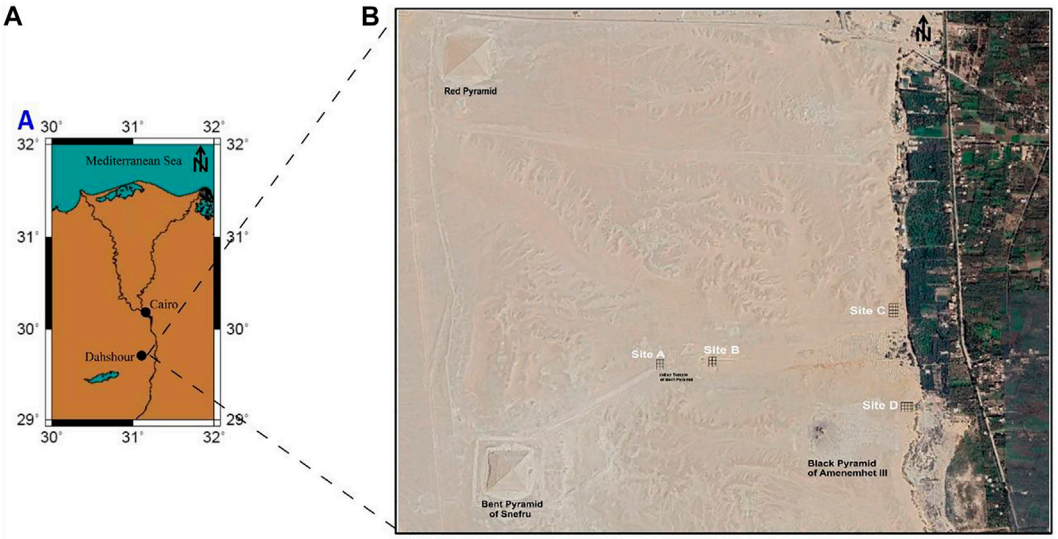

FIGURE 1 | (A) Map of Egypt showing the location of Dahshour area. **(B)** Satellite image showing the study areas as represented by sites (A, B, C, and D) (reproduced from Google Earth).

e.g., causeway, valley Temple, funeral Temple, and burial chambers). The Bent Pyramid has a very important archeological value, as it was the first attempt to build a smooth-sided pyramid by King Sneferu (2613–2589 BC), whereas his son King Khufu (2589–2566 BC) built the most famous the Great Pyramid of Giza.

The Pharaohs recorded earthquakes and their destructive effects on their temples. They built their temples to withstand the earthquakes. However, these monuments cannot defeat nature and time; therefore, they require protection and preservation. Consequently, this study includes both archaeological investigations and hazard assessment at Dahshour area. Usually, seismic hazard assessment studies are performed for structures rising above the ground surface where they are usually affected by ground shaking. Such studies are usually based on earthquake catalogs. Jena et al. (2020) gave a complete review of seismic hazard assessment methods. However, for buried structures like walls, the ground static load and the causative stresses play a major role in structure damage, especially during the excavation process. Underground structures have a lower rate of damage due to ground shaking than surface structures (Hashash et al., 2001). Therefore, this study includes crustal deformation analysis to determine the stresses at Dahshour area.

After the occurrence of October 12, 1992, earthquake, which has a magnitude of 5.9 on the Richter scale at Dahshour area, 30 km southwest the center of Cairo city at a depth of about 23 km, causing 545 deaths, injuring 6,512, and making 50,000 people homeless (Hussein et al., 1996), the National Research Institute of Astronomy and Geophysics (NRIAG) in Egypt proposed programs to study the crustal deformation in and around the Greater Cairo area. In 1995, a high-precision GPS geodetic network consisting of eleven geodetic stations was established in and around the Greater Cairo area including the archaeological Dahshour area, and it has been extended and renewed during the period of the present study (Mahmoud et al., 1996). This is very important to compute the stress affecting the study area, especially around Dahshour, to assess the seismotectonic setting of this vital area. This study is the first work to address the stress hazard before excavation with a detailed map of the expected features and their orientation with the stress direction.

HISTORICAL AND ARCHEOLOGICAL BACKGROUND

Dahshour area is a very interesting site for both archaeological investigations and tourists. It retains a diversity of enormous archaeological structures such as the Bent Pyramid (2613–2589 BC during the rule of King Sneferu from the fourth Dynasty-Old Kingdom); it was the first attempt to build a smooth-sided pyramid, succeeded by the Red Pyramid (the first smooth-sided pyramid) rising to 104 m height, the White Pyramid of Amenemhat II (1929–1895 BC), the Black Pyramid of Amenemhat III (1860–1814 BC), and the Pyramid of Senusret III (1878–1839 BC) from the Middle Kingdom (12th and 13th dynasties). Dahshour additionally contains various landmarks identified with each pyramid, like funeral home sanctuaries and helper burial chambers for the relatives and supported authorities. There are likewise the Mastabas (a unique burial chamber structure) of different princesses and queens containing noticeable instances of Middle Kingdom goldsmiths, a large portion of

which are currently in the Cairo Museum (Baines and Malek, 1992; Black and Norton, 1993).

The period of Sneferu witnesses a major evolution in the pyramid structure. It is well known that Sneferu built at least three pyramids that are still existing today (in Dahshour: the Bent Pyramid and the Red Pyramid, and in Faiyum: the Meidum Pyramid). Each pyramid was a step forward for the next with significant differences in the structure, materials, and design. Sneferu started with the Meidum pyramid, which was a step pyramid of sand and mud bricks covered with polished limestone. Only this pyramid has an associated mortuary temple. Finally, Sneferu constructed the Red Pyramid which is the first successfully constructed smooth-sided pyramid and the third largest pyramid in Egypt after those of Khufu and Khafre at Giza. The Red Pyramid complex contains mortuary and valley temples with a causeway in between. Nevertheless, the Bent Pyramid is a milestone in this progressive development in the pyramid's architecture. Key features start to appear in the pyramid's architecture, for example, using limestone as the main construction material in the pyramids, temples, and causeways.

PREVIOUS WORK

Geophysical surveying in Dahshour area was spearheading work to investigate the related archeological designs, particularly since Dahshour zone has been blocked for logical work for quite a while due to the security vacuum following the 2011 uprising. In July 2019, Egypt opens the Bent Pyramid for tourism for the first time since 1965. Geophysical methods have made a critical commitment to archeology, especially, the nondestructive methods which are generally utilized in locations that loosen the requirement for conventional excavation. Several geophysical techniques can be utilized together or independently to diagram archeological constructions (David, 1995). Magnetic techniques and ground-penetrating radar "GPR" are two such apparatuses that have been utilized to portray archeological highlights (Hounslow and Chroston, 2002; Abdallatif et al., 2003). The magnetic technique has become a significant tool for the scientific examination of archeological sites. It was first utilized during the 1950s (Aitken et al., 1958) and has since become the main instrument in archeological prospection. It is a quick and compelling procedure for planning the appropriation of archeological remaining parts in the shallow subsurface (Clark, 1986; Clark, 1990; Scollar et al., 1990; Reynolds, 1997). A recent review of the application of the magnetic technique in the exploration of Egyptian archeology is given by Abdallatif et al. (2019).

The data are directly obtained, dealt with, and interpreted, utilizing high goal instruments. Numerous topographical and hydrological uses of the GPR have been portrayed by Davis and Annan (1989), Annan et al. (1991), Doolittle (1993). In like manner, the procedure has been effectively utilized in archeological investigations (Goodman, 1994; Goodman et al., 1995; Conyers and Goodman, 1997; Leckebusch, 2000; Tomizawa et al., 2000).

Many previous geophysical studies have been carried out in Dahshour area. Abdallatif et al. (2010) have conducted near-surface magnetic investigations using the FM36 magnetic gradiometer in the area east of the Amenemhat II pyramid. They scan an area of 340 m × 200 m, which comprises four major archaeological features of different shapes and sizes that mostly consist of mud bricks. These main structures are the causeway that connected the mortuary temple with the valley temple during the Middle Kingdom of the 12th Dynasty, the mortuary temple and its associated rooms, ruins of an ancient working area, and a Mastaba. This work was followed by an integrated geophysical survey conducted by Abbas et al. (2011). The ground-penetrating radar (GPR, SIR-2000), the electrical resistance meter (Geoscan RM15), and the electromagnetic profiler (GEM300) have been utilized to acquire some geophysical data within the area scanned by Abdallatif et al. (2010). These techniques have been applied to selected zones to investigate specific objects and oriented to solve the problems questioned by the local archaeological inspectors. The study conveyed a superior image of the whole measured site and helped to identify most of the detected artifacts. Furthermore, the margins of the causeway and its infrastructure have been perfectly delineated. However, the possible locations for the pyramid's eastern entrance and the valley temple have been tentatively identified.

Mekkawi et al. (2013) conducted a conceptive work using a proton magnetic gradiometer to scan what is known as Mastaba (tomb) and Tell Athery (archeological hill) located to the south of the Bent Pyramid. The results indicated a distribution of some buried archeological features that are mostly tombs from the Old Kingdom.

FIELD SURVEY AND DATA ACQUISITION

The field survey was conducted in the study area to discover the archaeological structures made up of mud bricks and limestones such as tombs, temples, and walls. The sites were chosen close to existing or known archaeological features. Furthermore, site selection and their extensions were controlled by the ground topography and surface features. Two sites were surveyed to investigate the western and southern extensions of the valley temple of the Bent Pyramid. Meanwhile, another two sites were chosen to the east near the Nile Valley, where it was expected to have harbor and laborers' accommodation and facilities during the construction process of Dahshour pyramids.

Typical pyramid complex in the Fourth Dynasty usually consists of a valley temple, a causeway, a mortuary temple, and the king's pyramid. However, King Sneferu starts his ruling period by continuing building the Meidum Pyramid which seems never to have been completed. Beginning with Sneferu and to the 12th Dynasty, all pyramids had a valley temple, which is missing at Meidum. However, a mortuary temple was found under the rubble at the base of the Meidum Pyramid.

The remaining parts of what is believed to be the valley temple of the Bent Pyramid Complex of King Sneferu lie somewhere between the Pyramid of Sneferu and the Nile River (about 650 m northwest of the pyramid). Examination of the temple design and

the features enclosed within it presumed that it is similar to the Meidum temple. In actuality, the Bent Pyramid's prelude to the valley temple indicates that it is indeed somewhat a valley temple and a halfway funeral temple, containing components of both kinds of constructions, which makes it a unique design that resembles a transition in the construction strategy between the Third and the Fourth Dynasties. Since it is the principal temple associated with the pyramid complex, it has been explored archeologically (Baines and Malek, 1992). However, missing inscriptions and important features make archeologists believe that it has an associated complementary structure.

The temple is connected to the causeway from the west side and has a large opening on the eastern side that could connect it to the harbor. There may have been another causeway that led down to a harbor, but there are no excavated archaeological features that can prove this assumption yet (Hill, 2020).

Magnetic and GPR Data Acquisition

Acquisition Strategy

Four sites were surveyed using the vertical magnetic gradiometer FM36 (Geoscan Research, 1987). Each site was divided into small grids. The survey was conducted along parallel traverses with a station separation of 0.5 m. Standard working precautionary measures included instrument warm-up and site tidy up. A zero-reference point in a steady territory was chosen and utilized for instrument adjustment.

Powerful information obtaining is subject to a very much planned study and successful usage. Therefore, based on the magnetic survey results, two sites have been chosen to be further investigated using the GPR method. The survey was conducted using the SIR2000 instrument from GSSI with a monostatic antenna of a central frequency of 200 MHz. Each site is studied as one grid with a set of zigzag profiles. The offset distance between successive lines was 1 m. The radar was set up to procure 20 scans/m and a sampling rate of 512/trace over an absolute scope of 150 ns. A survey wheel that was utilized to control the studied distance and to trigger the electromagnetic wave was appended to the system.

Data Acquisition

Site (A)

Site A (**Figure 1B**) covers 120 m × 80 m (9600 m^2) at the western side of the north–south–oriented valley temple of the Sneferu Bent Pyramid. The vertical magnetic gradient survey was conducted in a half-meter station separation and a 1-m traverse separation. The survey began with an area of 40 m × 80 m. In light of the outcomes obtained from this underlying region, the survey was stretched out to follow up recognized highlights, covering 20 grids altogether, with every grid being 20 m × 20 m. The estimations were signed into the instrument each half-meter on 1 m dispersed traverses. Working more than 2 days, 16,000 readings were gathered and put away in the FM36 memory. Unavailable areas were viewed as fake grids (the grid layout is presented in **Supplementary Figure S1a**).

The procured data were then introduced in gray scale (the raw data are presented in **Supplementary Figure S1b**). The acquired raw data appear as if they were taken from an aerial photography. The dark areas in the gray scale magnetic image (**Supplementary Figure S1b**) indicate positive anomalies, while the lighter areas indicate negative anomalies. It shows some archeological structures that could be made from mud brick. The vertical magnetic gradient over this site was ranged from −10 to 10 nT/m. The surface topography was practically flat and suitable for the gradiometer survey. The estimations were not diurnally amended because diurnal varieties barely influence gradient data. They additionally favor close-by sources, given the quick tumble off of magnetic gradient amplitudes (converse fourth force of distance for dipole sources).

Site (B)

Site B (**Figure 1B**) is situated on the eastern side of the valley temple of the Sneferu Bent Pyramid. The area covers 60 m × 40 m (2400 m^2), which was divided into 10 grids, with each being 20 m × 10 m. This site was scanned in more detail than site A. The readings were signed each half-meter on half-meter spaced traverses. After working for more than 1 day, 8,000 readings were gathered and put away in the FM36 memory (see **Supplementary Figure S2a** for grid layout). The procured data were then introduced in gray scale (see **Supplementary Figure S2b** for raw data plot). The acquired raw data show an overall vertical magnetic gradient ranging between −200 and 60 nT/m.

Within Site B, a chosen area of 20 m × 40 m (see **Supplementary Figure S5a**) was further scanned using GPR to outline and follow the anomalies that appear in the magnetic survey. The GPR survey was carried out in the N–S direction along 20 zigzag profiles, with each being 40 m in length.

Site (C)

The investigation area covers 120 m × 40 m (4800 m^2) (**Figure 1B**). The Magnetic survey covers 12 grids, with each being 20 m× 20 m. The estimations were signed into the instrument each half-meter on 1 m traverses. Working more than 2 days, 9,600 readings were gathered and put away in the FM36 memory (the grids' layout is presented in **Supplementary Figure S3a**). The obtained data were then introduced in gray scale (see **Supplementary Figure S3b**). The attained raw data have an overall vertical magnetic gradient ranging between −220 and 60 nT/m.

Additionally, an area of 40 m× 40 m at site C (see **Supplementary Figure S5b**) was scanned using GPR to correlate them with the magnetic results. The GPR survey was carried out in the E–W direction along 40 zigzag profiles with 40 m length.

Site (D)

This site covers an area of 10 m × 20 m (200 m^2) (**Figure 1**). The survey covers one grid altogether. The estimations were signed into the instrument each half-meter on half-meter separated traverses. 800 readings were gathered and put away in the FM36 memory (see **Supplementary Figure S4a**). The procured data were then introduced in gray scale (see **Supplementary Figure S4b**) with an overall vertical magnetic gradient ranging between −60 and 40 nT/m.

GPS Data Acquisition

The field hardware incorporates receiver units and assistant gadgets like meteorological sensors, tribrachs with optical plummets, tribrach connectors, stands, compass, batteries, and other subordinate equipment. Geodetic receivers which perform exact baseline vector estimations should be thought of. Double recurrence receivers with P-code capacity are fundamental for the most exact positioning applications. The fieldworks of the GPS Greater Cairo geodetic network were completed by utilizing dual-frequency Trimble receiver 4,000 SSI with P-code and antennas compact L1/L2 with the ground plane. The Trimble receiver 4,000 SSI is naturally procured and tracks GPS satellites on the L1 and L2 stations. It additionally joins astoundingly low-noise code estimations with transporter and smoothing procedures to give exact position, velocity, and time solutions. Ten GPS campaigns from 2005 to 2011 were conducted with double-frequency Trimble 4000 SSI. The Greater Cairo network data of the ten GPS campaigns were handled utilizing Bernese V.5.0 (Dach et al., 2007).

DATA PROCESSING

Magnetic Data Processing

The raw magnetic data of sites (A, B, C, and D) are display magnetic impacts from numerous sources. Apart from the visible anomalies that appear at some parts of the images, most other archeologically critical peculiarities are not noticeable because of noise field abandons and other noise sources. To beat this, we actualized a handling arrangement that was recommended by the instrument producer. A run-of-the-mill preparing arrangement at first is to show and audit the data, cut outrageous qualities from the data, recognize the impact of major topographical and ferrous features, eliminate data assortment absconds, and at last, improve and present the archeological response. The introductory section diminishes the impact of iron spikes. Defect removal includes i) removal of grid slope, ii) removal of grid discontinuities, and iii) removal of traverse stripe effects. Improvement and introduction incorporate i) evacuation of iron spikes and ii) smoothing and insertion. The processing was conducted using the Geoplot software (Geoscan Research, 2005). More details about each processing step are provided by Geoscan Research (2005). The request for preparing can be vital for certain capacities—for instance, despiking ought to be performed before applying a low-pass channel to stay away from the spike energy spreading out. Some of the processing functions, however, may not be advisable to apply to the data as they could introduce artifacts and remove the archaeological features.

A few grids may show a progression of stripes orientated in the traverse direction. This impact is known as traverse stripping and was caused because of a slight contrast in the base level of substitute traverses. This difference could occur because of instrument tilting and the change in carrying angle while measuring in successive traverses. The difference in the mean gradient values between grids was corrected using a zero mean grid (ZMG) function, whereas the effect of traverse stripping was corrected using the zero mean traverse (ZMT) function. A low-pass filter (LPF) was utilized to stifle higher frequency parts, like noise in the data, and simultaneously save low frequency and enormous scope spatial anomalies, subsequently upgrading and smoothing the huge weak features. The low-pass filter with perusing window size two delivered the best outcomes and shows unmistakably the enormous, extended anomaly.

GPR Data Processing

The overall goal of data preparation, as applied to GPR, is to deliver an image that can be deciphered to distinguish buried targets. The gathered data were handled in 1D and 2D (time slicing). Manataki et al. (2015) gave a good review of the GPR practice and processing for archaeological investigation.

All through the 1D analysis, the data were exposed to noise removal and signal upgrade preparation. Four preparing steps were played out: a) Zero time adjustment (static shift): it is applied to connect zero time with zero depth, so any time offset because of instrument recording was eliminated before interpretation. b) X flip profile: it is applied to flip the profiles in the x-direction (reverse profiles). c) Background removal: filters follow up on the picked number of traces to take out transiently the predictable clamor from the entire profile and consequently perhaps make the signals visible. It additionally smothers horizontal coherent energy. Its impact is additionally to underscore signals, which differ laterally, for example, diffractions. d) Band-pass Butterworth: a low-pass vertical filter of 300 MHz was applied to remove the high-frequency signals, while a high-pass vertical filter of 80 MHz was applied to remove low-frequency signals. Filtering the data typically removed the unwanted background noise resulting from the electronic ringing of the antenna and power transmission line located in the survey area, etc. The GPR data processing was conducted using the Reflexw software package (Sandmeier, 2016).

GPS Data

First, the Greater Cairo network data were processed together with the Helwan (PHLW) permanent station and one of the IGS stations, so we used it as a fixed point.

Second, the data were processed session-by-session, and normal equations for all the sessions of each campaign were stored. Then, these normal equations were combined to obtain the final solutions for each campaign. Repeatability of station coordinates of the different campaigns was calculated to estimate the precision of the coordinates; hence, crustal deformation rates were estimated. The data were processed annually; that is, the parameters of the crustal deformation were computed for every year and finally for the total period from 2005 to 2011 to compute the mean velocity at each station.

MAIN RESULTS AND DISCUSSION

Magnetic Survey Results

Site (A)

The processed data image (**Figure 2A**) mirrors the principal discoveries uncovered by the magnetic technique in the zone

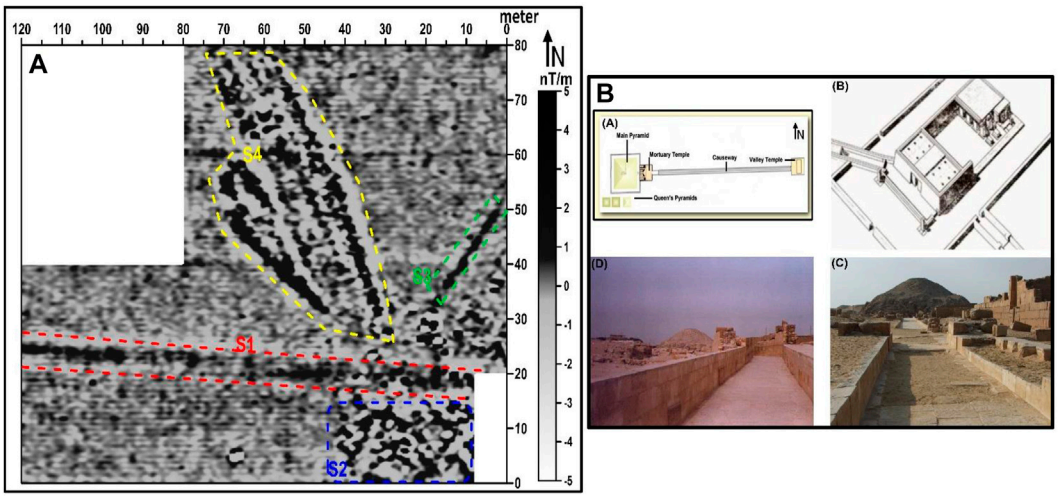

FIGURE 2 | (A) Gradiometer data of site A, after applying the processing functions. This plot shows the interested magnetic anomaly zones. S1, S2, S3, and S4 delineate the main discoveries in this study. **(B)** (a) A sketch of Sneferu Pyramid shows the causeway connects to the valley temple. (b) The ruins of the valley temple. (c) and (d) Examples for two causeways of two exposed pyramids at Saqqara (the causeway consists of parallel walls made up of limestone).

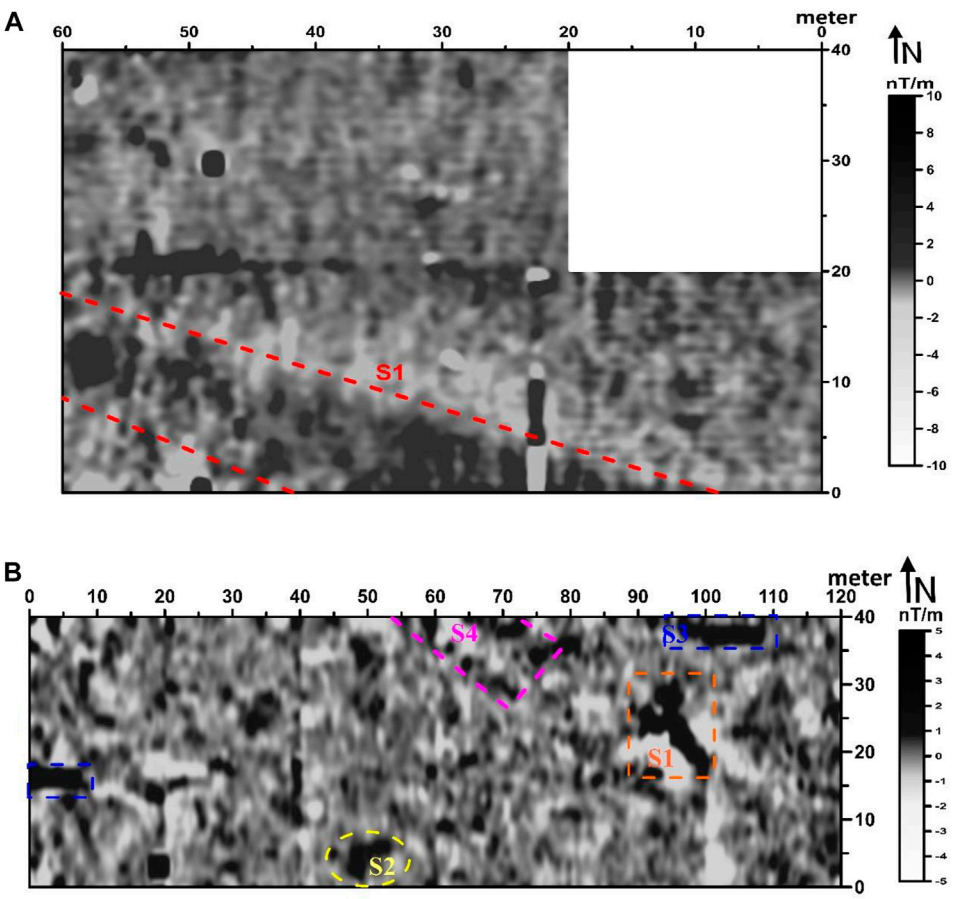

FIGURE 3 | (A) Gradiometer data of site B, after applying the processing functions. This plot shows the anomaly zone S1. **(B)** Gradiometer data of site C, after applying the processing functions. This plot shows the interested magnetic anomaly zones. S1, S2, S3, and S4 delineate the main discoveries in this area.

situated on the western side of the Bent Pyramid valley temple. Four fundamental anomalies have been distinguished as S1, S2, S3, and S4 (**Figure 2A**), which could reflect four archeological constructions covered around there. We expect the major part of these constructions to be made up of mud bricks. Our assumption depends on the positive extremity of the magnetic anomalies of these designs, the surface archeological record of the site, and the historical backdrop of old Egyptian constructions.

Structure S1 is an elongated high magnetic anomaly of about 100 m long and 5 m in width. This is strongly proposed to be part of the causeway. The causeway is a very important archaeological feature (**Figure 2B**) as it interfaces the funeral home temple with the valley temple, and its walls contain the popular pyramid contents composed by the most recent Egyptian Dynasty.

Structure S2 is represented by scattered positive magnetic anomalies that cover an area of about 30 m × 20 m which is considerably large enough to resemble some collapsed structure. This structure is not clear for deciding its archaeological origin.

Structure S3 is represented by a connected positive magnetic anomaly. This anomaly is about 20 m long and is parallel to the valley temple wall. This feature may be a mud-brick wall.

Structure S4 is represented by several dissected and ambiguous negative and positive anomalies with different shapes and sizes. However, its edges resemble straight lines. This structure is hazy and not clear for deciding its archaeological origin. However, the western edge of this anomaly is at a right angle to the detected feature S3.

Site (B)

The processed image (**Figure 3A**) shows an archaeological structure S1, which may be an extension of the causeway in the direction of the Nile Valley. The feature is resampled by scattered positive anomalies that are bounded by negative anomalies. This suggested that the positive (dark color) part of feature S1 is made up of mud, and the boundary negative anomaly (light color) is made up of limestone. Therefore, the GPR survey was proposed in this location to confirm the nature of these findings.

Site (C)

The processed image (**Figure 3B**) mirrors the primary revelations uncovered by the magnetic technique around there. Four primary atypical areas have been recognized as S1, S2, S3, and S4 (**Figure 3B**).

Structure S1 is addressed by a major associated positive magnetic anomaly. Moreover, it is seen that there are little irregular negative inconsistencies (white color), which may allude to the presence of an underground cavity structure that has been regularly filled with sediments. The first zone may address a mud-brick wall.

Structure S2 has a three-sided shape and may allude to the passage of burial place. In addition, it is seen that the little irregular negative anomalies (white color) are not addressing a magnetic dipole impact. These negative parts may allude to the presence of an underground cavity structure that has been frequently filled with silt (i.e., tomb).

Structure S3 is represented by a connected positive magnetic anomaly. This zone might be a piece of a mud-brick wall.

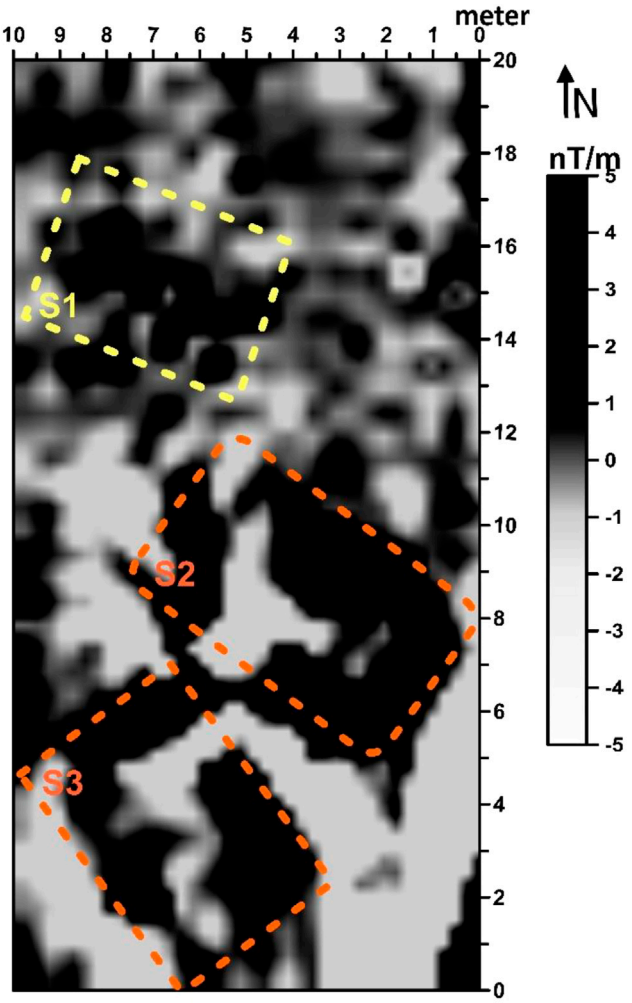

FIGURE 4 | Gradiometer data of site D, after applying the processing functions. This plot shows the interested magnetic anomaly zones. S1, S2, and S3 delineate the main discoveries in this area.

Structure S4 is addressed by an associated positive magnetic anomaly prolonged with a rectangular shape. The zone may address a burial place made up of mud-bricks.

Moreover, the results show an enormous number of small (1 m × 2 m) negative anomalies, which is a typical grave size. To further identify the nature of these anomalies, a GPR survey was proposed to start from the western side of feature S4 to cover feature S2 and extended 30 m to the west.

Site (D)

The prepared image (**Figure 4**) mirrors the fundamental discoveries uncovered by the magnetic technique around there. Three primary anomaly areas have been recognized as S1, S2, and S3 (**Figure 4**), reflecting single archeological designs covered around there.

Structure S1 is addressed by a major associated positive magnetic anomaly and recommends a piece of rectangular shape. This zone might be a mud-brick wall.

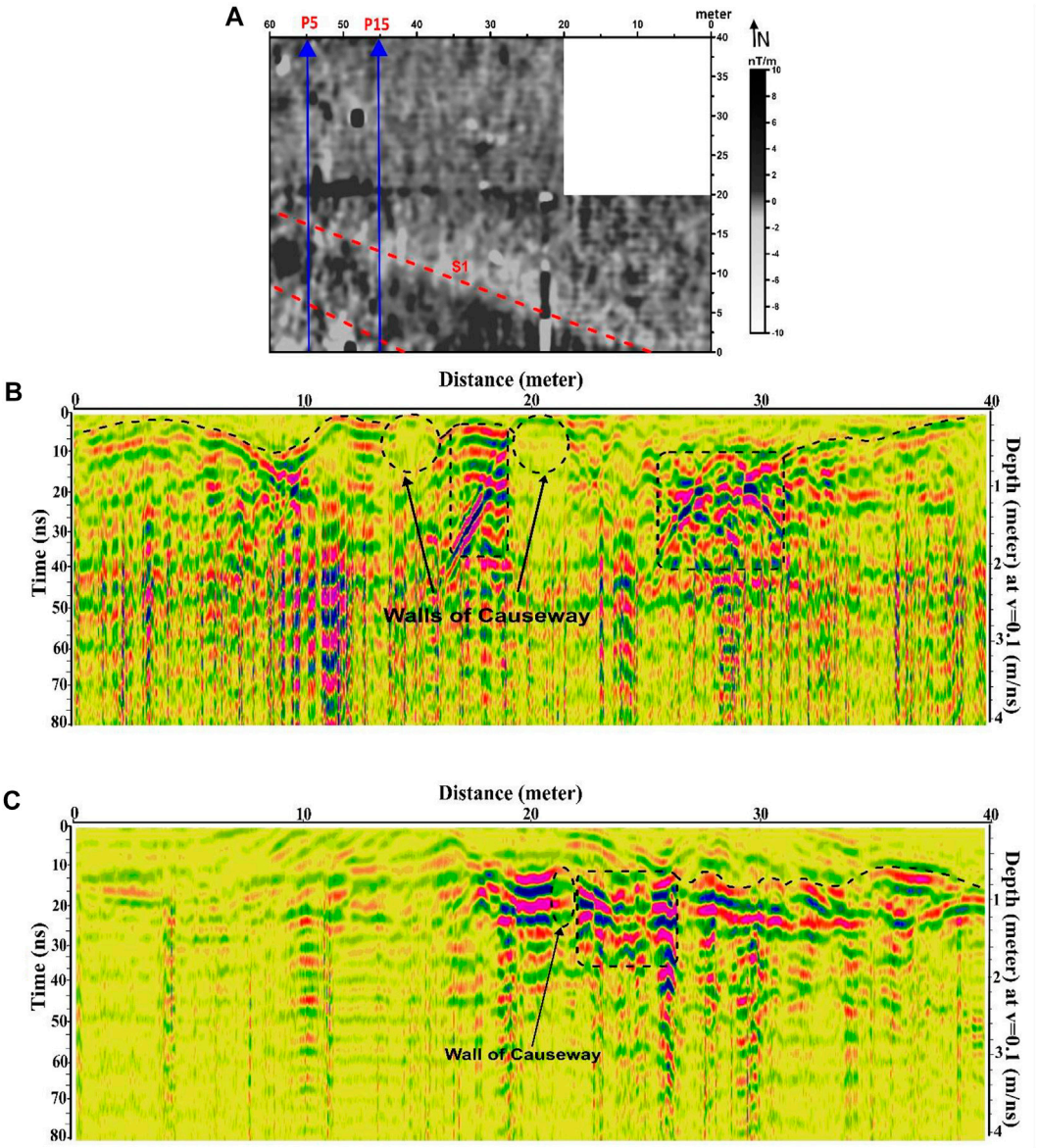

FIGURE 5 | (A) The location of the GPR profiles P5 and P15 at site B. **(B)** GPR display of radar profile P5. **(C)** GPR display of radar profile P15.

Structures S2 and S3 are represented by a big connected positive magnetic anomaly with a square shape. It may be the presence of buried walls (mud-brick wall structure supposed to be a tomb) with an entrance that leads to an inner chamber. Additionally, it is seen that the little irregular negative anomalies (white color) may allude to the presence of underground cavity structures that are regularly filled with sediments.

GPR Survey Results

Site (B)

The GPR data interpretation is usually based on the reflector's shapes and the horizontal continuity of the reflections. In this site, a convergence of reflections is seen in a zone of high reflectivity, for the most part between 0.2 m and 2 m depth in numerous GPR profiles.

Profile No.5 (P5): Trends N–S with a total length of about 40 m (**Figures 5A,B**). It shows two anomalies, which reveal parts of the two walls of the causeway. The two anomalies are far from each other separated by a distance of about 2.5 m. A disturbance zone is noticed between distances (26 and 31 m), which may be generated due to the presence of buried walls (mud-brick wall structure).

Profile No.15 (P15): Trends N–S with a total length of about 40 m (**Figures 5A,C**). This profile is located at a 10-m distance from the profile (P5). Its results are quite similar to those in the previous profile (P5), but the depth of the causeway increases to 0.4 m. A disturbance zone is noticed between distances 22 and 26 m, which may be generated due to the presence of buried walls (mud-brick wall structure).

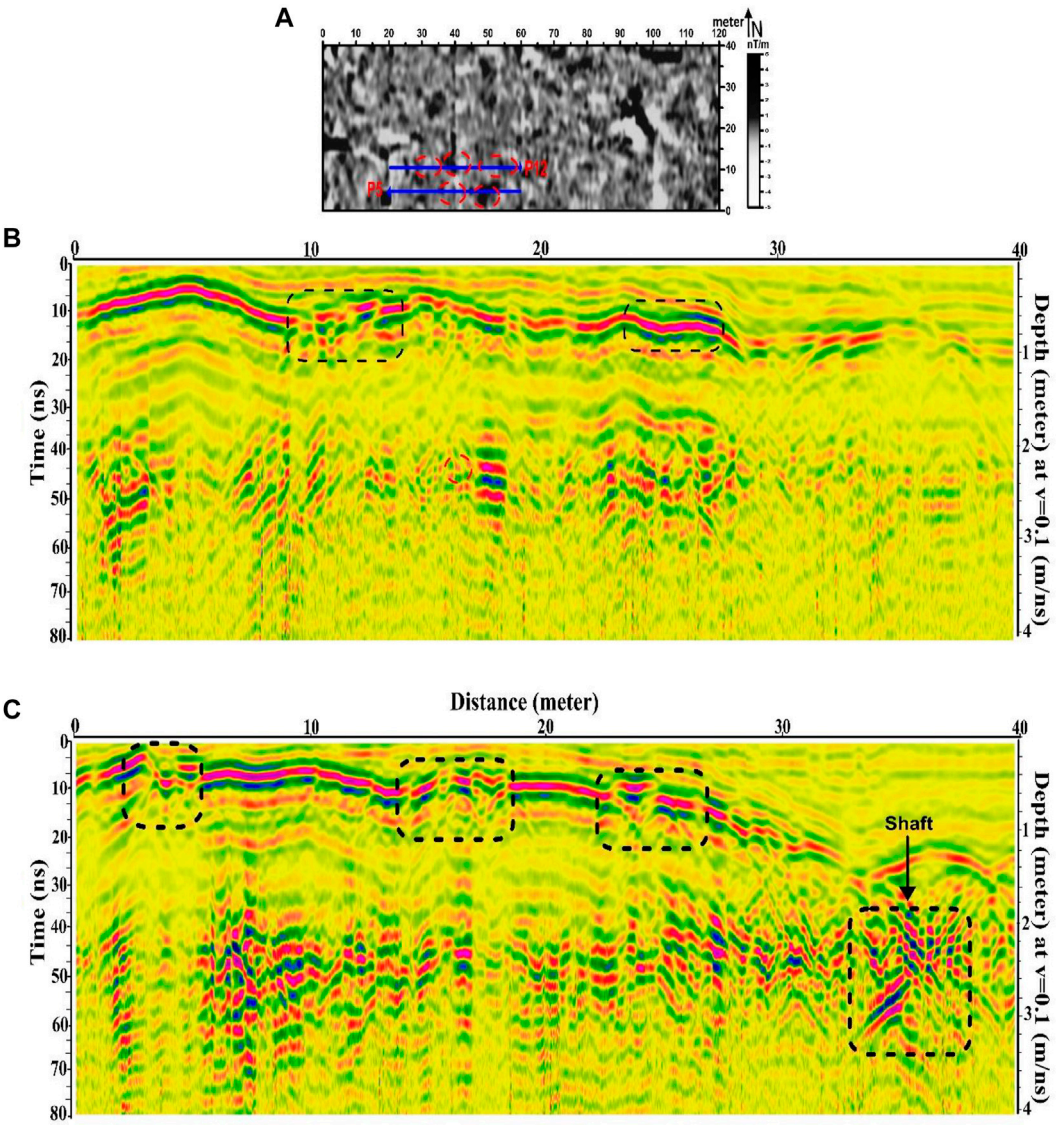

FIGURE 6 | (A) The location of the GPR profiles P5 and P12 at site C. **(B)** GPR display of profile P5. **(C)** GPR display of profile P12.

Site (C)

A convergence of reflections is seen in a zone of high reflectivity, for the most part between 0.5 and 3 m depth in numerous GPR profiles around the site.

Profile No.5 (P5): Trends W–E with a total length of about 40 m (**Figure 6A**). Through this profile, two anomalies appear obviously at distances of 10 m and 24 m, and comparable time of 8 and 10 ns, respectively (**Figure 6B**). These features correspond with the observed magnetic features. Their mean depth varies from 0.5 to 1 m.

Profile No.12 (P12): Trends W–E with a total length of about 40 m (**Figure 6A**). Through this profile, four anomalies appear obviously at distances of 4, 14, 22, and 34 m, and comparable times of 2, 4, 5, and 30 ns, respectively (**Figure 6C**).

The disturbance zones along this anomaly do not exist in the magnetic results, which may be owing to its nonmagnetic nature (e.g., limestone). The origin of these features may reflect a presence of a shaft. The walls of the shaft section can be observed from the surface. This mud-brick building of the shaft might have also been originally cased on the inner side of the courts with limestone. Also, they are filled with sand and gravel deposits in the entrance of the shaft. The shaft entrance may lead to several burial chambers found at the bottom.

Profile No.26 (P26): Trends W–E with a total length of about 40 m (**Figure 7A**). Through this profile, three anomalies appear obviously at distances of 0, 7, and 26 m, and comparable times of 1, 5, and 32 ns, respectively (**Figure 7B**).

The profile is showing a very big dipping planner reflection, which may represent an anomaly created and blown up against archaeological structure (may be considered as a vertical shaft leading to an underground burial chamber). The second anomaly appears at a distance of 7 m, which may represent a near-surface small shaft. At a distance of 28 m, we can notice a very clear and

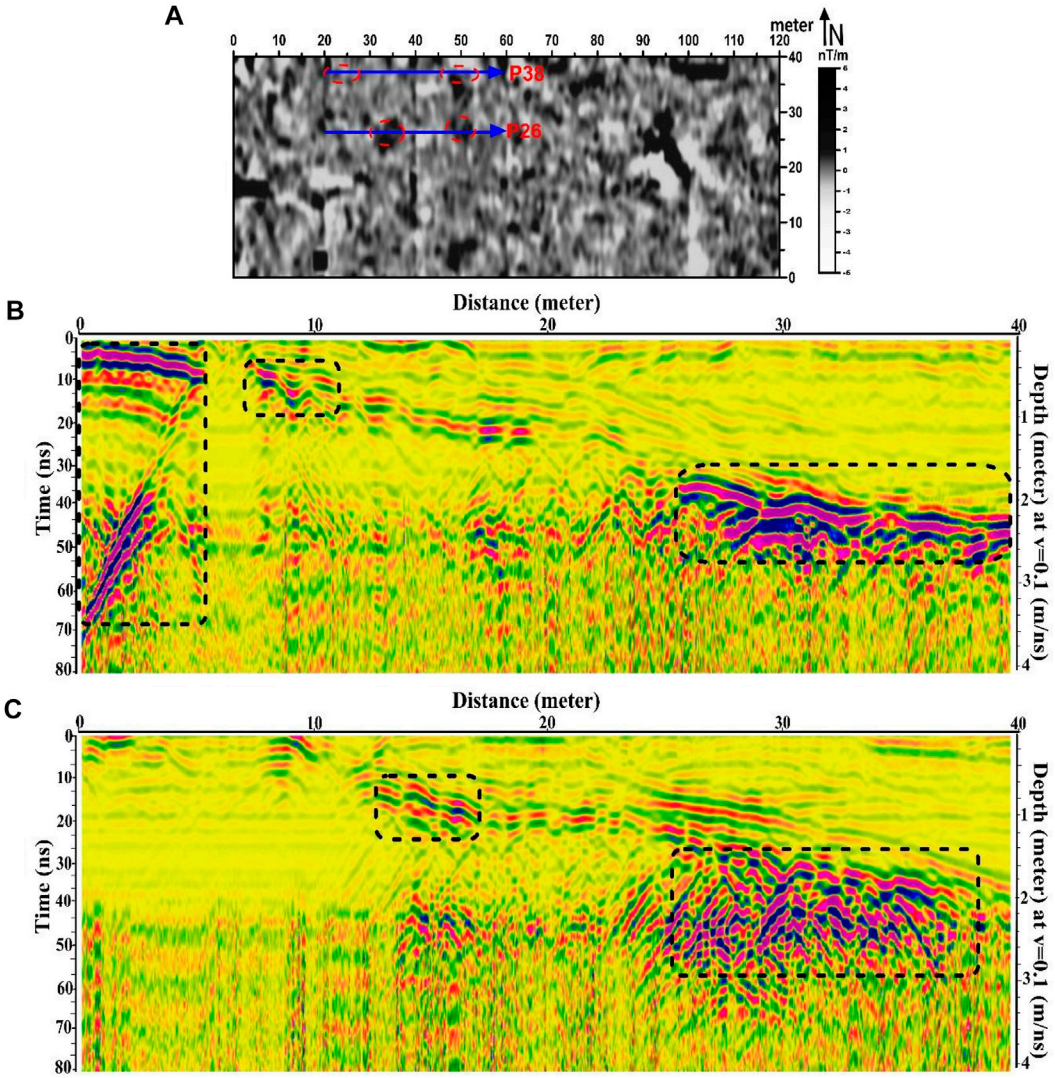

FIGURE 7 | (A) Magnetic image of site (B) shows the location of the GPR profiles (P26 and P38). **(B)** GPR display of profile 26. **(C)** GPR display of profile 38.

larger anomaly (at an offset from 26 to 40 m). This anomaly is too large to be interpreted as a mud-brick wall. It may be a mud-brick burial tomb, which is built of mud bricks with limestone revetments.

Profile No.38 (P38): Trends W–E with a total length of about 40 m (**Figure 7A**). Through this profile, two anomalies appear obviously at distances of 14 and 26 m, at comparable times of 14 and 32 ns, respectively (**Figure 7C**). The second anomaly may reveal a dissected area filled with sand and gravel, which may be due to the presence of mud-brick features. These features correspond with the observed magnetic features.

GPS Results

Horizontal Displacement Results

The displacement vectors at every GPS station were resolved under the imperative states of a supposition of free network adjustment. Horizontal components at each station were computed from the difference of adjusted coordinates of the stations from one epoch to another. The horizontal components of the displacement vectors with 95% confidence error ellipses and the seismicity events are shown in **Figure 8** (see **Supplementary Figure S6**). Here, the error ellipses mean the standard error on the whole bearing around the noticed site. A few stations of the network show critical changes, while other stations demonstrate no huge changes through the time of observations. The extents of the movements are inhomogeneous over the region.

As shown in (see **Supplementary Table S1**) **Figure 8**, for the period from 2005 to 2011, the movement rates are nearly distributed equally on the southern part of the study area, and this is clear from the horizontal displacement rates at stations of ELSF, WAHA, and MESA, and these rates are 14.8 mm/yr, 9.1 mm/yr, and 7.4 mm/yr, respectively. The northern part of the study area is not subjected to high movement rates. This is

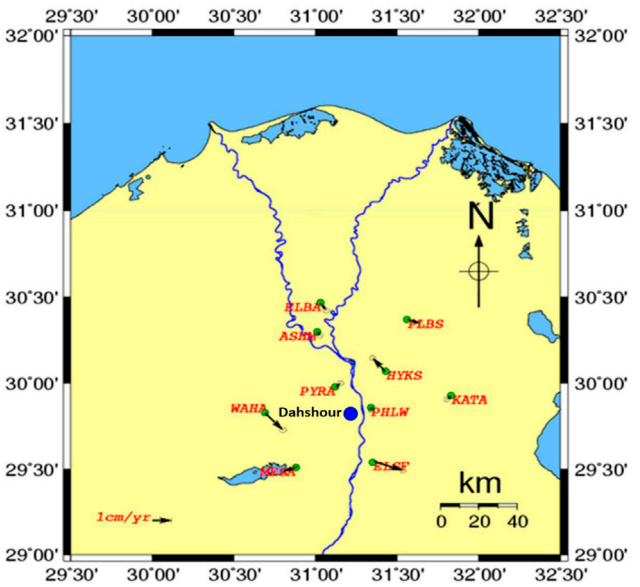

FIGURE 8 | Horizontal displacement rates of the study area from 2005 to 2011.

confirmed from the concentrations of the earthquake events at the southern part (see **Supplementary Figure S6**). This is due to the concentrations of the earthquakes that occurred in this period at the southwestern part of the study area. An earthquake with a magnitude greater than 4 mb (Richter scale) occurred in this area, between Dahshour and El-Fayoum area. Such a last feature requires additional studies to better determine the causative tectonic sources, therefore implying a thorough reevaluation of the seismic hazards in this important region.

Strain Results

The strain describes object deformation caused by external loads in terms of relative displacement of the object particles (Wu, 2005).

The horizontal components of the displacement vectors are used for estimating the strain tensor parameters: dilatations and maximum shear strains where they are estimated within the observation periods. The program used for calculating these parameters is called strain tensor (Dimitrios et al., 2018). The program implements Shen et al. (2015) method for interpolating the GPS-estimated horizontal displacement rates.

The area under study has been divided into four blocks, and the strain parameters for each block have been calculated.

Dilatation

The dilatation is the deformation component that defines the change in object volume (Dixit and Dixit, 2008). As shown in **Figure 9A** (see **Supplementary Table S2**), the Greater Cairo area was suffering from both compressional and extensional dilatation during the period from 2005 to 2011. The extensional forces are dominant at block I, 0.13 μs (microstrain), while the compressional forces are found clearly at blocks II and IV where the maximum value is −0.52 μs at block II. From the results, we can conclude that the southwestern part of the study area is suffering from both extensional and compressional forces.

From the obtained dilatation results, we can conclude that the entire study area is suffering from both compressional and extensional dilatation forces. But the highest values are found in the southern part of the study area, especially in the southwestern part including Dahshour area.

Maximum Shear Strain

The shear strain defines the angular shape deformation of the object under stress (Beer and Johnston, 1992). **Figure 9B** (see **Supplementary Table S2**) shows the total amount of maximum shear strain in the Greater Cairo area during the period from 2005 to 2011. The area could be classified into two zones, the northeastern part represented by blocks III and IV where the shear strain rate is high, 0.3 μs, and the southwestern part represented by blocks I and II where the shear strain rate is high too, 0.26 μs (Fujii, 1995), but it is lower than that of the northeastern part.

The maximum shear result shows that significant values are to be found at the southern part of the study area, especially at the southwestern part including stations of WAHA, MESA, and PYRA.

CONCLUSIONS AND DISCUSSIONS

Dahshour zone has been blocked for geophysical investigation for quite a while since the 2011 uprising. The area has a historically important value, especially during the Fourth Dynasty. Significantly, the period of Sneferu witnesses a major evolution in the pyramid's structure. The Bent Pyramid was a milestone in this progressive development in pyramid architecture.

Four archeological sites (A, B, C, and D) near the Bent Pyramid were chosen to complete the archaeo-prospection survey. The micro-magnetic survey was conducted using the FM36 fluxgate gradiometer through a raster of progressive parallel traverses. The site areas and survey grids are as follows:

- Site A covers an area of 9600 m^2 (120 m × 80 m) and was surveyed using 0.5 station separation and 1 m traverse separation.
- Site B covers an area of 2400 m^2 (60 m × 40 m) and was surveyed using 0.5 station separation and 0.5 m traverse separation.
- Site C covers an area of 4800m^2 (120 × 40 m) and was surveyed using 0.5 station separation and 1 m traverse separation.
- Site D covers an area of 200 m^2 (10 m × 20 m) and was surveyed using 0.5 station separation and 0.5 m traverse separation.

GPR survey was conducted within sites B and C to confirm the nature of the observed magnetic anomalies. The GPR surveys were conducted in zigzag lines with 1 m separation between successive lines.

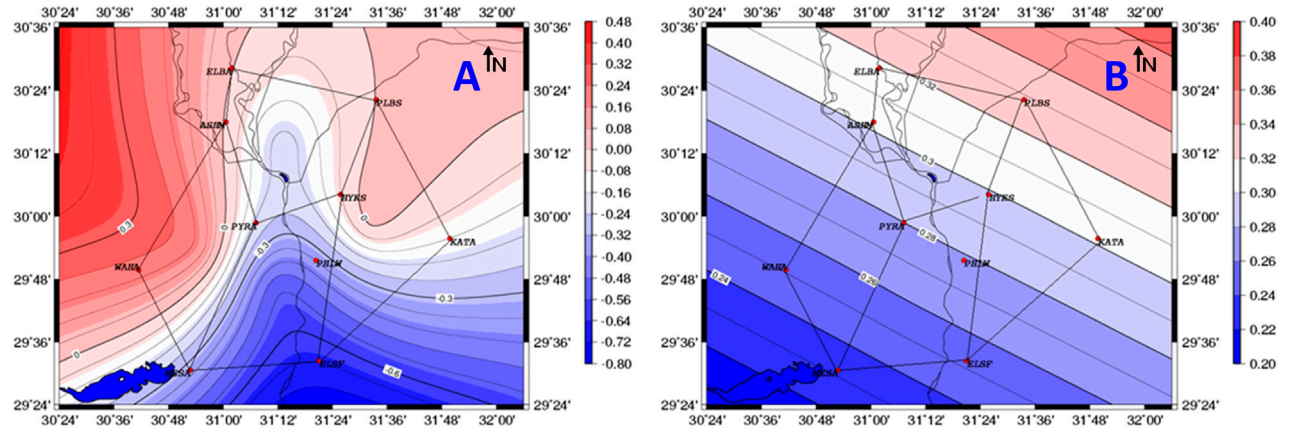

FIGURE 9 | (A) Dilatation rates of the study area from 2005 to 2011. **(B)** Maximum shear strain rates of the study area from 2005 to 2011.

The magnetic survey of Site A (**Figure 2**) reveals four interesting anomalies:

- S1: An elongated high-magnetic anomaly of about 100 m long and 5 m width. This is strongly proposed to be part of the causeway.
- S2: Scattered positive magnetic anomalies that cover an area of about 30 m × 20 m which is considerably large enough to resample some collapsed structure. This structure is not clear for deciding its archaeological origin.
- S3: Connected positive magnetic anomaly about 20 m long and is parallel to the valley temple wall. This feature may be a mud-brick wall.
- S4: Several dissected and ambiguous negative and positive anomalies with different shapes and sizes that are resampled in straight lines. However, the western edge of this anomaly is at a right angle to the detected feature S3.

We believe these features (S2, S3, and S4) could be the remains of a larger rectangular structure resample of another temple that was built in the same orientation as the existing valley temple. It seems that this mud structure was built even before the valley temple because the causeway is crossing it to the valley temple.

The geophysical survey at site B (**Figure 3A**, **5**) shows an archaeological structure that could be an extension of the causeway in the direction of the Nile Valley. The feature (**Figure 3A**) is resampled by scattered positive anomalies that are bounded by negative anomalies. The positive anomalies represent features made up of mud, and the negative anomalies may be due to limestone blocks. This could match the old structure of the causeways where the walking path (the wide part of the causeway) is made up of mud bricks and the side walls are made up of limestone bricks. This result was confirmed using the GPR survey (**Figure 5**).

The geophysical survey at site C (**Figures 3B**, **6**, **7**) shows some interesting features that could be attributed to the presence of an underground cavity structure that has been regularly filled with sediments. Some cavities are engraved in the natural ground (as appears from the GPR sections in **Figure 6**) in the form of shafts, and the others are built with mud bricks as they have a positive magnetic anomaly. However, deeper features that appear in the GPS sections (**Figure 7**) indicate the presence of burial chambers. We believe that this site contains a large grave cemetery that has its entrance located in the southern part of the site.

The magnetic survey of Site D (**Figure 4**) reveals three interesting anomalies. These anomalies may indicate the presence of buried mud-brick walls (positive anomalies) with an entrance that leads to an inner chamber (negative anomalies). These are typical for the excavated tombs built with mud brick and are situated close to this site, which may indicate the special structure of the zone.

Furthermore, a crustal deformation investigation was conducted to estimate the stresses and the expected strain on the detected features. The achieved results indicated that the southern and the southeastern sectors of the investigated area are currently accumulating strain, and this means that there is a possibility for future earthquakes to occur around this vital archaeological area. Meanwhile, buried structures are preserved by confinement in the burial materials like a large mold. However, external load or stress can still cause damage as the mold is considered to be of a soft material regarding the stress and load size.

The obtained dilatation and maximum shear strain results show that Dahshour area is suffering from compressional dilatation forces and has a high shear strain rate. The dilatation forces are directed from south to north. Therefore, it is highly recommended that excavation starts from the southern side of the detected features to reduce the soil stress on it and to avoid walls and soil collapse.

In conclusion, this study reveals the existence of a mud-brick structure that could be an older valley temple made up of mud bricks. It seems that they started building this temple from mud bricks, and then for some reason, they stopped and built the existing valley temple from limestone. This could be a normal act from Sneferu who was pursuing perfection and greatness. Therefore, excavation is recommended to reveal the true identity and the purpose of this structure. Further to the east, the survey confirms the existence of another causeway that led to the Nile Valley. Nevertheless, this is the first work to address the stress hazard before excavation with a detailed map of the expected features and their orientation with the stress direction.

DATA AVAILABILITY STATEMENT

The original contributions presented in the study are included in the article/**Supplementary Material**; further inquiries can be directed to the corresponding author.

AUTHOR CONTRIBUTIONS

All contributed in data acquisition, processing, interpretation, and writing the manuscript.

FUNDING

This work has been funded by the National Research Institute of Astronomy and Geophysics.

ACKNOWLEDGMENTS

The authors are appreciative to the National Research Institute of Astronomy and Geophysics (NRIAG, Egypt) for giving the Geoscan Gradiometer (FM36), the GPR (SIR-2000), and GPS instruments and other fundamental field equipment, vehicles, and field partners. The authors also thank the Egyptian Supreme Council of Antiquities for their consent to lead the fieldworks on Dahshour site and for the field inspectors who gave us the necessary archeological information. We would like to acknowledge the time and effort devoted by the reviewers to improving the quality of the manuscript. We appreciate the detailed and useful comments that we obtained from them.

SUPPLEMENTARY MATERIAL

The Supplementary Material for this article can be found online at: https://www.frontiersin.org/articles/10.3389/feart.2021.674953/full#supplementary-material

REFERENCES

Abbas, M.A., Atya, M., El Emam, A., Shaaban, F., Odah, H., and Lethy, A. (2011). Integrated Geophysical Studies to Image the Remains of Amenemht II Pyramid's Complex in Dahshour Necropolis, Giza, Egypt. *J. Pet. Min. Eng.* 14, 27–51.

Abdallatif, T. F., Mousa, S. E., and Elbassiony, A. (2003). Geophysical Investigation for Mapping the Archaeological Features at Qantir, Sharqyia, Egypt. *Archaeol. Prospect.* 10 (1), 27–42. doi:10.1002/arp.190

Abdallatif, T., El Emam, A. E., Suh, M., El Hemaly, I. A., Ghazala, H. H., Ibrahim, E. H., et al. (2010). Discovery of the Causeway and the Mortuary Temple of the Pyramid of Amenemhat II Using Near-Surface Magnetic Investigation, Dahshour, Giza, Egypt. *Geophys. Prospection* 58, 307–320. doi:10.1111/j.1365-2478.2009.00814.x

Abdallatif, T., Odah, H. H., El Emam, A. E., and Mohsen, A. (2019). Geomagnetism Exploration of the Egyptian Archaeology: Thirty-Years of Success and Challenges *Archaeogeophysics. Natural Science in Archaeology*. G. El-Qady and M. Metwaly Editors. Cham: Springer, 137–168. doi:10.1007/978-3-319-78861-6_7

Aitken, M. J., Webster, G., and Rees, A. (1958). Magnetic Prospecting. *Jour. Antiquity* 32, 270–271.

Annan, A. P., Coway, S. W., and Redman, J. D. (1991). "Water Table Detection with Ground Penetrating Radar," in 61st annual international meeting of the society of Exploration Geophysics (Houston, Texas: Society of Exploration Geophysics), 494–496. Expanded abstract.

Baines, J., and Malek, J. (1992). *Atlas of Ancient Egypt*. Oxford: Andromeda, 240.

Beer, F. P., and Johnston, E. R. (1992). *Mechanics of Materials*. 2nd edition. New York: McGraw-Hill.

Black, A. C., and Norton, W. W. (1993). *Blue Guide Egypt*. London: Bedford, 762.

Clark, A. J. (1986). Archaeological Geophysics in Britain. *Geophysics* 51, 1404–1413. doi:10.1190/1.1442189

Clark, A. J. (1990). *Seeing beneath the Soil Prospecting Methods in Archaeology*. London: Batsford Ltd, 176p.

Conyers, L. B., and Goodman, D. (1997). *Ground Penetrating Radar. An Introduction for Archaeologists*. Walnut Creek: Altamira Press.

Dach, R., Hugentobler, U., Fridez, P., and Meindl, M. (2007). in *Bernese GPS Software Version 5.0* (Bern: Astronomical Institute, University of Bern).

David, B., Collins, J., Barker, B., Flood, J., and Gunn, R. (1995). Archaeological Research in Wardaman Country, Northern Territory: The Lightning Brothers Project 1990-91 Field Seasons. *Aust. Archaeology* 41 (1), 1–8. doi:10.1080/03122417.1996.11681574

Davis, J. L., and Annan, A. P. (1989). Ground-penetrating Radar for High-Resolution Mapping of Soil and Rock Stratigraphy1. *Geophys. Prospect* 37 (5), 531–551. doi:10.1111/j.1365-2478.1989.tb02221.x

Dimitrios, G. A., Papanikolaou, X., Ganas, A., and Paradissis, D. (2018). StrainTool: A Software Package to Estimate Strain Tensor Parameters (Version v1.0-rc1.0). *Zenodo*. doi:10.5281/zenodo.1314151

Dixit, P., and Dixit, U. (2008). *Modeling of Metal Forming and Machining Processes*. London: Springer-Verlag London Limited.

Doolittle, J. A. (1993). *Characteristics and Monitoring the Vadose Zone with Ground Penetrating Radar: Technological Application*, 26-28. Columbus, Ohio, USA: October Ohio State University, 105–119.

Fujii, Y. (1995). Characteristics of Horizontal Crustal Deformation in Japan as Deduced from Frequency Distribution of Maximum Shear Strain Rate. *Pageoph* 144 (No. 1), 19–37. doi:10.1007/bf00876472

Geoscan Research (1987). *Instruction Manual Version 1.0 (Fluxgate Gradiometer FM9, FM18, FM36)*. Bradford, West Yorkshire, England: Geoscan Research.

Geoscan Research (2005). *Instruction Manual 1.01*. Bradford: Geoscan Research. (Geoplot 2.01).

Goodman, D., Nishimura, Y., and Rogers, J. D. (1995). GPR Time Slices in Archaeological prospect Ion. *Archaeological Prospection* 2, 85–89.

Goodman, D. (1994). Ground Penetrating Radar Simulation in Engineering and Archaeology. *Geophysics* 59 (No. 2), 224–232. doi:10.1190/1.1443584

Hashash, Y. M. A., Hook, J. J., Schmidt, B., and I-Chiang Yao, J. (2001). Seismic Design and Analysis of Underground Structures. *Tunnelling Underground Space Tech.* 16 (4), 247–293. doi:10.1016/s0886-7798(01)00051-7

Hill, J. (2020). *Dashur: Bent Pyramid of Sneferu"*. Jenny Hill. Ancient Egypt Online Retrieved. Available at: https://ancientegyptonline.co.uk/bent-pyramid-dashur/ (Accessed September 25, 2020).

Hounslow, M. W., and Chroston, P. N. (2002). Structural Layout of the Suburbs of Roman Butrint, Southern Albania: Results from a Gradiometer and Resistivity Survey. *Archaeol. Prospect.* 9, 229–242. doi:10.1002/arp.202

Hussein, H., M., Korrat, I., M., and Abd El-Fattah, A., K. (1996). *The October 12, 1992 Cairo Earthquake a Complex Multiple Shock*, 30. Japan: Bulletin of the International Institute of Seismology and Earthquake Engineering, 9–21.

Jena, R., Pradhan, B., Beydoun, G., Al-Amri, A., and Sofyan, H. (2020). Seismic hazard and Risk Assessment: a Review of State-Of-The-Art Traditional and GIS Models. *Arab J. Geosci.* 13, 50. doi:10.1007/s12517-019-5012-x

Leckebusch, J. r. (2000). Two- and Three-Dimensional Ground-Penetrating Radar Surveys across a Medieval Choir: a Case Study in Archaeology. *Archaeol. Prospect.* 7, 189–200. doi:10.1002/1099-0763(200009)7:3<189::aid-arp134>3.0.co;2-n

Mahmoud, S., M., Khalil, H., Sakr, K., O., and Rayan, A. (1996). "GPS Measurements at the Area Around Great Cairo and Southern Part of Delta, Egypt," in Proceedings of the Regional Symposium on Deformations and Crustal Movement Investigations using Geodetic Techniques, Aug. 31-Sep. 5, 1996 (Hungary: Szekesfehervar), 180–188.

Manataki, M., Sarris, A., Donati, J., Cuenca-García, C., and Kalayci, T. (2015). *GPR: Theory and Practice in Archaeological Prospection*. Oxford: Archaeopress. doi:10.13140/RG.2.1.3256.9363

Mekkawi, M., Arafa-Hamed, T., and Abdellatif, T. (2013). Detailed Magnetic Survey at Dahshour Archeological Sites Southwest Cairo, Egypt. *NRIAG J. Astron. Geophys.* 2, 175–183. doi:10.1016/j.nrjag.2013.06.020

Reynolds, J. M. (1997). *An Introduction to Applied and Environmental Geophysics*. Chichester: John Wiley and Sons Ltd.Inc, 796.

Sandmeier, K. J. (2016). *ReflexW Program for Processing of Seismic, Acoustic or Electromagnetic Reflection, Refraction and Transmission Data*. Karlsruhe, Germany: Software Manual.

Scollar, I., Tabbagh, T., hesse, A., and Herzog, I. (1990). *Archaeological Prospecting and Remote Sensing*. Cambridge: Cambridge University Press, 692p.

Shen, Z. K., Wang, M., Zeng, Y., and Wang, F. (2015). Optimal Interpolation of Spatially Discretized Geodetic Data. *Bull. Seismological Soc. America* 105 (4), 2117–2127. doi:10.1785/0120140247

Tomizawa, Y., Arai, I., Hirose, M., Suzuki, T., and Ohhashi, T. (2000). Archaeological Survey Using Pulse Compression Subsurface Radar. *Archaeol. Prospect.* 7, 241–247. doi:10.1002/1099-0763(200012)7:4<241::aid-arp140>3.0.co;2-2

Wu, H. (2005). *Continuum, Mechanics, and Plasticity*. Boca Raton, FL: Chapman & Hall/CRC.

Conflict of Interest: The authors declare that the research was conducted in the absence of any commercial or financial relationships that could be construed as a potential conflict of interest.

frontiers in Earth Science

ORIGINAL RESEARCH
published: 23 July 2021
doi: 10.3389/feart.2021.700873

Recovering Marine Gravity Over the Gulf of Guinea From Multi-Satellite Sea Surface Heights

*Richard Fiifi Annan and Xiaoyun Wan**

School of Land Science and Technology, China University of Geosciences (Beijing), Beijing, China

A regional gravity field product, comprising vertical deflections and gravity anomalies, of the Gulf of Guinea (15°W to 5°E, 4°S to 4°N) has been developed from sea surface heights (SSH) of five altimetry missions. Though the remove-restore technique was adopted, the deflections of the vertical were computed directly from the SSH without the influence of a global geopotential model. The north-component of vertical deflections was more accurate than the east-component by almost three times. Analysis of results showed each satellite can contribute almost equally in resolving the north-component. This is attributable to the nearly northern inclinations of the various satellites. However, Cryosat-2, Jason-1/GM, and SARAL/AltiKa contributed the most in resolving the east-component. We attribute this to the superior spatial resolution of Cryosat-2, the lower inclination of Jason-1/GM, and the high range accuracy of the Ka-band of SARAL/AltiKa. Weights of 0.687 and 0.313 were, respectively, assigned to the north and east components in order to minimize their non-uniform accuracy effect on the resultant gravity anomaly model. Histogram of computed gravity anomalies compared well with those from renowned models: DTU13, SIOv28, and EGM2008. It averagely deviates from the reference models by −0.33 mGal. Further assessment was done by comparing it with a quadratically adjusted shipborne free-air gravity anomalies. After some data cleaning, observations in shallow waters, as well as some ship tracks were still unreliable. By excluding the observations in shallow waters, the derived gravity field model compares well in ocean depths deeper than 2,000 m.

Keywords: sea surface heights, geoid gradients, vertical deflection, gravity anomaly, remove-restore technique, Gulf of Guinea

OPEN ACCESS

Edited by:
D. Sarah Stamps,
Virginia Tech, United States

Reviewed by:
Taoyong Jin,
Wuhan University, China
Shengjun Zhang,
Northeastern University, China

****Correspondence:***
Xiaoyun Wan
wanxy@cugb.edu.cn

Specialty section:
This article was submitted to Solid Earth Geophysics, a section of the journal Frontiers in Earth Science

Received: *27 April 2021*
Accepted: *14 July 2021*
Published: *23 July 2021*

Citation:
Annan RF and Wan X (2021) Recovering Marine Gravity Over the Gulf of Guinea From Multi-Satellite Sea Surface Heights. Front. Earth Sci. 9:700873. doi: 10.3389/feart.2021.700873

INTRODUCTION

The advancements in satellite altimetry since the past 4 decades has led to the proliferation of sea surface height (SSH) data which has contributed significantly to geodesy, geophysics, oceanography, and hydrology. Some of its applications include: sea level variation research (Cazenave et al., 2014; Ablain et al., 2015; Watson et al., 2015; Passaro et al., 2018), determination of mean dynamic topography (MDT) and mean sea surface (Andersen et al., 2016; Ophaug et al., 2021), construction of marine geoid (Dadzie and Li, 2007; Chander and Majumdar, 2016), monitoring of lakes and rivers (Villadsen et al., 2015; Zakharova et al., 2019) and inversion of marine gravity field (Sandwell et al., 2013; Sandwell et al., 2014; Zhu et al., 2019; Nguyen et al., 2020; Wan et al., 2020b).

Marine gravity anomaly is an important geophysical quantity with applications in marine resources exploration and exploitation (Becker et al., 2009), geoid modeling (Olgiati et al., 1995;

Hwang, 1998; Soltanpour et al., 2007), delimitation of continent–ocean boundaries (Sandwell et al., 2013), revelation of submarine tectonic structures (Hwang and Chang, 2014; Sandwell et al., 2014; Wan et al., 2020a), and bathymetry augmentation (Hwang, 1999). Marine gravity anomaly can be inverted from geoid heights after SSH is reduced to geoid by the removal of dynamic sea surface topography (Olgiati et al., 1995; Andersen et al., 2010; Nguyen et al., 2020). It can also be derived from the deflection of the vertical, whereby the geoid heights are differenced along satellite orbits to obtain geoid gradients. The along-track geoid gradients are then converted to vertical deflections. This along-track differentiation has the advantage of reducing the impact of long wavelength errors (Hwang et al., 2002; Zhu et al., 2019). Also, the vertical deflections approach does not require crossover adjustment (Hwang et al., 2002).

Since marine surface phenomena mostly have submarine origins, with these submarine activities best revealed through gravity anomalies, it is imperative to derive accurate marine gravity models to aid in understanding marine phenomena. Since the past decade, there have been an increase in the quantity and quality of altimetry data, as well as superior computing hardware. This has led to various researchers to develop gravity field models for their respective countries and economic blocs. For instance: over the South China Sea, Zhang et al. (2017) and Zhu et al. (2020) separately developed $1' \times 1'$ marine gravity models by amalgamating multi-satellite SSH data; Nguyen et al. (2020) merged gravity anomaly derived from Cryosat-2 and Saral/AltiKa SSH datasets with shipborne gravity data over the Gulf of Tonkin area of Vietnam. A recent study by Sandwell et al. (2013) has shown that gravity field models derived from modern altimeter satellites are more accurate than those obtained from some governmental shipborne gravity data. This shows the usefulness of satellite-derived gravity models in filling the gaps between tracks of shipborne gravimetry. It must be appreciated that though gravimetry via ships is still reliable, it is expensive, slow and mostly limited to the maritime waters of developed countries. Therefore, SSH datasets from altimetry satellites are the best and cheapest option for developing regions like West Africa.

It is expected that the development of the study region synchronizes with scientific investigations of its largest natural resource (the ocean); however, this is yet to be realised. Even though the region is oil-rich (Osaretin, 2011; Bazilian et al., 2013), the scantiness of reviewed literatures about the maritime waters of West Africa shows that the region's maritime waters is one of the least studied. The study area encompasses 15°W to 5°E, and 4°S to 4°N. Countries of interest include Guinea and Guinea Bissau at the western end, through to the central-south African country of The Congo.

The present study aims to study the gravity field of the region by using vertical deflections derived from the geodetic missions (GM) of Jason-1, Saral/AltiKa, Haiyang-2A; Cryosat-2, and Envisat. We achieve this objective through the remove-restore procedure using EGM2008 as the reference gravity filed model. The use of EGM2008 is due to the fact that it is the most frequently used global geopotential model for marine geodetic and geophysical research (Andersen et al., 2010; Sandwell et al., 2014; Zhang et al., 2017; Andersen and Knudsen, 2019; Zhu et al., 2019; Zhu et al., 2020).

TABLE 1 | Selection criteria for SSH computation.

Parameter	Constraint
Dry tropospheric correction (m)	−2.5 ~ −1.9
Wet tropospheric correction (m)	−0.5 ~ 0.001
Ionospheric correction (m)	−0.1 ~ 0.04
Sea state bias correction (m)	−0.5 ~ 0
Ocean tide correction (m)	−5 ~ 5
Solid earth tide correction (m)	−1 ~ 1
Pole tide correction (m)	−0.15 ~ 0.15
Inverse barometer correction (m)	−2 ~ 2
SSH (m)	−130 ~ 100
No. valid points to compute the range	Greater than 20
RMS of the range (m)	0 ~ 0.2
Significant wave height (m)	0 ~ 11
Backscatter coefficient (dB)	3 ~ 30
Wind speed (m/s)	0 ~ 30
Waveform-derived square of off nadir angle (deg^2)	−0.2 ~ 0.64
No. valid points to compute the backscatter coefficient	Greater than 20
RMS of the backscatter coefficient (dB)	0 ~ 1

MATERIALS AND METHODS

Altimetry Data

The altimetry datasets used in this research comprises GDR (geophysical data record) of eight cycles of Jason-1/GM, seven cycles of Saral/AltiKa, five cycles of Envisat, five cycles of Cryosat-2, and IGDR (interim geophysical data record) of seven cycles of HY-2A/GM. The Jason-1 GDRs were obtained from the Physical Oceanography Distributed Active Archive Center, Jet Propulsion Laboratory, NASA (https://podaac.jpl.nasa.gov/JASON1?sections=data). Saral/AltiKa GDRs were obtained from AVISO (https://www.aviso.altimetry.fr/), Envisat and Cryosat-2 GDRs were provided by the European Space Agency (http://earth.esa.int); while HY-2A GDRs were provided by the National Satellite Ocean Administration Service of China (ftp2.nsoas.org.cn). Along-track SSH is computed from each cycle as given by **Eq. 1**. **Table 1** is a summary of the various selection criteria applied to each satellite's dataset during SSH computation. **Figure 1** shows the spatial distribution of ground tracks of the different satellites.

$$SSH = altitude - range + corrections \tag{1}$$

where

$$corrections = \left\{ \begin{array}{l} wet\ troposphere\ correction + dry\ troposphere\ correction + \\ ionosphere\ correction + sea\ state\ bias\ correction + \\ pole\ tide\ correction + ocean\ tide\ correction + \\ solid\ earth\ tide\ correction + inverse\ barometric\ correction \end{array} \right\}$$

Reference Gravity Field

In implementing the remove-restore procedure, a global geopotential model (otherwise known as reference gravity

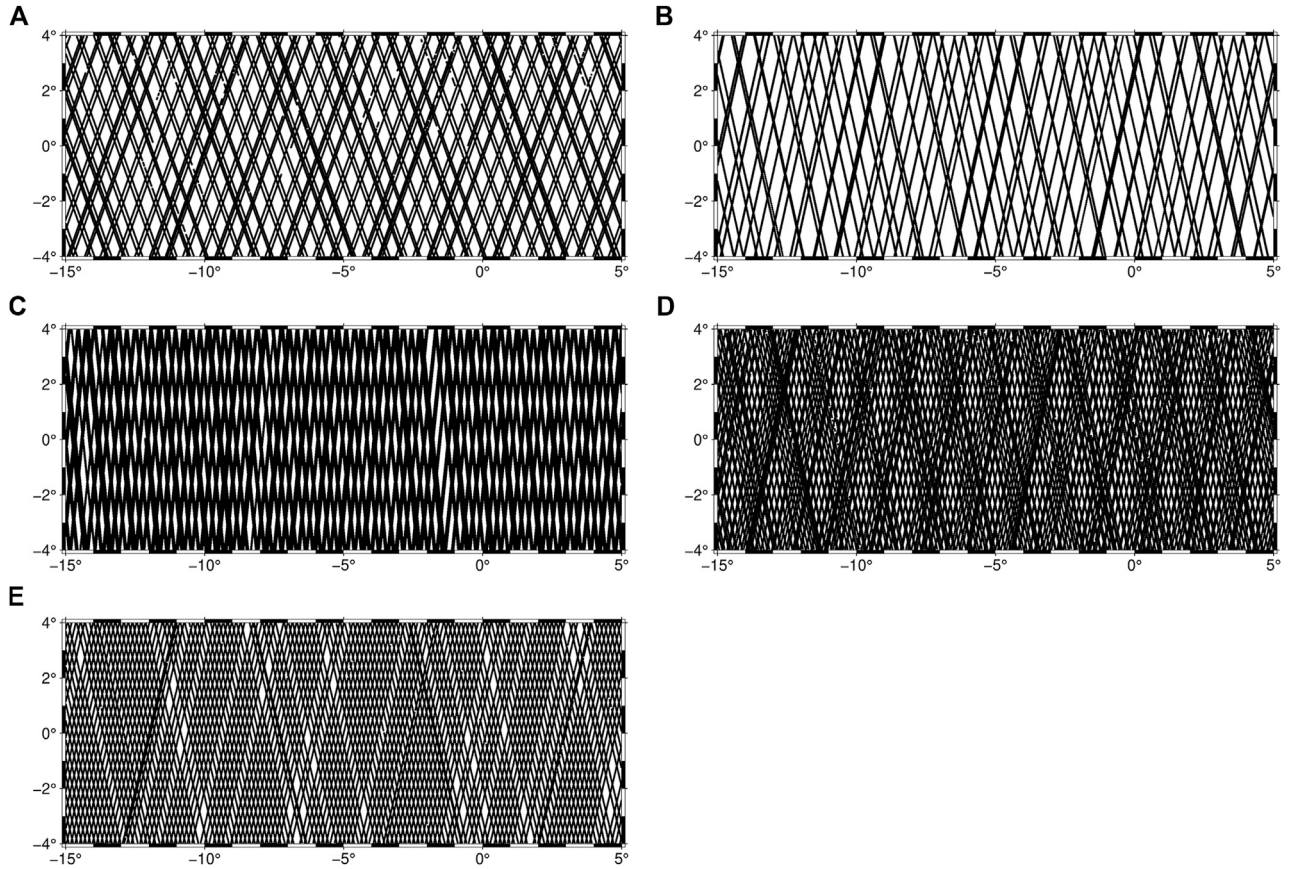

FIGURE 1 | Ground tracks of **(A)** Jason-1/GM, **(B)** Envisat, **(C)** Cryosat-2, **(D)** SARAL/AltiKa, and **(E)** HY-2A/GM.

field) is required. The reference gravity field of one quantity (which in this case is deflections of the vertical) is removed from its corresponding observed deflections of the vertical to obtain residual deflections of the vertical. The residual deflections of the vertical are then used to construct the residual gravity anomalies. Full gravity anomalies are later obtained by restoring the removed reference gravity field (now in the form of gravity anomalies). The removal of the reference gravity field ensures a more statistically homogeneous and smoother model. Also, it has the effect of ensuring that the gravity field outside the data extent is accounted for (Andersen, 2013). EGM2008 is expressed as coefficients of spherical harmonics and has a maximum degree of 2,190 (Pavlis et al., 2012). It was obtained from the International Centre for Global Earth Models (http://icgem.gfz-potsdam.de/).

Dynamic Topography

In the computation of gravity anomalies, the SSH data must initially be reduced to geoid heights. To achieve this, the time-dependent topography of the surface of the sea must be removed. It is well known that the geoid is linearly related to the mean sea surface through the mean dynamic topography (MDT) of the ocean surface. Therefore, to compute the geoid heights, this research used the mean dynamic topography DTU15MDT, obtained from the Technical University of Denmark. It is a product derived from EIGEN-6C4 and DTU15MSS mean sea surface model (Knudsen et al., 2016). The time-independent sea surface topography was removed through filtering similar to the method of Hwang et al. (2002).

Computation of Gravity Anomalies

The SSH_i at a point, i, computed from **Eq. 1** is transformed into geoid height, N_i, as given by **Eq. 2**:

$$N_i = SSH_i - MDT_i. \tag{2}$$

Geoid gradients, β_{ij}, between two consecutive points i and j along the satellite's ground track are then calculated by:

$$\beta_{ij} = \frac{N_j - N_i}{D_{ij}}, \tag{3}$$

where D_{ij} is the spherical distance between the two points i and j. For each geoid gradient, β_{ij}, its corresponding azimuth, α_{ij}, is also computed. To obtain the vertical deflections, the along-track geoid gradients and azimuths are gridded using biharmonic spline with a tension of 0.25. The biharmonic spline in tension was executed using the *surface* module of GMT (Generic Mapping Tools). The north-component, ξ, and

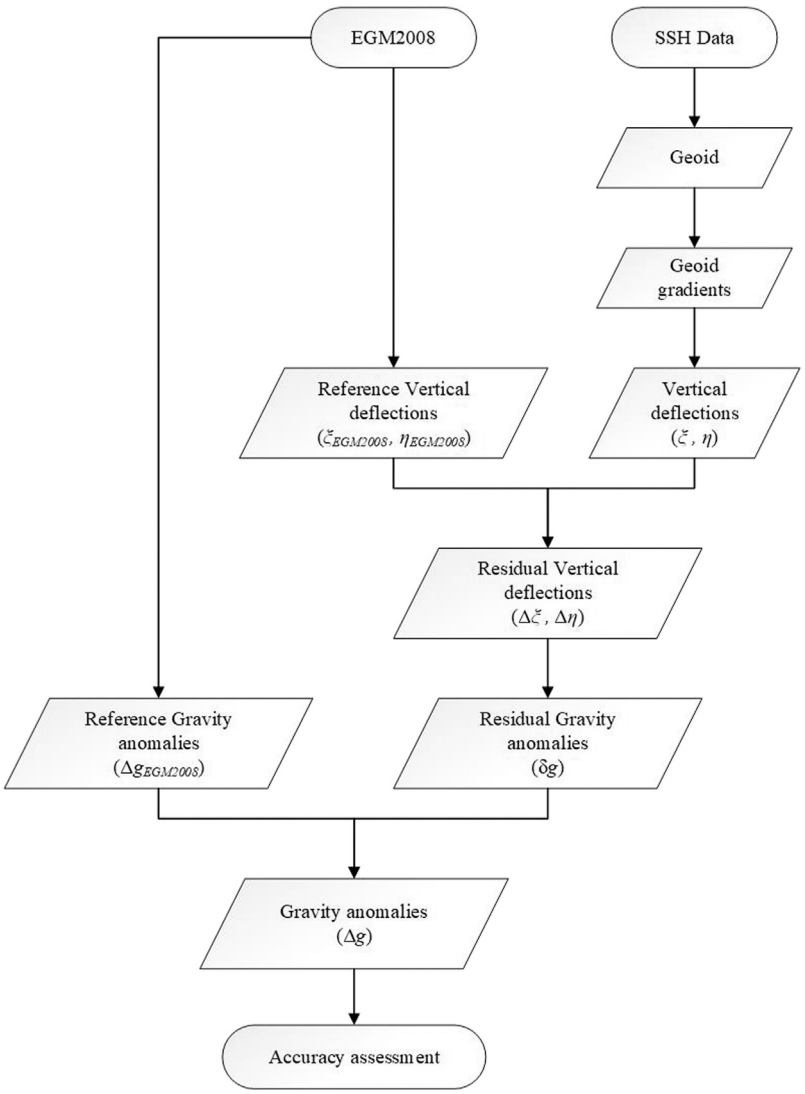

FIGURE 2 | Remove-restore technique used.

east-component, η, of the along-track deflections of the vertical are obtained by setting up a system of equations with several points in a small cell (Hwang et al., 2002), as given by **Eq. 4**:

$$\beta_k + v_k = \xi_k \cos\alpha_k + \eta_k \sin\alpha_k \qquad k = 1, 2, ..., n, \tag{4}$$

where v_k is the model error.

With reference to the remove-restore technique described in **Figure 2**, the computed components of deflections of the vertical are reduced to their residual version by subtracting EGM2008-simulated deflection components from them. The reference vertical deflections were simulated at the maximum degree/order of 2,190.

$$\left.\begin{aligned}\Delta\xi &= \xi - \xi_{EGM2008}\\ \Delta\eta &= \eta - \eta_{EGM2008}\end{aligned}\right\} \tag{5}$$

where $\Delta\xi$ and $\Delta\eta$ are, respectively, north-component and east-components of residual vertical deflections; $\xi_{EGM2008}$ and $\eta_{EGM2008}$ are the EGM2008-simulated north- and east-components of vertical deflections, respectively. The residual vertical deflection components are then used to invert residual gravity anomaly, δg, through Fourier transform as expressed in **Eq. 6**:

$$\delta g = -\frac{i\overline{\gamma}}{\sqrt{u^2 + v^2}} F^{-1}\{v\Delta X(u, v) + u\Delta E(u, v)\}, \tag{6}$$

where F^{-1} is the inverse Fourier transform, $\overline{\gamma}$ is mean value of gravity, u and v are the spatial frequencies. ΔX and ΔE are, respectively, the Fourier transforms of $\Delta\xi$ and $\Delta\eta$. Finally, using the remove-restore procedure, long wavelength gravity anomaly, $\Delta g_{EGM2008}$, from the reference gravity field at degree/order 2,190 is restored to the residual gravity

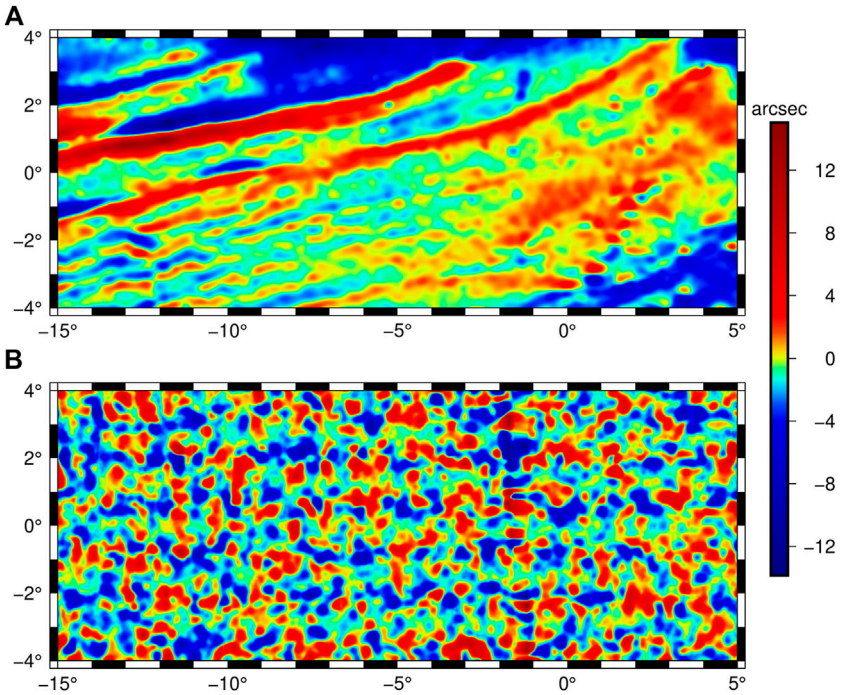

FIGURE 3 | Computed vertical deflections: **(A)** North component, **(B)** East component.

anomaly, δg, to recover the gravity anomaly, Δg. This is simply given as:

$$\Delta g = \delta g + \Delta g_{EGM2008} \tag{7}$$

Reviewed literatures have shown that for most altimetry-derived deflections of the vertical, the north component is often times more accurate than the east component. This is attributable to the inclinations of the satellites which usually are towards the north. The effect of this accuracy imbalance propagates to the resultant gravity anomalies derived from the deflections of the vertical (Small and Sandwell, 1992; Zhang, 2017; Wan et al., 2020b). In order to nullify this effect on the derived gravity anomaly model, weights are assigned to the vertical deflection components based on the covariance between them, and their error variances relative to the reference gravity field model. The residual gravity anomaly is derived from each component, δg_ξ and δg_η as (Small and Sandwell, 1992; Hwang and Parsons, 1996):

$$\left.\begin{aligned} \delta g_\xi &= -\frac{i\gamma}{\sqrt{u^2+v^2}} F^{-1}[v.\Delta X(u,v)], \\ \delta g_\eta &= -\frac{i\gamma}{\sqrt{u^2+v^2}} F^{-1}[u.\Delta E(u,v)] \end{aligned}\right\} \tag{8}$$

Using the constraints described in **Eq. 9**, the weights, w_ξ and w_η are computed as given by **Eq. 10** (Wan et al., 2020b):

$$\left.\begin{aligned} \delta g &= w_\xi \delta g_\xi + w_\eta \delta g_\eta \\ w_\xi &+ w_\eta = 1 \\ f_{\min} &= \min\left(w_\xi^2 \delta_{\Delta\xi}^2 + w_\eta^2 \delta_{\Delta\eta}^2 + 2 w_\xi w_\eta \delta_{\Delta\xi\Delta\eta}^2\right) \end{aligned}\right\} \tag{9}$$

$$\left.\begin{aligned} w_\xi &= \frac{\delta_{\Delta\eta}^2 - \delta_{\Delta\xi\Delta\eta}^2}{\delta_{\Delta\xi}^2 + \delta_{\Delta\eta}^2 - 2\delta_{\Delta\xi\Delta\eta}^2} \\ w_\eta &= \frac{\delta_{\Delta\xi}^2 - \delta_{\Delta\xi\Delta\eta}^2}{\delta_{\Delta\xi}^2 + \delta_{\Delta\eta}^2 - 2\delta_{\Delta\xi\Delta\eta}^2} \end{aligned}\right\} \tag{10}$$

where $\delta_{\Delta\xi}^2$ and $\delta_{\Delta\eta}^2$ are the corresponding error variances of $\Delta\xi$ and $\Delta\eta$, respectively; and $\delta_{\Delta\xi\Delta\eta}^2$ is the covariance between $\Delta\xi$ and $\Delta\eta$.

RESULTS

The computed vertical deflection components are shown as **Figure 3**. They were validated by comparing them with simulated components from EGM2008 at maximum degree/order 2,190. The result of this comparison is summarized in **Table 2**. With regard to standard deviation of differences, it can be seen from **Table 2** that the accuracy of the north component is slightly better than the east component by almost three times. A visual inspection shows that, in general, the positive deflections of the north component (**Figure 3A**) have a SW/NE orientation, whereas there is no distinct orientation in the east component (**Figure 3B**).

With reference to **Eqs. 8–10**, **Table 3** is a compilation of the vertical deflection components' error variances, covariance and their respective weights used for the construction of the residual gravity anomaly. The constructed gravity anomaly model is shown in **Figure 4**. It compares well with gravity anomalies from EGM2008, DTU13 (obtained from the Technical University of Denmark) and SIOv28 (obtained from Scripps Institution of

TABLE 2 | Summary statistics of vertical deflection components compared with EGM2008-simulated components (unit: arcsecond).

Statistic of difference	North-component	East-component
Minimum	−2.82	−8.58
Maximum	2.95	8.30
Mean	0.06	−0.09
Standard deviation	0.96	2.81

TABLE 3 | Variances, covariance and weights of vertical deflection components.

Statistic	Component	Value
Variance	$\delta^2_{\Delta\xi}$	2.888
	$\delta^2_{\Delta\eta}$	6.858
Covariance	$\delta^2_{\Delta\xi\Delta\eta}$	−0.426
Weights	w_ξ	0.687
	w_η	0.313

Oceanography) used as reference models. A summary of this comparison is presented in **Table 4**. **Figure 5** shows similar histograms of gravity anomalies for the inverted model and the reference models; this is an attestation of high accuracy of the derived gravity anomalies. **Figure 6** is a visual analysis of differences between the inverted gravity anomaly model and the reference models; this is a further attestation of the results presented in **Table 4**. On average, the model deviates from the reference models by −0.33 mGal. Further analysis of the histogram indicated that more than approximately 50% of gravity anomalies in the study region falls within the range of −80–80 mGal.

DISCUSSION

Comparing Derived Gravity Anomaly Model With Shipborne Gravimetry

The accuracy of the constructed gravity anomaly model is further analyzed by comparing it with gravity anomalies observed along tracks of ship cruises obtained from National Centers for Environmental Information of the National Oceanic and Atmospheric Administration (https://maps.ngdc.noaa.gov/viewers/geophysics/). However, the shipborne gravity data has the disadvantage of being very heterogenous with some erroneous observations made at some points. Some sources of these errors are: the absence of a uniform reference field at the time of measurement, drifting of the gravimeters, absence of base stations for references, etc. (Wessel and Watts, 1988). Therefore, in degree to amalgamate the shipborne gravity anomalies to a common reference, gravity anomalies simulated from EGM2008 were used as reference. With the exception of track RC1312, a second-degree polynomial model is then used to adjust the shipborne gravity anomalies. Track RC1312 was well adjusted by a first-degree polynomial. The adjustment model, given as **Eq. 11**, is applied separately on each ship track of observations.

$$\left.\begin{aligned} \widehat{\Delta g} &= \theta_0 + \theta_1 \Delta t + \theta_2 \Delta t^2 \\ \widehat{\Delta g} &= \Delta g_{ship} - \Delta g_{EGM2008} \\ \Delta t &= \Delta t_{observe} - \Delta t_{depart} \end{aligned}\right\} \tag{11}$$

where $\widehat{\Delta g}$ is the difference between shipborne, Δg_{ship}, and EGM2008-simulated, $\Delta g_{EGM2008}$, gravity anomalies; Δt is the difference between observation time, $\Delta t_{observe}$, and time of ship's departure, Δt_{depart}. The unknown parameters to be solved are θ_0, θ_1, and θ_2.

The adjusted shipborne gravity anomalies are presented in **Figure 7**. From **Figure 7**, it can be seen that the northern half of the study region generally has lower gravity anomalies. Higher values can be observed at the southern part, especially in the south-west. The middle section has anomalies ranging approximately from −60 to 45 mGal. These observations generally agree with observations made from the constructed gravity model presented in **Figure 4**.

For each ship track, statistical summary analysis of the differences between the shipborne anomalies and modelled anomalies is computed; the results are given in **Table 5**. A total of 288 points were discarded due to their difference

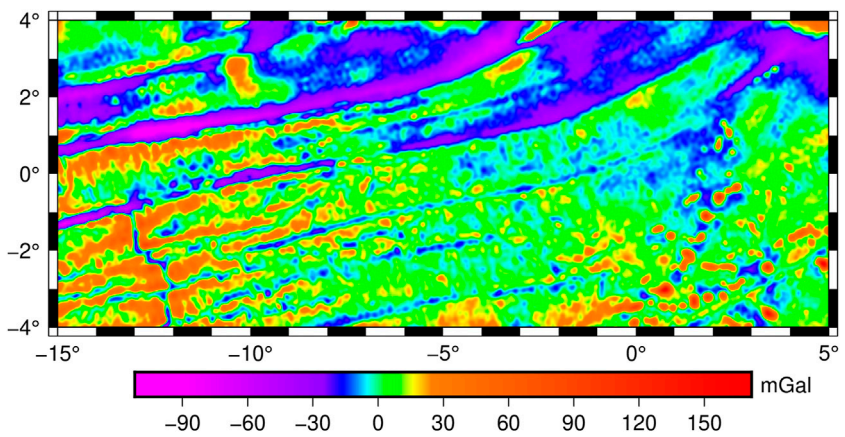

FIGURE 4 | Inverted gravity anomaly model.

TABLE 4 | Comparing modelled gravity anomaly with reference models.

Statistic of difference	Model−EGM2008	Model−DTU13	Model−SIO
Minimum (mGal)	−15.99	−16.59	−16.64
Maximum (mGal)	15.08	15.66	16.03
Mean (mGal)	−0.37	−0.37	−0.25
Std. Deviation (mGal)	5.18	5.38	5.44
Corr. Coefficient (%)	96.16	95.86	95.75

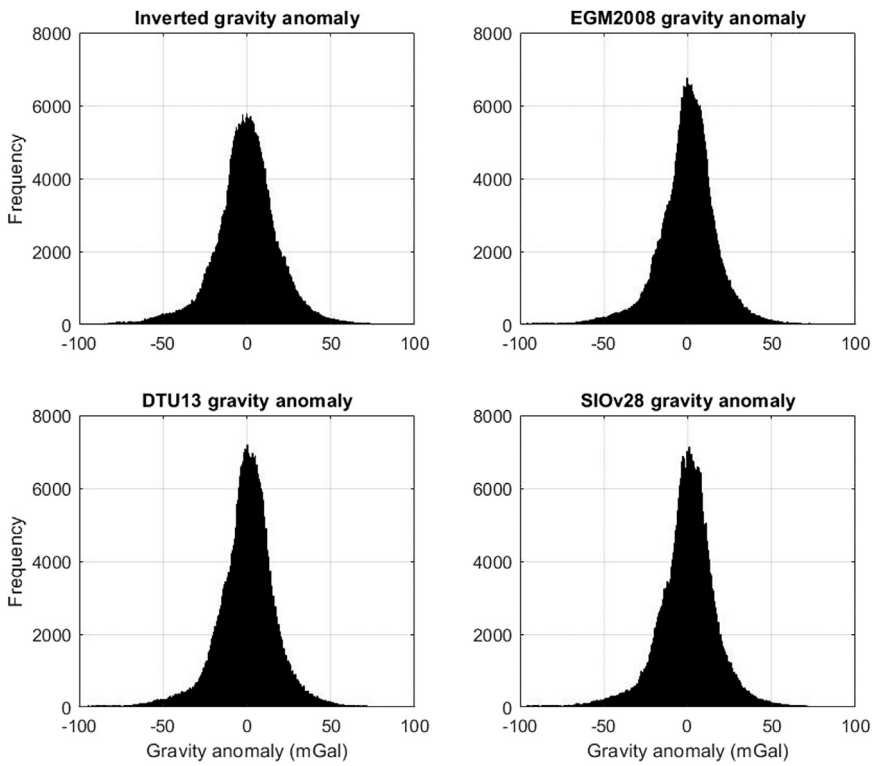

FIGURE 5 | Comparing histograms of gravity anomaly models over the study region.

exceeding three times the standard deviation. Tracks that have relatively high standard deviations are: 88000811, CD5591, and V2604, with standard deviations of 8.50, 8.52, and 9.22 mGal, respectively. With regard to the error standard deviations, the most precise track is RC2602, it compared with the modelled gravity anomalies and yielded a standard deviation of 2.15 mGal. Without considering the mean errors, which denote the systematic errors, for major tracks of shipborne gravimetry, the standard deviations of the differences between the shipborne observations and the modelled gravity anomalies are smaller than 5.5 mGal. The ratios of the tracks with standard deviations smaller than 5.5 mGal and 6.0 mGal are about 71.4 and 78.6%, respectively. This index is close to the results of **Table 4**. Furthermore, from **Table 5**, it must be appreciated that the adjustment was done using EGM2008 as true values; therefore, the standard deviations of differences between the adjusted shipborne and EGM2008 gravity anomalies are virtually negligible. However, the magnitudes of the mean differences range within 1–20 mGal, which indicates the contribution from altimetry observations.

In order to analyze the systematic errors depicted by the large mean errors in **Table 5**, the accuracy of gravity anomalies is assessed with respect to varying ocean depth. **Table 6** is a summary of this analysis. The gravity anomalies are more accurate at depths deeper than 2,000 m. The mean deviation is approximately 5.09 mGal, which signifies the existence of some systematic errors. Therefore, in order to nullify the effects of these errors, observations whose deviation exceeded the mean deviation of the entire dataset were removed. This resulted in removal of values in shallow depths (depth range of 1,001–2,000 m), with the new results compiled in **Table 7**. It is obvious from **Table 7** that the mean and standard deviation of differences escalate in shallow waters (i.e., in depth range of 1,001 ~ 2,000 m). This shows that observations in shallow waters (depths > 2,000 m) were the main source of systematic differences.

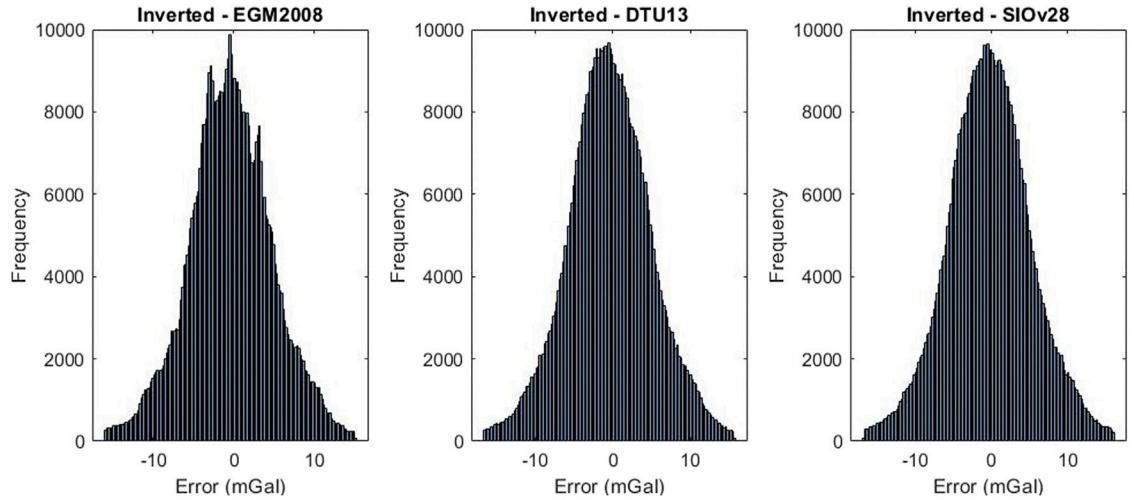

FIGURE 6 | Histograms of gravity anomaly deviations from reference models.

Analyzing each satellite's contribution in constructing the gravity anomaly model

In order to investigate the contribution of each satellite in the gravity field construction, the north, ξ_i, and east, η_j, components of deflections of the vertical were computed for each satellite. Summary of each satellite's contribution in establishing the integrated model, (ξ, η), is shown in **Table 8**. This was achieved by uniformly generating two sets of random numbers (each set contains five elements). The elements of each set are normalized so that their sum equates to one. These normalized values are now used as weights, w, applied to the satellite's vertical deflections as given in **Eq. 12**. The randomization process was repeated 100 times for each of the two sets; and for each iteration, normalization was performed correspondingly. Using the deflections of integrated model as true values, the set of weights that minimizes the standard deviation of errors was then chosen.

$$\left.\begin{aligned} w_i\xi_i + \ldots + w_5\xi_5 &= \overline{w}_i\xi \\ w_j\eta_j + \ldots + w_5\eta_5 &= \overline{w}_j\eta \\ w_i + \ldots + w_5 = \overline{w}_i = 1 \; i &= 1, 2, \ldots, 5 \\ w_j + \ldots + w_5 = \overline{w}_j = 1 \; j &= 1, 2, \ldots, 5 \end{aligned}\right\} \tag{12}$$

It can be seen from **Table 8** that SARAL/AltiKa contributed ~25% in resolving the north component. This can be attributed to the range accuracy of its Ka-band signal. It is also possible that its good drifting phase spatial resolution (Verron et al., 2021) could be a factor, though this is sometimes lower than that of Cryosat-2. Approximately, 19% proportion of north component was realized from each of HY-2A/GM, Cryosat-2, and Envisat. This can be attributed to the geodetic spatial resolutions of these satellites, except for Cryosat-2 and Envisat which are not geodetic. Even though the datasets from Jason-1/GM are also geodetic, it contributed the lowest north component due to its lower spatial resolution. Jason-1/

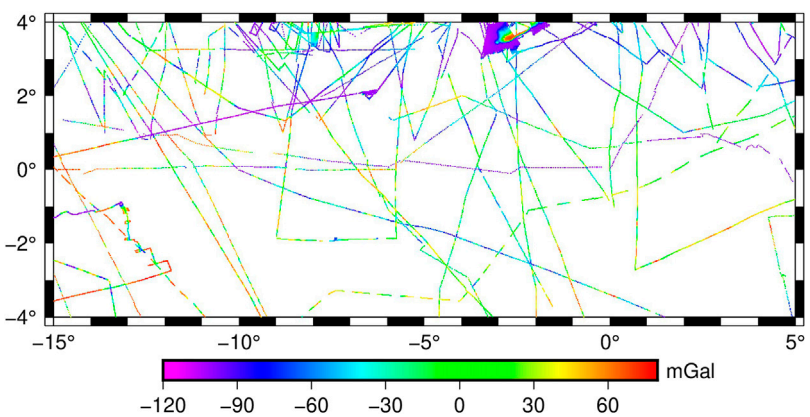

FIGURE 7 | Shipborne gravity anomalies over the study region.

TABLE 5 | Accuracy assessment of modelled gravity anomalies per track of shipborne gravimetry (unit: mGal).

Survey ID	Adj. Shipborne−EGM2008		Adj. Shipborne−Inverted		Survey ID	Adj. Shipborne−EGM2008		Adj. Shipborne−Inverted	
	Mean	Std. Dev	Mean	Std. Dev		Mean	Std. Dev	Mean	Std. Dev
71003311	6.972	0.002	4.072	5.518	RC1312	17.174	0.002	16.901	5.348
71003711	10.541	0.041	11.578	5.469	RC1702	3.895	0.001	2.865	3.270
88000711	3.787	0.001	3.860	5.060	RC1703	2.489	0.001	3.487	4.737
88000811	3.041	0.002	7.476	8.503	RC2602	18.297	0.001	26.353	2.150
A2067L02	1.358	0.002	0.777	4.933	RC2806	−8.005	0.003	−3.677	4.484
A2075L02	1.058	0.002	1.857	4.610	U571AF	4.269	0.056	5.400	2.190
A2075L03	2.551	0.012	1.993	4.480	V1912	17.273	0.031	15.277	4.461
A2075L04	3.969	0.002	5.125	6.194	V1913	12.332	0.001	11.192	2.270
AKU20	5.926	0.001	15.859	2.798	V2604	−4.408	0.001	−2.533	9.225
AKU28	49.555	0.020	47.924	3.516	V2712	4.741	0.002	5.151	4.950
CD5591	0.621	0.010	5.733	8.518	V2713	5.169	0.007	4.676	6.030
CH115L02	−1.186	0.002	−1.750	5.340	V2907	1.432	0.001	1.396	4.992
KIR1	2.492	0.002	0.887	3.532	V2908	6.482	0.002	4.203	4.160
RC1311	23.146	0.002	21.992	4.954	V3620	19.106	0.005	19.976	2.930

TABLE 6 | Initial accuracy assessment of modelled gravity anomalies with respect to change in ocean depth.

Range of depth (m)	Error range (mGal)	Mean error (mGal)	Std. Deviation of error (mGal)
−1,001 ~ −2,000	−6.07 ~ 46.13	32.37	13.71
−2001 ~ −3,000	−6.98 ~ 26.97	5.74	7.52
−3,001 ~ −4,000	−23.44 ~ 29.78	4.63	9.10
−4,001 ~ −5,000	−25.50 ~ 32.98	5.13	8.75
−5,001 ~ −6,000	−21.32 ~ 42.00	4.87	7.91

TABLE 7 | Improved accuracy assessment of modelled gravity anomalies with respect to change in ocean depth.

Range of depth (m)	Error range (mGal)	Mean error (mGal)	Std. Deviation of error (mGal)
−2,001 ~ −3,000	−6.9811 ~ 5.0888	−0.7609	2.8772
−3,001 ~ −4,000	−12.7752 ~ 5.0881	−1.5134	3.2243
−4,001 ~ −5,000	−14.4302 ~ 5.0885	−0.3484	4.3806
−5,001 ~ −6,000	−11.1749 ~ 5.0895	0.7098	3.0266

TABLE 8 | Contribution of each satellite in establishing the deflections of the vertical.

Satellite	Inclination (deg)	Spatial resolution at the equator (km)	North-component	East-component
			Weight	Weight
Jason-1/GM	66	7.5	0.1618	0.2804
SARAL/AltiKa	98.55	1 ~ 15	0.2486	0.2414
HY-2A/GM	99.3	8.7	0.1997	0.0643
Cryosat-2	92	7.5	0.1981	0.3373
Envisat	98.52	51	0.1918	0.0765

GM's lower contribution in resolving the north component could also be attributed to its inclination of only 66°. On the other hand, due to this low inclination of 66°, Jason-1/GM contributed ~28% of the east components, which is higher than that of SARAL/AltiKa. It was only surpassed by Cryosat-2 with ~34%, which has one of the best spatial resolutions amongst altimetry satellite missions. For Cryosat-2, since it resolved more deflections in east component than north component, it seems that the effect of spatial resolution is larger than the inclination.

CONCLUSION

A regional gravity anomaly model of the Gulf of Guinea has been constructed through the remove-restore method. It was constructed from deflections of the vertical derived from five different altimetry missions. The north-component of vertical deflections was more accurate than the east-component by almost three times. Analysis of the vertical deflections (**Table 8**) revealed that, on average, SSH data from each satellite can contribute almost equally in resolving the north component. However, Cryosat-2, Jason-1/GM, and SARAL/AltiKa were the dominant contributors of the east component. The gravity anomaly model was constructed by assigning weights of 0.687 and 0.313 to the north and east components, respectively. A comparison of histograms (refer to **Figure 5**) of the computed gravity anomaly model with renowned models from EGM2008, SIOv28, and DTU13 showed similar results. The computed gravity anomaly averagely deviated from these reference models by −0.33 mGal. Further assessment was done by comparing it with quadratically adjusted shipborne free-air gravity anomalies. By excluding observations in shallow waters, the derived gravity field model compares well in depths deeper than 2,000 m.

DATA AVAILABILITY STATEMENT

The original contributions presented in the study are included in the article/supplementary material, further inquiries can be directed to the corresponding author.

AUTHOR CONTRIBUTIONS

Conceptualization, RA; methodology, both authors; data curation, both authors; funding acquisition, XW; formal analysis, RA; investigation, both authors; writing—original draft preparation, RA; writing—review and editing, both authors.

FUNDING

This research was funded by the National Natural Science Foundation of China (Nos. 42074017, 41674026); Fundamental Research Funds for the Central Universities (No. 2652018027); Open Research Fund of Qian Xuesen Laboratory of Space Technology, CAST (No. GZZKFJJ2020006); China Geological Survey (No. 20191006).

ACKNOWLEDGMENTS

The authors are grateful to ESA for providing GDRs of Envisat and Cryosat-2. We are appreciative to NASA/JPL and AVISO for providing GDRs of Jason-1/GM and SARAL/AltiKa, respectively. We thank the National Satellite Ocean Application Service of China for providing HY-2A/GM data. We are appreciative to DTU for providing DTU13, as well as SIO for providing SIOv28. We acknowledge the use GMT (Generic Mapping Tools) for drawing the maps. EGM2008 was provided by ICGEM/GFZ Potsdam. We recognize the use of shipborne gravity data which was provided by the National Centers for Environmental Information of the National Oceanic and Atmospheric Administration.

REFERENCES

Ablain, M., Cazenave, A., Larnicol, G., Balmaseda, M., Cipollini, P., Faugère, Y., et al. (2015). Improved sea level record over the satellite altimetry era (1993-2010) from the Climate Change Initiative project. *Ocean Sci.* 11, 67–82. doi:10.5194/os-11-67-2015

Andersen, O. B., Knudsen, P., and Berry, P. A. M. (2010). The DNSC08GRA global marine gravity field from double retracked satellite altimetry. *J. Geod.* 84, 191–199. doi:10.1007/s00190-009-0355-9

Andersen, O. B., Knudsen, P., and Stenseng, L. (2016). "The DTU13 MSS (Mean Sea Surface) and MDT (Mean Dynamic Topography) from 20 Years of Satellite Altimetry," in *IGFS 2014: Proceedings of the 3rd International Gravity Field Service (IGFS), Shanghai, China, June 30 - July 6, 2014*. Editors S. Jin and R. Barzaghi (Cham: Springer), 111–121.

Andersen, O. B., and Knudsen, P. (2019). "The DTU17 Global Marine Gravity Field: First Validation Results," in Fiducial Reference Measurements for Altimetry *International Association of Geodesy Symposia.*. Editors S. P. Mertikas and R. Pail (Cham: Springer), 83–87. doi:10.1007/1345_2019_65

Andersen, O. B. (2013). "Marine Gravity and Geoid from Satellite Altimetry," in Geoid Determination: Theory and Methods *Lecture Notes in Earth System Sciences*. Editors F. Sanso and M. G. Sideris (Heidelberg: Springer-Verlag), 401–451. doi:10.1007/978-3-540-74700-0_9

Bazilian, M., Onyeji, I., Aqrawi, P.-K., Sovacool, B. K., Ofori, E., Kammen, D. M., et al. (2013). Oil, Energy Poverty and Resource Dependence in West Africa. *J. Energ. Nat. Resour. L.* 31, 33–53. doi:10.1080/02646811.2013.11435316

Becker, J. J., Sandwell, D. T., Smith, W. H. F., Braud, J., Binder, B., Depner, J., et al. (2009). Global Bathymetry and Elevation Data at 30 Arc Seconds Resolution: SRTM30_PLUS. *Mar. Geodesy* 32, 355–371. doi:10.1080/01490410903297766

Cazenave, A., Dieng, H.-B., Meyssignac, B., von Schuckmann, K., Decharme, B., and Berthier, E. (2014). The rate of sea-level rise. *Nat. Clim. Change* 4, 358–361. doi:10.1038/nclimate2159

Chander, S., and Majumdar, T. J. (2016). Comparison of SARAL and Jason-1/2 altimetry-derived geoids for geophysical exploration over the Indian offshore. *Geocarto Int.* 31, 158–175. doi:10.1080/10106049.2015.1041562

Dadzie, I., and Li, J. (2007). Determination of geoid over South China Sea and Philippine Sea from multi-satellite altimetry data. *Geo-spatial Inf. Sci.* 10, 27–32. doi:10.1007/s11806-006-0154-x

Hwang, C., and Chang, E. T. Y. (2014). Seafloor secrets revealed. *Science* 346, 32–33. doi:10.1126/science.1260459

Hwang, C., Hsu, H.-Y., and Jang, R.-J. (2002). Global mean sea surface and marine gravity anomaly from multi-satellite altimetry: applications of deflection-geoid and inverse Vening Meinesz formulaeflection-geoid and inverse Vening Meinesz formulae. *J. Geodesy* 76, 407–418. doi:10.1007/s00190-002-0265-6

Hwang, C. (1998). Inverse Vening Meinesz formula and deflection-geoid formula: applications to the predictions of gravity and geoid over the South China Sea. *J. Geodesy* 72, 304–312. doi:10.1007/s001900050169

Hwang, C., and Parsons, B. (1996). An optimal procedure for deriving marine gravity from multi-satellite altimetry. *Geophys. J. Int.* 125, 705–718. doi:10.1111/j.1365-246x.1996.tb06018.x

Hwang, C. (1999). A Bathymetric Model for the South China Sea from Satellite Altimetry and Depth Data. *Marine Geodesy* 22, 37–51. doi:10.1080/014904199273597

Knudsen, P., Andersen, O. B., and Maximenko, N. (2016). The updated geodetic mean dynamic topography model – DTU15MDT. Available at: http://lps16.esa.int/page_session122.php#998p.

Nguyen, V.-S., Pham, V.-T., Van Nguyen, L., Andersen, O. B., Forsberg, R., and Tien Bui, D. (2020). Marine gravity anomaly mapping for the Gulf of Tonkin area (Vietnam) using Cryosat-2 and Saral/AltiKa satellite altimetry data. *Adv. Space Res.* 66, 505–519. doi:10.1016/j.asr.2020.04.051

Olgiati, A., Balmino, G., Sarrailh, M., and Green, C. M. (1995). Gravity anomalies from satellite altimetry: comparison between computation via geoid heights and via deflections of the vertical. *Bull. Géodésique* 69, 252–260. doi:10.1007/BF00806737

Ophaug, V., Breili, K., and Andersen, O. B. (2021). A coastal mean sea surface with associated errors in Norway based on new-generation altimetry. *Adv. Space Res.* 68, 1103–1115. doi:10.1016/j.asr.2019.08.010

Osaretin, I. (2011). Energy Security in the Gulf of Guinea and the Challenges of the Great Powers. *J. Soc. Sci.* 27, 187–191. doi:10.1080/09718923.2011.11892919

Passaro, M., Nadzir, Z. A., and Quartly, G. D. (2018). Improving the precision of sea level data from satellite altimetry with high-frequency and regional sea state bias corrections. *Remote Sensing Environ.* 218, 245–254. doi:10.1016/j.rse.2018.09.007

Pavlis, N. K., Holmes, S. A., Kenyon, S. C., and Factor, J. K. (2012). The development and evaluation of the Earth Gravitational Model 2008 (EGM2008). *J. Geophys. Res.* 117, a–n. doi:10.1029/2011jb008916

Sandwell, D., Garcia, E., Soofi, K., Wessel, P., Chandler, M., and Smith, W. H. F. (2013). Toward 1-mGal accuracy in global marine gravity from CryoSat-2, Envisat, and Jason-1. *The Leading Edge* 32, 892–899. doi:10.1190/tle32080892.1

Sandwell, D. T., Müller, R. D., Smith, W. H. F., Garcia, E., and Francis, R. (2014). New global marine gravity model from CryoSat-2 and Jason-1 reveals buried tectonic structure. *Science* 346, 65–67. doi:10.1126/science.1258213

Small, C., and Sandwell, D. T. (1992). A comparison of satellite and shipboard gravity measurements in the Gulf of Mexico. *Geophysics* 57, 885–893. doi:10.1190/1.1443301

Soltanpour, A., Nahavandchi, H., and Ghazavi, K. (2007). Recovery of marine gravity anomalies from ERS1, ERS2 and ENVISAT satellite altimetry data for geoid computations over Norway. *Stud. Geophys. Geod.* 51, 369–389. doi:10.1007/s11200-007-0021-8

Verron, J., Bonnefond, P., Andersen, O., Ardhuin, F., Bergé-Nguyen, M., Bhowmick, S., et al. (2021). The SARAL/AltiKa mission: A step forward to the future of altimetry. *Adv. Space Res.* 68, 808–828. doi:10.1016/j.asr.2020.01.030

Villadsen, H., Andersen, O. B., Stenseng, L., Nielsen, K., and Knudsen, P. (2015). CryoSat-2 altimetry for river level monitoring - Evaluation in the Ganges-Brahmaputra River basin. *Remote Sensing Environ.* 168, 80–89. doi:10.1016/j.rse.2015.05.025

Wan, X., Annan, R. F., Jin, S., and Gong, X. (2020a). Vertical Deflections and Gravity Disturbances Derived from HY-2A Data. *Remote Sensing* 12, 2287. doi:10.3390/rs12142287

Wan, X., Annan, R. F., and Wang, W. (2020b). Assessment of HY-2A GM data by deriving the gravity field and bathymetry over the Gulf of Guinea. *Earth Planets Space* 72, 13. doi:10.1186/s40623-020-01291-2

Watson, C. S., White, N. J., Church, J. A., King, M. A., Burgette, R. J., and Legresy, B. (2015). Unabated global mean sea-level rise over the satellite altimeter era. *Nat. Clim. Change* 5, 565–568. doi:10.1038/nclimate2635

Wessel, P., and Watts, A. B. (1988). On the accuracy of marine gravity measurements. *J. Geophys. Res.* 93, 393–413. doi:10.1029/jb093ib01p00393

Zakharova, E. A., Krylenko, I. N., and Kouraev, A. V. (2019). Use of non-polar orbiting satellite radar altimeters of the Jason series for estimation of river input to the Arctic Ocean. *J. Hydrol.* 568, 322–333. doi:10.1016/j.jhydrol.2018.10.068

Zhang, S. (2017). *Research on Determination of Marine Gravity Anomalies from Multi-Satellite Altimeter Data*. Wuhan, China: Wuhan University.

Zhang, S., Sandwell, D. T., Jin, T., and Li, D. (2017). Inversion of marine gravity anomalies over southeastern China seas from multi-satellite altimeter vertical deflections. *J. Appl. Geophys.* 137, 128–137. doi:10.1016/j.jappgeo.2016.12.014

Zhu, C., Guo, J., Gao, J., Liu, X., Hwang, C., Yu, S., et al. (2020). Marine gravity determined from multi-satellite GM/ERM altimeter data over the South China Sea: SCSGA V1.0. *J. Geod.* 94, 50. doi:10.1007/s00190-020-01378-4

Zhu, C., Guo, J., Hwang, C., Gao, J., Yuan, J., and Liu, X. (2019). How HY-2A/GM altimeter performs in marine gravity derivation: assessment in the South China Sea. *Geophys. J. Int.* 219, 1056–1064. doi:10.1093/gji/ggz330

Conflict of Interest: The authors declare that the research was conducted in the absence of any commercial or financial relationships that could be construed as a potential conflict of interest.

Publisher's Note: All claims expressed in this article are solely those of the authors and do not necessarily represent those of their affiliated organizations, or those of the publisher, the editors and the reviewers. Any product that may be evaluated in this article, or claim that may be made by its manufacturer, is not guaranteed or endorsed by the publisher.

frontiers in Earth Science

ORIGINAL RESEARCH
published: 04 August 2021
doi: 10.3389/feart.2021.707869

Structural Inheritance Controls Strain Distribution During Early Continental Rifting, Rukwa Rift

Folarin Kolawole[1,2]*, *Thomas B. Phillips*[3], *Estella A. Atekwana*[4] and *Christopher A.-L. Jackson*[5]

[1]School of Geosciences, University of Oklahoma, Norman, OK, United States, [2]BP America, Houston, TX, United States, [3]Science Labs, Department of Earth Sciences, Durham University, Durham, United Kingdom, [4]Department of Earth Science, University of Delaware, Newark, DE, United States, [5]Department of Earth and Environmental Sciences, The University of Manchester, Manchester, United Kingdom

Little is known about rift kinematics and strain distribution during the earliest phase of extension due to the deep burial of the pre-rift and earliest rift structures beneath younger, rift-related deposits. Yet, this exact phase of basin development ultimately sets the stage for the location of continental plate divergence and breakup. Here, we investigate the structure and strain distribution in the multiphase Late Paleozoic-Cenozoic magma-poor Rukwa Rift, East Africa during the earliest phase of extension. We utilize aeromagnetic data that image the Precambrian Chisi Shear Zone (CSZ) and bounding terranes, and interpretations of 2-D seismic reflection data to show that, during the earliest rift phase (Permo-Triassic 'Karoo'): 1) the rift was defined by the Lupa border fault, which exploited colinear basement terrane boundaries, and a prominent intra-basinal fault cluster (329° ± 9.6) that trends parallel to and whose location was controlled by the CSZ (326°); 2) extensional strain in the NW section of the rift was accommodated by both the intra-basinal fault cluster and the border fault, where the intra-basinal faulting account for up to 64% of extension; in the SE where the CSZ is absent, strain is primarily focused on the Lupa Fault. Here, the early-rift strain is thus, not accommodated only by the border fault as suggested by existing magma-poor early-rift models; instead, strain focuses relatively quickly on a large border fault and intra-basinal fault clusters that follow pre-existing intra-basement structures; 3) two styles of early-rift strain localization are evident, in which strain is localized onto a narrow discrete zone of basement weakness in the form of a large rift fault (Style-1 localization), and onto a broader discrete zone of basement weakness in the form of a fault cluster (Style-2 localization). We argue that the CSZ and adjacent terrane boundaries represent zones of mechanical weakness that controlled the first-order strain distribution and rift development during the earliest phase of extension. The established early-rift structure, modulated by structural inheritance, then persisted through the subsequent rift phases. The results of our study, in a juvenile and relatively well-exposed and data-rich rift, are applicable to understanding the structural evolution of deeper, buried ancient rifts.

Keywords: continental rifting, tectonic strain, normal faults, rukwa rift basin, east african rift system

OPEN ACCESS

Edited by:
James D Muirhead,
The University of Auckland,
New Zealand

Reviewed by:
Giacomo Corti,
National Research Council (CNR), Italy
Damien Delvaux,
Royal Museum for Central Africa,
Belgium

***Correspondence:**
Folarin Kolawole
folarin.kol@gmail.com

Specialty section:
This article was submitted to Structural Geology and Tectonics, a section of the journal Frontiers in Earth Science

Received: *10 May 2021*
Accepted: *22 July 2021*
Published: *04 August 2021*

Citation:
Kolawole F, Phillips TB, Atekwana EA and Jackson CA-L (2021) Structural Inheritance Controls Strain Distribution During Early Continental Rifting, Rukwa Rift. Front. Earth Sci. 9:707869. doi: 10.3389/feart.2021.707869

INTRODUCTION

Tectonic extension of the continental lithosphere is typically accommodated by the brittle deformation of the upper crust, demonstrated by the emergence of normal fault populations (Cowie et al., 2005; Agostini et al., 2011; Muirhead et al., 2016, 2019). Some classic models for the evolution of continental rifts, suggest that during the early phase of extension, strain is initially accommodated by the development of distributed normal faults, with strain subsequently localizing onto a few large faults and subsequently migrating to the rift axis (e.g., Chorowicz, 2005; Gawthorpe and Leeder, 2008; Nixon et al., 2016; Naliboff et al., 2017). However, a comparison of juvenile, magma-rich and magma-poor segments of narrow rifting along the East African Rift System (EARS) show that in contrast to the magma-rich rift basins where strain is accommodated by both the large basin-bounding faults (border faults) and intra-basinal structures, the border faults accommodate most (~90%) of the strain in the magma-poor rift segment (Muirhead et al., 2019). Elsewhere along the EARS, the incipient (<3 Ma) magma-poor Zomba Graben, southern Malawi Rift, has already witnessed the localization of strain in the rift axis, with the related faults presently accounting for up to 55% (±24) of the extensional strain (Wedmore et al., 2020a). The evidence presented in these studies indicate that early-phase extensional strain along magma-poor continental rifts may or may not be primarily accommodated by only the border faults. Thus, there is a need to better understand other mechanisms that can facilitate early focusing of intra-basinal faulting and extensional strain in magma-poor continental rifts.

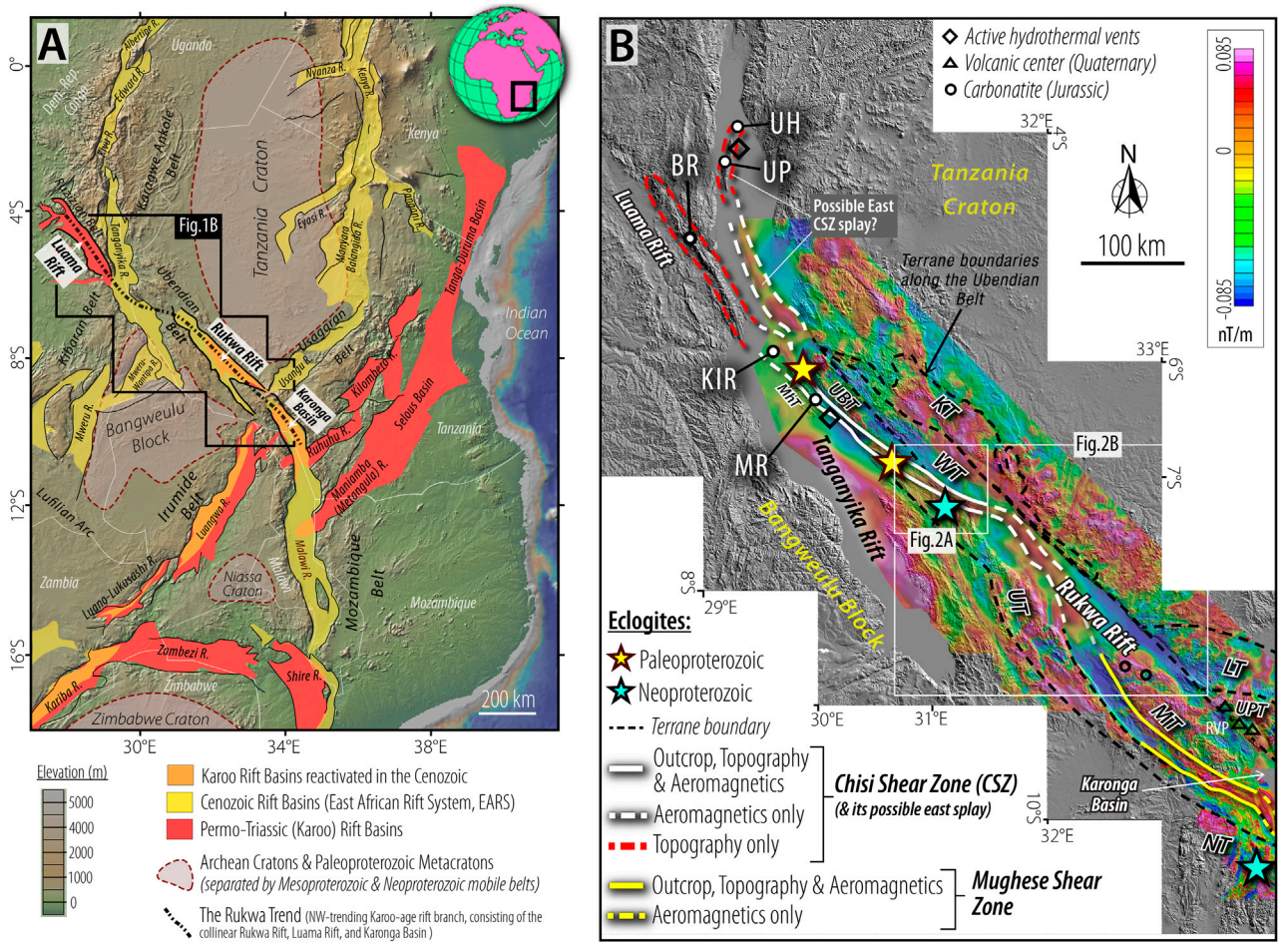

FIGURE 1 | (A): Map of East Africa showing the Permo-Triassic (i.e., Karoo rift system) rift segments, and the currently active rift segments (i.e., East African Rift System). **(B)**: Shuttle Radar Topography Mission (SRTM) Digital Elevation Model (DEM) hillshade map covering the Rukwa Rift Trend, overlaid with the vertical derivative aeromagnetic of SW Tanzania. Black dashed lines represent boundaries of the Precambrian terranes of the Rukwa Rift Trend (after Daly, 1988; Lenoir et al., 1994; Delvaux et al., 2012; Lemna et al., 2019; Heilman et al., 2019). Locations of Proterozoic eclogites in the Ubendian Belt are from Boniface et al. (2012) and Boniface and Schenk (2012). Locations of hydrothermal vents and Mesozoic-Cenozoic igneous centers (volcanics and carbonatites) are obtained from Hodgson et al. (2017). See uninterpreted aeromagnetic and hillshade maps in **Supplementary Figures 1**, **2**. Geomorphic features: BR (Busindi Ridge), KIR (Kavala Island Ridge), MR (Mahale Ridge), UP (Ubwari Peninsula), UH (Ubwari Horst). Terranes of the Ubendian Belt: KT (Katuma Terrane), LT (Lupa Terrane), MT (Mbozi Terrane), MhT (Mahale Terrane), RVP (Rungwe Volcanic Province), UBT (Ubende Terrane), UPT (Upangwa Terrane), UT (Ufipa Terrane), WT (Wakole Terrane).

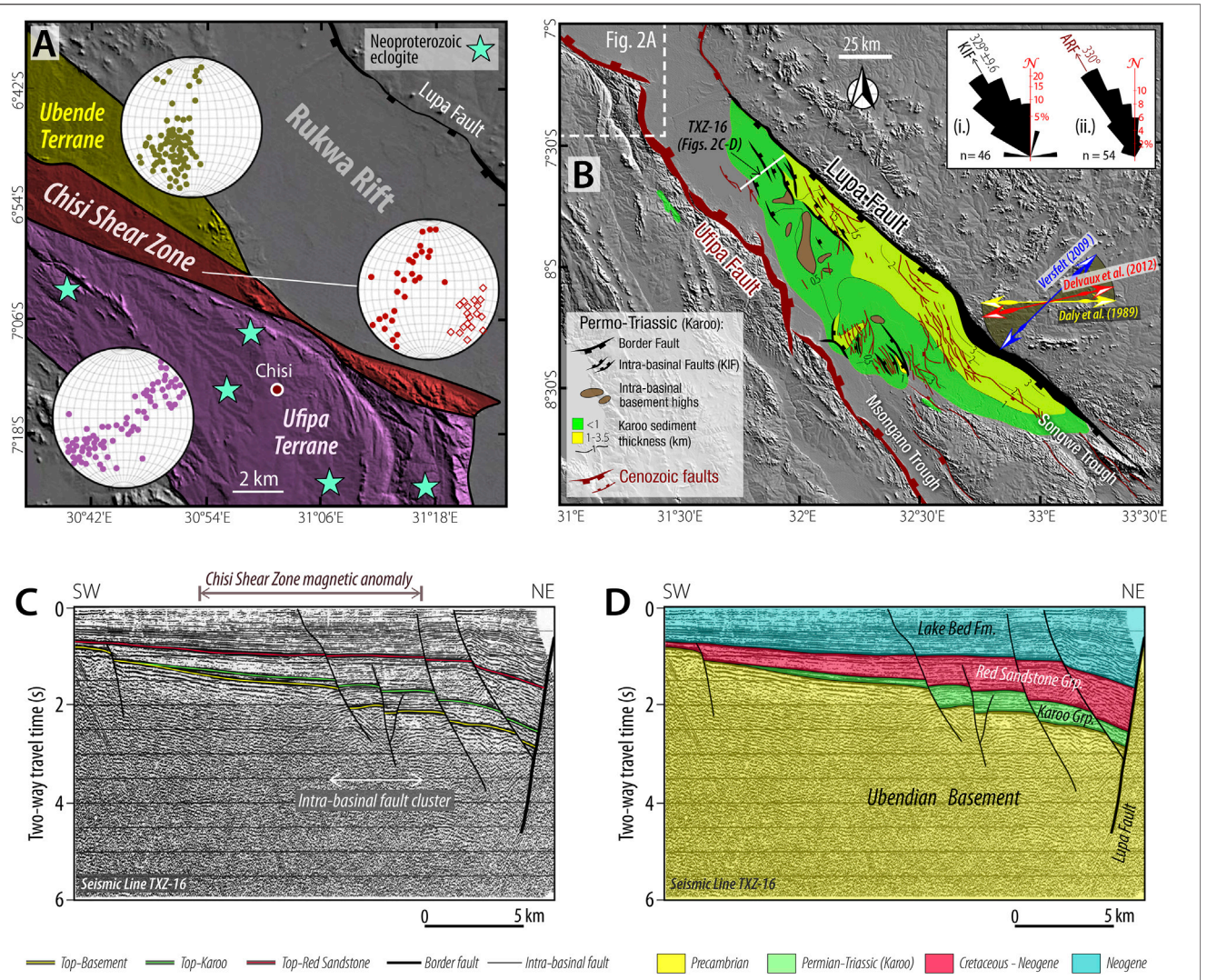

FIGURE 2 | (A): Shuttle radar digital elevation model (DEM) hillshade map of the NW Rukwa Rift shoulder (see **Figure 1B**, **2B** for location) showing the Precambrian Chisi Shear Zone exposure and its bounding basement terranes. The plots of equal area stereographic projection (lower hemisphere) show the poles to planes of gneissic foliation (filled circles), and poles of mineral elongation lineation and some fold axes of asymmetric intrafolial folds (diamonds in the Chisi Shear Zone stereonet) measured in field outcrops (from Boven et al., 1999). These structures represent the metamorphic basement fabrics of the basement. Locations of Neoproterozoic eclogites in the Chisi area are from Boniface and Schenk (2012). **(B)**: Map of the Rukwa Rift showing the interpreted Karoo and post-Karoo structural elements (structural elements are from Morley et al., 1992, 1999). Arrows represent the previously published inferred Karoo extension directions. *Inset:* Frequency-azimuth distribution plot for ***(i.)*** Karoo-age (Permo-Triassic) intra-basinal faults (KIF) with black arrow indicating their mean trend and standard error (measured in this study), and ***(ii.)*** All (Permian to Quaternary) Rukwa Rift faults (ARF) with their mean trend shown as brown arrow (digitized from Morley et al., 1992). **(C–D)**: 2-D seismic reflection profile line TXZ-16 and interpretation (modified from Morley et al., 1999; see location in **Figure 2B**) showing the major stratigraphic boundary horizons, the Lupa border fault, and intra-basinal faults.

Since continental rifts typically develop in previously deformed lithosphere (Wilson, 1966; Dewey and Spall, 1975; Buiter and Torsvik, 2014), the distribution of early-phase strain in magma-poor rifts can be complex due to the interaction between faults that exploit or reactivate pre-existing structures, and those that form independently of any pre-existing structure (e.g., Manatschal et al., 2015; Kolawole et al., 2018; Ragon et al., 2019; Schiffer et al., 2019; Phillips et al., 2019a,b; Heilman et al., 2019; Osagiede et al., 2020; Wang et al., 2021). Overall, very little is known about the earliest phase of continental extension, and even less of how strain is partitioned along inherited structures; this reflects the fact that the associated structures and related stratigraphic record are typically deeply buried beneath younger (i.e., post-rift or later rift phase) sequences and are thus difficult to image with geophysical data, or are overprinted by later tectonic events (e.g., post-rift plate collision). This knowledge gap limits a fuller understanding of the spectrum of processes that govern continental rifting and breakup in space and time.

The EARS (**Figure 1A**) is the largest active continental rift system on Earth. This system, which formed by the stretching of

previously deformed lithosphere, is characterized by segments that span the major stages of continental rifting from inception to transitional crust (e.g., Daly et al., 1989; Hayward and Ebinger, 1996; Delvaux, 2001; Chorowicz, 2005; Ebinger, 2005). We integrate available geophysical and geological datasets from the multiphase magma-poor Rukwa Rift (**Figures 1A,B**, **2A–D**) to explore how strain was distributed during the earliest phase of extension, and investigate the dominant controls. We show that the potentially lithosphere-scale Precambrian Chisi Shear Zone (CSZ) and its adjacent terrane boundaries (**Figure 1B**; Lemna et al., 2019; Heilman et al., 2019) represent major zones of pre-rift basement mechanical weakness that controlled the location, structure, and evolution of both the border and intra-basinal faults during the earliest phase of continental extension. We show how the geometry of the CSZ controlled along-rift variations in the early-phase tectonic extension and overall basin geometry, the effects of which persist through and thus influence the later rift geometry. We also expand our analysis to the nearby Luama Rift (located in DRC), which is coeval, colinear with, and parallel to the Rukwa Rift; both basins representing structural elements along a NW-trending Karoo-age rift branch herein referred to as "the Rukwa Trend" (**Figure 1A**). Our results resolve a long-standing controversy related to the geometrical structure and kinematics of rifting in this part of the East African Rift System.

GEOLOGICAL SETTING

The Precambrian (Pre-Rift) Basement of the Rukwa Trend

The crystalline basement of the Rukwa Trend is composed of the metamorphic and igneous rocks of the Precambrian (1.95–1.85 Ga) Ubendian Belt, which formed during the collision of the Archean Tanzania Craton and the Bangweulu Block, and which comprises the Ufipa, Katuma, Wakole, Lupa, Mbozi, Ubende, and Upangwa terranes (**Figures 1A,B**; Daly, 1988; Lenoir et al., 1994). This orogenic belt, which is defined by several NW-trending terranes (2.1–2.025 Ga) that are bounded by steeply dipping, ductile, amphibolite facies, strike-slip shear zones (**Figure 1B**; Daly, 1988; Lenoir et al., 1994; Theunissen et al., 1996; Kolawole et al., 2018). The terranes are composed of amphibolite to granulite facies gneisses with foliations that dominantly trend NW-SE and commonly steepen near the terrane boundaries (Lenoir et al., 1994). Although relative rare compared to gneisses, other metasediments along the belt consists of mica schists, marbles, meta-anorthosites, and ferruginous quartzites (Lenoir et al., 1994).

The geochronology, geochemistry, and metamorphic structure of the Ubendian Belt suggests that it formed in response to multiple episodes of wrench tectonic events (Theunissen et al., 1996) with phases of subduction extending from the Paleoproterozoic to the Neoproterozoic (Ganbat et al., 2021). The orogenic belt first developed during a phase of collisional orogeny along the SW margin of the Tanzanian Craton (ca 2.1–2.0 Ga), after which the belt experienced two episodes of wrench tectonics consisting of an initial phase of dextral strike-slip shear at ca. 1.8–2.0 Ga, followed by a ductile-brittle sinistral strike-slip reactivation in the Neoproterozoic (Lenoir et al., 1994). This Neoproterozoic shear reactivation recorded the development of thick mylonite and blastomylonite zones with low-grade metamorphic assemblages along shear zones that bound the terranes. The terranes and associated fabrics which are observable in basement exposures along the flanks of the Phanerozoic Rukwa Rift, are suggested to have exerted some control on the development of the basin (Wheeler and Karson, 1994; Theunissen et al., 1996; Klerkx et al., 1998; Boven et al., 1999; Heilman et al., 2019; Lemna et al., 2019).

The Chisi Shear Zone

Along the Ubendian Belt, the Chisi Shear Zone (CSZ) is a prominent shear zone which separates the Ufipa Terrane to the southwest, from the Wakole and Ubende Terranes to the northeast (**Figure 1B**). The structure was initially identified as the "Ikulu series" or "Ikulu Terrane", a broad (6–12 km-wide in Chisi area) shear belt composed of amphibolite, micaschist, and meta-calcareous rocks with high pressure blueschist or eclogitic associations (Lenoir et al., 1994; Boven et al., 1999). The mafic high-pressure sequences along the shear zone were interpreted to represent disrupted remnants of deeply subducted ophiolites (Smirnov et al., 1973; Lenoir et al., 1994; Klerkx et al., 1998; Sklyarov et al., 1998).

Along the "Ikulu" structure, amphibolites and amphibole gneisses exhibit metamorphic foliation with planes that dominantly strike WNW-ESE and dip steeply to the NNE and S-SSW (stereographic plot with red filled circles in **Figure 2A**; Theunissen et al., 1996; Boven et al., 1999). The rocks also exhibit mineral elongation lineation and some fold axes of asymmetric intrafolial folds that generally trend NW-SE and plunge shallowly-to-moderately to the ESE-SE (stereographic plot with open diamonds in **Figure 2A**). Mylonitic rocks along the SW margin of the granulitic Ubende Terrane exhibit P-T characteristics and shear fabrics suggesting an uplift and exhumation of the terrane relative to the felsic Ufipa Terrane on the SW flank of the "Ikulu" structure (Theunissen et al., 1996; Sklyarov et al., 1998; Boven et al., 1999). More detailed petrographic and geochemical investigation of the eclogites reveal striking similarities with oceanic island-arc volcanic rocks (Boniface and Schenk, 2012). Geochronologic analyses indicate a clustering of Paleoproterozoic eclogites to the northern segment of the structure (near Lake Tanganyika) and Neoproterozoic eclogites to the south (e.g., Chisi area and northern Malawi) (**Figure 1B**), suggesting multiple cycles of subduction-related orogenic events along the structure (Boniface et al., 2012; Boniface and Schenk, 2012; Ganbat et al., 2021). Thus, the "Ikulu" domain was proposed to be the primary Late Proterozoic (Pan African Orogeny) suture zone between the Tanzania and Bangweulu Cratons along the Ubendian Belt (Boniface and Schenk, 2012).

Further, the magnetic-high anomaly expression of the "Ikulu" domain, created by the dominance of mafic rocks along the belt, defines a prominent regional magnetic lineament that extends southeast beneath the Rukwa Rift sedimentary cover, sub-parallel to the northwest trend of the rift (**Figure 1B**; Lemna et al., 2019;

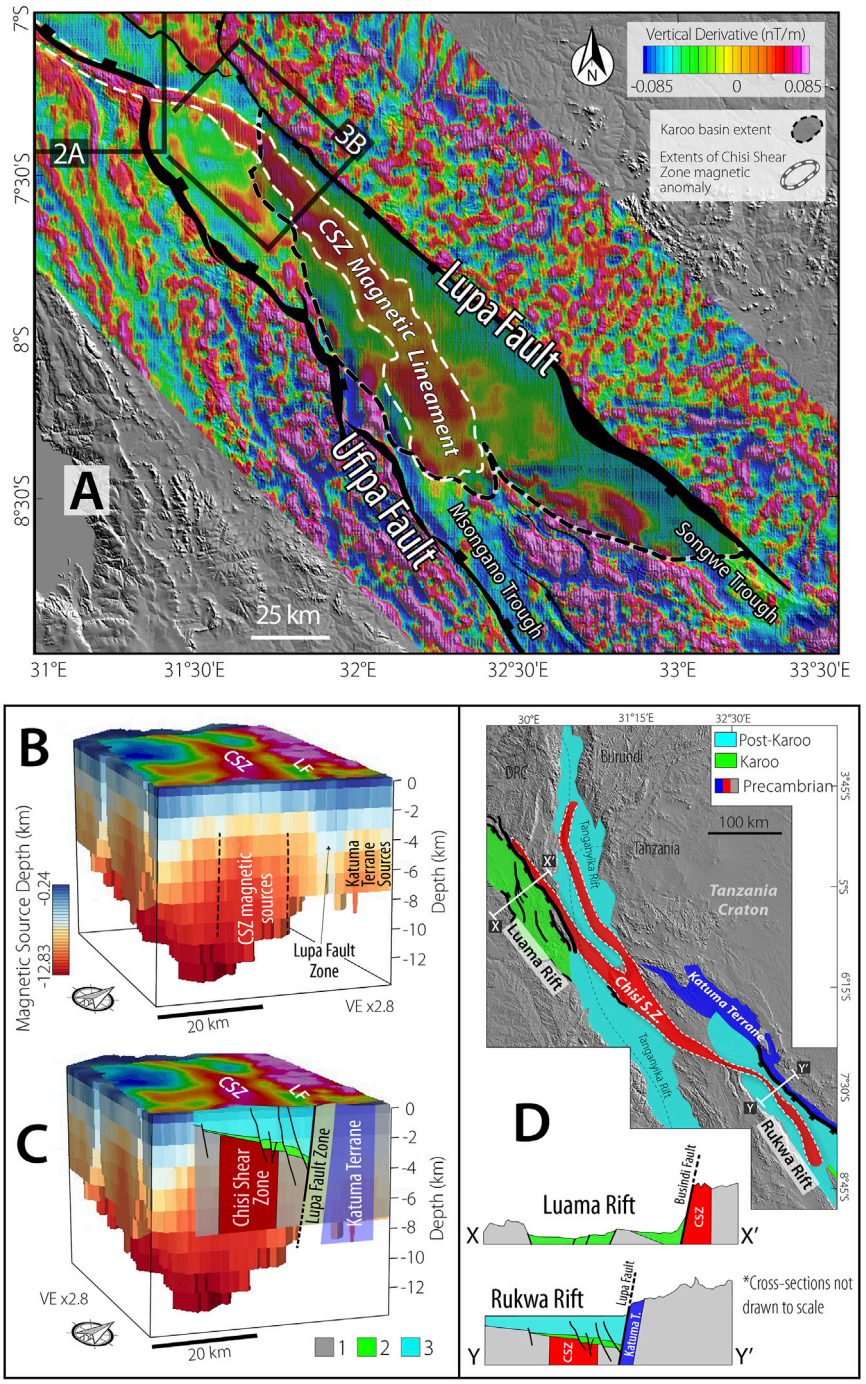

FIGURE 3 | (A): Vertical derivative of the aeromagnetic grid overlaid on satellite Digital Elevation Model (DEM) hillshade map, showing the rift border faults, rift shoulder basement fabrics and the aeromagnetic signature of the Chisi Shear Zone (CSZ) along the rift axis. See uninterpreted aeromagnetic maps in **Supplementary Figure 1**. **(B)**: 3-D gridded block of the Source Parameter Imaging (SPI) solutions from the transform of the aeromagnetic grid, showing the subsurface extents and geometry of CSZ and the shallower Katuma Terrane magnetic sources. **(C)**: 3-D gridded block overlaid with interpretations of the rift faults and simplified stratigraphy (interpretations from 2-D seismic line TXZ-16 of Morley et al., 1999 shown in **Figure 2C**). Stratigraphic units shown: 1 = Precambrian basement), 2 = Permo-Triassic (Karoo Grp.) sequences, 3 = Post-Karoo sequences i.e., Red Bed Grp. and Lake Bed Fm.). **(D):** Regional satellite DEM hillshade map showing the >600 km extent of the CSZ and its relationships with the Rukwa and Luama segments of the Rukwa Trend. The Luama Rift cross-section is based on legacy geologic maps and satellite DEM, and that of the Rukwa Rift is based on 2-D seismic data interpretation, satellite DEM, and aeromagnetics.

Heilman et al., 2019). Since the Chisi area of Tanzania represents a type-locality for the detailed studies of the structural fabrics, geochemistry, and petrology of the structure (Theunissen et al., 1996; Boven et al., 1999; Boniface and Schenk, 2012), the structure was recently officially re-introduced as "Chisi Shear Zone" (Lemna et al., 2019) or "Chisi Suture Zone" (Heilman et al., 2019). However, in this current study, we adopt the name "Chisi Shear Zone" to refer to the structure.

Phanerozoic Rifting Along the Rukwa Trend

The present-day configuration of the Rukwa Trend consists of multiple colinear, NNW-trending rift basins (Rukwa, Karonga, and Luama basins) that initially developed during Permo-Triassic (Karoo) phase of rifting (e.g., Delvaux, 2001). All three basins were reactivated by extensional tectonics in the Cretaceous (Roberts et al., 2010, 2012). However, only the Rukwa Rift and Karonga Basin (**Figure 1A**) experienced significant reactivation in the Cenozoic, and they are still currently active (e.g., Morley et al., 1999; Delvaux, 2001; Chorowicz, 2005). The Rukwa Rift, the primary focus of this study, currently defines a graben and is bounded to the northeast by the Lupa Fault and to the southwest by the Ufipa Fault (**Figure 2B**; Heilman et al., 2019; Morley et al., 1999). The basin initially developed as a NE-dipping half graben (with a shallow graben geometry only in the NW) during the Karoo rifting phase, bounded to the northeast by the principal border fault, the Lupa Fault (**Figures 2C,D**). The Karoo intra-basinal faults (KIF) and basement highs predominantly trend NNW, oblique to the Lupa Fault strike (**Figure 2B**). Estimates of the Karoo-age extension direction vary from NE-SW to E-W (**Figure 2B**).

DATASET AND METHODOLOGY

Along the Rukwa Trend, we compile structural mapping and structural measurement data from published 2-D seismic data (e.g., **Figure 2C**; Morley et al., 1999) and integrate these with aeromagnetic data (**Supplementary Figures S1A–B**) and Shuttle radar digital elevation model (DEM) (**Supplementary Figures S2A–B**).

Aeromagnetic Data, Shuttle Radar Topographic Data, and their Analyses

We use aeromagnetic data to map key pre-rift intra-basement structures along the axis of the Rukwa Rift and along-trend of the rift. We applied derivative filters to the aeromagnetic grid to enhance structural features (**Figure 3A**), and mathematical transforms to estimate the depths to magnetic sources in the basement (**Figures 3B–D**; see **Supplementary Material** information).

The aeromagnetic data (**Supplementary Figure S1A**), collected between 1977–1980 with flight height of 200 m and a flight line spacing of 1 km, was provided by the South African Council for Geoscience. First, we reduced the data to the magnetic pole (RTP) to correct for latitude-dependent skewness (Baranov, 1957), after which we applied a vertical derivative filter to better resolve magnetic gradients associated with structural features (**Figure 3A**, **Supplementary Figure S1B**) (Salem et al., 2007; Kolawole et al., 2017, 2018; Heilman et al., 2019). In this study, we delineate the boundaries of the Chisi Shear Zone along the edges of the high magnetic anomaly lineament in the vertical derivative map of the aeromagnetic grid. In areas where aeromagnetic data is not available, we augmented the basement mapping with 30 m-resolution Shuttle Radar Topography Mission (SRTM) Digital Elevation Model (DEM) hill shade maps (**Supplementary Figures S2A–B**).

Structural Data From Seismic Interpretation

We establish the initial (i.e., Karoo rift phase) geometry of the Rukwa Rift and related faults using published seismic reflection profiles, and associated fault trace maps and sediment thickness maps ("Karoo Isopach") presented by Morley et al. (1992, 1999). We also calculate along-rift variations in Karoo-age tectonic extension (geometrically-restored to Karoo time surface; **Figures 4A–D**) accommodated by slip on the Lupa Fault and intra-basinal faults, again using data published by Morley et al. (1992). We integrate these structural data with aeromagnetic data analysis to investigate the influence of the pre-rift basement structure on the early-rift structure and evolution of the Rukwa Rift (**Figures 4A–C**).

RESULTS

3-D Geometry and Extent of the CSZ

The petrology and geochemistry, local structure, and topographic expression of the CSZ is well-constrained in the Chisi area, located on the NW flank of the Rukwa Rift (**Figures 1B**, **2A**; Theunissen et al., 1996 and Boven et al., 1999; Boniface and Schenk, 2012). Field observations show that the CSZ is dominated by steep, NE- and SW-dipping, metamorphic fabrics hosted by eclogite facies rocks (**Figure 2A**). At this location, the CSZ is characterized by a prominent NW-trending, positive magnetic anomaly lineament (**Figure 1B**) and a topographic ridge (**Figure 2A** and **Supplementary Figure S2A**). Based on its distinct geophysical and geomorphic expression, as well as known field locations of eclogite rocks, we map the northwestward and southeastward continuations of the CSZ system beneath the Rukwa Rift and along the northeastern boundary zone of the Luama Rift respectively (**Figure 1B**).

Northwest of the Chisi area, the CSZ associated structures are colinear with the subaerial Mahale Ridge and the submerged Kavala Island Ridge (submerged beneath Lake Tanganyika), and continues northwest into the Busindi Ridge which itself represents the footwall of the Busindi border fault of the Luama Rift (**Figure 1B**, **Supplementary Figure S2A**). Along the Luama Rift, the inferred CSZ extension represents the boundary between the Kibaran Belt (to the south) and the Ruzizian Belt to the north (**Figure 1A**). Based on the occurrence of a prominent high magnetic lineament extending NNW across Lake Tanganyika from the northernmost known CSZ-related eclogite exposure, a possible East CSZ splay is delineated to continue northward and link with the N-trending

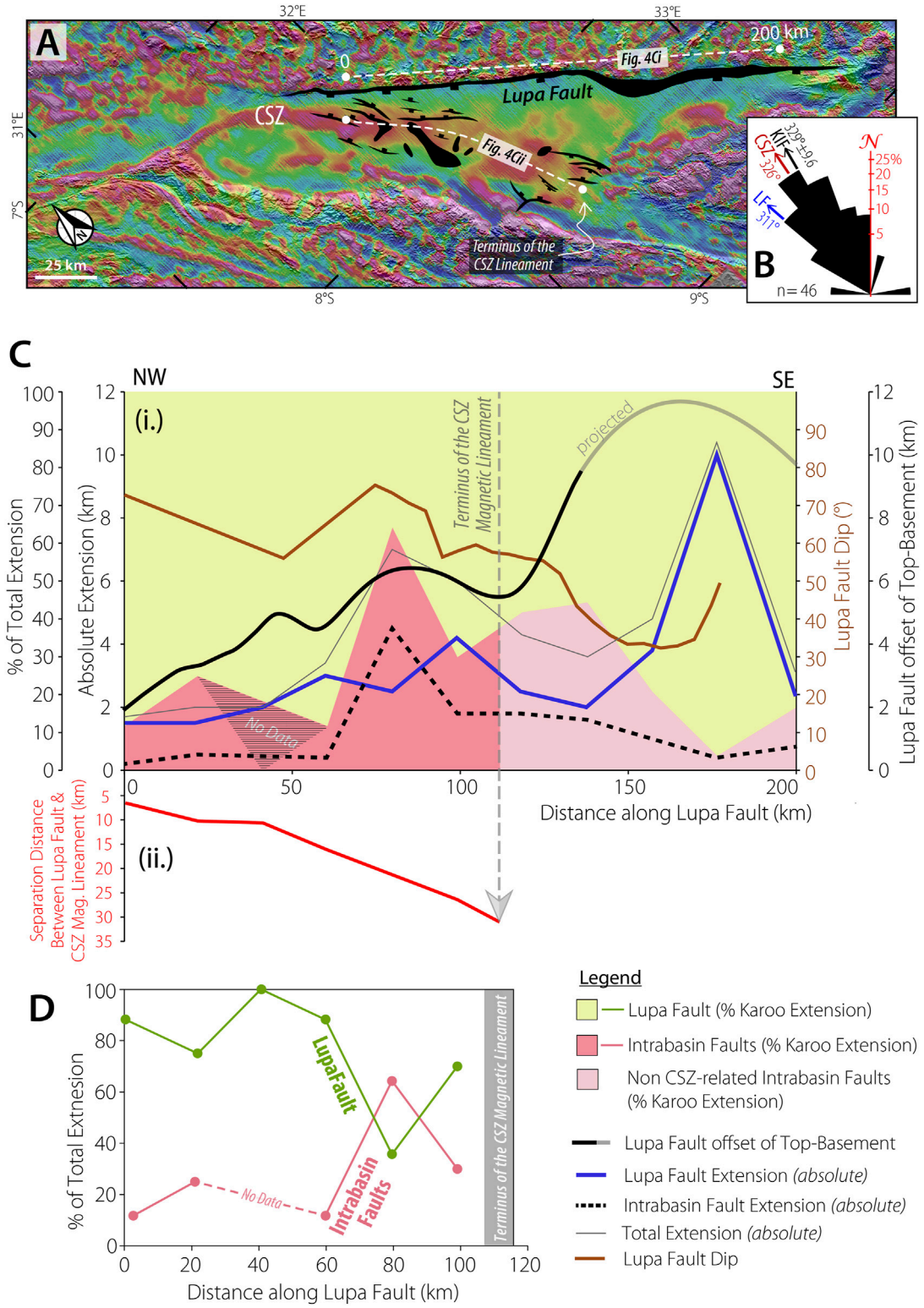

FIGURE 4 | (A): Map of vertical derivative of the aeromagnetic grid overlaid on satellite DEM hillshade map, showing the section of the Rukwa Rift (white dashed lines) along which, the measurements plotted in **Figures 4C,D** were taken. **(B)**: Frequency-azimuth distribution of the Karoo-age intra-basinal faults (KIF; measured in this study). CSZ = Chisi Shear Zone, LF = Lupa Fault. Arrows represent the mean trend of the associated structure. **(C)**: Plot showing along-rift distribution of **(i.)** line-length measurement of the Top-Karoo surface as estimates of Karoo-age tectonic extension (for the Lupa and intra-basinal faults), Lupa Fault dip angle, and Top-Basement offset along the Lupa Fault, and **(ii.)** lateral separation distance between the CSZ and the Lupa Fault. **(D)**: Plot showing the along-rift variation of % total Karoo-age extension accommodated by the Lupa Fault and the intra-basinal faults up till the CSZ termination (displayed as stacked area plot in **Figure 4C**).

Ubwari Ridge (buried horst and subaerial peninsula; **Figure 1B**, **Supplementary Figures S1A-B**). Although the Ubwari Ridge is a fault-bounded horst block in the Cenozoic Tanganyika Rift, its possible spatial association with the CSZ inferred based on both the colinearity with the continuation of the magnetic-high anomaly lineament of the CSZ, and the southeastward rotation of the N-trending metamorphic fabrics of the subaerial section of the horst (**Supplementary Figures S1B**, **S2B**).

The CSZ extends southeastwards from the Chisi area to continue beneath the Rukwa Rift, where it is sub-parallel to the rift border faults (**Figure 1B**, **2A**). Just southeast of the termination of the CSZ magnetic lineament, the >15 km-wide Mughese Shear Zone (MSZ) which separates the Ufipa and Mbozi Terranes of the Ubendian Belt (**Figure 1B**), extends beneath the Msongano Trough (bifurcation of the Rukwa Rift) and continues southeast into the Karonga Basin (**Figure 1B**, **2B**). Overall, the CSZ-associated aeromagnetic and geomorphic structures extend for >600 km from the Luama and Tanganyika rifts, southeastwards through the Rukwa Rift (**Figure 1B**). Although our mapping suggests an along-trend and perhaps genetic relationship between the CSZ and the Mughese Shear Zone (**Figure 1B**), we clarify that at the time of this contribution, there is no available data demonstrating that the Mughese Shear Zone is also a subduction-related suture. In the absence of this information, we define the southeast termination of the CSZ as the termination zone of its magnetic anomaly lineament beneath the Rukwa Rift (**Figure 1B**, **3A**).

Our 3D grid of the depth-distribution of intra-basement magnetic sources along the Rukwa Rift (**Figures 3A–C**, **Supplementary Figures S3A–B**, **S4A–B**) reveal a steeply-dipping, NW-trending zone of magnetic sources that extend to 12 km depth; this feature is spatially collocated with the surface trend of the CSZ aeromagnetic lineament (**Figure 3B**). Northeast of these CSZ-related magnetic sources, a narrow sub-vertical block of very shallow (<6 km deep) magnetic sources is spatially colocated with the Lupa Fault. This zone of Lupa Fault-related shallow sources separates the CSZ-related sources from another sub-vertical cluster of moderately deeper (~9 km-deep) magnetic sources that are spatially collocated with the Katuma Terrane (**Figures 3B–D**).

The CSZ and the Early-Rift (Karoo) Structure

The Karoo-age basin of the Rukwa Rift widens southeastwards from c. 16 km in the northwest to c. 57 km at the terminus of the CSZ magnetic lineament, before narrowing to <16 km towards the southeast (**Figure 2B**). The Karoo intra-basinal faults (KIF, 329° ± 9.6; **Figure 2Bi**) are dominated by a fault cluster, spaced 4–6 km apart and striking oblique to the Lupa Fault (311°). The fault cluster is collocated with the CSZ magnetic lineament and trends parallel to the lineament (**Figures 4A,B**). Although, some of the KIF faults dip to the SW, most of them dip to the NE (**Figure 2B**). A Karoo isopach map shows that the thickest sections (>1 km-thick) of the Karoo-age units are generally confined to the northeast of the CSZ anomaly (yellow polygon in **Figure 2B**; also see **Figures 2C,D**). Adjacent to the Katuma Terrane and CSZ lineament (i.e., northwestern half of the rift), the Lupa Fault has a relatively high dip (~69°); this decreases south-eastwards to <40° (**Figure 4C**). Also, within the rift, prominent basement ridges cluster along the CSZ, some of which appear to be fault-bounded (**Figure 2B**). We note the strong alignment between the CSZ mean trend (326°), KIF mean trend (329° ± 9.6), and that of all (Permian to Quaternary) rift faults (ARF, 330°; **Figure 2Bii**).

Strain Distribution Within the Rukwa Rift During Karoo Extension

In the northwestern half of the Rukwa Rift, the proportion of Karoo-phase tectonic extension accommodated by the KIF increased southeastwards from ~12 to 64% (**Figures 4C,D**). This trend is coincident with an increase in across-strike separation between the Lupa border fault and the CSZ, from <10 km in the NW to ~30 km at the SE terminus of CSZ magnetic lineament (**Figure 4C**; see also **Figure 4A**). However, southeastward from the CSZ terminus to the southeast tip of the basin, total extension was largely accommodated by the Lupa Fault (up to 83%; **Figure 4C**). Also, NW of the CSZ terminus, the curve for intra-basinal fault absolute extension tracks that of the total absolute extension, whereas SE of the CSZ terminus, total absolute extension curve is not tracked by that of the intra-basinal fault, rather, it is tracked by the Lupa Fault absolute extension (**Figure 4C**). The southeastward increase in the percentage of total extension accommodated by the Lupa Fault is consistent with the southeastward increase in the magnitude of Lupa Fault's offset of the Top-Basement which shows a more pronounced increase just southeast of the CSZ terminus (see "Lupa Fault offset of Top-Basement" curve in **Figure 4C**). Northwest of the CSZ terminus, Lupa Fault's offset of the Top-Basement shows a range of 2–6.4 km over a distance of 120 km, whereas SE of the CSZ terminus, the basement offset increases from ~5.5 km to >9 km within ~20 km distance.

CONTROLS OF THE CSZ AND TERRANE BOUNDARY ON EARLY-RIFT FAULTING, STRAIN DISTRIBUTION, AND BASIN ARCHITECTURE

Border Fault Development

The geometrical and spatial relationships between the Karoo rift-related structures, the CSZ, and the adjacent basement terrane boundaries reveal how strain was localized and spatially partitioned during the early phases of extension in the Rukwa Rift. The Lupa Fault is the largest rift-related structure in the Rukwa Rift, having formed at the very onset of rifting, thus representing the border fault (e.g., Kilembe and Rosendahl, 1992; Morley et al., 1992, 1999; Wheeler and Karson 1994). Studies suggest that the Lupa Fault localized along terrane boundaries (Katuma-Wakole boundary in the NW and Lupa-Mbozi boundary in the SE) and that its NW-SE trend is influenced by the structural fabrics in the bounding Katuma Terrane

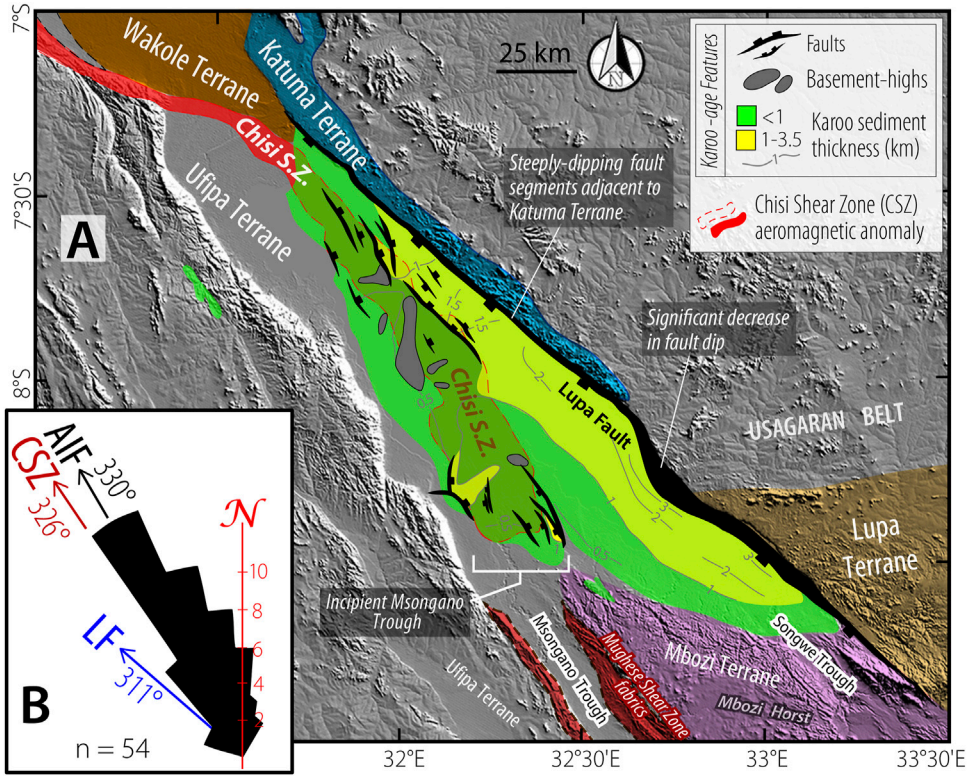

FIGURE 5 | (A): Satellite DEM hillshade map of the Rukwa Rift, overlaid with the Karoo structural features (faults and basement ridges), Karoo isopach map (from Morley et al., 1992, 1999), Chisi Shear Zone magnetic anomaly, and the relevant surrounding basement terranes. **(B)**: Frequency-azimuth distribution of all the faults (Permian-Quaternary) in the Rukwa Rift (digitized from Morley et al., 1992). ARF = "All Rukwa Rift faults" and black arrow showing their mean trend; LF = "Lupa Fault" and blue arrow showing its approximate trend; CSZ = "Chisi Shear Zone" and brown arrow showing its approximate trend within the rift axis.

(**Figures 1B**, **3B–D**; Daly et al., 1989; Wheeler and Karson, 1994; Theunissen et al., 1996; Lemna et al., 2019; Heilman et al., 2019). However, the observations supporting these hypotheses were based on the shallow geometries of structures observed in the field or the plan-view structural trends of metamorphic fabrics expressed in aeromagnetic data.

The sub-vertical dips described by the cluster of magnetic sources beneath the Katuma Terrane (**Figure 3B**) support previous studies that argue that the Katuma-Wakole terrane boundary, and fabrics within the Katuma Terrane, are steeply dipping. However, the Lupa Fault itself shows an abrupt and significant decrease in dip just southeast of the Katuma Terrane termination (**Figure 4C**), where it is coincident with the E-W-trending Usagaran Belt and Lupa Terrane (**Figure 5A**). Therefore, we suggest that both the Katuma-Wakole Terrane boundary and the tectonic structures in the Katuma Terrane are responsible for the steep dip of the Lupa border fault in the NW; in contrast, to the SE, the absence of favorably oriented intra-basement structures result in the fault having a lower dip.

The sub-vertical dip of the CSZ-related magnetic sources and southwest dip direction of the Lupa Fault (**Figure 3C**) also suggests that the deepest sections of the border fault could merge with the shear zone at the deeper crustal levels, although it would require a southwestward dip for the CSZ at depth. If this spatial and potentially kinematic relationship is true, we infer a depth-dependent partitioning of the control of structural inheritance on the early development of the Lupa border fault, such that the upper sections of the fault exploited the Katuma-Wakole Terrane boundary and structures in the Katuma Terrane, and the deepest section exploited the Chisi Shear Zone.

Intra-Basinal Faulting

The collocation and parallel trends of the KIF and CSZ suggest that the CSZ largely controlled the localization of the Karoo intra-basinal faulting (**Figure 4A**, **5A**). The prominence of NE-dip direction of the KIF faults (**Figure 4A**) suggests that the KIF exploited the NE-dipping metamorphic fabrics along the CSZ (**Figure 2A**). The confinement of the main Karoo-age rift fill between the Lupa Fault and CSZ (where present) (**Figure 5A**) indicates that the KIF cluster directly influenced the first-order sediment distribution during the early phases of extension. The Karoo-age basin is widest in the northwest where the CSZ is present (CSZ rotates from NW to NNW trend, away from the Lupa Fault), further indicating the influence of the CSZ and its geometry on the extent of the early rift-related depocenter (**Figure 4A**). The apparent confinement of earliest rift-related sediments also provides further age constraints on the timing of formation of the intra-basinal fault cluster. Overall, these observations indicate that the shear zone and terrane

boundary represent discrete zones of inherited mechanical weakness in the crust where brittle deformation was accommodated during the early stages of continental extension.

Early-Rift Paleotopography

The Karoo-age rift topography is likely dominated by the footwall uplift along the Lupa border fault in the northeastern basin margin (Van der Beek et al., 1998; Morley et al., 1999). However, the clustering of basement ridges along the submarine part of the CSZ, likely representative of early syn-rift erosionally-resistant topography, is consistent with observations of topographic ridges along the CSZ onshore (**Figure 1B** and **Supplementary Figure S2A**). Elsewhere, prominent, erosionally-resistant topographic ridges define the surface expression of the Mughese Shear Zone (Kolawole et al., 2018), which appears to be a southeast continuation of the CSZ trend in the Karonga Basin (**Figure 1B**). Such ridges represent elevated topographic domains that may represent important sediment sources (e.g., Gawthorpe and Leeder, 2000). Thus, the chain of ridges along the CSZ represents intra-basinal sediment-source regions near the southwestern basin margin, indicating an additional importance of the CSZ during initial sedimentation in the Rukwa Rift.

Early-Rift Distribution of Extension

Our analyses show that within the northwestern section of the basin, Karoo-age tectonic extension was largely accommodated on both the CSZ-related intra-basinal faults (KIF) and the Lupa border fault (**Figures 4C,D**); in fact, during this initial phase of extension, more strain was accommodated on intra-basinal faults than the (developing) border fault. In contrast, southeast of the CSZ termination beneath the basin (or at significantly large separation distance), extension was primarily accommodated along the Lupa border fault. These suggest that during the early phase of rifting, there was a competition for extensional strain localization between the CSZ and the Katuma-Wakole terrane boundary in the northwest. Due to the southward increase in separation between the CSZ and Katuma-Wakole/Lupa-Mbozi terrane boundaries, and the absence of CSZ in the southeastern section of the Karoo-age basin, tectonic extension was then primarily accommodated along the Lupa Fault, which ultimately exploited the Lupa-Mbozi terrane boundary (**Figures 4C,D**). The significant increase in the Lupa Fault Top-basement offset just south of the CSZ termination (**Figure 4C**) also supports the dominant localization of extensional strain on the border fault in the southeastern section of the basin where the CSZ-related KIF is absent. Thus, we suggest that the CSZ strongly controlled the early-phase distribution of tectonic extension along the Rukwa Rift.

This along-rift partitioning of strain resulted in a lateral change of the overall Karoo-age rift geometry from a shallower graben in the northwest, to a deep half graben in the southeast. This along-rift change in rift geometry was previously thought to be primarily related to variation in border fault strain accommodation controlled by oblique extensional kinematics (Morley et al., 1992). Also, the obliquity of the intra-basinal faults relative to the border fault trend (**Figures 4B**, **5B**) has been used as a basis for inferring pull-apart and oblique extension kinematics for the rift development (Kilembe and Rosendahl, 1992; Chattopadhyay and Chakra, 2013). However, detailed structural interpretation from seismic reflection data revealed a minor component of strike-slip-related deformation along the rift (Morley et al., 1999). Thus, we here suggest that the observed obliquity of intra-basinal faults to border fault trend is primarily controlled by the focusing of extensional strain along prominent pre-existing discrete zones of basement weakness during the early phase of rifting. The geometrical alignment of the intra-basinal faults to the CSZ trend could have been influenced by local stress rotation (SHmax) into CSZ-parallel/sub-parallel trend during the early rift phase; a mechanism that has been proposed to explain the influence of weak basement fabrics on the present-day orthogonal extension kinematics along the Rukwa Rift (Morley, 2010). This resolves a long-standing controversy related to the geometrical structure and kinematics of rift faulting in the Rukwa Rift. Elsewhere along the Rukwa Trend, farther northwest of the Rukwa Rift, the Busindi border fault of the Luama Rift exploited the NW continuation of the CSZ (**Figures 1B**, **3D**), demonstrating the broader influence of the CSZ on the development of the other Karoo rift segments of the Rukwa Trend. In the Tanganyika Rift, the along-rift distribution of tectonic extension is influenced by the lateral variation of the inherited crustal rheology (Wright et al., 2020), further demonstrating the strong influence of structural inheritance on the early localization and distribution of extension along continental rifts.

Post-Karoo Rift Architecture

Geological and geophysical evidence for post-Karoo strike-slip deformation has been recorded along the Rukwa Rift (Wheeler and Karson, 1994; Delvaux et al., 2012; Heilman et al., 2019), possibly associated with a plate-scale compressional event (Daly et al., 1991; Delvaux et al., 2021). However, the analyses of seismic reflection profiles across the Rukwa Rift show that post-Karoo strike-slip or compressional deformation in the basin was very minor (Morley et al., 1999). Therefore, it is not likely that the plate-scale compressional event significantly altered the karoo-age fault patterns in the Rukwa Rift.

The CSZ and adjacent terrane boundaries continued and still continue to influence rift geometry long after the Karoo phase of extension. First, the mean trend of the rift faults, all combined (Permian to Quaternary), generally remains the same as the Karoo-age mean intra-basinal fault trend (**Figures 2Bi–ii**; Morley et al., 1992; Kilembe and Rosendahl, 1992). Second, the along-strike projection of the CSZ southeast of its magnetic anomaly termination is coincident with location and orientation of the Msongano Trough, which represents a southeastward continuation of the Rukwa Rift during the Cenozoic rifting phase (**Figure 5A**). We suggest that the extension of the KIF to the CSZ termination zone already established the incipient graben of the Msongano Trough during the Karoo rifting phase (**Figure 5A**, **6**). We suggest that the CSZ and its colinear Mughese Shear Zone, along which the Msongano Trough developed (**Figure 5A**), both constitute coupled discrete zones of weakness in the basement that accommodated the continuous lateral southeastward propagation of the KIF as a narrow graben during the post-Karoo phases of extension. Thus, the present-day bifurcation of the Rukwa Rift into the Songwe and Msongano troughs

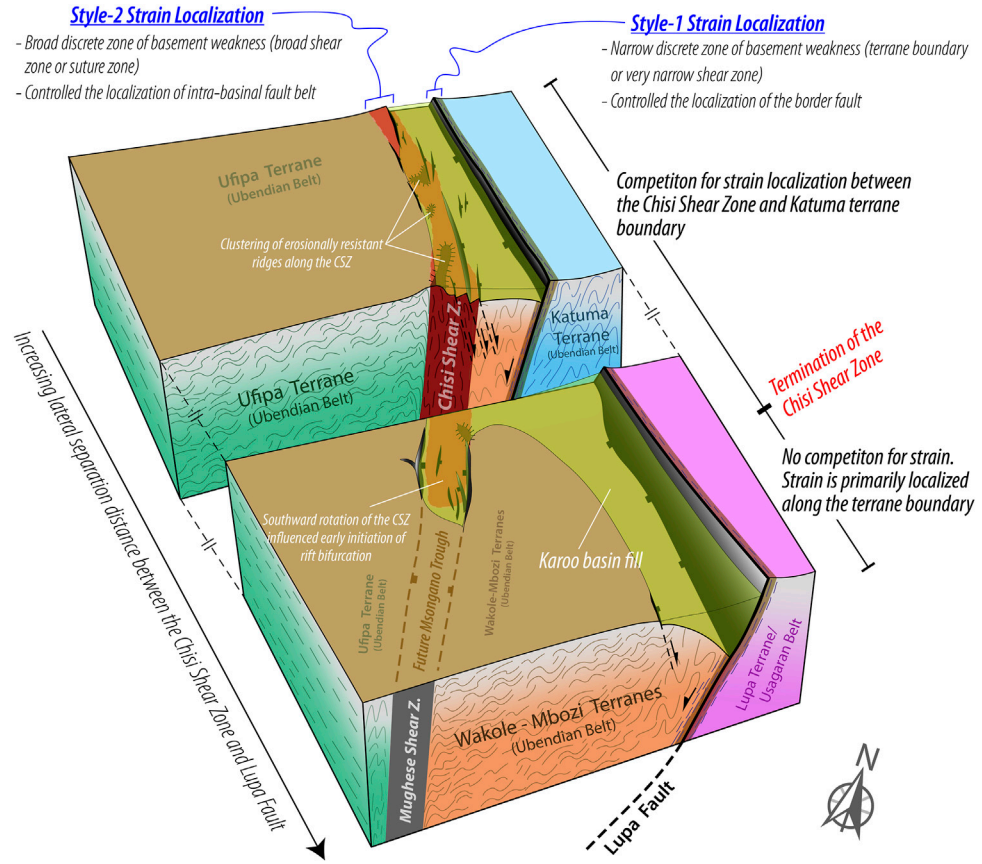

FIGURE 6 | Cartoon illustrating some of the key observations in this study, showing how the structure of discrete zones of basement weakness influenced strain localization styles and along-rift distribution of extension during the early phase of tectonic extension in the Rukwa Rift.

(**Figure 1C**) was established during the very earliest stage of rifting. In addition, the southeastern border fault of the Rukwa Rift (Ufipa Fault; **Figure 2B**) which developed in the Cenozoic, largely exploited the tectonic fabrics of the Ufipa Terrane (Heilman et al., 2019).

More broadly, in the Cenozoic Tanganyika Rift, located northwest of the Rukwa Rift (**Figures 1A,B**), the rift basin is segmented (Sander and Rosendahl, 1989; Muirhead et al., 2019; Wright et al., 2020). The segmentation occurs at the proposed splay of the CSZ magnetic lineaments (**Figure 1B**). The Ruzizi and East Kigoma sub-basins are separated by the northern section of the East CSZ splay, whereas the East and West Kigoma sub-basins are separated by the southern section of the East Splay, and the West Kigoma and Kalemie Sub-basins are separated by the CSZ segment extending into the Luama Rift. In essence, not only did the CSZ influence the early-phase architecture of the Karoo-age Rukwa and Luama rift basins, but also the structure of the relatively younger Tanganyika Rift. The spatial collocation of Cenozoic hydrothermal vents within different sections of the CSZ in the Tanganyika Rift (diamond symbols in **Figure 1B**) highlights the deep reaches of the rift faults that exploited the basement weakness of the shear zone.

Implications for Early-Stage Architecture of Continental Rift Basins

Our study of the Rukwa Rift suggests that early-phase rift strain is significantly accommodated by intra-basinal faults, contrary to observations in some other juvenile magma-poor continental rifts (e.g., Nixon et al., 2016; Muirhead et al., 2019), but it is localized onto pre-existing structures. The early-phase strain localization in the Rukwa Rift occurred via two different styles with associated deformational mechanisms. One style (Style-1 strain localization) is the localization of a large rift fault onto a narrow discrete zone of basement weakness, such as prominent basement terrane boundaries (this study), pre-existing fault zones, and narrow ductile shear zones, in which case the structures of the weak zone and the fabrics of the adjacent basement may influence the fault geometry (**Figure 6**). An example of this is the development of the Livingstone Fault in the Karonga Basin, northern Malawi Rift (Wheeler and Karson, 1989), the Thyolo border fault in the Shire Rift Zone (Wedmore et al., 2020b), and splay faulting at a terrane boundary during the Late Cretaceous extension between Zealandia and Australia (Phillips and McCaffrey, 2019b). A second style (Style-2 strain localization) is the localization of a fault cluster (or fault belt) onto a broader discrete zone of

basement weakness, such as wide pre-rift shear zones or subduction suture zones (this study), in which case the individual fault strands may exploit the smaller-scale mechanical heterogeneities within the broad zone of basement weakness (**Figure 6**). An example of Style-2 localization is the development of a fault cluster along the western margin of the Karonga Basin, northern Malawi Rift, where the fault cluster exploited the >15 km-wide Precambrian Mughese Shear Zone (Kolawole et al., 2018). Therefore, we hypothesize that during the earliest stages of continental rifting, strain initially localizes on pre-existing zones of crustal weakness, and the style of localization may be associated with the type of the inheritance and character of the inherited structure. In addition, we note that whilst pre-existing structure may exert a strong control on strain distribution and localization during the earliest phase of continental extension, the established early rift template, may persist through the subsequent phases of the stretching stage of rifting (i.e., prior to the necking and hyper-extension stages).

CONCLUSION

We investigated the distribution of strain during the earliest phase of extension in the Rukwa Rift, a Phanerozoic multiphase magma-poor rift basin that developed along the trend of the Precambrian Chisi Shear Zone (CSZ) and terrane boundary shear zones in East Africa.

Here are our main findings:

1) During the earliest phase of extension, although the border fault, Lupa Fault exploited the colinear Katuma-Wakole and Lupa-Mbozi terrane boundaries, the CSZ facilitated the early localization and development of a prominent intra-basinal fault cluster.
2) In the northwestern section of the rift, the presence and proximity of the CSZ and the Katuma-Wakole terrane boundary facilitated a competition for strain localization between the CSZ and the adjacent terrane boundary, whereas in the southeastern section where the CSZ is either absent or at a significantly large distance, strain is primarily localized along the Lupa-Mbozi terrane boundary.
3) The along-rift variation in early phase rift geometry, rift margin paleotopography, and depocenter extents were largely controlled by the CSZ.
4) The along-rift distribution of early-phase extension was largely influenced by structural inheritance, such that in the northwestern section of the rift, significant extension is accommodated by the intra-basinal fault cluster that exploited the CSZ, whereas in the southeast, extension is largely accommodated by the Lupa border fault.
5) Two styles of early-phase strain localization in which a.) strain is localized onto a narrow discrete zone of basement weakness in the form of a large rift fault (Style-1 strain localization), and b.) strain is localized onto a broad discrete zone of basement weakness in the form of a fault cluster (Style-2 strain localization).
6) Whilst pre-existing basement structure may exert the strong control on strain distribution and localization during the earliest phase of extension, the established early rift template, may persist through the subsequent phases of the stretching stage of rifting.

Our findings offer a window into the early stages of continental extension along a young evolving magma-poor rift, where early strain is not accommodated only by the border fault as suggested by existing magma-poor early-rift models; instead, strain focuses relatively quickly on a large border fault and intra-basinal fault clusters that follow pre-existing intra-basement structures. This study reveals the influence of structural inheritance on early-phase rift geometry and along-rift partitioning of strain along magma-poor rift basins.

DATA AVAILABILITY STATEMENT

Publicly available datasets were analyzed in this study. This data can be found here: The SADC aeromagnetic data is archived at http://sadc-gla.org/SADC/home.html. We have provided uninterpreted versions of the aeromagnetic data in our **Supplementary Material** document. The 2-D seismic reflection images of the Rukwa Rift shown in this study other 2-D seismic datasets from the basin are archived in the appendix of Morley et al. (1999), AAPG).

AUTHOR CONTRIBUTIONS

FK conceptualized and developed the project. FK and TP conducted the analyses and investigations. FK wrote the manuscript. TP, CJ, and EA edited and improved the manuscript. All authors read and approved the final manuscript.

ACKNOWLEDGMENTS

We thank reviewers Giacomo Corti and Damien Delvaux for their insightful comments that have helped to improve the quality of our paper, and we also thank the editor, James Muirhead for handling our paper. We thank Obeid Lemna for providing useful comments on the preprint of the initial version of the manuscript uploaded on EarthArXiv. We thank the South African Council for Geoscience for providing the aeromagnetic data to EA used in this study. The aeromagnetic data is archived at http://sadc-gla.org/SADC/home.html. We have provided uninterpreted versions of the aeromagnetic data in our **Supplementary Material** document. The seismic reflection cross-section of the Rukwa Rift shown in this study (**Figure 2C**) and other 2-D seismic datasets from the basin are archived in the appendix of Morley et al. (1999).

SUPPLEMENTARY MATERIAL

The Supplementary Material for this article can be found online at: https://www.frontiersin.org/articles/10.3389/feart.2021.707869/full#supplementary-material

REFERENCES

Agostini, A., Bonini, M., Corti, G., Sani, F., and Mazzarini, F. (2011). Fault Architecture in the Main Ethiopian Rift and Comparison with Experimental Models: Implications for Rift Evolution and Nubia–Somalia Kinematics. *Earth Planet. Sci. Lett.* 301 (3-4), 479–492. doi:10.1016/j.epsl.2010.11.024

Baranov, V. (1957). A New Method for Interpretation of Aeromagnetic Maps: Pseudo-gravimetric Anomalies. *Geophysics* 22 (2), 359–382. doi:10.1190/1.1438369

Boniface, N., Schenk, V., and Appel, P. (2012). Paleoproterozoic Eclogites of MORB-type Chemistry and Three Proterozoic Orogenic Cycles in the Ubendian Belt (Tanzania): Evidence from Monazite and Zircon Geochronology, and Geochemistry. *Precambrian Res.* 192-195, 16–33. doi:10.1016/j.precamres.2011.10.007

Boniface, N., and Schenk, V. (2012). Neoproterozoic Eclogites in the Paleoproterozoic Ubendian belt of Tanzania: Evidence for a Pan-African Suture between the Bangweulu Block and the Tanzania Craton. *Precambrian Res.* 208-211, 72–89. doi:10.1016/j.precamres.2012.03.014

Boven, A., Theunissen, K., Sklyarov, E., Klerkx, J., Melnikov, A., Mruma, A., et al. (1999). Timing of Exhumation of a High-Pressure Mafic Granulite Terrane of the Paleoproterozoic Ubende belt (West Tanzania). *Precambrian Res.* 93 (1), 119–137. doi:10.1016/s0301-9268(98)00101-6

Buiter, S. J. H., and Torsvik, T. H. (2014). A Review of Wilson Cycle Plate Margins: a Role for Mantle Plumes in continental Break-Up along Sutures? *Gondwana Res.* 26, 627–653. doi:10.1016/j.gr.2014.02.007

Chattopadhyay, A., and Chakra, M. (2013). Influence of Pre-existing Pervasive Fabrics on Fault Patterns during Orthogonal and Oblique Rifting: an Experimental Approach. *Mar. Pet. Geology.* 39 (1), 74–91. doi:10.1016/j.marpetgeo.2012.09.009

Chorowicz, J. (2005). The East African Rift System. *J. Afr. Earth Sci.* 43 (1-3), 379–410. doi:10.1016/j.jafrearsci.2005.07.019

Cowie, P. A., Underhill, J. R., Behn, M. D., Lin, J., and Gill, C. E. (2005). Spatio-Temporal Evolution of Strain Accumulation Derived from Multi-Scale Observations of Late Jurassic Rifting in the Northern North Sea: A Critical Test of Models for Lithospheric Extension. *Earth Planet. Sci. Lett.* 234 (3-4), 401–419.

Daly, M. C., Chorowicz, J., and Fairhead, J. D. (1989). Rift basin Evolution in Africa: The Influence of Reactivated Steep Basement Shear Zones. *Geol. Soc. Lond. Spec. Publications* 44 (1), 309–334. doi:10.1144/gsl.sp.1989.044.01.17

Daly, M. C. (1988). Crustal Shear Zones in Central Africa: a Kinematic Approach to Proterozoic Tectonics. *Episodes* 11 (1), 5–11. doi:10.18814/epiiugs/1988/v11i1/003

Daly, M. C., Lawrence, S. R., Kimun'a, D., and Binga, M. (1991). Late Palaeozoic Deformation in central Africa: a Result of Distant Collision? *Nature* 350 (6319), 605–607. doi:10.1038/350605a0

Delvaux, D. (2001). *Karoo Rifting in Western Tanzania: Precursor of Gondwana Breakup. Contributions to Geology and Paleontology of Gondwana in Honor of Helmut Wopfner:*. Cologne: Geological Institute, University of Cologne, 111–125.

Delvaux, D., Kervyn, F., Macheyeki, A. S., and Temu, E. B. (2012). Geodynamic Significance of the TRM Segment in the East African Rift (W-Tanzania): Active Tectonics and Paleostress in the Ufipa Plateau and Rukwa basin. *J. Struct. Geology.* 37, 161–180. doi:10.1016/j.jsg.2012.01.008

Delvaux, D., Maddaloni, F., Tesauro, M., and Braitenberg, C. (2021). The Congo Basin: Stratigraphy and Subsurface Structure Defined by Regional Seismic Reflection, Refraction and Well Data. *Glob. Planet. Change* 198, 103407. doi:10.1016/j.gloplacha.2020.103407

Dewey, J., and Spall, H. (1975). Pre-Mesozoic Plate Tectonics: How Far Back in Earth History Can the Wilson Cycle Be Extended? *Geol* 3, 422–424. doi:10.1130/0091-7613(1975)3<422:ppthfb>2.0.co;2

Ebinger, C. (2005). Continental Break-Up: the East African Perspective. *Astron. Geophys.* 46 (2), 2–16. doi:10.1111/j.1468-4004.2005.46216.x

Ganbat, A., Tsujimori, T., Boniface, N., Pastor-Galán, D., Aoki, S., and Aoki, K. (2021). Crustal Evolution of the Paleoproterozoic Ubendian Belt (SW Tanzania) Western Margin: A Central African Shield Amalgamation Tale. *Gondwana Res.* 91, 286–306. doi:10.1016/j.gr.2020.12.009

Gawthorpe, R. L., and Leeder, M. R. (2008). Tectono-sedimentary Evolution of Active Extensional Basins. *Basin Res.* 12 (3-4), 195–218. doi:10.1111/j.1365-2117.2000.00121.x

Hayward, N. J., and Ebinger, C. J. (1996). Variations in the along-axis Segmentation of the Afar Rift System. *Tectonics* 15 (2), 244–257. doi:10.1029/95tc02292

Heilman, E., Kolawole, F., Atekwana, E. A., and Mayle, M. (2019). Controls of Basement Fabric on the Linkage of Rift Segments. *Tectonics* 38 (4), 1337–1366. doi:10.1029/2018tc005362

Hodgson, I., Illsley-Kemp, F., Gallacher, R. J., Keir, D., Ebinger, C. J., and Mtelela, K. (2017). Crustal Structure at a Young continental Rift: A Receiver Function Study from the Tanganyika Rift. *Tectonics* 36 (12), 2806–2822. doi:10.1002/2017tc004477

Kilembe, E. A., and Rosendahl, B. R. (1992). "Structure and Stratigraphy of the Rukwa Rift," in *Tectonophysics*. Editors C. J. Ebinger, H. K. Gupta, and L.O. Nyambok (Nairobi, Kenya: Seismology and Related Sciences in Africa), 209, 143–158. doi:10.1016/0040-1951(92)90016-y

Klerkx, J., Theunissen, K., and Delvaux, D. (1998). Persistent Fault Controlled basin Formation since the Proterozoic along the Western Branch of the East African Rift. *J. Afr. Earth Sci.* 26 (3), 347–361. doi:10.1016/s0899-5362(98)00020-7

Kolawole, F., Atekwana, E. A., Laó-Dávila, D. A., Abdelsalam, M. G., Chindandali, P. R., Salima, J., et al. (2018). Active Deformation of Malawi Rift's north basin Hinge Zone Modulated by Reactivation of Preexisting Precambrian Shear Zone Fabric. *Tectonics* 37 (3), 683–704. doi:10.1002/2017tc004628

Kolawole, F., Atekwana, E. A., Malloy, S., Stamps, D. S., Grandin, R., Abdelsalam, M. G., et al. (2017). Aeromagnetic, Gravity, and Differential Interferometric Synthetic Aperture Radar Analyses Reveal the Causative Fault of the 3 April 2017Mw6.5 Moiyabana, Botswana, Earthquake. *Geophys. Res. Lett.* 44 (17), 8837–8846. doi:10.1002/2017gl074620

Lemna, O. S., Stephenson, R., and Cornwell, D. G. (2019). The Role of Pre-existing Precambrian Structures in the Development of Rukwa Rift Basin, Southwest Tanzania. *J. Afr. Earth Sci.* 150, 607–625. doi:10.1016/j.jafrearsci.2018.09.015

Lenoir, J. L., Liégeois, J.-P., Theunissen, K., and Klerkx, J. (1994). The Palaeoproterozoic Ubendian Shear belt in Tanzania: Geochronology and Structure. *J. Afr. Earth Sci.* 19 (3), 169–184. doi:10.1016/0899-5362(94)90059-0

Morley, C. K., Cunningham, S. M., Harper, R. M., and Wescott, W. A. (1992). Geology and Geophysics of the Rukwa Rift, East Africa. *Tectonics* 11 (1), 69–81. doi:10.1029/91tc02102

Morley, C. K. (2010). Stress Re-orientation along Zones of Weak Fabrics in Rifts: An Explanation for Pure Extension in 'oblique' Rift Segments? *Earth Planet. Sci. Lett.* 297 (3-4), 667–673. doi:10.1016/j.epsl.2010.07.022

Morley, C. K., Wescott, W. A., Harper, R. M., and Cunningham, S. M. (1999). Geology and Geophysics of the Rukwa Rift. Geoscience of Rift Systems-Evolution of East Africa. *AAPG Stud. Geology.* 44, 91–110.

Muirhead, J. D., Kattenhorn, S. A., Lee, H., Mana, S., Turrin, B. D., Fischer, T. P., et al. (2016). Evolution of Upper Crustal Faulting Assisted by Magmatic Volatile Release during Early-Stage continental Rift Development in the East African Rift. *Geosphere* 12, 1670–1700. doi:10.1130/ges01375.1

Muirhead, J. D., Wright, L. J. M., and Scholz, C. A. (2019). Rift Evolution in Regions of Low Magma Input in East Africa. *Earth Planet. Sci. Lett.* 506, 332–346. doi:10.1016/j.epsl.2018.11.004

Naliboff, J. B., Buiter, S. J., Péron-Pinvidic, G., Osmundsen, P. T., and Tetreault, J. (2017). Complex Fault Interaction Controls continental Rifting. *Nat. Commun.* 8 (1), 1–9. doi:10.1038/s41467-017-00904-x

Nixon, C. W., McNeill, L. C., Bull, J. M., Bell, R. E., Gawthorpe, R. L., Henstock, T. J., et al. (2016). Rapid Spatiotemporal Variations in Rift Structure during Development of the Corinth Rift, central Greece. *Tectonics* 35 (5), 1225–1248. doi:10.1002/2015tc004026

Osagiede, E. E., Rotevatn, A., Gawthorpe, R., Kristensen, T. B., Jackson, C. A.-L., and Marsh, N. (2020). Pre-existing Intra-basement Shear Zones Influence Growth and Geometry of Non-colinear normal Faults, Western Utsira High-Heimdal Terrace, North Sea. *J. Struct. Geology.* 130, 103908. doi:10.1016/j.jsg.2019.103908

Phillips, T. B., Fazlikhani, H., Gawthorpe, R. L., Fossen, H., Jackson, C. A. L., Bell, R. E., et al. (2019a). The Influence of Structural Inheritance and Multiphase Extension on Rift Development, the Northern North Sea. *Tectonics* 38. doi:10.1029/2019tc005756

Phillips, T. B., and McCaffrey, K. J. W. (2019b). Terrane Boundary Reactivation, Barriers to Lateral Fault Propagation and Reactivated Fabrics: Rifting across the Median Batholith Zone, Great South Basin, New Zealand. *Tectonics* 38 (11), 4027–4053. doi:10.1029/2019tc005772

Ragon, T., Nutz, A., Schuster, M., Ghienne, J. F., Ruffet, G., and Rubino, J. L. (2019). Evolution of the Northern Turkana Depression (East African Rift System, Kenya) during the Cenozoic Rifting: New Insights from the Ekitale Basin (28-25.5 Ma). *Geol. J.* 54 (6), 3468–3488. doi:10.1002/gj.3339

Roberts, E. M., O'Connor, P. M., Stevens, N. J., Gottfried, M. D., Jinnah, Z. A., Ngasala, S., et al. (2010). Sedimentology and Depositional Environments of the Red Sandstone Group, Rukwa Rift Basin, Southwestern Tanzania: New Insight into Cretaceous and Paleogene Terrestrial Ecosystems and Tectonics in Sub-equatorial Africa. *J. Afr. Earth Sci.* 57 (3), 179–212. doi:10.1016/j.jafrearsci.2009.09.002

Roberts, E. M., Stevens, N. J., O'Connor, P. M., Dirks, P. H. G. M., Gottfried, M. D., Clyde, W. C., et al. (2012). Initiation of the Western branch of the East African Rift Coeval with the Eastern branch. *Nat. Geosci* 5 (4), 289–294. doi:10.1038/ngeo1432

Salem, A., Williams, S., Fairhead, J. D., Smith, R., and Ravat, D. (2007). Interpretation of Magnetic Data Using Tilt-Angle Derivatives. *Geophysics* 73 (1), L1–L10.

Schiffer, C., Doré, A. G., Foulger, G. R., Franke, D., Geoffroy, L., Gernigon, L., et al. (2019). Structural Inheritance in the North Atlantic. *Earth-Science Rev.*.

Sklyarov, E. V., Theunissen, K., Melnikov, A. I., Klerkx, J., Gladkochub, D. P., and Mruma, A. (1998). Paleoproterozoic Eclogites and Garnet Pyroxenites of the Ubende Belt (Tanzania). *Schweizerische Mineralogische Petrographische Mitteilungen* 78, 257–271.

Smirnov, V., Pentelkov, V., Tolochko, V., Trifan, M., and Zhukov, S. (1973). *Geology and Minerals of the central Part of the Western Rift. Tech. rep., Mineral and Resource Division, Dodoma, Tanzania*. Dodoma, Tanzania: Unpublished report of the geological mapping. doi:10.1007/978-1-4684-1968-9

Theunissen, K., Klerkx, J., Melnikov, A., and Mruma, A. (1996). Mechanisms of Inheritance of Rift Faulting in the Western branch of the East African Rift, Tanzania. *Tectonics* 15 (4), 776–790. doi:10.1029/95tc03685

Van der Beek, P., Mbede, E., Andriessen, P., and Delvaux, D. (1998). Denudation History of the Malawi and Rukwa Rift Flanks (East African Rift System) from Apatite Fission Track Thermochronology. *J. Afr. Earth Sci.* 26 (3), 363–385. doi:10.1016/s0899-5362(98)00021-9

Wang, L., Maestrelli, D., Corti, G., Zou, Y., and Shen, C. (2021). Normal Fault Reactivation during Multiphase Extension: Analogue Models and Application to the Turkana Depression, East Africa. *Tectonophysics* 811, 228870. doi:10.1016/j.tecto.2021.228870

Wedmore, L. N., Biggs, J., Williams, J. N., Fagereng, Å., Dulanya, Z., Mphepo, F., et al. (2020a). Active Fault Scarps in Southern Malawi and Their Implications for the Distribution of Strain in Incipient continental Rifts. *Tectonics* 39 (3), e2019TC005834. doi:10.1029/2019tc005834

Wedmore, L. N. J., Williams, J. N., Biggs, J., Fagereng, Å., Mphepo, F., Dulanya, Z., et al. (2020b). Structural Inheritance and Border Fault Reactivation during Active Early-Stage Rifting along the Thyolo Fault, Malawi. *J. Struct. Geology.* 139, 104097. doi:10.1016/j.jsg.2020.104097

Wheeler, W. H., and Karson, J. A. (1994). Extension and Subsidence Adjacent to a "weak" continental Transform: An Example from the Rukwa Rift, East Africa. *Geol* 22 (7), 625–628. doi:10.1130/0091-7613(1994)022<0625:easata>2.3.co;2

Wheeler, W. H., and Karson, J. A. (1989). Structure and Kinematics of the Livingstone Mountains Border Fault Zone, Nyasa (Malawi) Rift, Southwestern Tanzania. *J. Afr. Earth Sci. (and Middle East)* 8 (2-4), 393–413. doi:10.1016/s0899-5362(89)80034-x

Wilson, J. T. (1966). Did the Atlantic Close and Then Re-open? *Nature* 211, 676–681. doi:10.1038/211676a0

Wright, L. J. M., Muirhead, J. D., and Scholz, C. A. (2020). Spatiotemporal Variations in Upper Crustal Extension across the Different Basement Terranes of the Lake Tanganyika Rift, East Africa. *Tectonics* 39, e2019TC006019. doi:10.1029/2019tc006019

Conflict of Interest: FK is currently employed by BP America. However, this study and the initial manuscript drafts were developed and completed during his stay at the University of Oklahoma, prior to joining BP.

The remaining authors declare that the research was conducted in the absence of any commercial or financial relationships that could be construed as a potential conflict of interest.

Publisher's Note: All claims expressed in this article are solely those of the authors and do not necessarily represent those of their affiliated organizations, or those of the publisher, the editors and the reviewers. Any product that may be evaluated in this article, or claim that may be made by its manufacturer, is not guaranteed or endorsed by the publisher.

frontiers in Earth Science

HYPOTHESIS AND THEORY
published: 20 September 2021
doi: 10.3389/feart.2021.716630

On the Origin of Orphan Tremors and Intraplate Seismicity in Western Africa

T. Olugboji[1], Manoochehr Shirzaei[2], Yingping Lu[1,3], A. A. Adepelumi[4‡] and F. Kolawole[5†]*

[1]Department of Earth and Environmental Sciences, University of Rochester, Rochester, NY, United States, [2]Department of Geosciences, Virginia Tech, Blacksburg, VA, United States, [3]Goergen Institute for Data Science, University of Rochester, Rochester, NY, United States, [4]Department of Geology, OAU, Ife, Nigeria, [5]School of Geology and Geophysics, University of Oklahoma, Norman, OK, United States

On September 5–7, 2018, a series of tremors were reported in Nigeria's capital city, Abuja. These events followed a growing list of tremors felt in the stable intraplate region, where earthquakes are not expected. Here, we review available seismological, geological, and geodetic data that may shed light on the origin of these tremors. First, we investigate the seismic records for parent location of the orphan tremors using a technique suitable when a single-seismic station is available such as the Western Africa region, which has a sparse seismic network. We find no evidence of the reported tremors within the seismic record of Western Africa. Next, we consider the possibility of a local amplification of earthquakes from regional tectonics, reactivation of local basement fractures by far-field tectonic stresses, post-rift crustal relaxation, landward continuation of oceanic fracture zones, or induced earthquakes triggered by groundwater extraction. Our assessments pose important implications for understanding Western Africa's intraplate seismicity and its potential connection to tectonic inheritance, active regional tectonics, and anthropogenic stress perturbation.

Keywords: intraplate seismicity, tremors, interferometric synthetic aperture radar, structural inheritance, seismology, polarization, West Africa

OPEN ACCESS

Edited by:
Pascal Audet, University of Ottawa, Canada

Reviewed by:
Cynthia J. Ebinger, Tulane University, United States
Ahzegbobor Philips Aizebeokhai, Covenant University, Nigeria

****Correspondence:***
T. Olugboji
tolulope.olugboji@rochester.edu

†Present address:
F. Kolawole, BP America, Houston, TX, United States

‡Deceased

Specialty section:
This article was submitted to Solid Earth Geophysics, a section of the journal Frontiers in Earth Science

Received: *28 May 2021*
Accepted: *12 August 2021*
Published: *20 September 2021*

Citation:
Olugboji T, Shirzaei M, Lu Y, Adepelumi AA and Kolawole F (2021) On the Origin of Orphan Tremors and Intraplate Seismicity in Western Africa. Front. Earth Sci. 9:716630. doi: 10.3389/feart.2021.716630

INTRODUCTION

On September 5–7, 2018, a series of low-magnitude tremors hit Nigeria's capital city in Mpape, Abuja (Government Report, 2018). These events followed a series of earthquakes felt in the region since 1933, a stable, intraplate setting, otherwise not being earthquake-prone (Akpan and Yakubu, 2010; Akpan et al., 2014; Tsalha et al., 2015). This seismicity highlights the issue of seismic hazards in the Western Africa region and the need for an improved seismic monitoring network (Alaneme and Okotete, 2018; Afegbua et al., 2019). Nigeria is located in the southern part of the Neoproterozoic Trans-Saharan Mobile Belt, separating the Archean West African Craton, Congo Craton, and the Archean-Proterozoic Sahara Metacraton. Within this mobile belt, a large continent-scale system of elongate rift basins (aulacogens) developed during the Cretaceous, among which is located the Benue Trough on whose flank the Abuja city is located (**Figure 1A**). The extent of areas that historical seismicity felt in Nigeria encompasses regions within the failed rifts and areas of the exposed basement on the flanks of the rift basins (**Figure 1A**). Note that in the context of this paper, the term "tremor" is used in its general meaning with no particular emphasis on the processes that are attributed to a tremor activity, such as fluid migration and slow slip events, observed in some volcanic and tectonic settings (Rogers and Dragert, 2003; McCausland et al., 2005; Nadeau and Dolenc, 2005; Wech et al., 2012; Montgomery-Brown et al., 2013).

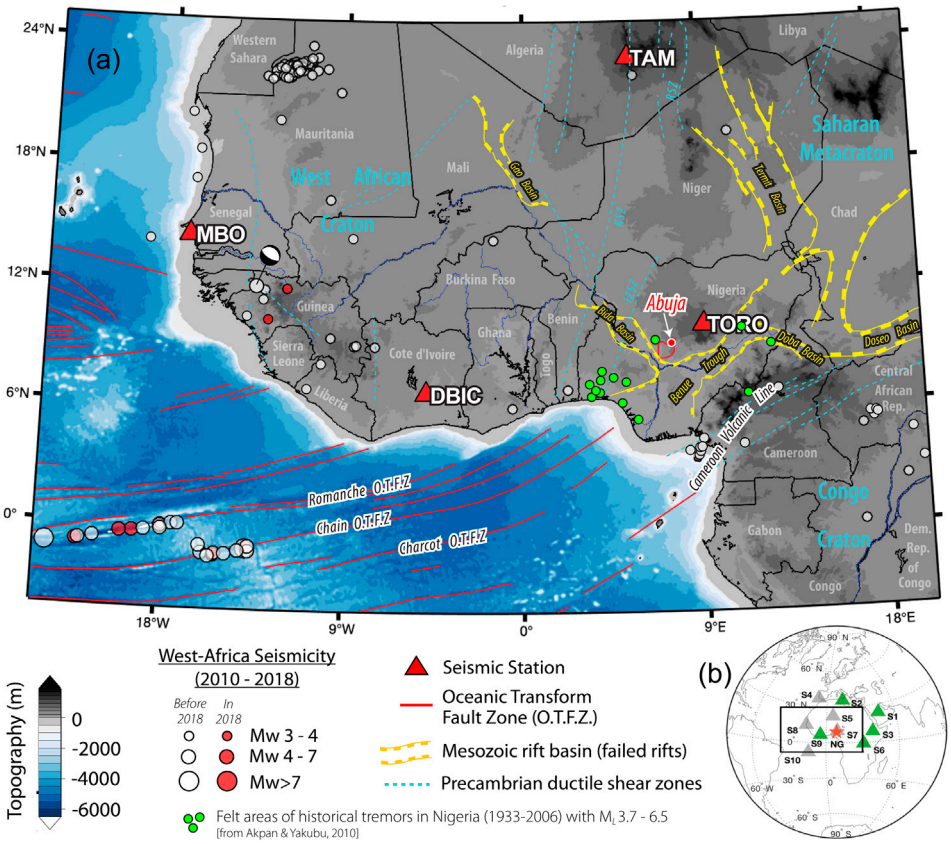

FIGURE 1 | (A) West African seismicity and tectonics, showing the epicenters (circles) for earthquakes in the past decade with M3.0 and greater, ocean fracture zones (red lines), and the seismic network (triangles) available for seismic detection. The 2018 earthquake events (red circles) are outside the Abuja area (red polygon north-east of TORO). OTFZ = oceanic transform fault zone (oceanic fracture zone). Tectonic structures are from Pérez-Díaz and Eagles (2014). The Mesosoic failed rifts shown in yellow lines define the West African Rift System. **(B)** Final selection of five stations (green triangle) used to search for an earthquake with a hypothetical epicenter (red star) located in Nigeria (NG). Gray stations do not pass the data quality selection criteria. Note that although TAM (S5) has good quality data, it is not used for single station detection since it only has one horizontal channel operating during the time of interest.

Compared to historical events, the series of shakings reported on September 2018 is located within the northern edge of Abuja. Because the capital city of Abuja is highly populated and relatively affluent, the considerable shaking (which was felt by most of the residents) was reported by the local news agencies and picked up by increased social media activity. Although the local population felt these events, very little observational evidence exists for the origin of the shaking and its connection to local geology, or regional tectonics. Here, we present the available geological and geophysical constraints that may offer clues about the shaking and examine the available seismic, geologic, and geodetic measurements and discuss several viable hypotheses regarding the origin of the felt shaking connected to the local or regional tectonics and anthropogenic activities. In particular, we evaluate the hypotheses that these events are due to 1) local amplification of earthquakes from regional tectonics, 2) distant teleseismic events large enough to be felt in Western Africa, 3) reactivation of local basement fractures by far-field tectonic stresses, post-rift crustal relaxation, or landward continuation of oceanic fracture zones, or 4) local anthropogenic activities such as groundwater extraction.

A comprehensive search of the global earthquake catalog in the decade leading up to September 2018 does not turn up any events located within Nigeria, although we point out that in the Western African region, these catalogs are incomplete below moment magnitude 4 (Kadiri and Kijko, 2021). In the region, most of the events are clustered around oceanic transform faults, with only a few inland earthquakes. Similarly, all earthquakes in 2018 occurred along the oceanic transform fault, except for a single event on February 2019, located in the country of Guinea about 10° northwest of Nigeria (**Figure 1**). Therefore, we examine the available seismic data from the Nigerian seismic network (Afegbua et al., 2011), supplementing them with seismic stations from the Western African region where long-term real-time monitoring is available. We conduct a rigorous search of the seismic record using a single-station detector method to examine the first two hypotheses, which investigate the possibility of the shaking being related to distant earthquakes and their ability to reactivate preexisting fault systems that may be preferentially primed for failure (Han et al., 2017; Neves et al., 2018). We then complement the seismic investigation with other geological and geophysical datasets. Surface geology and basement structure are

investigated using high-resolution satellite images and aeromagnetic data, and the observed patterns compared to the inferred prevailing stress field and the general trends dictated by the opening and closure of the failed rifts located close to the Abuja capital city. A final analysis explores the anthropogenic controls on earthquake nucleation and whether these may be related to the hydrological cycle within Nigeria. We measure surface deformation using Interferometric Synthetic Aperture Radar (InSAR) and correlate the observed patterns with the ongoing anthropogenic activities such as groundwater pumping and the addition of dams in the study area. Overall, the assessments presented in this study pose important implications for understanding Western Africa's intraplate seismicity and its connection to regional tectonics and local geology.

METHODS

Single-Station Seismology

Ideally, the detection of a low-magnitude local or regional event would require a proximal high-quality seismic array. Western Africa, on the other hand, has a sparse distribution of real-time seismic stations. Even recently deployed small-aperture seismic arrays located in Western Africa, e.g., Nigeria (Afegbua et al., 2011) and Ghana (Ahulu and Danuor, 2015), do not currently archive data on global waveform databases and only a few are real-time. Therefore, we use a single-station location method that is based on polarization analysis using eigen-decomposition of ground displacement (Vidale, 1986; Park et al., 1987; Bai and Kennett, 2000; Simons et al., 2009) for event detection, seismic phase identification (Earle, 1999), and source localization (Böse et al., 2017). Alternative methods such as beamforming analysis, which is widely applied to pin-pointing earthquake source direction (Rost, 2002; Rost et al., 2006; Nakata et al., 2019), are challenging to apply because of the sparsity of high-quality, continuously recording, and small-aperture seismic arrays present at regional distances to the location of the largest reported shaking.

The single-station location technique is based on the same principle for which polarization analysis is most commonly used, i.e., orienting seismometers on the bottom of the seafloor (Stachnik et al., 2012; Zha et al., 2013; Doran and Laske, 2017; Scholz et al., 2017) or identifying misoriented horizontal channels (Ojo et al., 2019). Used in this mode, the arrival direction (azimuth) and the distance of a seismic event can be inferred from a three-channel seismogram recorded on a single station on the African continent. The geographical orientation of the seismic channels is then determined, given a known arrival direction of a particular seismic phase (often the compression and Rayleigh waves). In the earthquake-location mode, however, the idea is reversed. We assume the channel orientations are known (or can be corrected for); then, in principle, we fix the source orientation by determining the azimuth of the incoming waves. The key idea is to identify the polarization of particular seismic phases which are parallel to the wave propagation (e.g., compressional and Rayleigh wave phases) and use this to determine the wave-arrival azimuth. A differential time between the first arriving compressional wave and other phases (e.g., S, Love, and Rayleigh), in conjunction with a given earth model, prescribes the epicentral distance and completes the process, providing coordinates of the earthquake.

The adaptation of polarization analysis for single-station event location (Magotra et al., 1987; Magotra et al., 1989; Frohlich and Pulliam, 1999; Agius and Galea, 2011; Böse et al., 2017) increases the likelihood of detecting earthquakes with smaller magnitudes. In our adaptation, we incorporate benefits from the coherence (Vidale, 1986) and covariance technique (Jurkevics, 1988; Schulte-Pelkum et al., 2004; Park and Ishii, 2018) and include multimode identification (Bai and Kennett, 2000; Bai and Kennett, 2001). Our idea bears some similarity to the technique proposed for locating Mars-quakes (Böse et al., 2017), or the identification of the source location of ambient seismic noise or micro-tremors (Koper and Hawley, 2010; Zha et al., 2013). We describe a successful application for locating the epicenter of moderate-to-large teleseismic earthquakes. We then describe the application to a few high-quality stations recording during the 3 days with the largest shaking, i.e., stations on the GEOSCOPE network (Roult et al., 2010), the Global Seismic Network (GSN) (Lay et al., 2002), and the Nigerian Seismic Network.

While single-station event location is sufficient for distinguishing between a teleseismic and a local/regional event, when more than one station is available, the uncertainty or bias (error) from a single-station detection can be improved by performing a second-stage association analysis (Ringdal and Husebye, 1982; Shearer, 1994; Ekström, 2006). This allows us to improve the confidence estimate for the location by comparing the estimated source locations from multiple stations when they are available. Suppose all the single-station locations agree (within uncertainty) that the hypothesized source location (Abuja, Nigeria) is not the epicenter of the detection, in that case, we can rule out this null hypothesis and explore the alternative hypothesis that the shaking is from a different source location (i.e., of teleseismic origin). We require only two stations to confirm detection for a particular source location. Application to the 360 polarization records derived from each of the five closest stations to Nigeria results in a space-time probability of a possible event detection (Böse et al., 2017) (see **Supplementary Appendix** for a detailed discussion of technique).

Structural Mapping From Aeromagnetic Data Analysis and Satellite Images

The largest shaking may have resulted from seismogenic slip on local faults or due to local amplification. To explore how local geology in and around Abuja may have contributed to significant shaking intensity, following standard practice, we analyze the subsurface structure and the spatial distribution of the sedimentary cover. The Abuja area is located in low magnetic latitude. Thus, we first perform a reduction of the magnetic data to the magnetic equator (RTE, e.g., Li and Oldenburg, 2001) using an IGRF 2005 model. This transformation corrects for the

skewness of the magnetic anomalies due to the oblique angles of magnetization at large distances from the magnetic pole.

We then upward-continue the RTE-corrected aeromagnetic grid to remove noise and apply a vertical derivative filter to better resolve the gradients that correspond to the geological structure. Further, we estimate the distribution of depths to the top of the magnetic sources (i.e., crystalline basement) using the Source Parameter Imaging (SPI) method (Smith et al., 2002; Smith and Salem, 2005). Although this technique has an accuracy of ±20%, it can reliably show the relative spatial pattern of the depth of the burial of the magnetized basement (e.g., Kolawole et al., 2018). Volcanic rocks are absent in the Abuja area; thus, the Precambrian metamorphic rocks and granitic intrusives define the primary magnetic basement. In order to identify the dominant structural trends associated with basement deformation (and possibly faulting) in the area, we manually digitize the linear traces defined by edges in the filtered (vertical derivative) aeromagnetic grid. Further, we map fracture systems in basement exposures in satellite images (Google Earth©) and compare with the aeromagnetic fabric trend to better constrain the dominant basement structures that may correspond to faulting.

InSAR Deformation Field

To map the surface deformation, we use 80 SAR images acquired in the ascending orbit of the Sentinel-1A/B C-band satellites between 2018/01/19 and 2020/09/05. We performed an advanced multitemporal SAR interferometric analysis to retrieve rates and time series of surface deformation over the study area. The analysis began with co-registering SLC images to a reference image, which includes a standard matching algorithm using a digital elevation model (DEM), precise orbital parameters, and amplitude images (Sansosti et al., 2006). For the Sentinel-1A/B datasets, the step mentioned above is followed by an enhanced spectral diversity (ESD) approach (Yagüe-Martínez et al., 2016; Shirzaei and Bürgmann, 2017). Using this dataset, we generate a set of high-quality interferograms, considering only those with short perpendicular and temporal baselines. We also apply a multi-looking operator of 32 and 6 pixels in range and azimuth to obtain a ground resolution cell of ~75 m × 75 m. To calculate and remove the effect of topographic phase and flat earth correction (Franceschetti and Lanari, 1999), we used a 1-arcsecond (~30 m) Shuttle Radar Topography Mission DEM (Farr et al., 2007) and precise satellite orbital information. To identify the elite (i.e., less noisy) pixels, we only consider pixels with an average temporal coherence larger than 0.65. In analogy to Global Navigation Satellite System (GNSS) stations, these elite pixels form a network of SAR observation points, for which we estimate the time series and rate of line-of-sight (LOS) surface deformation. To retrieve the absolute (unwrapped) phase values for sparsely distributed elite pixels, we applied a minimum cost flow (MCF) algorithm. Although the precise orbits are used, a few interferograms were still affected by a ramp-like signal, which was corrected by fitting a second order polynomial to their unwrapped phase (Shirzaei and Walter, 2011). We further applied several wavelet-based filters to correct for effects of spatially uncorrelated topography error and topography correlated atmospheric delay (Shirzaei and Bürgmann, 2012). Subsequently, we applied a re-weighted least square approach iteratively to invert the corrected measurement of the unwrapped phase at each elite pixel and solve the time series of the surface deformation. We further reduce the effect of residual atmospheric errors by applying a high pass filter based on continuous wavelet transform to the time series of surface deformation at each elite pixel. Finally, we estimate the long-term LOS deformation rates as the best-fitting line slope to the time series of surface deformation at each elite pixel.

DATA AND RESULTS

Earthquake Detection with a Sparse Network

We use the following station-selection criteria: 1) waveform data recorded during tremor activity archived and retrievable from a global waveform database, e.g., IRIS, 2) good back-azimuth coverage relative to Nigeria, 3) availability of three-channel seismograms necessary for polarization analysis, 4) high signal to noise ratio, and 5) correct orientations for the horizontal channels or new analysis reflecting the proper orientations (e.g., Ojo et al., 2019). Only five stations out of the ten initially selected pass our selection criteria, and their locations provide relatively good azimuthal coverage around Nigeria (see **Figure 1B** and **Tables 1**, **2**). We focus on the 3 days from September 5–7, 2018, when anecdotal reports agree on the strongest shaking in Nigeria, 1) three reports on September 5: ~13:30, 16:30, and 19:00 UTC, and 2) two on September 6 and 7: 01:30 and 05:30 UTC. We scan hour-long records of three-component seismograms at each station, allowing for a half-hour to extend detection duration. Our dataset results in 360 polarization records, representing 72-hour-long records (for the 3 days) at each of the five stations. A data quality check reveals that two of the five stations are particularly useful for seismic detection (i.e., G.TAM and G.DBIC). In particular, stations NJ.TORO, which the closest station to the main interest area, Abuja, is very noisy and is impractical for detection on its own (see **Figures 1A**, **2**). This analysis further highlights the challenge of earthquake location and the value of a single-station event detector.

Null Detection and Other Coincidences

We analyze the continuous data stream in hour-long sections during the 3 days of the largest reported shaking. In this 3-day scan, we detect a notable event in the hour following 18:00 UTC on September 5th with good SNR on most stations (**Figure 2**). Our attempt to associate the other tremor sequences to either a previously undetected global or regional event proved inconclusive (**Supplementary Figures S5A–D**). For the September 5 event, the stations detect P and S arrivals within only slight timing variations. We cross-reference our detection with the USGS earthquake catalog. The arrival time of the seismic phases is correctly matched with a source location that is consistent with the M6.6 Hokkaido Eastern Iburi, Japanese earthquake (**Figures 3**, **4B**). We note that this event is neither local nor regional (<30°) but clearly of teleseismic origin (compare **Figures 4A,B** with **Figure 3**).

TABLE 1 | Stations used to discriminate local and teleseismic events originating from Western Africa. Station G.TAM has only one horizontal channel, station II.ASCN is an island station, and station PM.PFVI is located in Portugal, but with very little propagation in the Atlantic Ocean. We include II.RAYN, which is a very quiet station, to broaden the back-azimuth coverage, even though it is technically in the Middle East.

No.	Code	Country	Coordinates (Lat., Lon.)	$X_{N\ angle}$[a]	Location code
1	**II-RAYN**	**Saudi Arabia**	**23.5224**, **45.5032**	**0°**	**00**
2	**MN-WDD**	**Malta**	**35.8373**, **14.5242**	**–3°**	**--**
3	**IU-FURI**	**Ethiopia**	**8.8952**, **38.6798**	**–1°**	**00**
4	PM-PFVI	Portugal	37.1328, –8.8268	6°	—
5	G-TAM	Algeria	22.7915, 5.5284	2°	00
6	**II-MBAR**	**Uganda**	**–0.6019**, **30.7382**	**0°**	**00**
7	NJ-TORO	Nigeria	10.055, 9.12	6°	—
8	G-MBO	Senegal	14.392, –16.9555	–8°	10
9	**GT-DBIC**	**Cote d'Ivoire**	**6.6702**, **–4.8566**	**15°**	**00**
10	II-ASCN	Ascension Island	–7.9327, –14.3601	–1°	00

*The bold indicates the five high-quality stations with very clear event detections (compare **Figure 3** with **Figure 2**).*
[a]*Proper orientation for the North Channel is retrieved from Ojo et al. (2019).*

TABLE 2 | Hypotheses test using distance and azimuth statistics. Low error confirms hypotheses H_1.

No.	Δ*	Φ*	ΔH_0	ΦH_0	ΔH_1	ΦH_1	$\varepsilon\Delta H_0$	$\varepsilon\Delta H_1$	$\varepsilon\Phi H_0$	$\varepsilon\Phi H_1$
1	85°	226°	38°	63°	79°	292°	123%	8%	258%	22%
2	86°	300°	27°	10°	88°	320°	218%	2%	2771%	6%
3	85°	294°	30°	88°	94°	286°	187%	9%	234%	3%
6	101°	272°	24°	112°	106°	284°	320%	5%	141%	5%
9	151°	270°	14°	261°	122°	320°	1007%	23%	4%	16%

H_0: Hypothesis that event is regional with epicenter in Nigeria.
H_1: Hypothesis that event is teleseismic with epicenter in Japan.
[Δ, Φ*]: Observed distance and azimuth (see **Figure 5**)*
*[ΔH, ΦH]: Calculated distance and azimuth assuming Hypothesis (compare **Figure 5** with **Figure 4**)*
ϵ: Normalized error between observation and hypothesis (low error confirms teleseismic hypotheses, H_1)

Despite the large station-earthquake distances (80–120°), we detect clear body-wave and surface-wave phases on the high-quality stations located around Nigeria. Even for the station at the largest epicentral distance (GT-DBIC), strong PP and SS phases are visibly detected and identified by our phase detector (**Figure 3** and **Table 2**).

The closest stations to the Japanese event are able to pick up at least one of the two direct P and S arrivals. For example, station II-RAYN demonstrates that our method provides effective picks for four of the incoming phases (*P, PP, S, SS, L,* and *R*: **Figure 3**). At stations MN-WDD and IU-FURI located at an epicentral distance less than 90°, we precisely identify all the main P and S arrivals, except for the reflected *SS* phase. At station II-MBAR, which is even further away (>90°) from the source location, our method is still able to detect the diffracted phases (*Pdiff* and *Sdiff*). However, at station GT-DBIC which is located ~120° from Japan, we are unable to detect the first-arriving diffracted *Pdiff* waves and only able to detect the diffracted *Sdiff* phase (with a slight time shift compared to the travel time predictions using the ak135 Earth model) and the reflected *PP* and *SS* phase. Association of the single-station detections shows that three of the five stations (WDD, FURI, and MBAR) provide a location match with an error <5°, while the other two stations (DBIC and RAYN) agree on the epicentral distance with some bias in the azimuth direction (**Figure 5**). This is clear evidence that the seismic event detected at all our stations is coincident in space and time with the teleseismic Japanese event reported by the global catalog and felt in Nigeria on September 5th.

Our search for a source-origin in Western Africa was inconclusive, which may suggest a low magnitude event that may have been attenuated before being detected by the regional seismic network. We emphasize that of the five events reported in anecdotal records; we are able to associate a single event to a teleseismic earthquake originating in Hokkaido, Japan, on September 5, 2018 (18:07 UTC). This event, from far-away Japan, triggered multiple landslides (~6,000) that lasted for a few minutes (Yamagishi and Yamazaki, 2018; Kameda et al., 2019; Shao et al., 2019; Wang et al., 2019). None of the other tremors in the sequence identified by anecdotal records are conclusively associated with either a local or teleseismic event. We explore briefly what explanation, if any, exists between the felt shaking and this landslide event. Alternatively, we evaluate how the local geology around Abuja could host the reactivation of existing faults. We also consider the possibility of induced earthquakes triggered by groundwater extraction.

Geological Framework from Aeromagnetic and Satellite Data

We integrate available surface and subsurface geological and geophysical datasets to constrain the first-order geological features in the Abuja area that could have localized or amplified ground shaking. First, we delineate satellite-scale fracture systems in basement outcrops using Google Earth

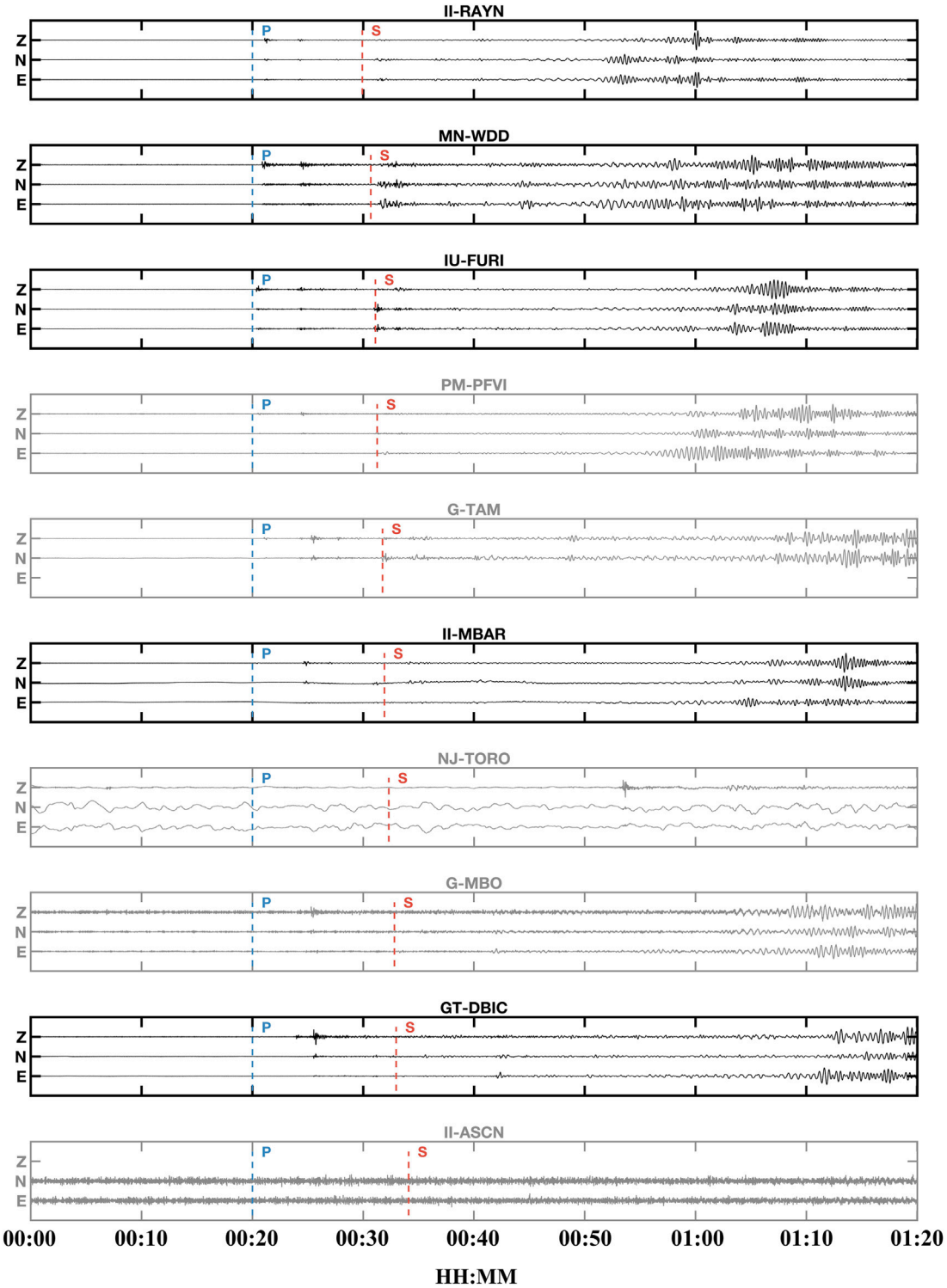

FIGURE 2 | Seismograms at stations in or close to Nigeria using an 80 min time window. Traces are amplitude normalized. Stations used for further analysis, marked in black, are those that pass the data selection criteria (green triangles in **Figure 1B**). In each trace, the first P (blue) and S (red) arrivals of the M6.6 Hokkaido event are shown with the station code to the top.

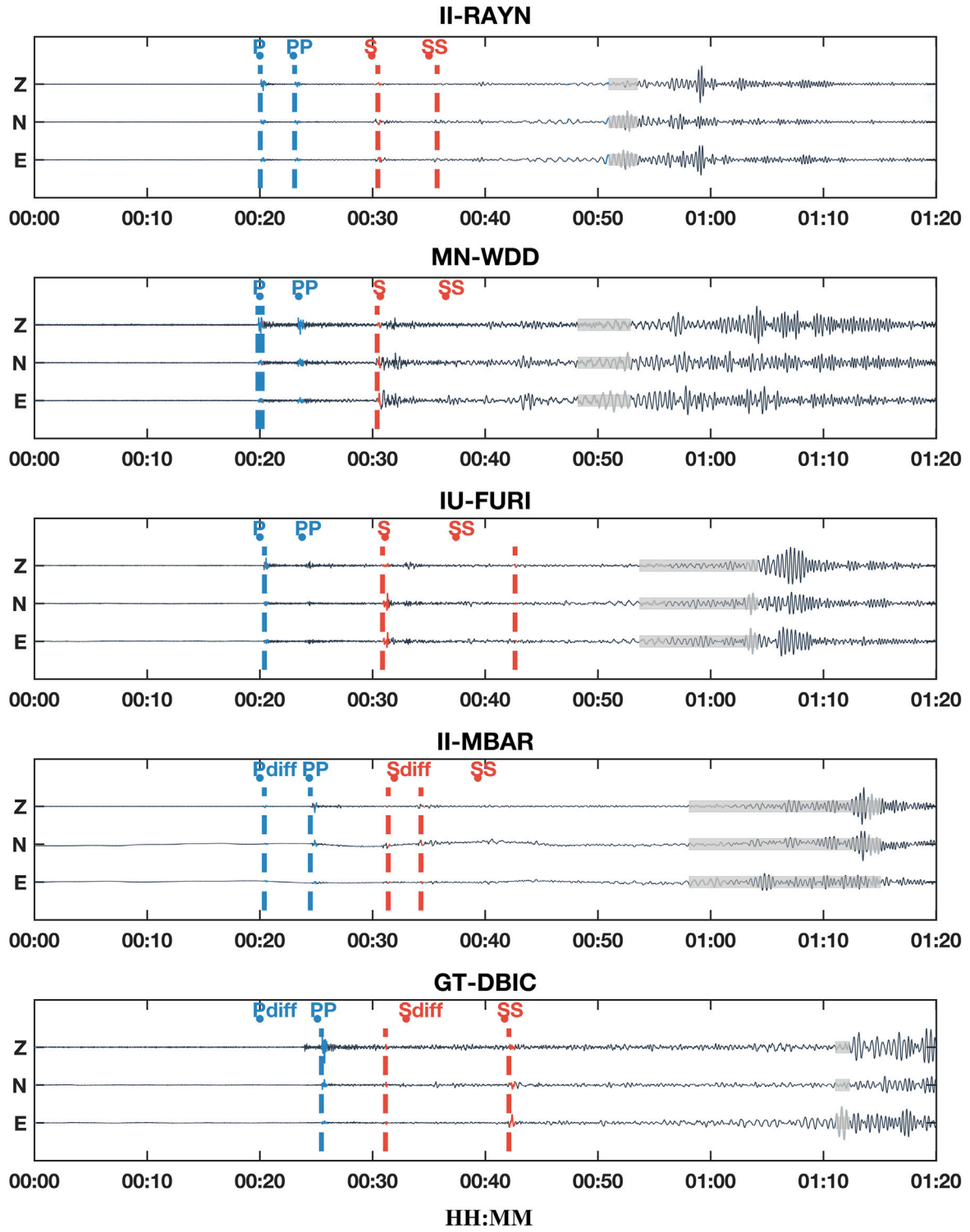

FIGURE 3 | Phase detection using polarization analysis applied to data recorded at the five high-quality stations during the Hokkaido event of September 5, 2018. The waveforms are for an 80 min-long time window, where time 0:00 is 20 min before the P arrival at each station following the event origin. The detected arrival of P and S waves is marked with blue and red dashed lines, respectively, while the first arriving linearly polarized surface wave is shaded in gray. The predicted arrival time calculated using the earthquake parameters and an earth model is indicated with dots and labels indicating the phase.

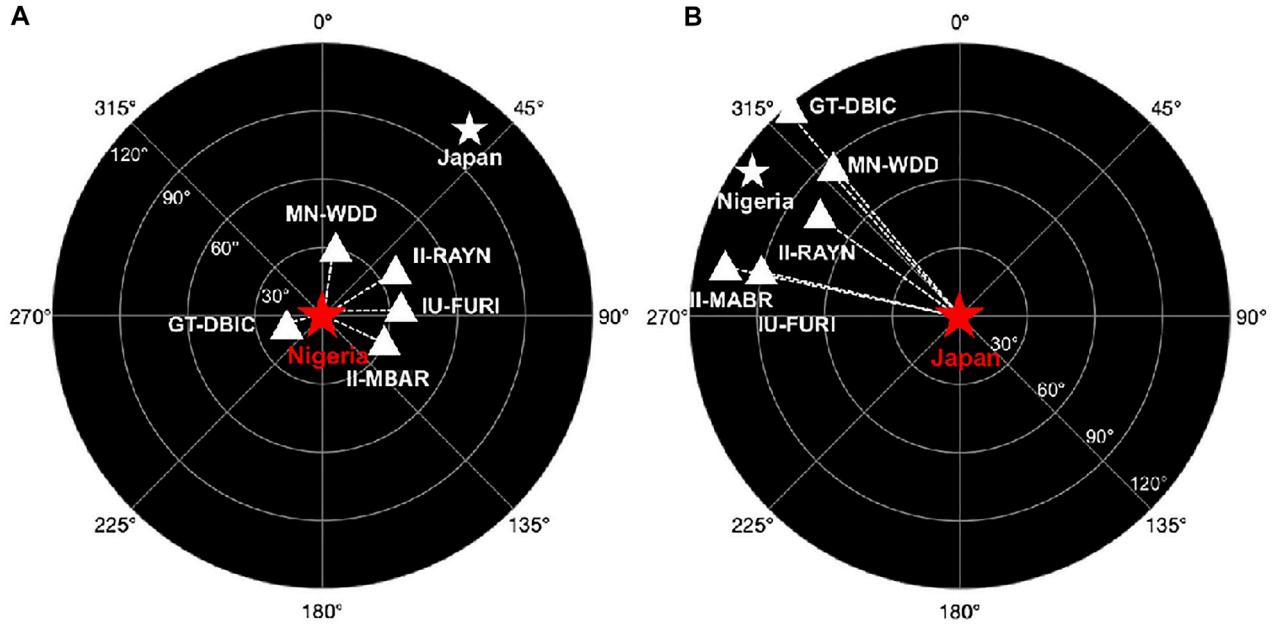

FIGURE 4 | Station locations relative to two hypothetical epicenters (star). **(A)** For a local or regional event originating from Nigeria or within Western Africa, all stations are expected to be within 30° of the event location (red star). **(B)** For the Hokkaido event, distance is 60–120° and azimuth 270–320° (compare **Figure 5**).

satellite images at a spatial resolution of 5 m (e.g., Kolawole et al., 2019). Then, we utilize high-resolution aeromagnetic data first to map sub surface structural fabrics in order to obtain information on the potential trends of fault lineaments in the crystalline basement and then to model the distribution and thickness of the sedimentary over-burden (e.g., Grauch and Hudson, 2007; Kolawole et al., 2018). The aeromagnetic data used in this study were acquired country-wide between 2005 and 2007 by the Nigerian Geological Survey Agency (NGSA), with 500 m line spacing and 80 m mean terrain clearance. The aeromagnetic data were provided as a grid of 100 m cell size.

Delineated Geological Structures in the Abuja Area

The satellite-scale fracture systems in the basement outcrops, mapped in the satellite images of the Abuja area (**Figures 6A,B**), show dominant trends of 049° ± 3.6° (NE-SW) and 136° ± 3.7°(NW-SE) (**Figure 6C**). Also, the larger-scale basement fabrics, delineated in filtered aeromagnetic data (**Figure 6D**), show dominant trends of 048° ± 6.4° (NE-SW), 124° ± 6.1° (NW-SE), and 086° ± 5.4° (E-W) (**Figure 6E**). Further, our depth-to-basement map, generated from the SPI transform of the aeromagnetic data (**Figures 6F,G**), shows that most of the Abuja area and mainly the areas where the tremor was felt are located within a small sedimentary basin. The thickness of this sedimentary cover ranges between ~200 and 800 m (**Figure 6G**). Although the three prominent trends (NE, NW, and E-W) can be observed in the northern half of the area where basement outcrops dominate, the NE-trending lineaments appear to dominate the southern part where the basin is located (**Figure 6D**).

InSAR Ground Deformation Map

Figure 7 shows the rate of LOS displacement field and selected time series at the sites of rapid subsidence. The negative values (cool colors) correspond with movement away from satellite, hereafter, subsidence. The map is characterized by widespread subsidence up to 35 mm/yr. Roughly the zone of subsidence is bounded by the administrative divides, suggesting an anthropogenic drive. A rapidly declining trend characterizes the selected time series of LOS displacement at sites (b), (c), and (d) until 2020. The slightly rising time series (**Figure 7E**) also follows a similar pattern, whose rising trend is interrupted by 2020. This behavior change might be attributed to the COVID-19 global pandemic, which has caused a reduction of economic activities worldwide.

DISCUSSION

Origin of Tremor: Perspective, Interpretation, and Outstanding Questions

In our study, we were able to associate only one of the tremor sequences to an event in the global catalog. Our attempt to associate the other events in the tremor sequences to either a previously undetected global or regional event proved inconclusive. This lack of corroborating seismic evidence confirming anecdotal reports could be due to either of the following: 1) the inaccuracy of the timing or the number of the reports; 2) localized low-magnitude shaking not detectable by the seismic station closest to Abuja, due to the quality of the data recovered from that seismic station (i.e., TORO). While this is an unsatisfactory conclusion, it emphasizes the need for high-quality

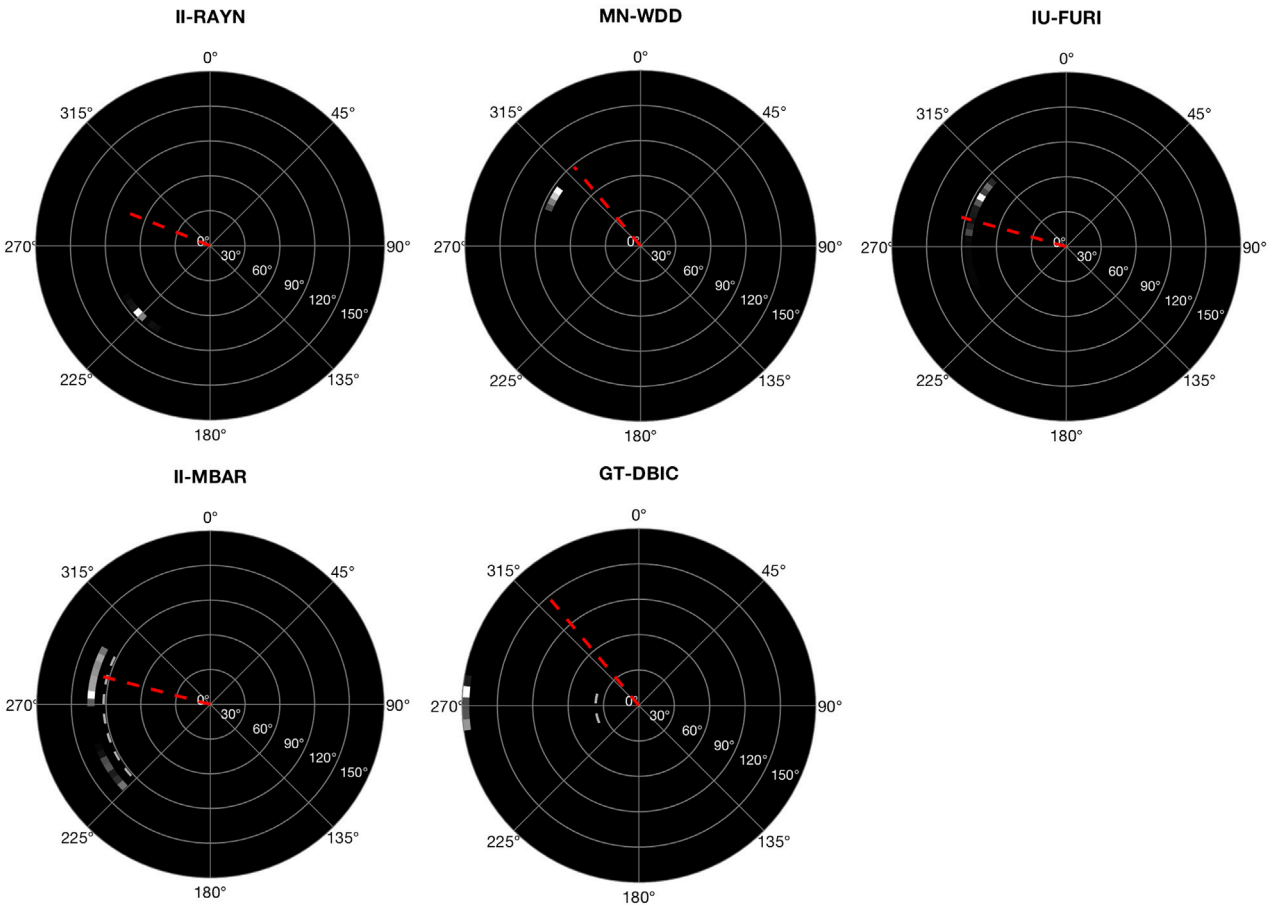

FIGURE 5 | Single-station location of Hokkaido, Japan, in the event reference frame (compare with station-event geometry in **Figure 1B**). All stations identify the correct epicentral distance and azimuth range (except for DBIC and RAYN with an azimuth bias of –50°).

data in regions that are often ignored due to the assumption of lack of seismicity. We also demonstrated that one of the reported tremor activities in Abuja, Nigeria, and recorded by the Western African stations coincides with the Hokkaido Eastern Iburi, Japanese earthquake of September 5, 2018. It is very puzzling that this moderate-sized earthquake (~M6.7) generated enough seismic energy to be felt in the capital city of Nigeria, considering that Japan is located at considerable teleseismic distances (~112°). Here, we discuss a few plausible scenarios that may offer more insights into these results taken together.

Hypothesis I: A Unique Teleseismic Event

Moderate teleseismic events are unlikely to cause significant shaking at such a considerable distance. However, we are persuaded to explore the possibility that there is a direct connection to the M6.6 Hokkaido Eastern Iburi, Japanese earthquake on September 5, 2018, given a large number of coseismic landslides (Zhang et al., 2019) generated significant long-period surface wave energy that propagated to large distances without much dissipation (Allstadt, 2013). Landslides can be effectively modeled by single forces, where the orientation of the force exerted on the ground is in the direction opposite to landslide acceleration, generating maximum surface wave amplitudes along the trajectory of mass loss (Kawakatsu, 1989; Ekström et al., 2003; Tsai and Ekström, 2007). For shallow landslides with estimated mass volumes and a simple trajectory, it should be straightforward to model the effective forces, using synthetic seismograms (Ekström and Stark, 2013). However, the Hokkaido Iburi Earthquake triggered ~6,000 landslides with complex trajectories (**Figure 8**), distributed over a large area making this a difficult task. Despite this complexity, we observe that the aggregate spatial distribution of the landslides can explain surface-wave radiation in the direction of Nigeria (310°, which is in the NW/SE direction from Japan) (**Figure 8**).

A comprehensive inventory of landslides (Wang et al., 2019; Zhang et al., 2019) document important characteristics that fit this pattern: a large concentration of 65% of the landslides (21 per square-km) in an elliptical area of 173 squared-km with major axis oriented NNW/SEE at 327.7° (within 18° of the direction of Abuja). We expect that a considerable portion of the radiated surface-wave energy is connected to the coseismic landslides

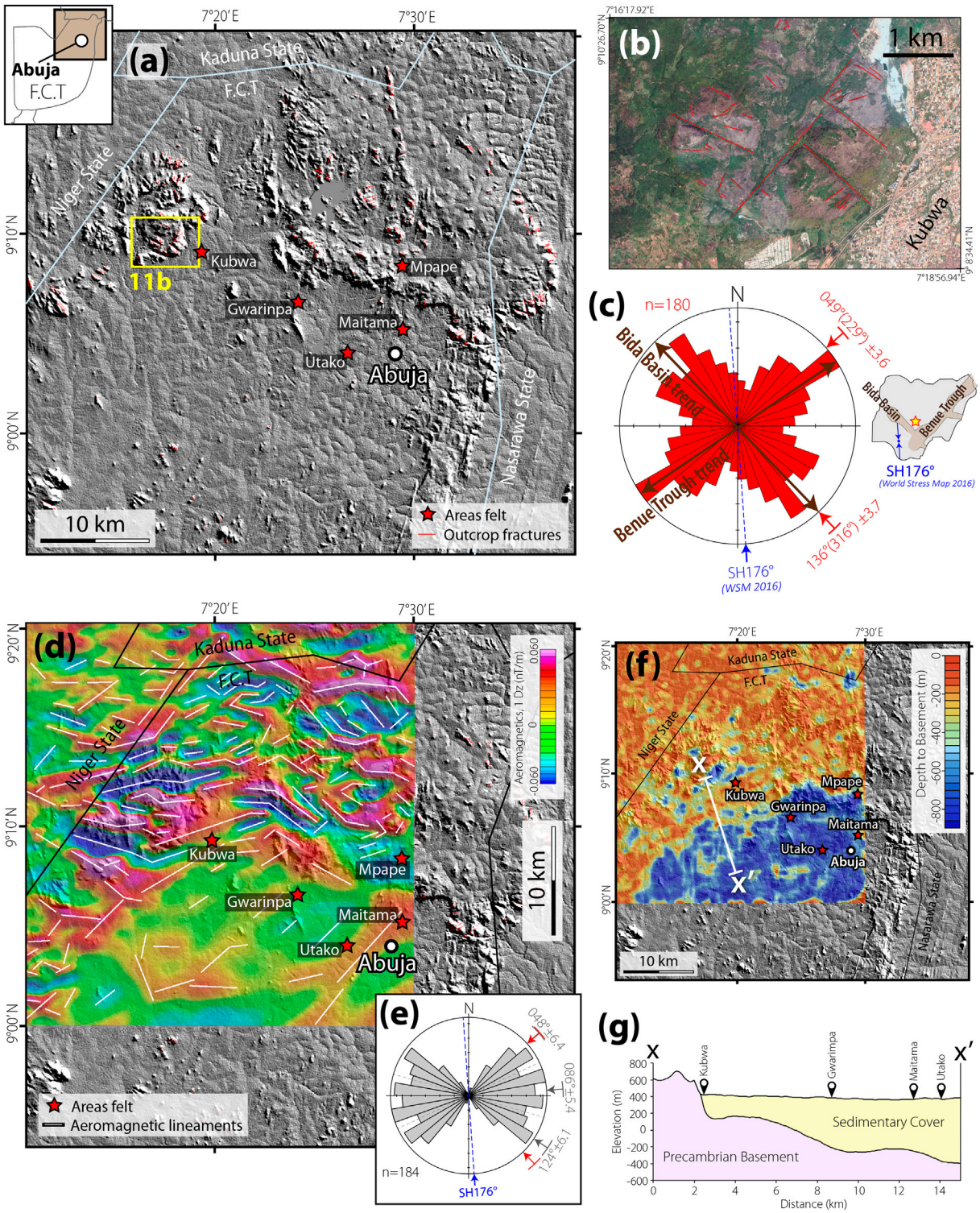

FIGURE 6 | (A) Satellite topography hillshade map of the Abuja area of the Federal Capital Territory (F.C.T.), Nigeria, showing areas where the tremor was felt (source: BBC Africa Hausa). **(B)** Google Earth© satellite image of a part of the Abuja area showing an example of satellite-scale fractures in the granitic basement outcrops. **(C)** Rose diagram showing the azimuth-frequency distribution of the satellite-scale outcrop fractures in the entire Abuja area shown in **Figure 6A**. SH = maximum horizontal compressional stress orientation (source: Heidbach et al., 2016). Inset: map of Nigeria showing the location and orientation of SH data (blue arrows), location of Abuja (red-yellow star), and Mesozoic rift basins (BT = Benue Trough; BB = Bida Basin). **(D)** The vertical derivative of the reduced to the equator (RTE) aeromagnetic map of the Abuja area. White lines represent the trends of basement magnetic anomaly lineaments. For "SH," see 6 **(C)**. **(E)** Rose diagram showing the azimuth-frequency distribution of the aeromagnetic lineaments, which represent the subsurface structural fabrics. The mean trends of the NW and NE dominant sets coincide considerably well with those of the satellite-scale outcrop fractures. **(F)** Depth to basement map, generated from the Source Parameter Imaging (SPI) transform of the aeromagnetic data, and the associated **(G)** cross-section, showing that the areas where the tremor was felt are located within a small sedimentary basin.

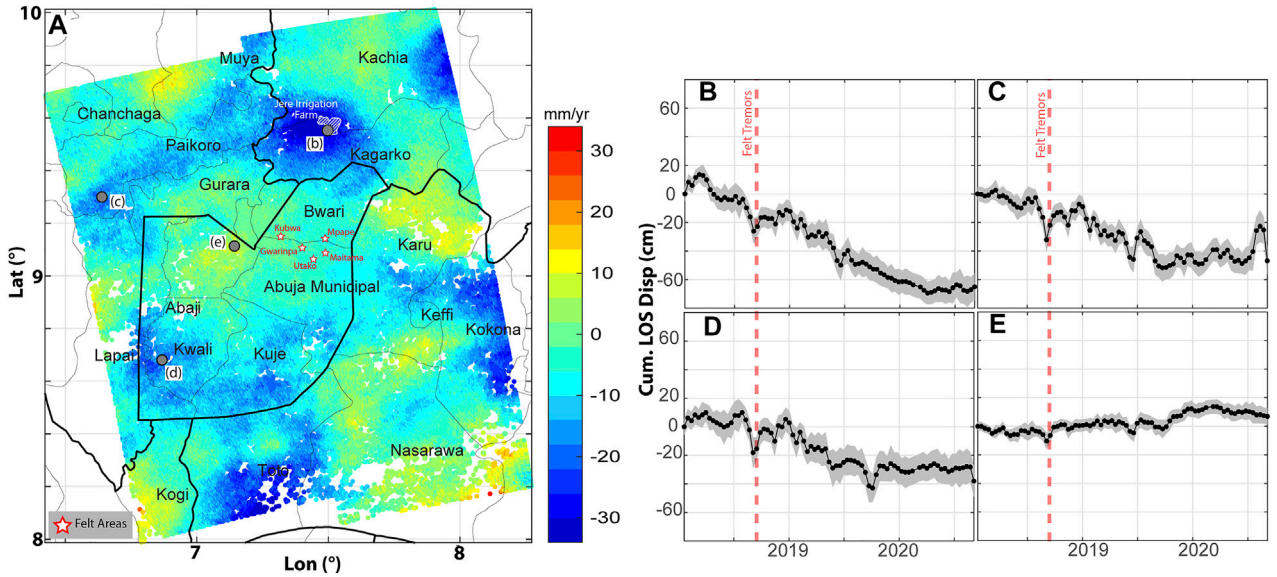

FIGURE 7 | InSAR deformation map obtained from Sentinel-1A/B ascending orbit (heading ~347° and incidence angle ~38.5°) SAR images for period 2018/01/19–2020/09/05. **(A)** LOS linear velocity. Colder colors indicate movement away from satellite or subsidence. Black polygons show administrative divisions. **(B)**–**(E)** Time series of LOS displacement at four locations shown in panel **(A)**. The gray shading indicates a 1-sigma uncertainty range for the estimated time series.

separate from the triggering earthquake, which has been modeled as a deep-crustal earthquake with different rupture processes, and surface wave radiation patterns (Gou et al., 2019; Hua et al., 2019; Kobayashi et al., 2019; Zang et al., 2019). Although we report an event detection, we do not expect significant shaking from radiated energy from the landslide.

Hypothesis II: Local Amplification of Earthquakes from Regional Tectonics

Previous studies have documented the occurrence of earthquakes in the Western African continental region and especially within continental Nigeria (Blundell, 1976; Wright, 1976; Williams and Williams, 1977; Scheidegger and Ajakaiye, 1985; Ajakaiye et al., 1987). These earthquakes have been attributed to 1) the inland continuation of oceanic fracture zones (Blundell, 1976; Wright, 1976) or 2) seismicity associated with faulting along the Cameroon volcanic line (Tabod et al., 1992; Nfomou et al., 2004). The apparent extension of the oceanic fracture zones across the continent-ocean boundary towards the shoreline in the Gulf of Guinea (**Figure 1A**; Granot and Dyment, 2015) may explain the clustering of historical seismicity close to the shorelines (**Figure 1A**), but may not explain the events reported from areas further inland. We note that historical tremors that were felt in the inland areas (north central part of Nigeria) are distributed across both the failed rifts and areas of the exposed basement on the rift flanks (**Figure 1A**).

We consider an alternative hypothesis that the series of shakings felt in the study area (Abuja, north central Nigeria) may be related to the local amplification of earthquakes associated with the active tectonics along the offshore oceanic fracture zones (transforms), or along the active Cameroon Volcanic Line in the east. The Abuja area is located within the broad basement complex terrain of Nigeria (i.e., outboard of the Mesozoic failed rifts), where the basement rocks are dominated by Precambrian migmatite gneiss and granitic intrusions (Oyawoye, 1964). The granitic intrusions occur as prominent topographic-highs in the landscape, and the gneissic host rocks occur as topographic-lows where small basins of unconsolidated sediments commonly accumulate. Our estimation of basement undulations in the Abuja area shows that the locations where the tremor was felt are within a small sedimentary basin (**Figure 6G**), indicating a vulnerability of the local geology of the Abuja area to seismic amplification. Although the oceanic transforms, coastal areas, and areas near the Cameroon Volcanic Line show historical seismic activity (**Figure 1A**), our catalog search did not identify any event along the offshore oceanic transforms or the Cameroon volcanic Line that coincides with the timing of the shaking.

Hypothesis III: Reactivation of Local Basement Fractures and Fault Systems by Post-Rift Crustal Relaxation or Far-Field Tectonic Stresses

Although we report inconclusive evidence for an earthquake in Nigeria, we emphasize that the absence of evidence is not the evidence of absence, considering the poor data quality from the closest station (TORO). As mentioned earlier, the historical earthquakes in Nigeria have been attributed to the inland continuation of oceanic fracture zones through the Precambrian basement shear zones (Blundell, 1976; Wright, 1976; Odeyemi, 1989; Anifowose et al., 2006; Odeyemi, 2006). However, these Precambrian basement shear zones (cyan dotted lines in **Figure 1A**) show a NNE trend that is markedly distinct from the ENE-to-NE trends of the oceanic fracture zones. Rather, the oceanic fracture zones show better

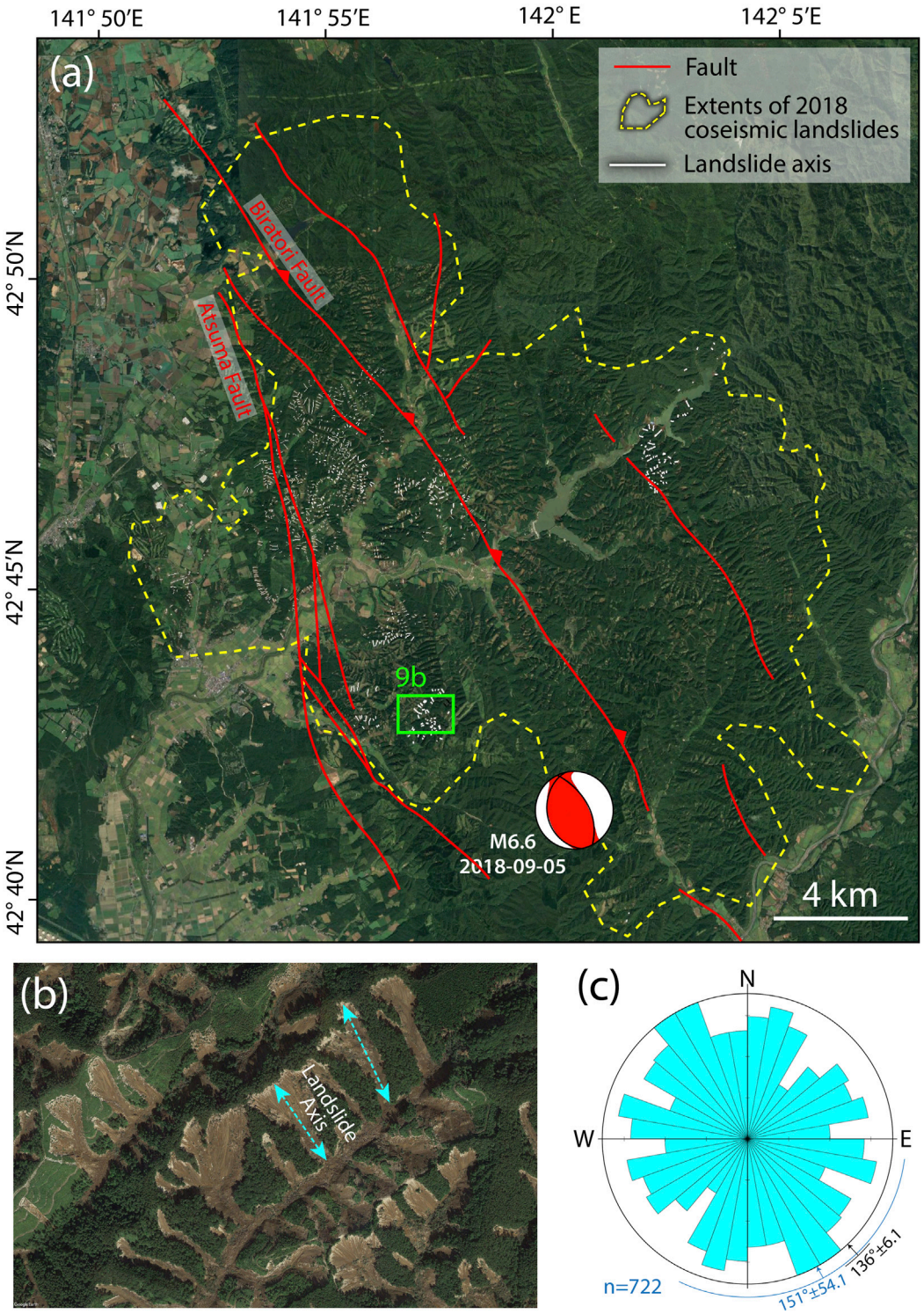

FIGURE 8 | (A) Google Earth© satellite image of the Hokkaido landslide region showing the 270 km^2 extent of coverage of the affected area. **(B)** A representative satellite image showing the distribution of the individual landslides and the manually digitized axial trends (long axes) of the landslides (see Dataset S1 for digitized data). **(C)** Azimuth-frequency distribution of the mapped axial trends of the coseismic landslides.

spatial and azimuthal correlation with the NE-trending Benue Trough (failed Mesozoic rift) than the onshore basement shear zones (**Figure 1A**). In addition, there exists no surficial evidence of recent fault scarps or collocated active brittle exploitation along the trend of the basement shear zones. Therefore, we examine the brittle structures in the basement of the Abuja area which is located on the flank of the Benue Trough, with a view of possible local seismic reactivation of pre-existing basement fracture systems.

Our analysis of the exposed basement fracture systems (**Figures 6A–C**) and deeper structures of the aeromagnetic lineaments (**Figures 6D,E**) show common prominent sets of conjugate NE-SW and NW-SE trends. Thus, we interpret these structural trends as the dominant patterns of the basement fracture systems and faults in the Abuja area. We note that the Abuja area is located near the nexus of two Mesozoic rift basins (failed rifts), the NW-trending Bida Basin and NE-trending Benue Trough (**Figures 1A**, **6C**). The basins are composed of basement-rooting structures associated with the opening (Mid Cretaceous) and closing (Late Cretaceous) of the Western and Central African Rift System. We find that the axial trends of these two rift structures are parallel to the most prominent structural trends in the Abuja area (**Figure 6C**). This suggests that the pre-existing discontinuities in the Abuja area are most likely inherited from the Mesozoic extensional tectonic deformation. We propose that these basement structures may be reactivated either by far-field tectonic stresses or post-rift relaxation of the crust. This reactivation can be accompanied by seismicity or developed aseismically.

Unfortunately, there exists no published stress field data in the interior of Nigeria (Heidbach et al., 2018). Nevertheless, to provide a first-order assessment, we consider the closest available measurement of the *in situ* azimuth of 176° for the maximum horizontal compressional stress (SHmax from borehole breakout) at a location in SW Nigeria (**Figure 6C** inset; Heidbach et al., 2018). If these available stress data are representative of the current σ1 magnitude and orientation in the Abuja area, the NW-trending fractures are more critically oriented for reactivation (in strike-slip mode) than those in the NE and E-W trends. We recommend future studies to explore the *in situ* stress field across the region in order to better understand the susceptibility of the inherited structures to seismic reactivation.

Based on the geological considerations presented above, we infer that in the Abuja area, there exist basement discontinuities that could be optimally oriented for seismic reactivation by stress perturbation of the assumed current stress field. On a regional scale of the Western Africa sub-continent, we highlight the occurrence of earthquakes in the Mesozoic rift structures and the Precambrian basement domains (earthquakes in Termit Basin, Benue Trough, Yola-Doba Basin, Ahaggar Massif, and West African Craton in **Figure 6A**), suggesting that inherited brittle structures in the basement pose important seismic hazards across the region. Overall, we emphasize that the faults and fracture systems of the failed Mesozoic rift basins in the Western Africa region (West African Rift System, **Figure 1A**) represent critical seismic hazards in the region that may be capable of hosting damaging earthquakes.

Hypothesis IV: Induced Earthquake Triggering by Groundwater Extraction

The widespread subsidence observed in the study area is consistent with those measured in other metro areas around the world and is likely to be associated with fluid (primarily groundwater) extraction (Chaussard et al., 2014; Miller and Shirzaei, 2015; Miller et al., 2017; Miller and Shirzaei, 2019; Herrera-García et al., 2021). A change in near-surface hydrologic loading has the potential to alter the local and regional stress field (Amos et al., 2014; Johnson et al., 2017a; Johnson et al., 2017b; Carlson et al., 2020; Johnson et al., 2020), which can encourage earthquake nucleation and may weakly modulate seismicity (Heki, 2003; Johnson et al., 2017a). In regions where elastic loading maintains a strong periodic signal, the same cyclic pattern is observed in seismic catalogs (Heki, 2003; Ader and Avouac, 2013). Furthermore, stress and pressure in the crust can be altered due to fluid injection and extraction, triggering earthquakes (Wang, 2001; Wang and Kümpel, 2003; Segall, 2010; Ellsworth, 2013; Segall and Lu, 2015; Shirzaei et al., 2016; Keranen and Weingarten, 2018; Kwiatek et al., 2019; Zhai et al., 2019; Zhai et al., 2021). The stress and pressure gain is a function of pumping and injection location, flux, and accumulated volume, while the rate of radial fluid migration is mainly controlled by crustal permeability (Wang, 2001; Segall and Lu, 2015).

Fault failure may occur when shear stress exceeds the fault shear strength for a given effective normal stress. Shear stress can be altered due to non-zero differential stress changes caused by the imparted stress. Also, effective normal stress depends on the magnitude of the stresses and the orientation of the fault in the tectonic stress field. The magnitude of fault-normal stresses can be reduced due to increased pore fluid pressure. However, establishing a threshold for stress and pressure change to trigger an earthquake is not trivial (e.g., Talwani and Acree, 1985). It is often assumed that faults are near critically stressed, if they have not ruptured recently (Townend and Zoback, 2000). Therefore, a small perturbation of the stress field due to the loading effect and fluid diffusion may trigger some earthquakes. Some examples include seasonal modulation of seismicity due to hydrological loading cycles (Christiansen et al., 2007; Johnson et al., 2017a; Carlson et al., 2020), triggering earthquakes due to tides (Wilcock, 2001; Tanaka et al., 2002), and induced seismicity due to pore pressure change by seasonal precipitation or snowmelt (Saar and Manga, 2003; Hainzl et al., 2006; Montgomery-Brown et al., 2019).

Despite scientific evidence from elsewhere, in the Abuja case study, investigating the hypothesis that the events similar to that of September 2018 are of hydrological origin is not straightforward due to the lack of dense hydrological observations (e.g., groundwater levels and stream discharge) and a complete seismic catalog. Therefore, we call for future efforts to generate new observations and develop models that constrain spatiotemporal variations in components of total water storage and establish a link to the local and regional tectonics and seismicity. Such data and models will further enhance the knowledge of water availability and improve the local communitie's resilience to drought in the era of climate change.

Summary: Preferred Hypotheses and Strategies for Further Tests

Our exploration of the limited yet very important geological and geophysical datasets has shed light on the most plausible cause of the shaking experienced in Abuja between September 5 and 7, 2018. Based on the available InSAR analysis, we find the strongest support for the hypotheses that these events were triggered by groundwater extraction (H-IV). Similarly, recently published strain rate modeling from country-wide GNSS network covering the period of 2012–2015 (i.e., before the 2018 tremors; Bawa et al., 2020) shows a localized subsidence zone (negative dilation) that is collocated with a prominent subsidence zone in our analyses (see location b of **Figure 7A**). This subsidence anomaly is located directly over the Jere Irrigation Project, which was reportedly active at the time of the reported tremors. Following closely, it is the hypothesis that at least one of the felt events could have been triggered by the remote teleseismic event in Japan (H-I). While this idea is plausible, we have no actual data to confirm this hypothesis, because the closest seismic station did not record good enough data to investigate this hypothesis any further (see examples, Han et al., 2017). This again underscores the need for a high-quality geodetic and seismic network in the region. Similarly, a thorough examination of both hypotheses related to local fault reactivation by regional tectonics would require a high quality seismic and geodetic network to evaluate its plausibility for future events (H-II and -III). All the evidence taken together, we point out that, although the Abuja area is located on a stable intraplate region within the continent, transient strain rates, e.g., recharge and discharge of aquifers, can be more important than the background tectonic strain rates when it comes to triggering an earthquake swarm (Sykes, 1978; Wolin et al., 2012; Calais et al., 2016; Gardonio et al., 2018). The Western African crystalline basement is dominated by inherited crustal weaknesses that may then fail due to the transient stress release. Should such events reoccur in the future, further evaluation of our proposed hypotheses would definitely benefit from a renewed geophysical investigation of the Western African region, which is currently grossly understudied and poorly instrumented.

CONCLUSION

We investigated the source of ground shaking reported during September 5–7, 2018, in the Abuja area, central Nigeria. We reviewed previous seismic activity in the region, speculated on how the shaking is related to unique teleseismic events, or may be connected to other alternative explanations, i.e., anthropogenically triggered, or whether regional tectonics and local geology could have made the region more susceptible to triggered fault rupture and amplification of seismic shaking. We explored the spatial and temporal origins of the shaking using seismology and studied the basement structure and surface deformation using aeromagnetic and SAR data. We found the strongest support for seismicity related to anthropogenic groundwater extraction. While other hypotheses cannot be ruled out completely for the case study presented here, we point out that more work is needed to establish a better understanding of the potential connections between inherited basement structure, active regional tectonics, and anthropogenic stress perturbations.

Data and Resources

All the seismic data used in this study are publicly available through USGS and IRIS. The MATLAB code for polarization was originally developed by Matt Haney based on the covariance method and coherency method discussed by Vidale (1986). M_idist (Pawlowicz, 2020) is used to calculate the distance between the station and source location and the corresponding azimuth, and Matlab_TauP based on (Crotwell et al., 1999) is used to calculate the travel time of seismic phases given a list of event parameters (such as origins and magnitude). We use the irisFetch FDSN event web service method (irisFetch.Events) to retrieve seismic data. Information on earthquake location, magnitude, and focal mechanisms are obtained from the NEIC-PDE and USGS catalogs.

DATA AVAILABILITY STATEMENT

Publicly available datasets were analyzed in this study. These data can be found here: https://doi.org/10.17632/W7KKG3G37D.1.

AUTHOR CONTRIBUTIONS

All authors listed have made a substantial, direct, and intellectual contribution to the work and approved it for publication.

ACKNOWLEDGMENTS

The authors acknowledge the use of the BlueHive Linux cluster at the University of Rochester's center for integrated research computing (CIRC). YL acknowledges a summer research grant from URSeismo and funding from the Georgen Institute of Data Science. The authors thank the Nigeria Geological Survey Agency (NGSA) for providing the aeromagnetic data used in this study. They acknowledge many helpful discussions with members of the URSeismo lab: Baowei Liu, Ziqi Zhang, Liam Moser, Trey Brink, and Faner Lin. The facilities of IRIS Data Services, and specifically the IRIS Data Management Center, were used for access to waveforms, related metadata, and/or derived products used in this study. IRIS Data Services are funded through the Seismological Facilities for the Advancement of Geoscience (SAGE) Award of the National Science Foundation under Cooperative Service Agreement EAR-1851048. The satellite (**Figure 6**) and aeromagnetic data (**Figure 8**) used for this research are published on a public repository at (Olugboji, 2020) and included as google KMZ files in the supplementary information files, Datasets S1 and S2. We thank the editor, PA, and two reviewers for their insightful comments which helped to increase the quality of the manuscript.

SUPPLEMENTARY MATERIAL

The Supplementary Material for this article can be found online at: https://www.frontiersin.org/articles/10.3389/feart.2021.716630/full#supplementary-material

REFERENCES

Ader, T. J., and Avouac, J.-P. (2013). Detecting Periodicities and Declustering in Earthquake Catalogs Using the Schuster Spectrum, Application to Himalayan Seismicity. *Earth Planet. Sci. Lett.* 377-378, 97–105. doi:10.1016/j.epsl.2013.06.032

Afegbua, K. U., Abubakar, Y. T., Umo, A. O., Dauda, D., and Saturday, U. E. (2011). Towards an Integrated Seismic hazard Monitoring in Nigeria Using Geophysical and Geodetic Techniques. *Int. J. Phys. Sci.* 6 (28), 6385–6393. doi:10.5897/ijps10.375

Afegbua, K. U., Ezomo, F. O., Osahon, O. D., Yakubu, T. A., and Sanni, H. T. (2019). Probabilistic Seismic Hazard Assessment for National Planning and Development in Nigeria. *J. Geodynamics.* 126, 46–55. doi:10.1016/j.jog.2019.03.004

Agius, M. R., and Galea, P. (2011). A Single-Station Automated Earthquake Location System at Wied Dalam Station, Malta. *Seismological Res. Lett.* 82 (4), 545–559. doi:10.1785/gssrl.82.4.545

Ahulu, S., and Danuor, S. K. (2015). Ghana's Experience in the Establishment of a National Digital Seismic Network Observatory. *J. Seismol.* 19 (3), 667–683. doi:10.1007/s10950-015-9486-z

Ajakaiye, D. E., Daniyan, M. A., Ojo, S. B., and Onuoha, K. M. (1987). The July 28, 1984 Southwestern Nigeria Earthquake and its Implications for the Understanding of the Tectonic Structure of Nigeria. *J. Geodynamics.* 7 (3), 205–214. doi:10.1016/0264-3707(87)90005-6

Akpan, O. U., Isogun, M. A., Yakubu, T. A., Adepelumi, A. A., Okereke, C. S., Oniku, A. S., et al. (2014). An Evaluation of the 11th September, 2009 Earthquake and its Implication for Understanding the Seismotectonics of South Western Nigeria. *Open J. Geol.* 04 (10), 542–550. doi:10.4236/ojg.2014.410040

Akpan, O. U., and Yakubu, T. A. (2010). A Review of Earthquake Occurrences and Observations in Nigeria. *Earthq Sci.* 23 (3), 289–294. doi:10.1007/s11589-010-0725-7

Alaneme, K. K., and Okotete, E. A. (2018). Critical Evaluation of Seismic Activities in Africa and Curtailment Policies - a Review. *Geoenviron Disasters.* 5 (1), 24. doi:10.1186/s40677-018-0116-2

Allen, R. (1982). Automatic Phase Pickers: Their Present Use and Future Prospects. *Bull. Seismological Soc. America.* 72 (6B), S225–S242. doi:10.1785/bssa07206b0225

Allstadt, K. (2013). Extracting Source Characteristics and Dynamics of the August 2010 Mount Meager Landslide From Broadband Seismograms. *J. Geophys. Res. Earth Surf.* 118 (3), 1472–1490. doi:10.1002/jgrf.20110

Amos, C. B., Audet, P., Hammond, W. C., Bürgmann, R., Johanson, I. A., and Blewitt, G. (2014). Uplift and Seismicity Driven by Groundwater Depletion in central California. *Nature.* 509 (7501), 483–486. doi:10.1038/nature13275

Anifowose, A. Y. B., Odeyemi, I. B., and Borode, A. M. (2006). The Tectonic Significance of the Ifewara-Zungeru Megastructure in Nigeria. In Teme SC and Ezeigbo C U. Proceedings of the 1st International Workshop on Geodesy and Geodynamics, Toro, Nigeria. Centre for Geodesy and Geodynamics, Vol. 1728.

Astiz, L., Earle, P., and Shearer, P. (1996). Global Stacking of Broadband Seismograms. *Seismological Res. Lett.* 67 (4), 8–18. doi:10.1785/gssrl.67.4.8

Bai, C.-Y., and Kennett, B. L. N. (2000). Automatic Phase-Detection and Identification by Full Use of a Single Three-Component Broadband Seismogram. *Bull. Seismological Soc. America.* 90 (1), 187–198. doi:10.1785/0119990070

Bai, C.-Y., and Kennett, B. L. N. (2001). Phase Identification and Attribute Analysis of Broadband Seismograms at Far-Regional Distances. *J. Seismology.* 5 (2), 217–231. doi:10.1023/A:1011436421196

Bawa, S., Ojigi, L. M., Dodo, J. D., and Lawal, K. M. (2020). Strain Rate Field on the Nigeria Lithosphere Derived from GNSS Velocity. *Appl. Geomat.* 13, 179–193. doi:10.1007/s12518-020-00336-1

Blundell, D. J. (1976). Active Faults in West Africa. *Earth Planet. Sci. Lett.* 31 (2), 287–290. doi:10.1016/0012-821X(76)90221-1

Böse, M., Clinton, J. F., Ceylan, S., Euchner, F., van Driel, M., Khan, A., et al. (2017). A Probabilistic Framework for Single-Station Location of Seismicity on Earth and Mars. *Phys. Earth Planet. Interiors.* 262, 48–65. doi:10.1016/j.pepi.2016.11.003

Calais, E., Camelbeeck, T., Stein, S., Liu, M., and Craig, T. J. (2016). A New Paradigm for Large Earthquakes in Stable Continental Plate Interiors. *Geophys. Res. Lett.* 43 (20), 10. doi:10.1002/2016gl070815

Carlson, G., Shirzaei, M., Werth, S., Zhai, G., and Ojha, C. (2020). Seasonal and Long-Term Groundwater Unloading in the Central Valley Modifies Crustal Stress. *J. Geophys. Res. Solid Earth.* 125 (1), 439. doi:10.1029/2019JB018490

Chaussard, E., Bürgmann, R., Shirzaei, M., Fielding, E. J., and Baker, B. (2014). Predictability of Hydraulic Head Changes and Characterization of Aquifer-System and Fault Properties from InSAR-Derived Ground Deformation. *J. Geophys. Res. Solid Earth.* 119, 6572–6590. doi:10.1002/2014jb011266],

Christiansen, L. B., Hurwitz, S., and Ingebritsen, S. E. (2007). Annual Modulation of Seismicity Along the San Andreas Fault Near Parkfield, CA. *Geophys. Res. Lett.* 34 (4), L04306. doi:10.1029/2006gl028634

Crotwell, H. P., Owens, T. J., and Ritsema, J. (1999). The TauP Toolkit: Flexible Seismic Travel-Time and Ray-Path Utilities. *Seismological Res. Lett.* 70 (c), 154–160. doi:10.1785/gssrl.70.2.154

Doran, A. K., and Laske, G. (2017). Ocean-Bottom Seismometer Instrument Orientations via Automated Rayleigh-Wave Arrival-Angle Measurements. *Bull. Seismological Soc. America.* 107 (2), 691–708. doi:10.1785/0120160165

Earle, P. S. (1999). Polarization of the Earth's Teleseismic Wavefield. *Geophys. J. Int.* 139 (1), 1–8. doi:10.1046/j.1365-246x.1999.00908.x

Ekström, G. (2006). Global Detection and Location of Seismic Sources by Using Surface Waves. *Bull. Seismological Soc. America.* 96 (4), 1201–1212. doi:10.1785/0120050175

Ekström, G., Nettles, M., and Abers, G. A. (2003). Glacial Earthquakes. *Science.* 302 (5645), 622–624. doi:10.1126/science.1088057

Ekström, G., and Stark, C. P. (2013). Simple Scaling of Catastrophic Landslide Dynamics. *Science.* 339 (6126), 1416–1419. doi:10.1126/science.1232887

Ellsworth, W. L. (2013). Injection-Induced Earthquakes. *Science.* 341 (6142), 1225942. doi:10.1126/science.1225942

Farr, T. G., Rosen, P. A., Caro, E., Crippen, R., Duren, R., Hensley, S., et al. (2007). The Shuttle Radar Topography Mission. *Rev. Geophys.* 45 (2), RG2004. doi:10.1029/2005rg000183

Franceschetti, G., and Lanari, R. (1999). Synthetic Aperture Radar Processing. *Synth. Aperture Radar Process.* CRC Press. doi:10.1201/9780203737484

Frohlich, C., and Pulliam, J. (1999). Single-Station Location of Seismic Events: a Review and a Plea for More Research. *Phys. Earth Planet. Interiors.* 113 (1), 277–291. doi:10.1016/S0031-9201(99)00055-2

Gardonio, B., Jolivet, R., Calais, E., and Leclère, H. (2018). The April 2017 Mw 6.5 Botswana Earthquake: An Intraplate Event Triggered by Deep Fluids. *Geophys. Res. Lett.* 45 (17), 8886–8896. doi:10.1029/2018GL078297

Gou, T., Huang, Z., Zhao, D., and Wang, L. (2019). Structural Heterogeneity and Anisotropy in the Source Zone of the 2018 Eastern Iburi Earthquake in Hokkaido, Japan. *J. Geophys. Res. Solid Earth.* 124 (7), 7052–7066. doi:10.1029/2019JB017388

Government Report (2018). Available at: https://www.minesandsteel.gov.ng/wp-content/uploads/2018/09/Mpape-Tremor.pdf (January March 12, 2020).

Granot, R., and Dyment, J. (2015). The Cretaceous Opening of the South Atlantic Ocean. *Earth Planet. Sci. Lett.* 414, 156–163. doi:10.1016/j.epsl.2015.01.015

Grauch, V. J. S., and Hudson, M. R. (2007). Guides to Understanding the Aeromagnetic Expression of Faults in Sedimentary Basins: Lessons Learned From the Central Rio Grande Rift, New Mexico. *Geosphere.* 3 (6), 596–623. doi:10.1130/GES00128.1

Hainzl, S., Kraft, T., Wassermann, J., Igel, H., and Schmedes, E. (2006). Evidence for Rainfall-Triggered Earthquake Activity. *Geophys. Res. Lett.* 33 (19), L19303. doi:10.1029/2006gl027642

Han, L., Peng, Z., Johnson, C. W., Pollitz, F. F., Li, L., Wang, B., et al. (2017). Shallow Microearthquakes Near Chongqing, China Triggered by the Rayleigh Waves of the 2015 M7.8 Gorkha, Nepal Earthquake. *Earth Planet. Sci. Lett.* 479, 231–240. doi:10.1016/j.epsl.2017.09.024

Heidbach, O., Rajabi, M., Cui, X., Fuchs, K., Müller, B., Reinecker, J., et al. (2018). The World Stress Map Database Release 2016: Crustal Stress Pattern across Scales. *Tectonophysics.* 744, 484–498. doi:10.1016/j.tecto.2018.07.007

Heki, K. (2003). Snow Load and Seasonal Variation of Earthquake Occurrence in Japan. *Earth Planet. Sci. Lett.* 207 (1), 159–164. doi:10.1016/S0012-821X(02)01148-2

Herrera-García, G., Ezquerro, P., Tomás, R., Béjar-Pizarro, M., López-Vinielles, J., Rossi, M., et al. (2021). Mapping the Global Threat of Land Subsidence. *Science.* 371 (6524), 34–36. doi:10.1126/science.abb8549

Hua, Y., Zhao, D., Xu, Y., and Wang, Z. (2019). Arc-arc Collision Caused the 2018 Eastern Iburi Earthquake (M 6.7) in Hokkaido, Japan. *Sci. Rep.* 9 (1), 13914. doi:10.1038/s41598-019-50305-x

Johnson, C. W., Fu, Y., and Bürgmann, R. (2020). Hydrospheric Modulation of Stress and Seismicity on Shallow Faults in Southern Alaska. *Earth Planet. Sci. Lett.* 530, 115904. doi:10.1016/j.epsl.2019.115904

Johnson, C. W., Fu, Y., and Bürgmann, R. (2017a). Seasonal Water Storage, Stress Modulation, and California Seismicity. *Science.* 356 (6343), 1161–1164. doi:10.1126/science.aak9547

Johnson, C. W., Fu, Y., and Bürgmann, R. (2017b). Stress Models of the Annual Hydrospheric, Atmospheric, Thermal, and Tidal Loading Cycles on California Faults: Perturbation of Background Stress and Changes in Seismicity. *J. Geophys. Res. Solid Earth.* 122, 605. doi:10.1002/2017jb014778

Jurkevics, B. Y. A. (1988). Polarization Analysis of Three-Component Array Data. *Bull. Seismological Soc. America.* 78 (5), 1725–1743. doi:10.1785/BSSA0780051725 Retrieved from: http://citeseerx.ist.psu.edu/viewdoc/download?doi=10.1.1.472.9669&rep=rep1&type=pdf.

Kadiri, A. U., and Kijko, A. (2021). Seismicity and Seismic Hazard Assessment in West Africa. *J. Afr. Earth Sci.* 183, 104305. doi:10.1016/j.jafrearsci.2021.104305

Kameda, J., Kamiya, H., Masumoto, H., Morisaki, T., Hiratsuka, T., and Inaoi, C. (2019). Fluidized Landslides Triggered by the Liquefaction of Subsurface Volcanic Deposits during the 2018 Iburi-Tobu Earthquake, Hokkaido. *Sci. Rep.* 9 (1), 13119. doi:10.1038/s41598-019-48820-y

Kawakatsu, H. (1989). Centroid Single Force Inversion of Seismic Waves Generated by Landslides. *J. Geophys. Res.* 94 (B9), 12363. doi:10.1029/JB094iB09p12363

Keranen, K. M., and Weingarten, M. (2018). Induced Seismicity. *Annu. Rev. Earth Planet. Sci.* 46 (1), 149–174. doi:10.1146/annurev-earth-082517-010054

Kobayashi, T., Hayashi, K., and Yarai, H. (2019). Geodetically Estimated Location and Geometry of the Fault Plane Involved in the 2018 Hokkaido Eastern Iburi Earthquake. *Earth Planets Space.* 71 (1), 62. doi:10.1186/s40623-019-1042-6

Kolawole, F., Atekwana, E. A., Laó-Dávila, D. A., Abdelsalam, M. G., Chindandali, P. R., Salima, J., et al. (2018). Active Deformation of Malawi Rift's North Basin Hinge Zone Modulated by Reactivation of Preexisting Precambrian Shear Zone Fabric. *Tectonics.* 37, 683–704. doi:10.1002/2017TC004628

Kolawole, F., Johnston, C. S., Morgan, C. B., Chang, J. C., Marfurt, K. J., Lockner, D. A., et al. (2019). The Susceptibility of Oklahoma's Basement to Seismic Reactivation. *Nat. Geosci.* 12 (10), 839–844. doi:10.1038/s41561-019-0440-5

Koper, K. D., and Hawley, V. L. (2010). Frequency Dependent Polarization Analysis of Ambient Seismic Noise Recorded at a Broadband Seismometer in the central United States. *Earthq Sci.* 23 (5), 439–447. doi:10.1007/s11589-010-0743-5

Kwiatek, G., Saarno, T., Ader, T., Bluemle, F., Bohnhoff, M., Chendorain, M., et al. (2019). Controlling Fluid-Induced Seismicity during a 6.1-Km-Deep Geothermal Stimulation in Finland. *Sci. Adv.* 5 (5), eaav7224. doi:10.1126/sciadv.aav7224

Lay, T., Berger, J., Buland, R., Butler, R., Ekström, G., Hutt, C. R., et al. (2002). Global Seismic Network Design Goals Update 2002. *IRIS.* 26. doi:10.1029/2004EO230001 Retrieved from: http://academic.aua.am/yelena_vardanyan/Web/flesh/Y/seis.pdf.

Li, Y., and Oldenburg, D. W. (2001). Stable Reduction to the Pole at the Magnetic Equator. *Geophysics.* 66 (2), 571–578. doi:10.1190/1.1444948

Magotra, N., Ahmed, N., and Chael, E. (1987). Seismic Event Detection and Source Location Using Single-Station (Three-component) Data. *Bull. Seismological Soc. America.* 77 (3), 958–971. doi:10.1785/bssa0770030958

Magotra, N., Ahmed, N., and Chael, E. (1989). Single-Station Seismic Event Detection and Location. *IEEE Trans. Geosci. Remote Sensing.* 27 (1), 15–23. doi:10.1109/36.20270

McCausland, W., Malone, S., and Johnson, D. (2005). Temporal and Spatial Occurrence of Deep Non-Volcanic Tremor: From Washington to Northern California. *Geophys. Res. Lett.* 32 (24), L24311. doi:10.1029/2005gl024349

Miller, M. M., Shirzaei, M., and Argus, D. (2017). Aquifer Mechanical Properties and Decelerated Compaction in Tucson, Arizona. *J. Geophys. Res. Solid Earth.* 122 (10), 8402–8416. doi:10.1002/2017jb014531

Miller, M. M., and Shirzaei, M. (2019). Land Subsidence in Houston Correlated With Flooding From Hurricane Harvey. *Remote Sensing Environ.* 225, 368–378. doi:10.1016/j.rse.2019.03.022

Miller, M. M., and Shirzaei, M. (2015). Spatiotemporal Characterization of Land Subsidence and Uplift in Phoenix Using InSAR Time Series and Wavelet Transforms. *J. Geophys. Res.* 120, 5822–5842. doi:10.1002/2015jb012017

Montgomery-Brown, E. K., Shelly, D. R., and Hsieh, P. A. (2019). Snowmelt-Triggered Earthquake Swarms at the Margin of Long Valley Caldera, California. *Geophys. Res. Lett.* 46 (7), 3698–3705. doi:10.1029/2019gl082254

Montgomery-Brown, E. K., Thurber, C. H., Wolfe, C. J., and Okubo, P. (2013). Slow Slip and Tremor Search at Kilauea Volcano, Hawaii. *Geochem. Geophys. Geosyst.* 14 (2), 367–384. doi:10.1002/ggge.20044

Nadeau, R. M., and Dolenc, D. (2005). Nonvolcanic Tremors Deep Beneath the San Andreas Fault. *Science.* 307 (5708), 389. doi:10.1126/science.1107142

Nakata, N., Gualtieri, L., and Fichtner, A. (2019). *Seismic Ambient Noise*. United Kingdom: Cambridge University Press.

Neves, M., Custódio, S., Peng, Z., and Ayorinde, A. (2018). Earthquake Triggering in Southeast Africa Following the 2012 Indian Ocean Earthquake. *Geophys. J. Int.* 212 (2), 1331–1343. doi:10.1093/gji/ggx462

Nfomou, N., Tongwa, A. F., Ubangoh, U. R., Bekoa, A., Metuk, N. J., and Victor, H. J. (2004). The July 2002 Earthquake in the Kribi Region: Geological Context and a Preliminary Evaluation of Seismic Risk in Southwestern Cameroon. *J. Afr. Earth Sci.* 40 (3), 163–172. doi:10.1016/j.jafrearsci.2004.09.002

Odeyemi, I. B. (1989). "Precambrian Crustal Fractures as Possible Sites of Seismic Activity in Nigeria: Ifewara Fault as a Case Example," Proceedings of the National Seminar on Earthquakes in Nigeria, Lagos, Nigeria. Editors DE Ajakaiye, SB Ojo, MA Daniyan, and AO Abatan (Bauchi: National Technical Committee on Earthquake Phenomena), Vol. 225.

Odeyemi, I. B. (2006). *The Ifewara Fault in Southwestern Nigeria: Its Relationship with Fracture Zones along the Nigerian Coast*. Centre for Geodesy and Geodynamics, Toro, Bauchi State, 113.

Ojo, A. O., Zhao, L., and Wang, X. (2019). Estimations of Sensor Misorientation for Broadband Seismic Stations in and Around Africa. *Seismological Res. Lett.* 90, 2188–2204. doi:10.1785/0220190103

Olugboji, T. M., Lu, Y., Adepelumi, A., and Kolawole, F. (2020). Satellite and Aeromagnetic Data for " Solving the Mystery of Orphan Tremors Detected in West Africa on Sept 5-7,2018" [Data Set]. *Mendeley*. doi:10.17632/W7KKG3G37D.1

Oyawoye, M. O. (1964). The Geology of the Nigerian Basement Complex—A Survey of Our Present Knowledge of Them. *J. Mining Geology. Metal.* 1 (2pp87-103), 80–91. Retrieved from: https://nmgs-journal.org/wp-content/uploads/journal/published_paper/volume-1/issue-2/ztf6mXF8.pdf.

Park, J., Vernon, F. L., III, and Lindberg, C. R. (1987). Frequency Dependent Polarization Analysis of High-Frequency Seismograms. *J. Geophys. Res.* 92 (B12), 12664. doi:10.1029/JB092iB12p12664

Park, S., and Ishii, M. (2018). Near-surface Compressional and Shear Wave Speeds Constrained by Body-Wave Polarization Analysis. *Geophys. J. Int.* 213, 1559. doi:10.1093/gji/ggy072

Pawlowicz, R. (2020). M_Map: A mapping package for MATLAB *version 1.4m, [Computer software]*. Available at: www.eoas.ubc.ca/~rich/map.html.

Pérez-Díaz, L., and Eagles, G. (2014). Constraining South Atlantic Growth with Seafloor Spreading Data. *Tectonics.* 33 (9), 1848–1873. doi:10.1002/2014TC003644

Reading, A. M., Mao, W., and Gubbins, D. (2001). Polarization Filtering for Automatic Picking of Seismic Data and Improved Converted Phase Detection. *Geophys. J. Int.* 147 (1), 227–234. doi:10.1046/j.1365-246X.2001.00501.x

Ringdal, F., and Husebye, E. S. (1982). Application of Arrays in the Detection, Location, and Identification of Seismic Events. *Bull. Seismological Soc. America.* 72 (6B), S201–S224. Retrieved from: https://pubs.geoscienceworld.org/ssa/bssa/article/72/6B/S201/102166/application-of-arrays-in-the-detection-location.

Rogers, G., and Dragert, H. (2003). Episodic Tremor and Slip on the Cascadia Subduction Zone: the Chatter of Silent Slip. *Science.* 300 (5627), 1942–1943. doi:10.1126/science.1084783

Rost, S. (2002). Array Seismology: Methods and Applications. *Rev. Geophys.* 40 (3), 1008. doi:10.1029/2000RG000100

Rost, S., Thorne, M. S., and Garnero, E. J. (2006). Imaging Global Seismic Phase Arrivals by Stacking Array Processed Short-Period Data. *Seismological Res. Lett.* 77 (6), 697–707. doi:10.1785/gssrl.77.6.697

Roult, G., Montagner, J. P., Romanowicz, B., Cara, M., Rouland, D., Pillet, R., et al. (2010). The GEOSCOPE Program: Progress and Challenges During the Past 30 Years. *Seismological Res. Lett.* 81 (3), 427–452. doi:10.1785/gssrl.81.3.427

Saar, M. O., and Manga, M. (2003). Seismicity Induced by Seasonal Groundwater Recharge at Mt. Hood, Oregon. *Earth Planet. Sci. Lett.* 214 (3), 605–618. doi:10.1016/S0012-821X(03)00418-7

Sansosti, E., Berardino, P., Manunta, M., Serafino, F., and Fornaro, G. (2006). Geometrical SAR Image Registration. *IEEE Trans. Geosci. Remote Sensing.* 44 (10), 2861–2870. doi:10.1109/TGRS.2006.875787

Scheidegger, A. E., and Ajakaiye, D. E. (1985). Geodynamics of Nigerian Shield Areas. *J. Afr. Earth Sci.* 3 (4), 461–470. doi:10.1016/S0899-5362(85)80089-0

Scholz, J.-R., Barruol, G., Fontaine, F. R., Sigloch, K., Crawford, W. C., and Deen, M. (2017). Orienting Ocean-Bottom Seismometers FromP-Wave and Rayleigh Wave Polarizations. *Geophys. J. Int.* 208 (3), 1277–1289. doi:10.1093/gji/ggw426

Schulte-Pelkum, V., Earle, P. S., and Vernon, F. L. (2004). Strong Directivity of Ocean-Generated Seismic Noise. *Geochem. Geophys. Geosystems.* 5 (3). doi:10.1029/2003gc000520

Segall, P. (2010). *Earthquake and Volcano Deformation*. Princeton University Press. Retrieved from: https://play.google.com/store/books/details?id=QLumDwAAQBAJ.

Segall, P., and Lu, S. (2015). Injection-Induced Seismicity: Poroelastic and Earthquake Nucleation Effects. *J. Geophys. Res. Solid Earth.* 120 (7), 5082–5103. doi:10.1002/2015jb012060

Shao, X., Ma, S., Xu, C., Zhang, P., Wen, B., Tian, Y., et al. (2019). Planet Image-Based Inventorying and Machine Learning-Based Susceptibility Mapping for the Landslides Triggered by the 2018 Mw6.6 Tomakomai, Japan Earthquake. *Remote Sensing.* 11, 978. doi:10.3390/rs11080978

Shearer, P. M. (1994). Global Seismic Event Detection Using a Matched Filter on Long-Period Seismograms. *J. Geophys. Res.* 99, 13713–13725. doi:10.1029/94JB00498

Shirzaei, M., and Bürgmann, R. (2012). Topography Correlated Atmospheric Delay Correction in Radar Interferometry Using Wavelet Transforms. *Geophys. Res. Lett.* 39 (1), a–n. doi:10.1029/2011gl049971

Shirzaei, M., and Bürgmann, R. (2017). Applicability of Sentinel-1 Terrain Observation by Progressive Scans Multitemporal Interferometry for Monitoring Slow Ground Motions in the San Francisco Bay Area. *Geophys. Res. Lett.* 44, 2733. doi:10.1002/2017gl072663

Shirzaei, M., Ellsworth, W. L., Tiampo, K. F., González, P. J., and Manga, M. (2016). Surface Uplift and Time-dependent Seismic hazard Due to Fluid Injection in Eastern Texas. *Science.* 353 (6306), 1416–1419. doi:10.1126/science.aag0262

Shirzaei, M., and Walter, T. R. (2011). Estimating the Effect of Satellite Orbital Error Using Wavelet-Based Robust Regression Applied to InSAR Deformation Data. *IEEE Trans. Geosci. Remote Sensing.* 49 (11), 4600–4605. doi:10.1109/TGRS.2011.2143419

Simons, F. J., Nolet, G., Georgief, P., Babcock, J. M., Regier, L. A., and Davis, R. E. (2009). On the Potential of Recording Earthquakes for Global Seismic Tomography by Low-Cost Autonomous Instruments in the Oceans. *J. Geophys. Res.* 114 (B5), 1217. doi:10.1029/2008JB006088

Smith, R. S., and Salem, A. (2005). Imaging Depth, Structure, and Susceptibility From Magnetic Data: The Advanced Source-Parameter Imaging Method. *Geophysics.* 70 (4), L31–L38. doi:10.1190/1.1990219

Smith, R. S., Thurston, J. B., Dai, T.-F., and MacLeod, I. N. (2002). ISPITM—the Improved Source Parameter Imaging Method. *Geophys. Prospecting.* 46 (2), 141–151. Retrieved fromhttps://www.earthdoc.org/content/journals/10.1046/j.1365-2478.1998.00084.x.

Stachnik, J. C., Sheehan, A. F., Zietlow, D. W., Yang, Z., Collins, J., and Ferris, A. (2012). Determination of New Zealand Ocean Bottom Seismometer Orientation via Rayleigh-Wave Polarization. *Seismological Res. Lett.* 83 (4), 704–713. doi:10.1785/0220110128

Sykes, L. R. (1978). Intraplate Seismicity, Reactivation of Preexisting Zones of Weakness, Alkaline Magmatism, and Other Tectonism Postdating continental Fragmentation. *Rev. Geophys.* 16 (4), 621–688. doi:10.1029/RG016i004p00621

Tabod, C. T., Fairhead, J. D., Stuart, G. W., Ateba, B., and Ntepe, N. (1992). Seismicity of the Cameroon Volcanic Line, 1982–1990. *Tectonophysics.* 212 (3), 303–320. doi:10.1016/0040-1951(92)90297-J

Talwani, P., and Acree, S. (1985). "Pore Pressure Diffusion and the Mechanism of Reservoir-Induced Seismicity," in *Earthquake Prediction*. Editors K. Shimazaki and W. Stuart (Basel: Birkhäuser Basel), 947–965. doi:10.1007/978-3-0348-6245-5_14

Tanaka, S., Ohtake, M., and Sato, H. (2002). Spatio-temporal Variation of the Tidal Triggering Effect on Earthquake Occurrence Associated With the 1982 South Tonga Earthquake of Mw 7.5. *Geophys. Res. Lett.* 29 (16), 3–1. doi:10.1029/2002gl015386

Townend, J., and Zoback, M. D. (2000). How Faulting Keeps the Crust strong. *Geology.* 28 (5), 399–402. doi:10.1130/0091-7613(2000)28<399:HFKTCS>2.0.CO;2

Tsai, V. C., and Ekström, G. (2007). Analysis of Glacial Earthquakes. *J. Geophys. Res.* 112 (F3), 959. doi:10.1029/2006JF000596

Tsalha, M. S., Lar, U. A., Yakubu, T. A., Kadiri, U. A., and Duncan, D. (2015). The Review of the Historical and Recent Seismic Activity in Nigeria. *IOSR J. Appl. Geol. Geophys.* 3 (1), 48–56. doi:10.9790/0990-0311456

Vidale, J. E. (1986). Complex Polarization Analysis of Particle Motion. *Bull. Seismological Soc. America.* 76 (5), 1393–1405. doi:10.1785/bssa0760051514

Wang, F., Fan, X., Yunus, A. P., Siva Subramanian, S., Alonso-Rodriguez, A., Dai, L., et al. (2019). Coseismic Landslides Triggered by the 2018 Hokkaido, Japan (Mw 6.6), Earthquake: Spatial Distribution, Controlling Factors, and Possible Failure Mechanism. *Landslides.* 16 (1), 1551–1566. doi:10.1007/s10346-019-01187-7

Wang, H. F. (2001). *Theory of Linear Poroelasticity with Applications to Geomechanics and Hydrogeology*. Princeton, NJ: Princeton University Press. doi:10.1515/9781400885688

Wang, R., and Kümpel, H. J. (2003). Poroelasticity: Efficient Modeling of Strongly Coupled, Slow Deformation Processes in a Multilayered Half-space. *Geophysics.* 68 (2), 705–717. doi:10.1190/1.1567241

Weber, R. C., Lin, P.-Y., Garnero, E. J., Williams, Q., and Lognonné, P. (2011). Seismic Detection of the Lunar Core. *Science.* 331 (6015), 309–312. doi:10.1126/science.1199375

Wech, A. G., Boese, C. M., Stern, T. A., and Townend, J. (2012). Tectonic Tremor and Deep Slow Slip on the Alpine Fault. *Geophys. Res. Lett.* 39 (10), a–n. doi:10.1029/2012gl051751

Wilcock, W. S. D. (2001). Tidal Triggering of Microearthquakes on the Juan de Fuca Ridge. *Geophys. Res. Lett.* 28 (20), 3999–4002. doi:10.1029/2001gl013370

Williams, H. R., and Williams, R. A. (1977). Kimberlites and Plate-Tectonics in West Africa. *Nature.* 270 (5637), 507–508. doi:10.1038/270507a0

Wolin, E., Stein, S., Pazzaglia, F., Meltzer, A., Kafka, A., and Berti, C. (2012). Mineral, Virginia, Earthquake Illustrates Seismicity of a Passive-Aggressive Margin. *Geophys. Res. Lett.* 39 (2), L02305. doi:10.1029/2011gl050310

Wright, J. B. (1976). Fracture Systems in Nigeria and Initiation of Fracture Zones in the South Atlantic. *Tectonophysics.* 34 (3), T43–T47. doi:10.1016/0040-1951(76)90093-7

Yagüe-Martínez, N., Prats-Iraola, P., Rodríguez González, F., Brcic, R., Shau, R., Geudtner, D., et al. (2016). Interferometric Processing of Sentinel-1 TOPS Data. *IEEE Trans. Geosci. Remote Sensing.* 54 (4), 2220–2234. doi:10.1109/TGRS.2015.2497902

Yamagishi, H., and Yamazaki, F. (2018). Landslides by the 2018 Hokkaido Iburi-Tobu Earthquake on September 6. *Landslides.* 15 (12), 2521–2524. doi:10.1007/s10346-018-1092-z

Zang, C., Ni, S., and Shen, Z. (2019). Rupture Directivity Analysis of the 2018 Hokkaido Eastern Iburi Earthquake and its Seismotectonic Implication. *Seismological Res. Lett.* 90 (6), 2121–2131. doi:10.1785/0220190131

Zha, Y., Webb, S. C., and Menke, W. (2013). Determining the Orientations of Ocean Bottom Seismometers Using Ambient Noise Correlation. *Geophys. Res. Lett.* 40 (14), 3585–3590. doi:10.1002/grl.50698

Zhai, G., Shirzaei, M., Manga, M., and Chen, X. (2019). Pore-pressure Diffusion, Enhanced by Poroelastic Stresses, Controls Induced Seismicity in Oklahoma. *Proc. Natl. Acad. Sci. USA.* 116 (33), 16228–16233. doi:10.1073/pnas.1819225116

Zhai, G., Shirzaei, M., and Manga, M. (2021). Widespread Deep Seismicity in the Delaware Basin, Texas, Is Mainly Driven by Shallow Wastewater Injection. *Proc. Natl. Acad. Sci. USA.* 118 (20), e2102338118. doi:10.1073/pnas.2102338118

Zhang, S., Li, R., Wang, F., and Iio, A. (2019). Characteristics of Landslides Triggered by the 2018 Hokkaido Eastern Iburi Earthquake, Northern Japan. *Landslides.* 16 (9), 1691–1708. doi:10.1007/s10346-019-01207-6

Conflict of Interest: FK is currently employed by BP.

The remaining authors declare that the research was conducted in the absence of any commercial or financial relationships that could be construed as a potential conflict of interest.

Publisher's Note: All claims expressed in this article are solely those of the authors and do not necessarily represent those of their affiliated organizations, or those of the publisher, the editors, and the reviewers. Any product that may be evaluated in this article, or claim that may be made by its manufacturer, is not guaranteed or endorsed by the publisher.

frontiers in Earth Science

ORIGINAL RESEARCH
published: 20 December 2021
doi: 10.3389/feart.2021.696674

Two-step Gravity Inversion Reveals Variable Architecture of African Cratons

Peter Haas[1]*, *Jörg Ebbing*[1], *Nicolas L. Celli*[2] and *Patrice F. Rey*[3]

[1]Institute of Geosciences, Kiel University, Kiel, Germany, [2]Dublin Institute for Advanced Studies, Geophysics Section, School of Cosmic Physics, Dublin, Ireland, [3]EarthByte, School of Geosciences, The University of Sydney, Sydney, NSW, Australia

The lithospheric build-up of the African continent is still to a large extent unexplored. In this contribution, we present a new Moho depth model to discuss the architecture of the three main African cratonic units, which are: West African Craton, Congo Craton, and Kalahari Craton. Our model is based on a two-step gravity inversion approach that allows variable density contrasts across the Moho depth. In the first step, the density contrasts are varied for all non-cratonic units, in the second step for the three cratons individually. The lateral extension of the tectonic units is defined by a regionalization map, which is calculated from a recent continental seismic tomography model. Our Moho depth is independently constrained by pointwise active seismics and receiver functions. Treating the constraints separately reveals a variable range of density contrasts and different trends in the estimated Moho depth for the three cratons. Some of the estimated density contrasts vary substantially, caused by sparse data coverage of the seismic constraints. With a density contrast of $\Delta\rho = 200$ kg/m^3 the Congo Craton features a cool and undisturbed lithosphere with smooth density contrasts across the Moho. The estimated Moho depth shows a bimodal pattern with average Moho depth of 39–40 km for the Kalahari and Congo Cratons and 33–34 km for the West African Craton. We link our estimated Moho depth with the cratonic extensions, imaged by seismic tomography, and with topographic patterns. The results indicate that cratonic lithosphere is not necessarily accompanied by thick crust. For the West African Craton, the estimated thin crust, i.e. shallow Moho, contrasts to thick lithosphere. This discrepancy remains enigmatic and requires further studies.

Keywords: African cratons, gravity inversion, Moho depth, Archean lithosphere, tectonic regionalization, Kalahari Craton, Congo Craton, West African Craton

OPEN ACCESS

Edited by:
Mohamed Sobh,
Freiberg University of Mining and Technology, Germany

Reviewed by:
Islam Fadel,
University of Twente, Netherlands
Tolulope Morayo Olugboji,
University of Rochester, United States
Christian Gerhards,
Freiberg University of Mining and Technology, Germany

***Correspondence:**
Peter Haas
peter.haas@ifg.uni-kiel.de

Specialty section:
This article was submitted to Solid Earth Geophysics, a section of the journal Frontiers in Earth Science

Received: *17 April 2021*
Accepted: *24 November 2021*
Published: *20 December 2021*

Citation:
Haas P, Ebbing J, Celli NL and Rey PF (2021) Two-step Gravity Inversion Reveals Variable Architecture of African Cratons. Front. Earth Sci. 9:696674. doi: 10.3389/feart.2021.696674

1 INTRODUCTION

Knowledge of the lithospheric architecture of cratons is crucial for understanding continental assembly in the Archean and Paleoproterozoic. While most cratons are characterized by a deep lithospheric keel and flat topography (Artemieva, 2009; Artemieva and Vinnik, 2016), African cratons display variable signatures of topography and lithosphere (Fishwick and Bastow, 2011; Hu et al., 2018; Celli et al., 2020). Furthermore, the crustal structure of the African cratons is to a large extent unknown (Szwillus et al., 2019). Here, we investigate the African continent and highlight the variable architecture of individual cratons, based on a new crustal model.

The African continent is to a large extent composed of Archean cratons and Proterozoic Belts that surround and connect them (Begg et al., 2009). It consists of three main cratonic units, namely the

West African Craton, the Congo Craton and the Kalahari Craton. Other portions include the smaller Uganda and Tanzania Cratons, as well as the enigmatic Sahara Metacraton (e.g., Sobh et al., 2020). To document the lithospheric architecture of these cratons seismic tomography is a powerful method.

Stable cratonic platforms contrast to the surrounding mantle by an anomalous high seismic velocity (e.g., Artemieva, 2009; Lebedev et al., 2009; Celli et al., 2020). For central and southern Africa, surface-wave tomography shows a variable velocity structure beneath the cratonic regions (Fishwick, 2010). Full-wave ambient noise tomography suggests multiple cratonic roots within the Congo Craton (Emry et al., 2019). However, both approaches are limited by data availability (Fishwick, 2010) and depth resolution (Emry et al., 2019). Recent seismic tomography with massive data sets reveals a clearer image of the extension and internal structure of the lithosphere beneath the African cratons (Celli et al., 2020). The individual cratons are more fragmented and partially eroded than previously assumed, and smaller cratonic bodies like the Cubango and Niassa Cratons have been proposed (Celli et al., 2020). This cratonic fragmentation might also be reflected in the topography, which is the first-order signature for continental studies.

Generally, the flat topography of stable cratonic platforms indicates long-term stability of the underlying lithosphere (François et al., 2013). The African continent shows a bimodal pattern with higher topography in the south and east and lower topography in the west (Doucouré and de Wit, 2003). Of the three main cratonic units the Kalahari Craton stands out with anomalous high topography, which originates from upwelling mantle flow, representing parts of the African superswell (Lithgow-Bertelloni and Silver, 1998) and/or low density of the mantle lithosphere (Artemieva and Vinnik, 2016). In contrast to that, the West African Craton shows the flat topography typical of cratons, implying long-term stability (François et al., 2013).

Topographic signals are not only sourced from anomalies in the deeper lithosphere or asthenosphere, identified by gravity or seismic data, but invoke a contribution of isostatically compensated crust (Fishwick and Bastow, 2011). This is especially relevant for smaller cratonic bodies like the elevated Cubango Craton (Celli et al., 2020). Quantifying the Moho depth helps to identify topographic patterns that deviate from the isostatic state, indicating additional intercrustal or upper mantle sources. To fully understand the cratonic fragmentation and the topographic patterns of the African continent a continental Moho depth model is required.

On a continental scale, the African Moho depth has been the subject of earlier studies with variable quality and accuracy. For example, a comparison of the gravity-based model of Tugume et al. (2013) with global models shows strong differences in the Moho depth, which are explained by individual data characteristics and different modelling techniques (van der Meijde et al., 2015). In another study, integrated modeling of elevation, geoid, and thermal data was performed to define a continental Moho model (Globig et al., 2016). While inversion of satellite gravity data provides a homogeneous resolved Moho depth model, seismic and seismological models suffer from sparse data distribution. Szwillus et al. (2019) used the USGS Global Seismic Catalogue of (Mooney, 2015) to quantify the uncertainty of active source seismic Moho depth estimates to more than 5 km for the majority of the African continent. Focussing on the three main cratonic units, only the Kalahari Craton is covered by a dense network of seismic stations. Analysis of receiver functions shows a heterogeneous crustal structure with short wavelength variations (Youssof et al., 2013). An individual study of the West African Craton shows little to no correlation for Moho models, which are obtained by seismic tomographic inversions, receiver functions, and gravity and magnetic data (Jessell et al., 2016). All these studies highlight that the Moho depth for the African cratons is to a large extent unknown.

In this study, we shed new light on the architecture of the African cratons by applying a two-step gravity inversion. Our approach is based on inversion of satellite gravity data using laterally variable density contrasts and pointwise seismic estimates as qualitative constraints to define the best-fitting Moho model (Haas et al., 2020). This method is extended by allowing flexible density contrasts of the individual cratons. The outcome is a new continental Moho depth model. We use this model to investigate the coupling between Moho depth, density contrasts, topography, and seismically imaged lithosphere. We highlight the variability of the individual cratons with a special focus on the West African Craton.

2 DATA AND METHODS

In this section, we first describe the gravity data and the seismic data used to constrain the gravity inversion. Next, we present how we obtained a new regionalization map for Africa, based on the AF2019 tomography model (Celli et al., 2020). This regionalization defines the boundaries for the density contrasts that are varied during gravity inversion. Here, we briefly describe the general steps of this inversion and focus on new improvement that we have introduced. For full technical details the reader is referred to Haas et al. (2020).

2.1 Gravity and Sediment Data

Gravity inversion of the Moho depth requires a regularly gridded initial data set. Theoretically, all gravity and gravity gradient components are available. Haas et al. (2020) showed that the vertical gravity gradient g_{zz} is the best-suited component to invert for the Moho depth on continental scale. Therefore, we chose g_{zz} as initial gravity data for the inversion.

Figure 1 shows the g_{zz} component of the GOCE gravity gradients at 225 km height (Bouman et al., 2016). The data are corrected for global topographic effects, as well as far-field isostatic effects (Szwillus et al., 2016). Haas et al. (2020) gives the details on selecting densities and reference depth for the topographic and isostatic corrections.

When possible, gravity data are corrected for the effect of sediments when applied to inversion for the Moho depth (e.g. Uieda and Barbosa, 2016; Zhao et al., 2020). However, the thickness of a large portion of the African sedimentary basins is unknown. The large uncertainties on lateral and depth extension of the sediment basins make them inappropriate to

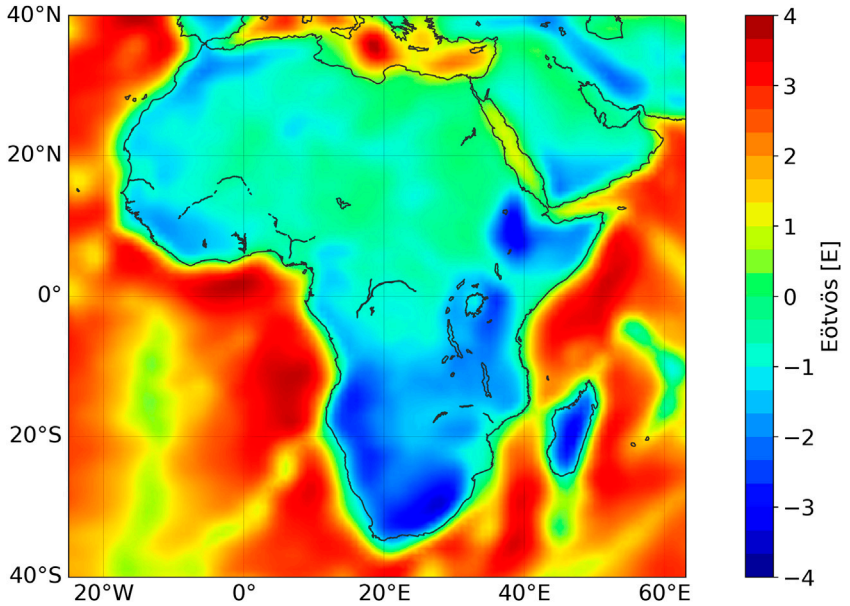

FIGURE 1 | Vertical gravity gradient at 225 km height, corrected for topographic and far field isostatic effects. This data set serves as input for the inversion.

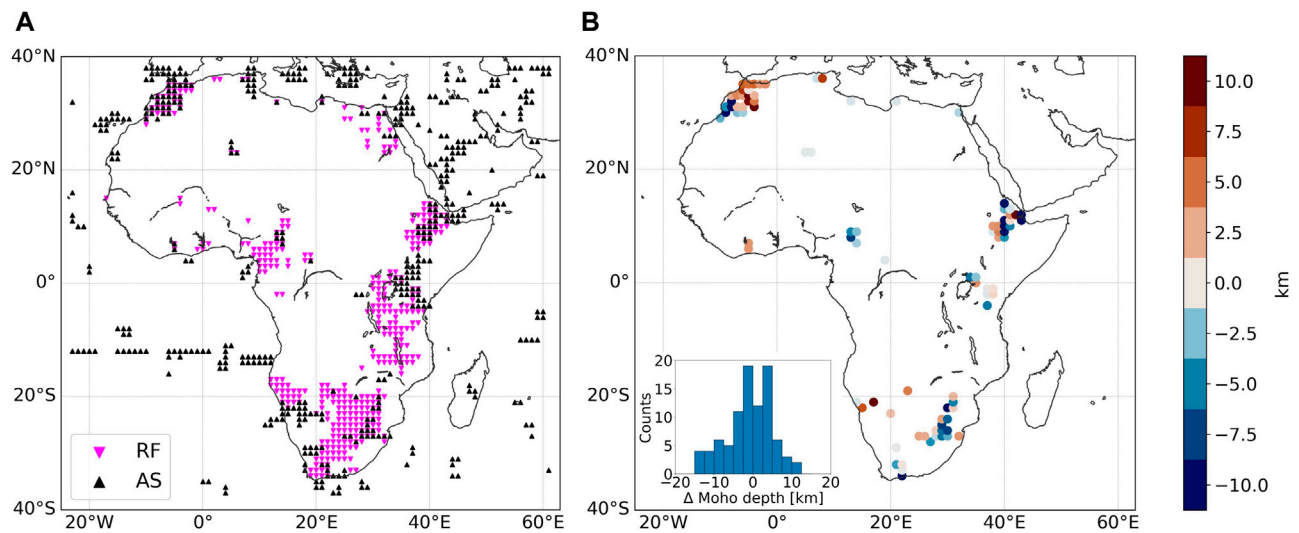

FIGURE 2 | Location of the seismic stations, binned on a 1° grid. **(A)** Active source seismic estimates (AS), marked as black triangles, and receiver functions (RF), marked as pink inverted triangles. **(B)** Differences of AS and RF estimates at overlapping stations. Red colours indicate deeper RF estimates, blue colours deeper AS estimates. The inset histogram shows the cumulative differences.

use as a reliable constraint for correction of the gravity data. In the **Supplementary Material** we show how the inversion performs with gravity data that has been corrected for the gravitational effect of sediments (**Supplementary Figures S1–S6**).

2.2 Seismic Data Base

To constrain a gravity-inverted Moho depth additional information on the Moho depth is required, such as a continental data base containing active and/or passive seismic depth estimates (e.g., Uieda and Barbosa, 2016; Haas et al., 2020). Here, we compile a new data base for our study area and decompose it into active (AS) and passive seismic Moho estimates, which are mostly obtained by receiver functions (RF). For the Moho estimates derived by active source seismics we use the data as listed in the USGS Global Seismic Catalogue (Mooney, 2015), which mostly represents reversed refraction data (Szwillus et al., 2019). Additionally, we add active source seismic estimates of the continental data base of

Globig et al. (2016). The USGS data base contains data for both the continental and oceanic domains, while the data base of Globig et al. (2016) contains data points over the continent only. For the second data base, we use the continental passive seismic Moho estimates as presented in Globig et al. (2016). We add recent receiver function studies in Namibia (Heit et al., 2015), Botswana (Yu et al., 2015; Fadel et al., 2018), Egypt (Hosny and Nyblade, 2016), Malawi (Sun et al., 2021), and Ethiopia (Wang et al., 2021).

In the next step, each data set is binned on a 1° lateral grid using inverse distance weighting (**Figure 2A**). This avoids small-scale clusters of seismic stations that may bias the estimated Moho depth and ensures that both gravity and seismic Moho depth are at the same coordinates, superseding a posterior interpolation of the gravity data. We select a search radius of 80 km for the inverse distance weighting. A representative study area in southern Africa shows that 34 receiver functions are removed during the interpolation (**Supplementary Figure S7**). At the same time, local clusters of different Moho depth estimates are removed, while the general trend of the receiver functions is preserved (**Supplementary Figure S7**). The final database contains 835 seismic stations, in which both components are almost equally represented (450 AS stations vs. 385 RF stations). For 91 of the stations, AS and RF data give different Moho depth estimates (**Figure 2B**) with differences up to ±15 km. This discrepancy motivates us to treat active and passive seismic constraints separately when applied to gravity inversion.

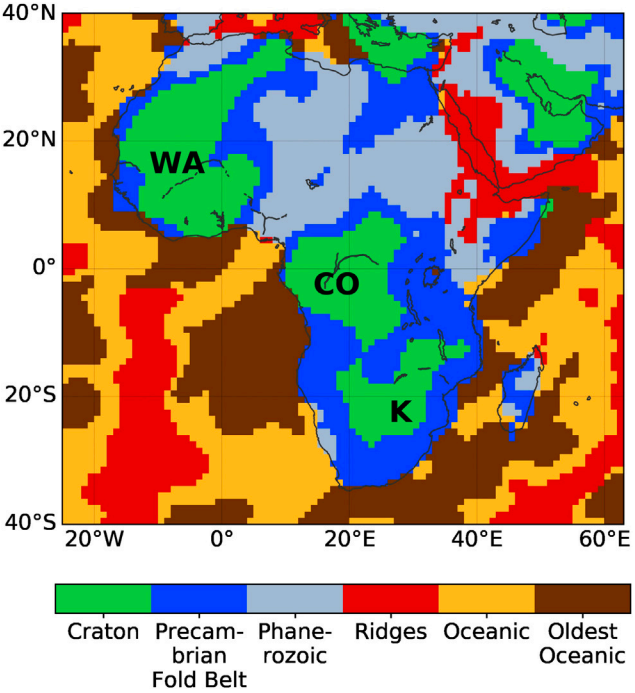

FIGURE 3 | Tectonic regionalization map of the AF2019 tomography model. The clusters are translated into distinct tectonic domains, based on the definitions of Lekic and Romanowicz (2011) and Schaeffer and Lebedev (2015). The three continental cratons are indicated as WA=West African Craton, CO=Congo Craton, K=Kalahari Craton.

2.3 K-Means Clustering of Seismic Tomography

A regionalization map is obtained by clustering seismic tomography data. We applied the *k*-means algorithm, which is an unsupervised machine learning algorithm. It has been frequently used to cluster seismic tomography data of different scale and resolution (e.g., Lekic and Romanowicz, 2011; Schaeffer and Lebedev, 2015; Garber et al., 2018; Eymold and Jordan, 2019). Compared to other algorithms, it is very fast and efficient. When applied to seismic tomography, it aids in identifying a certain number k of velocity-depth or 'centroid' profiles. Each single velocity-depth profile of the tomographic model is then allocated to a cluster in order to minimize the distance to the centroid profile.

The number of clusters k is the parameter that allows a high degree of freedom when clustering data. For a given data set, the number of clusters depends on its size and shape, as well as the target resolution. Lekic and Romanowicz (2011) applied the *k*-means algorithm to a set of upper mantle tomographies and found that $k = 6$ clusters "naturally group into families that correspond with known surface tectonics". Schaeffer and Lebedev (2015) adapted this method to provide a regionalization of their model SL 2013sv, producing six clusters that are translated into different tectonic units.

We tested this approach for the continental seismic tomography model AF2019 of Celli et al. (2020). AF2019 is an azimuthally anisotropic S-wave tomography model for Africa, extending from the crust to the mantle transition zone. In agreement with the parametrization of Schaeffer and Lebedev (2015) we clipped the model AF2019 to 30–350 km, which covers the lower crust and the underlying mantle lithosphere, and sliced the model at 10 km intervals. By using this depth extension, we map distinct tectonic domains that represent the entire lithospheric architecture, rather than internal crustal features. Setting the upper boundary of the model to 30 km additionally ensures that structures of the upper mantle in regions of shallower crust are mapped as well. To be consistent with the measured height of the gravity data and the regularization of the inversion we resampled the model laterally to 1°, which is roughly 100 km (Haas et al., 2020).

We used the elbow method to identify an appropriate number of clusters k for the given data set. Varying the cluster numbers between $k = 1$ and $k = 12$, we find no statistical justification for a certain cluster number (**Supplementary Figure S8**). Instead, $k = 6$ clusters separate the tomography model in three distinct continental and oceanic tectonic domains that are in accordance with the definition introduced by Schaeffer and Lebedev (2015) (**Supplementary Figure S9**). Interestingly, the same number of clusters has been independently chosen for models with very different resolution, indicating that the choice of $k = 6$ reflects distinct seismotectonic units and is not affected by the resolving power of each model. Therefore, we choose $k = 6$ to represent the seismic tomography in terms of distinct tectonic domains (**Figure 3**). Compared to the previous

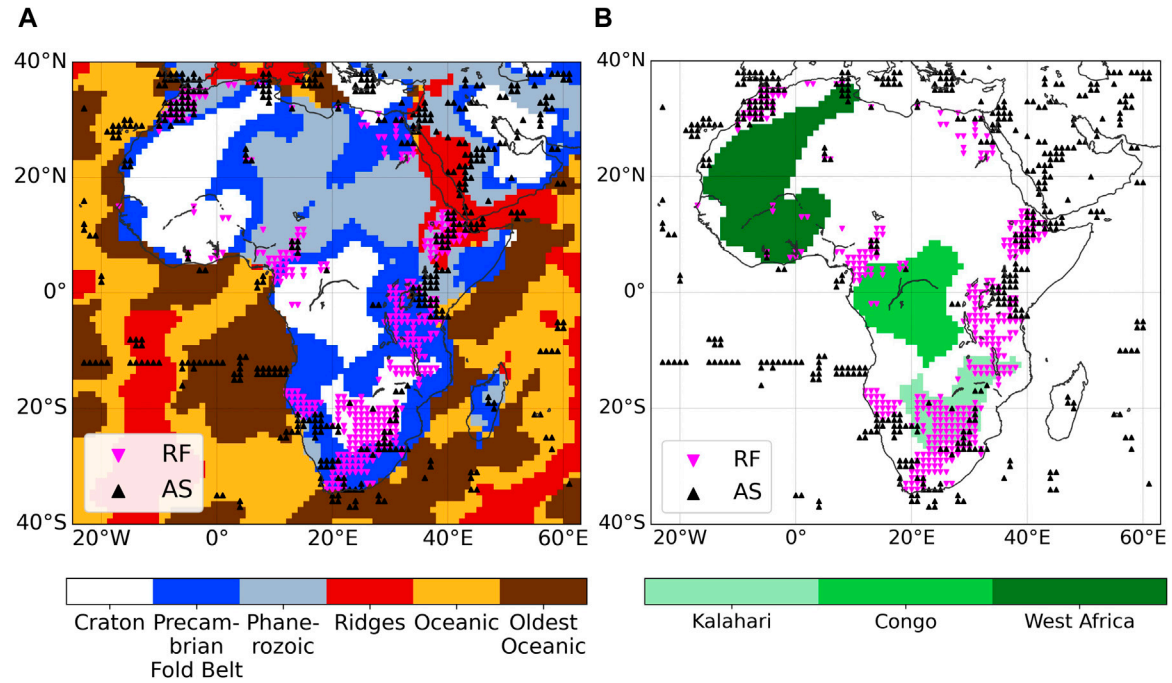

FIGURE 4 | Schematic overview on the two steps of the gravity inversion. The triangles indicate the location of AS and RF stations, respectively. **(A)** Step 1: Vary density contrasts of the units Precambrian, Phanerozoic, Ridges, Oceans, Oldest Oceans. Cratons are masked by white colour. **(B)** Step 2: Vary density contrasts of individual cratons, namely West African Craton (dark green), Congo Craton (green), Kalahari Craton (light green). Other tectonic units are masked by white colour.

regionalizations of Lekic and Romanowicz (2011) and Schaeffer and Lebedev (2015), our new regionalization map shows greater detail in the structure of all three cratons and particularly in the West African and Kalahari Cratons, previously seen as large, uniform blocks, retaining the resolution of AF2019 and validating their robustness across depths.

2.4 Two-step Gravity Inversion

We take the vertical gravity gradient g_{zz} at 225 km height as initial data to invert for the Moho depth. During the inversion, the density contrast at the Moho depth is kept laterally variable, as defined by the regionalization map. Together with the seismic data base the regionalization map constrains the estimated Moho depth.

We improve this approach by splitting the determination of lateral density variations into two steps. This ensures that closed polygons of the same tectonic domain can be varied individually. From a technical point of view, the imaged cratons of the African continent are well suited to be varied individually, as they form three coherent polygons, keeping the computational effort of the inversion reasonable (**Figure 3**).

In the first instance, the two hyperparameters, i.e. reference Moho depth $z_{ref} = 32\ km$ and reference density contrast $\Delta\ \rho_{ref} = 400\ \mathrm{kg}/m^3$, as well as an initial Moho depth of $z_0 = 30\ km$ are used to discretize a tesseroid model. According to Haas et al. (2020) A_{ref} is obtained by calculating the gravitational effect of shifting z_0 by $\delta z = 1\ km$. Hence, the dimension of each tesseroid is 1° in lateral direction and 1 km in vertical direction. Using these values, we calculate the Jacobian A_{ref} only once. A_{ref} contains the gravitational effect of every g_{zz} data point (column of matrix) for every tesseroid (row of matrix). In the inversion, we select a range of $\Delta\ \rho = 200 : 50 : 600\ \mathrm{kg}/m^3$, which is in accordance in terms of the compositional change at the Moho depth (Rabbel et al., 2013).

The two-step gravity inversion is based on the selection of tectonic units that are assigned with density contrasts during the inversion. The two steps are as follows:

1. Vary the density contrast for all tectonic units except the cratons (**Figure 4A**).
2. Vary the density contrast for cratons only (**Figure 4B**). Each craton is treated separately. Take the preferred density contrasts of step 1 for surrounding tectonic units.

In the first step, nine density contrasts are varied for five tectonic domains, giving a number of $n = 9^5 = 59.049$ combinations. For a certain density contrast i the Jacobian is defined as:

$$A_i = A_{ref}\frac{\Delta\rho_i}{\Delta\rho_{ref}} \tag{1}$$

Where the regionalization defines a craton, $\Delta\ \rho_i$ is set to $\Delta\ \rho_{ref}$.

For each iteration i a Moho depth z_i is estimated, derived from the Jacobian A_i (see Eqs. 4–6 in Haas et al., 2020). Together with the seismic estimates z_{seis} the inverted Moho depth z_i is used to calculate the RMS

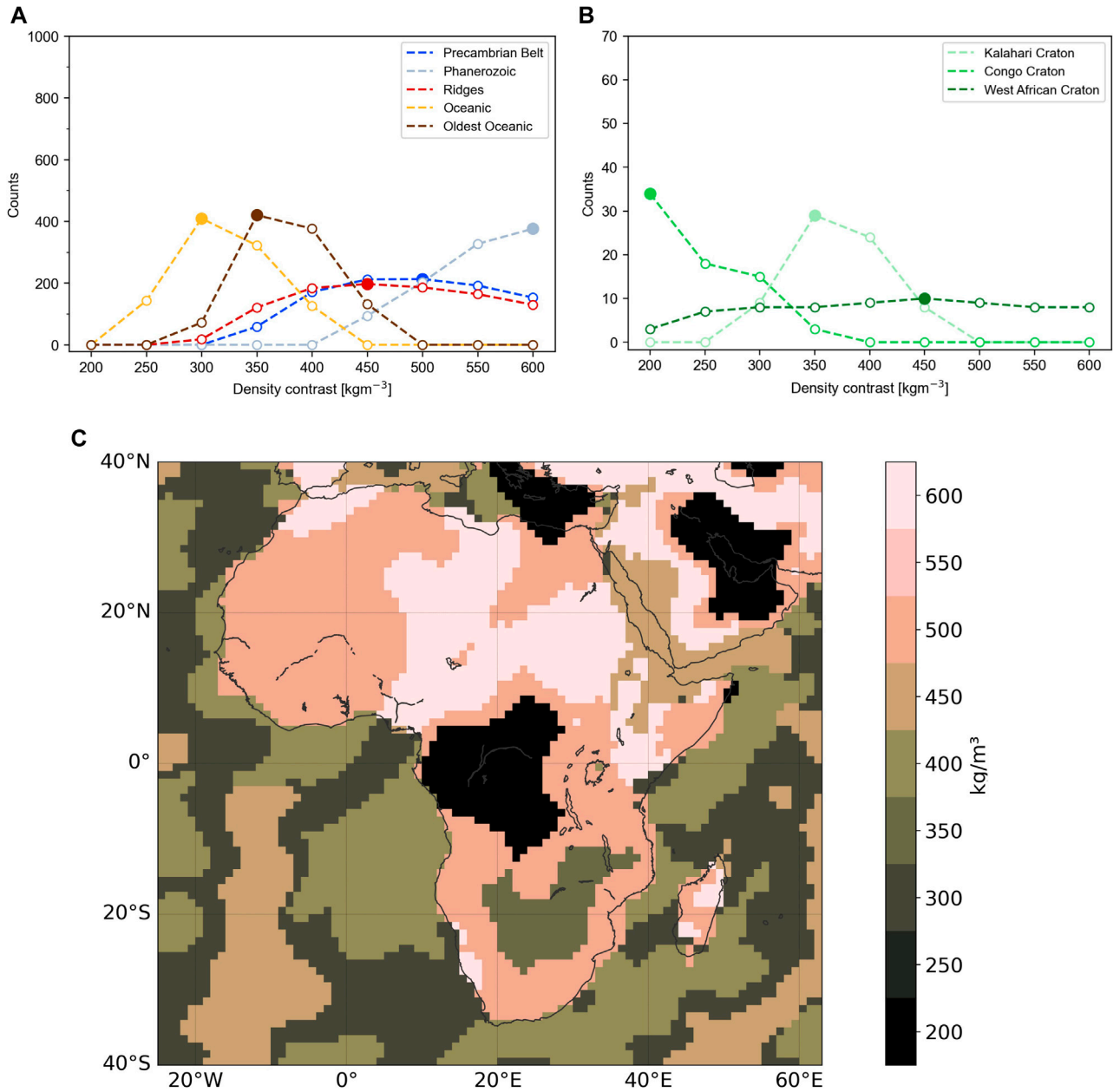

FIGURE 5 | (A) Distribution of the density contrasts for the 1,000 best-fitting models of the first inversion step. **(B)** Distribution of the density contrasts in the second inversion step. Due to a limited number of model solutions only 70 models are compared with each other. Both distributions are shown for the combined RMS of both constraints. **(C)** Final estimated density contrasts at the Moho depth for the best-fitting model in a gridded space.

$$RMS_i = \sqrt{\frac{\sum_{j=1}^{m} (z_{seis} - z_i)}{m}}, \tag{2}$$

where m is the number of seismic stations. Acknowledging the different station types the RMS is calculated for AS and RF stations separately (RMS_{AS} and RMS_{RF}). Afterwards, both RMS values are combined to a single value $RMS_{i,Comb}$, weighting the RMS of AS against the RMS of RF:

$$RMS_{i,Comb} = \frac{RMS_{i,AS} \cdot Q + RMS_{i,RF}}{Q + 1} \tag{3}$$

Q defines how much weight is given to the fit of the AS stations. We select $Q = 2$. This gives double weight to the RMS of the AS stations, as in continental scale data compilations receiver functions of different studies are prone to higher uncertainties (Szwillus et al., 2019). The specific density grid $\Delta \rho_i$, defining the best fitting $RMS_{i,Comb}$, is stored for the next step.

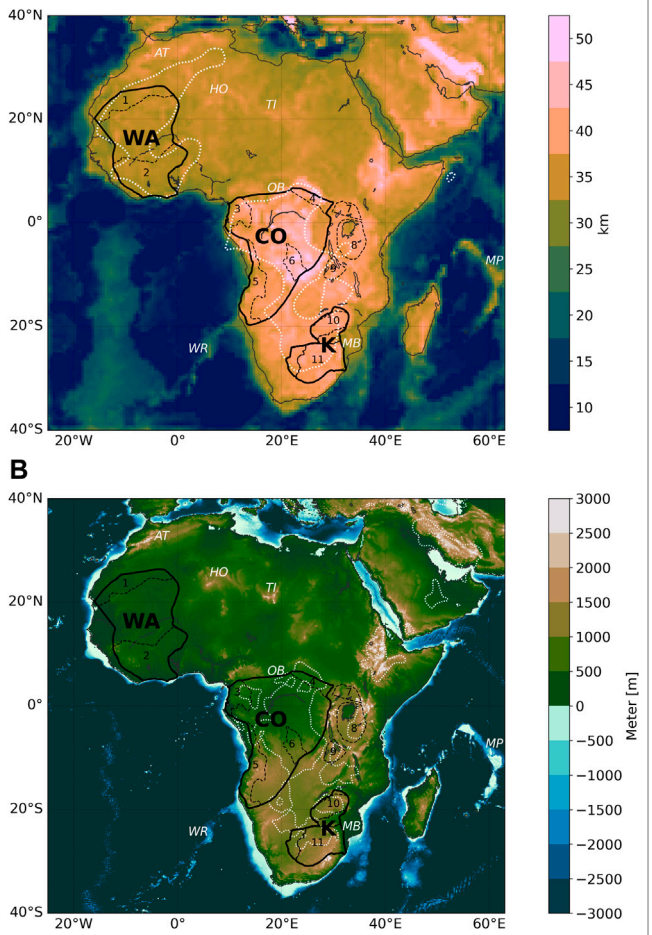

FIGURE 6 | (A) Final estimated Moho depth. Black solid contours indicate the extent of the West African Craton (WA), Congo Craton (CO) and Kalahari Craton (K), as seen in surface geology. Black dashed contours represent smaller cratons and individual shields. 1: Reguibat, 2: Man-Leo, 3: Gabon-Cameroon, 4: Bomu-Kibali, 5: Angola, 6: Kasai, 7: Uganda, 8: Tanzania, 9: Bangweulu, 10: Zimbabwe, 11: Kaapvaal. Contours are taken from Begg et al., 2009. Other tectonic domains that are discussed in the text are indicated in white italic letters. AT: Atlas Mountains, HO: Hoggar Mountains, TI: Tibesti Mountains, OB: Oubanguides Mobile Belt, MB: Mozambique Basin, WR: Walvis Ridge, MP: Mascarene Plateau. White dotted lines indicate the +4% dV_s contours between 80–150 km, calculated from the AF2019 model. **(B)** Topographic map with same contours of cratonic and shield extent as in a). White dotted lines indicate the 40 km contour of the estimated Moho depth of a).

In the second step, the density contrast of the three cratonic units are varied, resulting in $n = 9^3 = 729$ combinations. $\Delta\rho$ for the other units is taken from the first step. Finally, the density contrasts that define the best-fitting $RMS_{i,Comb}$ are taken to calculate the final Moho depth.

Splitting the density contrast variations in two steps significantly improves the total number of possible variations from $n = 9^8 = 43.046.721$ to $n = 9^5 + 9^3 = 59.778$ combinations, making this approach computationally very efficient. For details, the reader is referred Haas et al. (2020).

3 RESULTS

Figure 5 shows the density curves for the best-fitting models of both inversion steps, as defined by the combined RMS. The distribution for the individual constraints are documented in the Supplementary Material (**Supplementary Figure S10**). For the oceanic domains, including ridges, we estimate a density contrast between $\Delta\rho = 300 - 450$ kg/m^3 (**Figure 5A**). The flat curve for ridges is caused by different sensitivities of the constraints (**Supplementary Figure S10**). For the two continental domains, Precambrian Fold Belts and Phanerozoic, we estimate higher density contrasts. Phanerozoic is expressed as a pronounced maximum at a density contrast of $\Delta\rho = 600$ kg/m^3, whereas Precambrian Fold Belts show a rather flat distribution with a preferred density contrast of $\Delta\rho = 450$ kg/m^3. For the cratons, the Congo Craton reflects a distinct maximum at $\Delta\rho = 200$ kg/m^3, which is the lowest density contrast tested (**Figure 5B**). Like for the other domains, different sensitivities of AS and RF constraints cause shifts of the individual density curves (**Supplementary Figure S10**). For the Kalahari Craton, an intermediate density contrast of $\Delta\rho = 350$ kg/m^3 is preferred, while the West African Craton shows a smooth distribution of density contrasts with a slight plateau of higher density contrasts (**Figure 5B**).

In a gridded space, the density contrasts illustrate higher values for continental compared to oceanic domains (**Figure 5C**). However, for the continents, the range of estimated density contrasts is wider than for the oceans. In the north, the West African Craton is indistinguishable from its surrounding, as the adjacent Precambrian Fold Belts fit the same density contrast ($\Delta\rho = 450$ kg/m^3). In the south, the Kalahari Craton slightly contrasts to the surrounding fold belts $\Delta\rho = 350$ kg/m^3 vs. $\Delta\rho = 450$ kg/m^3). As the most prominent anomaly on the continent, the Congo Craton is clearly distinguished from the Precambrian Fold Belts ($\Delta\rho = 250$ kg/m^3 vs. $\Delta\rho = 450$ kg/m^3).

The differences of the estimated density contrasts are partly reflected in the corresponding Moho depth (**Figure 6A**). Offshore, deeper Moho correlates with ridge features like the Walvis Ridge and the Mascarene Plateau in the Indian Ocean. With an average Moho depth of 32.9 km Ridges and Backarks are overestimated in our Moho model (**Table 1**). There are two reasons for the deep Moho at ridges: First, the gravity data may contain a remnant signal of thermal anomalies in the oceanic lithosphere. For oceanic ridges, this effect is expected to be strongest, as the oceanic lithosphere is very young and hot (Chappell and Kusznir, 2008). Second, parts of the East African Rift System, which is densely covered by seismic stations, fall into the same cluster, causing a bias towards the continents (**Figure 4A**). For older oceanic lithosphere and deep ocean basins, the Moho depth is mainly shallower than 15 km.

On the African continent, western and northern Africa are characterized by a rather homogeneous Moho, extending from 30 to 35 km depth. Compared to the oceanic domains the estimated Moho depth is more constant for the individual domains, especially for the cratons, which is expressed by low standard deviation values (**Table 1**). With an average Moho depth of

TABLE 1 | Estimated density contrasts and distribution of seismic stations. STD = standard deviation.

Tectonic domain	Density contrast [kg/m^3]	Number of stations	Mean moho depth and STD [*km*]	Coverage of seismic stations [%]
Precambrian Fold Belts	500	247	36.7 ± 3.1	19.0
Phanerozoic Continents	600	188	35.8 ± 3.1	15.2
Ridges and Backarcs	450	92	32.9 ± 8.5	8.0
Oceanic	300	60	17.3 ± 9.9	3.9
Oldest Oceanic	350	74	16.3 ± 7.3	5.0
Kalahari Craton	350	111	39.9 ± 2.1	60.6
Congo Craton	200	12	39.7 ± 3.1	4.9
West African Craton	450	11	33.5 ± 2.0	3.7
Cratons total	200–450	134	39.2 ± 3.0	14.46

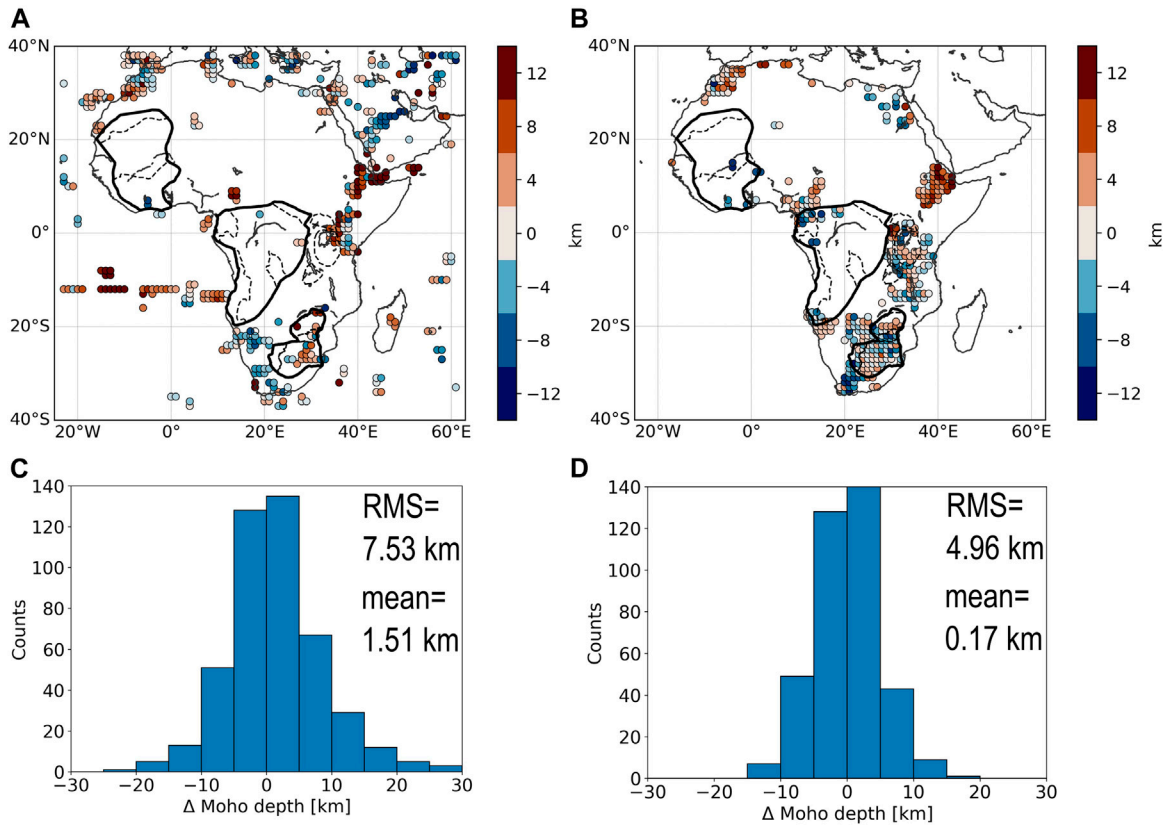

FIGURE 7 | Fit of the estimated Moho depth to the seismic constraints. Red colours indicate a deeper estimated Moho depth, while blue colours indicate a shallower Moho depth compared to the seismic constraints. **(A)** Estimated Moho depth minus AS constraints, **(B)** Estimated Moho depth minus RF constraints, **(C)** Histogram of differences for AS constraints, **(D)** Histogram of differences for RF constraints.

33.5 km (**Table 1**) the West African Craton does not contrast from the surrounding mobile belts. Deeper Moho depths for West and North-East Africa correlate with high topography, including Atlas, Hoggar, and Tibesti Mountains.

As the largest tectonic domain in Central Africa, the Moho of the Congo Craton reaches depths deeper than 50 km in the Kasai Shield, which is the deepest structure of the African continent. However, the average Moho depth is 39.7 km, indicating a Moho with a rather heterogeneous geometry. Towards the northern Oubanguides Mobile Belt the Moho depth displays a sharp contrast. This is well established in the Gabon-Cameroon and Bomu-Kibali Shields, where the Moho depth reveals deep anomalies. In between the two shields and at the eastern boundary, the Moho depth is uplifted to around 35 km.

The adjacent Archean shields to the east (Uganda, Tanzania and Bangweulu) are characterized by an intermediate continental Moho depth around 40 km. In the Afar region further north, the Moho depth reaches up to 50 km.

The deep Moho of the Congo Craton extends through the Proterozoic fold belts inside the Kalahari Craton, which has an average Moho depth of 39.9 km (**Table 1**). The Moho depth for the internal Archean sub-cratons (Kaapvaal and Zimbabwe) is

similar. This gives a homogeneous Moho depth of the Kalahari Craton, as expressed by a low standard deviation of 2.1 km (**Table 1**). Only the eastern boundary coincides with a sharp contrast in the Moho depth. Here, the Moho depth changes from 40 km in the Kalahari Craton to less than 30 km in the Mesozoic Mozambique Basin.

In many regions, the deep Moho depth correlates with high topography, i.e., in the East African Rift System, Tanzania Craton, Bangweulu Block, and parts of the Kalahari Craton (**Figure 6B**). In the southwestern Congo Craton, the high topography of the Angolan Shield partly correlates with a deep Moho. Towards the northern part of the Congo Craton, topography decreases to less than 500 m, while the deeper Moho is maintained to a large extent.

Our models for the Moho depth and associated density contrasts are estimated by the best-fitting Moho model compared to the initial seismic stations. **Figure 7** shows the fit to the seismic stations for AS and RF constraints separately. For the AS constraints, the estimated Moho depth is more than 10 km deeper in the East African Rift System and the Cameroon Volcanic Line (**Figure 7A**). The latter is constrained by five stations north of the Congo Craton. West of the Kalahari Craton several station clusters reveal Moho depth estimates more than 10 km shallower. Locally, the differences between Moho depth estimates and AS constraints can be higher than 20 km (**Figure 7C**). However, most stations are binned between ±10 km. With a mean value of 1.51 km the estimated Moho depth is slightly deeper than the AS constraints.

For the RF constraints, the estimated Moho depth of the East African Rift System is deeper as well (**Figure 7B**), even though the difference is less strong as for the AS constraints. The well covered Kalahari Craton, as well as the Tanzania and Uganda Shield show a good fit with differences mainly within ±4 km. In the area of the Gabon-Cameroon Shield the estimated Moho depth is locally more than 12 km shallower. To the north, in the adjacent Cameroon Volcanic Line, this trend changes and the Moho depth estimate is only up to 4 km deeper than the RF constraints.

Interestingly, the cumulative histogram shows a better fit for the RF estimates compared to the AS estimates (**Figure 7D**), which is also expressed in the RMS_{RF} value (4.96 km RF vs 7.53 km for AS). There are two reasons for the better fit of the RF estimates: First, offshore stations lack in the RF data base. As a consequence, the overestimated Moho depth for ridges are not reflected in the RMS. Second, more RF than AS estimates are available for the continent, resulting in a good match of RF estimates with the gravity-estimated Moho for large parts of the Kalahari, Tanzania, and Uganda Cratons.

4 DISCUSSION

4.1 Limitations of the Estimated Density Contrasts

The significance of the estimated density contrasts for each tectonic domain is manifested in the peaks of the density curves (**Figure 5**). Haas et al. (2020) showed that station coverage and amplitude of the gravity signal control the estimated density contrast distributions. This observation is also valid for the African continent, even though the poor station coverage in some tectonic domains hampers a progressive increase of density contrasts with tectonic age, as observed in the Amazonian Craton and its surroundings (Haas et al., 2020). The estimated density contrasts for the Phanerozoic domain and for the Congo Craton are located at the boundaries of the given range, representing realistic petrological assumptions (see Data and Methods). Nevertheless, the trend of the estimated density contrasts shows a flattening of the curve for the Phanerozoic domain, indicating that the estimated density contrasts are close to the theoretical peak. For the Congo Craton, the curve represents the dependence of the estimated density contrasts to a low number of receiver functions.

For the Phanerozoic domain, the seismic stations are predominantly located in mountainous regions (Atlas, Great Rift Valley, and Cameroon Volcanic Line), which are characterized by a deeper Moho that isostatically compensates the high topography. This coincides with a high density contrast across the Moho, which is also confirmed by gravity inversions in mountain ranges (e.g., Zhao et al., 2020). In the East African Rift System, the Moho depth is overestimated compared to both seismic constraints because of an unaccounted gravity signal of the upwelling mantle. Contrary to this, for the Cameroon Volcanic Line the AS constraints show a worse fit to the estimated Moho depth compared to the RF constraints of Tokam et al. (2010). However, in the same study, a deeper Moho depth between 43–48 km for the northern Congo Craton is identified, which is in stark contrast to our estimated Moho depth.

The impact of the poor station coverage is highly evident in the cratonic units. For the Congo Craton, the density curve of the AS constraints is flat, because no constraints are located in the Congo Craton (**Supplementary Figure S10** and **Table 1**). Here, only few receiver functions that are located in the vicinity of the Congo Basin (Tokam et al., 2010) can be used to make any assumptions on Moho depth and density contrast. Given the sparse distribution of seismic stations and the uncertainties of sediment thickness, the Congo Craton contrasts to the surrounding fold belts by a distinct low density contrast, which fits in the classical view of smooth density transitions in cratonic lithosphere. However, the impact of the available sediment data on the estimated Moho depth illustrates that it is almost impossible to predict the Moho depth precisely. Clearly, more seismic stations are required to shed light in the crustal architecture of the Congo Basin and Congo Craton.

The West African Craton reflects the smoothest density curve of all cratons, which is caused both by the lowest station coverage of all tectonic units and the low amplitude of the gravity data (**Table 1** and **Figure 1**). Generally, a low gravity signal inherently implies a flat Moho geometry. That means, even if the West African Craton was densely covered by seismic stations, the estimated Moho depth would not change significantly. Coincidentally, a wide range of density contrasts can explain the observed gravity signal, like it is the case for the West African Craton.

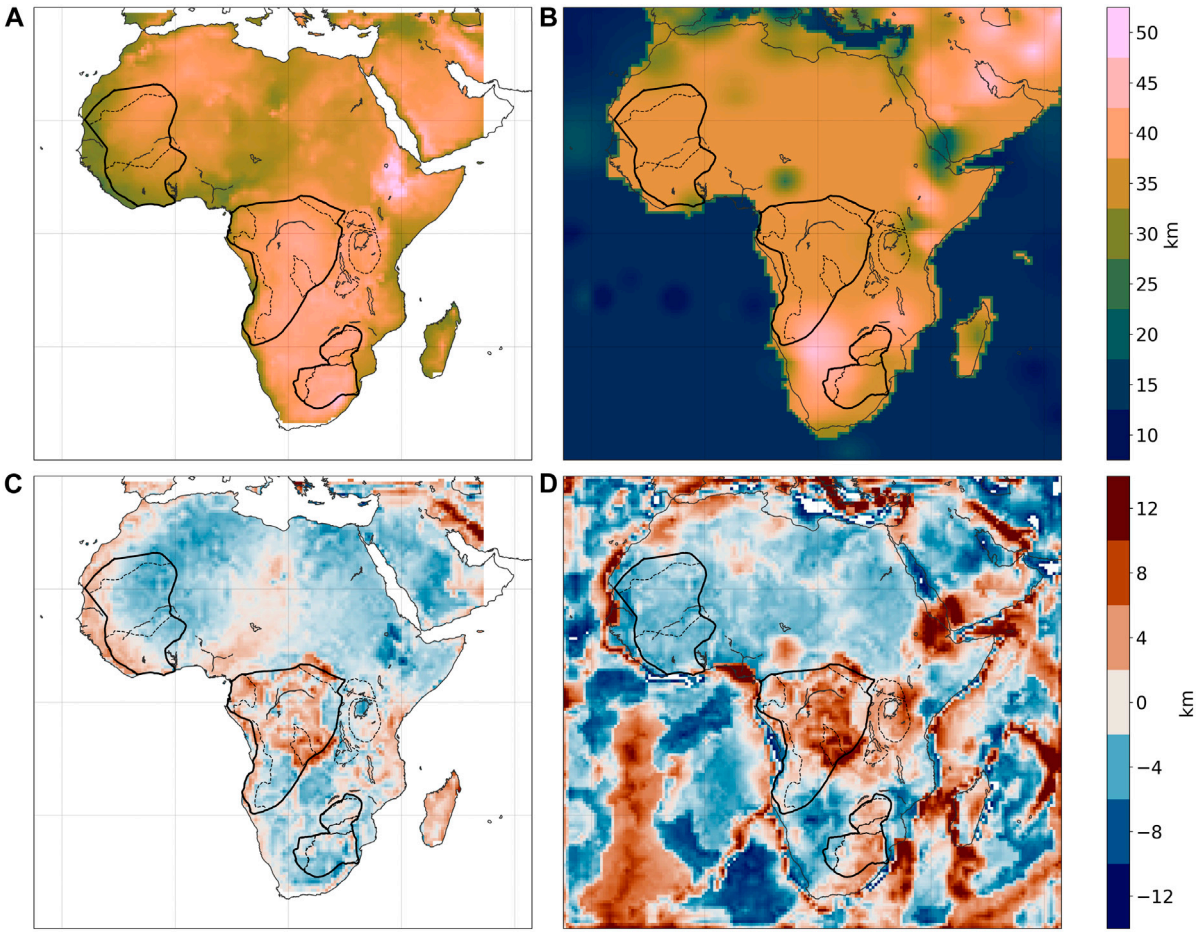

FIGURE 8 | Comparison of Moho depth models. **(A)** Moho depth model of Globig et al. (2016), which is only defined for the African continent. **(B)** Moho depth model of Szwillus et al. (2019). **(C)** Difference of our estimated Moho model minus Globig-Moho. **(D)** Difference of our estimated Moho model minus Szwillus-Moho. Contours indicate cratons and shields, taken from **Figure 6**.

The large Moho depth variations between gravity and receiver functions estimates on a small scale illustrate the limits of the constraining procedure. Velocity contrasts do not necessarily coincide with density contrasts, especially between different tectonic settings, and variations in temperature and anisotropy can affect the local velocity structure (e.g., Fullea et al., 2021). To overcome this discrepancy a more detailed analysis on combining the characteristics of both methods is required. One strategy forward would be to calculate synthetic receiver functions from the initial density model, using published density to velocity conversions (e.g. Julià, 2007; Masters et al., 2011).

4.2 Comparison With Other Moho Depth Models

In this section, we compare our estimated Moho depth model on continental scale with the continental model of Globig et al. (2016) (Globig-Moho) and the global model of Szwillus et al. (2019) (Szwillus-Moho). The Globig-Moho represents the latest continental Moho model, while the Szwillus-Moho is a global Moho model, obtained by interpolation of active source seismics only. It is derived by the USGS GSC data base that serves as pointwise constraint in our inversion. Therefore, a comparison with the Szwillus-Moho reflects the difference to the seismic Moho depth in a gridded space.

Like our estimated Moho depth model the Globig-Moho shows a deeper Moho for central and southern Africa, including the Congo and Kalahari Cratons (**Figure 8A**). However, the bimodal pattern is not as pronounced as in our model. In the Globig-Moho, the West African Craton progressively thickens towards the Atlas Mountains and thins towards the West African coast. In our model, the Moho of the West African Craton is mainly flat. The difference map shows a long-wavelength trend that documents the upper mantle contribution in the geoid anomaly map that Globig et al. (2016) used as input data (**Figure 8C**). Similar to our model, the Globig-Moho in the Afar region is characterized by a deep Moho. The deep Moho depth of both models represent isostatic compensation caused by high topography. This is also reflected in the gravity data (**Figure 1**). The question is then how

representative the isostatic state is for the Afar region. As the Afar region is underlain by an active plume, isostasy might be an inappropriate representation of the lithospheric state (Czechowski, 2019). Our Moho model rather shows the hypothetic isostatic state caused by the elevated topography in the Afar region.

The Szwillus-Moho predominantly displays long-wavelength structures that arise from the sparse coverage of seismic stations (**Figure 8B**). As in all data-sparse regions, like the West African and Congo Cratons, the Szwillus-Moho represents global mean values for continental Moho depth. Therefore, these two cratons cannot be differentiated. The only region where the Moho depth varies on small scale is the East African Rift System. Here, the Moho depth deepens from 20 km in the Afar Region to 45 km in the Ethiopian Highlands and back to 25 km in the Great Rift Valley of Ethiopia. In our model, this region is characterized by a Moho more than 12 km deeper than the Szwillus-Moho (**Figure 8D**). Most probably, the differences reflect an unaccounted gravity signal of the underlying Afar plume.

The general difference pattern reflects stronger amplitudes compared to the Globig-Moho. A shallower Moho is located in the East African System and Congo Craton, as well as in the southern Kalahari Craton, whereas deeper Moho can be found in the Mozambique Basin and Damara Belt, separating the Congo Craton from the Kalahari Craton. The comparison to the Szwillus-Moho reproduces the difference of the pointwise constraints (**Figure 7A**), as well as the difference to average continental Moho depth in data sparse regions in a gridded space.

4.3 Correlation Between Archean Crust and Archean Lithospheric Mantle

The general architecture of mid-Archean lithosphere is characterized by thick lithosphere and a shallow and sharp Moho (Artemieva, 2009; Abbott et al., 2013). In Paleoproterozoic regions, the crust gradually thickens and the Moho gets more diffuse in terms of v_p/v_s-ratios (Abbott et al., 2013; Yuan, 2015). The West Australian Craton can be regarded as a classic example that fulfills those criteria (Yuan, 2015). However, cratonic regions like the West African Craton might not fit in this uniform picture. In what follows, we investigate how the three African cratons fit in this uniform picture and link the gravity-derived Moho depth to the geographic extension of cratons, as imaged by seismic tomography (Celli et al., 2020).

Cratonic lithosphere can be affected by various mechanisms. On the one hand, the composition and temperature of cratonic mantle lithosphere can be modified by metasomatism and plume activity (e.g., Lee et al., 2011; Kusky et al., 2014; Dave and Li, 2016; Wenker and Beaumont, 2018). On the other hand, its thermal boundary layer can be mechanically eroded or recycled into the convective mantle. In addition, it is often proposed that in the Archean the denser lower crust was delaminated and recycled into the convective mantle, therefore before cratonization (Abbott et al., 2013). Using seismic tomography, bedrock geology, and diamondiferous kimberlites, Celli et al. (2020) showed that a large portion of the African cratons has been eroded by mantle plumes.

The lateral extension of the Congo and Kalahari Cratons coincides with a Moho deeper than 40 km (**Figure 6A**). This could suggest late-to post-Archean crustal thickening before stabilization of the crust. However, the stabilization of the Kalahari Craton is dated to mid-Archean (Abbott et al., 2013 and references within). For the Kalahari Craton, magmatic underplating triggered by the Karoo volcanism might be an alternative explanation for the deep crust (Cox, 1993). However, 3D modelling suggests that the high topography is largely isostatically compensated by the crust, accompanied by lateral changes in lithospheric mantle density (Scheiber-Enslin et al., 2016). In this study, only a small portion of the topographic signal is explained by buoyant asthenosphere, causing excess elevation of the African superswell (Lithgow-Bertelloni and Silver, 1998). We follow the study of Scheiber-Enslin et al. (2016) and interpret the deep Moho depth of the Kalahari Craton as isostatic compensation of high topography. The same mechanism might explain the deep Moho for the Congo Craton, even though missing data of stabilization age and Neoproterozoic subsidence of the Congo Basin are additional sources that need to be considered. Located in the center of the Congo Craton, the lighter sediments of the Congo Basin may uplift the Moho depth a few kilometers. However, the overall pattern of deeper Moho depth is preserved (**Supplementary Figure S4**). Furthermore, large uncertainties in the sedimentary data base hamper a valid assessment of the gravitational effect.

Some Archean shields are not imaged by seismic tomography (**Figure 6**). This is evident for the Angolan Shield, as well as the Uganda and Tanzania Cratons. Celli et al. (2020) propose that the missing cratonic root for the Angolan Shield is the result of Tristan Plume activity, and for the Tanzania and Uganda Cratons by ongoing activity of the Afar Plume. Our estimated Moho depth shows that Archean crust is still preserved, while the underlying lithosphere has been partially eroded, indicating that the crustal structure has been affected only little by the process of cratonic destruction. At the southeastern edge of the Angolan Shield, the deep Moho partly correlates with high topography (**Figure 6B**). This small scale topographic uplift ocurred in the Neogene, forming the so called Angola dome (Klöcking et al., 2020). The uplift of the Angola dome might be sourced from a small positive temperature anomaly in the asthenosphere, causing thinning of the overlying mantle (Klöcking et al., 2020), while the deep Moho has been preserved (**Figure 6A**). Such a rejuvenation of the lithospheric mantle has also been observed for other cratons like the Wyoming Craton and the North China Craton (Gao et al., 2004; Zhao et al., 2009; Dave and Li, 2016).

The West African Craton is in stark contrast to the other African cratons. While seismic tomography reveals a large lateral extension of cratonic lithosphere, the Moho depth is shallow and does not differentiate from the surrounding tectonic units. The sediments of the Neoproterozoic Taoudeni Basin contribute only minor the estimated Moho depth (**Supplementary Figures S4, S5**). As the West African Craton amalgamated in the Paleoproterozoic (e.g., Block et al., 2015), the Moho depth is

expected to be deeper than older cratons (Abbott et al., 2013). This raises the following question: Which process (es) caused the thinning of the crust without affecting the lithosphere?

Analysis of geological and geochronological data from NW Ghana suggests that the lower crust was largely exhumed and juxtaposed against the shallow crust during the Eburnean orogeny (2.15–2.0 Ga, Block et al., 2015). This exhumation involves extensional detachments that stretch and thin the upper crust, providing the space in the upper crust for the lower crust to flow into. The horizontal flow of the weak lower crust from regions of thicker crust towards regions of thinner crust would result in a thinner continental crust and a flat and shallower Moho. However, this process of gravitational collapse is often driven by to the convective removal of the thermal boundary layer of the lithosphere, which leads to thinning of the entire lithosphere (Rey et al., 2001; Rey et al., 2017). The preserved buoyancy of the Archean keel at the time of the Eburnean Orogeny may have prevented the recycling of the lithosphere thermal boundary layer into the convective mantle. Nevertheless, the association of a thinned crust, with a preserved thick lithospheric root remains enigmatic.

5 CONCLUSION

We have investigated the variable lithospheric architecture of the African cratons, based on a new gravity-derived continental Moho depth model. The model is constrained by a state-of-the-art tectonic regionalization map, calculated from the AF 2019 tomography model, and an updated seismic data base. This data base comprises different acquisition types that we distinguish between active source seismics and receiver functions.

Our two-step gravity inversion updates the method of Haas et al. (2020) by allowing flexible density contrasts for individual tectonic units. This splitting in two steps strongly decreases computation time. The estimated density contrasts at the Moho reveal large differences between the different tectonic domains and between the individual cratons. For the Congo Craton, we identify a density contrast of $\Delta\ \rho = 200\ kg/m^3$. The Kalahari Craton is the best-constrained tectonic unit and shows an intermediate density contrast of $\Delta\ \rho = 350\ kg/m^3$, which is typical of what we expect between the lower continental crust and the mantle. Uncertainties in the estimated density contrasts arise from different measuring techniques and sparse data coverage. This is well reflected in the poor distribution of density curves for the West African Craton.

The estimated Moho depth shows a bimodal pattern with deeper crust for the Congo and Kalahari Cratons and shallower crust for the West African Craton. The sediments of the intracratonic Congo and Taoudeni Basins, whose architecture is largely unknown, do not significantly change this observed pattern. We have demonstrated that the differences between the estimated Moho depth and the seismic constraints are not necessarily constant for both constraint types. This is well reflected in the Cameroon Volcanic Line, where the estimated Moho depth model fits receiver function constraints better than those from active source seismics.

We have analyzed the coupling between our Moho depth model and high seismic velocities in the mantle, as imaged by seismic tomography for the cratonic regions. For the southern and central cratons, the lithospheric keel matches with a deep Moho depth. Here, the deep Moho depth more likely represents an isostatic root of elevated topography and thick Archean crust. Contrary to that, the deep lithosphere of the West African Craton coincides with a flat and homogeneous Moho depth. Lower crustal exhumation with subsequent crustal flow and gravitational collapse cannot explain the observed pattern. Thus, for the West African Craton the observed lithospheric architecture remains enigmatic.

Clearly, more data from both active and seismic methods is required to further investigate the lithosphere of the West African and Congo Cratons. This would also help to disentangle the role of the yet very poorly explored big intracratonic sedimentary Congo and Taoudeni Basins for cratonic evolution.

In a next step, the variable build-up of the cratonic portions, as seen by the joint gravity inversion and seismological regionalization approach, should be tested for another continent. Moho depth variations between gravity and receiver functions estimates could be further investigated by calculating synthetic receiver functions from the accompanying density model. Special focus should be put to the coupling of the crustal and lithospheric structure, which is crucial for understanding the cratonization and destabilization of Earth's early crust.

DATA AVAILABILITY STATEMENT

Gravity gradient data are available from ESA: https://earth.esa.int/eogateway/missions/goce/goce-gravity-gradients-grids. The seismic tomography model AF2019 can be downloaded from the following webpage: https://nlscelli.wixsite.com/ncseismology/models. The constraints of seismic Moho depth are taken from the Globig et al. (2016) paper: https://agupubs.onlinelibrary.wiley.com/doi/full/10.100 2/2 016JB012972. Our estimated Moho depths, both with and without sediments, as well as the estimated density contrasts are available on the Github link below. We encourage the scientific community to test the presented inversion for their purposes. Therefore, we share our code on Github, where the inversion is reconstructed for a smaller test area: https://github.com/peterH105/Gradient_Inversion/.

AUTHOR CONTRIBUTIONS

All authors listed have made a substantial, direct, and intellectual contribution to the work and approved it for publication.

FUNDING

This work has been funded by the Deutsche Forschungsgemeinschaft (DFG) within the project "Linking the deep structures of the cratons of Africa and South America by integrated geophysical modelling" (project number

336717379), as well as by European Space Agency (ESA) as a Support to Science Element (STSE) within the project "3D Earth-A Dynamic Living Planet."

ACKNOWLEDGMENTS

We thank Wolfgang Szwillus for discussions on clustering of seismic tomography data and implementing the gravity inversion code. All figures have been created with Matplotlib. We are thankful for the valuable comments of three reviewers.

SUPPLEMENTARY MATERIAL

The Supplementary Material for this article can be found online at: https://www.frontiersin.org/articles/10.3389/feart.2021.696674/full#supplementary-material

REFERENCES

Abbott, D. H., Mooney, W. D., and VanTongeren, J. A. (2013). The Character of the Moho and Lower Crust within Archean Cratons and the Tectonic Implications. *Tectonophysics* 609, 690–705. doi:10.1016/j.tecto.2013.09.014

Artemieva, I. M. (2009). The continental Lithosphere: Reconciling thermal, Seismic, and Petrologic Data. *Lithos* 109, 23–46. doi:10.1016/j.lithos.2008.09.015

Artemieva, I. M., and Vinnik, L. P. (2016). Density Structure of the Cratonic Mantle in Southern Africa: 1. Implications for Dynamic Topography. *Gondwana Res.* 39, 204–216. doi:10.1016/j.gr.2016.03.002

Begg, G. C., Griffin, W. L., Natapov, L. M., O'Reilly, S. Y., Grand, S. P., O'Neill, C. J., et al. (2009). The Lithospheric Architecture of Africa: Seismic Tomography, Mantle Petrology, and Tectonic Evolution. *Geosphere* 5, 23–50. doi:10.1130/GES00179.1

Block, S., Ganne, J., Baratoux, L., Zeh, A., Parra-Avila, L. A., Jessell, M., et al. (2015). Petrological and Geochronological Constraints on Lower Crust Exhumation during Paleoproterozoic (Eburnean) Orogeny, NW Ghana, West African Craton. *J. Meta. Geol.* 33, 463–494. doi:10.1111/jmg.12129

Bouman, J., Ebbing, J., Fuchs, M., Sebera, J., Lieb, V., Szwillus, W., et al. (2016). Satellite Gravity Gradient Grids for Geophysics. *Sci. Rep.* 6, 21050. doi:10.1038/srep21050

Celli, N. L., Lebedev, S., Schaeffer, A. J., and Gaina, C. (2020). African Cratonic Lithosphere Carved by Mantle Plumes. *Nat. Commun.* 11, 92. doi:10.1038/s41467-019-13871-2

Chappell, A. R., and Kusznir, N. J. (2008). Three-dimensional Gravity Inversion for Moho Depth at Rifted continental Margins Incorporating a Lithosphere thermal Gravity Anomaly Correction. *Geophys. J. Int.* 174, 1–13. doi:10.1111/j.1365-246X.2008.03803.x

Cox, K. G. (1993). Continental Magmatic Underplating. *Phil. Trans. R. Soc. Lond. A.* 342, 155–166. doi:10.1098/rsta.1993.0011

Czechowski, L. (2019). Mantle Flow and Determining Position of LAB Assuming Isostasy. *Pure Appl. Geophys.* 176, 2451–2463. doi:10.1007/s00024-019-02093-8

Dave, R., and Li, A. (2016). Destruction of the Wyoming Craton: Seismic Evidence and Geodynamic Processes. *Geology* 44, 883–886. doi:10.1130/G38147.1

Doucouré, C. M., and de Wit, M. J. (2003). Old Inherited Origin for the Present Near-Bimodal Topography of Africa. *J. Afr. Earth Sci.* 36, 371–388. doi:10.1016/S0899-5362(03)00019-8

Emry, E. L., Shen, Y., Nyblade, A. A., Flinders, A., and Bao, X. (2019). Upper Mantle Earth Structure in Africa from Full-Wave Ambient Noise Tomography. *Geochem. Geophys. Geosyst.* 20, 120–147. doi:10.1029/2018GC007804

Eymold, W. K., and Jordan, T. H. (2019). Tectonic Regionalization of the Southern California Crust from Tomographic Cluster Analysis. *J. Geophys. Res. Solid Earth* 124, 11840–11865. doi:10.1029/2019JB018423

Fadel, I., van der Meijde, M., and Paulssen, H. (2018). Crustal Structure and Dynamics of Botswana. *J. Geophys. Res. Solid Earth* 123 (10659–10), 10659–10671. doi:10.1029/2018JB016190

Fishwick, S., and Bastow, I. D. (2011). Towards a Better Understanding of African Topography: A Review of Passive-Source Seismic Studies of the African Crust and Upper Mantle. *Geol. Soc. Lond. Spec. Publications* 357, 343–371. doi:10.1144/SP357.19

Fishwick, S. (2010). Surface Wave Tomography: Imaging of the Lithosphere-Asthenosphere Boundary beneath central and Southern Africa? *Lithos* 120, 63–73. doi:10.1016/j.lithos.2010.05.011

François, T., Burov, E., Meyer, B., and Agard, P. (2013). Surface Topography as Key Constraint on Thermo-Rheological Structure of Stable Cratons. *Tectonophysics* 602, 106–123. doi:10.1016/j.tecto.2012.10.009

Fullea, J., Lebedev, S., Martinec, Z., and Celli, N. L. (2021). WINTERC-G: Mapping the Upper Mantle Thermochemical Heterogeneity from Coupled Geophysical-Petrological Inversion of Seismic Waveforms, Heat Flow, Surface Elevation and Gravity Satellite Data. *Geophys. J. Int.* 226, 146–191. doi:10.1093/gji/ggab094

Gao, S., Rudnick, R. L., Yuan, H.-L., Liu, X.-M., Liu, Y.-S., Xu, W.-L., et al. (2004). Recycling Lower continental Crust in the North China Craton. *Nature* 432, 892–897. doi:10.1038/nature03162

Garber, J. M., Maurya, S., Hernandez, J. A., Duncan, M. S., Zeng, L., Zhang, H. L., et al. (2018). Multidisciplinary Constraints on the Abundance of diamond and Eclogite in the Cratonic Lithosphere. *Geochem. Geophys. Geosyst.* 19, 2062–2086. doi:10.1029/2018GC007534

Globig, J., Fernàndez, M., Torne, M., Vergés, J., Robert, A., and Faccenna, C. (2016). New Insights into the Crust and Lithospheric Mantle Structure of Africa from Elevation, Geoid, and thermal Analysis. *J. Geophys. Res. Solid Earth* 121, 5389–5424. doi:10.1002/2016JB012972

Haas, P., Ebbing, J., and Szwillus, W. (2020). Sensitivity Analysis of Gravity Gradient Inversion of the Moho Depth-A Case Example for the Amazonian Craton. *Geophys. J. Int.* 221, 1896–1912. doi:10.1093/gji/ggaa122

Heit, B., Yuan, X., Weber, M., Geissler, W., Jokat, W., Lushetile, B., et al. (2015). Crustal Thickness and Vp/Vs Ratio in NW Namibia from Receiver Functions: Evidence for Magmatic Underplating Due to Mantle Plume-Crust Interaction. *Geophys. Res. Lett.* 42, 3330–3337. doi:10.1002/2015GL063704

Hosny, A., and Nyblade, A. (2016). The Crustal Structure of Egypt and the Northern Red Sea Region. *Tectonophysics* 687, 257–267. doi:10.1016/j.tecto.2016.06.003

Hu, J., Liu, L., Faccenda, M., Zhou, Q., Fischer, K. M., Marshak, S., et al. (2018). Modification of the Western Gondwana Craton by Plume-Lithosphere Interaction. *Nat. Geosci* 11, 203–210. doi:10.1038/s41561-018-0064-1

Jessell, M. W., Begg, G. C., and Miller, M. S. (2016). The Geophysical Signatures of the West African Craton. *Precambrian Res.* 274, 3–24. doi:10.1016/j.precamres.2015.08.010

Julià, J. (2007). Constraining Velocity and Density Contrasts across the Crust-Mantle Boundary with Receiver Function Amplitudes. *Geophys. J. Int.* 171, 286–301. doi:10.1111/j.1365-2966.2007.03502.x

Klöcking, M., Hoggard, M. J., Rodríguez Tribaldos, V., Richards, F. D., Guimarães, A. R., Maclennan, J., et al. (2020). A Tale of Two Domes: Neogene to Recent Volcanism and Dynamic Uplift of Northeast Brazil and Southwest Africa. *Earth Planet. Sci. Lett.* 547, 116464. doi:10.1016/j.epsl.2020.116464

Kusky, T. M., Windley, B. F., Wang, L., Wang, Z., Li, X., and Zhu, P. (2014). Flat Slab Subduction, Trench Suction, and Craton Destruction: Comparison of the North China, Wyoming, and Brazilian Cratons. *Tectonophysics* 630, 208–221. doi:10.1016/j.tecto.2014.05.028

Lebedev, S., Boonen, J., and Trampert, J. (2009). Seismic Structure of Precambrian Lithosphere: New Constraints from Broad-Band Surface-Wave Dispersion. *Lithos* 109, 96–111. doi:10.1016/j.lithos.2008.06.010

Lee, C.-T. A., Luffi, P., and Chin, E. J. (2011). Building and Destroying continental Mantle. *Annu. Rev. Earth Planet. Sci.* 39, 59–90. doi:10.1146/annurev-earth-040610-133505

Lekic, V., and Romanowicz, B. (2011). Tectonic Regionalization without A Priori Information: A Cluster Analysis of Upper Mantle Tomography. *Earth Planet. Sci. Lett.* 308, 151–160. doi:10.1016/j.epsl.2011.05.050

Lithgow-Bertelloni, C., and Silver, P. G. (1998). Dynamic Topography, Plate Driving Forces and the African Superswell. *Nature* 395, 269–272. doi:10.1038/26212

Masters, G., Woodhouse, J. H., and Freeman, G. (2011). Mineos v1.0.2 [software], Computational Infrastructure for Geodynamics. Available at: https://geodynamics.org/cig/software/mineos/.

Mooney, W. D. (2015). "Crust and Lithospheric Structure – Global Crustal Structure," in *Treatise on Geophysics*. Editor G. Schubert (Amsterdam: Elsevier), 361–398.

Rabbel, W., Kaban, M., and Tesauro, M. (2013). Contrasts of Seismic Velocity, Density and Strength across the Moho. *Tectonophysics* 609, 437–455. doi:10.1016/j.tecto.2013.06.020

Rey, P. F., Mondy, L., Duclaux, G., Teyssier, C., Whitney, D. L., Bocher, M., et al. (2017). The Origin of Contractional Structures in Extensional Gneiss Domes. *Geology* 45, 263–266. doi:10.1130/G38595.1

Rey, P., Vanderhaeghe, O., and Teyssier, C. (2001). Gravitational Collapse of the continental Crust: Definition, Regimes and Modes. *Tectonophysics* 342, 435–449. doi:10.1016/S0040-1951(01)00174-3

Schaeffer, A. J., and Lebedev, S. (2015). "Global Heterogeneity of the Lithosphere and Underlying Mantle: A Seismological Appraisal Based on Multimode Surface-Wave Dispersion Analysis, Shear-Velocity Tomography, and Tectonic Regionalization," in *The Earth's Heterogeneous Mantle*. Editors A. Khan and F. Deschamps (Cham: Springer International Publishing), 3–46. doi:10.1007/978-3-319-15627-9_1

Scheiber-Enslin, S. E., Ebbing, J., and Webb, S. J. (2016). An Isostatic Study of the Karoo basin and Underlying Lithosphere in 3-d. *Geophys. J. Int.* 206, 774–791. doi:10.1093/gji/ggw164

Sobh, M., Ebbing, J., Mansi, A. H., Götze, H. J., Emry, E. L., and Abdelsalam, M. G. (2020). The Lithospheric Structure of the Saharan Metacraton from 3-D Integrated Geophysical-Petrological Modeling. *J. Geophys. Res. Solid Earth* 125, 2511. doi:10.1029/2019JB018747

Sun, M., Gao, S. S., Liu, K. H., Mickus, K., Fu, X., and Yu, Y. (2021). Receiver Function Investigation of Crustal Structure in the Malawi and Luangwa Rift Zones and Adjacent Areas. *Gondwana Res.* 89, 168–176. doi:10.1016/j.gr.2020.08.015

Szwillus, W., Afonso, J. C., Ebbing, J., and Mooney, W. D. (2019). Global Crustal Thickness and Velocity Structure from Geostatistical Analysis of Seismic Data. *J. Geophys. Res. Solid Earth* 124, 1626–1652. doi:10.1029/2018JB016593

Szwillus, W., Ebbing, J., and Holzrichter, N. (2016). Importance of Far-Field Topographic and Isostatic Corrections for Regional Density Modelling. *Geophys. J. Int.* 207, 274–287. doi:10.1093/gji/ggw270

Tokam, A.-P. K., Tabod, C. T., Nyblade, A. A., Julià, J., Wiens, D. A., and Pasyanos, M. E. (2010). Structure of the Crust beneath Cameroon, West Africa, from the Joint Inversion of Rayleigh Wave Group Velocities and Receiver Functions. *Geophys. J. Int.* 183, 1061–1076. doi:10.1111/j.1365-246X.2010.04776.x

Tugume, F., Nyblade, A., Julià, J., and van der Meijde, M. (2013). Precambrian Crustal Structure in Africa and Arabia: Evidence Lacking for Secular Variation. *Tectonophysics* 609, 250–266. doi:10.1016/j.tecto.2013.04.027

Uieda, L., and Barbosa, V. C. F. (2016). Fast Nonlinear Gravity Inversion in Spherical Coordinates with Application to the South American Moho. *Geophys. J. Int.* 208, 162–176. doi:10.1093/gji/ggw390

van der Meijde, M., Fadel, I., Ditmar, P., and Hamayun, M. (2015). Uncertainties in Crustal Thickness Models for Data Sparse Environments: A Review for South America and Africa. *J. Geodynamics* 84, 1–18. doi:10.1016/j.jog.2014.09.013

Wang, T., Gao, S. S., Yang, Q., and Liu, K. H. (2021). Crustal Structure beneath the Ethiopian Plateau and Adjacent Areas from Receiver Functions: Implications for Partial Melting and Magmatic Underplating. *Tectonophysics* 809, 228857. doi:10.1016/j.tecto.2021.228857

Wenker, S., and Beaumont, C. (2018). Can Metasomatic Weakening Result in the Rifting of Cratons? *Tectonophysics* 746, 3–21. doi:10.1016/j.tecto.2017.06.013

Youssof, M., Thybo, H., Artemieva, I. M., and Levander, A. (2013). Moho Depth and Crustal Composition in Southern Africa. *Tectonophysics* 609, 267–287. doi:10.1016/j.tecto.2013.09.001

Yu, Y., Liu, K. H., Reed, C. A., Moidaki, M., Mickus, K., Atekwana, E. A., et al. (2015). A Joint Receiver Function and Gravity Study of Crustal Structure beneath the Incipient Okavango Rift, Botswana. *Geophys. Res. Lett.* 42, 8398–8405. doi:10.1002/2015GL065811

Yuan, H. (2015). Secular Change in Archaean Crust Formation Recorded in Western Australia. *Nat. Geosci* 8, 808–813. doi:10.1038/ngeo2521

Zhao, G., Liu, J., Chen, B., Kaban, M. K., and Zheng, X. (2020). Moho beneath Tibet Based on a Joint Analysis of Gravity and Seismic Data. *Geochem. Geophys. Geosyst.* 21, 243. doi:10.1029/2019GC008849

Zhao, L., Allen, R. M., Zheng, T., and Hung, S.-H. (2009). Reactivation of an Archean Craton: Constraints from P- and S-Wave Tomography in North China. *Geophys. Res. Lett.* 36, 2089. doi:10.1029/2009GL039781

Conflict of Interest: The authors declare that the research was conducted in the absence of any commercial or financial relationships that could be construed as a potential conflict of interest.

The handling editor declared a past collaboration with one of the authors JE.

frontiers in Earth Science

REVIEW
published: 26 January 2022
doi: 10.3389/feart.2022.808503

Large-to Local-Scale Control of Pre-Existing Structures on Continental Rifting: Examples From the Main Ethiopian Rift, East Africa

Giacomo Corti[1]*, *Daniele Maestrelli*[1] *and Federico Sani*[2]

[1]Consiglio Nazionale Delle Ricerche, Istituto di Geoscienze e Georisorse, Firenze, Italy, [2]Dipartimento di Scienze Della Terra, Università di Firenze, Firenze, Italy

In the Main Ethiopian Rift (East Africa) a complex tectonic history preceded Tertiary rifting creating pre-existing discontinuities that influenced extension-related deformation. Therefore, this area offers the opportunity to analyze the control exerted by pre-existing structures on continental rifting at different scales. In this paper we present an overview of such an influence. We show that at a large scale (up to ~800–1,000 km) rift localization has been controlled by a lithospheric-scale inherited heterogeneity corresponding to a Precambrian suture zone, separating two different lithospheric domains beneath the plateaus surrounding the rift. The inherited rheological differences between these two lithospheric domains, as well as the presence of pre-existing lithospheric-scale transversal structures, largely controlled the along-axis segmentation and symmetry/asymmetry of different, ~80–100 km-long rift segments. Inherited transversal structures also controlled the development of off-axis volcano tectonic activity in the plateaus surrounding the rift. At a more local scale (<80 km), inherited fabrics controlled the geometry of normal faults and the distribution and characteristics of rift-related volcanism. These observations document a strong control exerted by pre-existing structures on continental rifting at all different scales.

Keywords: continental rifting, extensional tectonics, East African Rift System (EARS), Main Ethiopian Rift (MER), pre-existing structures, tectonic inheritance

OPEN ACCESS

Edited by:
D. Sarah Stamps, Virginia Tech, United States

Reviewed by:
Ken McCaffrey, Durham University, United Kingdom
Antonio Pedrera, Instituto Geológico y Minero de España (IGME), Spain

***Correspondence:**
Giacomo Corti
giacomo.corti@igg.cnr.it

Specialty section:
This article was submitted to Structural Geology and Tectonics, a section of the journal Frontiers in Earth Science

Received: *03 November 2021*
Accepted: *10 January 2022*
Published: *26 January 2022*

Citation:
Corti G, Maestrelli D and Sani F (2022) Large-to Local-Scale Control of Pre-Existing Structures on Continental Rifting: Examples From the Main Ethiopian Rift, East Africa. Front. Earth Sci. 10:808503. doi: 10.3389/feart.2022.808503

INTRODUCTION

Continental rift systems normally develop within a previously deformed lithosphere in which the distribution, architecture and evolution of deformation may be strongly influenced by pre-existing structures. Indeed, inherited mechanical heterogeneities (from the lithospheric scale, e.g., suture zones, to the upper crustal scale, e.g., foliations, shear zones, folds, faults, dykes) either weaker or stronger than the surrounding material, are able to significantly influence the pattern, propagation and overall evolution of continental rifts (e.g., Rosendahl, 1987; Dunbar and Sawyer, 1989; Smith and Mosley, 1993; Vauchez et al., 1998; Morley, 1999; Corti, 2012; Buiter and Torsvik, 2014; Purcell, 2017; Will and Frimmel, 2017).

Many extensional settings suggest such a control, including the North Sea (Bell et al., 2014; Phillips et al., 2019), the Rhine graben system (e.g., Schumacher, 2002; Michon and Sokoutis, 2005; Edel et al., 2007), the Tertiary rifts of Thailand (Morley et al., 2004; Pongwapee et al., 2019) and, finally, the East African Rift System (Chorowicz, 2005; Vétel and Le Gall, 2006; Corti et al., 2007;

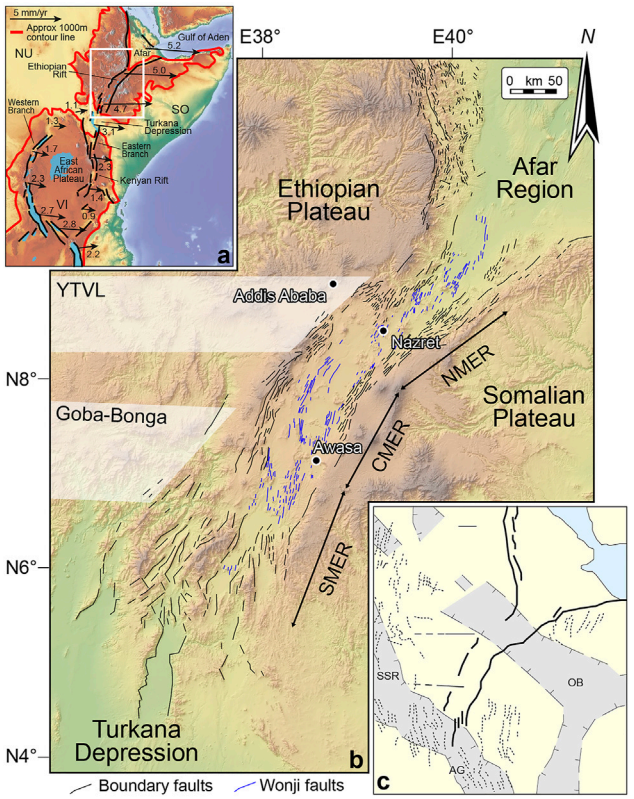

FIGURE 1 | Tectonic setting of the Main Ethiopian Rift. **(A)** Present-day plate kinematics of the East African Rift (modified from Corti et al., 2019). Black arrows show relative motions with respect to a stable Nubian reference frame; values besides arrows indicate motion in mm/yr. NU: Nubian plate; SO: Somalian plate; VI: Victoria microplate. **(B)** Main rift-related faults differentiated in Boundary and Wonji (axial) faults; indicated is the subdivision in the different segments: Northern MER (NMER), Central MER (CMER), Southern MER (SMER). Whitish pattern indicates the transversal lineaments of Yerer-Tullu Wellel (YTVL) and Goba-Bonga. **(C)** Inherited structures in Ethiopia (modified from Korme et al., 2004; Gani et al., 2009). Dashed lines indicate NE-SW- to N-S-trending basement foliations; solid lines illustrate E-W structures, corresponding to the main transversal lineaments affecting the rift; greyish pattern represents NW-SE-trending structures corresponding to sedimentary Mesozoic basins (AG: Anza graben; OB: Ogaden basin; SSR: South Sudan rifts).

Brune et al., 2017). Furthermore, several works show that many rifts developed in different, successive extensional phases (Whipp et al., 2014; Deng et al., 2017; Phillips et al., 2019; Wu et al., 2020), with normal faults formed during initial extensional events exerting a strong control on the structural architecture developed during the later rifting phases (Bell et al., 2014; Duffy et al., 2015; Henstra et al., 2015, 2019; Deng et al., 2018; Wang et al., 2021). Such a control exerted by early normal faults on structures formed during later extension is also supported by crustal and lithospheric scale analogue models (e.g., Corti et al., 2007; Sokoutis et al., 2007; Autin et al., 2013; Molnar et al., 2017, 2019, 2020; Zwaan and Schreurs, 2017; Maestrelli et al., 2020; Wang et al., 2021; Zwaan et al., 2021a).

The Main Ethiopian Rift (MER), in the East African Rift System (EARS), offers the possibility to analyse the control at different scales of pre-existing structures on rifting. Ethiopia has been indeed affected by several tectonic events that preceded Cenozoic rifting, from complex Precambrian phases of collision to extension during the Mesozoic (e.g., Korme et al., 2004; Chorowicz et al., 1994; Abbate et al., 2015 and references therein). This long tectonic history created pre-existing structures that controlled the development of the Ethiopian sector of the EARS from a regional to a local scale; the control of these mechanical heterogeneities (which are defined at different scales in the following sections) is the focus of this review paper.

TECTONIC SETTING

The MER is the northernmost portion of the EARS, extending from the Afar region in the north, to the Turkana depression in the south (**Figure 1**). This region of rifting results from active extension between the Nubia and Somalia Plates (e.g., Ebinger, 2005; Corti, 2009), with geodetic measurements indicating that extension is currently occurring in a roughly E-W direction at rates of ~4–6 mm/yr (e.g., Bendick et al., 2006; Saria et al., 2014; Birhanu et al., 2016). Extension in the northern EARS, Gulf of Aden and the Red Sea occurred contemporaneously with, and after, an intense phase of flood basalt volcanism at ~32–30 Ma (Wolfenden et al., 2004), which possibly resulted from upwelling of the African Superplume (e.g., Ritsema et al., 1999), although more complex scenarios have been recently proposed (e.g., Chang et al., 2020).

The MER is subdivided into three main sectors: Northern MER (NMER), Central MER (CMER) and Southern MER (SMER) (**Figure 1**). These sectors differ in terms of age and pattern of deformation, volcanic activity and lithospheric characteristics (e.g., Mohr, 1983; WoldeGabriel et al., 1990; Hayward and Ebinger, 1996; Bonini et al., 2005; Corti, 2009).

In the NMER, significant tectonic activity is localised at the rift axis along a belt of Pleistocene-Holocene volcano-tectonic structures, the so-called Wonji Fault Belt (WFB, e.g., Mohr, 1962; Boccaletti et al., 1998; Ebinger and Casey, 2001). The WFB is characterized by swarms of short, closely-spaced faults with minor vertical displacement, with associated focused volcanic activity and magma intrusion (e.g., Boccaletti et al., 1998; Tommasi and Vauchez, 2001). Large-offset boundary faults defining prominent marginal escarpments in this rift sector are interpreted to have accommodated deformation in the Mio-Pliocene, but they have been deactivated during the Pleistocene (e.g., Wolfenden et al., 2004; Casey et al., 2006; Keir et al., 2006). Voluminous magma intrusion beneath the axial WFB since 2 Ma caused important modifications of the composition, thermal structure and rheology of the crust/lithosphere in this rift sector (e.g., Beutel et al., 2010; Daniels et al., 2014). As a result, a combination of magma intrusion and normal faulting accommodates extension in this rift sector (e.g., Keranen et al., 2004; Dugda et al., 2005; Mackenzie et al., 2005; Keir et al., 2006; Bastow et al., 2010).

In the CMER and SMER, the large boundary faults are well developed and less eroded than in the Northern MER, and

geological, geodetical and seismicity data indicate that they still accommodate significant extension (Gouin, 1979; Keir et al., 2006; Pizzi et al., 2006; Agostini et al., 2011; Kogan et al., 2012; Molin and Corti, 2015; Corti et al., 2020). This occurs together with a decrease in the amount of extension taken up by axial Wonji faults, which are considered to be in an incipient stage of development in the CMER, but almost absent in the SMER (e.g., Ebinger et al., 2000; Agostini et al., 2011). Similarly, the volume of Quaternary volcanism decreases southwards and the volcano-tectonic activity within the rift is sparse in the SMER and limited to the rift margins.

All these variations of the distribution and characteristics of the tectonic and magmatic activity along the rift axis have been interpreted to reflect a transition from initial rifting in the SMER, with marginal deformation and rift morphology dominated by faulting, to more advanced rifting stages in the NMER, where prominent axial intrusion, dyking and related normal faulting testify a phase of magma-assisted rifting that precedes continental break-up (e.g., Kendall et al., 2005).

The several tectonic events that affected Ethiopia since the Precambrian created different sets of inherited structures that exerted an important control on Cenozoic rifting and can be classified into three main groups (**Figure 1C**; e.g., Korme et al., 2004): 1) Rift-parallel or subparallel structures (NE-SW- to N-S-trending) are mainly related to deformation connected to the closure of the Mozambique Ocean during the Proterozoic and to a suture zone which formed in relation to this event. 2) Roughly E-W structures correspond to Neoproterozoic weaknesses (e.g., faults, fractures) sub-parallel to the trend of the Gulf of Aden. 3) NW-SE-trending structures correspond to sedimentary basins (e.g., Ogaden basin, Anza graben, South Sudan rifts) and associated normal faults formed during Mesozoic extension, which in turn likely reactivated pre-existing Precambrian major crustal weakness zones.

CONTROL OF PRE-EXISTING LITHOSPHERIC WEAKNESSES ON RIFT LOCALISATION

Along with other processes (e.g., magma intrusion), the presence of large-scale zones of weakness such as ancient suture zones (e.g., Buiter and Torsvik, 2014), whose rheology is different from the surrounding regions, facilitates deformation of a continental lithosphere which would be otherwise too strong to be deformed by the available tectonic forces (e.g., Buck, 2004). This is why rift structures typically localise within pre-existing zones of weakness at a lithospheric scale, which tend to strongly favour extensional deformation (e.g., Dunbar and Sawyer, 1989; Buiter and Torsvik, 2014).

Previous studies in the MER based on geophysical data suggest that initial rift location has been controlled by a lithospheric-scale, up to ~800-1000 km-long, pre-existing Precambrian suture (**Figure 2**; e.g., Gashawbeza et al., 2004; Bastow et al., 2005; Daly et al., 2008; Keranen and Klemperer, 2008; Keranen et al., 2009; Cornwell et al., 2010; Purcell, 2017), resulting from the closure of the Mozambique Ocean and accretion of East to West Gondwana.

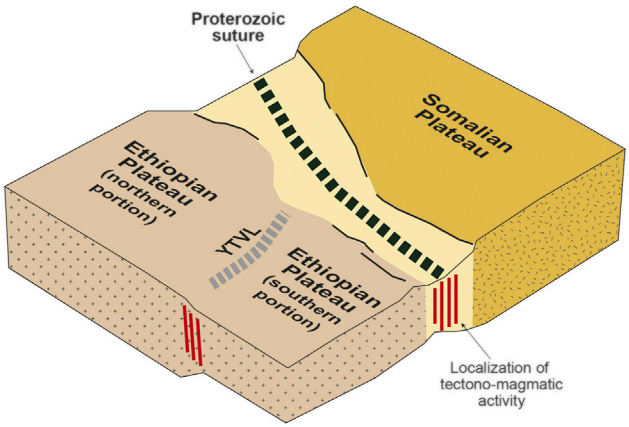

FIGURE 2 | Pre-rift lithospheric domains and location of Cenozoic volcano-tectonic activity in the MER (modified from Keranen and Klemperer, 2008). Cenozoic extension follows the rheological boundaries between two distinct Proterozoic basement terranes, underlying the Ethiopian and Somalian plateaus; this lithospheric weakness zone corresponds to an ancient suture zone (see text for details).

Ophiolites composing this suture zone have been dated between 880 and 690 Ma (Kroner et al., 1992; Claesson et al., 1984; Pallister et al., 1988). The existence of such a suture zone, which puts in contact 870 Ma Neo-Proterozoic juvenile crust with 2 Ga Archean basement (Kazmin et al., 1978; Vail, 1983; Berhe, 1990; Stern et al., 1990; Stern, 1994, 2002; Abdelsalam and Stern, 1996), is supported by differences in crustal/mantle properties between the Ethiopian and Somalian plateaus surrounding the rift. Several geophysical data (crustal thickness and bulk crustal Vp/Vs ratios, resistivity from magnetotelluric data, arrival-time body-wave tomographic models and effective elastic plate thickness) indicate indeed a strong and homogenous Somalian plateau, which contrasts with the more heterogeneous Ethiopian plateau composed of a strong and thick northern portion and a thinner and weaker southern portion (**Figure 2**; e.g., Corti et al., 2018a and references therein). The reactivation of this weakness zone is interpreted to have occurred at the eastern margin of the upwelling mantle plume, not above its center (e.g., Bastow et al., 2008), as documented in other flood basalt provinces (e.g., Deccan, Greenland, Parana, Central Atlantic; Courtillot et al., 1999). Magmatic activity and melt upraising through the upper mantle and crust may have promoted thermal and mechanical weakening of the continental lithosphere, possibly contributing its extension-related deformation (e.g., Díaz-Alvarado et al., 2021). The curved plan-view geometry of this inherited weakness significantly influenced the trend of the Cenozoic faulting (e.g., Mohr, 1962; Kazmin et al., 1980), with a variation from roughly N-S-trending in the south to roughly NE-SW-trending in the North. This resulted in an along-axis variation of the kinematics of rifting, from orthogonal in the southern MER to moderately oblique in the northern MER (Keir et al., 2015; Erbello et al., 2016), which had a major control on the segmentation and structural architecture of the rift (Corti, 2008). Notably, the

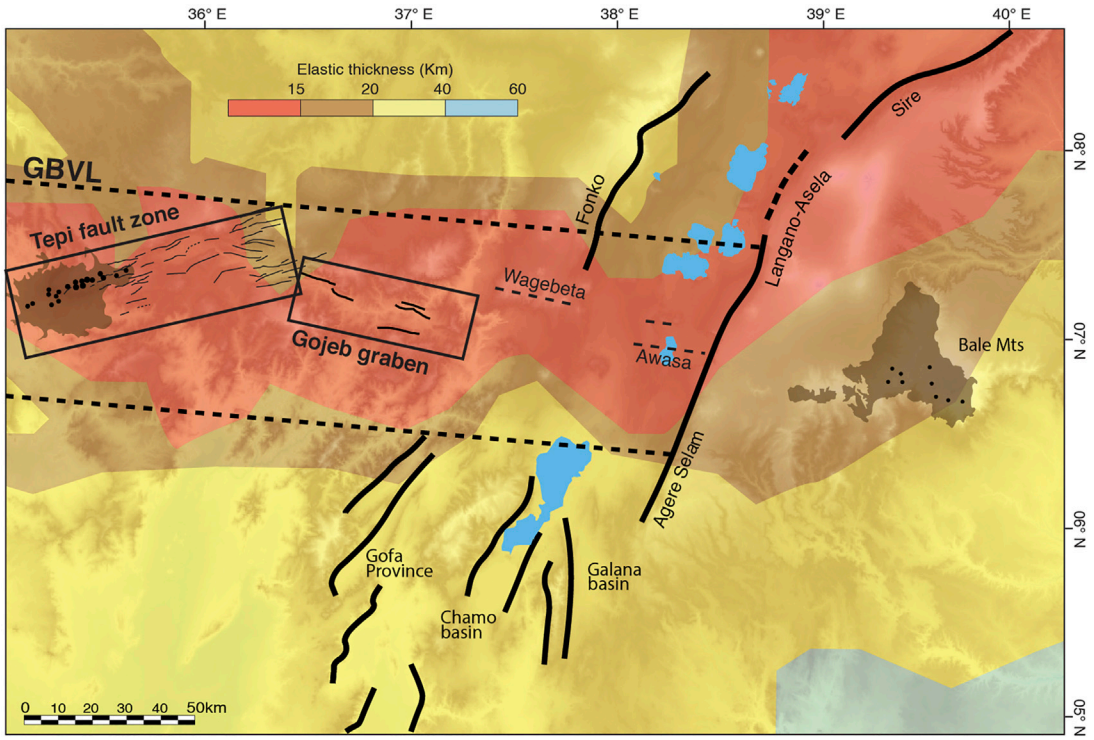

FIGURE 3 | Structural scheme of the Goba Bonga lineament (from Corti et al., 2018b) superimposed on a map of the elastic thickness of the lithosphere (Te), modified after Pérez-Gussinyé et al. (2009). Low Te values (<10–15 km) are observed in a narrow region extending in a roughly E-W direction in the region corresponding to the extent of the Goba Bonga lineament.

reactivation of an inherited weak zone oblique to the plate motion vector is able to impose a local reorientation of the extension direction at the rift margins, as illustrated in below **Section 6**.

CONTROL OF LARGE-SCALE TRANSVERSAL STRUCTURES ON OFF-AXIS DEFORMATION, RIFT INTERACTION AND LINKAGE

Transversal Lineaments and Off-Axis Deformation

The MER is characterised by the occurrence of major transversal lineaments, which affect the rift floor and the plateaus surrounding the rift valley (**Figure 1**; e.g., Abebe Adhana, 2014 and references therein). Specifically, the main structures correspond to the roughly E-W to WNW-ESE-trending Yerer-Tullu Wellel and Goba Bonga volcano-tectonic lineaments (**Figure 1**, **Figure 3**), causing deformation and volcanic activity to extend for hundreds of kilometres into the southern portion of the Ethiopian plateau and marking the transition between the different MER sectors. At a regional scale, these transversal structures have been interpreted to reflect the reactivation of inherited Neoproterozoic weaknesses roughly parallel to the trend of the Gulf of Aden (e.g., Abbate and Sagri, 1980; Abebe et al., 1998; Korme et al., 2004; Abebe Adhana, 2014; Corti et al., 2018b). As explained below, geophysical data support indeed the influence of inheritance on the development of these structures. The Yerer-Tullu Wellel lineament corresponds to a significant gradient in the thickness of the crust and marks the boundary between the northern and southern portions of the Ethiopian Plateau (**Figure 2**; Keranen and Klemperer, 2008). The P wave velocity model of Bastow et al. (2008) in its 75 km depth slice shows discrete low velocity anomalies that extend from the rift valley into the Ethiopian Plateau, beneath the Yerer-Tullu Wellel and Goba Bonga lineaments (see their **Figure 7**). A combination of a thermal anomaly and partial melting in response to asthenospheric upwelling and decompression, in turn related to localized lithospheric extension and thinning, best explains these low velocity anomalies beneath the two transversal lineaments (e.g., Bastow et al., 2010; Gallacher et al., 2016). The Goba Bonga lineament is also characterised by lower values of the elastic thickness of the lithosphere (T_e; Pérez-Gussinyé et al., 2009), which shows a decrease from values of up to 40 km beneath the Ethiopian plateau to values of 10–15 km (Pérez-Gussinyé et al., 2009) in a narrow E-W domain corresponding to the transversal structure (see **Figure 3**). These zones of thinned crust or lithosphere beneath the Yerer-Tullu Wellel and Goba Bonga lineaments were possibly caused by either inherited lithospheric thinned regions or by syn-rift extension exploiting pre-rift weakness zones. Overall, this indicates a pre-rift, structural control on the current structure of the lithosphere (Corti et al., 2018a).

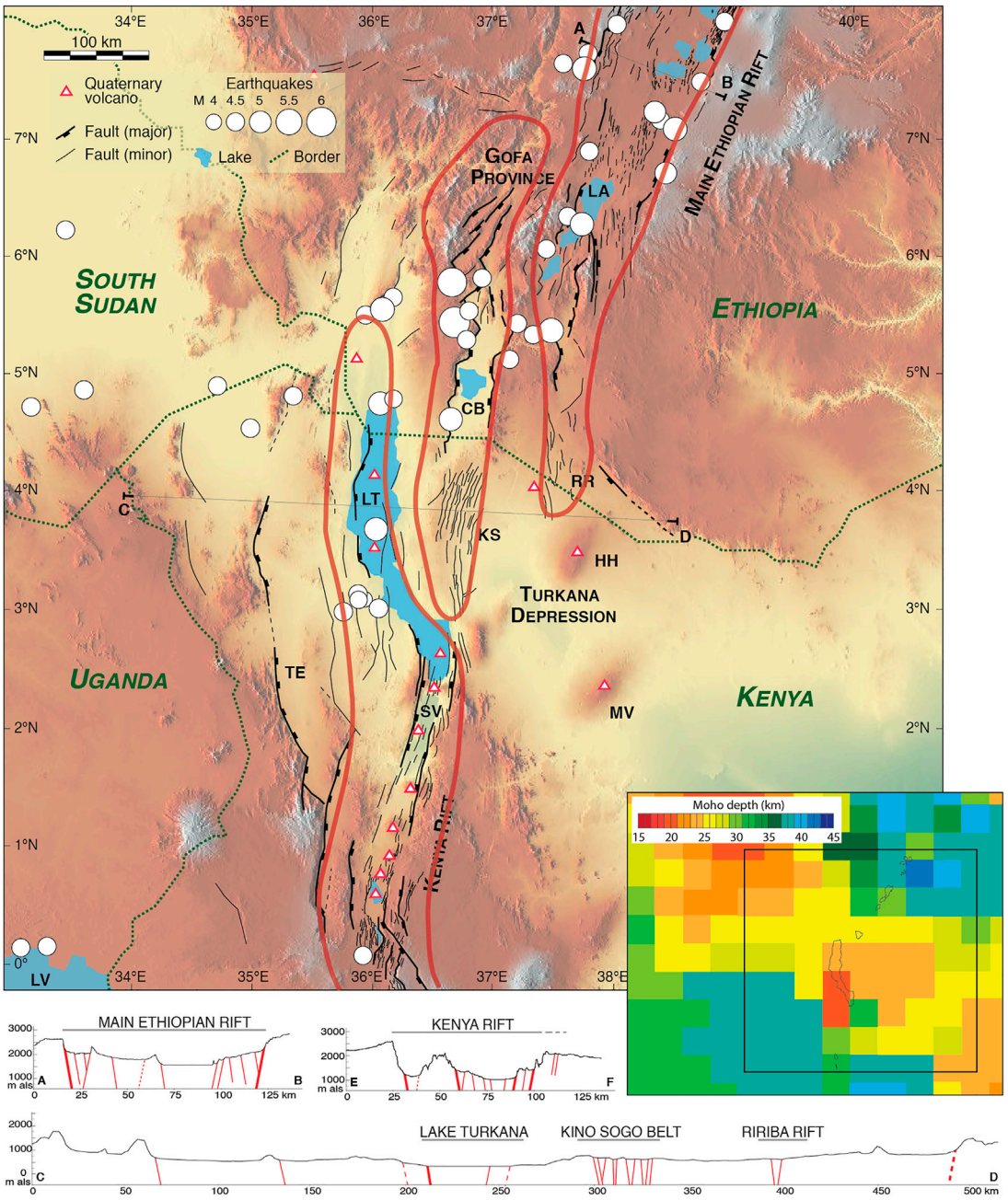

FIGURE 4 | Tectonic setting of the Turkana depression and surrounding regions, with Quaternary faults, seismicity and Quaternary volcanoes superimposed on a SRTM (Nasa Shuttle Radar Topography Mission, 30 m resolution) digital elevation model (modified from Brune et al., 2017). CB: Chew Bahir basin; HH: Hurri Hills; KS: Kino Sogo belt; LA: Lake Abaya; LT: Lake Turkana; LV: Lake Victoria; MV: Marsabit volcano; RR: Ririba Rift; SV: Suguta Valley; TE: Turkwell Escarpment. Areas encircled by red lines are the main deformation domains. Inset in the bottom right shows the crustal thickness in the region (from Benoit et al., 2006). Also illustrated are simplified cross sections highlighting the different architecture and distribution of deformation in the Turkana depression with respect to the Kenyan and Ethiopian rifts.

Rift Interaction and Linkage

At its southern termination, the MER interacts with the Kenya Rift within the Turkana depression, a low-land where deformation, seismic activity and Pleistocene-Holocene volcanism are distributed over a width of more than 450 km (**Figure 4**; e.g., Ebinger et al., 2000). Within this anomalously wide region of ongoing tectonic and magmatic activity, extension is accommodated by numerous small normal faults with limited vertical displacement. This is in striking contrast with the narrow rift valleys to the north and south, characterized by a typical rift valley morphology dominated by large fault escarpments and boundary faults with large vertical displacement. Previous studies have suggested an influence of the Mesozoic-Early Paleogene

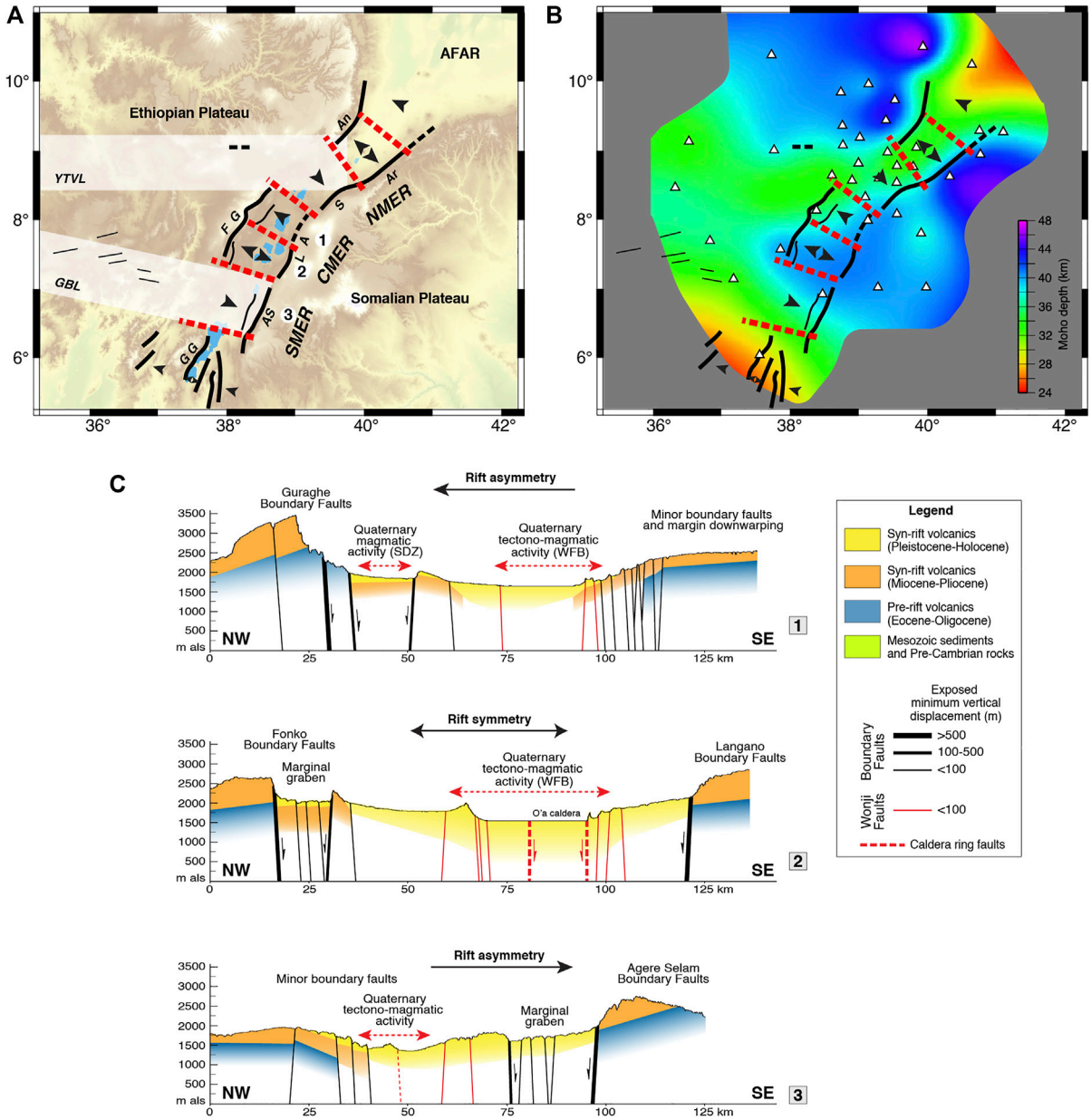

FIGURE 5 | Along-axis variations in the structure of the Main Ethiopian Rift (modified from Corti et al., 2018a). **(A)** Interpreted variations in rift symmetry and polarity: single arrows indicate the polarity of the different rift sectors; double arrows indicate symmetry of rifting. Whitish boxes indicate the hypothesised plan-view extent of the transversal structures: Yerer-Tullu Wellel (YTVL) and Goba-Bonga (GBL) volcano-tectonic lineaments. Rift segments labelled as NMER: Northern MER; CMER: Central MER, SMER: Southern MER. Other labels indicate the main rift escarpments as follows, An: Ankober; Ar: Arboye; AS: Agere Selam; FG: Fonko-Guraghe; GG: Gamo Gidole; LA: Langano Asela; S: Sire. **(B)** Map of depth of the Moho in the MER, modified after Keranen et al. (2009). **(C)** Simplified geological profiles across different sectors of the MER, with vertical exaggeration of x10. WFB: Wonji Fault Belt; SDZ: Silti Debre Zeit volcanic belt.

tectonic phase on the later extensional deformation related to the EARS (e.g., Brune et al., 2017; Corti et al., 2019; Emishaw and Abdelsalam, 2019): the location of the diffuse Cenozoic tectono-magmatic activity has been likely controlled by the presence of a wide region of thinned crust, trending NW-SE and resulting from Mesozoic extension (Anza graben, South Sudan rifts; **Figure 4**). More specifically, the anomalously wide rift zone is likely caused by the N-S direction of propagation of the Main Ethiopian and Kenya rift systems into this NW-SE-trending region of thinned crust and stronger mantle lithosphere (e.g., Brune et al., 2017). In this region, the Kenyan and Ethiopian rift valleys are left-laterally deflected away from one another, avoiding a direct linkage to form a thoroughgoing N-S depression (Brune et al., 2017). Therefore, the presence of pre-existing transversal structures has a

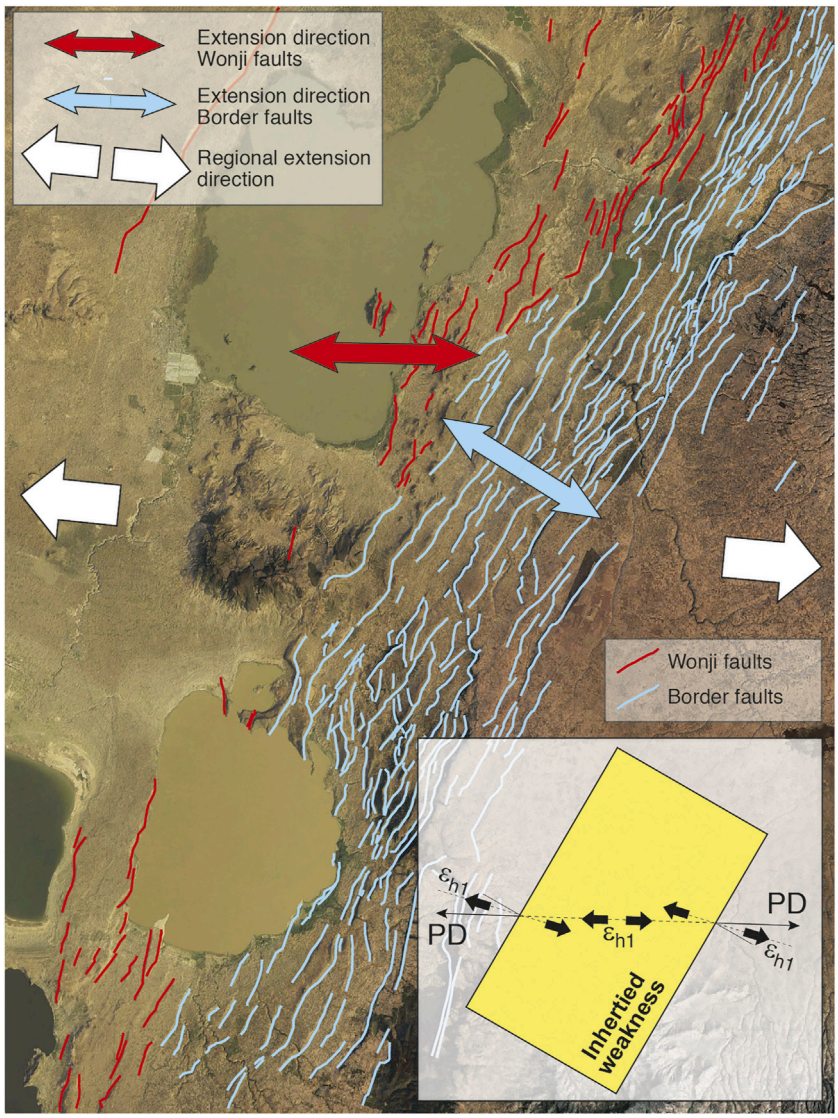

FIGURE 6 | Reorientation of the extension direction at the Asela-Langano margin. The local direction of extension at boundary and internal faults is indicated with light blue and red arrows, respectively; the regional direction of extension is illustrated with the big white arrows. Inset in the bottom right shows the relationship between the rift trend (or its perpendicular), the regional direction of extension (or plate divergence, PD) and the trend of the greatest horizontal principal strain (εh_1) in the different portions of the oblique rift (modified from Corti et al., 2020).

strong influence on the interaction and linkage of major rift segments.

CONTROL OF PRE-EXISTING STRUCTURES ON RIFT SEGMENTATION AND SYMMETRY

Recent studies in the MER (e.g., Corti et al., 2018a) have shown that the pre-rift structure of the Ethiopian and Somalian plateaus at two sides of the reactivated ancient suture zone has a major control on rift architecture and segmentation.

The eastern margin of the MER, where the lithosphere beneath the Somalian Plateau is strong and homogeneous (e.g., Keranen and Klemperer, 2008; Corti et al., 2018a), is characterised by the presence of a more or less continuous system of large boundary faults (**Figures 1**, **5**). Conversely, the western margin shows significant along-axis variations, with segments marked by large boundary faults (Ankober, Fonko-Guraghe, Gamo-Gidole) alternating with sectors characterised by flexures, with gentle monoclines dipping towards the rift axis (**Figures 1**, **5**). This has been interpreted to reflect a more heterogeneous and complex structure of the Ethiopian plateau lithosphere than the Somalian, with the Ethiopian plateau characterised by a strong northern portion and a southern

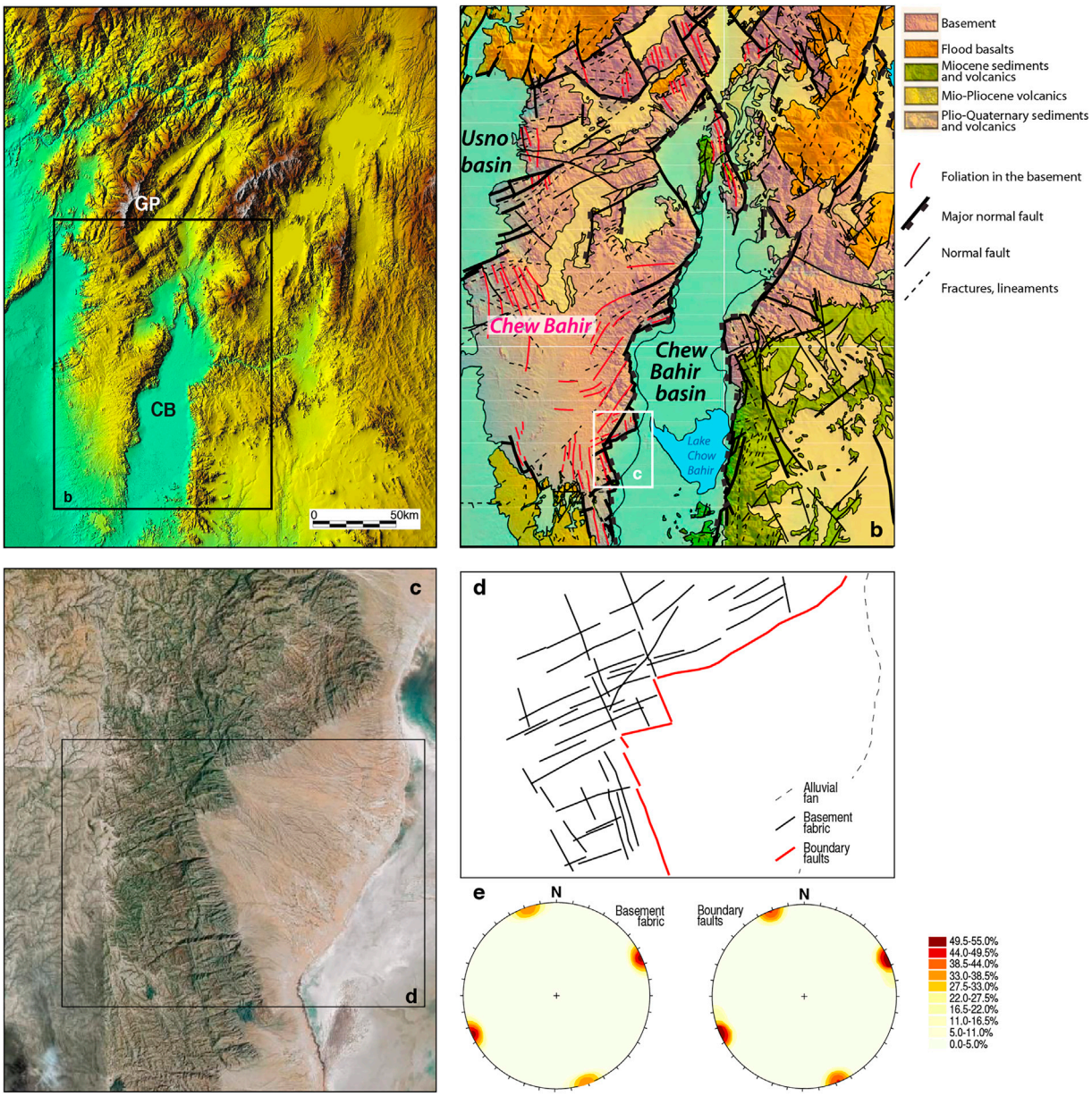

FIGURE 7 | (A) Digital elevation model (NASA-SRTM) of southern Ethiopia. CB: Chew Bahir; GP: Gofa province. **(B)** Geological map of the Chew Bahir basin and surrounding areas, illustrating the pattern of foliation on the basement. **(C)** Typical angular pattern of boundary faults of the Chow Bahir basin (see text for details); **(D)** structural sketch. **(E)** Distribution of inherited basement fabrics and boundary faults, illustrated as plots of weighted fault azimuths. Note the similarity between the trend of basement fabrics and that of boundary faults, supporting that the development of the latter is strongly influenced by basement inherited weaknesses. Panels **(A)**, **(C)**, **(D)**, **(E)** modified from Corti (2009); panel **(B)** modified from Philippon et al. (2014).

portion with a thinner and weaker crust (**Figure 5**; e.g., Keranen and Klemperer, 2008). This southern portion is marked by the presence of the E-W Yerer-Tullu Wellel and Goba Bonga volcano-tectonic lineaments (**Figure 5**). Where these pre-existing weaknesses intersect the rift at a high angle, major boundary faults are absent from the western margin and are instead replaced by gentle flexures; this, together with well-developed faults on the eastern side, gives rise to an overall asymmetry of the rift (**Figure 5**). Instead, where large boundary faults characterise the western margin, the rift is symmetric (**Figure 5**). Notably, southeast of Addis Ababa, the eastern rift margin is characterised by a prominent shift to the East, which occurs in spatial coincidence with the Yerer-Tullu Wellel volcano-tectonic lineament (**Figures 1**, **5**). This coincidence has been interpreted to reflect an influence exerted by the E-W-trending pre-existing weakness on the plan-view geometry of the rift valley at this latitude (e.g., Korme et al., 2004).

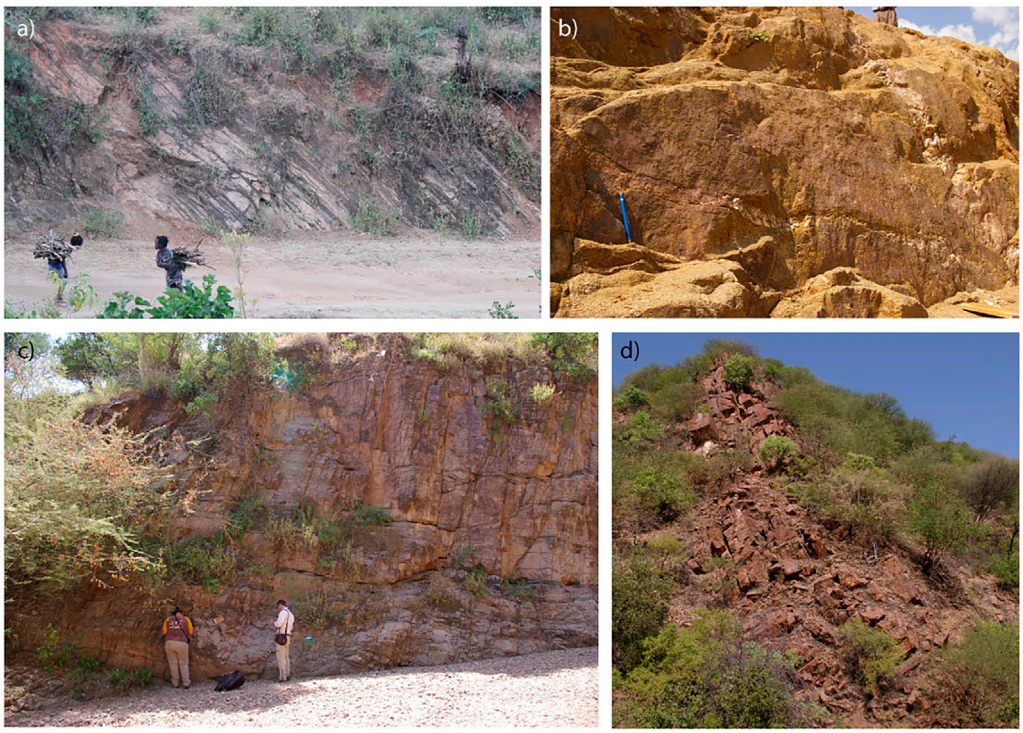

FIGURE 8 | Field examples of structures affecting the Precambrian basement in the southern MER: **(A)** magmatic foliation and **(B)** Cenozoic fault plane affecting basement and cutting quartz vein and aplitic dike in the Gofa province; **(C)** System of sub parallel fractures reactivated and associated to a major normal fault (not visible of the left) in the Chew Bahir basin; **(D)** basement foliation sub parallel to the major fault plane delimiting the Chew Bahir basin.

In summary, the above observations indicate that the MER is characterized by a segmentation strongly controlled by the inherited lithospheric structure, which results in 80–100 km-long rift segments with alternating symmetric/asymmetric basins.

CONTROL OF PRE-EXISTING STRUCTURES ON LOCAL-SCALE FAULT GEOMETRY AND ARCHITECTURE

Pre-existing structures have a significant influence on the geometry and segmentation of extension-related normal faults at a more local (<80 km) and shallower scale. The architecture and kinematics of boundary faults at the margins of the CMER and NMER are strongly influenced by the oblique inherited weakness described in **Section 3**. The boundary faults are at surface en-echelon arranged and oblique to both the pre-existing weakness (i.e., the rift trend) and the orthogonal to the regional plate motion vector; they trend orthogonal to the local direction of extension (**Figure 6**; Corti et al., 2013; Philippon et al., 2015). Inversion of fault-slip data and detailed analysis of fault kinematics in analogue models of oblique rifting indicate indeed a pure dip-slip motion on these faults, in which (given the oblique orientation with respect to the extension direction) a strike-slip component of motion could be expected (Corti et al., 2013; Philippon et al., 2015). This documents a reorientation in the extension direction at the margins of the rift, where the local extension direction does not correspond to the regional plate divergence, resulting in a pure dip-slip motion in an overall oblique kinematics (e.g., Morley, 2010; Corti et al., 2013; **Figure 6**).

Examples of an important control of inherited structures like fractures, faults, foliations, and dikes on the geometry of individual faults or fault segments are evident in the Gofa Basin and Range and in the Chew Bahir basin, in southern Ethiopia (**Figures 7**, **8**). In these regions, large boundary faults are typically highly segmented, with many short interacting segments characterised by sharp changes in orientation giving rise to zig-zag geometries and angular patterns (e.g., Moore and Davidson, 1978; Vétel et al., 2005; Vétel and Le Gall, 2006). Typically, the orientation of the boundary fault segments mimics the trend of foliations or mylonite zones indicating a strong control exerted by pre-existing basement structures (**Figures 7**, **8**; Moore and Davidson, 1978). Faults parallel to the extension direction are related to reactivation of basement fabrics rather than to recent transcurrent faults (Moore and Davidson, 1978; Philippon et al., 2014).

A similar control has been suggested by recent works in the Ririba rift, at the southern termination of the Ethiopian Rift (Corti et al., 2019). In this rift, besides the angular fault pattern and the parallelism between faults and inherited fabrics, the main boundary faults are characterised by an anomalously low displacement/length ratio (i.e. long faults have very low displacement) and by displacement/length (D-L) curves (with flat top profiles, low-end gradients and low D-L ratio values) typical of a 'constant length model' of fault growth (see Supplementary Fig. 4 in

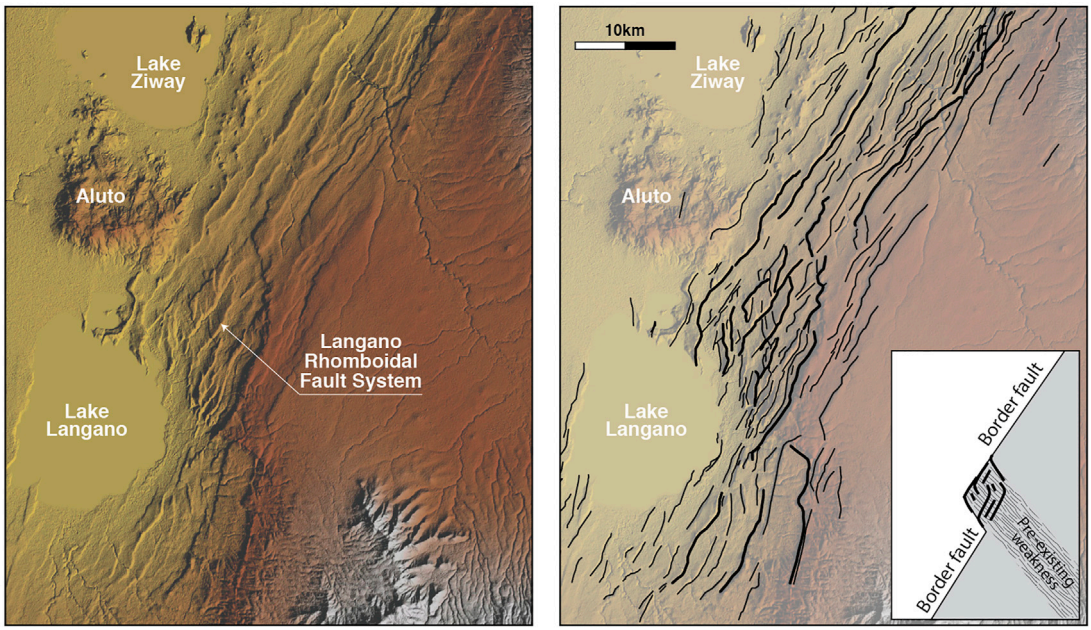

FIGURE 9 | Digital elevation model (NASA-Shuttle Radar Topography Mission, SRTM 30 m resolution; left panel), and faults superimposed onto a SRTM digital elevation model (right panel) of the Langano Rhomboidal Fault System. Inset in the bottom right shows a schematic representation of the possible influence of a NW-SE-trending inherited weakness on the fault pattern. See text for details.

Corti et al., 2019). This growth model is representative of reactivated fault systems in which fault lengths are inherited from underlying structures and established almost instantaneously on geological timescales, as also suggested for the nearby Kino Sogo fault belt in Kenya (Vétel et al., 2005; Vétel and Le Gall, 2006).

Another typical example is the Langano (or Haroresa) Rhomboidal Fault System (Le Turdu et al., 1999), located East of Lake Langano (**Figure 9**). In this area, the NE-SW-trending Asela-Langano escarpment curve to acquire a NW-SE trend and the interaction between NE-SW and NW-SE-trending structures give rise to a complex pattern of normal faults, with typical S- or Z-shaped plan-view geometries (**Figure 9**). This pattern and the curvature of the escarpment have been suggested to be controlled by a major NW-SE pre-existing crustal weakness zone, roughly parallel to the trend of the Red Sea (e.g., Korme et al., 2004). The existence of such pre-existing transverse structure close the Lake Langano is also supported by gravity data (Korme et al., 2004) which evidence the presence of NW-SE graben below the rift depression. A similar example of control on the local-scale fault pattern of inherited structures includes NW-SE faults East of Addis Ababa (Wolenchiti area) defining a NW-SE-trending graben filled by Pleistocene diatomite deposits (Korme et al., 2004).

CONTROL OF PRE-EXISTING STRUCTURES ON THE DISTRIBUTION VOLCANISM

Many examples in the MER document a strong control exerted by pre-existing structures on the distribution of volcanic vents and edifice geometries. In the Ririba rift, at the southern termination of the MER, the Quaternary volcanic fields are aligned in a NE-SW direction and show no apparent relationship with the N-S-trending Pliocene boundary faults of the rift (**Figure 10**) therefore indicating that these structures do not exert a control on the pathways of magma ascent. This volcanism aligns parallel with regional, NE-SW/NNE-SSW-trending pre-existing lineaments (such as the Buluk Fault Zone in **Figure 10**) suggesting that the distribution of volcanic centres may have been controlled by these major deep inherited structures (e.g., Vétel and Le Gall, 2006; Corti et al., 2019; Franceschini et al., 2020). Magma ascent along these pre-existing structures may have been caused by abandonment of the Ririba rift and consequent deactivation of the main rift faults, and a stress re-organization due to gradients in crustal thickness (Franceschini et al., 2020). This resulted in buoyancy forces causing a local stress field with maximum horizontal stress orthogonal to the Turkana depression, enabling the uprising and emplacement of magma along NE-SW pre-existing structures. At a more local scale, the distribution of vents and their preferential directions of elongation (within individual volcanic fields) suggest a second-order control by inherited basement fabrics (Franceschini et al., 2020), as documented by the above-mentioned angular networks of minor normal faults observed in the area. Overall, the Ririba example supports that major, lithospheric-scale inherited structures may represent zones of crustal weakness that magma can exploit during its ascent, controlling the volcanic spatial and temporal evolution, volcanic morphology, magma volume, and eruptive dynamics (e.g., Le Corvec et al., 2013; Wadge et al., 2016).

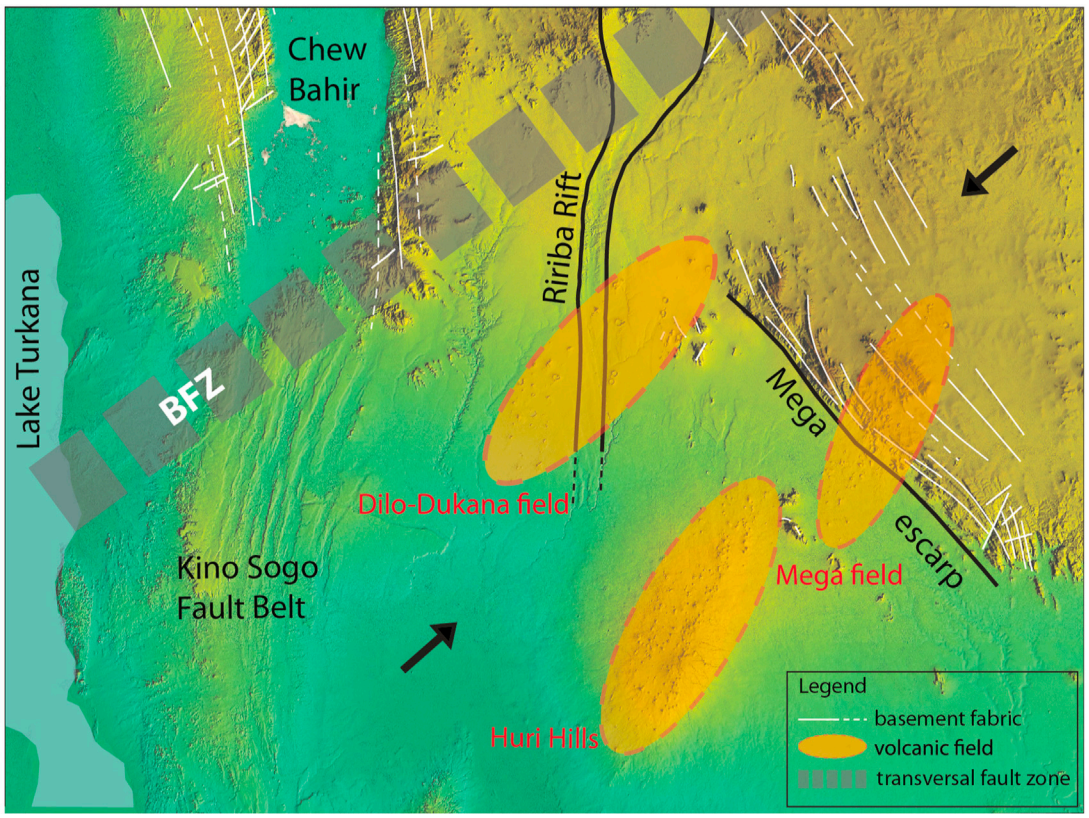

FIGURE 10 | Schematic relations between the distribution of the Quaternary volcanic fields of Dilo, Mega and Huri Hills (orange ellipses) and major inherited structures (dashed lines in the figure) such as the BFZ (Buluk Fault Zone), modified from Franceschini et al. (2020). Black arrows schematically indicate the main compressive stress resulting from buoyancy forces in the area related to variations in crustal thickness and topography. See text for details.

In a recent compilation, Maestrelli et al. (2021) suggested that at least some calderas in the MER (e.g., Fantale, Kone, Gedemsa and Corbetti) may have experienced a tectonic control exerted by pre-existing faults reactivated during the collapse (i.e., fault-controlled caldera rim; **Figure 11**). Furthermore, Acocella et al. (2002) hypothesized a control exerted by inherited structures, reactivated during rift extension, on the localization for Fantale, Kone and Gedemsa calderas. In this regard, Lloyd et al. (2018) suggested the presence of a E-W deep rooted inherited structures controlling the localization and the structural setting of the Corbetti Caldera. As supported by Corti et al. (2018b), this structure may be related to the regional-scale Goba Bonga lineament.

Previous works have also suggested the influence of inherited structures on the development of off-axis (or flank) volcanoes (**Figure 12**). Such volcanic edifices are located in the plateaus surrounding the rift, in an off-axis position with respect to the tectonic depression; a classic example of this volcanism is the Galama range, located in the Somalian plateau (**Figure 12**). Different models of magma generation and/or migration have been applied to explain the development of such volcanism (e.g., Bonini et al., 2001; Maccaferri et al., 2014; Chiasera et al., 2018). However, in most of the different models, the final uprising of magma at shallow crustal levels, resulting in the alignment of dikes and scoria cones in an area of thicker crust, has been related to ascending mafic dikes exploiting pre-existing basement faults and fractures slightly oblique to the rift margins (Mohr and Potter, 1976; Chiasera et al., 2018). Off-axis volcanism is also associated with pre-existing E-W lithospheric structures corresponding the Yerer-Tullu Wellel and Goba Bonga transversal lineaments (Abebe Adhana, 2014; Corti et al., 2018b).

DISCUSSIONS AND IMPLICATIONS FOR REACTIVATION OF PRE-EXISTING STRUCTURES DURING CONTINENTAL RIFTING

Understanding how the pre-existing structure of the continental lithosphere influences rifting is of primary importance, as it may have an impact on several aspects of the rifting process and its outcomes. These may include the potential architecture (e.g., symmetry/asymmetry) of resulting passive margins, the possible segmentation of oceanic domains and transform faults separating them, the characteristics (length, depth extent, segmentation) of seismogenic faults (with implications for maximum magnitude of earthquakes), the distribution, volumes, and dynamics of

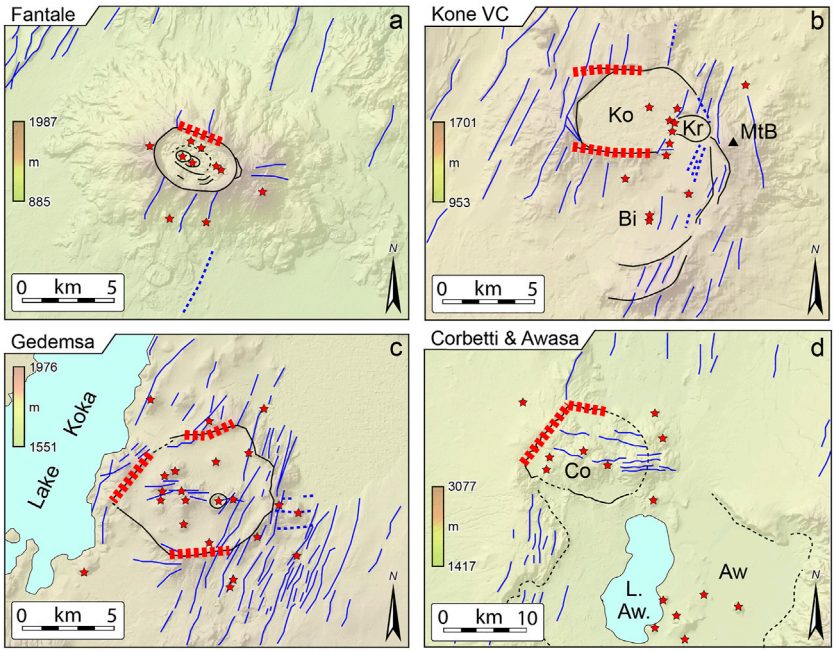

FIGURE 11 | Structural control on collapsed caldera margin at **(A)** Fantale, **(B)** Kone Volcanic complex (KVC), **(C)** Gedemsa and **(D)** Corbetti. Red dashed lines indicate caldera ring faults controlled by inherited structures reactivated during the collapse. Red stars mark volcanic emission points (modified from Maestrelli et al., 2021). Ko: Kone caldera; Kr: Korke caldera; Bi: Birenti caldera; MtB: Mount Birenti; Co.: Corbetti; L. Aw, Lake Awasa; Aw: Awasa caldera remnants.

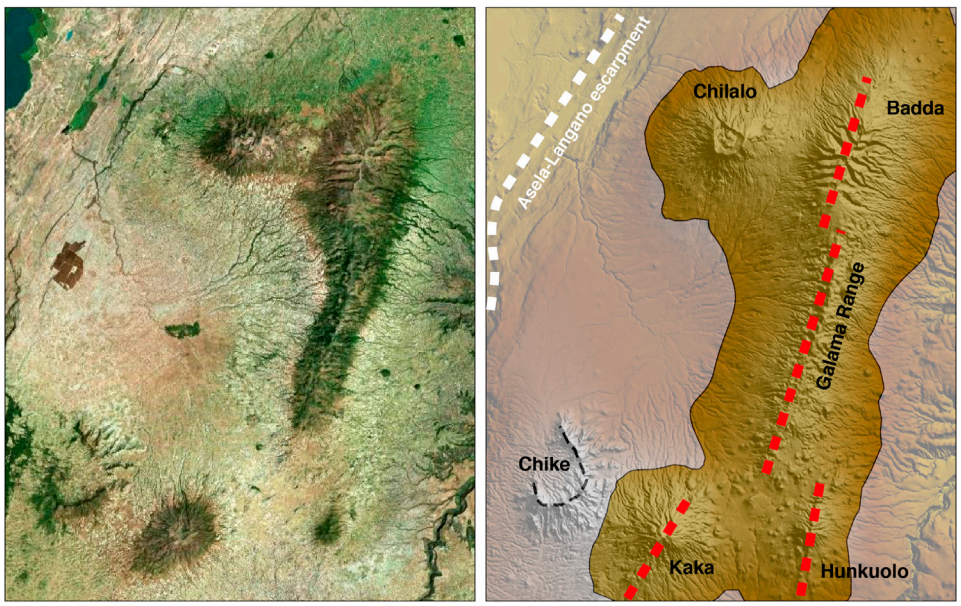

FIGURE 12 | Satellite image (left) and main off-axis volcanoes (right) in the Somalian Plateau. Red dashed lines indicate the trend of inherited fabrics that possibly feed the volcanoes.

associated volcanism (influencing volcanic risks and geo-resources such as geothermal energy). Because of this, the relationship between the Proterozoic crustal/lithospheric framework and the pattern of rift-related structures in East Africa has attracted considerable debate over the last decades (see Purcell, 2017).

Examples from the MER provide useful insights into this debate. Specifically, these examples document a significant

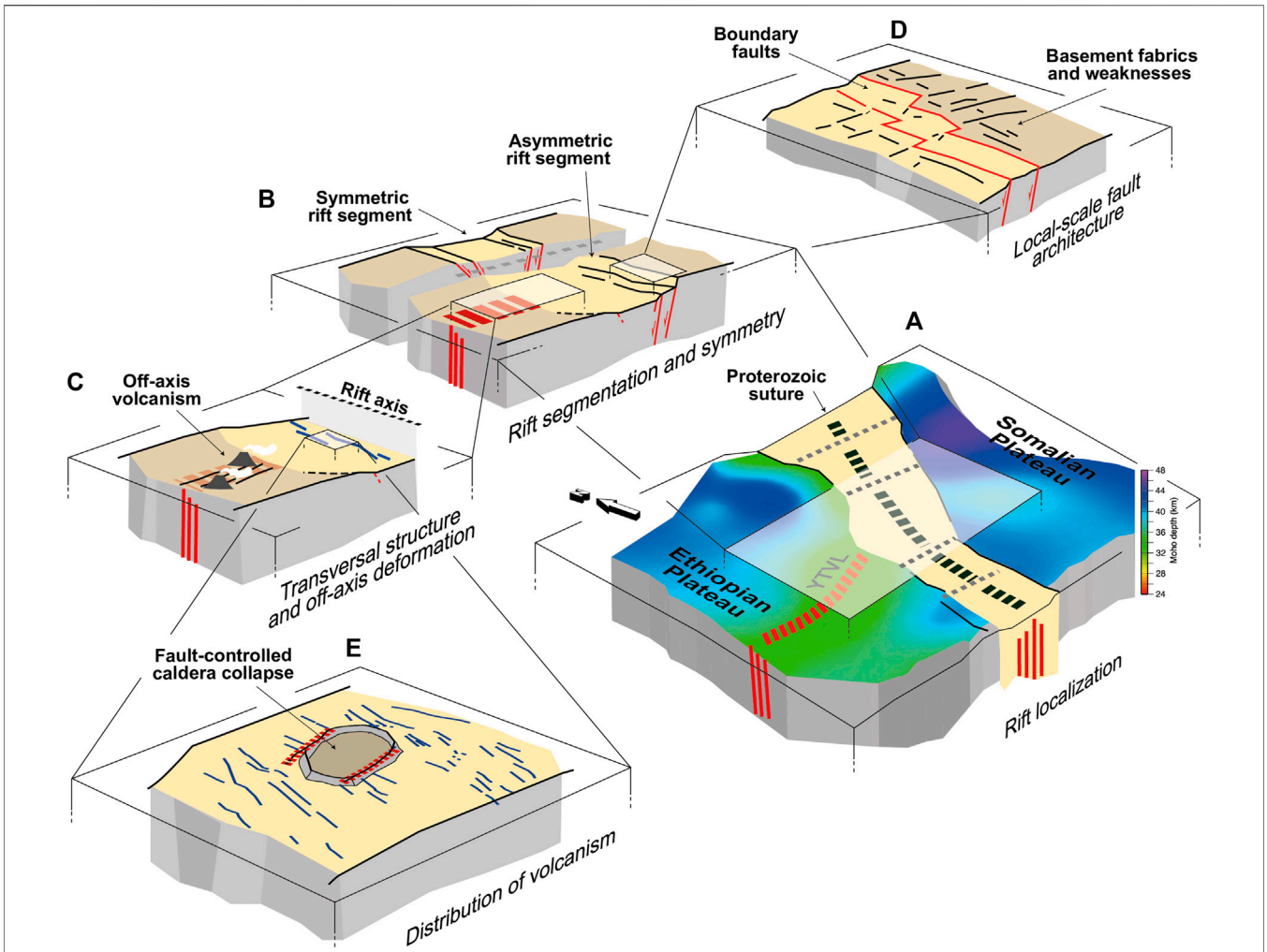

FIGURE 13 | Schematic illustration of the control exerted by inherited heterogeneities at different scales in the MER. From regional-scale to local-scale, we observe: **(A)** Rift localization controlled by Proterozoic suture. YTVL: Yerer-Tullu Wellel transversal structure; **(B)** Rift segmentation and asymmetry induced by large-scale transversal structures; **(C)** Off-Axis volcanism controlled by large-scale transversal structures; **(D)** Local-scale architecture controlled by inherited basement fabrics; **(E)** Distribution and setting of volcanism controlled by local scale-inherited structures.

control exerted by inherited heterogeneities at all different scales, which is illustrated in **Figure 13**.

At a large scale (up to ~800–1,000 km), the localisation of extensional deformation and the plan-view geometry of the rift valley is largely controlled by a NE-SW- to N-S-trending, lithospheric-scale Precambrian suture zone (**Figure 13A**). Suture zones may be indeed weaker than the normal lithosphere, because of processes including increased heat production in the thickened crust and the presence of inherited faults that can weaken the crust (Buiter and Torsvik, 2014). This explains why suture zones are typically reactivated during extension and localize extension-related deformation, as documented in many examples worldwide (see review in Buiter and Torsvik, 2014). In Ethiopia, the along-axis variations in the trend of the suture and the resulting rift valley, determine along-axis differences in the kinematics of rifting, from orthogonal in the southern MER to moderately oblique in the northern MER, which have important implications for rift architecture and evolution (see Keir et al., 2015).

Within the rift, the inherited rheological heterogeneities and different strength of the lithospheric domains surrounding the rift, and the presence of transversal structures, control the interaction between the Ethiopian and Kenyan rift, as well as the along-axis segmentation of the rift valley (**Figure 13B**). Specifically, the strength difference (or similarity) of the lithosphere beneath the plateaus controlled the development of 80–100 km-long rift portions characterised by asymmetry (or symmetry) of the rift valley. Recent analysis from other continental rifts (e.g., Malawi Rift, Upper Rhine Graben; Laó-Dávila et al., 2015; Grimmer et al., 2017) support that along-axis variations in inherited structures (e.g., basement fabrics) have a significant influence on basin architecture and segmentation, and on the characteristics of the rift margins.

Roughly E-W, lithospheric-scale inherited weaknesses control the development of off-axis volcano-tectonic activity in the plateaus surrounding the rift, an activity which may extend hundreds of kilometres away from the rift (**Figure 13C**). Transversal pre-existing structures may have controlled other characteristics of the MER, such as its plan-view geometry and its deflection southeast of Addis Ababa. Similar controls have been described in other regions of East Africa: for instance, the inherited Aswa Shear Zone has been suggested to control rift deflection in northern Kenya and the transfer of strain from the Western Branch to the Eastern Branch of the EARS (e.g., Purcell, 2017 and references therein).

At a local scale (<80 km), pre-existing structures may control the geometry of extension-related normal faults, causing anomalous fault patterns (**Figure 13D**): when controlled by inherited structures, normal faults may deviate from linear to zig-zag or sigmoidal plan-view geometries, with atypical displacement/length (D/L) curves and fault lengths established almost instantaneously on geological timescales (constant length model of fault growth). Examples from other sectors of the EARS (e.g., Malawi) confirm that pre-existing basement fabrics may have an important influence on the architecture of later rift-related faults (e.g., Williams et al., 2019; Wedmore et al., 2020; Kolawole et al., 2021). However, this may not always be the case: other studies have shown that pre-existing weaknesses only locally control border fault geometry at subsurface (e.g., Hodge et al., 2018) or that high-angle normal faults may cut through low-angle basement fabrics (e.g., Ebinger et al., 1989). In the Kenya rift, recent studies (Muirhead and Kattenhorn, 2018) points to a complex time-evolution of inheritance during rifting, with reactivation of pre-existing structures documented to postdate rift initiation and occur in an advanced rifting stage. In this case, later activation of inherited fabrics may reflect a complex contribution by magma-assisted deformation (Muirhead and Kattenhorn, 2018). A time-dependent reactivation of inherited structures has been also documented in other regions of the EARS, such as the Turkana depression of southern Ethiopia and northern Kenya. There, contrarily to what suggested for the Kenya rift, field analyses and seismic reflection data indicate that some NE-SW-trending basement structures have been reactivated during initial rifting but then abandoned during progressive extension, given their non-optimal orientation with respect to the roughly E-W extension direction (Nutz et al., 2021). Similarly, NW-SE-trending faults related to a previous Cretaceous-Early Paleogene extension phase are non-optimally oriented with respect to the roughly E-W extension of Cenozoic rifting. In this case, geodetic observations, and analysis of present-day deformation (Knappe et al., 2020) indicate no reactivation of these pre-existing faults during later extension, as also supported by analogue modelling of extension in the region (Wang et al., 2021). These analogue models indicate that the absence of fault reactivation may be related to a limited development of structures during the early rift phase, with a small volume of crust affected by pre-existing weak zones and a low reduction in strength in the brittle crust, and to their obliquity with respect to the later extension direction. In general, the strength contrast between the undeformed crust and that affected by pre-existing structures and the orientation, size and depth of inherited faults with respect to the extension direction are controlling factors in the reactivation of pre-existing structures as documented in many modelling works (e.g., Bellahsen and Daniel, 2005; Maestrelli et al., 2020; Molnar et al., 2017, 2019, 2020; Osagiede et al., 2021; Samsu et al., 2021; Schori et al., 2021; Wang et al., 2021, Zwaan and Schreurs, 2017; Zwaan et al., 2021a,b).

Inherited structures also control the patterns of migration and emplacement of rift-related magmas (**Figure 13E**), which may at some places show no direct relations to rift related faults and rather cut them. The MER examples support that pre-existing structures may control the spatial and temporal evolution of volcanic activity, its volume and eruptive dynamics, as observed in other parts of the EARS (such as the Chyulu Hills in the Kenya Rift; e.g., Mazzarini and Isola, 2021) and other regions undergoing extension (e.g., Gómez-Vasconcelos et al., 2020).

CONCLUDING REMARKS

We have shown how inherited structures have controlled the development of the MER from regional to local-scale. In general, as typically observed in other rift settings, the influence of inheritance on rift-related deformation is rather obvious at a regional scale, as rift valleys localise within lithospheric-scale weak zones avoiding stronger regions. Similarly, large, lithospheric-scale transversal structures influenced the MER segmentation, symmetry and off-axis volcanic activity. Examples in the MER document a local-scale influence of inherited structures on normal fault geometries and rift-related volcanism. However, comparison with other examples from the EARS suggests that the relations between pre-rift structures and individual rift basins or faults are more complex and several aspects of fault reactivation at a local scale remain enigmatic. These include, among others, the time-space variations of reactivation during rift progression and its dependence on parameters such as: the volume of crust affected by pre-existing weak zones and/or their dimensions, the strength contrast required for their re-use, and their dip and orientation with respect to the extension direction. Additional detailed studies in locations where we can clearly analyse, in 3D, crustal faults and ancient structures are therefore needed to improve our knowledge of these complex relations.

AUTHOR CONTRIBUTIONS

GC conceptualized and wrote the work; FS and DM contributed to the writing.

ACKNOWLEDGMENTS

We thank the reviewers for the comments that helped to improve previous versions of the manuscript. This work has been funded by the Italian Ministero dell'Università e della Ricerca (MiUR) through PRIN Grant 2017P9AT72.

REFERENCES

Abbate, E., Bruni, P., and Sagri, M. (2015). "Geology of Ethiopia: A Review and Geomorphological Perspectives," in *Landscapes and Landforms of Ethiopia, World Geomorphological Landscapes*. Editor P. Billi (Dordrecht: Springer Science+Business Media), 33–64. doi:10.1007/978-94-017-8026-1_2

Abbate, E., and Sagri, M. (1980). Volcanites of Ethiopian and Somali Plateaus and Major Tectonic Lines. *Atti Convegni Lincei* 47, 219–227.

Abdelsalam, M. G., and Stern, R. J. (1996). Sutures and Shear Zones in the Arabian-Nubian Shield. *J. Afr. Earth Sci.* 23, 289–310. doi:10.1016/s0899-5362(97)00003-1

Abebe Adhana, T. (2014). The Occurrence of a Complete continental Rift Type of Volcanic Rocks Suite along the Yerer-Tullu Wellel Volcano Tectonic Lineament, Central Ethiopia. *J. Afr. Earth Sci.* 99, 374–385. doi:10.1016/j.jafrearsci.2014.02.008

Abebe, T., Mazzarini, F., Innocenti, F., and Manetti, P. (1998). The Yerer-Tullu Wellel Volcanotectonic Lineament: a Transtensional Structure in central Ethiopia and the Associated Magmatic Activity. *J. Afr. Earth Sci.* 26, 135–150. doi:10.1016/s0899-5362(97)00141-3

Acocella, V., Korme, T., Salvini, F., and Funiciello, R. (2002). Elliptic Calderas in the Ethiopian Rift: Control of Pre-existing Structures. *J. Volcanol. Geotherm. Res.* 119 (1–4), 189–203. doi:10.1016/S0377-0273(02)00342-6

Agostini, A., Bonini, M., Corti, G., Sani, F., and Mazzarini, F. (2011). Fault Architecture in the Main Ethiopian Rift and Comparison with Experimental Models: Implications for Rift Evolution and Nubia-Somalia Kinematics. *Earth Planet. Sci. Lett.* 301, 479–492. doi:10.1016/j.epsl.2010.11.024

Autin, J., Bellahsen, N., Leroy, S., Husson, L., Beslier, M.-O., and d'Acremont, E. (2013). The Role of Structural Inheritance in Oblique Rifting: Insights from Analogue Models and Application to the Gulf of Aden. *Tectonophysics* 607, 51–64. doi:10.1016/j.tecto.2013.05.041

Bastow, I. D., Nyblade, A. A., Stuart, G. W., Rooney, T. O., and Benoit, M. H. (2008). Upper Mantle Seismic Structure beneath the Ethiopian Hot Spot: Rifting at the Edge of the African Low-Velocity Anomaly. *Geochem. Geophys. Geosyst.* 9 (12), na. doi:10.1029/2008GC002107

Bastow, I. D., Pilidou, S., Kendall, J.-M., and Stuart, G. W. (2010). Melt-induced Seismic Anisotropy and Magma Assisted Rifting in Ethiopia: Evidence from Surface Waves. *Geochem. Geophys. Geosyst.* 11 (6), na. doi:10.1029/2010GC003036

Bastow, I. D., Stuart, G. W., Kendall, J.-M., and Ebinger, C. J. (2005). Upper-mantle Seismic Structure in a Region of Incipient continental Breakup: Northern Ethiopian Rift. *Geophys. J. Int.* 162 (2), 479–493. doi:10.1111/j.1365-246x.2005.02666.x

Bell, R. E., Jackson, C. A. L., Whipp, P. S., and Clements, B. (2014). Strain Migration during Multiphase Extension: Observations from the Northern North Sea. *Tectonics* 33 (10), 1936–1963. doi:10.1002/2014tc003551

Bellahsen, N., and Daniel, J. M. (2005). Fault Reactivation Control on normal Fault Growth: an Experimental Study. *J. Struct. Geology.* 27, 769–780. doi:10.1016/j.jsg.2004.12.003

Bendick, R., McClusky, S., Bilham, R., Asfaw, L., and Klemperer, S. (2006). Distributed Nubia-Somalia Relative Motion and dike Intrusion in the Main Ethiopian Rift. *Geophys. J. Int.* 165 (1), 303–310. doi:10.1111/j.1365-246x.2006.02904.x

Benoit, M. H., Nyblade, A. A., and Pasyanos, M. E. (2006). Crustal Thinning between the Ethiopian and East African Plateaus from Modeling Rayleigh Wave Dispersion. *Geophys. Res. Lett.* 33 (13), L13301. doi:10.1029/2006GL025687

Berhe, S. M. (1990). Ophiolites in Northeast and East Africa: Implications for Proterozoic Crustal Growth. *J. Geol. Soc.* 147, 41–57. doi:10.1144/gsjgs.147.1.0041

Beutel, E., van Wijk, J., Ebinger, C., Keir, D., and Agostini, A. (2010). Formation and Stability of Magmatic Segments in the Main Ethiopian and Afar Rifts. *Earth Planet. Sci. Lett.* 293 (3-4), 225–235. doi:10.1016/j.epsl.2010.02.006

Birhanu, Y., Bendick, R., Fisseha, S., Lewi, E., Floyd, M., King, R., et al. (2016). GPS Constraints on Broad Scale Extension in the Ethiopian Highlands and Main Ethiopian Rift. *Geophys. Res. Lett.* 43 (13), 6844–6851. doi:10.1002/2016gl069890

Boccaletti, M., Bonini, M., Mazzuoli, R., Abebe, B., Piccardi, L., and Tortorici, L. (1998). Quaternary Oblique Extensional Tectonics in the Ethiopian Rift (Horn of Africa). *Tectonophysics* 287, 97–116. doi:10.1016/s0040-1951(98)80063-2

Bonini, M., Corti, G., Innocenti, F., Manetti, P., Mazzarini, F., Abebe, T., et al. (2005). Evolution of the Main Ethiopian Rift in the Frame of Afar and Kenya Rifts Propagation. *Tectonics* 24, na. doi:10.1029/2004TC001680

Bonini, M., Sokoutis, D., Mulugeta, G., Boccaletti, M., Corti, G., Innocenti, F., et al. (2001). Dynamics of Magma Emplacement in Centrifuge Models of continental Extension with Implications for Flank Volcanism. *Tectonics* 20, 1053–1065. doi:10.1029/2001tc900017

Brune, S., Corti, G., and Ranalli, G. (2017). Controls of Inherited Lithospheric Heterogeneity on Rift Linkage: Numerical and Analog Models of Interaction between the Kenyan and Ethiopian Rifts across the Turkana Depression. *Tectonics* 36, 1767–1786. doi:10.1002/2017TC004739

Buck, W. R. (2004). "1. Consequences of Asthenospheric Variability on Continental Rifting," in *Rheology and Deformation of the Lithosphere at Continental Margins*. Editors G. D. Karner, B. Taylor, N. W. Droscoll, and D. L. Kohlstedt (New York: Columbia Univ. Press), 1–30. doi:10.7312/karn12738-002

Buiter, S. J. H., and Torsvik, T. H. (2014). A Review of Wilson Cycle Plate Margins: a Role for Mantle Plumes in continental Break-Up along Sutures. *Gondwana Res.* 26, 627–653. doi:10.1016/j.gr.2014.02.007

Casey, M., Ebinger, C., Keir, D., Gloaguen, R., and Mohamed, F. (2006). "Strain Accommodation in Transitional Rifts: Extension by Magma Intrusion and Faulting in Ethiopian Rift Magmatic Segments," in *The Afar Volcanic Province within the East African Rift System*. Editors G. Yirgu, C. J. Ebinger, and P. K. H. Maguire (London: Geological Society Special Publication), 259, 143–163. doi:10.1144/gsl.sp.2006.259.01.13*Geol. Soc. Lond. Spec. Publications*

Chang, S.-J., Kendall, E., Davaille, A., and Ferreira, A. M. G. (2020). The Evolution of Mantle Plumes in East Africa. *J. Geophys. Res.* 125, e2020JB019929. doi:10.1029/2020JB019929

Chiasera, B., Rooney, T. O., Girard, G., Yirgu, G., Grosfils, E., Ayalew, D., et al. (2018). Magmatically Assisted Off-Rift Extension-The Case for Broadly Distributed Strain Accommodation. *Geosphere* 14 (4), 1544–1563. doi:10.1130/GES01615.1

Chorowicz, J., Collet, B., Bonavia, F. F., and Korme, T. (1994). Northwest to North-Northwest Extension Direction in the Ethiopian Rift Deduced from the Orientation of Extension Structures and Fault-Slip Analysis. *Geol. Soc. America Bull.* 106, 1560–1570. doi:10.1130/0016-7606(1994)105<1560:ntnned>2.3.co;2

Chorowicz, J. (2005). The East African Rift System. *J. Afr. Earth Sci.* 43, 379–410. doi:10.1016/j.jafrearsci.2005.07.019

Claesson, S., Pallister, J. S., and Tatsumoto, M. (1984). Samarium-neodymium Data on Two Late Proterozoic Ophiolites of Saudi Arabia and Implications for Crustal and Mantle Evolution. *Contr. Mineral. Petrol.* 85, 244–252. doi:10.1007/bf00378103

Cornwell, D. G., Maguire, P. K. H., England, R. W., and Stuart, G. W. (2010). Imaging Detailed Crustal Structure and Magmatic Intrusion across the Ethiopian Rift Using a Dense Linear Broadband Array. *Geochem. Geophys. Geosyst.* 11, na. doi:10.1029/2009GC002637

Corti, G., Cioni, R., Franceschini, Z., Sani, F., Scaillet, S., Molin, P., et al. (2019). Aborted Propagation of the Ethiopian Rift Caused by Linkage with the Kenyan Rift. *Nat. Commun.* 10, 1309. doi:10.1038/s41467-019-09335-2

Corti, G. (2009). Continental Rift Evolution: from Rift Initiation to Incipient Break-Up in the Main Ethiopian Rift, East Africa. *Earth-Science Rev.* 96, 1–53. doi:10.1016/j.earscirev.2009.06.005

Corti, G. (2008). Control of Rift Obliquity on the Evolution and Segmentation of the Main Ethiopian Rift. *Nat. Geosci* 1, 258–262. doi:10.1038/ngeo160

Corti, G. (2012). Evolution and Characteristics of continental Rifting: Analog Modeling-Inspired View and Comparison with Examples from the East African Rift System. *Tectonophysics* 522-523, 1–33. doi:10.1016/j.tecto.2011.06.010

Corti, G., Molin, P., Sembroni, A., Bastow, I. D., and Keir, D. (2018a). Control of Pre-rift Lithospheric Structure on the Architecture and Evolution of continental Rifts: Insights from the Main Ethiopian Rift, East Africa. *Tectonics* 37, 477–496. doi:10.1002/2017TC004799

Corti, G., Philippon, M., Sani, F., and Keir, D. (2013). Re-orientation of the Extension Direction and Pure Extensional Faulting at Oblique Rift Margins:

Comparison between the Main Ethiopian Rift and Laboratory Experiments. *Terra Nova* 25, 396–404. doi:10.1111/ter.12049

Corti, G., Sani, F., Agostini, S., Philippon, M., Sokoutis, D., and Willingshofer, E. (2018b). Off-axis Volcano-Tectonic Activity during continental Rifting: Insights from the Transversal Goba-Bonga Lineament, Main Ethiopian Rift (East Africa). *Tectonophysics* 728-729, 75–91. doi:10.1016/j.tecto.2018.02.011

Corti, G., Sani, F., Florio, A. A., Greenfield, T., Keir, D., Erbello, A., et al. (2020). Tectonics of the Asela-Langano Margin, Main Ethiopian Rift (East Africa). *Tectonics* 39, e2020TC006075. doi:10.1029/2020TC006075

Corti, G., van Wijk, J., Cloetingh, S., and Morley, C. K. (2007). Tectonic Inheritance and continental Rift Architecture: Numerical and Analogue Models of the East African Rift System. *Tectonics* 26 (6), na. doi:10.1029/2006tc002086

Courtillot, V., Jaupart, C., Manighetti, I., Tapponnier, P., and Besse, J. (1999). On Causal Links between Flood Basalts and continental Breakup. *Earth Planet. Sci. Lett.* 166, 177–195. doi:10.1016/s0012-821x(98)00282-9

Daly, E., Keir, D., Ebinger, C. J., Stuart, G. W., Bastow, I. D., and Ayele, A. (2008). Crustal Tomographic Imaging of a Transitional continental Rift: the Ethiopian Rift. *Geophys. J. Int.* 172, 1033–1048. doi:10.1111/j.1365-246x.2007.03682.x

Daniels, K. A., Bastow, I. D., Keir, D., Sparks, R. S. J., and Menand, T. (2014). Thermal Models of Dyke Intrusion during Development of Continent-Ocean Transition. *Earth Planet. Sci. Lett.* 385, 145–153. doi:10.1016/j.epsl.2013.09.018

Deng, C., Fossen, H., Gawthorpe, R. L., Rotevatn, A., Jackson, C. A. L., and FazliKhani, H. (2017). Influence of Fault Reactivation during Multiphase Rifting: the Oseberg Area, Northern North Sea Rift. *Mar. Pet. Geol.* 86, 1252–1272. doi:10.1016/j.marpetgeo.2017.07.025

Deng, C., Gawthorpe, R. L., Fossen, H., and Finch, E. (2018). How Does the Orientation of a Preexisting Basement Weakness Influence Fault Development during Renewed Rifting? Insights from Three-Dimensional Discrete Element Modeling. *Tectonics* 37 (7), 2221–2242. doi:10.1029/2017tc004776

Díaz-Alvarado, J., Pedrera, A., Azor, A., García-Senz, J., Alberto Díaz de Neira, J., and Rodríguez-Fernández, L. R. (2021). Submarine Basaltic Magmatism in the Subbetic Basin (Southern Spain): Insights into Melt-Weakening Processes during Mesozoic Continental Rifting. *Lithosphere* 2021 (1), 5505884. doi:10.2113/2021/5505884

Duffy, O. B., Bell, R. E., Jackson, C. A. L., Gawthorpe, R. L., and Whipp, P. S. (2015). Fault Growth and Interactions in a Multiphase Rift Fault Network: Horda Platform, Norwegian North Sea. *J. Struct. Geol.* 80, 99–119. doi:10.1016/j.jsg.2015.08.015

Dugda, M. T., Nyblade, A. A., Jordi, J., Langston, C. A., Ammon, C. J., and Simiyu, S. (2005). Crustal Structure in Ethiopia and Kenya from Receiver Function Analysis: Implications for Rift Development in Eastern Africa. *J. Geophys. Res.* 110 (B1), B01303. doi:10.1029/2004JB003065

Dunbar, J. A., and Sawyer, D. S. (1989). Continental Rifting at Pre-existing Lithospheric Weaknesses. *Nature* 242, 565–571.

Ebinger, C. (2005). Continental Breakup: The East African Perspective. *Astron. Geophys.* 46, 216–221. doi:10.1111/j.1468-4004.2005.46216.x

Ebinger, C. J., and Casey, M. (2001). Continental Breakup in Magmatic Provinces: An Ethiopian Example. *Geology* 29, 527–530. doi:10.1130/0091-7613(2001)029<0527:cbimpa>2.0.co;2

Ebinger, C. J., Yemane, T., Harding, D. J., Tesfaye, S., Kelley, S., and Rex, D. C. (2000). Rift Deflection, Migration, and Propagation: Linkage of the Ethiopian and Eastern Rifts, Africa. *Geol. Soc. America Bull.* 112 (2), 163–176. doi:10.1130/0016-7606(2000)112<163:rdmapl>2.0.co;2

Ebinger, C. J., Deino, A. L., Drake, R. E., and Tesha, A. L. (1989). Chronology of Volcanism and Rift Basin Propagation: Rungwe Volcanic Province, East Africa. *J. Geophys. Res.* 94, 15785–15803.

Edel, J. B., Schulmann, K., and Rotstein, Y. (2007). The Variscan Tectonic Inheritance of the Upper Rhine Graben: Evidence of Reactivations in the Lias, Late Eocene–Oligocene up to the Recent. *Int. J. Earth Sci.* 96 (2), 305. doi:10.1007/s00531-006-0092-8

Emishaw, L., and Abdelsalam, M. G. (2019). Development of Late Jurassic-Early Paleogene and Neogene-Quaternary Rifts within the Turkana Depression, East Africa from Satellite Gravity Data. *Tectonics* 38 (7), 2358–2377. doi:10.1029/2018tc005389

Erbello, A., Corti, G., Agostini, A., Sani, F., Kidane, T., and Buccianti, A. (2016). Modeling along-axis Variations in Fault Architecture in the Main Ethiopian Rift: Implications for Nubia-Somalia Kinematics. *J. Geodynamics* 102, 24–38. doi:10.1016/j.jog.2016.07.002

Franceschini, Z., Cioni, R., Scaillet, S., Corti, G., Sani, F., Isola, I., et al. (2020). Recent Volcano-Tectonic Activity of the Ririba Rift and the Evolution of Rifting in South Ethiopia. *J. Volcanology Geothermal Res.* 402, 106989. doi:10.1016/j.jvolgeores.2020.106989

Gallacher, R. J., Keir, Derek., Harmon, Nicholas., Stuart, G., Leroy, Sylvie., Hammond, James., et al. (2016). The Initiation of Segmented Buoyancy-Driven Melting during continental Breakup. *Nat. Commun.* 7, 13110. doi:10.1038/ncomms13110

Gani, N. D. S., Abdelsalam MGGera, S., and Gani, M. R. (2009). Stratigraphic and Structural Evolution of the Blue Nile Basin, Northwestern Ethiopian Plateau. *Geol. J.* 44, 30–56. doi:10.1002/gj.1127

Gashawbeza, E. M., Klemperer, S. L., Nyblade, A. A., Walker, K. T., and Keranen, K. M. (2004). Shear-wave Splitting in Ethiopia: Precambrian Mantle Anisotropy Locally Modified by Neogene Rifting. *Geophys. Res. Lett.* 31, L18602. doi:10.1029/2004GL020471

Gómez-Vasconcelos, M. G., Macías, J., Avellán, Denis., Sosa-Ceballos, Giovanni., Garduño-Monroy, Víctor., Cisneros, Guillermo., et al. (2020). The Control of Preexisting Faults on the Distribution, Morphology, and Volume of Monogenetic Volcanism in the Michoacán-Guanajuato Volcanic Field. *GSA Bull.* 132, 2455–2474. doi:10.1130/B35397.1

Gouin, P. (1979). *Earthquake History of Ethiopia and the Horn of Africa*. Ottawa: IDRC, 258.

Grimmer, J. C., Ritter, J. R. R., Eisbacher ·, G. H., and Fielitz, V. (2017). The Late Variscan Control on the Location and Asymmetry of the Upper Rhine Graben. *Int. J. Earth Sci. (Geol Rundsch)* 106, 827–853. doi:10.1007/s00531-016-1336-x

Hayward, N. J., and Ebinger, C. J. (1996). Variations in the along-axis Segmentation of the Afar Rift System. *Tectonics* 15, 244–257. doi:10.1029/95tc02292

Henstra, G. A., Berg Kristensen, T., Rotevatn, A., and Gawthorpe, R. L. (2019). How Do Pre-existing normal Faults Influence Rift Geometry? A Comparison of Adjacent Basins with Contrasting Underlying Structure on the Lofoten Margin, Norway. *Basin Res.* 31 (6), 1083–1097. doi:10.1111/bre.12358

Henstra, G. A., Rotevatn, A., Gawthorpe, R. L., and Ravnås, R. (2015). Evolution of a Major Segmented normal Fault during Multiphase Rifting: the Origin of Plan-View Zigzag Geometry. *J. Struct. Geol.* 74, 45–63. doi:10.1016/j.jsg.2015.02.005

Hodge, M., Fagereng, A., Biggs, J., and Mdala, H. (2018). Controls on Early-rift Geometry: New Perspectives from the Bilila-Mtakataka Fault, Malawi. *Geophys. Res. Lett.* 45 (9), 3896–3905. doi:10.1029/2018gl077343

Kazmin, V., Seife, M. B., Nicoletti, M., and Petrucciani, C. (1980). "Evolution of the Northern Part of the Ethiopian Rift," in *Geodynamic Evolution of the Afro-Arabian Rift System* (Roma: Accademia Nazionale Dei Lincei, Atti dei Convegni Lincei), 47, 275–292.

Kazmin, V., Shifferaw, A., and Balcha, T. (1978). The Ethiopian Basement: Stratigraphy and Possible Manner of Evolution. *Geologische Rundschau* 67 (2), 531–546. doi:10.1007/bf01802803

Keir, D., Bastow, I. D., Corti, G., Mazzarini, F., and Rooney, T. O. (2015). The Origin of Along-Rift Variations in Faulting and Magmatism in the Ethiopian Rift. *Tectonics* 34, 464–477. doi:10.1002/2014TC003698

Keir, D., Ebinger, C. J., Stuart, G. W., Daly, E., and Ayele, A. (2006). Strain Accommodation by Magmatism and Faulting as Rifting Proceeds to Breakup: Seismicity of the Northern Ethiopian Rift. *J. Geophys. Res.* 111 (B5), B05314. doi:10.1029/2005JB003748

Kendall, J. M., Stuart, G. W., Ebinger, C. J., Bastow, I. D., and Keir, D. (2005). Magma Assisted Rifting in Ethiopia. *Nature* 433, 146–148. doi:10.1038/nature03161

Keranen, K., and Klemperer, S. L. (2008). Discontinuous and Diachronous Evolution of the Main Ethiopian Rift: Implications for the Development of continental Rifts. *Earth Planet. Sci. Lettters* 265, 96–111. doi:10.1016/j.epsl.2007.09.038

Keranen, K., Klemperer, S. L., and Gloaguen, R.Eagle working group (2004). Three-dimensional Seismic Imaging of a Protoridge axis in the Main Ethiopian Rift. *Geology* 32, 949–952. doi:10.1130/g20737.1

Keranen, K., Klemperer, S. L., Julia, J., Lawrence, J. L., and Nyblade, A. (2009). Low Lower-Crustal Velocity across Ethiopia: Is the Main Ethiopian Rift a Narrow Rift in a Hot Craton. *Geochem. Geophys. Geosyst.* 10, Q0AB01. doi:10.1029/2008GC002293

Knappe, E., Bendick, R., Ebinger, C., Birhanu, Y., Lewi, E., Floyd, M., et al. (2020). Accommodation of East African Rifting across the Turkana Depression. *J. Geophys. Res. Solid Earth* 125 (2), e2019JB018469. doi:10.1029/2019jb018469

Kogan, L., Fisseha, S., Bendick, R., Reilinger, R., McClusky, S., King, R., et al. (2012). Lithospheric Strength and Strain Localization in continental Extension from Observations of the East African Rift. *J. Geophys. Res.* 117, B03402. doi:10.1029/2011JB008516

Kolawole, F., Phillips, T. B., Atekwana, E. A., and Jackson, C. A. L. (2021). Structural Inheritance Controls Strain Distribution during Early Continental Rifting, Rukwa Rift. *Front. Earth Sci.* 9, 707869 doi:10.3389/feart.2021.707869

Korme, T., Acocella, V., and Abebe, B. (2004). The Role of Pre-existing Structures in the Origin, Propagation and Architecture of Faults in the Main Ethiopian Rift. *Gondwana Res.* 7, 467–479. doi:10.1016/s1342-937x(05)70798-x

Kroner, A., Todt, W., Hussein, I. M., Mansour, M., and Rashwan, A. A. (1992). Dating of Late Proterozoic Ophiolites in Egypt and the Sudan Using the Single Grain Zircon Evaporation Technique. *Precambrian Res.* 59, 15–32. doi:10.1016/0301-9268(92)90049-t

Laó-Dávila, D. A., Al-Salmi, H. S., Abdelsalam, M. G., and Atekwana, E. A. (2015). Hierarchical Segmentation of the Malawi Rift: The Influence of Inherited Lithospheric Heterogeneity and Kinematics in the Evolution of continental Rifts. *Tectonics* 34, 2399–2417. doi:10.1002/2015TC003953

Le Corvec, N., Menand, T., and Lindsay, J. (2013). Interaction of Ascending Magma with Pre-existing Crustal Fractures in Monogenetic Basaltic Volcanism: an Experimental Approach. *J. Geophys. Res. Solid Earth* 118, 968–984. doi:10.1002/jgrb.50142

Le Turdu, C., Tiercelin, J. J., Gibert, E., Travi, Y., Lezzar, K. E., Richert, J. P., et al. (1999). The Ziway–Shala lake basin System, Main Ethiopian Rift: Influence of Volcanism, Tectonics, and Climatic Forcing on basin Formation and Sedimentation. *Palaeogeogr. Palaeoclimatol. Palaeoecol.* 150, 135–177. doi:10.1016/S0031-0182(98)00220-X

Lloy, R., Biggs, J., Wilks, M., Nowacki, A., Kendall, J. M., Ayele, A., et al. (2018). Evidence for Cross Rift Structural Controls on Deformation and Seismicity at a Continental Rift Caldera. *Earth Planet. Sci. Lett.* 487, 190–200. doi:10.1016/j.epsl.2018.01.037

Maccaferri, F., Rivalta, E., Keir, D., and Acocella, V. (2014). Off-rift Volcanism in Rift Zones Determined by Crustal Unloading. *Nat. Geosci.* 7, 297–300. doi:10.1038/ngeo2110

Mackenzie, G. H., Thybo, G. H., and Maguire, P. (2005). Crustal Velocity Structure across the Main Ethiopian Rift: Results from 2-dimenional Wide-Angle Seismic Modeling. *Geophys. J. Int.* 162, 994–1006. doi:10.1111/j.1365-246x.2005.02710.x

Maestrelli, D., Corti, G., Bonini, M., Montanari, D., and Sani, F. (2021). Caldera Collapse and Tectonics along the Main Ethiopian Rift: Reviewing Possible Relationships. *Comptes Rendus Geosci.* 353 (S2), 1–19. doi:10.5802/crgeos.63

Maestrelli, D., Montanari, D., Corti, G., Del Ventisette, C., Moratti, G., and Bonini, M. (2020). Exploring the Interactions between Rift Propagation and Inherited Crustal Fabrics through Experimental Modeling. *Tectonics* 39 (12), e2020TC006211. doi:10.1029/2020TC006211

Mazzarini, F., and Isola, I. (2021). Vent Distribution and Structural Inheritance in an Embryonic Rift: The Example of the Chyulu Hills Off-Rift Magmatic Range (South Kenya). *J. Volcanology Geothermal Res.* 416, 107268. doi:10.1016/j.jvolgeores.2021.107268

Michon, L., and Sokoutis, D. (2005). Interaction between Structural Inheritance and Extension Direction during Graben and Depocentre Formation: an Experimental Approach. *Tectonophysics* 409 (1–4), 125–146. doi:10.1016/j.tecto.2005.08.020

Mohr, P. A., and Potter, E. C. (1976). The Sagatu Ridge dike Swarms, Ethiopian Rift Margin. *J. Volcanol. Geotherm. Res.* 1, 55–71. doi:10.1016/0377-0273(76)90018-4

Mohr, P. (1962). The Ethiopian Rift System. *Bull. Geophys. Observatory Addis Ababa* 5, 33–62.

Mohr, P. (1983). Volcanotectonic Aspects of the Ethiopian Rift Evolution. *Bull. Centre Recherches Elf Aquitaine Exploration Prod.* 7, 175–189.

Molin, P., and Corti, G. (2015). Topography, River Network and Recent Fault Activity at the Margins of the Central Main Ethiopian Rift (East Africa). *Tectonophysics* 664, 67–82. doi:10.1016/j.tecto.2015.08.045

Molnar, N., Cruden, A., and Betts, P. (2020). The Role of Inherited Crustal and Lithospheric Architecture during the Evolution of the Red Sea: Insights from Three Dimensional Analogue Experiments. *Earth Planet. Sci. Lett.* 544, 116377. doi:10.1016/j.epsl.2020.116377

Molnar, N. E., Cruden, A. R., and Betts, P. G. (2019). Interactions between Propagating Rifts and Linear Weaknesses in the Lower Crust. *Geosphere* 15 (5), 1617–1640. doi:10.1130/GES02119.1

Molnar, N. E., Cruden, A. R., and Betts, P. G. (2017). Interactions between Propagating Rotational Rifts and Linear Rheological Heterogeneities: Insights from Three-dimensional Laboratory Experiments. *Tectonics* 36 (3), 420–443. doi:10.1002/2016TC004447

Moore, J. M., and Davidson, A. (1978). Rift Structure in Southern Ethiopia. *Tectonophysics* 46, 159–173. doi:10.1016/0040-1951(78)90111-7

Morley, C. K., Haranya, C., Phoosongsee, W., Pongwapee, S., Kornsawan, A., and Wonganan, N. (2004). Activation of Rift Oblique and Rift Parallel Pre-existing Fabrics during Extension and Their Effect on Deformation Style: Examples from the Rifts of Thailand. *J. Struct. Geol.* 26 (10), 1803–1829. doi:10.1016/j.jsg.2004.02.014

Morley, C. K. (1999). "Influence of Pre-existing Fabrics on Rift Structure," in *Geoscience of Rift Systems, Evolution of East Africa*. Editor C. K. Morley (Tulsa, Oklahoma: AAPG Studies in Geology), 44, 151–160.

Morley, C. K. (2010). Stress Re-orientation along Zones of Weak Fabrics in Rifts: An Explanation for Pure Extension in 'oblique' Rift Segments. *Earth Planet. Sci. Lett.* 297, 667–673. doi:10.1016/j.epsl.2010.07.022

Muirhead, J. D., and Kattenhorn, S. A. (2018). Activation of Preexisting Transverse Structures in an Evolving Magmatic Rift in East Africa. *J. Struct. Geology.* 106, 1–18. doi:10.1016/j.jsg.2017.11.004

Nutz, A., Ragon, T., and Schuster, M. (2021). Cenozoic Tectono-Sedimentary Evolution of the Northern Turkana Depression (East African Rift System) and its Significance for continental Rifts. *Earth Planet. Sci. Lett.*, 117285. doi:10.1016/j.epsl.2021.117285

Osagiede, E. E., Rosenau, M., Rotevatn, A., Gawthorpe, R., Jackson, C. A. L., and Rudolf, M. (2021). Influence of Zones of Pre-Existing Crustal Weakness on Strain Localization and Partitioning during Rifting: Insights from Analog Modeling Using High-Resolution 3D Digital Image Correlation. *Tectonics* 40 (10), e2021TC006970. doi:10.1029/2021TC006970

Pallister, J. S., Stacey, J. S., Fischer, L. B., and Premo, W. R. (1988). Precambrian Ophiolites of Arabia: Geologic Settings, U-Pn Geochronology, Pb-Isotope Characteristics, and Implications for continental Accretion. *Precambrian Res.* 38, 1–54. doi:10.1016/0301-9268(88)90092-7

Pérez-Gussinyé, M., Metois, M., Fernández, M., Vergés, J., Fullea, J., and Lowry, A. R. (2009). Effective Elastic Thickness of Africa and its Relationship to Other Proxies for Lithospheric Structure and Surface Tectonics. *Earth Planet. Sci. Lett.* 287, 152–167. doi:10.1016/j.epsl.2009.08.004

Philippon, M., Corti, G., Sani, F., Bonini, M., Balestrieri, M. L., Molin, P., et al. (2014). Evolution, Distribution and Characteristics of Rifting in Southern Ethiopia. *Tectonics* 33, 485–508. doi:10.1002/2013TC003430

Philippon, M., Willingshofer, E., Sokoutis, D., Corti, G., Sani, F., Bonini, M., et al. (2015). Slip Re-orientation in Oblique Rifts. *Geology* 43, 147–150. doi:10.1130/g36208.1

Phillips, T. B., Fazlikhani, H., Gawthorpe, R. L., Fossen, H., Jackson, C. A. L., Bell, R. E., et al. (2019). The Influence of Structural Inheritance and Multiphase Extension on Rift Development, the Northern North Sea. *Tectonics* 38 (12), 4099–4126. doi:10.1029/2019tc005756

Pizzi, A., Coltorti, M., Abebe, B., Disperati, L., Sacchi, G., and Salvini, R. (2006). "The Wonji Fault belt (Main Ethiopian Rift): Structural and Geomorphological Constraints and GPS Monitoring," in *The Afar Volcanic Province within the East African Rift System*. Editors G. Yirgu, C. J. Ebinger, and P. K. H. Maguire (Geol. Soc. Spec. Publ.), 259, 191–207. doi:10.1144/gsl.sp.2006.259.01.16

Pongwapee, S., Morley, C. K., and Won-in, K. (2019). Impact of Pre-existing Fabrics and Multi-phase Oblique Extension on Cenozoic Fault Patterns, Wichianburi Sub-basin of the Phetchabun Rift, Thailand. *J. Struct. Geology.* 118, 340–361. doi:10.1016/j.jsg.2018.11.012

Purcell, P. G. (2017). Re-imagining and Re-imaging the Development of the East African Rift. *Pet. Geosci.* 24 (1), 21–40. doi:10.1144/petgeo2017-036

Ritsema, J., van Heijst, H. J., and Woodhouse, J. H. (1999). Complex Shear Wave Velocity Structure Imaged beneath Africa and Iceland. *Science* 286, 1925–1928. doi:10.1126/science.286.5446.1925

Rosendahl, B. L. (1987). Architecture of continental Rifts with Special Reference to East Africa. *Annu. Rev. Earth Planet. Sci.* 15, 445–503. doi:10.1146/annurev.ea.15.050187.002305

Samsu, A., Cruden, A. R., Molnar, N. E., and Weinberg, R. F. (2021). Inheritance of Penetrative Basement Anisotropies by Extension-Oblique Faults: Insights from

Analogue Experiments. *Tectonics* 40 (5), e2020TC006596. doi:10.1029/2020TC006596

Saria, E., Calais, E., Stamps, D. S., Delvaux, D., and Hartnady, C. J. H. (2014). Present-day Kinematics of the East African Rift. *J. Geophys. Res. Solid Earth* 119, 3584–3600. doi:10.1002/2013JB010901

Schori, M., Zwaan, F., Schreurs, G., and Mosar, J. (2021). Pre-existing Basement Faults Controlling Deformation in the Jura Mountains Fold-And-Thrust belt: Insights from Analogue Models. *Tectonophysics* 814, 228980. doi:10.1016/j.tecto.2021.228980

Schumacher, M. E. (2002). Upper Rhine Graben: Role of Preexisting Structures during Rift Evolution. *Tectonics* 21 (1), 61–617. doi:10.1029/2001TC900022

Smith, M., and Mosley, P. (1993). Crustal Heterogeneity and Basement Influence on the Development of the Kenya Rift, East Africa. *Tectonics* 12, 591–606. doi:10.1029/92TC01710

Sokoutis, D., Corti, G., Bonini, M., Brun, J. P., Cloetingh, S., Mauduit, T., et al. (2007). Modelling the Extension of Heterogeneous Hot Lithosphere. *Tectonophysics* 444 (1-4), 63–79. doi:10.1016/j.tecto.2007.08.012

Stern, R. J. (1994). Arc Assembly and continental Collision in the Neoproterozoic East African Orogen. *Annu. Rev. Earth Planet. Sci.* 22, 319–351. doi:10.1146/annurev.ea.22.050194.001535

Stern, R. J. (2002). Crustal Evolution in the East African Orogen: a Neodymium Isotopic Perspective. *J. Afr. Earth Sci.* 34, 109–117. doi:10.1016/s0899-5362(02)00012-x

Stern, R. J., Nielsen, K. C., Best, E., Sultan, M., Arvidson, R. E., and Kroner, A. (1990). Orientation of the Late Precambrian Sutures in the Arabian-Nubian Shield. *Geology* 18, 1103–1106. doi:10.1130/0091-7613(1990)018<1103:oolpsi>2.3.co;2

Tommasi, A., and Vauchez, A. (2001). Continental Rifting Parallel to Ancient Collisional Belts: an Effect of the Mechanical Anisotropy of the Lithospheric Mantle. *Earth Planet. Sci. Lett.* 185, 199–210. doi:10.1016/s0012-821x(00)00350-2

Vail, J. R. (1983). Pan-African Crustal Accretion in the North-East Africa. *J. African Earth Sci.* 1, 285–294.

Vauchez, A., Tommasi, A., and Barrruol, G. (1998). Rheological Heterogeneity, Mechanical Anisotropy and Deformation of the continental Lithosphere. *Tectonophysics* 296, 61–86. doi:10.1016/s0040-1951(98)00137-1

Vétel, W., and Le Gall, B. (2006). Dynamics of Prolonged continental Extension in Magmatic Rifts: the Turkana Rift Case Study (North Kenya). *Geol. Soc. Lond. Spec. Publications* 259, 209–233. doi:10.1144/gsl.sp.2006.259.01.17

Vétel, W., Le Gall, B., and Walsh, J. J. (2005). Geometry and Growth of an Inner Rift Fault Pattern: the Kino Sogo Fault Belt, Turkana Rift (North Kenya). *J. Struct. Geol.* 27, 2204–2222. doi:10.1016/j.jsg.2005.07.003

Wadge, G., Biggs, J., Lloyd, R., and Kendall, J. M. (2016). Historical Volcanism and the State of Stress in the East African Rift System. *Front. Earth Sci.* 4, 86. doi:10.3389/feart.2016.00086

Wang, L., Maestrelli, D., Corti, G., Zou, Y., and Shen, C. (2021). Normal Fault Reactivation during Multiphase Extension: Analogue Models and Application to the Turkana Depression, East Africa. *Tectonophysics* 811, 228870. doi:10.1016/j.tecto.2021.228870

Wedmore, L. N. J., Williams, J. N., Biggs, J., Fagereng, A., Mphepo, F., Dulanya, Z., et al. (2020). Structural Inheritance and Border Fault Reactivation during Active Early-Stage Rifting along the Thyolo Fault, Malawi. *J. Struct. Geology.* 139, 104097. doi:10.1016/j.jsg.2020.104097

Whipp, P. S., Jackson, C. A. L., Gawthorpe, R. L., Dreyer, T., and Quinn, D. (2014). Normal Fault Array Evolution above a Reactivated Rift Fabric; a Subsurface Example from the Northern Horda Platform, Norwegian North Sea. *Basin Res.* 26 (4), 523–549. doi:10.1111/bre.12050

Will, T. M., and Frimmel, H. E. (2017). Where Does a Continent Prefer to Break up? Some Lessons from the South Atlantic Margins. *Gondwana Res.* 53, 9–19. doi:10.1016/j.gr.2017.04.014

Williams, J. N., Fagereng, A., Wedmore, L. N., Biggs, J., Mphepo, F., Dulanya, Z., et al. (2019). How Do Variably Striking Faults Reactivate during Rifting? Insights from Southern Malawi. *Geochem. Geophys. Geosystems* 20 (7), 3588–3607. doi:10.1029/2019gc008219

WoldeGabriel, G., Aronson, J. L., and Walter, R. C. (1990). Geology, Geochronology, and Rift basin Development in the central Sector of the Main Ethiopia Rift. *Geol. Soc. America Bull.* 102, 439–458. doi:10.1130/0016-7606(1990)102<0439:ggarbd>2.3.co;2

Wolfenden, E., Ebinger, C., Yirgu, G., Deino, A., and Ayale, D. (2004). Evolution of the Northern Main Ethiopian Rift: Birth of a Triple junction. *Earth Planet. Sci. Lett.* 224, 213–228. doi:10.1016/j.epsl.2004.04.022

Wu, L., Mei, L., Paton, D. A., Liu, Y., Shen, C., Liu, Z., et al. (2020). Basement Structures Have Crucial Influence on Rift Development: Insights from the Jianghan Basin, Central China. *Tectonics* 39 (2). doi:10.1029/2019tc005671

Zwaan, F., Chenin, P., Erratt, D., Manatschal, G., and Scheurs, G. (2021a). Competition between 3D Structural Inheritance and Kinematics during Rifting: Insights from Analogue Models. *Basin Res.* 00, 1–31 doi:10.1111/bre.12642

Zwaan, F., Chenin, P., Erratt, D., Manatschal, G., and Schreurs, G. (2021b). Complex Rift Patterns, a Result of Interacting Crustal and Mantle Weaknesses, or Multiphase Rifting? Insights from Analogue Models. *Solid Earth Discuss.* 12 (7), 1473–1495. doi:10.5194/se-12-1473-2021

Zwaan, F., and Schreurs, G. (2017). How Oblique Extension and Structural Inheritance Influence Rift Segment Interaction: Insights from 4D Analog Models. *Interpretation*; 5 (1): SD119–SD138. doi:10.1190/INT-2016-0063.1

Conflict of Interest: The authors declare that the research was conducted in the absence of any commercial or financial relationships that could be construed as a potential conflict of interest.

Publisher's Note: All claims expressed in this article are solely those of the authors and do not necessarily represent those of their affiliated organizations, or those of the publisher, the editors and the reviewers. Any product that may be evaluated in this article, or claim that may be made by its manufacturer, is not guaranteed or endorsed by the publisher.

frontiers in Earth Science

REVIEW
published: 22 February 2022
doi: 10.3389/feart.2022.838993

Insights Into the Source of Magmatic Hot-Lines: Forty Years of Geophysical Studies of the Cameroon Volcanic Line

Aubreya Adams *

Colgate University, Department of Geology, Hamilton, NY, United States

The Cameroon Volcanic Line (CVL) of west Africa poses many challenges to common models of mantle processes and volcanic system genesis. Although the CVL superficially resembles the hot-spot trace of a mantle plume, there is no evidence for age progression of initiation or cessation of volcanic activity, making the CVL one of several hot-lines observed on Earth, which exhibit asynchronous volcanism along each line. This unusual form of volcanic system, together with the complexity of the surrounding geology, which includes a Mesozoic rift, an Archean Craton, a Proterozoic mobile belt, and a major continental-scale shear zone, have fueled numerous geophysical investigations of the crust and upper mantle structure within the region. This review highlights major findings from geophysical studies, including controlled source and passive source seismic studies and gravimetric modeling, conducted in the late 20th and early 21st centuries. Potential geodynamic models for the formation of the CVL are examined and evaluated based on the body of geophysical evidence. Finally, several key outstanding questions about the structure and formation of the CVL are highlighted, potentially guiding future studies of this region.

Keywords: mantle convection, mantle plume, africa, volcanic line, tectonics, volcanism, lithosphere

OPEN ACCESS

Edited by:
Mohamed Sobh,
Freiberg University of Mining and Technology, Germany

Reviewed by:
Mohamed Abdelsalam,
Oklahoma State University, United States
Emmanuel Njinju,
Virginia Tech, United States

***Correspondence:**
Aubreya Adams
aadams@colgate.edu

Specialty section:
This article was submitted to Solid Earth Geophysics, a section of the journal Frontiers in Earth Science

Received: *19 December 2021*
Accepted: *24 January 2022*
Published: *22 February 2022*

Citation:
Adams A (2022) Insights Into the Source of Magmatic Hot-Lines: Forty Years of Geophysical Studies of the Cameroon Volcanic Line. Front. Earth Sci. 10:838993. doi: 10.3389/feart.2022.838993

INTRODUCTION

The Cameroon Volcanic Line (CVL) in west Africa is a geologic enigma that challenges many current models for mantle dynamics, tectonics, and volcanism. The CVL consists of an 1800 km long linear chain of active volcanoes and plutonic structures. It is comprised of two sections of roughly equal lengths—an onshore section within the Adamawa Plateau of Cameroon, and an offshore section of volcanic islands including Annobòn (Pagalú) and Bioko as well as the island nation of São Tomé and Príncipe (**Figure 1**). Volcanism along the CVL dates from 66 Ma to the present, without any systematic change in the onset of volcanism or in the age of the most recent volcanic activity (**Figure 2**; e.g., Hedberg, 1969; Deruelle et al., 1991; Deruelle et al., 2007; Marzoli et al., 1999; Marzoli et al., 2000; Ngounouno et al., 2005; Ngounouno et al., 2006; Kamgang et al., 2010; Asaah et al., 2015).

The linear nature of the CVL has led many studies to describe it as a classic Wilson-Morgan hot spot trail created by a mantle plume, in which a linear chain of age-progressive volcanoes are produced (e.g., Morgan, 1972; Morgan, 1983; Van Houten, 1983; Duncan and Richards, 1991; O'Connor and Le Roex, 1992; Lee et al., 1994; Burke, 2001). The CVL, however, displays several first-order characteristics that fundamentally differ from those that define a hot spot trail, leading other studies to conclude that the CVL is inherently inconsistent with its formation by a mantle plume (e.g., Poudjom Djomani et al., 1995; Reusch et al., 2010; Adams et al., 2015).

The characteristics of a mantle plume are debated in scientific literature. The traditional Wilson-Morgan model of a mantle plume includes a narrow thermal anomaly seated in the deep mantle,

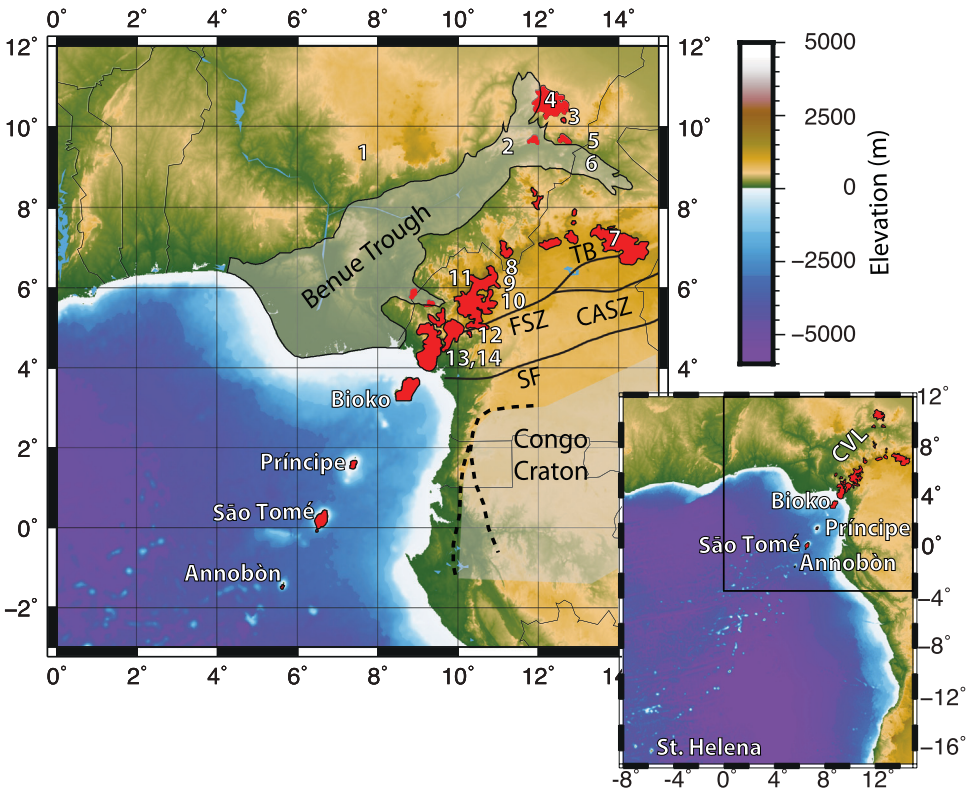

FIGURE 1 | Geologic map of the CVL and surrounding regions. Volcanic provinces of the CVL are shown in red, and the Congo Craton and the Benue Trough are shade in gray. Bold lines represent the CASZ, including the Foumbian Shear Zone (FSZ), Tcholliré-Banyo Shear Zone (TB), and the Sanaga Fault (SZ). White numbers and labels indicate the locations of volcanic centers dated in **Figure 2**. The inset shows the CVL in relation to St. Helena and nearby seamounts. The area of the primary map is shown with a black rectangle.

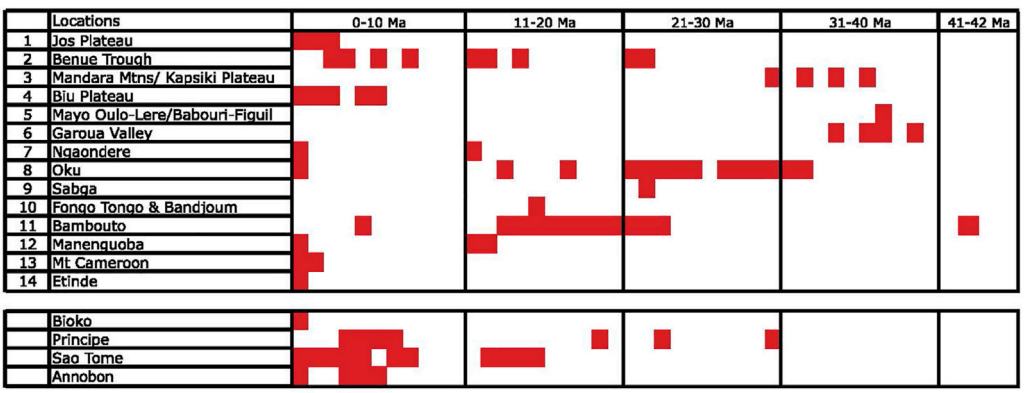

FIGURE 2 | Ages of volcanic activity at volcanic centers along the continental CVL (#1–14) and the oceanic portions (by island name) of the CVL. Volcanic center locations are shown in **Figure 1** (Hedberg, 1969; Grant et al., 1972; Grunau et al., 1975; Dunlap and Fitton, 1979; Cornen and Maury, 1980; Dunlap, 1983; Fitton and Dunlap, 1985; Lee et al., 1994; Ngounouno et al., 1997; Marzoli et al., 1999; 2000; Ngounouno et al., 2001; 2003; Njilah et al., 2004; Ngounouno et al., 2005; 2006), illustrating the lack of age progression for initiation or cessation of volcanism along the CVL. Reproduced with permission from Reusch et al. (2010).

which is stationary within the mantle over time (Wilson, 1963; Morgan, 1971; Morgan, 1972). Such a plume should 1) produce a linear chain of volcanos that parallels plate motion, 2) extend from an older large igneous province produced by the initial plume head, 3) show a progression in age of onset and cessation of volcanic activity along the line, and 4) produce basalts with geochemical signatures distinct from mid-ocean ridge basalts (e.g., Wilson, 1963; Morgan, 1971; Campbell, 2007; and

sources therein). More recent adaptations to the plume hypothesis include plumes that are not stationary within the mantle (e.g., Molnar and Stock, 1987; Steinberger et al., 2004), plumes that originate from shallower depths of the mantle (e.g., Burke and Torsvik, 2004), plumes that lack an initial plume head forming a large igneous province (e.g., Farnetani and Samuel, 2005; Davies and Bunge, 2006), or plumes with significant geochemical overlap with mid-ocean ridge basalts (Chadwick et al., 2005; White, 2010). All theories for the existence of mantle plumes, however, concur that a plume should produce a line of volcanos with age progression and an orientation parallel to plate motion. The CVL notably does not meet these "minimum requirements", displaying no age progression and having an orientation that is sub-perpendicular to plate motion in a hot-spot frame of reference (Gripp and Gordon, 1990). Furthermore, geochemical evidence to support or refute the presence of a mantle plume associated with the CVL is equivocal.

Numerous geophysical and geochemical studies have been conducted across the CVL since 1980 to delineate the characteristics of this volcanic line and to gain insight into the processes that formed and continue to drive it. Geochemical studies of the CVL were reviewed and analyzed by Asaah et al. (2015). In this study, I present a review of insights from geophysical studies from the last 40 years, and analyze the potential geodynamic models that may have formed the enigmatic CVL.

GEOLOGIC SETTING

The Cameroon Volcanic Line

The CVL consists of multiple volcanic and plutonic bodies arrayed a narrow line that roughly bifurcates the bend of central western Africa at the Gulf of Guinea. The onshore CVL lays atop the Adamawa Plateau, a broad topographic region with approximately 1 km of uplift and consists of seven major volcanic centers including Mt. Cameroon as well as Mts. Bambouto, Entinde, Mandara, Manengouba, and Oku (Tabod et al., 1992). The offshore CVL lays atop an asymmetrical 200 km wide crustal arch with up to 3 km of uplift, with major volcanic centers marked by the islands of Annobòn, São Tomé, Príncipe, and Bioko (Meyers and Rosendahl, 1991; Meyers et al., 1998). Igneous materials consist primarily of alkaline plutonic rings and alkaline basalts (Hedberg, 1969;Deruelle et al., 1991; Deruelle et al., 2007). Continental Precambrian crystalline basement rocks are part of the Oubanguides Belt, a zone of Neoproterozoic metamorphosed mobile belts dating to the Neoproterozoic Pan-African orogeny, and forming part of the Central African Orogenic Belt (e.g., Nzenti et al., 1988; Castaing et al., 1994; Marzoli et al., 2000).

The CVL strikes at approximately N30°E, with little apparent change in orientation within the continental and oceanic sections. Both distal ends of the CVL show divergence from the central line. In the northeast, the northern CVL splits into two distinct lines extending 300 km north and 200 km east, creating a Y-shaped terminus. Southwest of Annobòn, the CVL connects to a broad field of numerous seamounts, 700 km across, extending to St. Helena. It is notable that the long axis of this broad Annobòn-Helena seamount field roughly follows the overall orientation of the CVL (see inset of **Figure 1**). The apparent connection between the CVL, the Annobòn-Helena seamount field, and the island of St. Helena have led some authors to suggest that the CVL may be part of a broader mantle feature (e.g., Morgan, 1972; Morgan, 1983; Duncan and Richards, 1991; Meyers et al., 1998).

Surrounding Regions

North of the CVL and along the northern border of the Adamawa Plateau lies the Benue Trough, a linear sediment-filled dormant rift formed during the rifting of the Atlantic Ocean, 140–84 Ma (e.g., Burke et al., 1970; Fitton, 1980; Maluski et al., 1995). The Benue Trough is oriented sub-parallel to the CVL, and splits into two smaller rifts near the northeastern termination, forming a Y-shaped intersection and mirroring the shape of the northern CVL. The eastern most portions of the Benue Trough overlap with the northern most extension of the CVL in the Garoua Rift region. The Benue Trough was also volcanically active during and after rifting, with andesitic and basaltic deposits dating to 147–106 Ma in the north and 97–9 Ma in the south (e.g., Carter et al., 1963; Burke et al., 1970; Uzuakpunwa, 1974; Olade, 1978; Maluski et al., 1995). These morphologic and volcanic similarities between the Benue Trough and the CVL have led many authors to infer some dynamic relationship between the two features (e.g., Fitton 1980; Fitton et al., 1983; Fitton, 1987). For example, Fitton et al. (1983) suggested that a thermal anomaly in the upper mantle may have migrated from the Benue Trough to the CVL due to changes in mantle convection or plate motion. More recent geophysical studies, however, identify key differences between the crustal and upper mantle structures in these regions, suggesting that the two features may not share a common cause. The relationship between the two features, or even if any causal relationship exists, remains unanswered.

The CVL is roughly aligned with the Central African Shear Zone (CASZ), which locally includes the Foumbian Shear Zone, Tcholliré-Banyo Shear Zone, and the Sanaga Fault (SZ) as the Foumbian Shear Zone (Dorbath et al., 1986; Toteu et al., 2004; Nzenti et al., 2006). The CASZ in Cameroon consists of several mylonitic shear zones within the Oubanguides Belt and shows a complex series of both dextral and sinistral shear that began with the collision of multiple cratons during the formation of Gondwana (Toteu et al., 2004). This major intercontinental structure runs from northeastern Africa, through the central African continent, and along southern boundary of the CVL (Fairhead and Okereke 1987). Prior to the opening of the Atlantic Ocean during the Mesozoic, the CASZ continued into what is now the Pernambuco lineament of South America. Within the Atlantic Ocean, the previously existing CASZ may have influenced the large transform offsets observed for the Ascension Fracture Zone at the mid-Atlantic Ridge (Burke et al., 1971; Browne and Fairhead 1983).

The CASZ separates the CVL from the Congo Craton, the largest of several pre-Cambrian blocks that form the framework of the African continent. Archean to Paleoproterozoic in age, the Congo Craton occupies a substantial portion of sub-Saharan Africa, but is buried by major sedimentary basins in many locations. The Congo Craton is exposed in southern

Cameroon as the Ntem Complex, which forms the northwestern boundary of the craton (Vicat et al., 1996). The northern boundary is overthrust by the Oubanguides Belt, while the western boundary is obscured by coastal sediments, making the delineation of the Congo Craton's boundary relative to the CVL challenging in these locations (Boukeke, 1994).

Dating and Mantle "Hot Lines"

Igneous activity associated with the CVL began in the Paleocene, with the intrusion of alkaline plutonic ring complexes 66–30 Ma (Deruelle et al., 1991; Deruelle et al., 2007). Volcanic activity began 42 Ma within the continental portion of the CVL, while offshore volcanism began 30 Ma (**Figure 2**; e.g., Grunau et al., 1975). The initiation of offshore volcanism correlated with the formation of the offshore crustal arch, but uplift of the Adamawa Plateau began in the Miocene, after the onset of both plutonic and volcanic activity (Hedberg, 1969; Browne and Fairhead, 1983; Fitton et al., 1983; Fitton, 1987; Okereke, 1988; Meyers and Rosendahl, 1991; Meyers et al., 1998).

Volcanism continues to the present across both the oceanic and the continental CVL. No clear age progression along the line is observed either for age of onset or for the most recent volcanic activity, nor is any consistent pattern seen in the duration of active volcanism (**Figure 2**; e.g., Hedberg, 1969; Grant et al., 1972; Grunau et al., 1975; Dunlap and Fitton, 1979; Cornen and Maury, 1980; Dunlap, 1983; Fitton and Dunlap, 1985; Lee et al., 1994; Ngounouno et al., 1997; Marzoli et al., 1999, Marzoli et al., 2000; Ngounouno et al., 2001, Ngounouno et al., 2003; Njilah et al., 2004; Ngounouno et al., 2005, Ngounouno et al., 2006; Aka et al., 2009; Kagou Dongmo et al., 2010; Kamgang et al., 2010). Some studies of basalts from the oceanic sector suggest a possible progression in age of onset—but not in age of cessation—from the islands of Annobòn to Príncipe, but this apparent trend may reflect bias due to the very limited sampling from these islands (Grunau et al., 1975; Meyers and Rosendahl, 1991; Meyers et al., 1998).

This lack of age progression along the CVL has long been recognized as a challenge to the interpretation of the volcanic chain as a hot spot trace from a mantle plume, leading some studies to dub this and other linear volcanic chains without age progression as "hot lines" in the mantle (e.g., Bonatti and Harrison, 1976; Meyers et al., 1998). Numerous alternative causal mechanisms have been proposed for the formation of the CVL. Some models for formation are adaptations of the plume hypothesis, including the superposition of multiple mantle plumes with overprinting ages (Ngako et al., 2006; Njome and Wit, 2014) or the diversion of plume material from east Africa along the CASZ, reaching the surface at the CVL (Ebinger and Sleep, 1998). Other studies suggest that the CVL formation was influenced by the Benue Trough (e.g., Fitton 1980; Fitton et al., 1983; Stuart et al., 1985; Fitton, 1987) or by active rifting (e.g., Okereke, 1988). A number of studies attribute the formation of the CVL to local or regional patterns in mantle convection. Two studies suggest that local edge convection may be induced along the northern boundary of the Congo Craton. This edge convection would flow laterally from the Craton to the CVL at shallow sub-lithospheric depths if the asthenosphere beneath the Craton is heated due to insulation (King and Anderson, 1995) or would form a downwelling beneath the edge of the Craton and an upwelling beneath the CVL if the asthenosphere beneath the Craton is not anomalously warm (King and Anderson, 1998; King and Ritsema, 2000). Analog models by Milleli et al. (2012) indicate that edge convection may also be induced perpendicular to a continental margin due to the contrast in lithospheric thickness between continental and oceanic lithosphere. Meyers et al. (1998) alternatively suggest that the CVL may result from a convective roll induced by shear along the base of the mantle transition zone.

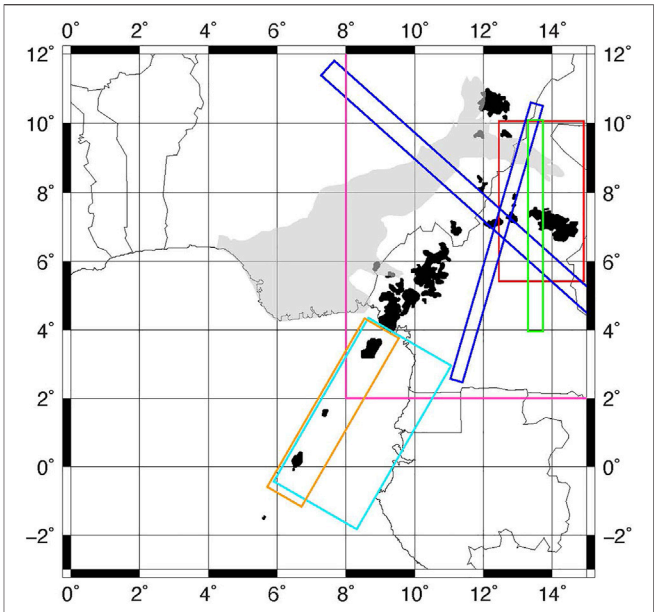

FIGURE 3 | Locations of select geophysical studies from 1985 to 1999. Red = Areal extent of Stuart et al. (1985) and Dorbath et al. (1986); Royal Blue = Cross-sections from Okereke (1988); Magenta = Focus area of Poudjom Djomani et al. (1995); Green = Cross-section from Poudjom Djomani et al. (1997); Cyan = Focus area of Meyers and Rosendahl (1991); Orange = Focus area of Meyers et al. (1998).

Volcanic lines lacking age progression also exist in other regions, most notably in the south Pacific. The Austral-Cook line of volcanos in the south Pacific, for example, lacks the clear age progression typical of a mantle plume. It has instead been suggested that this line of volcanos is formed by three superimposed mantle plumes rooted in the South Pacific Superplume (Bonneville et al., 2006). To the north, the central Pacific Line Islands also lack a clear age progression, which has been attributed to interactions with a spreading ridge or transform fault or to thermal feedback (Epp, 1984). Still other studies in this region attribute these "hot-lines" to a combination of shallow, short-lived plumes and lithospheric extension (Koppers et al., 2003).

19TH CENTURY GEOPHYSICAL STUDIES (1985–1999)

Early geophysical studies of the CVL and surrounding regions during the 1980s focused primarily on the crustal and lithospheric structures. These studies used a combination of

gravity (Fairhead and Okereke, 1987; Okereke, 1988), controlled source seismic refraction (Stuart et al., 1985), and teleseismic delay times (Dorbath et al., 1986) to image structures beneath the land portion of the CVL on the Adamawa Plateau and surrounding regions. Most of these studies focused on the northernmost portions of these features, where the Benue Trough, the CVL, and the CASZ overlap. In the 1990s, additional data were gathered and analyzed on land (Poudjom Djomani et al., 1995; Poudjom Djomani et al., 1997), and the study of the CVL expanded to include imaging of the oceanic sector using seismic reflection and gravity data (Meyers and Rosendahl, 1991; Meyers et al., 1998). By the end of the 1990s, a number of first-order characteristics of the CVL lithosphere were determined. **Figure 3** shows the areas of focus for selected 20th century geophysical studies described below.

Studies of the Land Sector

One of the earliest geophysical studies of crustal structure of this region used seismic refraction of 5 months of quarry blasts recorded on 40 vertical seismometers to image the crustal structure for a 200 km long transect across the northernmost Benue Trough into the Adamawa Plateau (Stuart et al., 1985). One dimensional velocity models were developed for both the Benue Trough and the Adamawa Plateau. Similar crustal velocities were found in both regions, but a notable change was observed in crustal thickness and upper-most mantle velocities. Crustal thickness changed from 23 km beneath the rifted Benue Trough to 33 km beneath the Adamawa Plateau and the northernmost CVL. This change was primarily due to a thinned lower crust beneath the Benue Trough. Upper mantle P-wave velocities beneath the Benue Trough are reduced to 7.8 km/s compared to 8.0 km/s beneath the Adamawa Plateau, suggesting that rifting has affected the lower crust and upper lithospheric mantle in the Benue Trough in the north, but that the formation of the CVL has not thinned the crust nor altered the upper lithospheric mantle. This is corroborated by the presence of a positive Bouguer gravity anomaly beneath the rift, and the lack of a similar corresponding anomaly beneath the CVL (Collignon, 1968; Stuart et al., 1985). The nature of the transition from the thinned Benue Trough to the thicker crust of the Adamawa Plateau is not clearly imaged but must occur over a narrow zone. This sharp transition likely predated the formation of the CVL and may have provided a pre-existing zone of weakness along which subsequent volcanic activity was concentrated, possibly leading to the similarity in the shape of the Benue Trough and the CVL (Stuart et al., 1985).

Dorbath et al. (1986) used teleseismic P-wave delay times recorded on the same seismic deployment used by Stuart et al. (1985) to build the earliest 3D P-wave velocity model of the CVL. This study focused on lithospheric-scale velocity structure to a depth of 190 km in the Garoua Rift region at the northern end of the Benue Trough and Adamawa Plateau. A region of low velocities was found directly beneath the location where the CASZ crosses the northernmost CVL near the Garoua Rift. This low velocity region is bounded to the north and south by lithospheric blocks with higher velocities. The contrast between velocities in these regions extends to all depths within the model and increases with depth; however, the greatest velocity contrast at any depth is 2.5%, which is considerably lower than velocity contrasts in other volcanically active regions (Dorbath et al., 1986). The authors suggest based on this shallow regional model that a large upper mantle velocity anomaly might lie beneath the entire Adamawa Plateau, but that previously existing zones of weakness associated with the CASZ allow heat and magma to reach the surface at the intersection of the CASZ and the CVL (Dorbath et al., 1986).

A regional survey of Bouguer gravity anomalies was conducted across west-central Africa by Fairhead and Okereke (1987), and two cross-sections from the gravity model through the northern CVL were interpreted and modeled by Okereke (1988). The data showed a long-wavelength positive Bouguer anomaly beneath the Benue Trough, paralleled by a long-wavelength negative anomaly beneath the Adamawa Plateau (Fairhead and Okereke, 1987). Forward models of the data suggested the positive anomaly beneath the Benue Trough represents thinned crust formed through extension, with low density lower crust replaced by high density lithospheric mantle. The negative anomaly beneath the Adamawa Plateau, however, is best modeled with thinned lithosphere but minimal crustal thinning (Okereke, 1988). Okereke (1988) notes the similarity between the broad negative Bouguer anomaly beneath the Adamawa Plateau and a similar anomaly beneath the East African Plateau associated with the East African Rift System. This pattern of anomalies is interpreted to reflect passive-style rifting in the Benue Trough due to tensional forces in the crust, and to reflect active-style rifting in the CVL due to upwelling of the asthenospheric mantle (Okereke, 1988).

Regional gravity anomalies were reexamined in the 1990s using data from higher resolution surveys. Poudjom Djomani et al. (1995) built new gravity and topography datasets combined from multiple sources, including data from approximately 32,000 locations. Combining both datasets, they determined effective elastic thickness (T_e) and crustal thickness (T_c) across the Benue Trough, Adamawa Plateau, the CVL, and the northernmost Congo Craton. They found a first-order pattern of decreasing crustal thickness from south to north, with T_c reaching a maximum of 50 km beneath the Congo Craton to the south and reaching a minimum of 14 km north of the Benue Trough. Poudjom Djomani et al. (1995) found a secondary pattern similar to the regional patterns observed by earlier studies, with thinner crust beneath the Benue Trough relative to the Adamawa Plateau, but considerable variation was found within each region. Within the Benue Trough, the CVL, and the Adamawa Plateau T_e was low. Within the Benue Trough, a spatial change was observed, with T_e transitioning from 16 km in the south to 23 km in the north. T_e for the CVL was estimated to be 18 +2/-4 km, and a similar value of 14–16 km was estimated for the remainder of the Adamawa Plateau. Notably, T_e values in these regions are lower than values typically found in rifted or volcanically active areas in Africa (26–35 km; Betchtel et al., 1987; Ebinger et al., 1989), suggesting the presence of an unusually weak lithosphere in these regions. The CVL and the Benue Trough, however, are separated by an area with high T_e, up to 34 +4/−8 km, suggesting that a block of strong lithosphere separates the two features. The Congo

Craton is marked by high values of T_e, varying between 30 and 40 km, and reflecting the existence of strong, cratonic lithosphere. Poudjom Djomani et al. (1995) conclude that there is a consistent relationship between low values of T_e and regions of volcanic activity and rifting. They suggest that low values of T_e for the CVL are probably due to volcanism and thermal alteration, while low T_e values for the Benue Trough are likely due to weakening of the lower crust through extension and shearing (Poudjom Djomani et al., 1995).

Poudjom Djomani et al. (1997) built an updated 2D model of lithospheric densities along a north-south profile through the eastern portion of the CVL using the combined gravity model of Poudjom Djomani et al. (1995). This profile shows the same long-wavelength positive and negative Bouguer anomalies beneath the Benue Trough and the Adamawa Plateau, respectively, that were observed by Okereke (1988), but also resolves a small 80 km wide positive anomaly superimposed on the Adamawa negative anomaly. The broad positive anomaly beneath the Benue Trough results from a gradual thinning of the crust from 33 km at its edge to 22 km at its center. The superposition of the narrow positive anomaly on the broad negative anomaly of the Adamawa Plateau is interpreted as a thinned 23 km thick crust beneath the CASZ, underlain by a thinned lithosphere ranging from 120 to 80 km thick. This is a notable difference from the prior studies of crustal structure from Bouguer gravity anomalies and seismic refraction, which found no evidence of crustal thinning beneath the Adamawa Plateau (Stuart et al., 1985; Okereke, 1988). The authors note that while their models show similar degrees of crustal thinning beneath the CVL and the Benue Trough, other characteristics of these regions are distinct. The Benue Trough is characterized by a positive Bouguer anomaly, low topography, and no lithospheric thinning, while the Adamawa Plateau is characterized by a small positive anomaly within a broader negative Bouguer anomaly, high topography, and a thinned lithosphere. These findings support a conclusion similar to that of Poudjom Djomani et al. (1995), that the Benue Trough formed through passive extensional rifting from far-field forces, while the CVL formed through active upwelling from the mantle, which has been influenced by the weakened crust of the CASZ (Poudjom Djomani et al., 1997).

Studies of the Oceanic Sector

During the 1990s, several key studies were conducted to characterize the deep crustal and lithospheric structure of the offshore portions of the CVL. Earlier seismic reflection studies conducted in the Gulf of Guinea focused on sedimentary layers, with limited resolution of crystalline basement rocks (e.g., Pautot et al., 1973; Emery et al., 1975; Grunau et al., 1975; Lehner and de Ruiter, 1977). Meyers and Rosendahl (1991) used long-offset seismic reflection to image both sedimentary layers and deep crustal structure between the oceanic sector of the CVL and the Gulf of Guinea, revealing that the CVL sits on arched oceanic crust, with an estimated maximum uplift of 3 km. The crustal arch is asymmetrical with a steeper limb on the southern side and may represent an extension of the uplift associated with the Adamawa Plateau (Meyers and Rosendahl, 1991). Regional stratigraphy showed that uplift began during the Miocene and was synchronous along-strike. This apparent lack of age progression in uplift, together with lack of age progression in volcanism suggests that the oceanic CVL was not formed by a traditional mantle plume. Meyers and Rosendahl (1991) note the spatial correlation between the oceanic arch and the CASZ and suggest that the previously existing structures formed by the CASZ may have influenced the surficial expression of a broad asthenospheric upwelling. These pre-existing structures may have led to the asymmetry of the arch and permitted the flow of magma through fracture zones, forming the regularly spaced volcanos that comprise the oceanic CVL (Meyers and Rosendahl, 1991).

A later study used a combination of gravity and 2D seismic reflection surveys along-strike and sub-perpendicular to the oceanic crustal arch of the CVL and lent further insights into the structure and geologic history of the oceanic CVL (Meyers et al., 1998). Although Moho reflections directly beneath the axis were not imaged, Moho reflections shallowed towards the axis of the arch, suggesting that the crust likely maintains a constant thickness across the arch. Normal faulting of the Precambrian crystalline basement and sedimentary layers were observed near the axis of the arch, but the uplift of the arch was primarily accommodated by bending of the lithosphere, rather than by large amounts of slip on these faults or accumulation on surface materials (Meyers et al., 1998). The study finds distinct differences between the crustal structure of the CVL and that of traditional mantle plume traces in the ocean. Most notably, the CVL crustal arch is built primarily of sediments, with less than 2 km of mixed igneous and syn-volcanic sedimentary layers capping 4–5 km of sediments (Meyers et al., 1998). This pattern is in stark contrast to the crustal structure of the Hawaiian hot spot, which consists primarily of thick deposits of volcanic material on top of oceanic crust and sediments of typical thickness, forming large shield volcanos (e.g., Watts et al., 1985). The authors note similarities in orientation for other volcanic island chains in the southeast Atlantic, which also show evidence of crustal uplift and limited evidence for age progression. These observations lead to one hypothesized mechanism for the formation of the CVL, shear induced convective rolls, which is described in detail in **Section 5** (Meyers et al., 1998).

Seismicity

The CVL and surrounding regions show limited levels of seismicity compared with other tectonically or volcanically active regions, but small earthquakes have long been felt and reported during eruptive episodes (Fairhead, 1985; Ambraseys and Adams, 1986), and a limited number of regional stations were used to record seismic activity around the CVL by the 1960s (Tabod et al., 1992). To better characterize seismicity in the region, the first seismometer was installed in Cameroon in 1982 and detected increased seismic activity during an eruption at Mt. Cameroon later that year (Fairhead, 1985). Following the fatal emission of concentrated CO_2 in 1984 due to the overturning of the deep volcanic lake, Lake Monoun, additional seismic monitoring stations were installed in Cameroon and were operating during a second fatal emission

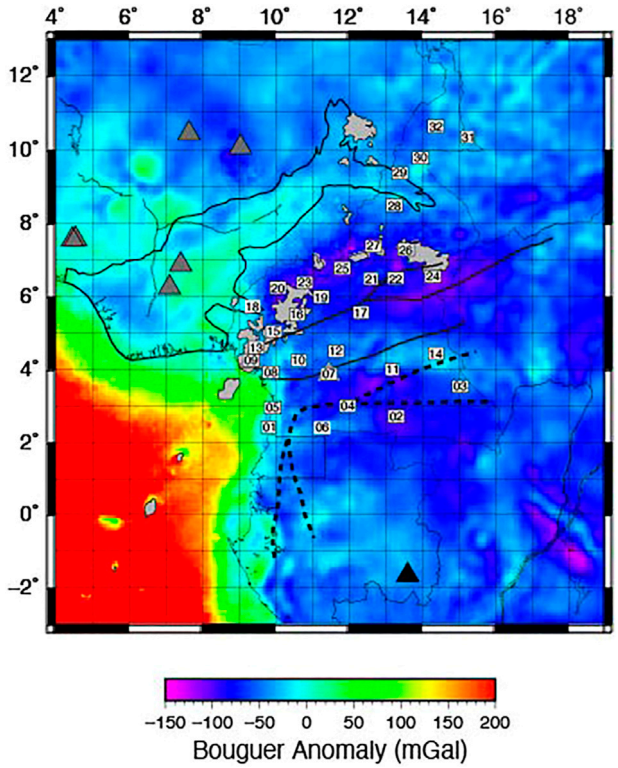

FIGURE 4 | Location of permanent (black triangle = GSN station, Albuquerque Seismological Laboratory/USGS, 1988; dark gray triangles = AfricaArray stations, Penn State University, 2004) and temporary seismic stations (white rectangles = CBSE, Wiens and Nyblade, 2005), superimposed on the bouguer anomaly from the COCE and EGM2008 combined model (GECO; Gilardoni and ReguzzoniSampietro, 2016). Numerical labels indicated station number for the CBSE. Light gray regions indicate volcanic centers, and bold lines show the borders of key regional features (see **Figure 1**).

TABLE 1 | Crustal thickness estimates from seismic and gravity studies beneath stations of the CBSE. Tokam = Tokam et al., 2010; Gallacher = Gallacher and Bastow, 2012; Ngalamo = Goussi Ngalamo et al., 2018; Ghomsi = Kemgang Ghomsi et al., 2020.

	Station #	Crustal thickness (km)			
		Tokam	Gallacher	Ngalamo	Ghomsi
Adamawa Plateau	21	35.50	34.10	34.00	39.31
	22	35.50	35.80	33.00	35.27
	24	35.50	38.20	35.00	38.93
	25	38.00	38.20	39.00	34.12
	26	33.00	34.90	37.00	37.80
	27	35.50	39.00	34.00	37.43
	AVERAGE	35.50	36.70	35.33	37.14
Coastal Plain	01	28.00	37.60	42.00	27.02
	05	28.00	37.40	43.00	28.40
	AVERAGE	28.00	37.50	42.50	27.71
Congo Craton	02	43.00	44.60	43.00	43.21
	04	45.00	47.50	39.00	35.34
	06	45.00	41.80	42.00	30.51
	07	43.00	41.80	37.00	36.47
	11	48.00	43.30	44.00	40.34
	14	-	-	42.00	-
	AVERAGE	44.80	43.80	41.17	37.17
Northern CVL	28	30.50	-	38.00	38.44
	29	25.50	25.30	26.00	32.10
	30	28.00	26.50	29.00	34.38
	31	30.50	-	35.00	31.30
	32	33.00	33.30	34.00	32.80
	AVERAGE	29.50	28.37	32.40	33.80
Oubangides	03	43.00	44.60	41.00	39.96
	08	-	-	38.00	-
	10	38.00	35.80	37.00	37.42
	12	38.00	37.80	37.00	34.33
	17	35.50	37.80	37.00	36.41
	AVERAGE	38.63	39.00	38.00	37.03
Southern CVL	09	-	-	30.00	34.24
	13	28.00	36.50	44.00	32.28
	15	33.00	-	40.00	34.99
	16	35.50	34.10	40.00	40.30
	18	30.50	-	39.00	36.15
	19	35.50	-	38.00	31.53
	20	33.00	33.70	36.00	37.75
	23	40.50	38.30	37.00	40.02
	AVERAGE	33.71	35.65	38.00	35.91

of CO_2 from the overturning of Lake Nyos (Ambeh et al., 1989; Ambeh and Fairhead, 1991). No seismic activity was observed during or prior to the overturning of Lake Nyos, suggesting the seismic shaking did not contribute to this fatal event (Tabod et al., 1992).

Tabod et al. (1992) compared temporal-spatial patterns in seismicity in and around the CVL from 1982 to 1990. Seismic activity in this region was primarily associated with Mt. Cameroon, which experienced small magnitude earthquakes, with the largest magnitude during the study time period reaching m_b = 4.8. Earthquakes occurred, on average, twice a day near Mt. Cameroon, but typically clustered in earthquake swarms lasting several months. Earthquakes along the northern CVL are more limited. Through the duration of the study, only 200 earthquakes were detected in the northern region, of which only 57 could be located with the seismic networks available at that time (Tabod et al., 1992). These infrequent northern earthquakes, however, included the largest earthquakes recorded during the experiment (m_b 4.1 and 4.8; Tabod et al., 1992). Tabod et al. (1992) concluded that seismicity associated with the CVL consists of frequent lower magnitude earthquakes near the active Mt. Cameroon, often occurring in swarms, and infrequent higher magnitude earthquakes occurring in the northeastern CVL, possibly associated with the CASZ.

20TH CENTURY GEOPHYSICAL STUDIES (2000–2021)

Recent geophysical studies have focused on the continental portion of the CVL, yielding enhanced views of subsurface structure beneath and near the CVL (e.g., Tokam et al., 2010; Reusch et al., 2010; Reusch et al., 2011; Gallacher and Bastow, 2012; Adams et al., 2015; Goussi Ngalamo et al., 2018; Ojo et al., 2019; Kemgang Ghomsi et al., 2020 and others). These studies were enabled by renewed data collection efforts, including the

Cameroon Broadband Seismic Experiment (CBSE) lasting from 2005 to 2008 (Wiens and Nyblade, 2005), installation of several permanent seismic stations in and around Cameroon (Penn State University, 2004), and detailed satellite measurements of gravity including the Challenging Minisatellite Payload (CHAMP; Reigber et al., 2002), Gravity Recovery and Climate Experiment (GRACE; Tapley et al., 2004) and Gravity Field and Steady-State Ocean Circulation Explorer (GOCE; Floberghagen et al., 2011) datasets (**Figure 4**). These higher resolution datasets combined with new modeling techniques led to more detailed models of the lithosphere and the extension of models deeper into the upper mantle beneath the continental portion of the CVL.

Crustal Thickness

Numerous recent studies have estimated crustal thickness and crustal structure using a wide variety of techniques (**Table 1**). Using a joint inversion of receiver functions and Rayleigh wave group velocities, Tokam et al. (2010) found that crustal thicknesses beneath the southern and central CVL and the Oubanguides Belt along its southern border are similar (35–39 km), while thicker crust (43–48 km) underlies the northern edge of the Congo Craton and thinner crust (26–31 km) is found beneath rifted regions along the coastal plain and the Garoua rift to the north. These estimates of crustal thickness from receiver functions are broadly similar to those from early 1D velocity models (Stuart et al., 1985) and from gravity studies (e.g., Fairhead and Okereke, 1987; Okereke, 1988), but provide greater spatial coverage and detail. The thick crust beneath the Congo Craton likely represents a crustal suture formed during the amalgamation of Gondwana, while thin crust beneath the Garoua rift and the coastal plains are attributed to the rifting of the Benue trough and the formation of the Atlantic ocean, respectively (Tokam et al., 2010).

Gallacher and Bastow (2012) used teleseismic receiver functions and H-κ analysis to estimate the crustal thickness and velocity structure beneath the CVL. Their patterns in crustal thickness closely follow those indicated by previous studies, with thick crust beneath stations in the Congo Craton, thin crust beneath stations in the Garoua Rift, and moderate crustal thickness beneath the CVL and the Obanguides Belt. Reported crustal thicknesses beneath the stations near the coastal plains is nearly 10 km thicker than those found by previous studies (e.g., Tadjou et al., 2009; Tokam et al., 2010), but this is likely due to biases induced by the predominance of raypaths traveling through the Congo Craton to the east (Gallacher and Bastow, 2012).

Crustal thickness has also been estimated using modeling of World Gravity Map data (WGM 2012; Goussi Ngalamo et al., 2018) and joint inversion of the Experimental Gravity Field Model (XGM 2016) with topographic and seismic data (Kemgang Ghomsi et al., 2020). Fundamental patterns in crustal thickness estimates from both gravity-based models are similar to those from seismic imaging, exhibiting thicker crust beneath the Congo Craton and thinner crust, with limited variability in thickness, beneath the southern CVL, the Oubangides Belt, and the Adamawa Plateau (Goussi Ngalamo et al., 2018; Kemgang Ghomsi et al., 2020). Numerical averages of crustal thickness within each region, however, show a more complex story and differ from seismic estimates in several ways (see **Table 1** for a comparison). Beneath the northern CVL and the Adamawa Plateau, and the Oubangides Belt, crustal thickness estimates are consistent for all studies (**Table 1**). For the southern CVL, crustal thickness estimates are similar in most studies, with only gravity estimates by Goussi Ngalamo et al. (2018) showing a slight difference averaging 4.5 km. Crustal thickness estimates for the Congo Craton are thinner in both gravity studies than estimates in seismic models. Beneath the coastal plain, Goussi Ngalamo et al. (2018) report crustal thicknesses that are similar to those for Congo Craton, which are greater than those reported for coastal stations by either seismic studies. Kemgang Ghomsi et al. (2020), however, find evidence for thinned crust beneath the coastal plains, consistent with the findings of Tokam et al. (2010), but smaller than estimates from Gallacher and Bastow (2012) or Goussi Ngalamo et al. (2018). Differences between crustal thickness estimates from seismic and gravity modeling may reflect a complex and laterally varying structure, resulting in heterogeneous density structures of the crust.

Crustal Structure

Average crustal velocities for the Congo Craton are consistent across multiple studies and methodologies, ranging from 3.84 to 3.9 km/s, comparable to other global cratonic regions (Tokam et al., 2010; Guidarelli and Aoudia, 2016; Ojo et al., 2018; Ojo et al., 2019). The lower crust is characterized by a thick layer with higher velocities greater than 4.0 km/s (Tokam et al., 2010; Ojo et al., 2019). Tokam et al. (2010) interpret this high velocity layer as a region of mafic intrusions into the lower crust, however evidence of low Vp/Vs ratios throughout the crust alternatively suggests a felsic-to-intermediate crustal composition. Low Vp/Vs ratios (1.76 - Gallacher and Bastow, 2012; 1.73 - Ojo et al., 2019) are consistent with other global cratons exhibiting a Tonalite-Trondhjemite-Granodiorite composition (Thompson et al., 2010; Ojo et al., 2019). Furthermore, Ojo et al. (2019) find that Vp/Vs ratios are lower in the middle to lower crust than in the upper crust, suggesting a notable lack of mafic material in the lower crust of the Congo Craton.

Both the southern and northern CVL are characterized by a uniform average crustal shear wave velocity between 3.6–3.8 km/s (Tokam et al., 2010; Guidarelli and Aoudia, 2016; Ojo et al., 2018; Ojo et al., 2019) and by low Vp/Vs ratios (Gallacher and Bastow, 2012; Ojo et al., 2019), which together suggest a lack of large-scale mafic intrusions into the lower crust of the CVL or the surrounding Adamawa Plateau. This is a notable difference from the rifted Benue Trough to the north, where gravimetric models indicate the presence of a mafic lower crust (Eyike and Ebbing, 2015). Low Vp/Vs ratios beneath the CVL also suggest that the volcanic line lacks large qualities of crustal melt at present or within the past 1MY (Gallacher and Bastow, 2012; Ojo et al., 2019). Rifts and hot spots from localities around the globe typically display both high elevations supported by the accumulation of mafic lower crust and melt within the crust, reflected in high seismic velocities, gravity, and Vp/Vs ratios (e.g.,

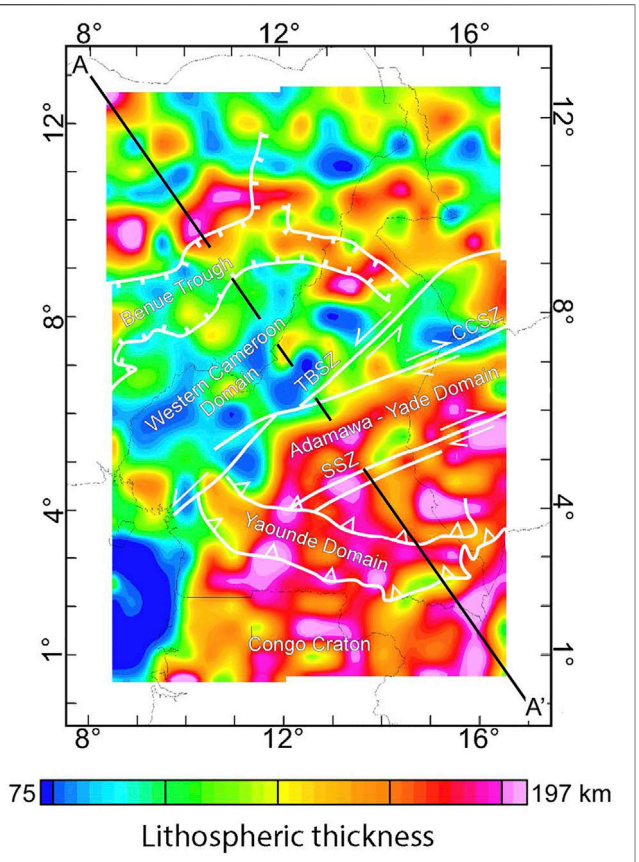

FIGURE 5 | Lithospheric thickness from radially averaged power spectral modeling of WGM2012 Bouguer gravity anomalies (Bonvalot et al., 2012). Reproduced with permission from Goussi Ngalamo et al. (2018). Components of the CASZ are labeled TBSQ = Tchollire-Banyo shear zone, CCSZ—Central Cameroon Shear Zone system, and SSZ = Sanaga Shear Zone.

Ebinger et al., 2017). The lack of these properties in the CVL provides support for the hypothesis that the uplift of the CVL and the surrounding Adamawa Plateau is due to thermal anomalies in the upper mantle (e.g., Fairhead and Okereke 1987), which is further supported by geophysical imaging of the upper mantle (see **Section 4.3**; Gallacher and Bastow, 2012).

Although average crustal structure is broadly consistent along the northern and southern CVL, a few localized deviations are observed. Shear wave velocities beneath several stations within the southern CVL show a thin fast velocity zone at the base of the crust, which is lacking or very thin beneath stations in the northern CVL (Tokam et al., 2010). A similar difference in the northern and southern CVL is observed in average crustal density, with higher density rocks in the southern CVL and the neighboring Oubangides Belt and lower density rocks in the northern CVL, possibly due to the prevalence of granitoid intrusions in that region (Kemgang Ghomsi et al., 2020). Isolated fast velocity layers are also found in the upper crust beneath many stations across Cameroon using joint inversion of receiver functions and surface wave velocities (Tokam et al., 2010). Similarly, ambient noise tomography shows a region of fast velocities in the upper to mid-crust around 5°N and 10.5°E (Guidarelli and Aoudia, 2016). These isolated fast velocity layers and bodies may reflect mafic intrusions into the shallow crust associated with CVL volcanism (Tokam et al., 2010; Guidarelli and Aoudia, 2016). Finally, the regions immediately surrounding Mt. Cameroon exhibit pronounced low surface wave velocities, which likely reflect ongoing magmatic processes at depth, as suggested by high rates of seismicity restricted to this region (Tabod et al., 1992; De Plaen et al., 2014; Guidarelli and Aoudia, 2016).

Lithospheric and Mantle Structure

Lithospheric thickness and structure vary dramatically across the areas surrounding the CVL. The Congo Craton is characterized by a thick lithosphere with high seismic velocities. Spectral analysis of Bouguer anomalies indicate a lithospheric thickness of 150–200 km for the Congo Craton and the Oubangides Belt, with a thinner lithosphere beneath the CVL, ranging from 113 to 162 km (**Figure 5**; Goussi Ngalamo et al., 2018). Shear wave velocities derived from regional Rayleigh wave tomography yield a similar estimate for lithospheric thickness beneath the Congo Craton and the Oubangides Belt of 175–200 km (Adams et al., 2015). Beneath the CVL, however, shear wave velocities in this model are greatly reduced at depths greater than 50 km in the southern CVL and 75 km in the northern CVL, indicating either a thermally eroded or thinned and altered lithosphere for the CVL (Adams et al., 2015). Analysis of continental scale shear wave velocity models also suggests greatly reduced lithospheric thicknesses of 72–133 km beneath the CVL (Sebai et al., 2006; Fishwick, 2010). These differences between gravity and seismic based lithospheric thicknesses are a reflection of the different physical properties measured by the methods. It is possible that these differences may reflect substantial variations in sublithospheric structure not included in gravity modeling (seismic evidence suggests substantial sublithospheric heterogeneity within the region, see below), or alternatively the velocity reduction at 50–75 km in seismic models may indicate thermal alteration but not erosion of the lithosphere at greater depths. All models, however, note significantly thinner lithosphere beneath the CVL when compared to the Congo Craton and Oubangides Belt to the south.

Low seismic velocities beneath the CVL continue deeper into the upper mantle. Teleseismic body wave tomography reveals a vertical, tabular low velocity zone directly beneath the CVL extending to at least 300 km, in which P-wave velocities are reduced -1-2% and S-wave velocities are reduced -2-3% compared to the regional average, with maximum velocity reduction at 200 km (**Figure 6A**; Reusch et al., 2010). The Congo Craton has fast velocities (>+2% Reusch et al., 2010). Shear wave velocities derived from Rayleigh wave tomography show a very similar pattern, with a tabular-shaped region in which velocities are reduced up to -5.5% beneath the CVL and positive velocity anomaly of up to 5% beneath the Congo Craton, when compared to the mobile belts in the region (**Figure 6B**; Adams et al., 2015). Adams et al. (2015) observe maximum velocity reduction at depths of 70–120 km, slightly shallower than the depth of maximum velocity reduction found by body wave tomography, which may be exhibit small amounts of

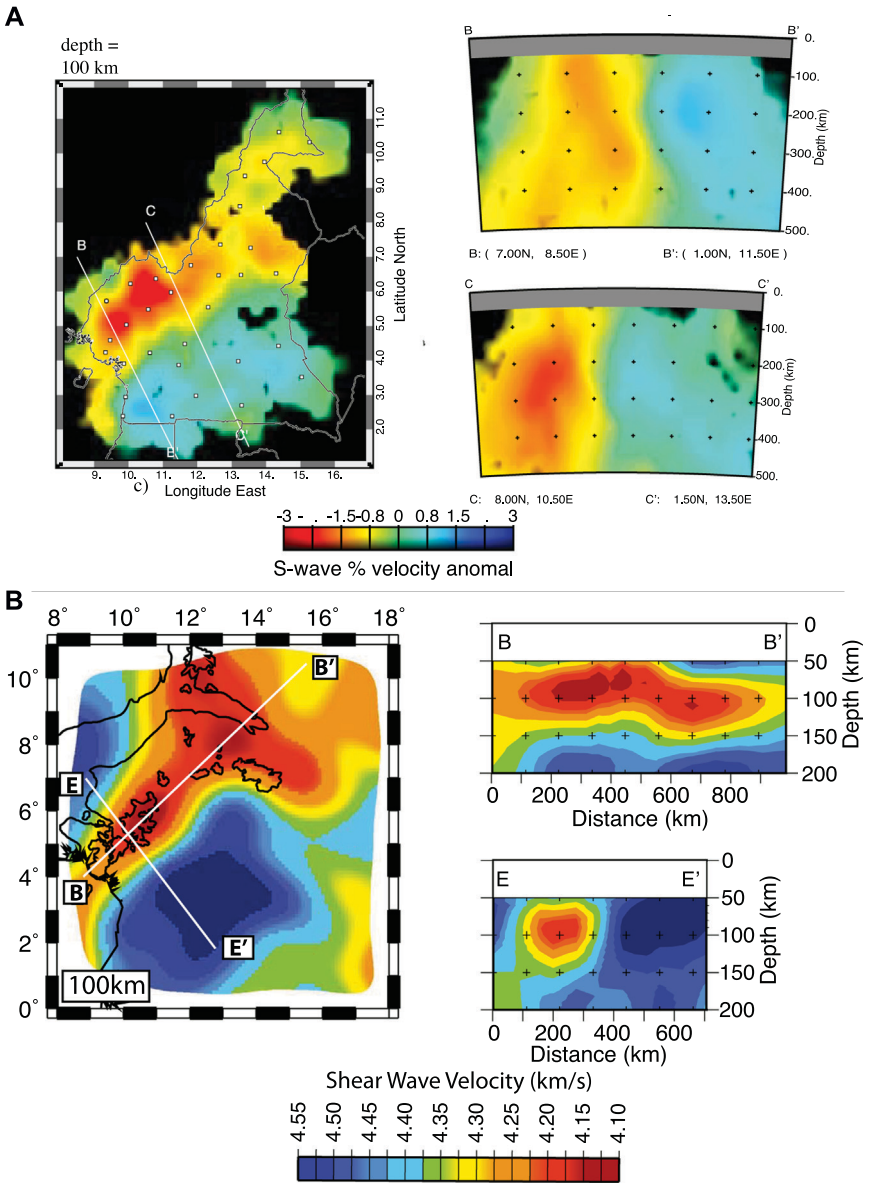

FIGURE 6 | Tomographic models. **(A)** A 100 km depth slice and selected cross-sections from an S-wave body wave tomography model (adapted with permission from Reusch et al., 2010). **(B)** A 100 km depth slice and selected cross-sections from an S-wave model derived from Rayleigh wave tomography (adapted with permission from Adams et al., 2015).

vertical smearing from the vertically oriented body waves (Reusch et al., 2010). Both of these tomography models that extend to sublithospheric depths find a sharp vertical transition between the CVL and the Congo Craton, extending into the asthenosphere to at least 200 km (Adams et al., 2015) or 300 km (Reusch et al., 2010). Neither study finds evidence of reduced mantle velocities beneath other regions of the Adamawa Plateau as suggested by earlier smaller-scale tomographic models (Dorbath et al., 1986). These regional findings by Reusch et al. (2010) and Adams et al. (2015) are consistent with larger-scale, lower resolution continental tomography studies, which also suggest that low velocities below the CVL are isolated to the shallow mantle (e.g., Sebai et al., 2006; Fishwick, 2010; Emry et al., 2019).

Receiver function analysis of the mantle transition zone indicates a transition zone with a typical thickness, suggesting that the low velocity anomaly beneath the CVL does not extend to the transition zone or into the lower mantle (Reusch et al., 2011). Some studies note the presence of low velocities in the deep mantle (>1,000 km) beneath the CVL (e.g., French and Romanowicz, 2015). Tomographic evidence restricting low velocities to depths less than 300 km (e.g., Reusch et al., 2010; Adams et al., 2015) together with a thermally unperturbed mantle transition zone (Reusch et al., 2011), however, show that this lower mantle feature is not directly connected to the CVL. It may instead be associated with the broader African Superplume.

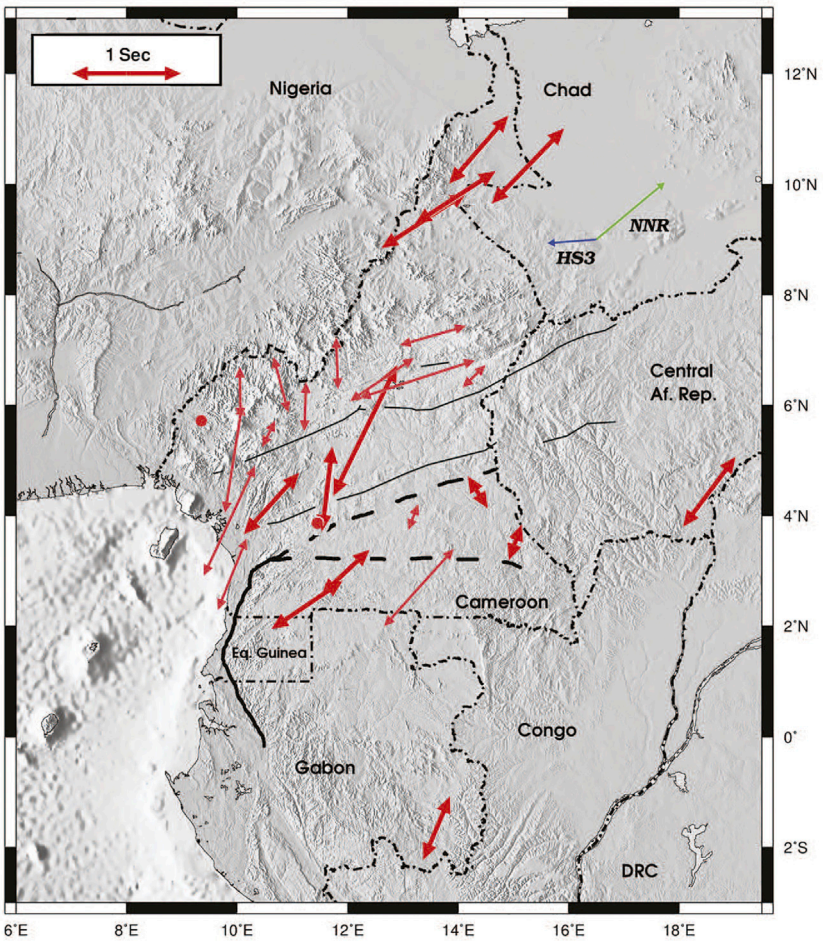

FIGURE 7 | Fast directions and delay times from shear wave splitting for stations from the CBSE. Reproduced with permission from Koch et al. (2012).

Insights From Anisotropy

Several studies have used shear wave splitting to investigate azimuthal anisotropy beneath the CVL and surrounding regions. While the observed patterns in these studies are broadly similar, the interpretations and implications for the formation of the CVL differ tremendously. Koch et al. (2012) found a NE-SW fast direction with split times of approximately 1s beneath the Congo Craton and the northern CVL, and a N-S fast direction with split times of approximately 0.7s beneath the southern CVL. The CVL and the Congo Craton are separated by a region with variable orientations and low delay times (**Figure 7**). Elsheikh et al. (2014) found generally similar spatial patterns in the orientation fast propagation. Notable deviations in fast direction were noted at only five stations, but differences at these stations did not affect the overall spatial patterns. Elsheikh et al. (2014) did, however, observe greater delay times that averaged twice those observed by Koch et al. (2012). De Plaen et al. (2014) find orientations of fast directions and delay times for stations in the Congo Craton and the northern CVL that are similar to those found by Koch et al. (2012). Beneath the southern CVL and the Oubangides Belt, they find only null solutions. De Plaen et al. (2014) note, however, that these null stations typically have very low delay times (<0.53 s) in Koch et al. (2012). Thus, all studies observe fast directions oriented NE-SW in the Congo Craton and the northern CVL, with a great range of delay times. There is a lack of consensus for the patterns of anisotropy beneath the southern CVL, as observations differ significantly with one study finding N-S orientations with large delay times (Elsheikh et al., 2014), one study finding N-S orientations with small delay times (Koch et al., 2012), and another study finding null results within the southern CVL (De Plaen et al., 2014).

Interpretations of the implications for the formation of the CVL are similarly variable including 1) northeastern sublithospheric flow resulting in thinned lithosphere (Elsheikh et al., 2014), 2) small-scale asthenospheric convection (Koch et al., 2012), and 3) strong vertical flow from asthenospheric convection or a plume resulting in high radial anisotropy and low azimuthal anisotropy (De Plaen et al., 2014).

An anisotropic velocity model from ambient noise and earthquake Rayleigh waves indicates complex multi-layered anisotropy in this region (Ojo et al., 2018). This tomographic

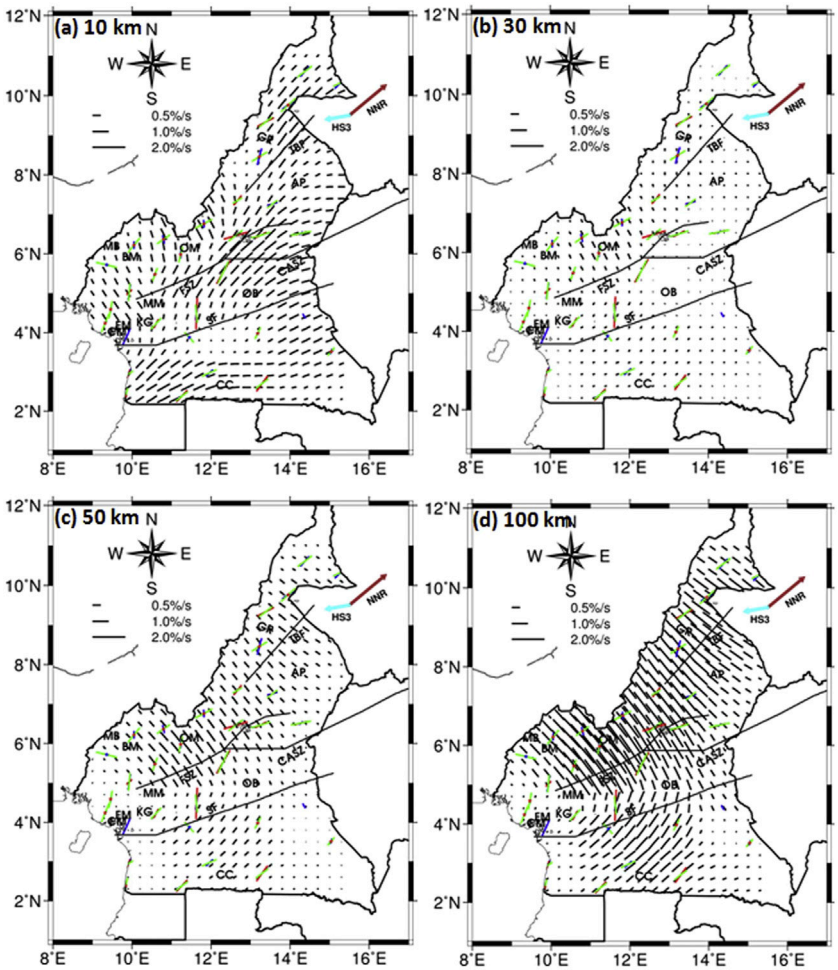

FIGURE 8 | Anisotropic fast directions within Cameroon. Black lines show azimuthal anisotropy from Rayleigh wave tomography at 10 km **(A)**, 30 km **(B)**, 50 km **(C)**, and 100 km **(D)**. Blue, red, and green lines show anisotropy from shear wave splitting from (Koch et al., 2012), De Plaen et al. (2014), and Elsheikh et al. (2014) respesectively. Reproduced with permission from Ojo et al. (2018).

model of anisotropy shows 1) strong NE-SW fast direction at a depth of 10 km through most of the study region, with weak N-S or NW-SE anisotropy in the southern CVL, 2) a primarily isotropic lower crust, and 3) strong anisotropy in the lithospheric mantle, oriented NW-SE in the northern and central CVL, NE-SW in the Congo Craton, and null to NW-SE orientations in the southern CVL near Mt. Cameroon (**Figure 8**). This observed change in fast directions with depth is supported by average regional anisotropy from Rayleigh wave tomography, which shows a change in average fast direction from NNE-SSW at periods less than 50 s to NW-SE at periods greater than 110 s for the CVL (Adams et al., 2015). These finding are consistent with those from shear wave splitting by Koch et al. (2012) at crustal depths but are inconsistent at lithospheric mantle depths for the northern and central CVL. This suggests that measured anisotropy beneath the Congo Craton and the southern CVL may derive exclusively from the lithosphere, but that there must be a significant contribution from the lower lithosphere or asthenosphere in the central and northern CVL, which is not constrained by the model of Ojo et al. (2018).

Plate Motions

Some studies have suggested that the CVL may be undergoing extension, forming a rift similar to the now dormant Benue Trough or the early stages of rifting in the East African Rift System (e.g., Fairhead and Okereke, 1987; Okereke, 1988). Geodetic studies are limited in this region, but analysis of GPS and Doppler orbitography and radiopositioning integrated by satellite (DORIS) across the African continent finds that plate motions near the CVL are best fit by a single Nubian plate, without evidence for a microplate boundary at or near the CVL (Saria et al., 2013).

Seismicity

Recent studies of seismicity near the CVL built upon studies from the 1980s and 1990s (**Section 3.3**), using the expanded CBSE seismic network and more numerous permanent stations deployed in the early 2000s. Analysis of five months of continuous seismic data from the CBSE, found 203 earthquakes with magnitudes between 1.4—4 M_L (De Plaen

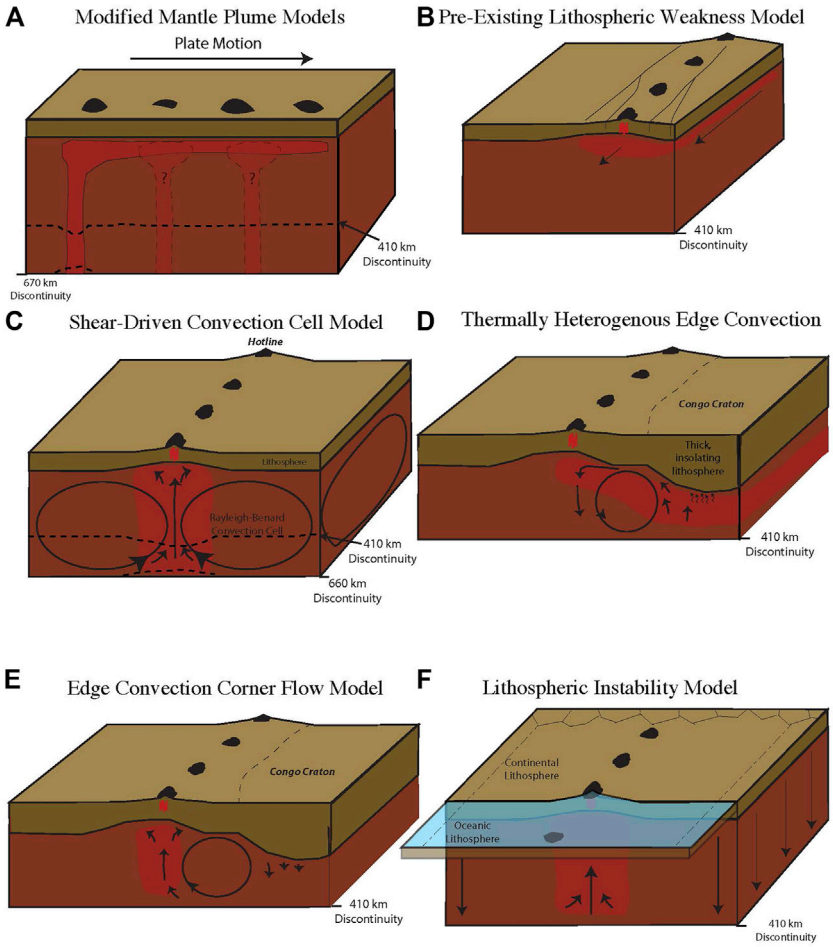

FIGURE 9 | Geodynamic models for the formation of the CVL, included modifications of mantle plume trace **(A)**, diversion of material along the CASZ **(B)**, convection driven by shear along the base of the transition zone **(C)**, convection driven by thermal contrasts combined with contrasts in lithospheric thickness **(D)**, convection driven by contrasts in lithospheric thickness in a thermally homogenous mantle **(E)**, and lithospheric instabilities driven by the juxtaposition of oceanic and continental lithosphere **(F)** after Adams et al. (2015).

et al., 2014). Of these events, three-quarters were centered around Mount Cameroon, and the rest lay in a roughly linear swath between Bioko and Mount Cameroon, aligned with the strike of the CVL. Away from this region, which has exhibited recent volcanic activity, the rest of the CVL and surrounding region appears largely aseismic. The spatial distribution of earthquakes during this study are consistent with seismicity studies from the previous decade, although a lower average rate of seismicity was recorded during this more recent study, despite the broader seismic array available for detection (Tabod et al., 1992; De Plaen et al., 2014). The majority of earthquakes nucleated in the upper 15 km and exhibited low frequency contents and emergent arrivals, suggesting they derived from magma or volatile migration in the upper crust. A small number of earthquakes were detected along the eastern and southern flanks of the Mount Cameroon at depths of 25–30 km, suggesting magmatic activity at these depths associated with the active volcano (De Plaen et al., 2014). The association of seismicity in the CVL with regions of active volcanism differs from earthquake distributions in continental rifts (e.g., Mulibo and Nyblade, 2013; Ebinger et al., 2017), and suggests that the CVL is not undergoing rifting as suggested by some early studies (e.g., Okereke, 1988).

GEODYNAMIC MODELS FOR FORMATION

Numerous models have been proposed for the formation of the CVL. Some models have proven untenable as new or improved evidence arises. For example, early speculation that the CVL might represent a simple Wilson-Morgan style mantle plume (e.g., Morgan, 1983; Van Houten, 1983; Lee et al., 1994; Burke, 2001) have generally been dismissed due to the lack of age progression along the line. Similarly, speculation that the CVL represents an early stage rift (e.g., Fairhead and Okereke, 1987; Okereke, 1988) now appears unlikely due to the lack of discernable extension from GPS measurements (e.g., Saria et al., 2013). Other models remain in circulation, and typically

invoke modifications to a simple plume model, mantle convection, and/or interaction between the asthenospheric and lithospheric mantle. The most prominent of these hypotheses for formation, their implications for crust and mantle structure, and evaluations based on existing geophysical data are discussed below and illustrated in **Figure 9**.

Modified Mantle Plume Origin

Lack of age progression along the CVL makes the formation of this feature by a Wilson-Morgan plume unlikely, however, other characteristics of the CVL show similarities to mantle plumes and many studies continue to attribute the formation of the CVL to a mantle plume. For example, Steinberger (2000) suggests that a non-stationary plume moving in the same direction as plate motion might lead to a lack of age progression along the CVL and other African volcanic centers, while also acknowledging the possible role of other mechanisms. A recent whole-mantle velocity model categorizes the CVL as a "clearly resolved" plume based on shear wave velocity perturbations in the lower most mantle (French and Romanowicz, 2014; 2015). Still other studies suggest that the CVL might be formed by multiple mantle plumes, with volcanic material from one plume overprinting material from other plumes and concealing any age progression (Ngako et al., 2006; Njome and Wit, 2014), similar to the multiple-plume hypothesis that has been suggested for volcanic lines in the south Pacific (**Figure 9A**; see **Section 2.3**). These adapted plume models, however, are inconsistent with seismic and gravimetric data beneath the continental section of the CVL, which indicate a linear-shaped upper mantle anomaly, restricted to the upper 200–300 km (e.g., Okereke, 1988; Poudjom Djomani et al., 1995; Reusch et al., 2010; Adams et al., 2015; Goussi Ngalamo et al., 2018), with no evidence for perturbation of the mantle transition zone beneath the continental portion of the CVL (Reusch et al., 2011). Anisotropic measurements are complex and vary both laterally and with depth (e.g., Ojo et al., 2018), and do not display spatially consistent patterns expected for mantle plumes. Current geophysical models cannot, however, constrain the presence or absence of a mantle plume or plumes for the offshore portions of the CVL.

Other studies suggest that the CVL is formed though the complex interactions between a mantle plume and lithospheric structures associated with the CASZ. The most prominent of these models is the suggested diversion of material produced by the Afar plume in eastern Africa through the CASZ to the CVL (**Figure 9B**; Ebinger and Sleep, 1998). This model, however, should create a progression in the age of initiation of volcanism, although not for cessation of volcanism, with the oldest volcanic centers in the east and younger volcanic centers in the west, which is not observed along the continental sector (see **Figure 2** and references therein). The linear nature of the mantle low velocity zone tomographically imaged beneath the CVL (e.g., Reusch et al., 2010; Adams et al., 2015) is consistent with the sublithospheric thermal anomaly expected for this model. The inconsistency of azimuthal anisotropy (e.g., Koch et al., 2012; De Plaen et al., 2014; Elsheikh et al., 2014) and the change to a NW-SE fast orientation at mantle depths (Adams et al., 2015; Ojo et al., 2018), however, are inconsistent with the along-strike sublithospheric flow described in these models.

Upwelling From Shear Driven Convection Cells

Meyers et al. (1998) noted that many volcanic centers on the African Plate, including the CVL, can be projected into parallel lines stretching across the plate, evenly spaced approximately 1800 km apart and oriented in a northeast-southwest direction. Volcanic centers within these projected lines share characteristics with the CVL, including a lack of age progression and an apparent uplift along-axis. These observations led Meyers et al. (1998) to hypothesize that these "hot-lines" observed across the African Plate, including the CVL, were formed by intermediate-scale convective rolls within the upper mantle. This proposed mechanism builds upon prior studies that predict cylindrical Rayleigh-Baynard convection cells with alternating convective directions may be generated by shearing at the base of the lithosphere in the presence of fast plate motion (Richter, 1973; Richter and Parsons, 1975). Because the motion of the Nubian Plate is slow, however, such convective rolls generated by shear at the base of the lithosphere would require more than 200 Ma to form (Meyers et al., 1998). Meyers et al. (1998) propose a variation on this mechanism, in which convective rolls are instead produced by shear along the base of the mantle transition zone, with limited shear at the base of the lithosphere. In this proposed model, the CVL and other hot-lines are formed at the convergence of two convective rolls (**Figure 9C**). Due to the alternation of convective directions, the two rolls would converge to form a large linear mantle upwelling, and a corresponding thermal anomaly, extending from the base of the transition zone to the base of the lithosphere (Meyers et al., 1998).

The tabular nature of the mantle low velocity zone imaged beneath the CVL (e.g., Reusch et al., 2010; Adams et al., 2015) and the thinning of the lithosphere (e.g., Okereke, 1988; Poudjom Djomani et al., 1995; Fishwick, 2010; Adams et al., 2015; Goussi Ngalamo et al., 2018) are consistent with the linear upwelling predicted by this model. The isolation of low velocities to the upper 200–300 km imaged by seismic tomography (Reusch et al., 2010; Adams et al., 2015) and the lack of perturbation to the mantle transition zone in receiver function studies (Reusch et al., 2011), however, suggest that no thermal anomaly extends into the transition zone as predicted by this model.

Edge Convection Driven by the Congo Craton

An alternate group of models attribute the formation of the CVL to edge convection along contrasts in lithospheric thicknesses. In one such model, King and Anderson (1995) suggest that a thick and insulating lithosphere, such as that which may exist beneath the Congo Craton, may lead to asthenospheric heating in the sub-lithospheric mantle. This thermally buoyant material would then flow laterally at shallow depths to the adjacent thinner lithosphere beneath the CASZ. This higher temperature mantle material would then lead to the formation of volcanism near the juxtaposition of thick and thin lithosphere, similar to the location of the CVL just north of the edge of the Congo

Craton. This thermally heterogeneous mechanism would produce a thermal anomaly dipping from shallow depths beneath the CVL to deeper depths at the base of the lithosphere beneath the Congo Craton to the south (**Figure 9D**).

The thermal convection model of King and Anderson (1995) was later expanded to consider the role of initial mantle temperatures on edge convection based on contrasts in lithospheric thickness (King and Anderson, 1998). King and Anderson (1998) demonstrated that the style and orientation of convection induced at an abrupt change in lithospheric thickness is strongly dependent on the thermal conditions of the sub-lithospheric mantle. If the sub-lithospheric mantle is warmed due to insulation by the thick cratonic lithosphere, convection flows laterally at shallow depths from beneath the thicker lithosphere to the thinner lithosphere, where non-erupted material cools and sinks, as described by King and Anderson (1995). If the sub-lithospheric mantle is not thermally perturbed beneath the thicker lithosphere, convection is induced in the opposite direction, with a downwelling beneath the thicker lithosphere and a corresponding upwelling beneath the thinner lithosphere (King and Anderson, 1998). Based on this model, if the asthenosphere beneath the Congo Craton has not been heated by thermal insulation, a corner flow edge should form, with a downwelling directly beneath the Congo Craton and a corresponding upwelling beneath the CVL, forming vertically-oriented thermal anomaly directly beneath the CVL (**Figure 9E**; King and Ritsema, 2000).

Both edge convection models would produce a shallow thermal anomaly, restricted to the upper few hundred kilometers of the upper mantle, which is consistent with findings from seismic tomography (Reusch et al., 2010; Adams et al., 2015) and transition zone receiver functions (Reusch et al., 2011). The shapes and lateral extent of the anomalies, however, would differ between the two models. In the thermally heterogeneous model of King and Anderson (1995), the thermal anomaly would be tilted, at shallow mantle depths beneath the CVL and reaching deeper depth beneath the Congo Craton (**Figure 9D**). This is not supported by tomographic evidence, which indicates a vertically oriented low velocity zone directly beneath the CVL (Reusch et al., 2010; Adams et al., 2015) nor by gravimetric models, which indicate that density anomalies are restricted beneath the CVL (e.g., Okereke, 1988; Poudjom Djomani et al., 1995; Goussi Ngalamo et al., 2018). Existing geophysical evidence instead supports the vertically oriented thermal upwelling predicted by the corner flow model (**Figure 9E**; King and Anderson, 1998; King and Ritsema, 2000).

Continental and Oceanic Lithosphere Instability

The impacts of lithospheric contrasts on convection were re-examined using analog models in a study by Milelli et al. (2012). Milelli et al. (2012) build upon prior experimental results demonstrating that a system that is heated from below and cooled from above, such as the heating of the lithosphere from the mantle and cooling at the surface boundary layer, forms a system of hexagonal convection cells (Jaupart et al., 2007). Milelli et al. (2012) modified this system to include a step-change in the thickness of the lid being heated from below and cooled from above, with a thick lid surrounded by a thinner lid, mimicking the contrast between oceanic and continental lithosphere. In this scenario, a complex system of convective cells was produced. Within the thick-lidded interior representing continental lithosphere, hexagonal convection cells formed as in prior studies (Jaupart et al., 2007). Near the change in lid thickness representing the continental margin, however, these hexagonal cells transition to linear convection cells, radiating outwards from the thicker simulated continental interior (Milelli et al., 2012). This model predicts that the contrast between thick continental lithosphere and thin oceanic lithosphere should produce upwellings and downwelling at and perpendicular to continental margins. Milelli et al. (2012) describe this system as a lithospheric instability, and propose the CVL as an example of this complex convective system, with the interior "Y" shape of the CVL indicating the boundary between hexagonal and linear convective cells (**Figure 9F**). This model would produce a vertically oriented thermal anomaly, restricted to the upper mantle, where upwellings occur, similar in shape to that predicted by the corner flow model (King and Anderson, 1998) but driven by the contrast in the lithospheric thickness beneath the continental and oceanic lithosphere instead of by the contrast between the lithosphere of the Congo Craton and the Oubangides Belt (Milelli et al., 2012). This model is equally supported by geophysical imaging of a shallow, vertically oriented, tabular upper mantle anomaly described in **section 5.3** (Okereke, 1988; Poudjom Djomani et al., 1995; Reusch et al., 2010; Reusch et al., 2011; Adams et al., 2015; Goussi Ngalamo et al., 2018).

DISCUSSION AND KEY QUESTIONS

Geophysical studies have given numerous insights into the crust and upper mantle structures of the CVL and surrounding areas during the past 40 years. Studies have revealed regional patterns in crustal thickness and structure, with thinned crust beneath the Benue Trough, thicker crust beneath the Congo Craton, and a generally consistent crustal thickness for the CVL and the surrounding Oubangides Belt, with some disagreement between studies on the relative thickness of stations along the coastal plain.

The crust of the Congo Craton displays velocities and Vp/Vs ratios characteristic of other Archean Cratons (Tokam et al., 2010; Guidarelli and Aoudia, 2016; Ojo et al., 2018; Ojo et al., 2019), although the potential existence of mafic intrusions into the lower-most crust is debated (Tokam et al., 2010; Gallacher and Bastow, 2012; Ojo et al., 2019). The northern and southern CVL are both characterized by low crustal bulk velocities and low Vp/Vs ratios, suggesting a lack of large-scale mafic intrusions into the crust (Tokam et al., 2010; Gallacher and Bastow, 2012; Guidarelli and Aoudia, 2016; Ojo et al., 2018; Ojo et al., 2019), while a decrease in crustal density is observed for the northern CVL, likely reflecting the increasing prevalence of granitoid

intrusions in that region. Localized high velocity layers and pockets across the CVL and the Adamawa Plateau may reflect small-scale intrusion of mafic materials into those regions (Tokam et al., 2010; Guidarelli and Aoudia, 2016). Offshore, crustal thickness remains constant, with uplift accommodated by lithospheric bending (Meyers et al., 1998).

Unlike the consistent crustal thickness observed beneath the Adamawa Plateau, both gravimetric (Goussi Ngalamo et al., 2018) and seismic studies (Fishwick, 2010; Adams et al., 2015) indicate substantially thinner lithosphere beneath the CVL, although the degree of thinning differs between methods. Thinned lithosphere beneath the continental CVL is underlain by a vertical, linear anomaly of low velocities, which extends to 200–300 km (Reusch et al., 2010; Adams et al., 2015) with no evidence for anomalies in the transition zone (Reusch et al., 2011). Studies of shear wave splitting indicate NE-SW fast directions beneath the northern CVL and N-S or null measurements beneath the southern CVL, with the relative contributions of crustal, lithospheric mantle, and sublithospheric mantle varying across the region (Koch et al., 2012; De Plaen et al., 2014; Elsheikh et al., 2014; Ojo et al., 2018). The causes of azimuthal anisotropy remain debated between studies. Neither deep lithospheric and sublithospheric mantle structure nor anisotropy is modeled for the oceanic portion of the CVL.

The CVL has displayed only low levels of small magnitude (<4.8 M_b) seismicity since monitoring began using local stations in the 1980s. Seismicity is primarily concentrated around the active volcanic center of Mt. Cameroon, where lower magnitude earthquakes primarily nucleate in the upper 15 km, appearing in swarms likely associated with migration of volatiles and magma (Tabod et al., 1992; De Plaen et al., 2014). Smaller numbers of earthquakes are detected in the northern portion of the CVL, but these infrequent earthquakes have a slightly higher average magnitude (Tabod et al., 1992).

The observed geophysical characteristics allow evaluation of the numerous geodynamic models that have been proposed for the formation of the CVL. The linear nature of the upper mantle low velocity anomalies, their restriction to the uppermost mantle, and the orientations of seismic anisotropy suggest a lack of mantle plume activity at the CVL, at least beneath the continental sector. Similarly, the restriction of the low velocities to the upper most mantle indicate that the CVL is not formed by shear at the base of the transition zone, and the vertical nature of the low velocity anomaly is inconsistent with edge convection driven by thermal heterogeneities in the sublithospheric mantle. The rapid spatial variation in azimuthal anisotropy (e.g., Koch et al., 2012; De Plaen et al., 2014; Elsheikh et al., 2014) and the NW-SE fast orientation at mantle depths (Adams et al., 2015; Ojo et al., 2018) are inconsistent with models of channelized sublithospheric flow. Current evidence suggests that the most likely models for the formation of the continental CVL are corner flow edge convection (King and Anderson, 1998) or lithospheric instability (Milleli et al., 2012).

The mantle structure of the oceanic CVL, however, remains largely unexplored except through continental or global scale models. Some large scale models suggest that first order structures observed onshore may continue offshore (e.g., Sebai et al., 2006; Fishwick, 2010), while others suggest a change in structure offshore (e.g., Hansen et al., 2012), but resolution is limited in these large-scale models. The detailed structure of the offshore CVL remains an important unresolved question, with key implications for the mechanisms forming and influencing the CVL. For example, no evidence is seen onshore for age progression from a mantle plume, yet there is some evidence for age progression offshore (see **Figure 2**). The lack of geophysical models for the mantle offshore means that it is possible that the offshore portion of the CVL could be formed or influenced by a mantle plume, giving the overall CVL a complex geodynamic history, in which the oceanic and continental sectors are formed by separate mechanisms. This possibility is supported by studies that resolve low velocities in this region within the deep mantle (e.g., French and Romanowicz, 2015). On the other hand, the two primary candidate models for the formation of the continental CVL, corner flow edge convection (King and Anderson, 1998) and lithospheric instability (Milelli et al., 2012), would likely produce different offshore structures in the mantle, with convective flow following the curve of the Congo Craton at depth for the corner flow model or continuing to extend perpendicular to the coast for the lithospheric instability model.

Additional first-order questions also remain for the onshore CVL. No study, for example, has found a causal link between the Benue Trough and the CVL that is consistent with both geological and geophysical evidence. Thus, uncertainty remains about the cause of the characteristic Y-shape shared by the neighboring features. Similarly, although the proximity and similar azimuth of the CVL and the CASZ are compelling, no consensus has been reached regarding the degree of influence held by the preexisting CASZ on the formation of the CVL.

Finally, while the geophysical studies of the past 40 years have yielded tremendous insights into the crust structure and onshore mantle structure of the CVL, these finding have in turn led to new questions. For example, several differences are observed in crustal and upper mantle velocity structure and density for the southern and northern continental CVL, yet these regions share a similar eruptive history and are presumed to have formed from the same mechanism. Therefore, what are the causes for these differences in structure? Measurements of anisotropy are often inconsistent between studies and variable at short distances within studies, and there is evidence for significant changes in anisotropic structure with depth. So, what are the causes of anisotropy in this region and why does it vary rapidly in three dimension? And, two of the leading candidate models for the formation of the continental CVL are dependent on the rapidly changing lithospheric thickness at the boundaries of the Congo Craton and the continental margin. How might these two significant boundaries in the lithosphere interact to influence the CVL?

As a volcanic line without age progression, the CVL challenges many of our current understandings of mantle dynamics and drivers of volcanic activity. Recent studies have yielded insights into the seismicity and crustal and upper mantle structure of the CVL, suggesting that the CVL does not form primarily from a mantle plume or from multiple mantle plumes as suggested for non-age progressive volcanic lines in the south Pacific. Instead,

the CVL is likely influenced by the interaction between mantle convection and the unique preexisting lithospheric structures in the region. Questions still remain about the relative contributions of different preexisting structure and about the nature of the offshore portions of the CVL. Further study focusing on the oceanic sector and finer scale structures of the continental sector are needed to address key outstanding questions.

AUTHOR CONTRIBUTIONS

AA performed the analysis, wrote the text, and designed all original figures.

FUNDING

This work is funded by Colgate University.

ACKNOWLEDGMENTS

The author has benefited from numerous conversations about the CVL and forms of mantle convection, and particularly wishes to thank Douglas Wiens, Andrew Nyblade, Karen Harpp, Samantha Hansen, and Angela Reusch for their insights. The author thanks the reviewers for their comments, which improved the manuscript.

REFERENCES

Adams, A. N., Wiens, D. A., Nyblade, A. A., Euler, G. G., Shore, P. J., and Tibi, R. (2015). Lithospheric Instability and the Source of the Cameroon Volcanic Line: Evidence from Rayleigh Wave Phase Velocity Tomography. *J. Geophys. Res. Solid Earth* 120, 1708–1727. doi:10.1002/2014jb011580

Aka, F. T., Nagao, K., Kusakabe, M., and Nfomou, N. (2009). Cosmogenic Helium and Neon in Mantle Xenoliths from the Cameroon Volcanic Line (West Africa): Preliminary Observations. *J. Afr. Earth Sci.* 55, 175–184. doi:10.1016/j.jafrearsci.2009.04.002

Albuquerque Seismological Laboratory (ASL)/USGS (1988). *Data from Global Seismograph Network - IRIS/USGS*. International Federation of Digital Seismograph Networks. doi:10.7914/SN/IU

Ambeh, W. B., Fairhead, J. D., Francis, D. J., Nnange, J. M., and Djallo, S. (1989). Seismicity of the Mount Cameroon Region, West Africa. *J. Afr. Earth Sci.* 7, 107. doi:10.1016/0899-5362(89)90002-x

Ambeh, W. B., and Fairhead, J. D. (1991). Regular, Deep Seismicity beneath Mt Cameroon Volcano: Lack of Evidence for Tidal Triggering. *Geophys. J. Int.* 106, 287–291. doi:10.1111/j.1365-246x.1991.tb04618.x

Ambraseys, N. N., and Adams, R. D. (1986). Seismicity of West Africa. *Ann. Geophys. Series B Terr. Planet. Phys.* 4 (6), 679–702.

Asaah, A. N. E., Yokoyama, T., Aka, F. T., Usui, T., Wirmvem, M. J., Tchamabe, B. C., et al. (2015). A Comparative Review of Petrogenetic Processes beneath the Cameroon Volcanic Line: Geochemical Constraints. *Geosci. Front.* 6, 557–570. doi:10.1016/j.gsf.2014.04.012

Betchtel, T. D. D., Forsyth, D. W., and Swain, C. (1987). Mechanism of Isostatic Compensation in the Vicinity of the East African Rift, Kenya. *Geophys. J. R. Astron. Soc.* 90, 445–465. doi:10.1111/j.1365-246x.1987.tb00734.x

Bonatti, E., and Harrison, C. G. A. (1976). Hot Lines in the Earth's Mantle. *Nature* 263, 402–404. doi:10.1038/263402a0

Bonneville, A., Dosso, L., and Hildenbrand, A. (2006). Temporal Evolution and Geochemical Variability of the South Pacific Superplume Activity. *Earth Planet. Sci. Lett.* 244 (1–2), 251–269. doi:10.1016/j.epsl.2005.12.037

Bonvalot, S., Balmino, G., Briais, A., Kuhn, M., Peyrefitte, A., Vales, N., et al. (2012). in *World Gravity Map. Commission for the Geological Map of the World* (Paris: BGI-CGMW-CNES-IRD).

Boukeke, D. B. (1994). *Structures crustales d'Afrique Centrale déduites des anomalies gravimétriques et magnétiques: le domaine précambrien de la République Centrafricaine et du Sud Cameroun*. Thèse Univ. Paris XI, Orsay, 263 pg.

Browne, S. E., and Fairhead, J. D. (1983). Gravity Study of the Central African Rift System: A Model of Continental Disruption: 1. The Ngaoundere and ABU Gabra Rifts. *Tectonophysics* 94 (1-4), 187–203. doi:10.1016/b978-0-444-42198-2.50018-3

Burke, K. C., Dessauvagie, T. F. J., and Whiteman, A. J. (1970). "Geological History of the Benue Valley and Adjacent Areas," in *African Geology*. Editors T. F. J. Dessauvagie and A. J. Whiteman (Nigeria: University of Ibadan), 187–205.

Burke, K., Dessauvagie, T. F. J., and Whiteman, A. J. (1971). Opening of the Gulf of Guinea and Geological History of the Benue Depression and Niger delta. *Nat. Phys. Sci.* 233 (38), 51–55. doi:10.1038/physci233051a0

Burke, K. (2001). Origin of the Cameroon Line of Volcano-Capped Swells. *J. Geology.* 109 (3), 349–362. doi:10.1086/319977

Burke, K., and Torsvik, T. H. (2004). Derivation of Large Igneous Provinces of the Past 200 Million Years from Long-Term Heterogeneities in the Deep Mantle. *Earth Planet. Sci. Lett.* 227, 531–538. doi:10.1016/j.epsl.2004.09.015

Campbell, I. H. (2007). Testing the Plume Theory. *Chem. Geology.* 241, 153–176. doi:10.1016/j.chemgeo.2007.01.024

Carter, J. D., Barber, W., and Tait, E. A. (1963). The Geology of Parts of Adamawa, Bauchi and Bornu Provinces in Northeastern Nigeria. *Bull. Geol. Surv. Nigeria* 30, 109.

Castaing, C., Feybesse, J. L., Thiéblemont, D., Triboulet, C., and Chèvremont, P. (1994). Palaeogeographical Reconstructions of the Pan-African/Brasiliano Orogen: Closure of an Oceanic Domain or Intracontinental Convergence between Major Blocks. *Precambrian Res.* 69, 327–344. doi:10.1016/0301-9268(94)90095-7

Chadwick, J., Perfit, M. R., Ridley, I. A., Jonasson, I. R., Kamenov, G. D., Chadwick, W. W., et al. (2005). Magmatic effects of the Cobb hot spot on the Juan de Fuca Ridge. *J. Geophys. Res.* 110, 1–16. doi:10.1029/2003jb002767

Collignon, F. (1968). *Gravimetrie de Reconnaissance*. Paris: Cameroun ORSTOM.

Cornen, G., and Maury, R. C. (1980). Petrology of the Volcanic Island of Annobon, Gulf of Guinea. *Mar. Geology.* 36 (3-4), 253–267. doi:10.1016/0025-3227(80)90090-0

Davies, J. H., and Bunge, H.-P. (2006). Are Splash Plumes the Origin of Minor Hotspots. *Geol* 34, 349–352. doi:10.1130/g22193.1

Déruelle, B., Moreau, C., Nkoumbou, C., Kambou, R., Lissom, J., Njonfang, E., et al. (1991). "The Cameroon Line: A Review," in *Magmatism in Extensional Tectonic Structural Settings*. Editors A. B. Kampunzu and R. T. Lubala (Berlin: Springer), 274–327.

Déruelle, B., Ngounouno, I., and Demaiffe, D. (2007). The 'Cameroon Hot Line' (CHL): A Unique Example of Active Alkaline Intraplate Structure in Both Oceanic and continental Lithospheres. *Comptes Rendus Geosci.* 339, 589–600. doi:10.1016/j.crte.2007.07.007

De Plaen, R. S. M., Bastow, I. D., Chambers, E. L., Keir, D., Gallacher, R. J., and Keane, J. (2014). The Development of Magmatism along the Cameroon Volcanic Line: Evidence from Seismicity and Seismic Anisotropy. *J. Geophys. Res. Solid Earth* 119, 4233–4252. doi:10.1002/2013JB010583

Dorbath, C., Dorbath, L., Fairhead, J. D., and Stuart, G. W. (1986). A Teleseismic Delay Time Study across the Central African Shear Zone in the Adamawa Region of Cameroon, West Africa. *Geophys. J. Int.* 86 (3), 751–766. doi:10.1111/j.1365-246x.1986.tb00658.x

Duncan, R. A., and Richards, M. A. (1991). Hotspots, Mantle Plumes, Flood Basalts, and True Polar Wander. *Rev. Geophys.* 29, 31–50. doi:10.1029/90rg02372

Dunlap, H. M. (1983). *Strontium Isotope Geochemistry and Potassium-Argon Studies on Volcanic Rocks from the Cameroon Line*. West Africa, Ph.D thesis. Edinburgh, U.K: University of Edinburgh.

Dunlop, H. M., and Fitter, J. G. (1979). A K-Ar and Sr-Isotopic Study of the Volcanic Rocks of the Island of Principe, West Africa ? Evidence for Mantle Heterogeneity beneath the Gulf of Guinea. *Contrib. Mineral. Petrol.* 71 (2), 125–131. doi:10.1007/BF00375428

Ebinger, C. J., Bechtel, T. D., Forsyth, D. W., and Bowin, C. O. (1989). Effective Elastic Plate Thickness beneath the East African and Afar Plateaus and

Dynamic Compensation of the Uplifts. *J. Geophys. Res.* 94, 2883–2901. doi:10.1029/jb094ib03p02883

Ebinger, C. J., Keir, D., Bastow, I. D., Whaler, K., Hammond, J. O. S., Ayele, A., et al. (2017). Crustal Structure of Active Deformation Zones in Africa: Implications for Global Crustal Processes. *Tectonics* 36, 3298–3332. doi:10.1002/2017tc004526

Ebinger, C. J., and Sleep, N. H. (1998). Cenozoic Magmatism throughout East Africa Resulting from Impact of a Single Plume. *Nature* 395, 788–791. doi:10.1038/27417

Elsheikh, A. A., Gao, S. S., and Liu, K. H. (2014). Formation of the Cameroon Volcanic Line by Lithospheric Basal Erosion: Insight from Mantle Seismic Anisotropy. *J. Afr. Earth Sci.* 100, 96–108. doi:10.1016/j.jafrearsci.2014.06.011

Emery, K. O., Uchupi, E., Phillips, J., Brown, C., and Mascle, J. (1975). Continental Margin off West Africa: Angola to Sierra Leone. *AAPG Bull.* 59, 2209–2265. doi:10.1306/83d92249-16c7-11d7-8645000102c1865d

Emry, E. L., Shen, Y., Nyblade, A. A., Flinders, A., and Bao, X. (2019). Upper Mantle Earth Structure in Africa from Full-Wave Ambient Noise Tomography. *Geochem. Geophys. Geosyst.* 20, 120–147. doi:10.1029/2018GC007804

Epp, D. (1984). Possible Perturbations to Hotspot Traces and Implications for the Origin and Structure of the Line Islands. *J. Geophys. Res.* 89 (273–11), 286. doi:10.1029/jb089ib13p11273

Eyike, A., and Ebbing, J. (2015). Lithospheric Structure of the West and Central African Rift System from Regional Three-Dimensional Gravity Modelling. *South. Afr. J. Geology.* 118, 285–298. doi:10.2113/gssajg.118.3.285

Fairhead, J. D., and Okereke, C. S. (1987). A Regional Gravity Study of the West African Rift System in Nigeria and Cameroon and its Tectonic Interpretation. *Tectonophysics* 143 (1-3), 141–159. doi:10.1016/0040-1951(87)90084-9

Fairhead, J. D. (1985). Preliminary Study of the Seismicity Associated with the Cameroon Volcanic Province during the Volcanic Eruption of Mt. Cameroon in 1982. *J. Afr. Earth Sciencies* 3, 197–301. doi:10.1016/0899-5362(85)90003-x

Farnetani, C. G., and Samuel, H. (2005). Beyond the thermal Plume Paradigm. *Geophys. Res. Lett.* 32, a–n. doi:10.1029/2005GL022360

Fishwick, S. (2010). Surface Wave Tomography: Imaging of the Lithosphere-Asthenosphere Boundary beneath central and Southern Africa. *Lithos* 120, 63–73. doi:10.1016/j.lithos.2010.05.011

Fitton, J. G., and Dunlop, H. M. (1985). The Cameroon Line, West Africa, and its Bearing on the Origin of Oceanic and continental Alkali basalt. *Earth Planet. Sci. Lett.* 72 (1), 23–38. doi:10.1016/0012-821X(85)90114-1

Fitton, J. G., Kilburn, C. R. J., Thirlwall, M. F., and Hughes, D. J. (1983). 1982 Eruption of Mount Cameroon, West Africa. *Nature* 306, 327–332. doi:10.1038/306327a0

Fitton, J. G. (1980). The Benue Trough and cameroon Line - A Migrating Rift System in West Africa. *Earth Planet. Sci. Lett.* 51 (1), 132–138. doi:10.1016/0012-821x(80)90261-7

Fitton, J. G. (1987). The Cameroon Line, West Africa: a Comparison between Oceanic and continental Alkaline Volcanism. *Geol. Soc. Lond. Spec. Publications* 30, 273–291. doi:10.1144/gsl.sp.1987.030.01.13

Floberghagen, R., Fehringer, M., Lamarre, D., Muzi, D., Frommknecht, B., Steiger, C., et al. (2011). Mission Design, Operation and Exploitation of the Gravity Field and Steady-State Ocean Circulation Explorer mission. *J. Geod* 85 (11), 749–758. doi:10.1007/s00190-011-0498-3

French, S. W., and Romanowicz, B. A. (2014). Whole-mantle Radially Anisotropic Shear Velocity Structure from Spectral-Element Waveform Tomography. *Geophys. J. Int.* 199, 1303–1327. doi:10.1093/gji/ggu334

French, S. W., and Romanowicz, B. (2015). Broad Plumes Rooted at the Base of the Earth's Mantle beneath Major Hotspots. *Nature* 525, 95–99. doi:10.1038/nature14876

Gallacher, R. J., and Bastow, I. D. (2012). The Development of Magmatism along the Cameroon Volcanic Line: Evidence from Teleseismic Receiver Functions. *Tectonics* 31, a–n. doi:10.1029/2011TC003028

Gilardoni, M., Reguzzoni, M., and Sampietro, D. (2016). GECO: a Global Gravity Model by Locally Combining GOCE Data and EGM2008. *Stud. Geophys. Geod* 60, 228–247. doi:10.1007/s11200-015-1114-4

Goussi Ngalamo, J. F., Sobh, M., Bisso, D., Abdelsalam, M. G., Atekwana, E., and Ekodeck, G. E. (2018). Lithospheric Structure beneath the Central Africa Orogenic Belt in Cameroon from the Analysis of Satellite Gravity and Passive Seismic Data. *Tectonophysics* 745, 326–337. doi:10.1016/j.tecto.2018.08.015

Grant, N. K., Rex, D. C., and Freeth, S. J. (1972). Potassium-argon Ages and Strontium Isotope Ratio Measurements from Volcanic Rocks in Northeastern Nigeria. *Contr. Mineral. Petrol.* 35 (4), 277–292. doi:10.1007/BF00371310

Gripp, A. E., and Gordon, R. G. (1990). Current Plate Velocities Relative to the Hotspots Incorporating the NUVEL-1 Global Plate Motion Model. *Geophys. Res. Lett.* 17, 1109–1112. doi:10.1029/GL017i008p01109

Grunau, H. R., Lehner, P., Cleintuar, M. R., Allenbach, P., and Bakker, G. (1975). "New Radiometric Ages and Seismic Data from Fuerteventura (Canary Islands)," in *Maio (Caper Verde Islands), and São Tomé (Gulf of Guinea)* (New York: North-Holland), 90–118.

Guidarelli, M., and Aoudia, A. (2016). Ambient Noise Tomography of the Cameroon Volcanic Line and Northern Congo Craton: New Constraints on the Structure of the Lithosphere. *Geophys. J. Int.* 204, 1756–1765. doi:10.1093/gji/ggv561

Hansen, S. E., Nyblade, A. A., and Benoit, M. H. (2012). Mantle Structure beneath Africa and Arabia from Adaptively Parameterized P-Wave Tomography: Implications for the Origin of Cenozoic Afro-Arabian Tectonism. *Earth Planet. Sci. Lett.* 319-320, 23–34. doi:10.1016/j.epsl.2011.12.023

Hedberg, J. D. (1969). *A Geological Analysis of the Cameroon Trend*. Ph.D. thesis. Princeton, New Jersey: Princeton University.

Jaupart, C., Molnar, P., and Cottrell, E. (2007). Instability of a Chemically Dense Layer Heated from below and Overlain by a Deep Less Viscous Fluid. *J. Fluid Mech.* 572, 433–469. doi:10.1017/s0022112006003521

Kagou Dongmo, A., Nkouathio, D., Pouclet, A., Bardintzeff, J.-M., Wandji, P., Nono, A., et al. (2010). The Discovery of Late Quaternary basalt on Mount Bambouto: Implications for Recent Widespread Volcanic Activity in the Southern Cameroon Line. *J. Afr. Earth Sci.* 57, 96–108. doi:10.1016/j.jafrearsci.2009.07.015

Kamgang, P., Njonfang, E., Nono, A., Dedzo, M. G., and Tchoua, F. M. (2010). Petrogenesis of a Silicic Magma System: Geochemical Evidence from Bamenda Mountains, NW Cameroon, Cameroon Volcanic Line. *J. Afr. Earth Sci.* 58, 285–304. doi:10.1016/j.jafrearsci.2010.03.008

Kemgang Ghomsi, F., Severin, N., Mandal, A., Nyam, F. E., Tenzer, R., and Tokam Kamga, A. (2020). Cameroon's Crustal Configuration from Global Gravity and Topographic Models and Seismic Data. *J. Afr. Earth Sci.*, 161. doi:10.1016/j.jafrearsci.2019.103657

King, S. D., and Anderson, D. L. (1995). An Alternative Mechanism of Flood basalt Formation. *Earth Planet. Sci. Lett.* 136, 269–279. doi:10.1016/0012-821x(95)00205-q

King, S. D., and Anderson, D. L. (1998). Edge-driven Convection. *Earth Planet. Sci. Lett.* 160, 289–296. doi:10.1016/s0012-821x(98)00089-2

King, S. D., and Ritsema, J. (2000). African Hot Spot Volcanism: Small-Scale Convection in the Upper Mantle beneath Cratons. *Science* 290 (5494), 1137–1140. doi:10.1126/science.290.5494.1137

Koch, F. W., Wiens, D. A., Nyblade, A. A., Shore, P. J., Tibi, R., Ateba, B., et al. (2012). Upper-mantle Anisotropy beneath the Cameroon Volcanic Line and Congo Craton from Shear Wave Splitting Measurements. *Geophys. J. Int.* 190, 75–86. doi:10.1111/j.1365-246X.2012.05497.x

Koppers, A. A. P., Staudigel, H., Pringle, M. S., and Wijbrans, J. R. (2003). Short-lived and Discontinuous Intraplate Volcanism in the South Pacific: Hot Spots or Extensional Volcanism. *Geochem. Geophys. Geosyst.* 4 (10), 1089. doi:10.1029/2003GC000533

Lee, D.-C., Halliday, A. N., Fitton, J. G., and Poli, G. (1994). Isotopic Variations with Distace and Time in the Volcanic Islands of the Cameroon Line: Evidence for a Mantle Plume Origin. *Earth Planet. Sci. Lett.* 123 (1-3), 119–138. doi:10.1016/0012-821X(94)90262-3

Lehner, P., and de Ruiter, P. A. C. (1977). Structural History of Atlantic Margin of Africa. *AAPG Bull.* 61, 961–981. doi:10.1306/c1ea43b0-16c9-11d7-8645000102c1865d

Maluski, H., Coulon, C., Popoff, M., and Baudin, P. (1995). 40Ar/39Ar Chronology, Petrology and Geodynamic Setting of Mesozoic to Early Cenozoic Magmatism from the Benue Trough, Nigeria. *J. Geol. Soc.* 152, 311–326. doi:10.1144/gsjgs.152.2.0311

Marzoli, A., Renne, P. R., Piccirillo, E. M., Francesca, C., Bellieni, G., Melfi, A. J., et al. (1999). Silicic Magmas from the continental Cameroon Volcanic Line (Oku, Bambouto and Ngaoundere): 40Ar-39Ar Dates, Petrology, Sr-Nd-O Isotopes and Their Petrogenetic Significance. *Contrib. Mineral. Petrol.* 135 (2-3), 133–150. doi:10.1007/s004100050502

Marzoli, A., Piccirillo, E. M., Renne, P. R., Bellieni, G., Iacumin, M., Nyobe, J. B., et al. (2000). The Cameroon Volcanic Line Revisited: Petrogenesis of continental Basaltic Magmas from Lithospheric and Asthenospheric Mantle Sources. *J. Pet.* 41 (1), 87–109. doi:10.1093/petrology/41.1.87

Meyers, J. B., Rosendahl, B. R., Harrison, C. G. A., and Ding, Z.-D. (1998). Deep-imaging Seismic and Gravity Results from the Offshore Cameroon Volcanic Line, and Speculation of African Hotlines. *Tectonophysics* 284, 31–63. doi:10.1016/s0040-1951(97)00173-x

Meyers, J. B., and Rosendahl, B. R. (1991). Seismic Reflection Character of the Cameroon Volcanic Line: Evidence for Uplifted Oceanic Crust. *Geol* 19, 1072–1076. doi:10.1130/0091-7613(1991)019<1072:srcotc>2.3.co;2

Milelli, L., Fourel, L., and Jaupart, C. (2012). A Lithospheric Instability Origin for the Cameroon Volcanic Line. *Earth Planet. Sci. Lett.* 335-336, 80–87. doi:10.1016/j.epsl.2012.04.028

Molnar, P., and Stock, J. (1987). Relative Motions of Hotspots in the Pacific, Atlantic and Indian Oceans since Late Cretaceous Time. *Nature* 327, 587–591. doi:10.1038/327587a0

Morgan, W. J. (1971). Convection Plumes in the Lower Mantle. *Nature* 230, 42–43. doi:10.1038/230042a0

Morgan, W. J. (1972). Plate Motions and Deep Mantle Convection. *Geol. Soc. America Mem. Stud. Earth Space Sci.* 132, 7–22. doi:10.1130/MEM132-p7

Morgan, W. J. (1983). Hotspot Tracks and the Early Rifting of the Atlantic. *Tectonophysics* 94, 123–139. doi:10.1016/0040-1951(83)90013-6

Mulibo, G. D., and Nyblade, A. A. (2013). The P and S Wave Velocity Structure of the Mantle beneath Eastern Africa and the African Superplume Anomaly. *Geochem. Geophys. Geosyst.* 14, 2696–2715. doi:10.1002/ggge.20150

Ngako, V., Njonfang, E., Aka, F. T., Affaton, P., and Nnange, J. M. (2006). The North-South Paleozoic to Quaternary Trend of Alkaline Magmatism from Niger-Nigeria to Cameroon: Complex Interaction between Hotspots and Precambrian Faults. *J. Afr. Earth Sci.* 45 (3), 241–256. doi:10.1016/j.jafrearsci.2006.03.003

Ngounouno, I., Deruelle, B., Demaiffe, D., and Montigny, R. (1997). New Data on the Cenozoic Volcanism of the Garoua valley (Upper Benue Trough, Northern Cameroon). *C. r. Acad. Sci. Ser. Earth Planet. Sci.* 325 (2), 87–94.

Ngounouno, I., Moreau, C., Deruelle, B., Demaiffe, D., and Montigny, R. (2001). Petrologie du complexe alcalin sous-sature de Kokoumi (Cameroun). *Bull. Soc. Geol. Fr.* 172 (6), 675–686. doi:10.2113/172.6.675

Ngounouno, I., Déruelle, B., Demaiffe, D., and Montigny, R. (2003). Les monchiquites de Tchircotché, vallée de la haute Bénoué (Nord du Cameroun). *Comptes Rendus Geosci.* 335 (3), 289–296. doi:10.1016/S1631-0713(03)00047-6

Ngounouno, I., Druelle, B., Montigny, R., and Demaiffe, D. (2005). Petrology and Geochemistry of Monchiquites from Tchircotch (Garoua Rift, north Cameroon, Central Africa). *Mineralogy Pet.* 83 (3-4), 167–190. doi:10.1007/s00710-004-0068-y

Ngounouno, I., Déruelle, B., Montigny, R., and Demaiffe, D. (2006). Les camptonites du mont Cameroun, Cameroun, Afrique. *Comptes Rendus Geosci.* 338 (8), 537–544. doi:10.1016/j.crte.2006.03.015

Njilah, I. K., Ajonina, H. N., Kamgang, K. V., and Tchindjang, M. (2004). K-Ar Ages, Mineralogy, Major and Trace Element Geochemistry of the Tertiary-Quaternary Lavas from the Ndu Volcanic Ridge N.W. Cameroon. *Afr. J. Sci. Technol.* 5 (1), 47–56. doi:10.4314/ajst.v5i1.15318

Njome, M. S., and de Wit, M. J. (2014). The Cameroon Line: Analysis of an Intraplate Magmatic Province Transecting Both Oceanic and continental Lithospheres: Constraints, Controversies and Models. *Earth-Science Rev.* 139, 168–194. doi:10.1016/j.earscirev.2014.09.003

Nzenti, J. P., Barbey, P., Macaudiere, J., and Soba, D. (1988). Origin and Evolution of the Late Precambrian High-Grade Yaounde Gneisses (Cameroon). *Precambrian Res.* 38 (2), 91–109. doi:10.1016/0301-9268(88)90086-1

Nzenti, J. P., Kapajika, B., Wörner, G., and Lubala, T. R. (2006). Synkinematic Emplacement of Granitoids in a Pan-African Shear Zone in Central Cameroon. *J. Afr. Earth Sci.* 45 (1), 74–86. doi:10.1016/j.jafrearsci.2006.01.005

O'Connor, J. M., and Le Roex, A. P. (1992). South Atlantic Hot Spot-Plume Systems: 1. Distribution of Volcanism in Time and Space. *Earth Planet. Sci. Lett.* 113, 343–364. doi:10.1016/0012-821x(92)90138-l

Ojo, A. O., Ni, S., Chen, H., and Xie, J. (2018). Crust-mantle Coupling Mechanism in Cameroon, West Africa, Revealed by 3D S-Wave Velocity and Azimuthal Anisotropy. *Phys. Earth Planet. Interiors* 274, 195–213. doi:10.1016/j.pepi.2017.12.006

Ojo, A. O., Ni, S., Xie, J., and Zhao, L. (2019). Further Constraints on the Shear Wave Velocity Structure of Cameroon from Joint Inversion of Receiver Function, Rayleigh Wave Dispersion and Ellipticity Measurements. *Geophys. J. Int.* 217, 589–619. doi:10.1093/gji/ggz008

Okereke, C. S. (1988). Contrasting Modes of Rifting: The Benue Trough and Cameroon Volcanic Line, West Africa. *Tectonics* 7, 775–784. doi:10.1029/tc007i004p00775

Olade, M. A. (1978). Early Cretaceous basalt Volcanism and Initial continental Rifting in Benue Trough, Nigeria. *Nature* 273, 458–459. doi:10.1038/273458a0

Pautot, G., Renard, V., Daniel, J., and Dupont, J. (1973). Morphology, Limits, Origin, and Age of Salt Layer along South Atlantic Margin. *Am. Assoc. Pet. Geologists Bull.* 57, 1658–1671. doi:10.1306/83d91024-16c7-11d7-8645000102c1865d

Penn State University (2004). *Data from: AfricaArray*. International Federation of Digital Seismograph Networks. doi:10.7914/SN/AF

Poudjom Djomani, Y. H., Nnange, J. M., Diament, M., Ebinger, C. J., and Fairhead, J. D. (1995). Effective Elastic Thickness and Crustal Thickness Variations in West central Africa Inferred from Gravity Data. *J. Geophys. Res.* 100 (B11), 22047–22070. doi:10.1029/95JB01149

Poudjom Djomani, Y. H., Diament, M., and Wilson, M. (1997). Lithospheric Structure across the Adamawa Plateau (Cameroon) from Gravity Studies. *Tectonophysics* 273 (3-4), 317–327. doi:10.1016/s0040-1951(96)00280-6

Reigber, C., Lühr, H., and Schwintzer, P. (2002). CHAMP mission Status. *Adv. Space Res.* 30 (2), 129–134. doi:10.1016/s0273-1177(02)00276-4

Reusch, A. M., Nyblade, A. A., Ateba, B., Wiens, D. A., Shore, P. J., Tabod, C. T., et al. (2010). Upper Mantle Structure beneath Cameroon from Body Wave Tomography and the Origin of the Cameroon Volcanic Line. *Geochem. Geophys. Geosyst.* 11 (10), a–n. doi:10.1029/2010GC003200

Reusch, A. M., Nyblade, A. A., Tibi, R., Wiens, D. A., Shore, P. J., Bekoa, A., et al. (2011). Mantle Transition Zone Thickness beneath Cameroon: Evidence for an Upper Mantle Origin for the Cameroon Volcanic Line. *Geophys. J. Int.* 187, 1146–1150. doi:10.1111/j.1365-246X.2011.05239.x

Richter, F. M. (1973). Convection and the Large-Scale Circulation of the Mantle. *J. Geophys. Res.* 78, 8735–8745. doi:10.1029/jb078i035p08735

Richter, F. M., and Parsons, B. (1975). On the Interaction of Two Scales of Convection in the Mantle. *J. Geophys. Res.* 80, 2529–2541. doi:10.1029/jb080i017p02529

Saria, E., Calais, E., Altamimi, Z., Willis, P., and Farah, H. (2013). A New Velocity Field for Africa from Combined GPS and DORIS Space Geodetic Solutions: Contribution to the Definition of the African Reference Frame (AFREF). *JGR Solid Earth* 118, 1677–1697. doi:10.1002/jgrb.50137

Sebai, A., Stutzmann, E., Montagner, J.-P., Sicilia, D., and Beucler, E. (2006). Anisotropic Structure of the African Upper Mantle from Rayleigh and Love Wave Tomography. *Phys. Earth Planet. Interiors* 155, 48–62. doi:10.1016/j.pepi.2005.09.009

Steinberger, B. (2000). Plumes in a Convecting Mantle: Models and Observations for Individual Hotspots. *J. Geophys. Res.* 105 (B5), 11127–11152. doi:10.1029/1999JB900398

Steinberger, B., Sutherland, R., and O'Connell, R. J. (2004). Prediction of Emperor-Hawaii Seamount Locations from a Revised Model of Global Plate Motion and Mantle Flow. *Nature* 430, 167–173. doi:10.1038/nature02660

Stuart, G. W., Fairhead, J. D., Dorbath, L., and Dorbath, C. (1985). A Seismic Refraction Study of the Crustal Structure Associated with the Adamawa Plateau and Garoua Rift, Cameroon, West Africa. *Geophys. J. Int.* 81, 1–12. doi:10.1111/j.1365-246x.1985.tb01346.x

Tabod, C. T., Fairhead, J. D., Stuart, G. W., Ateba, B., and Ntepe, N. (1992). Seismicity of the Cameroon Volcanic Line, 1982–1990. *Tectonophysics* 212 (3–4), 303–320. doi:10.1016/0040-1951(92)90297-J

Tadjou, J. M., Nouayou, R., Kamguia, J., Kande, H. L., and Manguelle-Dicoum, E. (2009). Gravity Analysis of the Boundary between the Congo Craton and the Pan-African Belt of Cameroon. *Austrian J. Earth Sci.* 102 (1), 71–79.

Tapley, B. D., Bettadpur, S., Watkins, M., and Reigber, C. (2004). The Gravity Recovery and Climate experiment: mission Overview and Early Results. *Geophys. Res. Lett.* 31, L09607. doi:10.1029/2004GL01977910.1029/2004gl019920

Thompson, D. A., Bastow, I. D., Helffrich, G., Kendall, J.-M., Wookey, J., Snyder, D. B., et al. (2010). Precambrian Crustal Evolution: Seismic Constraints from the Canadian Shield. *Earth Planet. Sci. Lett.* 297, 655–666. doi:10.1016/j.epsl.2010.07.021

Tokam, A.-P. K., Tabod, C. T., Nyblade, A. A., Julià, J., Wiens, D. A., and Pasyanos, M. E. (2010). Structure of the Crust beneath Cameroon, West Africa, from the Joint Inversion of Rayleigh Wave Group Velocities and Receiver Functions. *Geophys. J. Int.* 183, 1061–1076. doi:10.1111/j.1365-246X.2010.04776.x

Toteu, S. F., Penaye, J., and Djomani, Y. P. (2004). Geodynamic Evolution of the Pan-African belt in central Africa with Special Reference to Cameroon. *Can. J. Earth Sci.* 41 (1), 73–85. doi:10.1139/e03-079

Uzuakpunwa, A. B. (1974). The Abakaliki Pyroclastics - Eastern Nigeria: New Age and Tectonic Implications. *Geol. Mag.* 111, 65–69. doi:10.1017/s0016756800000467

Van Houten, F. B. (1983). Sirte Basin, north-central Libya: Cretaceous Rifting above a Fixed Mantle Hotspot. *Geol* 11, 115–118. doi:10.1130/0091-7613(1983)11<115:sbnlcr>2.0.co;2

Vicat, J., Leger, J., Nsifa, E., Piguet, P., Nzenti, J., Tchameni, R., et al. (1996). "Distinction within the Congo Craton in South-West Cameroon of Two Doleritic Episodes Initiating the Eburnean (Paleoproterozoic) and Pan-African (Neoproterozoic) Orogenic Cycles,". *Comptes Rendus de l'Academie de Sciences – Serie IIa: Sciences de la Terre et des Planetes*, 323, 575–582.

Watts, A. B., ten Brink, U. S., Buhl, P., and Brocher, T. M. (1985). A Multichannel Seismic Study of Lithospheric Flexure across the Hawaiian-Emperor Seamount Chain. *Nature* 315, 105–111. doi:10.1038/315105a0

White, W. M. (2010). Oceanic Island Basalts and Mantle Plumes: The Geochemical Perspective. *Annu. Rev. Earth Planet. Sci.* 38, 133–160. doi:10.1146/annurev-earth-040809-152450

Wiens, D., and Nyblade, A. (2005). *Data from: Broadband Seismic Investigation of the Cameroon Volcanic Line*. International Federation of Digital Seismograph Networks. doi:10.7914/SN/XB_2005

Wilson, J. T. (1963). A Possible Origin of the Hawaiian Islands. *Can. J. Phys.* 41, 863–870. doi:10.1139/p63-094

Conflict of Interest: The author declares that the research was conducted in the absence of any commercial or financial relationships that could be construed as a potential conflict of interest.

frontiers in Earth Science

ORIGINAL RESEARCH
published: 17 March 2022
doi: 10.3389/feart.2022.773783

Modelling S-Wave Velocity Structure Beneath the Central Main Ethiopian Rift Using Receiver Functions

Birhanu A. Kibret[1]*, *Atalay Ayele*[1] and *Derek Keir*[2,3]

[1]Institute of Geophysics, Space Science and Astronomy, Addis Ababa University, Addis Ababa, Ethiopia, [2]School of Ocean and Earth Science, University of Southampton, Southampton, United Kingdom, [3]Dipartimento di Scienze Della Terra, Università Degli Studi di Firenze, Florence, Italy

We applied the receiver function (RF) technique on high-quality teleseismic earthquake data recorded by the RiftVolc broadband network from February 2016 to October 2017. We calculate RFs at 17 stations, which are inverted to estimate Vs, and Vp/Vs structure beneath the Central Main Ethiopian Rift and the Eastern plateau. The observed slow S-wave velocity (Vs) in the uppermost crust (<6 km depth) is interpreted as sedimentary and/or volcanic layers. Beneath the rift valley, crustal Vs is heterogeneous both laterally and with depth. In particular, slow Vs (~2–3 km/s) is localised beneath volcanic centres in the upper-mid crust but ubiquitously slow in the lower crust with Vs as low as ~3.5 km/s common. The slow lower crust is associated with high Vp/Vs ratios of ~1.9–2.0. The Vs and Vp are consistent with the observed seismic velocities, and interpreted the presence of the small fraction (<5%) of partial melt from previous seismic imaging studies of the lower crust. In addition, the velocity contrast is small between the lower crust and upper mantle. The results suggest that partial melt in the lower crust beneath magmatically active rifts might be more widespread than previously thought and an important component of the magma plumbing system. In contrast, Vs is far more homogeneous and faster beneath the Eastern Plateau, with a distinct velocity contrast between the crust and upper mantle suggesting less crustal deformation than what is observed beneath the central rift zone.

Keywords: Vp/Vs, magma plumbing, volcanic centres, crustal structure, partial melt, moho depth, intrusion, Main Ethiopian rift

OPEN ACCESS

Edited by:
Tolulope Morayo Olugboji, University of Rochester, United States

Reviewed by:
Tim Greenfield, University of Cambridge, United Kingdom
Mohammad Youssof, University of Copenhagen, Denmark

***Correspondence:**
Birhanu A. Kibret
birhanu.abera@aau.edu.et

Specialty section:
This article was submitted to Solid Earth Geophysics, a section of the journal Frontiers in Earth Science

Received: *10 September 2021*
Accepted: *24 January 2022*
Published: *17 March 2022*

Citation:
Kibret BA, Ayele A and Keir D (2022) Modelling S-Wave Velocity Structure Beneath the Central Main Ethiopian Rift Using Receiver Functions. Front. Earth Sci. 10:773783. doi: 10.3389/feart.2022.773783

INTRODUCTION

The Main Ethiopian Rift (MER) is an active continental rift where magmatic intrusion is thought to play a key role by accommodating extension and thermally weakening the lithosphere (Kendall et al., 2005; Daniels et al., 2014). Since the start of the Ethiopia-Afar Geoscientific Lithospheric Experiment (Bastow et al., 2011) in the early 2000s, consecutive and successful controlled and passive seismic deployments helped to delineate the seismic structure of the MER crust, especially the P-wave velocity (Vp) structure and crustal thickness (e.g., Ebinger et al., 2017). A major finding of previous P-wave images is that the Vp of the crust beneath the MER is faster than that of standard continental crust (Zandt and Ammon, 1995), a feature interpreted as caused by post-Miocene mafic intrusions that have accommodated extension (e.g., Keranen et al., 2004; Mackenzie et al., 2005).

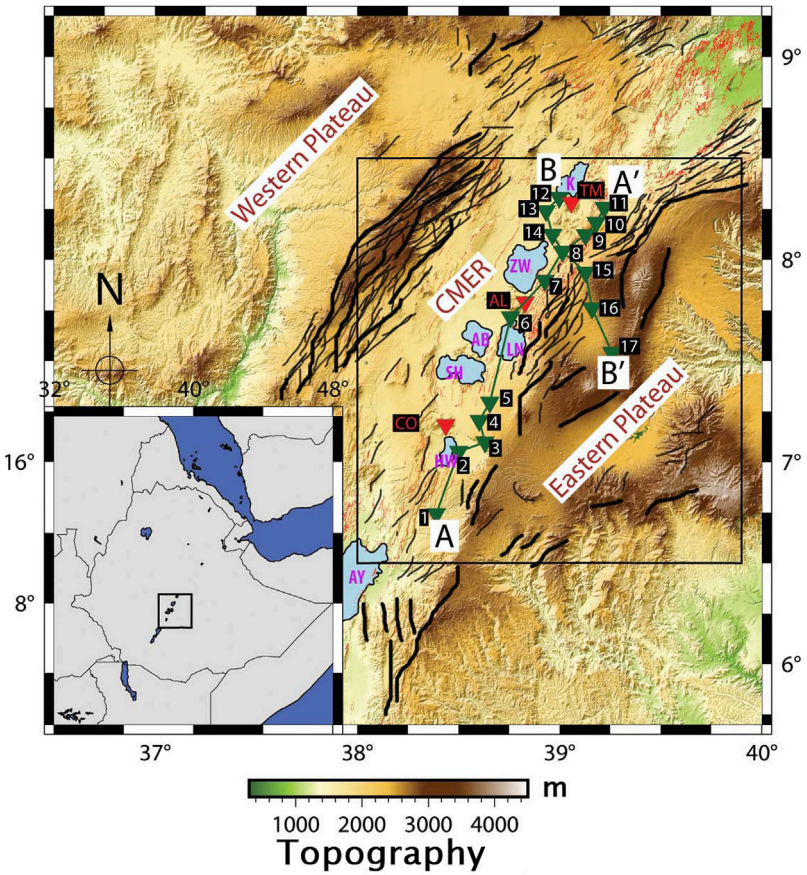

FIGURE 1 | The black rectangle is the study area in the Central Main Ethiopian Rift. Profile AA′ is along the eastern side of the Central Main Ethiopian Rift floor (along-rift) profile. Profile BB′ is the across-rift profile. Green reversed triangles represent the station location of 17 stations. Red -reversed triangles represent the locations of Corbetti (CO), Aluto (AL), and Tulu Moye (TM) calderas. The red thin and dense line represents the faults of the Main Ethiopian Rift (MER) (Corti et al., 2020). The bottom left corner inset shows the regional map, with a square for the area of our study. Names of the lakes are labelled by pink-coloured letters as AY (Abaya), HW (Hawasa), SH (Shala), AB (Abayata), LN (Langano), ZW (Ziway), and K (Koka).

More recently, however, the advent of ambient noise tomography at periods sufficiently short has facilitated imaging of shear-wave velocity (Vs) of the crust (e.g., Kim et al., 2012; Chambers et al., 2019). Results from these studies show that the MER crust has far slower Vs than the standard continental crust, with the absolute magnitude of the velocities in places interpreted to require the presence of partial melt (e.g., Chambers et al., 2019). The joint crustal seismic properties of relatively fast Vp and slow Vs are peculiar and poorly explored in previous literature. In addition, all previous constraints on the Vs structure of the MER come from models derived from surface wave imaging techniques, such as ambient noise tomography, with a lack of independent constraints provided by alternative methods.

In order to address this and provide additional and independent constraints on the Vs structure of the MER crust, we applied the receiver function (RF) techniques using open-source codes from Computer Programs for Seismology (CPS) (Herrmann and Ammon, 2004) to estimate the velocity of the crust and upper mantle. To this effect, we have used 17 new seismic stations deployed as part of the 2016–2017 RiftVolc project (Greenfield et al., 2019; Lavayssière et al., 2019) to improve our understanding of the spatial variations of the crustal Vs structure within the central MER (CMER) and adjacent Eastern Plateau. In addition, we use the RF technique to constrain the Vp and Vp/Vs ratio. In investigating the heterogeneous structure, we have chosen two vertical cross-sections to represent the area of our study (**Figure 1**). One profile (A–A′) is along the rift, and the other profile is across the rift (B–B′). This study improves on the previous velocity models and Moho depth estimates of the CMER and Eastern Plateau (Dugda et al., 2005; Keranen et al., 2009) by using a relatively large number of broadband seismic stations compared with the previous studies.

TECTONIC SETTING AND CRUSTAL STRUCTURE

The CMER formed within the Oligocene Ethiopian flood basalt province and is thought to have initiated at between ~20 and ~10 Ma (e.g., Wolfenden et al., 2004; Bonini et al., 2005; Corti, 2009). The extension was initially localized to several ~60-km-long, NE-SW striking, high-angle (>60°) border faults that bound

the rift, such as the Boru-Toru and the Goba-Bonga structural lineament on the western side of the rift, and the Asela-Sire Border Fault on the eastern side of the rift (Bonini et al., 2005; Corti et al., 2020). Since the Quaternary, the locus of tectonic and magmatic activity within the CMER is thought to have become focused to a ~20-km-wide zone of small offset faults, aligned cones, and active volcanic centres within the rift valley floor known as the Wonji Fault Belt (WFB), and also at a few rift marginal magmatic systems, such as the Silti-Debre Zeyit Fault Zone (SDFZ) towards the western side of the rift (Woldegabriel et al., 1990; Rooney et al., 2014; Chiasera et al., 2018).

Constraints on the crustal structure in the CMER come from several geophysical techniques including seismology, magnetotellurics (MT), and inversion of gravity data. Constraints on crustal thickness come from sparse RF measurements (Dugda et al., 2005; Keranen et al., 2009; Kibret et al., 2019), the wide-angle controlled-source along-rift EAGLE project line, and the intra-crustal Vs structure using ambient noise tomography (Kim et al., 2012; Chambers et al., 2019).

Previous RF studies in the CMER using relatively sparse station spacing show that the crust is 27- to 40-km thick in the rift (Dugda et al., 2005; Keranen et al., 2009) and 33- to 44-km thick beneath the plateaus (Dugda et al., 2005; Kibret et al., 2019). The crustal structure beneath the Western Plateau is more heterogeneous (33- to 44-km thick) (Keranen et al., 2009) than that beneath the Eastern Plateau (38- to 41 km thick) (Dugda et al., 2005; Keranen et al., 2009; Kibret et al., 2019). Wide-angle controlled-source seismology provides further constraints in the CMER, and Western and Eastern Plateaus. The EAGLE across-rift line shows similar crustal thicknesses of 38–40 km beneath the CMER (Dugda et al., 2005; Maguire et al., 2006; Stuart et al., 2006), and 35–45 and 37–42 km beneath the Western and Eastern Plateaus, respectively (Dugda et al., 2005; Stuart et al., 2006; Cornwell et al., 2010; Hammond et al., 2011; Kibret et al., 2019).

The southern end of the EAGLE along-rift wide-angle controlled-source line is as far south as Lake Hawasa (near HAWA station) and shows a varied along-rift crustal structure in the CMER (Mackenzie et al., 2005; Maguire et al., 2006). The Vp structure, modelled by the wide-angle 2D profile studies, shows that the velocities of the upper crustal layers beneath the rift are 5%–10% higher than outside the rift, a feature interpreted to be caused by mafic intrusions associated with magmatic centres (Mackenzie et al., 2005; Maguire et al., 2006). Consistent with this, 3D controlled-source tomography of the upper crust by Keranen et al. (2004) imaged rift parallel high Vp (~6.5–6.8 km/s) elongated bodies with a size of 20-km wide and 50-km long, and interpreted them as cooled mafic intrusions that are separated laterally from one another in a right-stepping en-echelon pattern, which corresponds with the surface segmentation of the WFB. These fast Vp regions correlate to a region of distinct positive Bouguer anomalies in gravity studies that are modelled as regions of dense rock (~3,000 kg/m^3) such a gabbro (e.g., Mahatsente et al., 1999; Cornwell et al., 2006).

In addition to the earliest studies revealing crustal structure in the MER based on Vp structure, later studies applied surface waves to render the Vs structure. Ambient noise tomography has been used to construct Rayleigh-wave group velocity maps covering the northern MER (NMER), CMER, and southern MER (SMER), and parts of the surrounding plateaus (Kim et al., 2012; Chambers et al., 2019). Chambers et al. (2019) also presented an absolute 3D Vs model of the crust and uppermost mantle of the region. An important feature of the Vs images is that the MER crust is mostly significantly slower than away from the rift, in contrast to the Vp, which is generally faster within the rift. The absolute Vs of less than 3.20 km/s + 0.03 in the lower crust are difficult to explain except with the presence of a fluid phase in the rock, such as partial melt (Chambers et al., 2019). In addition, slow Vs (<3.6 km/s) in the uppermost crust observed by Chambers et al. (2019) is consistent with the presence of sediments and/or partial melt (Diaferia and Cammarano, 2017).

Some studies reported that the anomalous high temperature is an important player on velocity structure in the case when it can trigger the transition of α–β quartz. In case of hydrated compositions (as one can presume about the current case study for the rift zone), the amphibole breakdown at increasing pressure and temperature produces a discontinuity that can be detected by RF or refraction studies (Guerri et al., 2015; Diaferia and Cammarano, 2017).

Similarly, several MT studies carried out in the CMER identify high conductivity anomalies associated with young surface volcanism (Whaler and Hautot, 2006). These conductive anomalies tend to be imaged in the uppermost crust at <1–2 km, in the upper crust at ~3–6 km depth, and in the mid-lower crust at 20–25 km depth (Ebinger et al., 2017; Hübert et al., 2018). The shallowest anomaly is interpreted as being caused by hydrothermal fluids, whereas the other deeper high conductivity anomalies are interpreted to be caused by partial melt in the subvolcanic plumbing system (Ebinger et al., 2017; Hübert et al., 2018). Broadly speaking, there is a good correlation between the loci of slow Vs from seismology and high conductivities, giving additional remark to the idea that these anomalies are caused by partial melt (Chambers et al., 2019).

DATA AND METHODS

Data

The data were acquired from the RiftVolc temporary network project that was conducted from February 2016 to October 2017 and recorded by three-component broadband Guralp CMG-6TD and Guralp CMG-ESPCD seismometers with a 50-Hz sampling rate. We downloaded the teleseismic waveform data and instrument responses of the RiftVolc project data archived at the Incorporated Research Institutions for Seismology (IRIS) Data Management Center (DMC).

To constrain the Vs and Vp/Vs structure beneath 17 stations, which are deployed along and across the CMER 60 teleseismic earthquakes with magnitudes, Mw ≥ 6 and source-to-receiver epicentral distances between 30° and 90° (**Figure 2**) were chosen. However, after calculating the RFs, only 8–38 signals were selected per station based on the percentage of signal power fit (**Table 1**).

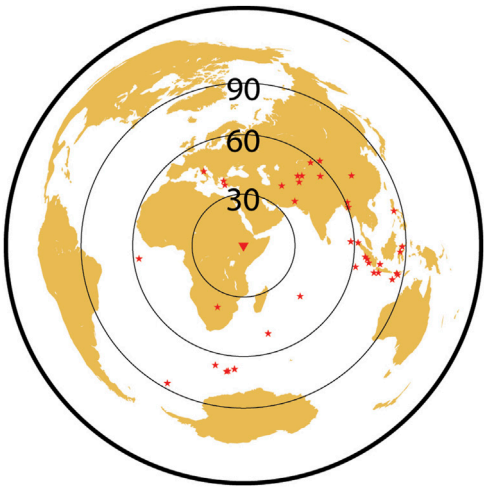

FIGURE 2 | Red circles are locations of the teleseismic earthquakes used for the study. The data collected are in the distance ranging from 30° to 90° in the time range of February 2016 to October 2017. The dark blue triangle is the central location of the 17 seismic stations used in this study.

TABLE 1 | The table shows the names of stations, the percent of signal power fit between observed and synthetic seismograms, and the number of receiver functions (RFs) used in the analysis during the model fit calculations.

NO	Name of stations	Percent of signal power fit (%)	Number of RFs used (RFTN)	Average ray Parameter
1	YIRG	76.6	20	0.060
2	HAWA	79.4	35	0.063
3	WOND	79.0	34	0.065
	SHAS	77.6	14	0.058
5	KADO	79.2	27	0.064
6	OHIT	80.9	18	0.063
7	BESH	77.8	24	0.063
8	OGOL	76.6	25	0.061
9	HURT	83.3	10	0.076
10	ANOL	84.5	18	0.065
11	CHKA	85.3	11	0.069
12	JIMA	88.2	8	0.057
13	JIRE	78.2	19	0.065
14	ODAS	81.1	28	0.067
15	ASSE	92.3	38	0.058
16	SAGU	90.4	31	0.059
17	BEKO	85.6	60	0.059

Note. From one earthquake, more than one RFs were calculated for the different values of Gaussian width parameters.

Data were processed in SAC format. We applied a cosine taper function for the P-waveform signal for a length of 50 s (10 s before and 40 s after the onset of the P-wave arrival) before computing the RFs. To reduce the influence of low-frequency noise on the RFs, all the signals were filtered with a Butterworth bandpass filter of between 0.01 and 5 Hz to ensure the stability of the RFs and to avoid aliasing when decimating the data. Finally, each three-component signal was reviewed to remove signals that contained low signal-to-noise ratios and/or when any of the three components were not recorded properly due to instrument malfunction.

METHODS

We applied an RF technique using time series teleseismic earthquakes to provide constraints on the local velocity structure of the crustal and upper mantle (Langston, 1979; Ammon et al., 1990). To extract the RF for each event, we first window the three-component seismograms starting from 10 s before and 40 s after the predicted P arrival. Selected teleseismic seismograms are rotated to radial (R), tangential (T), and vertical (Z) components from east–west, north–south, and vertical components, respectively. Each pair of horizontal-component signals (i.e., north–south and east–west components) was rotated to their corresponding radial and transverse directions.

A straightforward frequency domain deconvolution can be unstable due to spectral holes in the vertical component, and stabilization of this process can be obtained by either "pre-whitening" (Roninson, 1982; Yilmaz, 2001); or "water-level" algorithms. The former adds a small component of random noise to the vertical component, while the latter sets a lower bound on the magnitude of the denominator terms (the vertical seismogram spectral elements) in a frequency domain spectral division. In this study, converted phases are isolated by iterative, time-domain spiking deconvolution (Gurrola et al., 1995; Ligorria and Ammon, 1999) with pre-whitening to stabilize the filtering. Iterative time domain deconvolution works well even with complex signals. However, regardless of a deconvolution algorithm, the response at the receiver depends on the complexity of structures. Simple structures generally lead to better RF images (Ligorria and Ammon, 1999). After deconvolving the vertical from the radial component, we removed the signature of source, travel path, and instrumental response effects (Langston, 1979; Ammon et al., 1990; Dugda et al., 2005; Kibret et al., 2019) employing the signals coming from four different back azimuths (**Figure 3**).

The RF technique is a time series when the radial component trace is deconvolved from its vertical component seismogram, where the timing and amplitude of the RF phases are sensitive to the near receiver local Earth structure beneath the seismic station (Langston, 1979). The dominant signal in the first few seconds of the RF is the Ps conversion from the Moho and/or intracrustal velocity contrast followed by reverberated phases within the crust (e.g., Last et al., 1997; Hammond, 2014). In case of using a relatively dense array, RFs can show the fine crustal heterogeneity, anisotropy, and dipping structures (Eckhardt and Rabbel, 2011; Liu and Niu, 2012; Niu and James, 2002; Thybo et al., 2019; Youssof et al., 2013, Youssof et al., 2015).

Each RF was deconvolved for 20 iterations with a limiting error of 0.001 by applying three different Gaussian width parameters of 0.5, 1.0, and 2.5. We applied an iterative deconvolution algorithm (Kiknchi and Kanamori, 1982), which is calculated by the division of the denominator from the numerator (Herrmann and Ammon, 2004). Also, in each case, we allowed iteration to continue until the change in misfit

TABLE 2 | A summary of the findings of previous gravity and seismic methods studied in the SE plateau and the central main Ethiopian rift valley for the determination of Moho depth.

Geophysical methods	Moho depth (Km)	Study areas	Author/s
Seismic refraction/wide angle reflection	~39–40	SE MER	Mackenzie et al. (2005)
Gravity and topography data	~40	SE MER	Tiberi et al. (2005)
High-precision gravity data	~38–51	MER flanks	Cornwell et al. (2006)
RFs and Rayleigh wave group velocities	~38	CMER	Keranen et al. (2009)
RFs and Rayleigh wave group velocities	~38–41	Easter shoulder	Keranen et al. (2009)
A 2D forward gravity model	~38	CMER	(Emishawa et al., 2017)
Receiver function analysis	33–44	Ethiopian plateau	Dugda et al. (2005)
Receiver function analysis	27–38	MER	Dugda et al. (2005)
3D gravity modelling	30–50	MER & Adjoining plateau	Mahatsente et al. (1999)

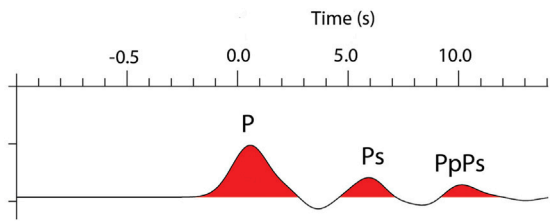

FIGURE 3 | This is a sampled receiver function (RF), which is calculated from the deconvolution of the horizontal from the vertical component. The deconvolution is processed from the data collected by the ASSE station from an earthquake coming from a ~178° azimuth. The diagram shows the direct P and the converted Ps and the PpPs multiples.

resulting from the addition of a spike was 0.01% (Ligorria and Ammon, 1999). The degree of fit between the synthetic and observed RFs is calculated from the three Gaussian width parameters. A sample of two RFs is selected from 17 stations based on their percent of fit to demonstrate the overall results throughout each step (**Figures 4**, **5**).

The study applies the ak135 velocity model (Kennett et al., 1995) as the initial velocity model to calculate the best fit velocity structure. Finally, we identified the level of the model fit of the observed and synthetic models by using both visual inspection and the calculated percentage of signal power fit. When the synthetic signals show a high degree of a misfit from the calculated RFs, both RFs and the synthetic models are automatically discarded.

The observed (red colour) and synthetic (blue colour) RFs (**Figure 5**) as well as the initial and the final velocity models (**Figure 6**) are calculated by using programs from Herrmann and Ammon (2004). The final velocity models are calculated from the global velocity model ak135. The calculated absolute velocity values at every 2-km depth are obtained from the inversions of the RFs. The uncertainties of the calculated RFs are estimated from the percentage of fit between the observed and the calculated RF. Subsequently, well-constrained Vs structures of the crust and upper mantle are provided in the 2D profiles.

We applied the Delaunay triangulation interpolation method to estimate unknown velocities based on several known calculated velocities (Ping et al., 2009). The method uses three velocities at a time by assuming no points inside the circumference of any triangle. We applied this interpolation method as implemented in the GMT plotting software (Wessel et al., 2019) by triangulating and contouring the calculated velocity values to image the 2D velocity versus depth plots.

Crustal thickness and Vp/Vs ratio are estimated from the *a priori* known Vp value obtained from two-dimensional wide-angle seismic modelling from the EAGLE controlled-source survey (Mackenzie et al., 2005; Maguire et al., 2006) in the region. During our inversion, we calculated Vs values at 2-km-depth intervals. Again, we employed the mathematical model by Last et al. (1997) and Zhu and Kanamori, (2000) to get the Moho depth (H) at each station, where $t_{Ps} - t_P$ is the time interval between the arrival of the direct P wave and the Moho Ps converted phase, and p is the average ray parameter calculated from RFs.

RESULTS

We computed observed and synthetic RFs at 17 stations where the degree of fit is between 77%–92% (at station OGOL and ASSE, respectively), as shown in **Table 1**. The range of degree of fit between observed and synthetic seismograms is similar to what is previously reported (70%–90%) in Ethiopia and Kenya by Dugda et al. (2005).

The current RFs are obtained with two clusters of range of back-azimuths of 30°–110° and 185°–260° (**Figure 4**). The first arrival spike is the direct incident P wave at the surface; however, the subsequent arrivals correspond to the partition of converted and reverberated phases (**Figures 3** and 5).

For the two examples of observed RF in **Figure 4**, we present the RF of each event with the corresponding synthetic RF in **Figure 5**. In this model, the red-coloured RFs are the observed signals, whereas the blue colour shows the synthetic ones. The observed and synthetic RFs (**Figure 5**) show a high degree of fit for the Gaussian width parameters of $\alpha = 0.5$ and $\alpha = 1.0$.

Figure 6 indicates the 1D velocity models for the chosen two stations. These velocity models are calculated from the blue-coloured synthetic RFs shown in **Figure 5**. They are calculated in the depth range of 2–100 km. The blue-coloured nearly vertical line is the initial velocity model, which is assumed as a homogeneous half space with a Vs of ~4.48 km/s, which is the value of most of the lithosphere in the ak135 velocity model (Kennett et al., 1995).

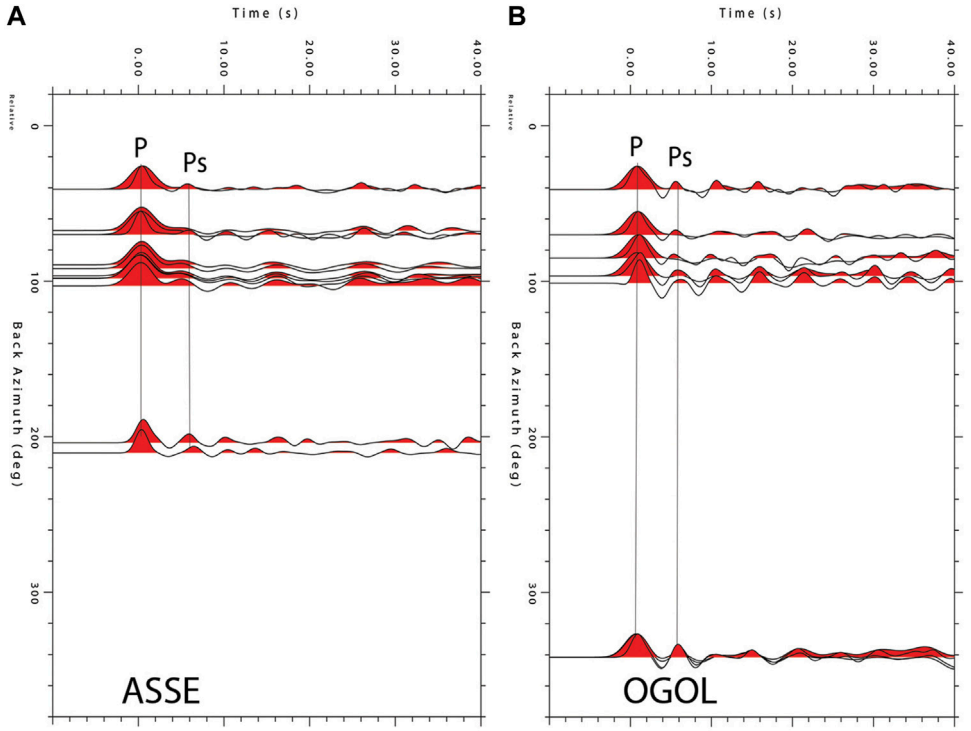

FIGURE 4 | (A) and **(B)** are examples of RFs calculated for signals coming from different azimuths. Positive values were filled with red ink to emphasize prominent features, such as the direct P and the Ps phase, which is the P-to-S conversion.

From the calculated 1D Vs models shown in **Figure 6**, the red-coloured 1D velocity value is the final and best fit calculated Vs model. From the models, the ASSE station, which is located on the Eastern Plateau shows very small heterogeneity in the upper and lower crust. However, station OGOL is located on the CMER floor and shows a heterogeneous velocity structure with a relatively high velocity of up to ~4.6 ± 0.1 km/s in the upper crust and a relatively low velocity of as low as 3.4 ± 0.1 km/s in the lower crust.

For the remainder of the stations, we have shown the results in the form of the along- and across-rift profiles (**Figure 7**). Broadly speaking, the velocity models show a distinctive reduction in Vs in the mid to lower crust similar to that observed at OGOL (**Figure 6**), or a more regular increase in Vs with depth as observed at ASSE (**Figure 6**). Closer inspection for the stations along the rift shows that the velocity model varies considerably spatially with both styles of velocity structure observed in different places within the rift. In contrast, the across-rift profile shows that the stations on the Eastern Plateau have a velocity structure more similar to ASSE.

The upper to mid crustal high-velocity material (~4–4.5 ± 0.1 km/s) observed in OGOL is also observed in the rift beneath YIRG, SHAS, KADO, and BESH stations for the depth range of 4–25 km (**Figure 7**). At these stations and beneath the observed high-velocity upper to mid crust, there is a relatively slow Vs (~3.5 ± 0.1 km/s) for the depth range of ~24–45 km. The slow velocity deep crust is commonly beneath normal upper-to-middle crust (4–4.3 km/s) such as beneath the JIMA station. In contrast, beneath JIRE, ODAS, ASSE, and SAGU stations (**Figure 7**), crustal Vs are relatively homogeneous.

Figure 8B1 shows the 2D Vs structure and **Figure 8B2** the corresponding Vp/Vs ratio of the along-rift profile in the CMER obtained from the Delaunay triangulation interpolation method. Throughout the crust, the depth to particular velocity contours generally deepens with proximity to the major volcanic centres. This is especially pronounced in the 5- to 20-km depth range where the Vs increase significantly in regions in between the major volcanic centres. For example, beneath the two high topographic peaks (marked as Aluto and Tulumoye) observed in **Figures 8A1,A2**, there are slow velocity (<3.8 km/s) and high Vp/Vs ratio zones in the upper-mid crust. A similar slow velocity zone in the upper-mid crust is also observed beneath the Wondo-Genet remnant Mega caldera rim. Vs is generally slow (~3.1–3.7 ± 0.1 km/s) in the lower crust beneath the CMER, with less spatial variation in velocities compared with that observed in the upper-mid crust. Generally, our findings are consistent with previous ambient noise tomography results showing the presence of slow S-velocity shallow crust beneath mega calderas, such as beneath Aluto and Tulu Moye, and slow Vs found more ubiquitously in the lower crust (Chambers et al., 2019).

Figures 9B1,B2 show the variations in Vs and Vp/Vs structure across the rift, respectively. In a similar fashion to the along-rift profile, the topmost ~5 km of the upper crust of the across-rift profile is a very low seismic velocity (2.0–3.2 km/s) material. The border fault of the eastern

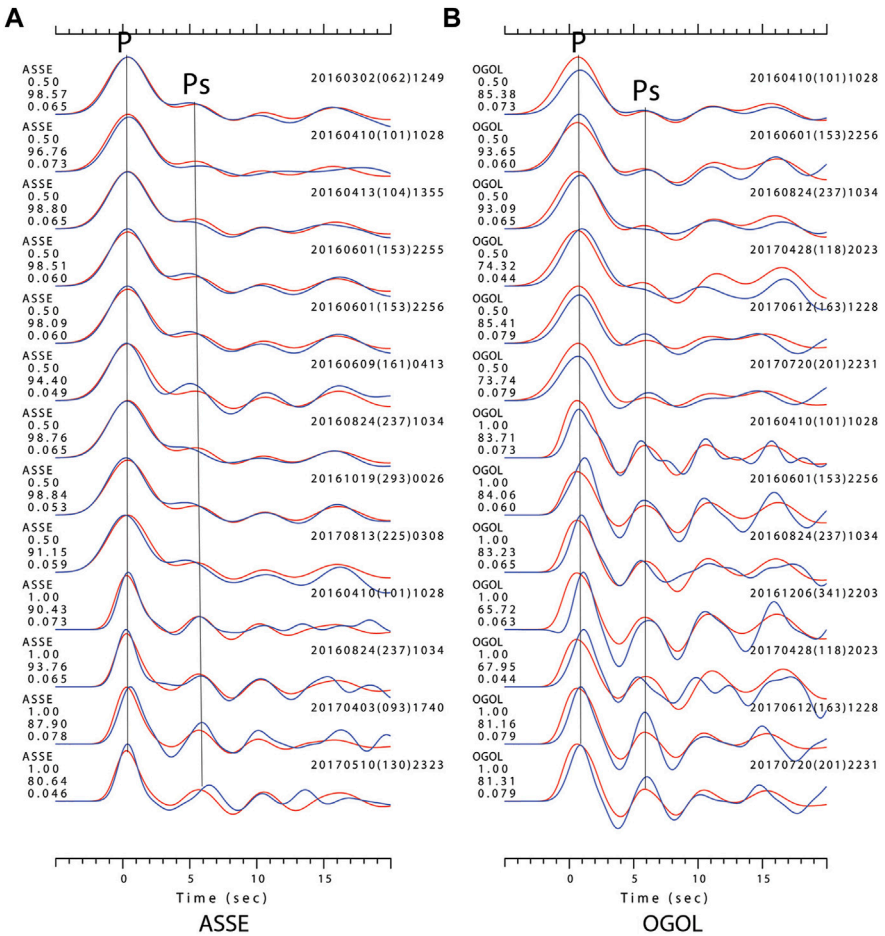

FIGURE 5 | (A) and **(B)** are RFs of ASSE and OGOL stations. The ASSE station located on the eastern plateau, which is the best fit RF of this study, whereas station OGOL is located in the central MER (CMER) rift margin near the eastern plateau, which has the largest misfit of all the RFs. Blue-coloured RFs in the background are synthetic, whereas the red-coloured RFs on top are the observed RFs. P represents the direct primary wave, and Ps is the converted phase at the Moho. The numbers on the left show the station name, Gaussian width parameter, percentage of fit, and the applied ray parameters for the specified RF. The numbers to the right of the RFs are the occurrence time of the earthquakes. In **(A)**, two signals and in **(B)** six signals are calculated twice for the Gaussian width parameters of 0.5 and 1.0.

side of the CMER is marked by a topographic step from ~1,700 m in the rift to ~2,700 m on the rift margin (**Figure 9**). Outside of the rift on the rift flank, we observe a fairly homogeneous crustal structure with a distinct lack of slow velocities in the lower crust. Instead, the seismic velocity mostly increases with depth. In addition, there is a sharp increase in seismic velocity at ~45 km depth, where previous studies based on different methods showed this change as Moho discontinuity (e.g., Mahatsente et al., 1999; Mackenzie et al., 2005; Cornwell et al., 2006), as shown in **Table 2**. However, similar to the along-rift profile, within the rift on the across rift profile, we see a more heterogenous velocity structure. At 20- to 35-km depths, particularly slow Vs and high Vp/Vs ratios are found beneath the eastern part of the across-rift profile beneath the JIMA and OGOL stations. In this depth interval, the lowest velocities are found beneath the eastern side of the CMER spatially associated with the surface position of the WFB volcanic centres.

DISCUSSION

We discuss here the Vs and Vp/Vs structure of the rift obtained from our data analysis in the context of magmatic and tectonic extensional processes, and with the aid of *a priori* constraints of Vp ~6.8 km/s (e.g., Dugda et al., 2005; Mackenzie et al., 2005; Maguire et al., 2006). We also compare our findings with constraints inferred from density and conductivity analysis conducted in the area. We use both one- and two-dimensional Vs profiles to interpret velocity variations in the lithosphere to answer basic questions about the nature of the crust and upper mantle when rifting modifies the lithosphere.

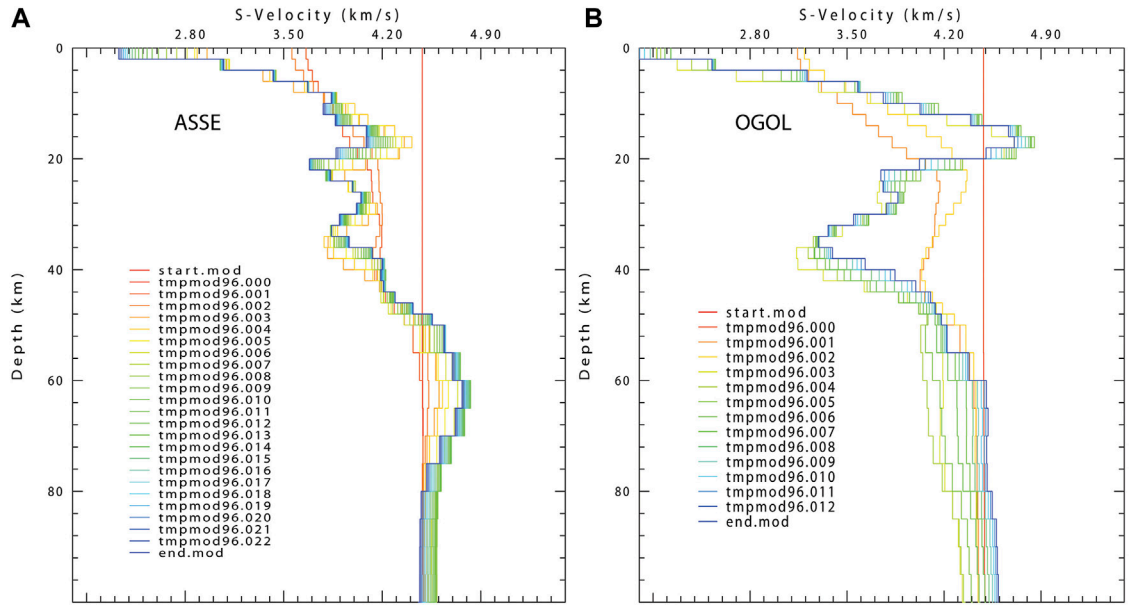

FIGURE 6 | Panels **(A)** and **(B)** are the two representative velocity models for the ASSE and OGOL stations. The nearly vertical start. mod is an initial half space velocity model derived from the ak135 global velocity model (Kennett et al., 1995) and the end. mod is the final and best-fit velocity model. The tmpmod96. xxx are the calculated velocity models from the relatively less fit RFs during an inversion.

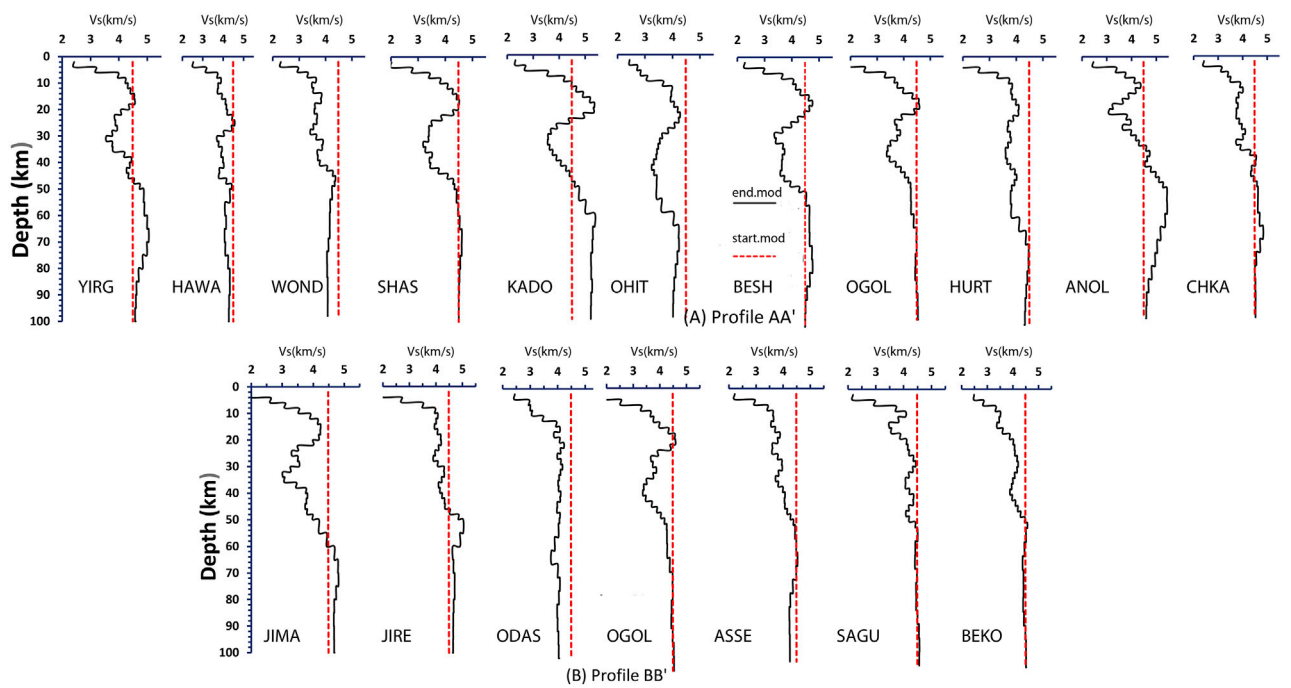

FIGURE 7 | Figure **(A)** The 1D velocity model for the along-rift profile AA′, which is located along the eastern margin of the central main Ethiopian rift profile. **(B)** The 1D velocity model for the across-rift profile, which includes the rift side (JIMA, JIRE, ODAS, and OGOL) and plateau side (ASSE, SAGU, and BEKO) stations.

S-wave velocity structure within the rift

The slow velocity (2–3 km/s) imaged at 2–6 km depth is similar to the proposed Vs of ~1.9–2.8 km/s typical of layered sediments (Benoit et al. (2006). This is also in good agreement with the work of Chambers et al. (2019), which interprets a similarly low velocity at the topmost upper crust as sedimentary and/or

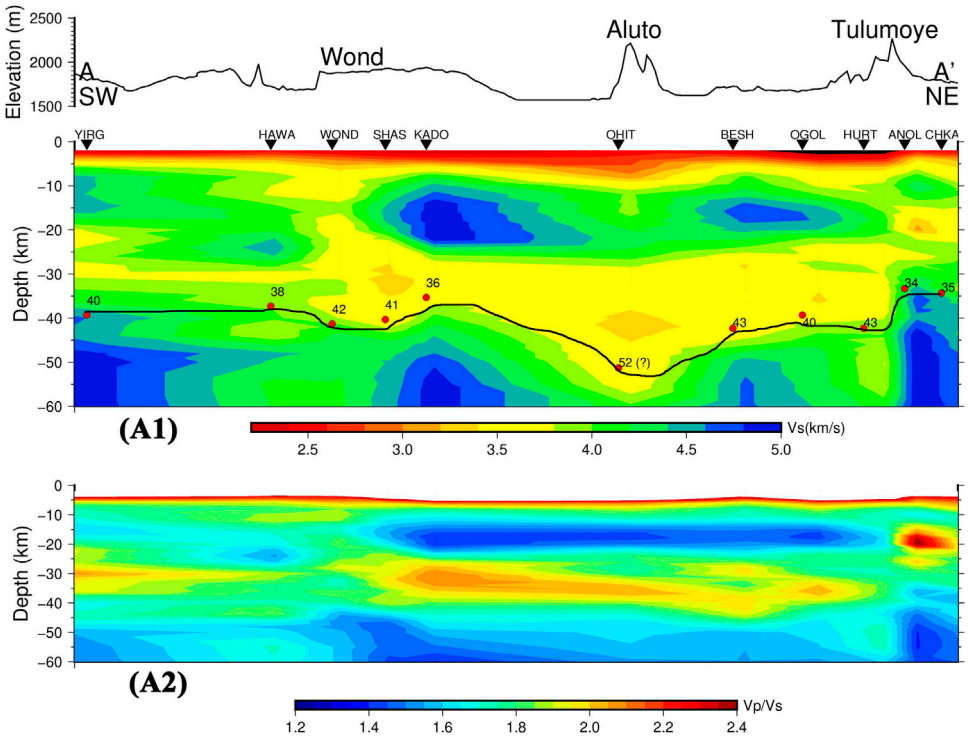

FIGURE 8 | (A1) shows a 2D vertical slice along the eastern margin of the central Main Ethiopian Rift, which is obtained from profile AA′ of **Figure 1** covering from station YIRG (1,756 m) to CHKA (1,604 m). **(A2)** shows the Vp/Vs ratio values at various depth points. Red indicates slower velocity and blue faster velocity. B2 shows the values of Vp/Vs for the rift and the plateau side of the profile. Blue indicates low Vp/Vs, and red indicates high Vp/Vs ratio.

volcanic layers. This result agree with the interpretation of Cornwell et al. (2006), which interprets the existence of an upper crustal low-density (2,380 kg/m^3) layer that represents interspersed volcaniclastics, lava flows, and lacustrine sediments within the rift valley (Wolfenden et al., 2004). In support of this interpretation, the low Vs of the uppermost crust extends to greatest depths within the rift valley than outside of it (**Figure 9**).

Both profiles shown in **Figure 7** represent significant variations in the 1D velocity models. In particular, a number of the stations show elevated seismic velocity at 6–25 km, while others are less fast. When stations are organised spatially from NW to NE in **Figure 8A1**, the spatial variability of this is clearer. Typically, along rift, in-between the magmatic centres (such as beneath station YIRG, SHAS, KADO, BESH, and OGOL), the high Vs (~4–4.5 km/s) is present in the upper-to-mid crust. The across-rift profile in **Figure 9** shows that these regions of higher Vs in the upper/mid crust are localised beneath the Wonji Fault Belt. The high seismic velocities coupled with their Wonji Fault belt position favours an interpretation of their origin being a solidified mafic intrusion, an interpretation in line with previous seismic imaging (Chambers et al., 2019), and spatially match high positive Bouguer anomalies constrained in gravity studies (Mahatsente et al., 1999; Tiberi et al., 2005; Cornwell et al., 2006). The average slow-velocity (~3.5 ± 0.1 km/s) regions at ~24–45 km depth may represent a less mafic modification of a normal continental crust of Vp/Vs <1.85 (Zandt and Ammon, 1995), or a more complex modification from felsic intrusion, and/or presence of partial melt with a Vp/Vs value of >1.9.

Beneath 25-km depth in the lower crust, the 1D models show that the majority of seismic stations show a reduction in Vs in the lower crust to 3.1–3.7 ± 0.1 km/s (**Figure 7**). **Figure 8** shows that this feature is spatially ubiquitous. There is some spatial variability in the magnitude of the velocity inversion (**Figures 8A1,A2**), with a hint that the most pronounced slow Vs regions in the lower crust are beneath the volcanic centres, such as Aluto, although this pattern is not particularly clear elsewhere. These regions of slow Vs correlate to high Vp/Vs of ~1.9–2.1. The observation of slow Vs and high Vp/Vs in the lower crust in the rift valley is consistent with the ambient noise tomography by Chambers et al. (2019), which shows that the slowest velocities for all depths within the MER range from 3.28 ± 0.01 km/s at 10-km depth to 3.83 ± 0.01 km/s at 40-km depth. The magnitude of the slow Vs at this depth range, combined with the high Vp/Vs, is consistent with previous deep crustal imaging studies, which combined interpret between 0.5% and 5% partial melt (e.g., Chambers et al., 2019). More tightly constraining melt fraction from the seismic velocities alone is difficult since Vp and Vs measurements are potentially explainable by either lower melt fractions aligned vertically as dikes or more elevated melt fractions aligned as sills (Paulatto et al., 2010; Paulatto et al., 2012; Paulatto et al., 2019; Dvorkin, 2020). However, dominance of horizontal sill-like melt alignment is favoured by inversions for radial anisotropy derived from surface waves for the MER (e.g.,

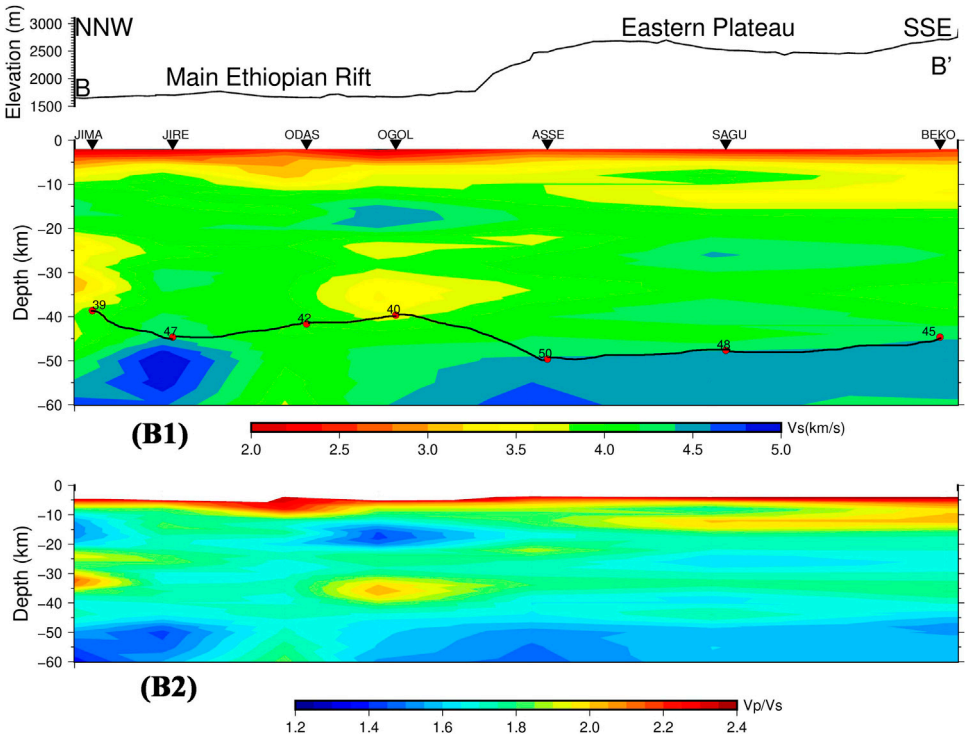

FIGURE 9 | (B1) shows a 2D vertical slice across the rift profile BB′ of **Figure 1** ranging from JIMA (in Central WFB) with an altitude of 1,659 m to BEKO (Eastern Plateau) having an elevation of 2,848 m. Red indicates slower velocity and blue faster velocity. **B2** shows the values of Vp/Vs for the rift and the plateau side of the profile. Blue indicates low Vp/Vs, and red indicates high Vp/Vs ratio.

Chambers et al., 2021), and petrological models of the deep crustal magma plumbing system globally (e.g., Annen et al., 2006). The interpretation of partial melt in the lower crust is also supported by high conductivities in the lower crust observed in crustal-scale MT studies at comparable depths (Whaler and Hautot, 2006).

Profile AA′ in **Figure 8** shows variations in the Vs structure, which provides insights into the crustal-scale magma plumbing system. The ubiquitous slow Vs suggests a diffuse interconnected melt-rich lower crust beneath most of the rift valley, with potentially higher melt concentration beneath the volcanic centres. In contrast, in the upper half of the crust, slower Vs beneath the volcanic centres, with anomalously fast Vs in between the volcanic centres, is consistent with volcanic segment-centred melt supply, in which subvolcanic melt reservoirs focus and store melt, which is delivered episodically mafic intrusion along the rift axis. Such an upper crustal plumbing system has been proposed in Afar on the basis of episodic segment-centred fed dyke intrusions observed with InSAR and seismicity (Keir et al., 2009; Barnie et al., 2016). Here in the MER, a similar subvolcanic plumbing system is consistent with the seismic velocity structure of the upper/mid crust. In addition, in the MER, observations of such rifting episodes are lacking, with geodetic observations of magma-related ground deformation being restricted to volcanic centres such as Aluto and Tulu Moye (Biggs et al., 2011; Albino and Biggs, 2021). Similarly, localised subvolcanic pockets of melt beneath the volcanic centres (Gleeson et al., 2017) suggest localised longer-lived magma bodies in the shallow crust of the volcanic centres. However, our seismic imaging of the deeper crust suggests that the distribution of melt in the lower crust might well be widespread and enable significant melt transport along rift.

S-wave velocity structure of the Eastern Plateau

In contrast to the rift valley floor, the Vs structure beneath the Eastern Plateau is remarkably homogeneous (**Figure 9B1**). In addition, the distinctive increase in Vs at ~45 km depth, is remarkably similar to constraints on the Moho depth computed in our study, consistent with a previous wide-angle active source, and passive source RF studies (Mackenzie et al., 2005; Maguire et al., 2006), and adds support observations that the Moho beneath the Eastern Plateau is a sharp and distinctive seismological boundary (e.g., Ogden et al., 2019). This profile shows a smooth transition toward the shoulder compared with the western plateau margin in which sharp lateral contrast between plateau and rift is observed (Chambers et al., 2019). Limited heterogeneity of the crustal and mantle structure beneath the Eastern Plateau is typical of regions of stable continental crust with limited history of deformation and modification by magmatism (e.g., Thompson et al., 2010; Youssof et al., 2013,

Youssof et al., 2015). The strong contrast in velocity structure from the Eastern Plateau into the rift (**Figure 9**) is in sharp contrast to the conjugate side of the rift valley, with the Western Plateau showing evidence for significant magmatic modification (e.g., Mackenzie et al., 2005; Chambers et al., 2019), indicating strong asymmetry to the rifting process. The lack of evidence for magmatic modification of the crust beneath the Eastern Plateau also favours a model of dynamic uplift from a deep-seated asthenospheric anomaly (e.g., Sembroni et al., 2016), as opposed to uplift being compensated by crustal magmatic additions (e.g., Keranen et al., 2009; Chambers et al., 2019).

Our study reveals new important insights regarding the variability in crustal structure and melt fraction on a local scale beneath the volcanic regions of the MER. The results demonstrate the continued need for more future efforts to understand crustal structure and distribution of partial melt in the wider sense beneath and near the East African rift. We would like to point out the need to have more international collaboration—although we would imagine that long-term and sustainable research in Ethiopia really needs local scientists to lead the way.

CONCLUSION

We use RF to delineate the Vs structure of the lithosphere beneath 17 stations in the CMER, which are arranged in two profiles along and across the rift valley. The observed low Vs (~2–3 km/s) uppermost crust (<6-km depth) is interpreted as sedimentary and/or volcanic layers. Beneath the rift valley crust, Vs is heterogeneous laterally and with depth. In particular, slow Vs and high Vp/Vs ratio is localised beneath volcanic centres in the upper-mid crust but ubiquitously slow in the lower crust. The Vs and Vp are consistent with the presence of the small fraction (<5%) partial melt interpreted in previous seismic imaging studies of the lower crust. In addition, the velocity contrast is small between the lower crust and upper mantle in the rift. The results suggest that partial melt in the lower crust beneath magmatically active rifts might be more widespread than previously thought and is an important component of the magma plumbing system. In contrast, Vs is more homogeneous and faster beneath the Eastern Plateau, with a distinct and sharp velocity contrast observed between the crust and upper mantle at Moho, jointly indicative of very little crustal modification from magmatism.

DATA AVAILABILITY STATEMENT

The datasets presented in this study can be found in online repositories. The names of the repository/repositories and accession number(s) can be found at: https://ds.iris.edu/wilber3/find_event.

AUTHOR CONTRIBUTIONS

BK customized the Computer Program for Seismology software and wrote some essential scripts. All the three authors developed the concept of this paper. BK selected and processed the teleseismic signals, conducted the modelling of all datasets, and led the writing of the paper. All authors contributed to the write up, discussion, and interpretation of the result of the paper.

FUNDING

The research work is sponsored by Addis Ababa University. The project was funded by the Natural Environment Research Council under NERC Grant NE/L013932/1. The publication charges were covered by the University of Southampton, and the laptop used to conduct the analysis was purchased using GCRF-UKRI funding from Ian Bastow, Imperial Collage London.

ACKNOWLEDGMENTS

We would like to thank those who participated in the RiftVolc project. We also want to acknowledge the IRIS Data Management Center (IRIS DMC). Similarly, I would like to furnish my deepest thanks to Prof. Robert Herrmann who affords his software packages entitled “Computer Program for Seismology” to the scientific community. We would also like to thank Prof. Giacomo Corti for allowing us to use the fault pattern in the location map. Ultimately, we would like to acknowledge Addis Ababa University for providing the opportunity to conduct this research.

SUPPLEMENTARY MATERIAL

The Supplementary Material for this article can be found online at: https://www.frontiersin.org/articles/10.3389/feart.2022.773783/full#supplementary-material

REFERENCES

Albino, F., and Biggs, J. (2021). Magmatic Processes in the East African Rift System: Insights from a 2015–2020 Sentinel-1 InSAR Survey. *Geochem. Geophys. Geosyst.* 22, 1–24. doi:10.1029/2020gc009488

Ammon, C. J., Randall, G. E., and Zandt, G. (1990). On the Nonuniqueness of Receiver Function Inversions. *J. Geophys. Res.* 95 (B10), 15303–15318. doi:10.1029/JB095iB10p15303

Annen, C., Blundy, J. D., and Sparks, R. S. J. (2006). The Genesis of Intermediate and Silicic Magmas in Deep Crustal Hot Zones. *J. Pet.* 47, 505–539. doi:10.1093/petrology/egi084

Barnie, T. D., Oppenheimer, C., and Pagli, C. (2016). Does the Lava lake of Erta ‘Ale Volcano Respond to Regional Magmatic and Tectonic Events? an Investigation Using Earth Observation Data. *Geol. Soc. Lond. Spec. Publications* 420 (1), 181–208. doi:10.1144/sp420.15

Bastow, I. D., Keir, D., and Daly, E. (2011). The Ethiopia Afar Geoscientific Lithospheric Experiment (EAGLE): Probing the Transition from continental Rifting to Incipient Seafloor Spreading. *Geol. Soc. America Bull.* 478, 51–76. doi:10.1130/2011.2478(04)

Benoit, M. H., Nyblade, A. A., and Pasyanos, M. E. (2006). Crustal Thinning between the Ethiopian and East African Plateaus from Modeling Rayleigh Wave Dispersion. *Geophys. Res. Lett.* 33, 1–5. doi:10.1029/2006gl025687

Biggs, J., Bastow, I. D., Keir, D., and Lewi, E. (2011). Pulses of Deformation Reveal Frequently Recurring Shallow Magmatic Activity beneath the Main Ethiopian Rift. *Geochem. Geophys. Geosyst.* 12, 1–11. doi:10.1029/2011gc003662

Bonini, M., Corti, G., Innocenti, F., Manetti, P., Mazzarini, F., Abebe, T., et al. (2005). Evolution of the Main Ethiopian Rift in the Frame of Afar and Kenya Rifts Propagation. *Tectonics* 24 (1), a–n. doi:10.1029/2004TC001680

Chambers, E. L., Harmon, N., Keir, D., and Rychert, C. A. (2019). Using Ambient Noise to Image the Northern East African Rift. *Geochem. Geophys. Geosystems* 20, 2091–2109. doi:10.1029/2018gc008129

Chambers, E. L., Harmon, N., Rychert, C., and Keir, D. (2021). Variations in Melt Emplacement beneath the Northern East African Rift from Radial Anisotropy. *Earth Planet. Sci. Lett.* 573, 1–13. doi:10.1016/j.epsl.2021.117150

Chiasera, B., Rooney, T. O., Girard, G., Yirgu, G., Grosfils, E., Ayalew, D., et al. (2018). Magmatically Assisted Off-Rift Extension-The Case for Broadly Distributed Strain Accommodation. *Geosphere* 14, 1544–1563. doi:10.1130/ges01615.1

Cornwell, D. G., Mackenzie, G. D., England, R. W., Maguire, P. K. H., Asfaw, L. M., and Oluma, B. (2006). Northern Main Ethiopian Rift Crustal Structure from New High-Precision Gravity Data. *Geol. Soc. Lond. Spec. Publications* 259, 307–321. doi:10.1144/gsl.sp.2006.259.01.23

Cornwell, D. G., Maguire, P. K. H., England, R. W., and Stuart, G. W. (2010). Imaging Detailed Crustal Structure and Magmatic Intrusion across the Ethiopian Rift Using a Dense Linear Broadband Array. *Geochem. Geophys. Geosystems* 11, n/a. doi:10.1029/2009gc002637

Corti, G. (2009). Continental Rift Evolution: From Rift Initiation to Incipient Break-Up in the Main Ethiopian Rift, East Africa. *Earth-Science Rev.* 96, 1–53. doi:10.1016/j.earscirev.2009.06.005

Corti, G., Sani, F., Florio, A. A., Greenfield, T., Keir, D., Erbello, A., et al. (2020). Tectonics of the Asela-Langano Margin, Main Ethiopian Rift (East Africa). *America Geophys. Union* 412, 1–43. doi:10.1038/35084058

Daniels, K. A., Bastow, I. D., Keir, D., Sparks, R. S. J., and Menand, T. (2014). Thermal Models of Dyke Intrusion during Development of Continent–Ocean Transition. *Earth Planet. Sci. Lett.* 385, 145–153. doi:10.1016/j.epsl.2013.09.018

Diaferia, G., and Cammarano, F. (2017). Seismic Signature of the continental Crust: What Thermodynamics Says. An Example from the Italian peninsula. *Tectonics* 36, 3192–3208. doi:10.1002/2016tc004405

Dugda, M. T., Nyblade, A. A., Julia, J., Langston, C. A., Ammon, C. J., and Simiyu, S. (2005). Crustal Structure in Ethiopia and Kenya from Receiver Function Analysis: Implications for Rift Development in Eastern Africa. *J. Geophys. Res.* 110, B01303. doi:10.1029/2004jb003065

Dvorkin, J. (2020). "Rock Physics: Recent History and Advances", in. *Geophys. Ocean Waves Stud.* Editors. K. S. Essa, M. Di Risio, D. Celli, and D. Pasquali (London, United Kingdom: IntechOpen), 1–24. doi:10.5772/intechopen.92161

Ebinger, C. J., Keir, D., Bastow, I., Whaler, K., Hammond, J., Ayele, A., et al. (2017). Crustal Structure of Active Deformation Zones in Africa: Implications for Global Crustal Processes: Africa Crust. *Tectonics* 36, 37–57. doi:10.1002/2017tc004526Avaliable At: https://agupubs.onlinelibrary.wiley.com/doi/full/10.1002/2017TC004526

Eckhardt, C., and Rabbel, W. (2011). P-receiver Functions of Anisotropic continental Crust: a Hierarchic Catalogue of Crustal Models and Azimuthal Waveform Patterns. *Geophys. J. Int.* 187 (1), 439–479. doi:10.1111/j.1365-246x.2011.05159.x

Emishaw, L., Laó-Dávila, D. A., Abdelsalam, M. G., Atekwana, E. A., and Gao, S. S. (2017). Evolution of the Broadly Rifted Zone in Southern Ethiopia Through Gravitational Collapse and Extension of Dynamic Topography. *Tectonophysics* 699, 213–226.

Gleeson, M. L. M., Michael, J. S., David, M. P., Tamsin, A. M., William, H., Gezahegn, Y., et al. (2017). Constraining Magma Storage Conditions at a Restless Volcano in the Main Ethiopian Rift Using Phase Equilibria Models. *J. Volcanology Geothermal Res.* 337, 44–61. doi:10.1016/j.jvolgeores.2017.02.026

Greenfield, T., Keir, D., Kendall, J.-M., and Ayele, A. (2019). Seismicity of the Bora-Tullu Moye Volcanicfield, 2016-2017. *Geochem. Geophys. Geosyst.* 20, 548–570. doi:10.1029/2018gc007648

Guerri, M., Cammarano, F., and Connolly, J. A. D. (2015). Effects of Chemical Composition, Water and Temperature on the Physical Properties of the continental Crust. *Geochem. Geophys. Geosyst.* 16, 2431–2449. doi:10.1002/2015gc005819

Gurrola, H., Baker, G. E., and Minster, J. B. (1995). Simultaneous Time-Domain Deconvolution with Application to the Computation of Receiver Functions. *Geophys. J. Int.* 120 (3), 537–543. doi:10.1111/j.1365-246X.1995.tb01837.x

Hammond, J. O. S. (2014). Constraining Melt Geometries beneath the Afar Depression, Ethiopia from Teleseismic Receiver Functions: The Anisotropic H-K Stacking Technique. *Geochem. Geophys. Geosyst.* 15, 1316–1332. doi:10.1002/2013gc005186

Hammond, J. O. S., Kendall, J. M., Stuart, G., Keir, D., Ebinger, C., Ayele, A., et al. (2011). The Nature of the Crust beneath the Afar Triple junction: Evidence from Receiver Functions. *Geochem. Geophys. Geosyst.* 12, 1–24. doi:10.1029/2011gc003738

Herrmann, R. B., and Ammon, C. J. (2004). *Surface Waves, Receiver Functions and Crustal Structure, Computer Programs in Seismology* Version 3.30. Saint Louis, MO: Saint Louis University.

Hübert, J., Whaler, K., and Fisseha, S. (2018). The Electrical Structure of the Central Main Ethiopian Rift as Imaged by Magnetotellurics: Implications for Magma Storage and Pathways. *J. Geophys. Res.* 123, 6019–6032. doi:10.1029/2017jb015160

Keir, D., Hamling, I. J., Ayele, A., Calais, E., Ebinger, C., Wright, T., et al. (2009). Evidence for Focused Magmatic Accretion at Segment Centers from Lateral dike Injections Captured beneath the Red Sea Rift in Afar. *The Geol. Soc. America* 37, 59–62. doi:10.1130/g25147a.1

Kendall, J. M., Stuart, G., Ebinger, C., Bastow, I., and Keir, D. (2005). Magma-assisted Rifting in Ethiopia. *Nature* 433, 146–148. doi:10.1038/nature03161

Kennett, B. L. N., Engdah, E. R., and Buland, R. (1995). Constraints on Seismic Velocities in the Earth from Traveltimes. *Geophys. J. Int.* 122, 108–124. doi:10.1111/j.1365-246x.1995.tb03540.x

Keranen, K. M., Klemperer, S. L., and Gloaguen, R. (2004). Three-dimensional Seismic Imaging of a Proto-ridge axis in the Main Ethiopian Rift. *Geology* 32, 949–952. doi:10.1130/g20737.1

Keranen, K. M., Klemperer, S. L., Julia, J., Lawrence, J. F., and Nyblade, A. A. (2009). Low Lower Crustal Velocity across Ethiopia: Is the Main Ethiopian Rift a Narrow Rift in a Hot Craton. *Geochem. Geophys. Geosystems* 10 (5), n/a. doi:10.1029/2008GC002293

Kibret, B. A., Ayele, A., and Keir, D. (2019). Crustal Thickness Estimates beneath Four Seismic Stations in Ethiopia Inferred from P-Wave Receiver Function Studies. *J. Afr. Earth Sci.* 150, 264–271. doi:10.1016/j.jafrearsci.2018.11.005

Kiknchi, M., and Kanamori, H. (1982). Inversion of Complex Body Waves. *Bull. Seismol. Soc. Am.* 72, 491–506.

Kim, S., Nyblade, A. A., Rhie, J., Baag, C. E., and Kang, T. S. (2012). Crustal S-Wave Velocity Structure of the Main Ethiopian Rift from Ambient Noise Tomography. *Geophys. J. Int.* 191 (2), 865–878. doi:10.1111/j.1365-246x.2012.05664.x

Langston, C. A. (1979). Structure under Mount Rainier, Washington, Inferred from Teleseismic Body Waves. *J. Geophys. Res. Solid Earth* 84 (B9), 4749–4762. doi:10.1029/JB084iB09p04749

Last, R. J., Nyblade, A. A., and Langston, C. A. (1997). Crustal Structure of the East African Plateau from Receiver Functions and Rayleigh Wave Phase Velocities. *J. Geophys. Res.* 102 (24), 469483–470424. doi:10.1029/97jb02156

Lavayssière, A., Greenfield, T., Keir, D., Ayele, A., and Kendall, J. (2019). Local Seismicity Near the Actively Deforming Corbetti Volcano in the Main Ethiopian Rift. *J. Volcanology Geothermal Res.* 381, 227–237. doi:10.5194/egusphere-egu2020-21585

Ligorria, J. P., and Ammon, C. (1999). Iterative Deconvolution and Receiver Function Estimation. *Bull. Seismol. Soc. Am.* 89, 1395–1400. doi:10.1785/bssa0890051395

Liu, H., and Niu, F. (2012). Estimating Crustal Seismic Anisotropy with a Joint Analysis of Radial and Transverse Receiver Function Data. *Geophys. J. Int.* 188, 144–164. doi:10.1111/j.1365-246x.2011.05249.x

Mackenzie, G., Thybo, H., and Maguire, P. (2005). Crustal Velocity Structure across the Main Ethiopian Rift: Results from Two-Dimensional Wide-Angle Seismic Modelling. *Geophys. J. Int.* 162, 994–106. doi:10.1111/j.1365-246x.2005.02710.x

Maguire, P., Keller, R., Klemperer, S., Mackenzie, G. D., Keranen, K., Harder, S., et al. (2006). Crustal Structure of the Northern Main Ethiopian Rift from the EAGLE Controlled Source Survey; a Snapshot of Incipient Lithospheric Break-Up. *Geol. Soc. Spec. Publ.* 259, 269–292. doi:10.1144/gsl.sp.2006.259.01.21

Mahatsente, R., Jentzsch, G., and Jahr, T. (1999). Crustal Structure of the Main Ethiopian Rift from Gravity Data: 3-dimensional Modeling. *Tectonophysics* 313, 363–382. doi:10.1016/s0040-1951(99)00213-9

Niu, F., and James, D. E. (2002). Fine Structure of the Lowermost Crust beneath the Kaapvaal Craton and its Implications for Crustal Formation and Evolution. *Earth Planet. Sci. Lett.* 200, 121–130. doi:10.1016/s0012-821x(02)00584-8

Ogden, C. S., Bastow, I. D., Gilligan, A., and Rondenay, S. (2019). A Reappraisal of the H–κ Stacking Technique: Implications for Global Crustal Structure. *Geophys. J. Int.* 219, 1491–1513. doi:10.1093/gji/ggz364

Paulatto, M., Annen, C., Henstock, T. J., Kiddle, E., Minshull, T. A., Sparks, R. S. J., et al. (2012). Magma Chamber Properties Fromintegrated Seismic Tomography and thermal Modeling at Montserrat. *Geochem. Geophys. Geosyst.* 13, 1–18. doi:10.1029/2011gc003892

Paulatto, M., Minshull, T. A., Baptie, B., Dean, S., Hammond, J. O. S., Henstock, T., et al. (2010). Upper Crustal Structure of an Active Volcano from Refraction/reflection Tomography, Montserrat, Lesser Antilles. *Geophys. J. Int.* 180 (2), 685–696. doi:10.1111/j.1365-246x.2009.04445.x

Paulatto, M., Moorkamp, M., Hautmann, S., Hooft, E., Morgan, J. V., and Sparks, R. S. J. (2019). Vertically Extensive Magma Reservoir Revealed from Joint Inversion and Quantitative Interpretation of Seismic and Gravity Data. *J. Geophys. Res.* 124 (11), 170–111. doi:10.1029/2019jb018476

Ping, D., Jiatian, L., Xiaoqing, Z., and Jia, L. (2009). "A New Interpolation Model of Convex Hull in Delaunay Triangulation," in International Symposium on Spatial Analysis, Spatial-Temporal Data Modeling, and Data Mining, Wuhan, China, October 13–14, 2009 (Wuhan, China: SPIE), 7492 1–9. doi:10.1117/12.838405

Rooney, T. O., Bastow, I. D., Keir, D., Mazzarini, F., Movsesian, E., Grosfils, E., et al. (2014). The Protracted Development of Focused Magmatic Intrusion during continental Rifting. *Tectonics* 33, 875–897. doi:10.1002/2013tc003514

Roninson, E. A. (1982). A Historical Perspective of Spectrum Estimation. *Proceedings of the IEEE* 70, 885–907.

Sembroni, A., Faccenna, C., Becker, T. W., Molin, P., and Abebe, B. (2016). Long-Term, Deep-Mantle Support of the Ethiopia-Yemen Plateau. *Tectonics* 35, 469–488. doi:10.1002/2015tc004000

Stuart, G., Bastow, I. D., and Ebinger, C. J. (2006). Crustal Structure of the Northern Main Ethiopian Rift from Receiver Function Studies. *Geol. Soc. Lond. Spec. Publications* 259, 253–267. doi:10.1144/gsl.sp.2006.259.01.20

Thompson, D. A., Bastow, I. D., Helffrich, G., Kendall, J. M., Wookey, J., Snyder, D. B., et al. (2010). Precambrian Crustal Evolution: Seismic Constraints from the Canadian Shield. *Earth Planet. Sci. Lett.* 297 (3-4), 655–666. doi:10.1016/j.epsl.2010.07.021

Thybo, H., Youssof, M., and Artemieva, I. M. (2019). Southern Africa Crustal Anisotropy Reveals Coupled Crust-Mantle Evolution for over 2 Billion Years. *Nat. Commun.* 10, 1–10. doi:10.1038/s41467-019-13267-2

Tiberi, C., Ebinger, C., Ballu, V., Stuart, G., and Oluma, B. (2005). Inverse Models of Gravity Data from the Red Sea–Aden–East African Rifts Triple junction Zone. *Geophys. J. Int.* 163 (2), 775–787. doi:10.1111/j.1365-246x.2005.02736.x

Wessel, P., Luis, J. F., Uieda, L., Scharroo, R., Wobbe, F., Smith, W. H. F., et al. (2019). The Generic Mapping Tools Version 6. *Geochem. Geophys. Geosystems* 20, 1–9. doi:10.1029/2019gc008515

Whaler, K., and Hautot, S. (2006). The Electrical Resistivity Structure of the Crust beneath the Northern Ethiopian Rift. *Geol. Soc. Lond. Spec. Publications* 251, 293–305. doi:10.1144/gsl.sp.2006.259.01.22

Woldegabriel, G., Aronson, J., and Walter, R. (1990). Geology, Geochronology, and Rift basin Development in the central Sector of the Main Ethiopia Rift. *Geol. Soc. America Bull. - GEOL SOC AMER BULL* 102, 439–458. doi:10.1130/0016-7606(1990)102<0439:ggarbd>2.3.co;2

Wolfenden, E., Ebinger, C., Yirgu, G., Deino, A., and Ayalew, D. (2004). Evolution of the Northern Main Ethiopian Rift: Birth of a Triple junction. *Earth Planet. Sci. Lett.* 224, 213–228. doi:10.1016/j.epsl.2004.04.022

Yilmaz, Ö. (2001). Seismic Data Analysis: Processing, Inversion, and Interpretation of Seismic Data. *Society of Exploration Geophysicists*. Tulsa.

Youssof, M., Thybo, H., Artemieva, I. M., and Levander, A. (2013). Moho Depth and Crustal Composition in the Southern Africa. *Tectonophysics* 609, 267–287. doi:10.1016/j.tecto.2013.09.001

Youssof, M., Thybo, H., Artemieva, I. M., and Levander, A. (2015). Upper Mantle Structure beneath Southern African Cratons from Seismic Finite-Frequency P- and S-Body Wave Tomography. *Earth Planet. Sci. Lett.* 420, 174–186. doi:10.1016/j.epsl.2015.01.034

Zandt, G., and Ammon, C. J. (1995). Continental Crustal Composition Constrained by Measurements of Crustal Poisson's Ratio. *Nature* 374, 152–154. doi:10.1038/374152a0

Zhu, L., and Kanamori, H. (2000). Moho Depth Variation in Southern California from Teleseismic Receiver Functions. *J. Geophys. Res. Solid Earth* 105 (B2), 2969–2980. doi:10.1029/1999JB900322

Conflict of Interest: The authors declare that the research was conducted in the absence of any commercial or financial relationships that could be construed as a potential conflict of interest.

Publisher's Note: All claims expressed in this article are solely those of the authors and do not necessarily represent those of their affiliated organizations, or those of the publisher, the editors, and the reviewers. Any product that may be evaluated in this article, or claim that may be made by its manufacturer, is not guaranteed nor endorsed by the publisher.

frontiers | Frontiers in Earth Science

ORIGINAL RESEARCH
published: 07 April 2022
doi: 10.3389/feart.2022.846389

Under-Displaced Normal Faults: Strain Accommodation Along an Early-Stage Rift-Bounding Fault in the Southern Malawi Rift

Oyewande O. Ojo[1], Leonard O. Ohenhen[2], Folarin Kolawole[3,4], Steven G. Johnson[1], Patrick R. Chindandali[5], Estella A. Atekwana[6] and Daniel A. Laó-Dávila[1]*

[1]Boone Pickens School of Geology, Oklahoma State University, Stillwater, OK, United States, [2]Department of Geosciences, Virginia Tech, Blacksburg, VA, United States, [3]BP America, Houston, TX, United States, [4]Lamont-Doherty Earth Observatory, Columbia University, Palisades, NY, United States, [5]Geological Survey Department, Zomba, Malawi, [6]Department of Earth and Planetary Sciences, University of California, Davis, Davis, CA, United States

One of the fundamental problems in continental rift segmentation and propagation is how strain is accommodated along large rift-bounding faults (border faults) since the segmentation of propagating border faults control the expression of rift zones, syn-rift depo-centers, and long-term basin evolution. In the Southern Malawi Rift, where previous studies on the early-stage rifting only assessed border fault structure from surficial and topographic expression, we integrate surface and subsurface data to investigate border fault segmentation, linkage, and growth as proxies for strain accommodation along the Bilila-Mtakataka Fault (BMF) System. We used 30 m-resolution topographic relief maps, electrical resistivity tomography (ERT), and high-resolution aeromagnetic data to characterize the detailed fault geometry and provide a more robust estimate of along-fault displacement distribution. Our results reveal a discrepancy between sub-aerial segmentation of the BMF geometry (six segments), scarp height (five segments) reflecting the most recent episodes of fault offset, and cumulative throw (three composite segments) reflecting the long-term fault offset. We also observe that although the BMF exhibits continuity of sub-aerial scarps along its length, the throw distribution shows a higher estimate at the Northern-to-Central segment relay zone (423 m absolute, 364 m moving median) compared to the Central-to-Southern segment relay zone (371 m absolute, 297 m moving median). The ERT profiles across the relay zones suggest a shallower basement and a possible canyon-mouth alluvial fan stratigraphy at the Central-to-Southern segment relay zone, contrasting the deeper basement and "simpler" electrical stratigraphy at the Northern-to-Central relay. The results suggest a more complex long-term evolution of the BMF than was assumed in previous studies. A comparison of BMF's maximum displacement-vs-length with those of other Malawi Rift border faults and global normal fault populations suggest that although the BMF has possibly reached its maximum length, it remains largely under-displaced as its 580–837 m maximum displacement is significantly lower than that of faults of equivalent length. We suggest that the BMF may continue to accrue significant strain as tectonic extension progresses in the Southern Malawi Rift, thus posing a major seismic hazard in the region.

Keywords: strain accommodation, normal faults, early-stage rift-bounding fault, bilila-mtakataka fault, under-displaced normal faults, fault scarp height, fault segmentation and growth

OPEN ACCESS

Edited by:
James D. Muirhead, The University of Auckland, New Zealand

Reviewed by:
Chris Elders, Curtin University, Australia
Craig Magee, University of Leeds, United Kingdom
Carolina Pagli, University of Pisa, Italy

****Correspondence:***
Oyewande O. Ojo
oyewande.ojo@okstate.edu

Specialty section:
This article was submitted to Structural Geology and Tectonics, a section of the journal Frontiers in Earth Science

Received: *31 December 2021*
Accepted: *15 March 2022*
Published: *07 April 2022*

Citation:
Ojo OO, Ohenhen LO, Kolawole F, Johnson SG, Chindandali PR, Atekwana EA and Laó-Dávila DA (2022) Under-Displaced Normal Faults: Strain Accommodation Along an Early-Stage Rift-Bounding Fault in the Southern Malawi Rift. Front. Earth Sci. 10:846389. doi: 10.3389/feart.2022.846389

1 INTRODUCTION

Normal faults grow as tectonic extension causes them to slip. During continental rifting, normal faults grow by strain accommodation leading to the progressive evolution of their associated rift basins (Calais et al., 2008; Nixon et al., 2016; Muirhead et al., 2019). Strain accommodation, strain transfer, and deformational styles in early-stage continental rifts are often influenced by regional tectonics, stress orientation, lateral variation in crustal stretching rates, pre-existing basement structures, lithology, magmatism, and lithosphere rheology (e.g., Nixon et al., 2016; Peacock et al., 2017; Muirhead et al., 2019; Rotevatn et al., 2019; Wright et al., 2020; Kolawole et al., 2021a; Gouiza and Naliboff, 2021). During continental extension, strain is accommodated by crustal deformation in the form of rift faulting, and the distribution and pattern of faulting can be quantified from a series of structural and tectonic attributes associated with fault growth (Bonini et al., 2005). These attributes include the younging direction of the border faults (Abbate and Sagri, 1980; WoldeGabriel et al., 1990; 2016), the changes in border fault length and the elastic thickness of the lithosphere (Hayward and Ebinger, 1996), lateral variation in ages of syn-rift deposits (Maguire et al., 2003; Furman et al., 2004), and lateral migration of magmatic activity (Zanettin et al., 1979).

In rift basins, upper crustal extension is accommodated by two groups of fault systems: border faults and intra-rift faults (e.g., Corti, 2009). The border faults are the largest faults bounding a rift segment and often accommodate the most offset, whereas intra-rift faults are the smaller faults that are found within the inner depressions of rift basins (Scholz and Contreras, 1998; Goldsworthy and Jackson, 2001; Ebinger, 2005; Corti, 2009; Muirhead et al., 2019). However, the new and recent 2015 multidisciplinary Study of Extension and maGmatism in Malawi and Tanzania (SEGMeNT) project provided seismic data data over Lake Malawi that show some very long intra rift faults with large throws of several km, even larger than the throw of some border faults in Southern Malawi Rift (Scholz et al., 2020; Shillington et al., 2016; 2020).

Large normal faults typically develop by an initial nucleation of isolated segments, which progressively propagate and link up with one another. The interaction and linkage of adjacent propagating fault segments typically create structurally complex areas, referred to as "strain transfer zones" or "relay zones" (e.g., Morley et al., 1990; Morley, 1999; Jackson and Rotevatn, 2013; Childs et al., 2017). These relay zones accommodate the along- and across-axis variations in the magnitude of subsidence of grabens and the elevation of uplifted rift flanks or normal fault footwall blocks (Rosendahl, 1987; Morley et al., 1990; Faulds and Varga, 1998; Morley, 1999).

There exists an empirical relationship between fault length and displacement, which provides insight into the mechanics of fault growth. It presents a useful tool for characterizing the extent and rates of tectonic deformation in continental rift zones (Bergen and Shaw, 2010). Scaling laws of maximum displacement versus fault length exhibit a power-law relationship (e.g., Walsh and Watterson, 1988; Peacock and Sanderson, 1991; Cowie and Scholz, 1992a; Cowie and Scholz, 1992b; Dawers et al., 1993; Manighetti et al., 2001). Normal fault propagation models suggest that faults grow along fault tips, and that there is a proportional increase in the length of the fault and maximum displacement throughout the slip history of the fault ("propagating fault model", e.g., Walsh and Watterson, 1988; Dawers et al., 1993; Cartwright et al., 1995; Walsh et al., 2003). Another model ("constant-length model") suggest that the total length of the fault is attained early in the fault history and that most displacement is accumulated after the total length has been established (Walsh et al., 2003; Nicol et al., 2005; Densmore et al., 2007; Schlagenhauf et al., 2008; Jackson and Rotevatn, 2013; Nixon et al., 2016). Rotevatn et al. (2019) proposed a hybrid fault growth model which suggests that normal faults initially grow by lateral propagation in the early stages of the fault lifespan (20–30% of the fault lifespan) to establish the total length of the fault, then, subsequently grow by constant-length model for the rest of the fault lifespan (70–80% of the fault lifespan). Also, recent numerical models by Pan et al. (2020) revealed that normal fault arrays evolve *via* alternating phases of fault-lengthening and localization. However, the process of strain accommodation by normal fault growth during the early stages of continental extension remains incompletely understood. Since the segments of important rift faults are often established during early-stage rifting, this knowledge-gap limits the complete understanding of the processes that govern the variation of structural architecture along margins of continental break-up.

In this contribution, we investigate the detailed structure and distribution of displacement along the Bilila-Mtakataka Fault (BMF), an active border fault in the Southern Malawi Rift, East Africa (**Figures 1A–C**), to understand the pattern of fault growth and strain accommodation in areas of early-stage continental extension. This fault is suggested to be seismogenic and may have hosted the M 6.2 earthquake, 9 km NNW of Salima, Malawi at a depth of about 30.3 km (from USGS earthquake hazard program). In addition, the results of the study provide insight into the seismic hazard of large rift-bounding normal faults.

1.1 Geologic and Tectonic Setting of the Malawi Rift

Eastern Africa has witnessed three phases of tectonic extension during the Phanerozoic. The East African Rift System (EARS) represents the third and currently active phase of extension which began in the Oligocene (Delvaux, 1991; Ebinger and Scholz, 2011; Roberts et al., 2012; Ebinger et al., 2019). The ~750 km-long N-S trending Malawi rift represents a prominent segment of the EARS (Ebinger et al., 1987; Ebinger et al., 1989), and is located near the southern tip of the magma-poor western branch of the rift system (**Figures 1A,B**). The Malawi Rift is sub-divided into eight distinct 100–150 km-long grabens and half grabens which exhibit alternating polarities along-strike (Laó-Dávila et al., 2015). Using a complete dataset that incorporated seismic imaging across Lake Malawi and estimation of fault throws and displacements, Scholz et al. (2020) provide an alternative

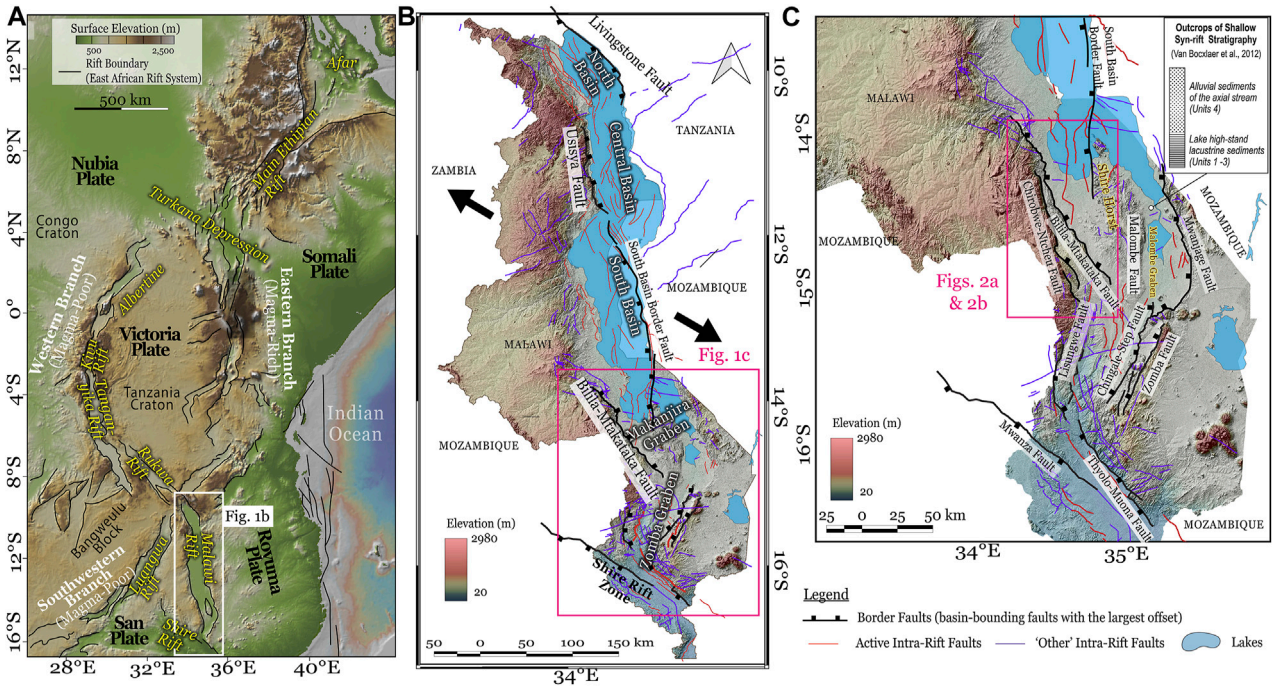

FIGURE 1 | (A) Simplified tectonic map of the East African Rift systems (EARS). Topographic relief basemap is obtained from GeoMapApp (Ryan et al., 2009), **(B)** Digital elevation model (DEM) hillshade map of the study area highlighting the surface topography, faults, and sub-basins along the Malawi Rift, **(C)** DEM hillshade map covering the southern Malawi showing structures in both the Southern Malawi Rift and the Shire Rift Zone further south. The fault traces are obtained from Malawi Rift's fault database in Williams et al. (2021). The inset shows the shallow syn-rift sediments revealed in outcrops of the Chipalamawamba Beds along the Malombe Graben (Van Bocxlaer et al., 2012).

and simpler structural framework than Laó-Dávila et al. (2015) for the Malawi Rift where only three main segments are presented. To the north, the northernmost graben, the "Karonga" or North Basin terminates at the Rungwe Volcanic Province, whereas, the southernmost graben of the Malawi Rift is defined by the Zomba Graben which terminates at a zone of exposed basement extending into the Shire Rift Zone (Kolawole et al., 2021b).

Although the Malawi Rift largely developed during the Cenozoic evolution of the EARS, it is proposed to have propagated southwards based on: 1) the extensive outcrops of Cenozoic syn-rift sequences in the northern basins of the rift which are absent in the south (Delvaux, 2001), and southward thinning of the syn-rift sedimentary cover (Specht and Rosendahl, 1989; Flannery and Rosendahl, 1990), and 2) southward decrease in the throw of border faults with corresponding changes in the seismic depositional facies of the syn-rift sequences (Scholz et al., 2020). However, it is also plausible that the initiation of Cenozoic rifting across the entire length of the Malawi Rift could have been synchronous and that rifting occurs at different rates along the rift length (Ojo et al., 2021). Overall, crustal stretching rates decrease from north (4.5 mm yr^{-1}) to south 1.3 mm yr^{-1} (Stamps et al., 2008; 2018; 2021). The major graben and some associated major border faults in the Southern Malawi Rift are the Makanjira Graben (Bilila-Mtakataka and Malombe faults), and the Zomba Graben (Zomba and Lisungwe faults).

1.2 The Bilila-Mtakataka Fault

The Bilila-Mtakataka Fault (BMF) is one of the most prominent rift-bounding faults in Southern Malawi Rift, characterized by a steep, clean fault scarp of about 4–15 m height, and was first highlighted in Walshaw (1965) and Dawson and Kirkpatrick (1968) based on its clear topographic expression in topographic relief maps (**Figures 2A–E**) and in the field (**Figures 2F,G**). Although the fault has been estimated to be an outstanding >100 km-long continuous normal fault scarp (Jackson and Blenkinsop, 1997; Hodge et al., 2018), the subsurface structure of the fault remains unknown. Based on the large length of the BMF, Jackson and Blenkinsop (1997) proposed the possible control of a thick seismogenic layer on the fault evolution. The BMF is suggested to have developed within a strong lithosphere with an effective elastic thickness of about 30 km (Jackson and Blenkinsop, 1993).

The surficial geomorphology of the BMF comprises a metamorphic basement that is composed of fractured and weathered basement rock at near-surface but still intact at depth. It is also made up of a deeper fresh basement, above which the syn-rift sediments accumulate in the hanging wall of the BMF. The sediments are primarily alluvial sediments with colluvial lobes confined to the foot of the fault escarpment (Walshaw, 1965). The sedimentary basin in the hanging wall is a fluvio-lacustrine depositional environment with occasional sediment inundation from 100-year cycles of over-flooding events in Lake Malawi (Dulanya et al., 2014; Dulanya, 2017).

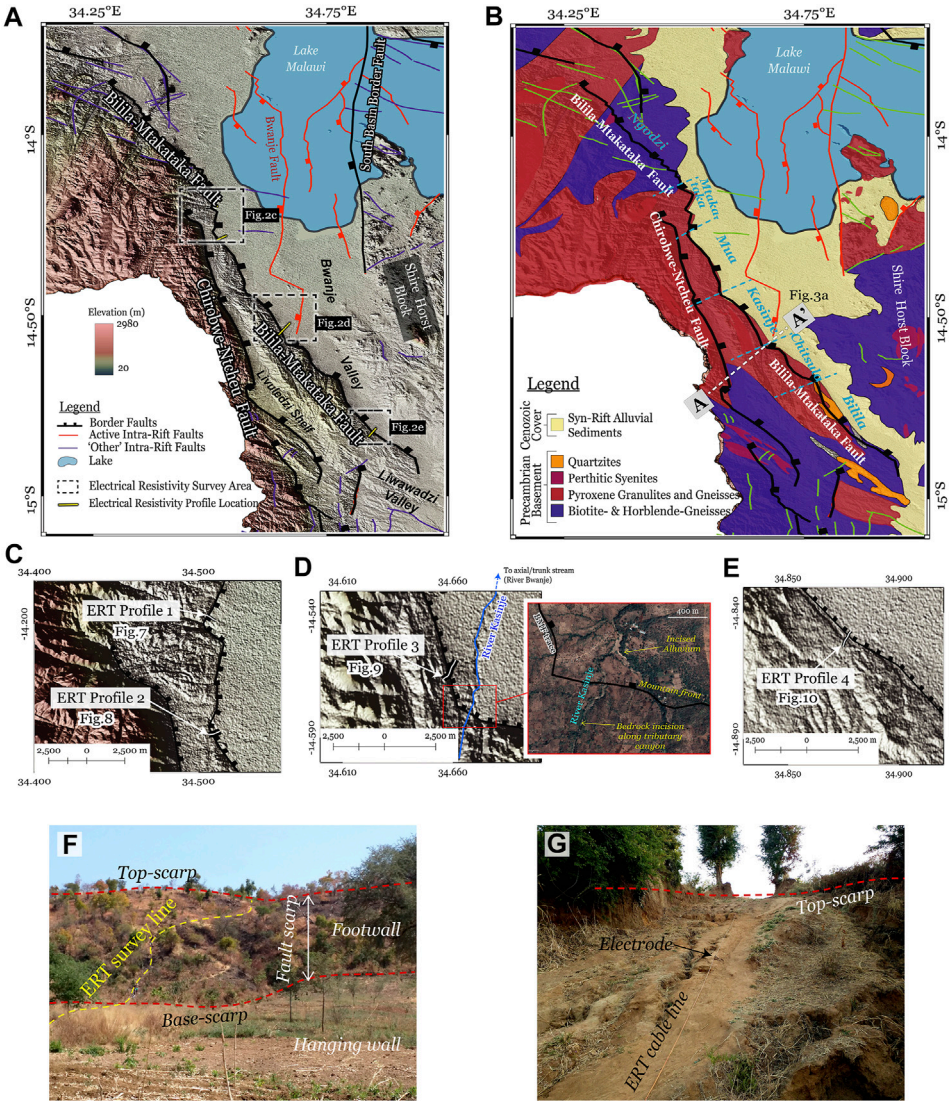

FIGURE 2 | (A) Hillshade map of the study area highlighting the surface topography across the Bilila-Mtakataka Fault (BMF) **(B)** Simplified geologic map of the study area along the BMF showing the major border showing the various lithologic units and BMF and CNF fault traces (BMF—Bilila—Mtakataka Fault; CNF—Chirobwe—Ntcheu Fault) **(C–E)** Electrical resistivity profiles across the BMF; **(C)** shows the location of electrical resistivity (ERT) Profiles 1 and 2; **(D)** shows Profile 3, and **(E)** shows the location of Profile 4. **(D)** Inset: Google Earth© image showing the modern sedimentary geomorphological features in the vicinity of ERT profile 3. **(F,G)** Field photographs of the deployment and acquisition of ERT profiles across the surface escarpment of the BMF.

The fluvio-lacustrine depositional environment is due to several transverse cutting streams that originate from the elevated footwall areas (e.g., Nsipe-Livelezi Shelf watershed) and flow downslope, across the BMF escarpment into the basin where they either empty into Lake Malawi or join the Bwanje River which is the prominent axial stream draining the Makanjira Sub-basin (**Figure 2D**). The northward-flowing Bwanje River originates from a watershed in an elevated area near Balaka that marks the southern tip of the BMF, separating the Bwanje valley in the Makajinra Trough from the Liwawadzi Valley in Zomba Graben to the south (Walshaw, 1965).

Hodge et al. (2018) investigated the sub-aerial map-view geometry of the BMF trace and controls of basement fabrics using high-resolution satellite topography data and field measurements. Based on the map-view along-trend changes in fault geometry and the along-fault distribution of vertical surface separation, six segments were identified. These segments consist of Ngodzi, Mtakataka, Mua, Kasinje, Chitsulo, and Bilila geometrical segments. The BMF was suggested to have a scarp height distribution that is likely influenced by the map-view fault geometry, and that the fault geometry developed as an exploitation of the local metamorphic foliations (Hodge et al., 2018; 2019). In this contribution, we describe the surface expression of the sub-aerial BMF trace as a representation of its map-view geometrical segmentation, using the names given by Hodge et al. (2018).

2 METHODOLOGY

In this study, we integrate topographic analysis with geophysical imaging of the subsurface structure along the Bilila-Mtakataka Fault (BMF). We obtain along-fault scarp height and footwall height measurements from one arc-second (30 m spatial resolution) Shuttle Radar Topography Mission (SRTM) elevation data. Scarp height provides the sub-aerial component of recent fault throw, and footwall height provides a measure of sub-aerial component of long-term cumulative fault throw. We utilize aeromagnetic transform techniques to generate a depth-to-magnetic basement map which provides estimates of the subsurface component of long-term cumulative fault throw.

Our sampling points from both the SRTM topographic data and aeromagnetic depth-to-basement are approximately the same along the entire trace length of the fault. At each sample point, the estimated throw represents its relative value across a fault surface, i.e., relative to depth, or its maximum value (Tao and Alves, 2019). Profiles were taken perpendicularly across the fault at every 1 km because the sampling interval/fault length ratio (δ) has to be <0.05 for adequate resolution and to avoid loss of vital information. The $\delta = 0.05$ threshold value is recommended for faults of any scale and profiles should be taken at intervals that are <5% of the total length of fault if they are believed to be segmented (Tao and Alves, 2019). We utilize Electrical Resistivity Tomography (ERT) to investigate the fault zone and assess the lateral variation of local hanging wall stratigraphic architecture along the trend of the fault.

2.1 Scarp and Footwall Height Measurements From Digital Elevation Models

The fault scarp indicates the most recent slip along a normal fault. The scarp heights were extracted and measured from a 30-m resolution Shuttle Radar Topography Mission (SRTM)-Digital Elevation Model (DEM). Fault scarps were outlined and traced from a hillshade map created on QGIS using the SRTM-DEM. The scarp height (h) is the vertical distance of the steepest slope along the local footwall elevation. The vertical distance of the local footwall slope is the local footwall elevation, i.e., the top of the local footwall slope to the top of the local hanging wall within which the fault scarp is hosted (h'; Caskey, 1995; Hornsby et al., 2020). We measured the vertical distance of the footwall between the steepest points along the fault scarps (as shown in **Figure 3**). The scarp heights and local footwall heights were measured and plotted against fault length to produce a displacement-length relationship. The methodology adopted in this study accounts for variables such as ancient topography, weathering and erosion, and structural irregularities due to the subjective nature of this process and observed irregularities along the fault trace. Our measurements are likely to be underestimated as the escarpment continues up to a higher elevation, however, since it is difficult to constrain the component of paleotopography in the footwall elevation, we take a conservative approach.

We note that the method of scarp height measurement adopted in this study is different from the methodology used by Hodge et al. (2018; 2019) which adopted a semi-automated approach for extraction of relief height from satellite topography data. Their study measured the "vertical separation" as an estimate of fault throw rather than scarp height. Vertical separation (or surface offset) is distinguished from scarp height in literature (Bucknam and Anderson, 1979). Further, to better capture the full length of the BMF and understand the long-term fault growth, we extended our study to include the northern extents of the BMF fault trace than the extent covered in Hodge et al. (2018). Segments on the scarp height plot along the fault length were classified as part of the fault between two consecutive minima separated by the maximum point between them. Relay zones on the along-fault scarp height plot are classified as flat parts of the fault between two consecutive minima and not separated by any maximum points.

2.2 Estimation of Depth-to-Magnetic Basement From Aeromagnetic Data

To assess the along-fault distribution of subsurface components of fault throw, we estimated the depth to the top of the magnetic basement (d) in the hanging wall of the BMF using 62 m spatial resolution aeromagnetic data from Malawi. The aeromagnetic data were acquired in 2013 (source: Geological Survey Department of Malawi) with 80 m terrane clearance along NE-SW lines with a line spacing of 250 m. Since the primary and dominant magnetic source in the study area is the Precmabrian gneissic basement (**Figure 2B**), d is taken to be a measure of the depth to the crystalline basement. For our basement depth calculation, we use the Source Parameter Imaging (SPI) transform of the total magnetic intensity (TMI) anomaly grid (Blakely and Simpson, 1986; Thurston and Smith, 1997; Smith et al., 1998).

The SPI formulation assumes a step-type source in which the depth to the top of the magnetic source is an inverse of the peak value of the local wavenumber over the step source.

$$\text{SPI Depth} = 1/K_{max} \tag{1}$$

$$K = \sqrt{\left([\mathrm{dT/dx}]^2 + [\mathrm{dy/dy}]^2\right)} \tag{2}$$

$$\mathrm{T} = \tan^{-1}(\mathrm{VDR/THDR}) \tag{3}$$

$$\mathrm{VDR} = \mathrm{dM/dz} \tag{4}$$

$$\mathrm{THDR} = \sqrt{\left([\mathrm{dM/dx}]^2 + [\mathrm{dM/dy}]^2\right)} \tag{5}$$

where K_{max} is the peak value of the local wavenumber K over the step source, T is the Tilt derivative, VDR is the first vertical derivative, THDR is the total horizontal derivative, and M is the total magnetic field anomaly (TMI).

The computation of the SPI depth solutions across a TMI grid involves an initial computation of the local wavenumber from the tilt derivative, then smoothing of the wavenumber grid using a Hanning filter to reduce noise, and finally, localized peak wavenumber detection using a Blakely test (Blakely and Simpson, 1986). Finally, we extracted the values of depth-to-magnetic basement in the hanging wall at a distance of 1 km basinward from the base of the fault scarp at each scarp height

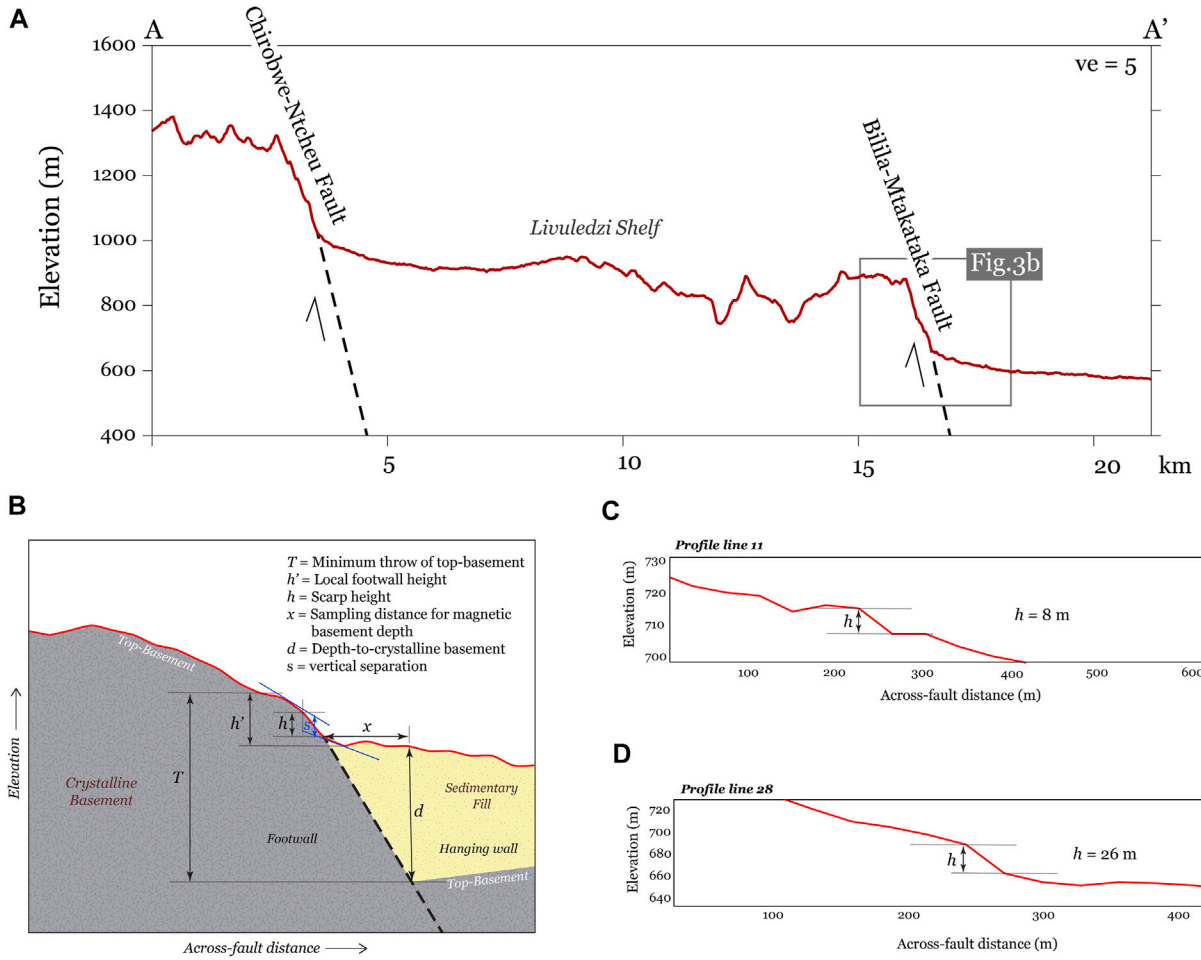

FIGURE 3 | (A) Elevation profile across the Bilila-Mtakataka and the Chirobwe-Ntcheu faults. **(B)** How the minimum throw (T) was estimated from the measured scarp height (h) and corresponding points of extraction for aeromagnetic depth to magnetic basement (d). **(C,D)** examples of scarp height measurements.

sample point (**Figure 3**). We use the 1 km extraction distance to maintain consistency, since the deepest sections near the BMF segment centers, and shallowest sections in the relay zones commonly occur within this distance from the base-scarp. The estimation of depth-to-magnetic basement from aeromagnetic data has an inferred accuracy of ±20% (Gay, 2009). Thus, we indicate an error bar of ±20% of the measurements in the depth-to-basement scatter plot.

2.3 Estimation of Cumulative Fault Throw and Maximum Displacement along the Bilila-Mtakataka Fault

Fault throw is the vertical component of fault offset between correlative footwall and hanging-wall of the fault (Muirhead et al., 2016; Tao and Alves, 2019). Thus, we estimate the cumulative fault throw as the sum total of both the surface and subsurface components of throw along the fault. To obtain the minimum throw (T) at each sample point along the BMF, we use:

$$T = h' + d \tag{6}$$

where h' is the measured local footwall height, and d is the depth-to-magnetic basement. Along-fault throw-distance plots present a view of fault segmentation which then provides insights into the complex structural evolution of the BMF in terms of its linkage and long-term growth. Therefore, the measured throws along the BMF serve as proxies for the overall displacement along the fault. However, to calculate maximum dip-displacement along the BMF fault plane D, we use dip magnitudes θ measured directly from the electrical resistivity tomography images (**section 3.4**) and the estimated maximum throw T_{max} following the relation:

$$D = T_{max}/\sin(\theta) \tag{7}$$

Based on pure normal faulting focal mechanism solutions along the BMF (Stevens et al., 2021), we assume a fault-orthogonal slip vector for the BMF. In addition, the lateral projection of clusters of microseismicity at depth beneath the BMF delineates a dip of ~42° (Stevens et al., 2021), thus expanding

the range of our estimated maximum displacement for the fault, considering the possibility of non-planarity of faults at depth. To better understand the long-term growth of the BMF, we compare its displacement-length ratio with those of other well-studied Malawi Rift border faults (Livingstone, Usisya, and South Basin border faults; **Figure 1B**). For these other border faults, we obtain estimates of their dip, sub-aerial components of throw and dip-displacement from previously published seismic reflection images along Lake Malawi, assuming a normal slip vector for the faults (Specht and Rosendahl, 1989; Scholz et al., 2020; Shillington et al., 2020). The cumulative throws and displacements for these other border faults were estimated by adding the sub-aerial components from seismic data to the surface components of the fault escarpments.

2.4 Electrical Resistivity Tomography of Fault Zone and Local Hanging Wall Stratigraphic Architecture

The BMF is composed of multiple segments as defined by surface scarp height variation and plan-view geometry (this study and Hodge et al., 2018). To characterize the local subsurface electrical structure in the hanging wall of the BMF, we acquired four 2-D electrical resistivity profiles across the segments and their relay zones (**Figure 2A**). Two of the survey profiles were acquired near the central part of two of the fault segments (ERT Profiles 1 and 4), and the other two profiles were acquired near two of the relay zones (ERT Profiles 2 and 3). The survey transects are oriented perpendicular to the fault trend, extending across the BMF fault scarp at each of the survey locations, except for a section along ERT Profile 3 which is slightly oblique to the fault trend due to land accessibility challenges in the field (**Figures 2C–E**). Along ERT Profile 3, the fault-oblique section occurs across the fault scarp, whereas the southwestern and northeastern sections of the profile are at higher angles to the fault trend (**Figure 2D**). At all the survey locations, the profiles extend from the footwall of the fault, across the top and base scarps, and terminate at a considerable distance into the hanging wall (**Figures 2F,G**).

We utilized a 10 channel Iris Syscal Pro resistivity meter with 72 electrodes and a 10 m electrode spacing along the four profiles (**Figures 2H,I**). Due to field constraints, three of the profiles (ERT Profiles 1, 2, and 4) were each 710 m-long, and the fourth (ERT Profile 3) was 1,070 m-long (acquired using roll-along sequence). Based on the ERT profile lengths, we consider that the surveys only image the fault zone and electrical stratigraphy of the local hanging wall slope of the fault. Except for ERT Profile 1 at which only the dipole-dipole array was acquired, we acquired both Wenner-Schlumberger and dipole-dipole arrays for all the profiles. The Wenner-Schlumberger array is sensitive to both horizontal and vertical structures, while the dipole-dipole array is good for mapping vertical structures (Loke, 2002).

To obtain a dense dataset with good lateral and vertical resolution, we combined the data from both array types to create a mixed array using Prosys II (Zhou, et al., 2002). Bad data points were culled using the RMS statistics based on preliminary inversion, and the final inversion model results have RMS error <10%. **Supplementary Table S1** contains the relevant details of the inversion parameters applied. The data processing and inversion were performed using RES2DINV software (Loke and Barker, 1996) using the smoothness-constrained least-squares method (Claerbout and Muir 1973; deGroot-Hedlin and Constable 1990). The least squares formulation provides a RMS (root-mean-squared) value which is the factor of discrepancy that describes the differences between the logarithms of the measured and calculated apparent resistivity values, such that the RMS error value of a model inversion is the measure of data fit for the inversion. The parameterization of the inversion carried out in our study is provided in **Supplementary Table S1** of the supplementary document. We present the results of the 2-D resistivity tomography along with plots of model sensitivity estimates.

The model sensitivity is a measure of the reliability of the inversion model (Loke, 2002). The higher the sensitivity value, the more reliable the model resistivity value and vice-versa (Loke, 2002). We defined low (less than 0.1), medium (values between 0.1 and 2.0), and high (greater than 2.0) sensitivity values for each inversion model (**Supplementary Figures S1, S2**) and used the model sensitivity to constrain the interpretation of the resistivity sections. Low-sensitivity regions are the shaded polygons in the ERT inverse models (**Figures 7–10**), and are given less weight in the interpretations.

Although there is no borehole data available in the study area to provide a strong constraint on the inversion profile interpretations, we adopt an "in-context" approach for interpretation, which relies on the tectono-geomorphic setting of the target structure (NE-dipping active normal fault with exposed basement footwall uplift; **Figure 2A**), the surface locations of the exposed crystalline basement and sedimentary cover along the survey profiles (**Figure 2B**), and the depositional environment of the basin (humid fluvio-lacustrine setting; Dulanya et al., 2014; Dulanya, 2017). Overall, the typical resistivity values for crystalline basement have a range of 1,000–100,000 Ω-m, and those of unconsolidated sedimentary deposits and weathered basement rocks range 2–1,000 Ω-m (Palacky, 1987; Minsley et al., 2010). We describe <10 Ω-m layers as low-resistivity units, ~10–600 Ω-m as low to moderate-resistivity units, and ~600 to >3,000 Ω-m as moderate-to high-resistivity units.

3 RESULTS

3.1 Along-Fault Distribution of Scarp Height (*h*) and Local Footwall Height (*h'*)

At the surface, the NW-trending BMF trace is approximately 152 km in length and exhibits plan-view geometrical (**Figure 2A**) and scarp segmentation (**Figure 4**). Based on the along-fault distribution of scarp height and local footwall height, the profiles (**Figure 4**) show that the border fault is subdivided into five scarp segments (Scarp Segments 1–5). Scarp Segment 1 is the northernmost segment along the BMF and it is 57 km long and has a maximum scarp height of 31 m and a maximum local footwall height of 61 m, which clearly contrasts the plan-view geometrical segmentation of this section of the fault (Ngodzi

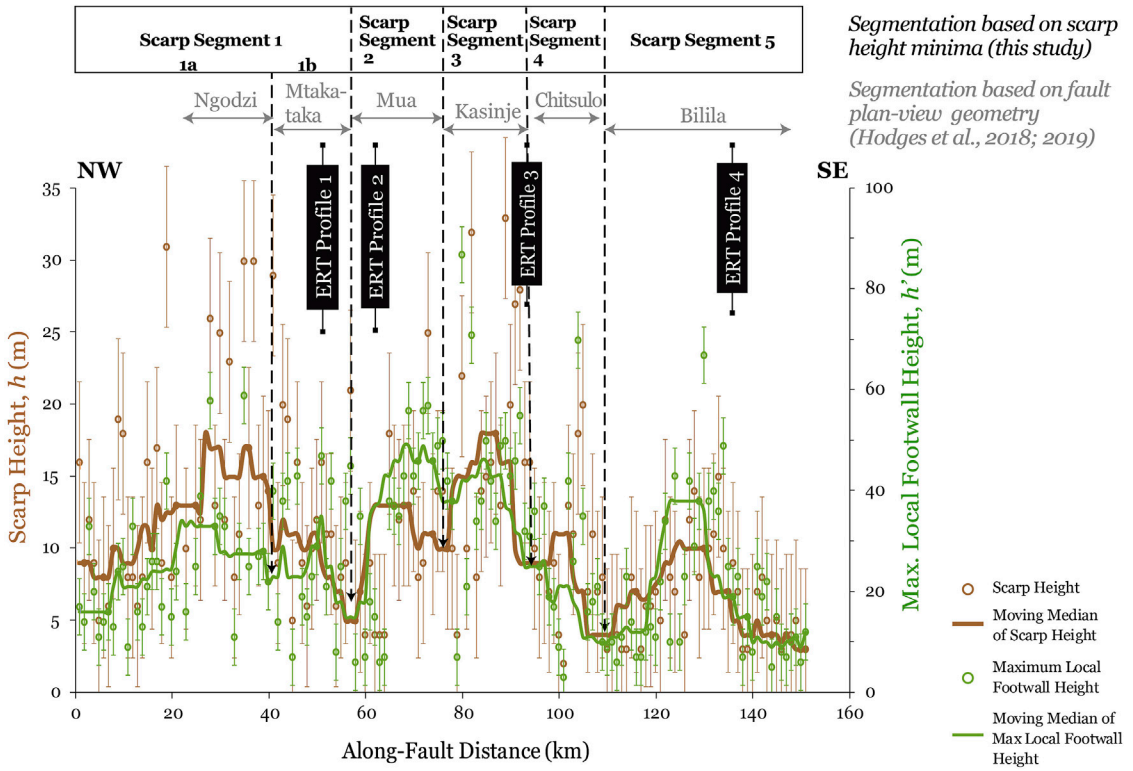

FIGURE 4 | Distribution of scarp height (*h*) and maximum local footwall elevation (*h'*) versus distance along-strike of the BMF. The "scarp segments" indicate the fault segmentation based on the scarp height minima along the moving median curve. Segmentation based on plan-view fault geometry is from Hodge et al. (2018). Dashed vertical lines show the location of the locations of the moving median minima which is consistent with the transition from one geometrical segment to another. The error bars show 5.6 m absolute error associated with SRTM-DEM in the vertical directions. Note that the vertical scales are different for scarp height and maximum footwall height plots.

and Mtakataka geometrical segments). Scarp Segment 2 is 20 km in length with a maximum scarp of 25 m and a maximum local footwall height of 56 m. Scarp Segment 3 has a length of 17 km, maximum scarp height of 33 m and maximum local footwall height of 86 m. Scarp Segment 4 which is 15 km long with 20 m of scarp height has 72 m of maximum local footwall height. To the south along the BMF, Scarp Segment 5 has a length of 43 km with scarp height of about 15 m and maximum local footwall height of about 65 m.

We note that the relay zone (zone of transition between segments) between Scarp Segments 4 and 5 shows the greatest magnitude of scarp height minima compared to the other relay zones. Also, we note that in both plan-view geometry (**Figure 2**) and scarp height distribution (**Figure 4**), the longest "continuous" segments along the BMF are the northern-most segment (Scarp Segment 1) and the southernmost segment (Scarp Segment 5). In between these two long segments, three smaller segments (Scarp Segment 2, 3 and 4) are found.

Overall, segmentation is generally consistent with the sub-aerial fault trace geometry (from Hodge et al., 2018) except for scarp height segment 1 where our scarp height does not show a pronounced minima between Ngdozi and Mtakataka segments. However, our maximum footwall height distribution shows a slight minima between Ngodzi and Mtakataka segments and based on these we subdivided scarp height segment 1 into scarp height segments 1a and 1b. The broad trends illustrated by the moving median curves suggest that these five sub-aerial segments can be grouped into three large composite segments considering the relative magnitudes of scarp height minima along the profile. These composite segments consist of a northern composite segment (includes Ngodzi and Mtakataka geometrical segments), a central composite segment (Mua, Kasinje, and Chitsulo geometrical segments), and a southern composite segment (Bilila geometrical segment). The scarp height and local footwall height plots show similar but higher magnitudes in both the northern and central composite segments and appear to gently decrease towards the southern end of the border fault system. Whereas, the maximum local footwall height shows the highest values in the central composite segment and somewhat similar magnitudes in the northern and southern composite segments.

3.2 Along-Fault Distribution of Depth-to-Basement

The calculation of depth-to-magnetic basement from the total magnetic intensity aeromagnetic grid (**Figure 5A**) using the SPI method produced a grid map of the depth solutions (**Figure 5B**). In

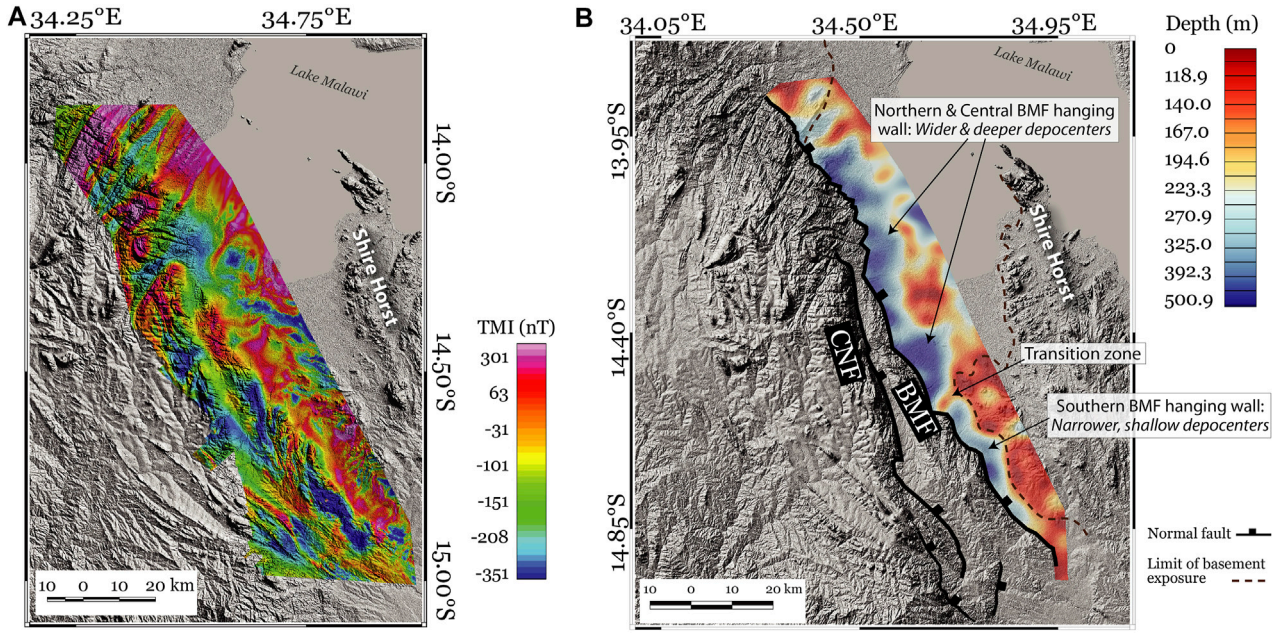

FIGURE 5 | (A) Hillshade map of the study area overlaid with the Total Magnetic Intensity (TMI) aeromagnetic grid, **(B)** Hillshade map of the study area overlaid with the grid of depth-to-basement solutions estimated from aeromagnetic data, using the Source Parameter Imaging (SPI) technique.

general, the SPI map shows <500 m basement depths which increases westward towards the BMF escarpment and shallows eastward towards the Shire Horst to the southeast and Lake Malawi to the northeast (**Figure 5B**). The shallowing of the basement is most pronounced in the southeast, along the Chitsulo and Bilila segments where the width of sediment cover in the BMF hanging wall is narrow (<7 km-wide) compared to 8–28 km-wide regions further north along the Mtakataka-to-Kasinje segments. We note the presence of a prominent narrow region of shallow basement (~120 m) that extends southwest from the Shire Horst into the relay zone between the Kasinje and Chitsula segments of the BMF (**Figure 5B**). In comparison to the other relay zones along the BMF, this relay zone exhibits the shallowest basement. In addition, the narrow region of shallow basement marks the transition from the southern BMF hanging wall region with narrow sedimentary cover to the northern BMF hanging wall region with wider sedimentary cover (**Figure 5B**).

Along the BMF, the extracted basement depth values show a distribution that roughly mimics the general trend of the maximum local footwall height (**Figure 6**). The values are highest near the center but decrease to ~180 m near the northern fault tip and ~100 m near the southern tip. We observe two prominent minima along the moving median curve: one at distance ~42 km, and the other at distance 100 km, thus delineating three large segments which are consistent with the composite segments of the scarp height fitting curve except for the Northern Segment. We refer to these large segments as the Northern Segment (extending between distance 0–40 km; 0–57 km for scarp height fitting curve), Central Segment (distance 45–100 km), and the Southern Segment (distance 105–150 km). The basement attains a maximum depth of ~460 m in the Northern Segment, ~500 m in the Central Segment, and ~460 m in the Southern Segment (**Figure 6**).

3.3 Along-Fault Distribution of Cumulative Throw, *T*

We estimated the minimum cumulative throw, *T*, at each sampling point to produce a distance-throw plot along the BMF by adding the maximum local footwall height and SPI depth-to-basement results (**Figure 6**). The fitting curve of the moving median of minimum cumulative throw shows a similar trend as those of both the depth-to-basement and maximum local footwall height, consistent with the delineation of three large segments along the BMF (**Figure 6**). Overall, the maximum *T* along the fault is ~560 m, located near the center of the entire fault system. The minimum *T* estimates are ~120 m at the southern tip of the fault and ~190 m near the northern fault tip. However, the Northern Composite Segment shows a maximum *T* of ~500 m, the Central Composite Segment ~560 m, and the Southern Composite Segment ~480 m. We consider that the smaller lobes on the throw-distance distribution plot could be data artifacts from either the SPI transform, the moving median fitting curve, or may be possibly representative of early-growth sub-segments of the fault, and that the broader lobes are more representative of the long-term fault growth.

3.4 Subsurface Electrical Resistivity Structure

In general, the ERT Profiles 1 to 4 (**Figures 7–10**) commonly show three geoelectrical layers that are truncated and offset by

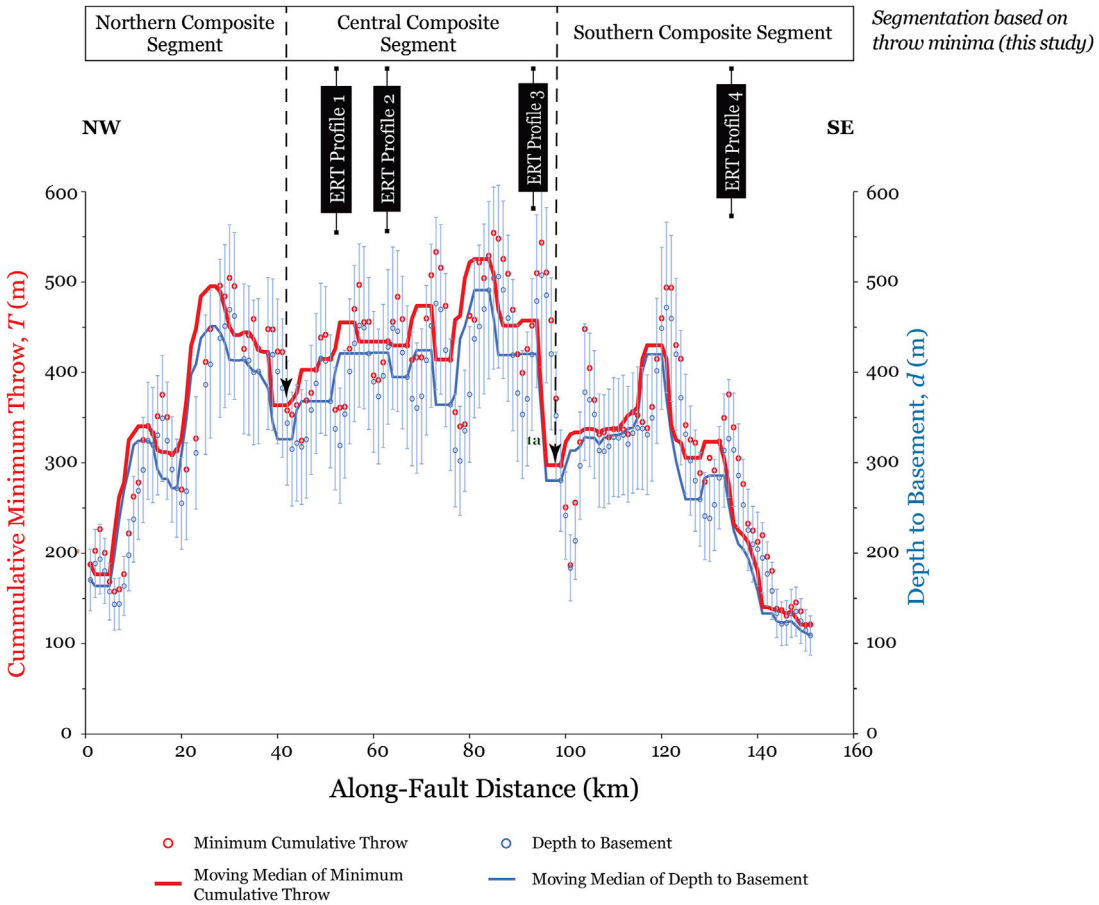

FIGURE 6 | The distribution of cumulative minimum throw estimate based on the addition of depth-to-basement, *d* and maximum local footwall height, *h'* at each sampling point along-strike of the fault trace. The error bars on the *d* data represents ±20% accuracy of depth-to-magnetic basement estimates from potential fields data (Gay, 2009), and those on the *h'* measurements is 5.6 m absolute vertical error of the Shuttle Radar Topography Mission (SRTM) DEM. The dashed lines with arrow-heads indicate the locations of throw minima delineating the large-scale relay zones (i.e., segmentation zones) along the fault.

sub-vertical discontinuities. On each profile, the most prominent among the sub-vertical discontinuities is colocated with the base of the BMF escarpment at the surface. The relative sensitivity of the inverse models is mostly composed of model blocks of medium and high sensitivities, particularly within the upper 40 m interval (**Supplementary Information S1**). Also, the regions with high resistivity values compared to the surrounding regions generally show low sensitivities (**Supplementary Information S1**).

ERT Profile 1 was acquired near the center of Scarp Segment 1 (Ngodzi) in the north-western section of the BMF (**Figure 2C**) and shows three geoelectric layers (**Figure 7**). The topmost layer is a ~10 m thick laterally-continuous layer dominated by low-to moderate-resistivity values (~10–100 Ω-m). This layer overlies a 120 m-thick layer that is dominated by generally low-resistivity zones (<10 Ω-m). The third and basal geoelectric layer appears to be a moderate-to high-resistivity layer (>1,000 Ω-m) that extends up to the near-surface in the northwestern part of all the profiles where it is confined to the footwall of the BMF escarpment. However, we note that the model sensitivity is low in the basal part of the model.

ERT Profile 2 (**Figure 8**) was acquired near the zone of segmentation (relay zone) between Scarp Segments 1 and 2 (transition from Mtakataka to Mua geometrical segments) in the northwestern section of the BMF (**Figure 2C**). The inversion model shows three geoelectrical layers with a 20–40 m-thick topmost layer dominated by ~10–300 Ω-m resistivity anomalies, which appear to mimic the electrical character of the topmost layer in ERT Profile line 1. This topmost layer is underlain by a ~100 m-thick low-resistivity (<10 Ω-m) layer, which is underlain by a basal layer of elevated resistivity values (>30 Ω-m). Similar to ERT Profile 1, the footwall of the BMF scarp is dominated by high-resistivity anomalies (>1,000 Ω-m).

ERT Profile 3 (**Figure 9**) was acquired at the relay zone in-between Scarp Segments 3 and 4 (transition from Kasinje to Citsulo geometrical segments) in the central section of the BMF (**Figure 2**). The inversion result of this profile contrasts with the other ERT profiles in that it shows a complex geoelectrical model in which the top of the basal high-resistivity layer defines a gently-dipping (not

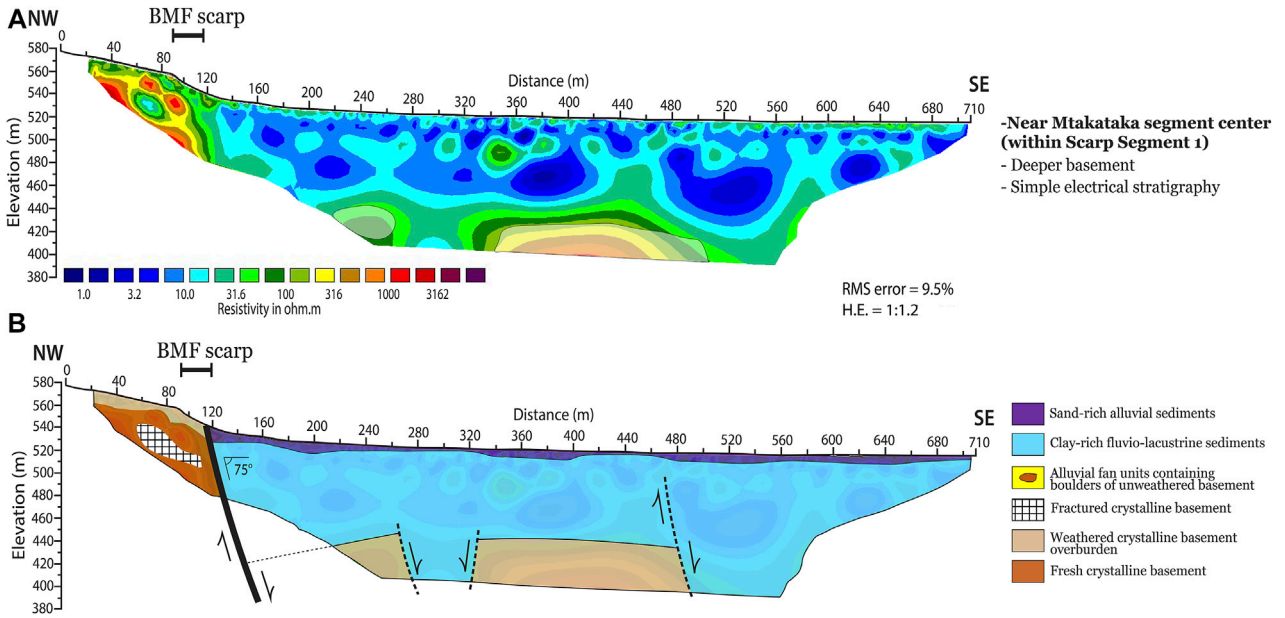

FIGURE 7 | (A) Inverse model of the ERT Profile 1 acquired near the center of Scarp Segment 1 (Ngodzi) in the north-western section of the Bilila-Mtakataka Fault (BMF) (**Figure 2C**). The white transparent polygons are areas of low model sensitivity (**Supplementary Figure S1A**). **(B)** Geologic model and interpretation of the resistivity model.

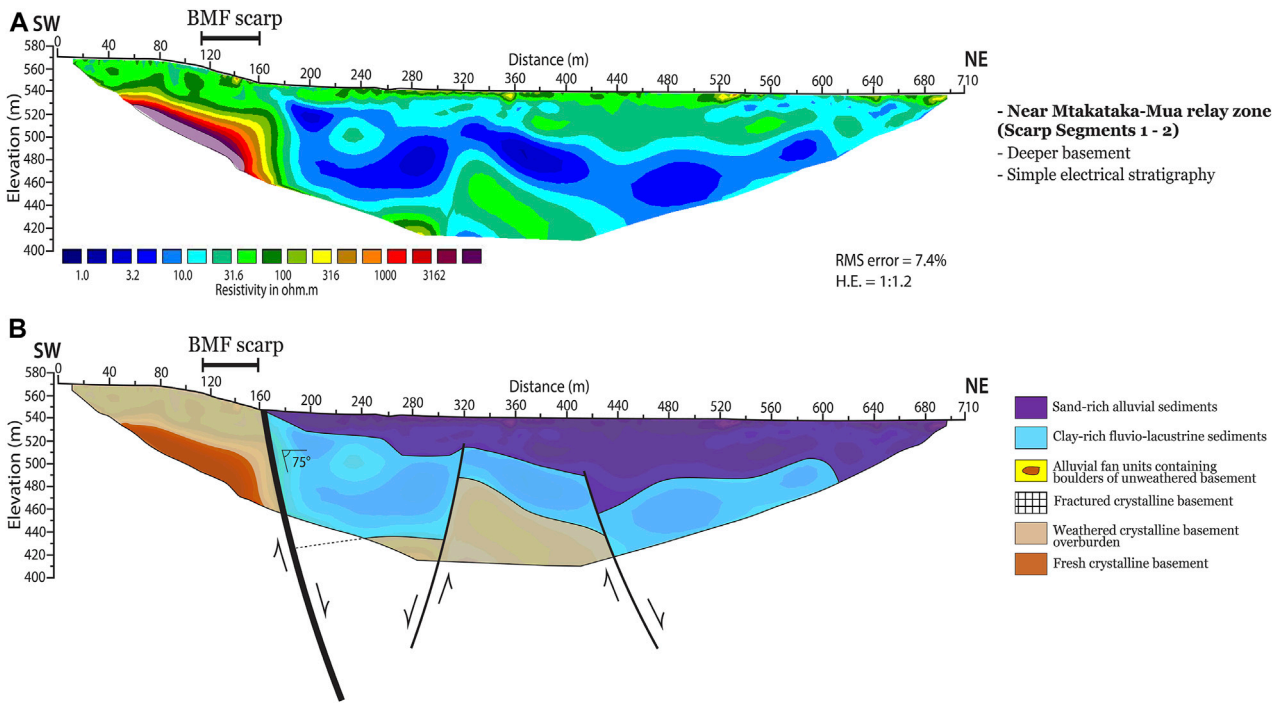

FIGURE 8 | (A) Inverse model of the ERT Profile 2 acquired near the zone of segmentation (relay zone) between Scarp Segments 1 and 2 (transition from Mtakataka to Mua geometrical segments) in the northwestern section of the Bilila-Mtakataka Fault (BMF) (**Figure 2C**). The white transparent polygons are areas of low model sensitivity (**Supplementary Figure S1B**). **(B)** Geologic model and interpretation of the resistivity model.

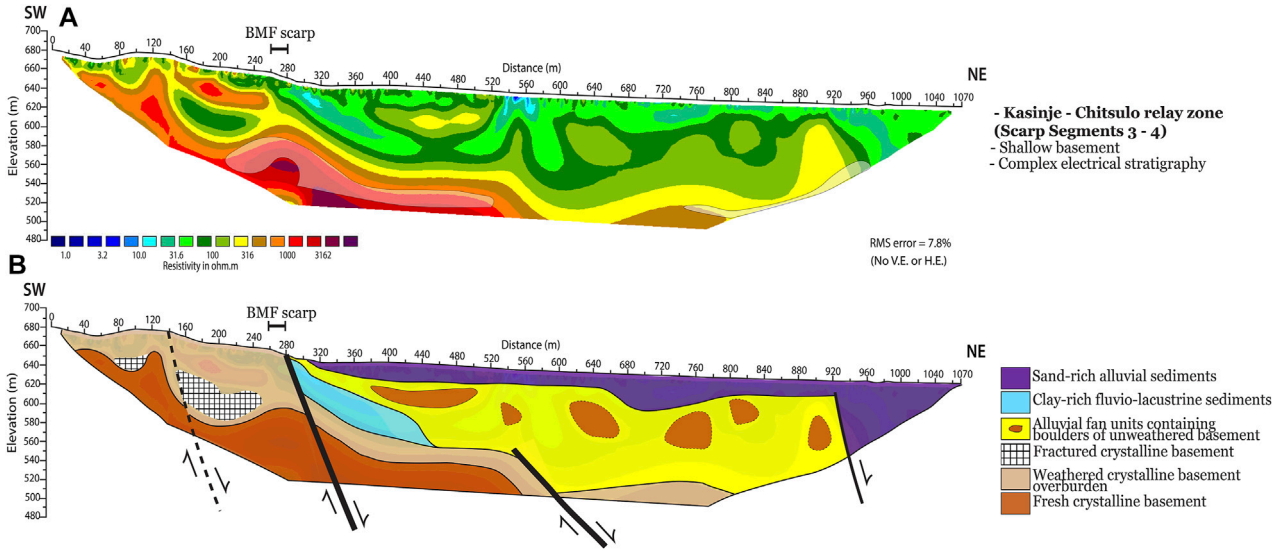

FIGURE 9 | (A) Inverse model of the ERT Profile 3, acquired at the relay zone in-between Scarp Segments 3 and 4 (transition from Kasinje to Citsulo geometrical segments) in the central section of the BMF. The white transparent polygons are areas of low model sensitivity (**Supplementary Figure S2A**). **(B)** Geologic model and interpretation of the resistivity model. The inversion model and interpretation reflects a low angle fault plane along the BMF because the survey profile was acquired at an oblique angle to the strike of the fault scarp due to land accessibility challenges encountered on the field.

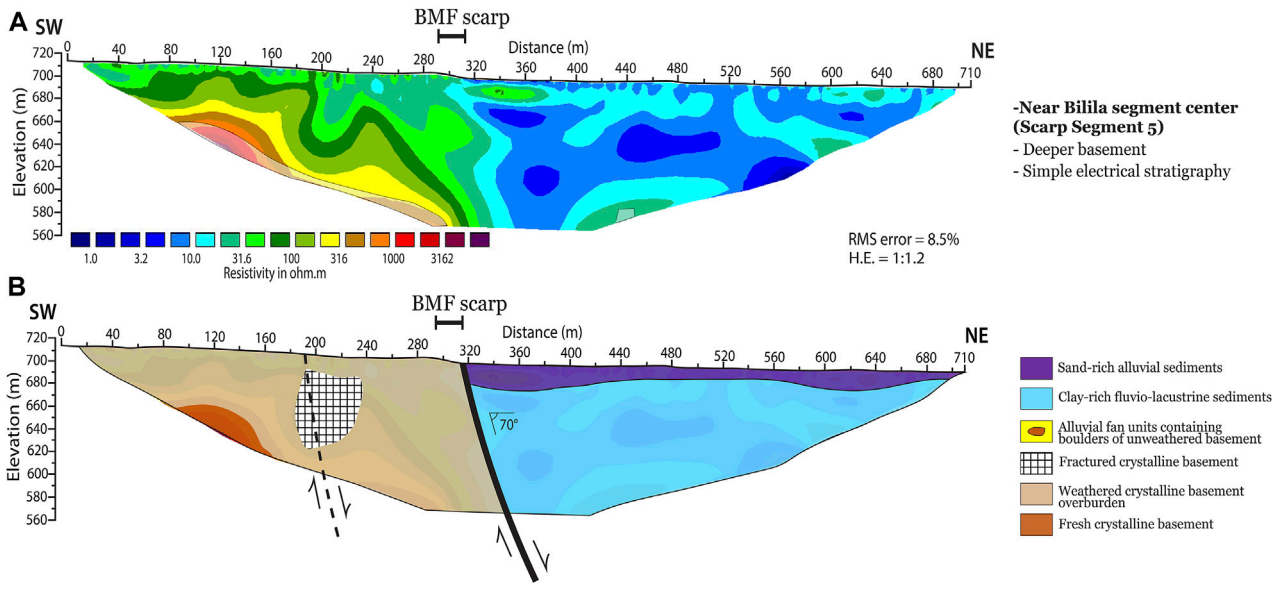

FIGURE 10 | (A) Inverse model of the ERT Profile 4, acquired near the center of the Scarp Segment 5 (Bilila geometrical segment) in the southernmost section of the BMF. The white transparent polygons are areas of low model sensitivity (**Supplementary Figure S2B**). **(B)** Geologic model and interpretation of the resistivity model.

sub-vertical) slope that is colocated with the base of the BMF scarp. The top-most geoelectric layer is characterized by low-to moderate-resistivity (10–60 Ω-m) and has a thickness of 20–40 m which thickens to at least 70 m basinward (near the far eastern end of the profile). This shallow layer overlies a thicker interval (~110 m) defined by discrete bodies of moderately resistive bodies (60–300 Ω-m) hosted within a ~60 Ω-m background resistivity anomaly. Similar to other profiles, the basal geoelectric layer is composed of high resistivity values (>1,000 Ω-m), extends into and dominates the footwall of the BMF. ERT Profile 4 (**Figure 10**), acquired near the center of the Scarp Segment 5 (Bilila geometrical segment) in the southernmost section of the BMF, is generally characterized by low-resistivity zones (<30 Ω-m) in the hanging wall of the BMF scarp and very high-resistivity zones in the footwall of the scarp. The BMF scarp is colocated with a strongly subvertical discontinuity that extends across the inversion model.

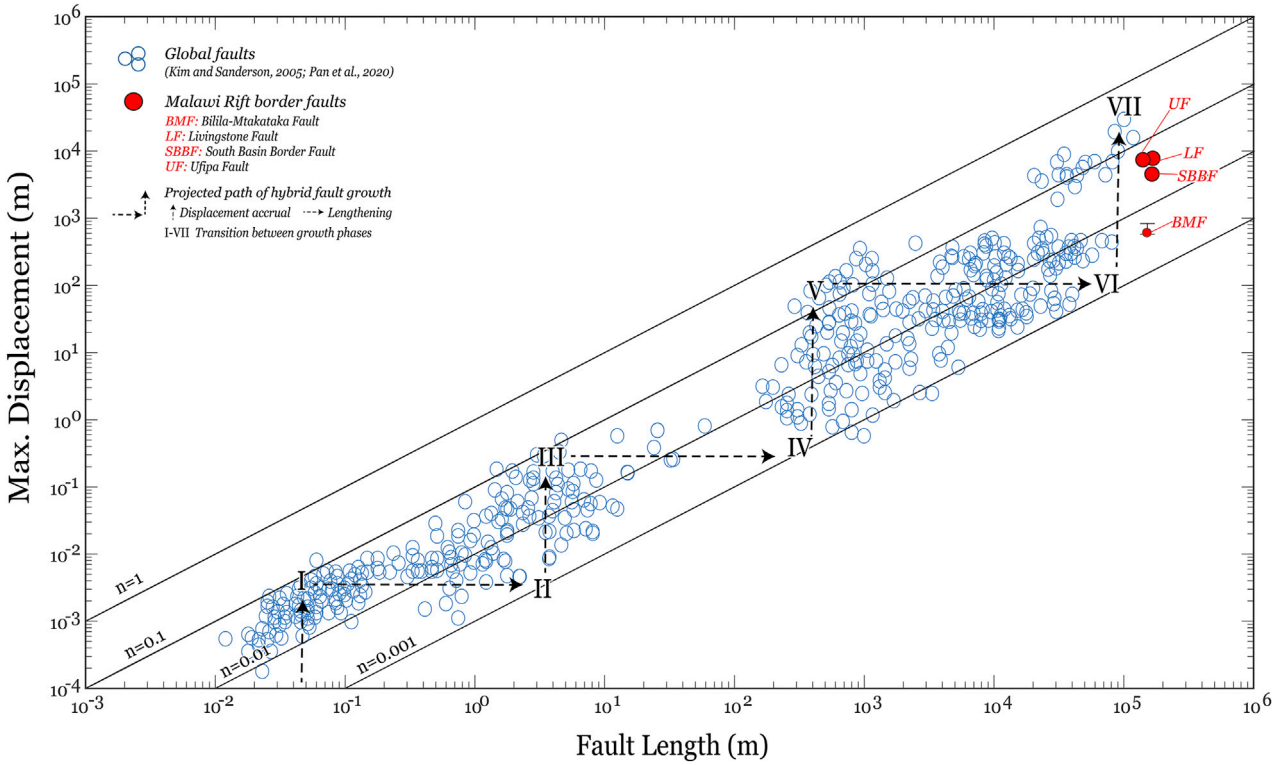

FIGURE 11 | Fault length trace along strike against maximum displacement relationship. The figure shows the stages of strain evolution (I–VII) the Bilila-Mtakataka (BMF) fault is compared with Livingstone Fault (LF) Usisya Fault (UF) and South Basin Border Fault (SBBF) (Specht and Rosendahl, 1989; Scholz et al., 2020; Shillington et al., 2020) and the tendency for the faults to still accumulate more strain. The arrow lines show the path a fault would follow at different stages (I–VII) as it grows and evolve from initiation to termination (lengthening phase (horizontal arrows); isolated fault initiation and displacement accrual phase (vertical arrows); transition between the normal fault growth phases (I–VI); and at stage VII, fault becomes inactive. The global D-L plots were modified from Kim and Sanderson, (2005) and Pan et al. (2020).

The inversion results for ERT Profiles 1 and 2 show a 75° dip angle for the BMF electrical gradient (**Figures 7**, **8**), whereas a 70° dip angle is observed on ERT Profile 4 (**Figure 10**). These are useful estimates of shallow crustal dip of the BMF, considering that the profiles are orthogonal to the fault trend. Based on a 560 m maximum throw along the BMF, and dips of 70–75° from ERT and 42° from deep microseismicity clusters, we estimate the maximum dip displacement to range between 837 m (upper bound), 580 m (lower bound), and a median of 596 m (**Figure 11**). Further north along the Malawi Rift (**Figure 1B**), the Livingstone border fault records a maximum displacement of ~7.4 km, Usisya border fault records ~7.3 km, and South Basin Border Fault records ~3.85 km (**Figure 11**; Specht and Rosendahl, 1989; Scholz et al., 2020; Shillington et al., 2020).

4 DISCUSSION

4.1 Integration of Topographic and Subsurface Observations Along the Bilila-Mtakataka Fault Zone

The results of this study reveal a distinct difference in the segmentation pattern observable along the surface trace of the BMF (i.e., scarp and geometrical segmentation; **Figure 4**) and the segmentation pattern shown by the along-fault distribution of depth-to-basement (**Figure 6**). Faults usually initiate as isolated fault segments which evolve over time through fault growth and linkage of the isolated fault segments into larger faults (Jackson and Rotevatn, 2013; Childs et al., 2017). As the faults grow through linkage and interactions between the isolated segments, the magnitude of displacement and throw along the resulting fault become cumulative and change over time. The longer the time that has passed since isolated fault segments linked up, the harder it is to identify all the different segments that make up the fault. Thus, different tiers of segmentation along a fault may develop due to the various stages of growth and history of the fault (Jackson and Rotevatn, 2013). As such, the lower tier of segmentation associated with recent surface-rupturing fault offsets (observable along surface fault traces) may not necessarily mimic the higher tier of segmentation associated with long-term fault growth and is observable in the along-fault distribution of cumulative fault offset.

For this study, our scale of observation encompasses the entire length of the fault and maximum vertical offset of the pre-rift basement, thus providing a robust basis for the tier/classification of the segments. The geometrical segmentation

shows six segments (**Figure 4**; Hodge et al., 2018) and scarp segmentation shows five segments (**Figure 4**), whereas the depth-to-basement and overall cumulative throw segmentation show three segments (**Figure 6**). Since the cumulative throw is most representative of the long-term displacement pattern along a fault, we posit that the subsurface component of displacement should not be ignored in the investigation of fault zone structure and segmentation as it can contrast observations at the surface. We argue that fault segmentation that is based on scarp height and surface fault trace geometry are more representative of the patterns of most recent coseismic surface rupturing events along the fault. As such, segments with overlapping rupture patches associated with multiple episodes of coseismic surface rupture may show significant cumulative scarp height which may not necessarily be representative of the longer-term displacement history of the other fault segments.

However, we note that although local footwall height (*h'*) is also part of the subaerial component of fault displacement (**Figure 3**), the similarity of its long-wavelength segmentation pattern with that of depth-to-basement (**Figure 6**) suggest that the *h'* may preserve some information on the long-term displacement pattern along a fault. In essence, our results suggest that for evolving normal faults such as the BMF, the geometrical complexity observed along their surface fault trace might not always be present at depth.

At the scale of the Makanjira Sub-basin (i.e., western branch of the Malawi Rift), the map of depth-to-basement shows that the hanging wall of the BMF exhibits a much wider and deeper zone of subsidence in the northern and central sections than in the south (**Figure 5B**). The zone of transition between both regions is marked by a shallowly buried pre-rift basement. This shallowly buried basement also coincides with the footwall of the Bwanje Fault, an antithetic fault within the hanging wall of the BMF (**Figure 2A**). Overall, we interpret this "top-basement" topography to represent a partitioning of depocenters along the BMF hanging wall in which the depocenters in the northern/central sections were once separated from those in the south by a basement-high. This basement-high has not been significantly buried since the coalescence of the northern/central and southern depocenters. This interpretation is supported (or at least not contradicted) by the relatively shallow basement and distinct hanging wall electrical stratigraphy of ERT Profile 3 (acquired near the transition zone) which contrasts those of the other profiles.

4.2 Evolution of Segmentation and Linkage Along the Bilila-Mtakataka Fault

The along-fault distribution of cumulative throw provides insight into how tectonic processes might have contributed to the present-day architecture of normal faults. Our results show the BMF is characterized by a series of relay zones (defined by throw minima) among which the most prominent are those located between the three composite segments (**Figure 6**). The lateral continuity of the fault scarp (**Figure 2A**) as well as the continuity of offset along the entire fault (**Figure 6**) indicate that the relay zones have been breached and that the composite segments are hard-linked. However, among the two major relay zones, the relay zone connecting the Central and Southern composite segments (Kasinje-Chitsulo relay zone in **Figure 4**) has the least cumulative throw (Figure 6), suggesting that it has not accommodated significant long-term tectonic strain post-linkage of the composite segments.

At the surface, the base of the BMF escarpment (mountain front) is covered by floodplain deposits of the Bwanje River (axial stream) and incised alluvial fan deposits of transverse streams flowing down from the footwall of the BMF (e.g., **Figure 2D**). This is consistent with observations in the outcrops of the Quaternary Chipalamawamba Beds nearby in Malombe Graben (**Figure 1C**; Van Bocxlaer et al., 2012) where axial stream alluvial deposits overlay a deeper unit of lacustrine origin. This deeper lacustrine unit is possibly associated with infrequent flooding of Lake Malawi which deposited thick clay-rich sediments into the southern branches of the Malawi Rift (Dulanya et al., 2014; Dulanya, 2017). Most of our resistivity profiles commonly show a general geoelectric stratigraphy in which a shallow low-to moderate-resistivity layer is underlain by a deeper and relatively thicker low-resistivity layer within the syn-rift sedimentary cover, consistent with geoelectrical stratigraphy onshore of Lake Malawi in the northern Malawi Rift (Kolawole et al., 2018). We interpret that the ubiquitous deep-seated low-resistivity geoelectric layer within the syn-rift stratigraphy represents clay-rich lacustrine sediments deposited during an episode of flooding of Lake Malawi, and that the topmost low-to moderate-resistivity layer represent floodplain deposits of the axial streams and incised alluvial fan deposits.

In contrast, the local hanging wall geoelectrical stratigraphy at the Kasinje-Chitsulo relay zone (ERT Profile 3; **Figures 9A,B**) shows a deep sedimentary geoelectric layer that hosts 100–300 Ω-m discrete bodies within a background of 32–100 Ω-m, interpreted to be colluvial deposits of less-weathered basement material dispersed within a mountain front alluvial fan stratigraphy (**Figure 2D**). The absence of this unique electrical stratigraphy in the other ERT profiles (this study and onshore of northern Lake Malawi) suggests that this relay zone is, perhaps, a major long-lived entry point for alluvial and colluvial sediments sourced from the BMF footwall into the Makanjira Trough sub-basin.

Based on these observations, and the collocation of this relay zone with the zone of transition between the northern/central and southern BMF depocenters, we infer that the Central-to-Southern composite segment relay zone is likely the most recently breached relay zone along the BMF. It is possible that after the nucleation of the three composite BMF segments, the northern and central composite segments linked first and continued to localize strain which facilitated the early coalescence of their depocenters. It is also likely that progressive offset on the antithetic faults within the BMF hanging wall (e.g., Bwanje Fault) further amplified the subsidence and broadening of the northern and central BMF depocenters (**Figure 5B**). In addition, the results of our study suggest that the Southern Composite Segment has

accommodated the least cumulative offset and thus, long-term tectonic strain relative to the other composite segments along the BMF. Thus, we interpret that the BMF segments have been accruing vertical offset over the fault life so far, a portion of the long-term faulting activity has been dominated by the breaching of relay zones and linkage of the fault segments leading to the large-scale lengthening of the BMF.

4.3 Implications for Strain Localization During Early-Stage Rifting and Associated Earthquake Hazards

Various studies have investigated the magnitudes of cumulative displacement that a border fault may accommodate before it becomes mechanically incapable of accommodating more strain (Scholz and Contreras, 1998; Goldsworthy and Jackson, 2001; Ebinger, 2005; Corti, 2009; Muirhead et al., 2016, 2019). During this period, the border faults accrue throws greater than 1 km and induce extension within their hanging walls, which is then accommodated by the localization of intra-rift faults as slip rates of border faults progressively reduce (Muirhead et al., 2016). However, it has been shown that pre-existing structures may localize tectonic strain along the rift axis during the early stages of rifting prior to significant displacement accrual on the border faults (Wedmore et al., 2020; Kolawole et al., 2021a). The Malawi Rift has been proposed to have propagated southwards (e.g., Scholz et al., 2020); which implies that the border faults in the south (such as the BMF) may be relatively less developed than those in the northern sections of the rift, and that a comparison of the long-term displacement on the northern and central Malawi Rift faults with the BMF may provide a template for understanding the future growth of the BMF.

Further north along the Malawi Rift (**Figure 1B**), where the intra-rift faults account for a significant portion of the overall tectonic strain (Shillington et al., 2020), the 170 km-long Livingstone, 140 km-long Usisya, and the 162 km-long South Basin border faults record significant maximum displacements (~7.4, ~7.3 and ~3.85 km respectively; **Figure 11**) (Specht and Rosendahl, 1989; Scholz et al., 2020; Shillington et al., 2020). It is possible that these faults may have reached their maximum displacements and might no longer be accommodating increasing strain as seismic slips (Cowie et al., 2005). Nevertheless, we note that the Livingstone, Usisya, and South Basin Border Faults have similar fault lengths as the BMF (**Figure 11**).

Considering the empirical displacement-length ratio relationships for normal faults (**Figure 11**; Kim and Sanderson, 2005; Pan et al., 2020), the BMF should have a similar magnitude of maximum cumulative displacement as the northern and central Malawi Rift border faults with which it has comparable lengths, but this is not the case (**Figure 11**). Based on the integration of both the subsurface and subaerial components of fault offset and dips from ERT and microseismicity cluster, we estimate the maximum displacements along the BMF to be ~580–837 m (median of 596 m), which are significantly exceeded by those of other Malawi Rift border faults and global normal faults of equivalent length. Thus, we suggest that the BMF is in fact an under-displaced border fault. Furthermore, we posit that this discrepancy in the displacement-length ratio implies that large magnitude seismic activity along the BMF is possible because there is still room for displacement to be accumulated before the border fault potentially becomes inactive as it progressively attains the displacement-length ratio of the larger-offset northern and central Malawi border faults.

Also, considering the mathematical expression for the fault displacement-length relationship ($D = CL^n$), the direct proportionality of these two attributes of the fault is dependent on the constant C, which could be influenced by factors such as lithology, rheology, strain rate and direction of tectonic stretching, and strain inhibition or transfer to neighboring pre-existing or subsequent structures (Bergen and Shaw, 2010). In the case of the BMF, we speculate that its under-displaced history could be a result of strain inhibition by and/or distributed transfer of strain to its synthetic Chirobwe-Ntcheu Fault, the southern sections of the South Basin Border Fault, and the Malombe Fault (prominent fault in the Malombe Graben east of the BMF; Kolawole et al., 2021b; **Figure 1C**). In addition, we speculate that Malombe Graben could probably be an equally or more active branch of the Malawi Rift and therefore may be accommodating most of the recent strain.

Furthermore, we estimate strain rates along the BMF as a function of cumulative strain (cumulative displacement) against time (initiation of rift faulting at 23 Ma; Van Der Beek et al., 1998; Mortimer et al., 2016; Ojo et al., 2021) using the relationship *strain rate = displacement/time*. The BMF has lower strain rates (0.025 mm/yr) compared to the most prominent and larger offset border faults along the Malawi Rift which include the Livingstone Fault (0.32 mm/yr), Usisya Fault (0.31 mm/yr), and the South Basin Border Fault (0.20 mm/yr). We suggest that the disparity in displacement may also be due to a combination of lower strain rate of the BMF compared to the Livingstone Fault, Usisya Fault and South Basin Border Fault, the difference in the normal fault growth model, and to inherited heterogeneities of the crust (Williams et al., 2021 *preprint*).

The presence of potentially recent linkage of composite segments along the BMF indicates a history of prolonged coalescence and offset accrual within the composite segments and a delayed fault lengthening by linkage and coalescence of the composite segments. Thus, we consider a model whereby the BMF could have evolved through alternating stages of lengthening and displacement accrual demonstrating the hybrid fault growth model (**Figure 11**; Pan et al., 2020) and/or by fault segment linkage (Peacock, 1991; Peacock and Sanderson, 1991; Cartwright et al., 1995; Peacock et al., 2017).

5 CONCLUSION

We integrated SRTM-DEM, electrical resistivity tomography, and aeromagnetic methods to investigate the architecture, cumulative throw distribution, and maximum displacement along the Bilila-Mtakataka Fault (BMF). The results show that although the BMF has attained a possible maximum length similar to the other prominent border faults along the Malawi

Rift and global normal fault populations, it has significantly lower cumulative displacement. We provide evidence suggesting "recent" linkage and coalescence of the composite segments of the BMF, indicating that much of the fault life has been spent on the coalescence and offset accrual within the composite segments and a delayed fault lengthening by linkage and coalescence of the composite segments. In essence, the BMF is an under-displaced border fault. Our observations highlight the potential for large magnitude seismic activity along the BMF because there is still room for displacement to be accumulated before the border fault potentially becomes inactive, and it progressively attains the displacement-length ratio of the larger-offset northern and central Malawi border faults.

In a wider context, the multidisciplinary research approach used in this study is useful for investigating the long-term and short-term structural and tectonic evolution of active normal faults in early-stage continental rift settings such as the Malawi Rift. The research approach is especially useful in regions where geological and environmental conditions are unfavorable for the preservation of short-term tectonic indicators [e.g., Rhine Graben and Andean Pre-Cordillera of Western Argentina (Megharoui et al., 2000; Fazzito et al., 2009)].

DATA AVAILABILITY STATEMENT

The original contributions presented in the study are included in the article/**Supplementary Material**, further inquiries can be directed to the corresponding author.

AUTHOR CONTRIBUTIONS

All authors listed have made a substantial, direct, and intellectual contribution to the work and approved it for publication.

ACKNOWLEDGMENTS

We thank the associate editor, and reviewers (CP, CM, CE) for their useful comments that have helped to improve the quality of this paper. The ERT data used in this study were collected under the support of NSF II-1358150 grant. Data supporting the conclusions can be found in the cited references and in the supporting information provided as a published supplement to this manuscript. S.C.M. Beresh, W.G. Mynatt, K. Mȳndez Mȳndez, E.A. Elifritz, M. Mkumbura, C. Chisenga, S. Gondwe, M. Mayle, and D. Kalaguluka helped to collect the electrical resistivity data. L. Kalindekafe and J. Salima provided support while in the field. This is the Oklahoma State University Boone Pickens School of Geology contribution number 2022-128.

SUPPLEMENTARY MATERIAL

The Supplementary Material for this article can be found online at: https://www.frontiersin.org/articles/10.3389/feart.2022.846389/full#supplementary-material

REFERENCES

Abbate, E., and Sagri, M. (1980). Volcanites of Ethiopian and Somali Plateaus and Major Tectonic Lines. *Atti Convegni Lincei* 47, 219–227.

Bergen, K. J., and Shaw, J. H. (2010). Displacement Profiles and Displacement-Length Scaling Relationships of Thrust Faults Constrained by Seismic-Reflection Data. *Bulletin* 122 (7-8), 1209–1219. doi:10.1130/b26373.1

Blakely, R. J., and Simpson, R. W. (1986). Approximating Edges of Source Bodies from Magnetic or Gravity Anomalies. *Geophysics* 51, 1494–1498. doi:10.1190/1.1442197

Bonini, M., Corti, G., Innocenti, F., Manetti, P., Mazzarini, F., Abebe, T., et al. (2005). Evolution of the Main Ethiopian Rift in the Frame of Afar and Kenya Rifts Propagation. *Tectonics* 24, a–n. doi:10.1029/2004TC001680

Bucknam, R. C., and Anderson, R. E. (1979). Estimation of Fault-Scarp Ages from a Scarp-Height-Slope-Angle Relationship. *Geol* 7 (1), 11–14. doi:10.1130/0091-7613(1979)7<11:eofafa>2.0.co;2

Calais, E., d'Oreye, N., Albaric, J., Deschamps, A., Delvaux, D., Déverchère, J., Ebinger, C., Ferdinand, R. W., Kervyn, F., Macheyeki, A. S., Oyen, A., Perrot, J., Saria, E., Smets, B., Stamps, D. S., and Wauthier, C. (2008). Strain Accommodation by Slow Slip and Dyking in a Youthful continental Rift, East Africa. *Nature* 456 (7223), 783–787. doi:10.1038/nature07478

Cartwright, J. A., Trudgill, B. D., and Mansfield, C. S. (1995). Fault Growth by Segment Linkage: an Explanation for Scatter in Maximum Displacement and Trace Length Data from the Canyonlands Grabens of SE Utah. *J. Struct. Geology*. 17 (9), 1319–1326. doi:10.1016/0191-8141(95)00033-a

Caskey, S. J. (1995). Geometric Relations of Dip Slip to a Faulted Ground Surface: New Nomograms for Estimating Components of Fault Displacement. *J. Struct. Geology*. 17 (8), 1197–1202. doi:10.1016/0191-8141(95)00023-7

Childs, C., Holdsworth, R. E., Jackson, C. A.-L., Manzocchi, T., Walsh, J. J., and Yielding, G. (2017). Introduction to the Geometry and Growth of normal Faults. *Geol. Soc. Lond. Spec. Publications* 439 (1), 1–9. doi:10.1144/sp439.24

Claerbout, J. F., and Muir, F. (1973). Robust Modeling with Erratic Data. *Geophysics* 38 (5), 826–844. doi:10.1190/1.1440378

Corti, G. (2009). Continental Rift Evolution: from Rift Initiation to Incipient Break-Up in the Main Ethiopian Rift, East Africa. *Earth-science Rev.* 96 (1-2), 1–53. doi:10.1016/j.earscirev.2009.06.005

Cowie, P. A., and Scholz, C. H. (1992b). Displacement-length Scaling Relationship for Faults: Data Synthesis and Discussion. *J. Struct. Geology*. 14 (10), 1149–1156. doi:10.1016/0191-8141(92)90066-6

Cowie, P. A., and Scholz, C. H. (1992a). Physical Explanation for the Displacement-Length Relationship of Faults Using a post-yield Fracture Mechanics Model. *J. Struct. Geology*. 14 (10), 1133–1148. doi:10.1016/0191-8141(92)90065-5

Cowie, P. A., Underhill, J. R., Behn, M. D., Lin, J., and Gill, C. E. (2005). Spatio-temporal Evolution of Strain Accumulation Derived from Multi-Scale Observations of Late Jurassic Rifting in the Northern North Sea: A Critical Test of Models for Lithospheric Extension. *Earth Planet. Sci. Lett.* 234 (3-4), 401–419. doi:10.1016/j.epsl.2005.01.039

Dawers, N. H., Anders, M. H., and Scholz, C. H. (1993). Growth of normal Faults: Displacement-Length Scaling. *Geol* 21 (12), 1107–1110. doi:10.1130/0091-7613(1993)021<1107:gonfdl>2.3.co;2

Dawson, A. L., and Kirkpatrick, I. K. (1968). The Geology of the Cape Maclear peninsula and Lower Bwanje valley. *Bull. Geol. Surv. Malaẇi* 71, 71. doi:10.1177/0040571x6807100120

deGroot-Hedlin, C., and Constable, S. (1990). Occam's Inversion to Generate Smooth, Two Dimensional Models from Magnetotelluric Data. *Geophysics* 55 (12), 1613–1624.

Delvaux, D. (2001). Tectonic and Palaeostress Evolution of the Tanganyika-Rukwa-Malawi Rift Segment, East African Rift System. *Peri-Tethys Memoir* 6, 545–567.

Delvaux, D. (19911991). The Karoo to Recent Rifting in the Western branch of the East-African Rift System: A Bibliographical Synthesis. *Mus. Roy. Afr. centr., Tervuren (Belg.), Dépt. Géol. Min., Rapp. Ann.* 1990, 63–83.

Densmore, A. L., Gupta, S., Allen, P. A., and Dawers, N. H. (2007). Transient Landscapes at Fault Tips. *J. Geophys. Res. earth Surf.* 112 (F3). doi:10.1029/2006jf000560

Dulanya, Z. (2017). A Review of the Geomorphotectonic Evolution of the South Malawi Rift. *J. Afr. Earth Sci.* 129, 728–738. doi:10.1016/j.jafrearsci.2017.02.016

Dulanya, Z., Croudace, I., Reed, J., and Trauth, M. (2014). Palaeolimnological Reconstruction of Recent Environmental Change in Lake Malombe (S. Malawi) Using Multiple Proxies. *Wsa* 40 (4), 717–728. doi:10.4314/wsa.v40i4.17

Ebinger, C. (2005). Continental Break-Up: the East African Perspective. *Astron. Geophys.* 46 (2), 2–16. doi:10.1111/j.1468-4004.2005.46216.x

Ebinger, C. J., Deino, A. L., Drake, R. E., and Tesha, A. L. (1989). Chronology of Volcanism and Rift basin Propagation: Rungwe Volcanic Province, East Africa. *J. Geophys. Res.* 94 (B11), 15785–15803. doi:10.1029/jb094ib11p15785

Ebinger, C. J., Oliva, S. J., Pham, T. Q., Peterson, K., Chindandali, P., Illsley-Kemp, F., et al. (2019). Kinematics of Active Deformation in the Malawi Rift and Rungwe Volcanic Province, Africa. *Geochem. Geophys. Geosyst.* 20, 3928–3951. doi:10.1029/2019GC008354

Ebinger, C. J., Rosendahl, B. R., and Reynolds, D. J. (1987). Tectonic Model of the Malaŵi Rift, Africa. *Tectonophysics* 141 (1-3), 215–235. doi:10.1016/0040-1951(87)90187-9

Ebinger, C., and Scholz, C. A. (2011). Continental Rift Basins: the East African Perspective. *Tectonics Sediment. basins: Recent Adv.*, 183–208.

Faulds, J. E., and Varga, R. J. (1998). The Role of Accommodation Zones and Transfer Zones in the Regional Segmentation of Extended Terranes. *Geol. Soc. America Spec. Pap.* 323, 1–45. doi:10.1130/0-8137-2323-x.1

Fazzito, S. Y., Rapalini, A. E., Cortés, J. M., and Terrizzano, C. M. (2009). Characterization of Quaternary Faults by Electric Resistivity Tomography in the Andean Precordillera of Western Argentina. *J. South Am. Earth Sci.* 28 (3), 217–228. doi:10.1016/j.jsames.2009.06.001

Flannery, J. W., and Rosendahl, B. R. (1990). The Seismic Stratigraphy of Lake Malawi, Africa: Implications for Interpreting Geological Processes in Lacustrine Rifts. *J. Afr. Earth Sci. (and Middle East)* 10 (3), 519–548. doi:10.1016/0899-5362(90)90104-m

Furman, T., Bryce, J. G., Karson, J., and Iotti, A. (2004). East African Rift System (EARS) Plume Structure: Insights from Quaternary Mafic Lavas of Turkana, Kenya. *J. Pet.* 45 (5), 1069–1088. doi:10.1093/petrology/egh004

Gay, S. P. (2009). *Reactivation Tectonics: The Evidence and the Consequences*. Salt Lake City, Utah.

Goldsworthy, M., and Jackson, J. (2001). Migration of Activity within normal Fault Systems: Examples from the Quaternary of mainland Greece. *J. Struct. Geology.* 23 (2-3), 489–506. doi:10.1016/s0191-8141(00)00121-8

Gouiza, M., and Naliboff, J. (2021). Rheological Inheritance Controls the Formation of Segmented Rifted Margins in Cratonic Lithosphere. *Nat. Commun.* 12 (1), 4653–4659. doi:10.1038/s41467-021-24945-5

Hayward, N. J., and Ebinger, C. J. (1996). Variations in the along-axis Segmentation of the Afar Rift System. *Tectonics* 15 (2), 244–257. doi:10.1029/95tc02292

Hodge, M., Biggs, J., Fagereng, Å., Elliott, A., Mdala, H., and Mphepo, F. (2019). A Semi-automated Algorithm to Quantify Scarp Morphology (SPARTA): Application to normal Faults in Southern Malawi. *Solid Earth* 10 (1), 27–57. doi:10.5194/se-10-27-2019

Hodge, M., Fagereng, Å., Biggs, J., and Mdala, H. (2018). Controls on Early-Rift Geometry: New Perspectives from the Bilila-Mtakataka Fault, Malawi. *Geophys. Res. Lett.* 45 (9), 3896–3905. doi:10.1029/2018gl077343

Hornsby, K. T., Streig, A. R., Bennett, S. E. K., Chang, J. C., and Mahan, S. (2020). Neotectonic and Paleoseismic Analysis of the Northwest Extent of Holocene Surface Deformation along the Meers Fault, Oklahoma. *Bull. Seismological Soc. America* 110 (1), 49–66. doi:10.1785/0120180148

Jackson, C. A.-L., and Rotevatn, A. (2013). 3D Seismic Analysis of the Structure and Evolution of a Salt-Influenced normal Fault Zone: a Test of Competing Fault Growth Models. *J. Struct. Geology*. 54, 215–234. doi:10.1016/j.jsg.2013.06.012

Jackson, J., and Blenkinsop, T. (1997). The Bilila-Mtakataka Fault in Malaŵi: An Active, 100-km Long, normal Fault Segment in Thick Seismogenic Crust. *Tectonics* 16 (1), 137–150. doi:10.1029/96TC02494

Jackson, J., and Blenkinsop, T. (1993). THE Malaŵi Earthquake of March 10, 1989: DEep Faulting within the East African Rift System. *Tectonics* 12, 1131–1139. doi:10.1029/93tc01064

Kim, Y. S., and Sanderson, D. J. (2005). The Relationship between Displacement and Length of Faults: a Review. *Earth-Science Rev.* 68 (3-4), 317–334. doi:10.1016/j.earscirev.2004.06.003

Kolawole, F., Atekwana, E. A., Laó-Dávila, D. A., Abdelsalam, M. G., Chindandali, P. R., Salima, J., et al. (2018). High-resolution Electrical Resistivity and Aeromagnetic Imaging Reveal the Causative Fault of the 2009 Mw 6.0 Karonga, Malawi Earthquake. *Geophys. J. Int.* 213 (2), 1412–1425. doi:10.1093/gji/ggy066

Kolawole, F., Firkins, M. C., Al Wahaibi, T. S., Atekwana, E. A., and Soreghan, M. J. (2021b). Rift Interaction Zones and the Stages of Rift Linkage in Active Segmented continental Rift Systems. *Basin Res.* 33 (6), 2984–3020. doi:10.1111/bre.12592

Kolawole, F., Phillips, T. B., Atekwana, E. A., and Jackson, C. A. L. (2021a). Structural Inheritance Controls Strain Distribution during Early continental Rifting, Rukwa Rift. *Front. Earth Sci.*, 670. doi:10.3389/feart.2021.707869

Laó-Dávila, D. A., Al-Salmi, H. S., Abdelsalam, M. G., and Atekwana, E. A. (2015). Hierarchical Segmentation of the Malawi Rift: The Influence of Inherited Lithospheric Heterogeneity and Kinematics in the Evolution of continental Rifts. *Tectonics* 34 (12), 2399–2417. doi:10.1002/2015TC003953

Loke, M. H., and Barker, R. D. (1996). Rapid Least-Squares Inversion of Apparent Resistivity Pseudosections by a Quasi-Newton Method1. *Geophys. Prospect.* 44 (1), 131–152. doi:10.1111/j.1365-2478.1996.tb00142.x

Loke, M. H. (2002). *Electrical Imaging Surveys for Environmental and Engineering Studies, A Practical Guide to 2-D and 3-D Surveys: RES2DINV Manual*. IRIS Instruments.

Maguire, P. K. H., Ebinger, C. J., Stuart, G. W., Mackenzie, G. D., Whaler, K. A., Kendall, J.-M., Khan, M. A., Fowler, C. M. R., Klemperer, S. L., Keller, G. R., Harder, S., Furman, T., Mickus, K., Asfaw, L., Ayele, A., and Abebe, B. (2003). Geophysical Project in Ethiopia Studies continental Breakup. *Eos Trans. AGU* 84 (35), 337–343. doi:10.1029/2003eo350002

Manighetti, I., King, G. C. P., Gaudemer, Y., Scholz, C. H., and Doubre, C. (2001). Slip Accumulation and Lateral Propagation of Active normal Faults in Afar. *J. Geophys. Res.* 106 (B7), 13667–13696. doi:10.1029/2000jb900471

Meghraoui, M., Camelbeeck, T., Vanneste, K., Brondeel, M., and Jongmans, D. (2000). Active Faulting and Paleoseismology along the Bree Fault, Lower Rhine Graben, Belgium. *J. Geophys. Res.* 105 (B6), 13–841. doi:10.1029/1999jb900236

Minsley, B. J., Ball, L. B., Burton, B. L., Caine, J. S., Curry-Elrod, E., and Manning, A. H. (2010). Geophysical Characterization of Subsurface Properties Relevant to the Hydrology of the Standard Mine in Elk Basin, Colorado, U.S. *Geol. Surv. Open-File Rep.* 2009, 1284–1287.

Morley, C. K., Nelson, R. A., Patton, T. L., and Munn, S. G. (1990). Transfer Zones in the East African Rift System and Their Relevance to Hydrocarbon Exploration in Rifts. *AAPG Bull.* 74 (8), 1234–1253. doi:10.1306/0c9b2475-1710-11d7-8645000102c1865d

Morley, C. K. (1999). Patterns of Displacement along Large normal Faults: Implications for basin Evolution and Fault Propagation, Based on Examples from East Africa. *AAPG Bull.* 83 (4), 613–634. doi:10.1306/00aa9c0a-1730-11d7-8645000102c1865d

Mortimer, E., Kirstein, L. A., Stuart, F. M., and Strecker, M. R. (2016). Spatio-temporal Trends in normal-fault Segmentation Recorded by Low-Temperature Thermochronology: Livingstone Fault Scarp, Malawi Rift, East African Rift System. *Earth Planet. Sci. Lett.* 455, 62–72. doi:10.1016/j.epsl.2016.08.040

Muirhead, J. D., Kattenhorn, S. A., Lee, H., Mana, S., Turrin, B. D., Fischer, T. P., Kianji, G., Dindi, E., and Stamps, D. S. (2016). Evolution of Upper Crustal Faulting Assisted by Magmatic Volatile Release during Early-Stage continental Rift Development in the East African Rift. *Geosphere* 12 (6), 1670–1700. doi:10.1130/ges01375.1

Muirhead, J. D., Wright, L. J. M., and Scholz, C. A. (2019). Rift Evolution in Regions of Low Magma Input in East Africa. *Earth Planet. Sci. Lett.* 506, 332–346. doi:10.1016/j.epsl.2018.11.004

Nicol, A., Walsh, J., Berryman, K., and Nodder, S. (2005). Growth of a normal Fault by the Accumulation of Slip over Millions of Years. *J. Struct. Geology*. 27 (2), 327–342. doi:10.1016/j.jsg.2004.09.002

Nixon, C. W., McNeill, L. C., Bull, J. M., Bell, R. E., Gawthorpe, R. L., Henstock, T. J., Christodoulou, D., Ford, M., Taylor, B., Sakellariou, D., Ferentinos, G., Papatheodorou, G., Leeder, M. R., Collier, R. E. L., Goodliffe, A. M., Sachpazi, M., and Kranis, H. (2016). Rapid Spatiotemporal Variations in Rift Structure during Development of the Corinth Rift, central Greece. *Tectonics* 35 (5), 1225–1248. doi:10.1002/2015tc004026

Ojo, O., Thomson, S. N., Thomson, S. N., and Lao-Davila, D. (2021). Neogene - Quaternary Rifting of the Southern Malawi Rift and Linkage to the Late Carboniferous - Early Jurassic Shire Rift. *Geol. Soc. America Abstr. Programs* 53–6. (*currently under review at AGU Tectonics*). doi:10.1130/abs/2021AM-368982

Palacky, G. (1987). "Resistivity Characteristics of Geological Targets," in *Electromagnetic Methods in Applied Geophysics-Theory*. Editor M. Nabighian (Tulsa, OK: Society of Exploration Geophysicists), 53–129.

Pan, S., Bell, R. E., Jackson, C. A. L., and Naliboff, J. (2020). Evolution of normal Fault Displacement and Length as continental Lithosphere Stretches. *Basin Res.* 34, 121–140. doi:10.1111/bre.12613

Peacock, D. C. P. (1991). Displacements and Segment Linkage in Strike-Slip Fault Zones. *J. Struct. Geology*. 13 (9), 1025–1035. doi:10.1016/0191-8141(91)90054-m

Peacock, D. C. P., Nixon, C. W., Rotevatn, A., Sanderson, D. J., and Zuluaga, L. F. (2017). Interacting Faults. *J. Struct. Geology*. 97, 1–22. doi:10.1016/j.jsg.2017.02.008

Peacock, D. C. P., and Sanderson, D. J. (1991). Displacements, Segment Linkage and Relay Ramps in normal Fault Zones. *J. Struct. Geology*. 13 (6), 721–733. doi:10.1016/0191-8141(91)90033-f

Roberts, E. M., Stevens, N. J., O'Connor, P. M., Dirks, P. H. G. M., Gottfried, M. D., Clyde, W. C., et al. (2012). Initiation of the Western branch of the East African Rift Coeval with the Eastern branch. *Nat. Geosci* 5 (4), 289–294. doi:10.1038/ngeo1432

Rosendahl, B. R. (1987). Architecture of continental Rifts with Special Reference to East Africa. *Annu. Rev. Earth Planet. Sci.* 15, 445–503. doi:10.1146/annurev.ea.15.050187.002305

Rotevatn, A., Jackson, C. A.-L., Tvedt, A. B. M., Bell, R. E., and Blækkan, I. (2019). How Do normal Faults Grow? *J. Struct. Geology*. 125, 174–184. doi:10.1016/j.jsg.2018.08.005

Ryan, W. B., Carbotte, S. M., Coplan, J. O., O'Hara, S., Melkonian, A., Arko, R., and Zemsky, R. (2009). Global Multi-resolution Topography Synthesis. *Geochem. Geophys. Geosystems* 10 (3). doi:10.1029/2008gc002332

Schlagenhauf, A., Manighetti, I., Malavieille, J., and Dominguez, S. (2008). Incremental Growth of normal Faults: Insights from a Laser-Equipped Analog experiment. *Earth Planet. Sci. Lett.* 273 (3-4), 299–311. doi:10.1016/j.epsl.2008.06.042

Scholz, C. A., Shillington, D. J., Wright, L. J. M., Accardo, N., Gaherty, J. B., and Chindandali, P. (2020). Intrarift Fault Fabric, Segmentation, and basin Evolution of the Lake Malawi (Nyasa) Rift, East Africa. *Geosphere* 16 (5), 1293–1311. doi:10.1130/ges02228.1

Scholz, C. H., and Contreras, J. C. (1998). Mechanics of continental Rift Architecture. *Geol* 26 (11), 967–970. doi:10.1130/0091-7613(1998)026<0967:mocra>2.3.co;2

Shillington, D. J., Gaherty, J. B., Ebinger, C. J., Scholz, C. A., Selway, K., Nyblade, A. A., Bedrosian, P. A., Class, C., Nooner, S. L., Pritchard, M. E., Elliott, J., Chindandali, P. R. N., Mbogoni, G., Ferdinand, R. W., Boniface, N., Manya, S., Kamihanda, G., Saria, E., Mulibo, G., Salima, J., Mruma, A., Kalindekafe, L., Accardo, N. J., Ntambila, D., Kachingwe, M., Mesko, G. T., McCartney, T., Maquay, M., O'Donnell, J. P., Tepp, G., Mtelela, K., Trinhammer, P., Wood, D., Aaron, E., Gibaud, M., Rapa, M., Pfeifer, C., Mphepo, F., Gondwe, D., Arroyo, G., Eddy, C., Kamoga, B., and Moshi, M. (2016). Acquisition of a Unique Onshore/offshore Geophysical and Geochemical Dataset in the Northern Malawi (Nyasa) Rift. *Seismological Res. Lett.* 87 (6), 1406–1416. doi:10.1785/0220160112

Shillington, D. J., Scholz, C. A., Chindandali, P. R., Gaherty, J. B., Accardo, N. J., Onyango, E., et al. (2020). Controls on Rift Faulting in the North Basin of the Malawi (Nyasa) Rift, East Africa. *Tectonics* 39 (3), e2019TC005633. doi:10.1029/2019tc005633

Smith, R. S., Thurston, J. B., Dai, T. F., and MacLeod, I. N. (1998). iSPI TM - the Improved Source Parameter Imaging Method. *Geophys. prospecting* 46 (2), 141–151. doi:10.1046/j.1365-2478.1998.00084.x

Specht, T. D., and Rosendahl, B. R. (1989). Architecture of the Lake Malawi Rift, East Africa. *J. Afr. Earth Sci.* 8 (2–4), 355–382. doi:10.1016/s0899-5362(89)80032-6

Stamps, D. S., Saria, E., and Kreemer, C. (2018). A Geodetic Strain Rate Model for the East African Rift System. *Sci. Rep.* 8 (1), 732–739. doi:10.1038/s41598-017-19097-w

Stamps, D. S., Calais, E., Saria, E., Hartnady, C., Nocquet, J. M., Ebinger, C. J., et al. (2008). A Kinematic Model for the East African Rift. *Geophys. Res. Lett.* 35 (5). doi:10.1029/2007gl032781

Stamps, D. S., Kreemer, C., Fernandes, R., Rajaonarison, T. A., and Rambolamanana, G. (2021). Redefining East African Rift System Kinematics. *Geology* 49 (2), 150–155. doi:10.1130/g47985.1

Stevens, V. L., Sloan, R. A., Chindandali, P. R., Wedmore, L. N. J., Salomon, G. W., and Muir, R. A. (2021). The entire crust can be seismogenic: Evidence from southern Malawi. *Tectonics*, 40, e2020TC006654. doi:10.1029/2020TC006654

Tao, Z., and Alves, T. M. (2019). Impacts of data sampling on the interpretation of normal fault propagation and segment linkage. *Tectonophysics* 762, 79–96. doi:10.1016/j.tecto.2019.03.013

Thurston, J. B., and Smith, R. S. (1997). Automatic Conversion of Magnetic Data to Depth, Dip, and Susceptibility Contrast Using the SPI (TM) Method. *Geophysics* 62 (3), 807–813. doi:10.1190/1.1444190

Van Bocxlaer, B., Salenbien, W., Praet, N., and Verniers, J. (2012). Stratigraphy and Paleoenvironments of the Early to Middle Holocene Chipalamawamba Beds (Malawi Basin, Africa). *Biogeosciences* 9 (11), 4497–4512. doi:10.5194/bg-9-4497-2012

Van der Beek, P., Mbede, E., Andriessen, P., and Delvaux, D. (1998). Denudation History of the Malawi and Rukwa Rift Flanks (East African Rift System) from Apatite Fission Track Thermochronology. *J. Afr. Earth Sci.* 26 (3), 363–385. doi:10.1016/s0899-5362(98)00021-9

Walsh, J. J., Bailey, W. R., Childs, C., Nicol, A., and Bonson, C. G. (2003). Formation of Segmented normal Faults: a 3-D Perspective. *J. Struct. Geology*. 25 (8), 1251–1262. doi:10.1016/s0191-8141(02)00161-x

Walsh, J. J., and Watterson, J. (1988). Analysis of the Relationship between Displacements and Dimensions of Faults. *J. Struct. Geology*. 10 (3), 239–247. doi:10.1016/0191-8141(88)90057-0

Walshaw, R. D. (1965). *The Geology of the Ncheu-Balaka Area*. Zomba, Malawi: Government Printer. No. 19.

Wedmore, L. N., Biggs, J., Williams, J. N., Fagereng, Å., Dulanya, Z., Mphepo, F., et al. (2020). Active Fault Scarps in Southern Malawi and Their Implications for the Distribution of Strain in Incipient continental Rifts. *Tectonics* 39 (3), e2019TC005834. doi:10.1029/2019tc005834

Williams, J. N., Fagereng, A., Wedmore, L. N. J., Biggs, J., Mdala, H., Mphepo, F., et al. (2021). Low Dissipation of Earthquake Energy along Faults that Follow Pre-existing Weaknesses: Field and Microstructural Observations of Malawi's Bilila-Mtakataka Fault. *Earth Space Sci. Open Archive*. doi:10.1002/essoar.10507584.1

WoldeGabriel, G., Aronson, J. L., and Walter, R. C. (1990). Geology, Geochronology, and Rift basin Development in the central Sector of the Main Ethiopia Rift. *Geol. Soc. America Bull.* 102 (4), 439–458. doi:10.1130/0016-7606(1990)102<0439:ggarbd>2.3.co;2

WoldeGabriel, G., Olago, D., Dindi, E., and Owor, M. (2016). "Genesis of the East African Rift System," in *Soda Lakes of East Africa*. Editor M. Schagerl (Cham: Springer). doi:10.1007/978-3-319-28622-8_2

Wright, L. J., Muirhead, J. D., and Scholz, C. A. (2020). Spatiotemporal Variations in Upper Crustal Extension across the Different Basement Terranes of the Lake Tanganyika Rift, East Africa. *Tectonics* 39 (3), e2019TC006019. doi:10.1029/2019tc006019

Zanettin, B., Ej, V., and Em, P. (1979). *Correlation Among Ethiopian Volcanic Formation with Special Reference to the Chronological and Stratigraphical Problems of the Trap Series*.

Zhou, W., Beck, B., and Adams, A. (2002). Effective Electrode Array in Mapping Karst Hazards in Electrical Resistivity Tomography. *Environ. Geology.* 42 (8), 922–928. doi:10.1007/s00254-002-0594-z

Conflict of Interest: FK was employed by the company BP America.

The remaining authors declare that the research was conducted in the absence of any commercial or financial relationships that could be construed as a potential conflict of interest.

Publisher's Note: All claims expressed in this article are solely those of the authors and do not necessarily represent those of their affiliated organizations, or those of the publisher, the editors and the reviewers. Any product that may be evaluated in this article, or claim that may be made by its manufacturer, is not guaranteed or endorsed by the publisher.

frontiers | Frontiers in Earth Science

ORIGINAL RESEARCH
published: 19 April 2022
doi: 10.3389/feart.2022.839995

Seismic Constraints on the Trompsburg Layered Igneous Intrusion Complex in South Africa Using Two Deep Reflection Seismic Profiles

Michael Westgate[1], *Musa S. D. Manzi*[1]*, *Ian James*[2], *Marco A. G. Andreoli*[1,3] *and Raymond J. Durrheim*[1]

[1]School of Geosciences, University of the Witwatersrand, Johannesburg, , South Africa, [2]Southern Geoscience Consultants, West Perth, WA, Australia, [3]Department of Mechanical Engineering Science, University of Johannesburg, Johannesburg, South Africa

The discovery and characterization of layered intrusions around the globe have been predicated to a large degree on the imaging capabilities of the reflection seismic method. The ability of this tool to detect mineralization zones and structural controls such as faults and folds has been critical in unlocking the economic potential of igneous complexes, most notably the Bushveld Complex in South Africa. In this study, we present novel seismic constraints on the lesser-known Trompsburg Complex in South Africa. Two yet-unpublished seismic profiles were conducted end-to-end in the early 1990s, with a southwest-to-northeast trend through the centre of the ~2,400 km^2 Trompsberg potential field anomaly in South Africa, attributed to a 1915 ± 6 Ma buried layered intrusion complex. The complex was first detected by magnetic and gravity measurements near the town of Trompsburg in 1939 and was subsequently confirmed as a layered intrusion by borehole cores drilled thereafter. The combined length of the two profiles is 108 km. Both profiles have been reprocessed and interpreted to further constrain the subsurface expanse of the Trompsberg Complex along the seismic traverse. Processing and interpretation of the seismic profiles were aided by a handful of studies found in the literature: stratigraphy and physical property measurements of borehole cores that were drilled into the complex in the 1940s; pre-Karoo (~317 Ma) lithological maps that were constructed based on boreholes in and around the investigation area; and potential field maps of the intrusion area near the town of Trompsburg. Most of the seismic reflection energy is concentrated within the top 1 km in both profiles, where localized reflectors with strong amplitudes are observed, due likely to the dolerite sills that permeate the Karoo cover. These sills obstruct seismic illumination of underlying structures due to their high acoustic impedance contrast with the surrounding soft rock sediments, rendering underlying reflections challenging to identify and enhance. The base of the Karoo is confidently identified to be at an average depth of 1.5 km and several reflection packages have been identified thereunder. These are linked to Proterozoic supracrustals associated with the Witwatersrand, Ventersdorp, Transvaal/Griqualand West, and Kheis Supergroups, as well as the Trompsburg Complex that intruded into them. The

OPEN ACCESS

Edited by:
Bjarne Sven Gustav Almqvist, Uppsala University, Sweden

Reviewed by:
Craig Magee, University of Leeds, United Kingdom
John McBride, Brigham Young University, United States

***Correspondence:**
Musa S. D. Manzi
musa.manzi@wits.ac.za

Specialty section:
This article was submitted to Solid Earth Geophysics, a section of the journal Frontiers in Earth Science

Received: *20 December 2021*
Accepted: *22 March 2022*
Published: *19 April 2022*

Citation:
Westgate M, Manzi MSD, James I, Andreoli MAG and Durrheim RJ (2022) Seismic Constraints on the Trompsburg Layered Igneous Intrusion Complex in South Africa Using Two Deep Reflection Seismic Profiles. Front. Earth Sci. 10:839995. doi: 10.3389/feart.2022.839995

geometry of the Trompsburg Complex along the seismic traverse has been constrained with a moderate degree of confidence. It comprises a series of 30° northeasterly dipping reflectors near its southwestern boundary, flat reflectors near its centre at the town of Trompsburg, and 45° southwesterly dipping reflectors near its northeastern boundary. The lateral sub-Karoo extent of the complex is 60 km and its total thickness is difficult to constrain due to lack of deep reflections, but is likely between 6.6 and 7.5 km. The complex subcrops against the Karoo cover except near the southwestern region, where it is overlaid by Waterberg Group sediments.

Keywords: reflection, seismic, 2D, Trompsburg complex, hardrock, South Africa

INTRODUCTION

The reflection seismic method has been used extensively for, among others, mineral exploration and hardrock prospection (e.g., Pretorius, 1986; Durrheim, 2015; Manzi et al., 2019; Malehmir et al., 2021). Challenges presented by these environments are related to complex wavefield phenomena, such as scattering and diffraction, which are caused by sharp

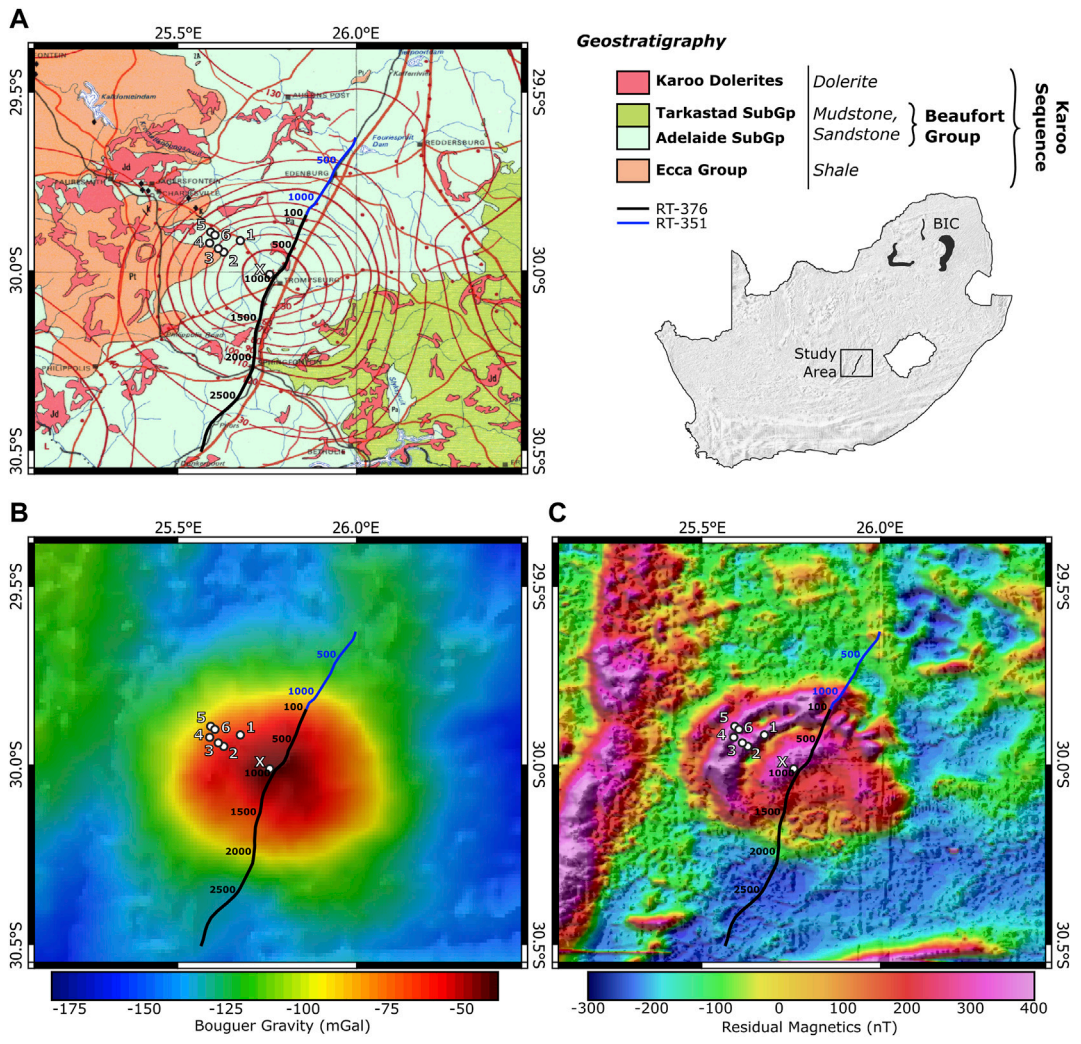

FIGURE 1 | Geological **(A)** and potential field maps, gravity in **(B)** and magnetic in **(C)**, of the Trompsburg anomaly with seismic profiles P1 (RT-376) and P2 (RT-351) overlaid in black and blue, respectively. Profile CMP numbers are labelled every 500th CMP. Boreholes are labelled 1 through 6 in the NW and X in the centre, corresponding to boreholes TG1 through TG6 and TGX, respectively. BIC, Bushveld Igneous Complex.

discontinuities, heterogeneities and anisotropies in the seismic velocity and density fields. Complex layering of rocks, metamorphic scars, and structural constraints that typify the hardrock setting hinder seismic detection and interpretation (Pretorius et al., 2003; Buske et al., 2015). Despite these challenges, the robustness of this method in imaging the subsurface with unprecedented accuracy and resolution renders it exceedingly valuable in the exploration and mining industry. In particular, structural constraints on mineral deposits and host rocks associated with igneous plumbing systems have been successfully mapped using the reflection seismic approach across diverse sets of geological, tectonic, and geomorphological environments (e.g., Scheiber-Enslin and Manzi, 2018; Manzi et al., 2019; Sehoole et al., 2020).

In South Africa, a substantial portion of the world-class gold and platinum deposits were characterized using the reflection seismic method prior to their exploitation. Such projects included the vast amount of corporate-funded seismic surveys that targeted the Bushveld Igneous Complex, the world's largest layered igneous intrusion, now accountable for 90% of the world's platinum group matals (PGM) reserves, as well as its substantial contribution to production of chromite and palladium. In this study, the reflection seismic method is used to image complex lithostratigraphic and structural features of the ~1915 Ma layered igneous intrusion in South Africa called the Trompsburg Complex, named after the town located at its centre (**Figure 1**).

Following the discovery of the positive, 50-km-wide Trompsburg gravity anomaly in 1944 near the town of Trompsburg, South Africa, several efforts were made to investigate the geology lying beneath the overlying sedimentary cover of the Carboniferous to Jurassic Karoo basin. Gravimetric and magnetometric surveys were conducted, followed by the drilling of seven exploration boreholes into the centre and northwestern rim of the geophysical anomaly, where the magnetic map of the anomaly exhibited concentric arcs of high amplitudes (**Figure 1**). The results of these surveys were initially documented by Ortlepp (1959) and Buchmann, (1960), which revealed a series of layered igneous intrusions beneath the Karoo cover, leading both authors to conclude the presence of a buried igneous complex. The former suggested an average total thickness of 3 km for the complex, and the latter a thickness of 10 km. The six boreholes in the northwestern region of the anomaly revealed several layers of mafic intrusions, including gabbros, anorthosite and magnetite, beneath the Karoo sedimentary rocks and dolerite sills, while the borehole near the centre of the anomaly only intersected granite beneath the Karoo.

Significant amounts of magnetite were observed within the layered intrusions, prompting multiple studies into the economic potential of the complex (Logan, 1979; Reynolds, 1979). Such studies revealed strong mineralogical and chemical correlations between the Trompsburg Complex and regions of the Bushveld Igneous Complex, suggesting the former to be a satellite intrusion of the latter (McCarthy et al., 2018). However, Rb-Sr isotopic and zircon dating of core samples from the Trompsburg Complex by Maier et al. (2003) yielded an age of 1915 ± 6 Ma, ~140 Ma younger than the crystallization of the Bushveld Igneous Complex at 2056 ± 4 Ma (cf. Walraven and Hattingh, 1993; Buick et al., 2001), and a derivation from a different, relatively depleted mantle source (Maier et al., 2003). McCarthy et al. (2018) comment on the striking similarity of lithologies between the two complexes and suggest that redating of the Trompsburg Complex should be undertaken.

The first attempt at a 3D model of the Trompsburg Complex was made by Maré and Cole (2006) based on physical property measurements they had conducted on retrieved core from the 1960 exploration boreholes. Density and magnetic susceptibility measurements conducted on the core samples were used to forward model the potential field anomaly of the Trompsburg Complex. Their model comprises an 8-km-thick layered intrusion with an average diameter of 65 km and an 8 km thick central feeder, totaling a thickness of 16 km near the centre of the complex. While the modelled potential field data correlate well with the observed field data, Maré and Cole (2006) Stress the ambiguity of potential field modelling, which in their study was exacerbated by the restriction of constraining borehole data to the centre and NW region of the complex. No further geological or geophysical investigations into the structure of the Trompsburg Complex have been conducted to verify or constrain its three-dimensional extent.

In the late 1980s and early 1990s, AngloGold Ashanti Ltd., then the Gold Division of the Anglo-American Corporation, commissioned several 6 and 16 s 2D seismic profiles to map crustal-scale structures across the Kaapvaal Craton in search of gold-bearing Witwatersrand Supergroup outliers (Durrheim, 2015). Most of these data have been donated to the Seismic Research Centre at the University of the Witwatersrand, South Africa, for crustal and mineralogical research. Since their acquisition, a handful of these profiles have been published in the literature (e.g. Stettler et al., 1999; Tinker et al., 2002; Westgate et al., 2020; Westgate et al., 2021), but many remain unpublished. Amongst the undisclosed surveys are two 6 s profiles that traverse the centre of the Trompsburg Complex with a SW-NE bearing (shown in **Figure 1**), namely profiles RT-376 in the SW and RT-351 in the NE. For simplicity, we refer to profiles RT-376 and RT-351 throughout the rest of this paper as P1 and P2, respectively. We have reprocessed these profiles separately using a standard reflection processing flow to obtain a migrated image of the subsurface that extends to a depth of ~15 km. Our reprocessing and interpretation of the seismic profiles have been informed by the aforementioned borehole and physical property studies, as well as geophysical and geological maps in the literature.

The primary objective of reprocessing the two seismic profiles is to image structural features beneath the Karoo sediments and dolerites that are related to the Trompsburg Complex. Secondary objectives include constraining the Karoo cover thickness and investigating pre-Trompsburg structures beneath the Karoo.

REGIONAL GEOLOGY AND GEOPHYSICS

Seismic profiles P1 and P2 are plotted on surface geology, gravity, and magnetic maps in **Figure 1**. The Trompsburg Complex

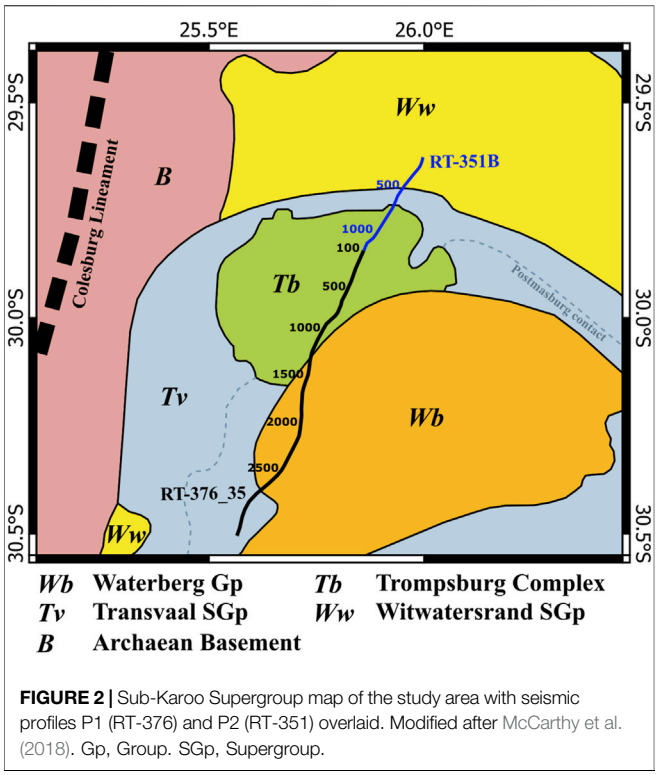

FIGURE 2 | Sub-Karoo Supergroup map of the study area with seismic profiles P1 (RT-376) and P2 (RT-351) overlaid. Modified after McCarthy et al. (2018). Gp, Group. SGp, Supergroup.

manifests as a 50-km-wide circular anomaly in both geophysical maps whose circumference intersects P1 at common midpoint (CMP) 2000 in the SW and P2 at CMP 760 in the NE. The magnetic map exhibits concentric arcs of high amplitudes in the NW that taper off in the NE and SW regions, and the overall magnetic signature of the complex is weaker in the SE.

The surface geological map in **Figure 1** consists entirely of ~360–145 Ma Karoo Supergroup rocks, which comprise basal tillite from the Carboniferous Dwyka Group, shale from the Permian Ecca Group, mudstone and sandstone from the Permian to Triassic Beaufort Group, and dolerites from the Karoo Dolerite Suite (KDS), which intruded the Karoo following crustal rupture around 182 Ma under an extensional regime. These dolerite dykes and sills permeate most of the Karoo Supergroup. They typically exhibit saucer-shape geometry and vary in size from a few centimeters to hundreds of meters thick (Coetzee and Kisters, 2016). Scheiber-Enslin et al. (2014; 2021) noted the effect of the KDS on the seismic imaging of structures located thereunder; in regions where dolerite sills were located, a lack of seismic illumination was observed in the traces within these regions. This lack of illumination is likely due to a strong reflection coefficient along the boundary of the weathered overburden and the high-density sills (Elde et al., 2018; Scheiber-Enslin et al., 2021). The seismic profiles traverse exclusively the sandstones from the Adelaide Subgroup of the Beaufort Group, as well as various dolerite outcrops from the KDS.

Due to lack of outcrop as well as ~1.5 km thick Karoo cover, mapping of sub-Karoo geology in the Trompsburg area has been inferred primarily from geophysical maps and boreholes (Borchers, 1964; Stratten, 1970; Pretorius, 1986; McCarthy et al., 2018). A sub-Karoo map of the southern Kaapvaal Craton was created by McCarthy et al. (2018) that details proposed extents of sub-Karoo lithologies with varying degrees of confidence. In their analysis, 22 boreholes were used to construct the sub-Karoo map in the region of the Trompsburg Complex. A simplified version of this map is shown in **Figure 2** with seismic profiles P1 and P2 overlaid.

Lying on the Archaean granite basement are quartzites, shales and diamictites that were intersected by boreholes to the east and NE of the Trompsburg Complex. Based on borehole correlations and zircon dating of the core samples, McCarthy et al. (2018) interpreted these as belonging to the West Rand and Central Rand Groups of the Archaean Witwatersrand Supergroup (2.9–2.7 Ga), which collectively compose the Colesburg Basin in the study area.

Sandwiched between the Witwatersrand and overlying rocks are the basalts and more localized quartzites and mafic units that comprise the late Archaean Ventersdorp Supergroup in the study region. McCarthy et al. (2018) note that these predominantly basaltic rocks underlie most of the Transvaal Supergroup across the Kaapvaal Craton and are present in boreholes ~50 km SW of the centre of the Trompsburg complex, just off the southernmost extent of seismic profile P1. According to the pre-Karoo map in **Figure 2**, the Ventersdorp rocks do not subcrop against the Karoo cover. They are thus expected to pinch out somewhere along the traverse of the seismic profiles before the Witwatersrand metasediments subcrop near the NE end of the profile (**Figure 2**).

The Neoarchaean-Paleoproterozoic Transvaal Supergroup (2.65–2.05 Ga) overlies the Witwatersrand and Ventersdorp Supergroups. In our study area, the Supergroup is confirmed by boreholes to be composed of dolomites and BIFs of the Chuniespoort Group, and basalts of the Pretoria Group. Two of the outer boreholes drilled into the Trompsburg geophysical anomaly intersected dolomites that Ortlepp (1959) first interpreted as belonging to the Transvaal Supergroup, which is now generally accepted. McCarthy et al. (2018) note that the BIFs are responsible for a strong v-shaped magnetic signature south of Trompsburg and infer from the anomaly shape that these formations are part of a NE plunging syncline.

The only pre-Karoo stratigraphic units observed in the area that are potentially younger than the 1915 ± 6 Ma Trompsburg Complex belong to what McCarthy et al. (2018) generically related to the Paleoproterozoic Waterberg Group (~2–1.8 Ga). This interpretation needs to be revisited considering recent work by Van Niekerk and Beukes (2019) on the Kheis Supergroup, a Waterberg equivalent with regional extent in the Northern Cape, far closer to the study area than the latter basin situated in the Limpopo Province. The oldest age obtained from the Hartley Formation, near the base of Kheis Supergroup is 1915.6 ± 1.4 Ma (Van Niekerk and Beukes, 2019), coinciding within error with the age of the underlying Trompsburg intrusion. Red arenites which exhibited similar composition and ages to those found in the Kheis Supergroup/Waterberg group were intersected by boreholes SE of the complex, implying the presence of an outlier of the basin in the vicinity of the complex (McCarthy et al., 2018). While Buchmann (1960) attributed the weak

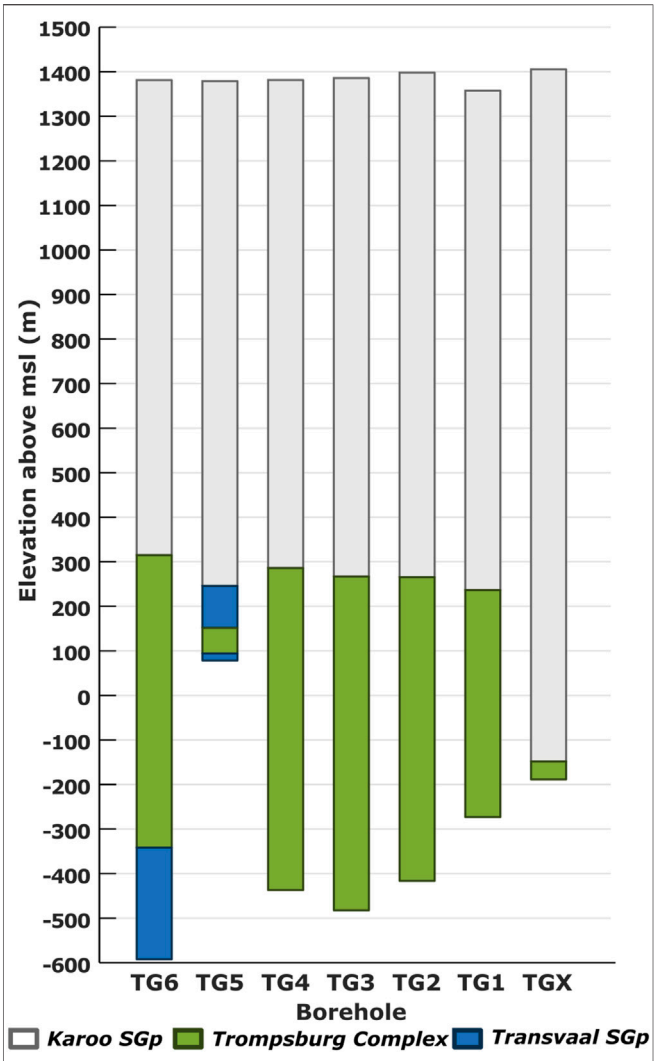

FIGURE 3 | Summary of cores of boreholes TG1 through TGX. Locations of boreholes can be seen in **Figure 1**.

geophysical signal in the SE portion of the Trompsburg Complex (**Figure 1**) to a lack of crystalline limestone within the Transvaal metasediments and thicker Karoo cover, McCarthy et al. (2018) suggested that the complex is overlain by Waterberg sediments (**Figure 2**) in this region, resulting in a weaker geophysical signature.

GEOLOGY OF TROMPSBURG COMPLEX

Boreholes

Logs of the boreholes that were drilled into the Trompsburg Complex in the 1950s are summarized in **Figure 3**. A more detailed log of the lithostratigraphy can be found in Ortlepp (1959) and Buchmann (1960). Holes TG1 through TG6 are located within the NW extents of the complex while hole TGX is located 200 m off the centre of the two seismic profiles (**Figure 1**). Each of the former six boreholes intersected mafic to ultramafic units belonging to the Trompsburg Complex, which are mostly gabbroic with intermittent magnetite, troctolite and anorthosite. The gabbro is dominated by plagioclase and olivine, and includes intermittent samples of clino-pyroxene and ortho-pyroxene. The two outermost boreholes (TG5 and TG6) contained samples of marble from the Transvaal Supergroup into which the complex intruded (Maier et al., 2003). The only igneous rock belonging to the complex that was interested by, and

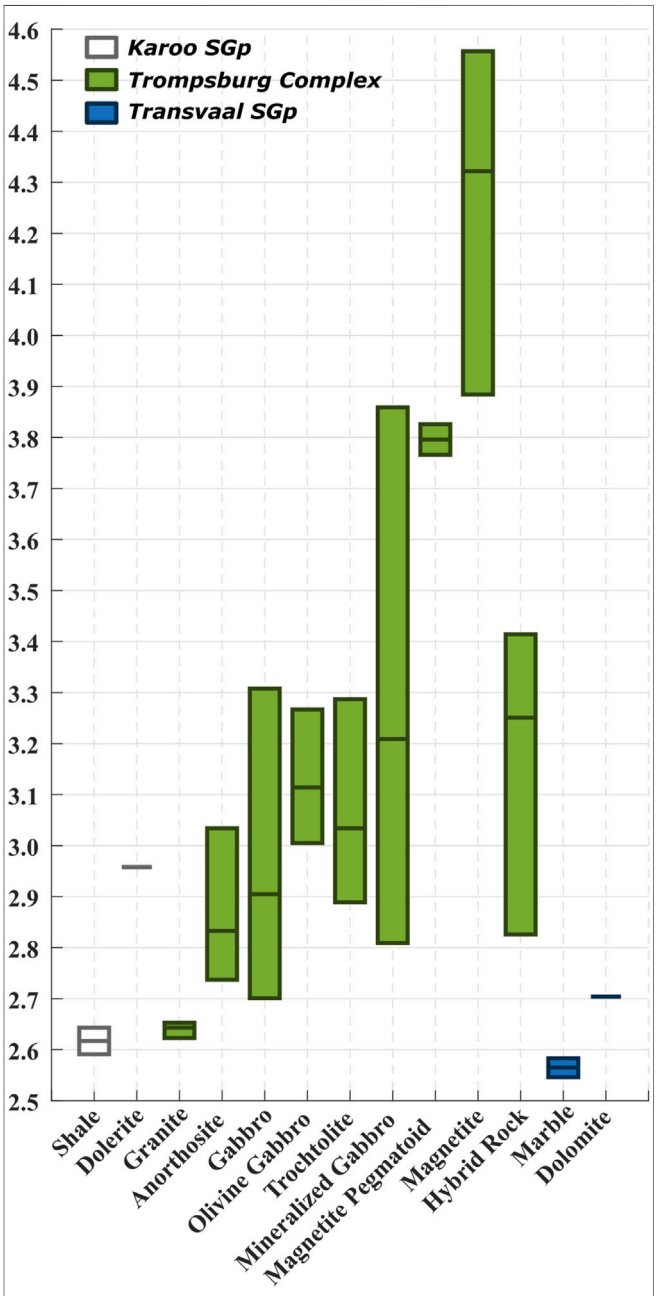

FIGURE 4 | Summary of density measurements of lithologies identified by Maré and Cole (2006). Bar limits denote maximum and minimum density values and centre lines denote average density values. Note that only one measurement was made on dolerite and dolomite samples.

found exclusively in, borehole TGX was a course-grained granophyric granite containing quartz, orthoclase and oligoclase grains (Ortlepp 1959).

Karoo sediments in each of the boreholes exhibit composite thicknesses of 1,558 m near the centre of the Trompsburg complex (borehole TGX), and 1,051–1,137 m near the outer rim of the complex (boreholes TG1 to TG6). As the latter six boreholes are clustered in the NW region of the complex and TGX located approximately 14 km to the SE, an explanation for the change in thickness is mostly conjectural. Ortlepp (1959) attributes the change in thickness either to a gentle NW-SE dip of the sub-Karoo topography, in which the sediment package was tilted prior to erosion, or a local valley/depression prior to deposition of the Karoo sediments. McCarthy et al. (2018) record Karoo thicknesses equal to those of TGX in boreholes located 33 km northeast, and 35 km south, of TGX.

Buchmann's (1960) interpretation of the boreholes and geophysical maps consisted of a gently NW-SE dipping Karoo cover, which overlie Trompsburg intrusions. The latter are characterized in the NW by gabbro and anorthosite layers with a 30° dip towards the centre of the intrusion, where granitic intrusions dominate the complex, reaching depths of 11 km.

Physical Properties

The 3D model of the Trompsburg Complex produced by Maré and Cole (2006) is based on physical property measurements on core retrieved from the TG1-TGX boreholes. The authors categorized samples of the cores, based primarily on their physical property contrasts and informed by the principal rock types logged by Ortlepp (1959), into quasilithological units (that is, representative units grouped by physical properties without further distinction).

Included in the physical property measurements made by Maré and Cole (2006) were density measurements, which are summarized in **Figure 4**. Due to lack of sonic measurements within the boreholes, acoustic impedance calculations, and therefore reflectivity modelling, is not possible. However, the density measurements can serve as first-order proxies of the reflectivity along boundaries between the quasilithological units. This can aid in a cautious interpretation of the reflection seismic profiles.

The relatively lower density values are attributed to shales from the Karoo Supergroup (2.61 g/cm^3) as well as marble and dolomites from the Transvaal Supergroup (2.56 g/cm^3 and 2.7 g/cm^3 respectively), which are substantially less dense than those of the Trompsburg intrusive rocks. Other than the 2.62 g/cm^3 granite, the rocks belonging to the Trompsburg complex exhibit densities much higher than the surrounding units, with values ranging from 2.7 to 4.5 g/cm^3. Within the Trompsburg suite, magnetite exhibits the highest average density of 4.32 g/cm^3 (**Figure 4**).

While these values do not give a direct measure of the seismic reflectivity in the region, it is useful to note the most significant density contrasts serve to inform the interpretation of the seismic profile rather than to serve as a basis thereof. Where the Karoo shales overlie the mafic components of the Trompsburg complex, there is a strong density contrast averaging 0.69 g/cm^3. A significant density contrast of 0.3 g/cm^3 occurs between Karoo shales and Karoo dolerites. However, a less significant contrast is found between the densities of the Karoo shales and the Trompsburg granites (0.02 g/cm^3), the latter of which are present near the centre of the Trompsburg Complex within borehole TGX. A strong density contrast (0.6 g/cm^3) is also present between the Trompsburg igneous rocks and the Transvaal dolomites and marble. Within the Trompsburg units, magnetite samples exhibit significantly higher density values than the rest of the igneous rocks, which could be the source of reflections within the complex.

METHODOLOGY

Seismic Acquisition

Acquisition of seismic profiles P1 and P2 were commissioned separately by Anglo-American, the former in 1990 and the latter in 1991, and share mostly identical acquisition parameters, which are summarized in **Table 1**. Both profiles utilized four seismic vibrators in a linear array with a linear sweep of 10–61 Hz. Shot and receiver spacing for each profile were both 50 m. Each shot record of both profiles comprised a total of 120 channels in a split-spread geometry that spanned a total distance of 5,950 m. Sercel SM4U 10 Hz geophones were used for both profiles and the sampling rate for both was 4 ms, with a total record length of 6 s. The profiles were acquired end-to-end with a SSW-NNE bearing that traversed roads through the centre of the Trompsburg potential field anomaly (**Figure 1**), spanning a total distance of 110 km, with a 3 km overlap.

Seismic Processing

The full processing flow of the reflection seismic profiles is summarized in **Table 2**. After verifying and integrating the retrieved geometry with the seismic data, the prestack component of the processing was conducted. This comprised initial datum and refraction statics, followed by a spiking deconvolution and bandpass frequency filter (60–10–99–120 Hz). A frequency-wavenumber (*f-k*) filter was then applied to remove ground roll and low-velocity (<3,500 m/s) linear signals. Velocity analysis consisted of constant velocity stack analysis on every 50th CMP gather and accompanied with iterative residual static corrections. **Figure 5** illustrates the improvement in reflection signals via the pre-stack workflow (blue arrows), as well as the suppression of ground roll (orange arrows) and first break arrivals (red arrows). Finally, before conversion to the depth domain, a Kirchoff pre-stack time migration was conducted to place reflections in their correct orientation and to collapse diffractions associated with sharp velocity contrasts. Due to the lack of velocity logs or other constraining depth data, the conversion to depth was performed using a smoothed version of the RMS velocity model.

TABLE 1 | Acquisition parameters for profiles P1 and P2

Acquisition parameter	RT-376 (P1)	RT-351 (P2)
Shooting Direction	N-S	
Spread	Split spread: 2975m-25m-25m–2975m. 120 active channels	
Recording Instrument	Sercel SN368	
Geophones	Sercel SM4U 1C–10 Hz	
Receiver Spacing	50 m	
Sampling Interval	4 ms	
Source	4 vibs, 3 sweeps per vib point	
Sweep Parameters	10–61 Hz linear sweep	
Source Spacing	50 m	
Profile Length	80 km	30
Nominal Fold	60	

TABLE 2 | Processing flow of seismic profiles.

Processing Step	Parameters: RT-376 (P1)	Parameters: RT-351 (P2)
1. Geometry	Write geometry to SEGY headers	
2. CMP binning	Crooked line. CMP bin spacing: 25 m	
3. Static corrections	Floating datum 1,550 m SRD 3,000 m/s rep. vel Refraction Statics: 6.2 ms RMS	Floating Datum 1,475 m SRD 3,000 m/s rep. vel Refraction Statics: 8.8 ms RMS
4. Deconvolution	Spiking deconvolution	
5. Frequency filter	Bandpass: 6–10–99–120 Hz	
6. F-K filter	Mute signals with velocities <3,500 m/s	
7. Velocity Analysis	Constant velocity stack analysis every 50th CMP	
8. Residual statics	4 iterations	
9. Migration	2D Kirchoff pre-stack time migration	
10. Stack	Normalized stacking	
11. Frequency filter	Bandpass: 10–18–50–70 Hz	
12. Depth conversion	Time-to-depth conversion using smoothed interval velocity model	

RESULTS

The final migrated and depth-converted seismic sections, along with CMP fold plots and potential field plots, for profiles P1 and P2 are shown in **Figures 6A,B**, respectively. CMP labels of the sections decrease from left to right in **Figure 6** because acquisition of the profiles was from NE to SW. Presented here are the observed seismic facies and boundaries.

A first glance at **Figures 6A,B** reveals that a significant amount of the seismic energy is contained within the top half of the sections. In particular, most of the high-amplitude reflections are restricted to the top 2 km of both sections. Lying beneath these is a reflection package that is present throughout both profiles at a constant 0 m-above-sea-level (msl), which is labelled R1 in **Figures 6B,C**. R1 has a high amplitude, with exception to areas of low fold such as at CMPs 2,700 and 1,000 of P1, as well as a distinctive reflectivity reminiscent of bedding.

Beneath R1, between CMPs 2000 and 1,200 of P1, is another strong reflection with a 30° dip to the SW. This reflector bears similar seismic reflectivity and (reverse) dip to a reflector located between CMPs 3,000 and 2,200 of P1. These reflectors, collectively labelled R2 in **Figure 6**, trace out a concave bowl beneath R1 with a discontinuous apex at CMP 2250 and elevation -2,500 msl. The discontinuity displaces the SW R2 reflector about 500 m above the NE reflector and is interpreted as a reverse fault that extends into deeper units.

The region of the profiles where Trompsburg reflectors are expected is characterized by chaotic reflection zones and weak, discontinuous reflections (**Figure 6C**). The reflections can be

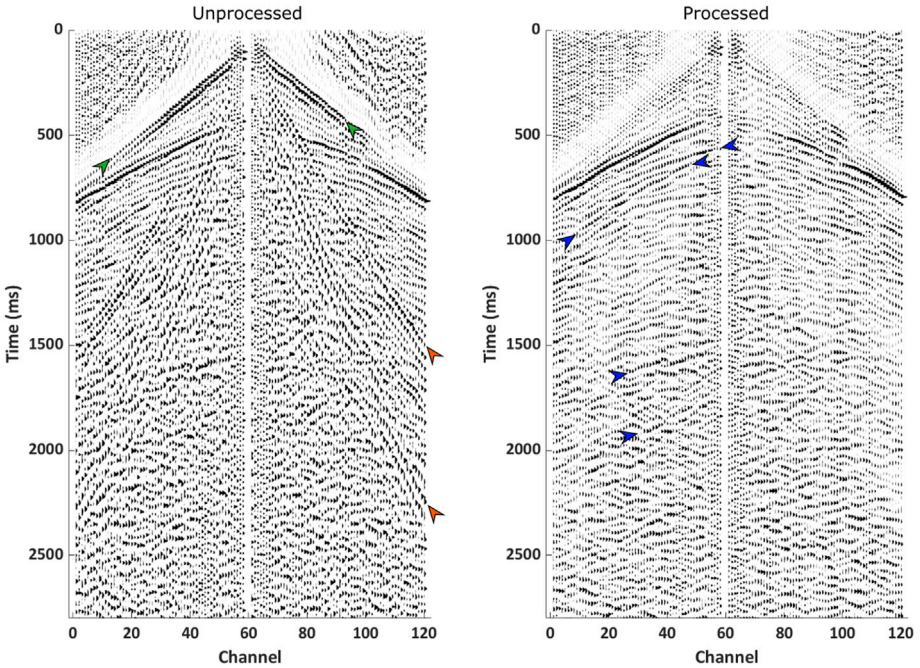

FIGURE 5 | Example shot gather from profile P1 (RT-376) before and after prestack processing flow. Green and orange arrows indicate first break and ground roll signals, respectively, that were removed. Blue arrows highlight enhanced reflection signals.

grouped by dip into three groups. The first group of reflections dip to the NE and are labelled R4. They lie between CMPs 2,200 and 1,100 of P1 and have a consistent dip of ~30°. The second group of reflections, labelled R5, has near-zero dip between CMPs 1700 and 1,000 and exhibits seismic facies characteristic of complex layering. The third group consists of reflections with a SW dip labelled R6. The R6 reflections have either a ~30° or a 45° dip; the former are observed closer to the centre of the expected complex and the latter along the NE bounds.

Approximately 1 km below and parallel to the SW R2 reflector is a more attenuated reflector labelled R3 (**Figure 6C**). Accompanying R3 is a weaker parallel reflector ~500 m below it. A series of weak, almost horizontal reflectors, labelled R8, are located beneath R3 at an elevation of -3,000 msl (**Figure 6C**). Two reflector packages labelled R9 and R10 in **Figures 6B,C** lie beneath R8. In profile P1 (**Figure 6C**), both R9 and R10 exhibit strong reflection amplitudes and appear to have a high degree of thrust-faulting.

Interpretation

In **Figures 6B,C**, strong reflections have been traced in black and interpreted stratigraphic units, as discussed in this section, have been overlaid on the migrated seismic sections of the respective profiles. While the focus of the seismic interpretation is on the Trompsburg Complex, first order interpretations of other supracrustals belonging to the Witwatersrand, Ventersdorp, Transvaal, Kheis, and Karoo Supergroups are given. Most of the seismic energy is concentrated in the top 2 km of the section, leaving less energy to transmit to deeper strata including the target Trompsburg Complex. Thus, our interpretations are informed largely by the *a priori* geophysical and geological datasets: magnetic, gravimetric, and geological maps, as well as the physical property data. The interpretation presented here provides, in our estimation, the model that best explains the combined set of these datasets with the observed seismic reflections.

Another factor that must be considered in the interpretation is that the depth conversion was performed using the RMS velocity model due to lack of constraining data in the area. This means that accuracy in depth is limited by the presence and accuracy in picked velocities. Where velocity picks were sparse, i.e., where there were no clear coherent reflection events, there is no strong tie between time and depth. Furthermore, any coherent events in time that are preceded by a gap in the velocity model are also limited in accuracy of depth. This makes it challenging to produce an accurate model in the depth domain. Despite these challenges, depth conversions based on picked velocities, or even with constant velocity models, have proven to be robust in multiple hardrock settings (e.g. Markovic et al., 2019; Westgate et al., 2020), and we are relying on this robustness in our interpretation.

The reflections in the top 2 km are due primarily to the dolerite suite within the Karoo cover. The characteristic saucer shape of the sills is evident throughout the Karoo in **Figures 6B,C**. We interpret the high-amplitude and bedding-like reflectivity of R2 as resulting from the basal Dwyka Group of the Karoo Supergroup. This interpretation is consistent with the density contrasts in **Figure 4**. With this interpretation, the average total thickness of the Karoo cover across the seismic profiles is 1,400 m, which correlates with observations from borehole TGX, located near

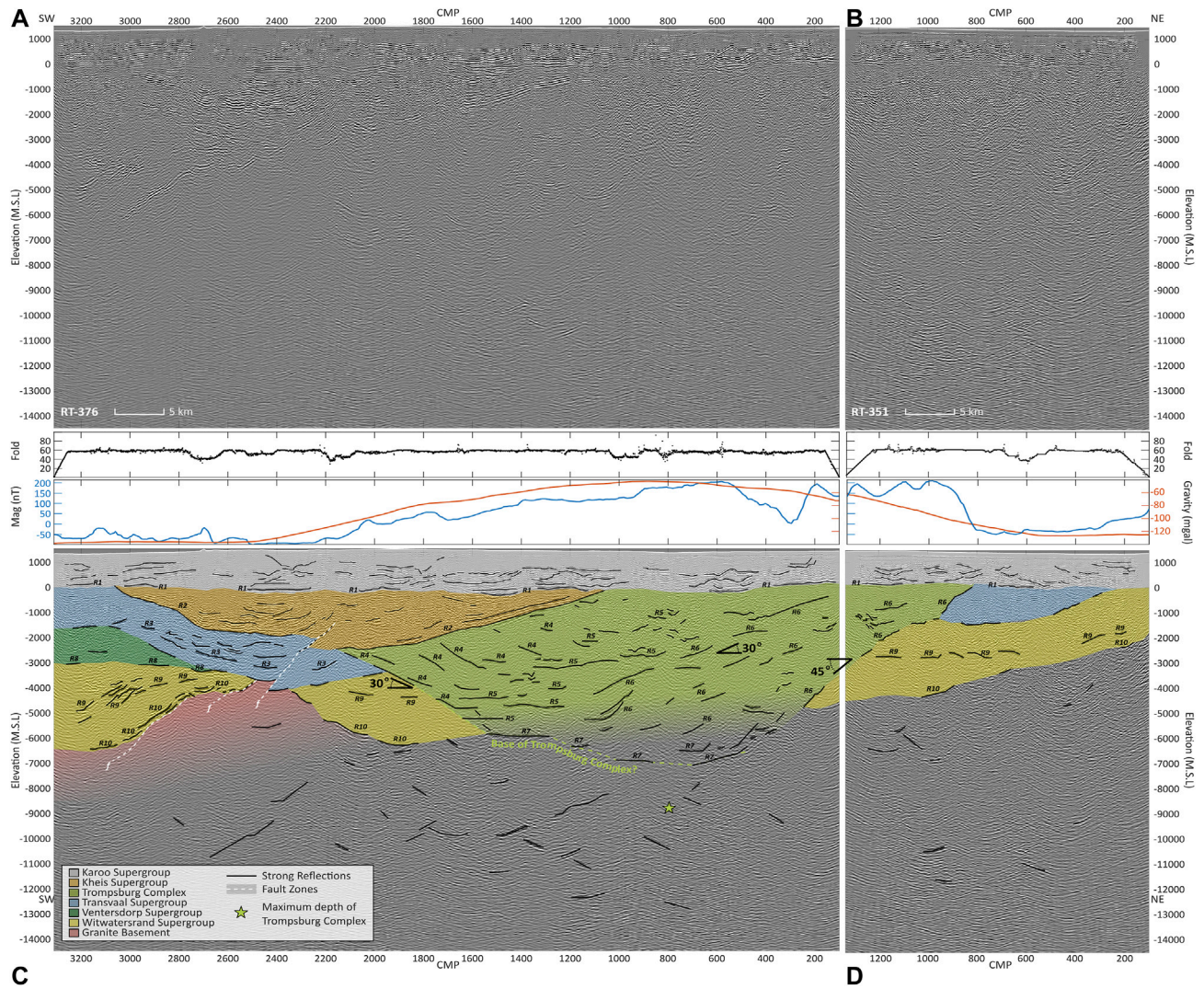

FIGURE 6 | Uninterpreted migrated sections of profiles P1 (RT-376; **A**) and P2 (RT-351; **B**) as well as fold plots, potential field plots, and interpreted sections **(C,D)**. Potential field data were obtained by sampling the relevant maps displayed in **Figure 1** along the seismic profiles. Interpreted sections comprise black lines denoting identified reflections, faults in dotted white lines, and stratigraphic units in colour. Identified reflectors are labelled as cited in the text.

CMP 900 of P1 (**Figure 6C**), as well as other boreholes in the region (McCarthy et al., 2018).

The R2 reflectors pinch out against the Karoo cover where P1 intersects the boundary of the Waterberg Group (i.e., Kheis Supergroup) in the pre-Karoo map by McCarthy et al. (2018) (**Figure 2**). The R2 reflectors are thus interpreted as the base of the Kheis Supergroup, which attains a maximum thickness at CMP 2200 of 2.5 km, and has a total lateral sub-Karoo expanse of 45 km along the traverse of P1.

R4 and R6 are interpreted as comprising the SW and NE boundaries of the Trompsburg Complex, respectively. With this interpretation, the total sub-Karoo expanse of the complex along the profiles is 60 km. The SW third of the complex is overlain by Kheis Supergroup sediments and the NE boundary of the Trompsburg Complex is located beneath the Karoo cover near CMP 800 of P2. Both of these observations are consistent with the geophysical maps in **Figure 1** and the pre-Karoo map in **Figure 2**. The potential field plots in **Figure 6** reinforce this interpretation: maximum values in both magnetic and gravity data are located above the R5 reflectors, centred between the R4 and R6 pinch-outs. Additionally, the potential field profiles both exhibit, especially the magnetic profile, a more gradual increase of amplitude in the SW approaching the centre of the interpreted complex, and a rapid decrease in the NE. The gradual SW limb can be explained by the overlying Kheis rocks and a 30° dip of the Trompsburg intrusions, while a steeper 45° dip and no overlying rocks beneath the Karoo yield a steeper NE potential field limb. The magnetic data exhibits short wavelength (~5 km) amplitude fluctuations near the overlap region of the two profiles. We interpret this as intermittent mineralization within the Trompsburg Complex. The lack of

strong and coherent reflections below −5,000 msl obscures distinction between Trompsburg-related reflections and basement reflections, resulting in an unconstrained basal reflection of the complex. A series of weak reflections at about −7,000 msl, labelled R7, are tentatively interpreted as the base of the complex, rendering it with a maximum thickness of ~6.6 km.

The R3 reflector is interpreted to be from iron mineralization within the BIFs of the Chuniespoort Group of the Transvaal Supergroup. Its fluctuating amplitude could be resultant of varying degrees of mineralization density along the horizon. The underlying weaker reflector is interpreted as the quartzites that comprise the base of the Transvaal metasediments (McCarthy et al., 2018). Between CMPs 2,400 and 2,200 (**Figure 6C**) the metasediments are disrupted by the aforementioned reverse fault that displaced the base of the Kheis Supergroup, before they pinch out against the boundary of the Trompsburg Complex. In profile P2 (**Figure 6D**), the Transvaal Supergroup is interpreted to lie NE of the Trompsburg Complex with a thickness of 1 km, which tapers off at CMP 250.

R8 is interpreted as the base of the Ventersdorp Supergoup, which averages in thickness of 1.2 km and pinches out beneath the Transvaal metasediments near CMP 2600. This interpretation is consistent with boreholes lying ~50 km SW of the town of Trompsburg as detailed by McCarthy et al. (2018).

R10 is interpreted as the base of the Witwatersrand Supergroup and R9 as an internal reflection, likely associated with the base of the Central Rand Group. R10 pinches out against the Transvaal Supergroup at CMP 2500 of P1 due to a reverse fault that terminates at the base of the Transvaal Supergroup and is subparallel to the aforementioned reverse fault that extends into the Kheis. The Witwatersrand strata are interpreted to reemerge near CMP 2300 and extend further NE until being truncated by the Trompsburg Complex. On the NE side of the complex, the Witwatersrand rocks directly underlie the Transvaal metasediments before subcroping against the Karoo Supergroup at CMP 220 in P2.

The basement, which is interpreted to exist at depths greater than 6 km, exhibits a collection of both discontinuous reflections with randomly distributed orientations and migration "smile" signals. These could be computational artefacts caused by the migration or related to changes in the basement facies (such as localized metamorphism, for example).

DISCUSSION AND CONCLUSION

Certainty in the geological interpretation of seismic data is reduced when dealing with 2D data. True dips and thicknesses cannot be determined from a 2D section and out-of-plane reflections can lead to misinterpretations of in-plane features. This is exacerbated by implications of the hardrock setting and layered igneous plumbing systems: seismic energy that is scattered ubiquitously due to heterogeneities in rock characteristics, and complex subsurface structures as the result of metamorphism, all lead to a complex wavefield and seismic reflections that have weak amplitudes and coherence across traces. Seismic interpretation is non-unique and there can be multiple plausible geological models that fit the same seismic data, especially if it is 2D. The interpretation we present in **Figures 6C,D** is based to a large degree on the constraining datasets (magnetic, gravimetric and geological maps, as well as the borehole and physical property measurements).

In addition to these factors, as is the case with seismic profiles P1 and P2, the surficial Karoo Supergroup is laden with dolerite intrusions. The large acoustic impedance contrast along the boundaries between the igneous dolerites and the Karoo sediments causes scattering of seismic energy and diminishes transmission of seismic energy to deeper layers. This is a common obstacle in the reflection seismic method (e.g., Eide et al., 2018; Scheiber-Enslin et al., 2021). There are thus varying degrees of confidence in the interpreted units laid out in **Figures 6C,D**, with the highest confidence placed on the interpretations pertaining to the Karoo Supergroup and Kheis Supergroup. Interpretations of the other supracrustal units, including the Trompsburg Complex, rely heavily on the supporting literature mentioned in earlier chapters (Ortlepp, 1959; Buchmann, 1960; McCarthy et al., 2018).

Seismic interval velocities within the two profiles range from 4,000 m/s to 6,500 m/s, with the former being attributed to Karoo sediments and the latter to metamorphosed basement granite. These velocities coincide with those recorded in the literature (Stettler et al., 1999; Tinker et al., 2002; Durrheim, 2015). The average seismic velocity of the sub-Karoo seismic waves was 5,000 m/s and the dominant frequency of the migrated data is 30 Hz. Using the Widess quarter-wavelength criterion (Widess, 1973), the vertical seismic resolution is thus 40 m. Our first order interpretation of sub-Karoo supracrustals requires a significantly less stringent resolution limit. Upon migration, this is also the horizontal resolution of the seismic data (Yilmaz, 2001).

The centre of the Trompsburg geophysical anomaly (**Figure 1**) is located near CMP 1000 of profile P1, and tapers off near CMP 2000 of P1 to the SW, and CMP 1000 of P2 to the NE. The bounds of the seismically interpreted Trompsburg Complex (**Figure 6**) correlate well with these locations. Borehole TGX, located near CMP 900, intersected Trompsburg granite at an elevation of −150 msl (**Figure 3**), which is the same elevation that the complex subcrops against the Karoo in our model (**Figure 6**). Additionally, our model conforms with the interpretation by McCarthy et al. (2018) that the weaker potential field signature of the Trompsburg Complex in its southern region is attributed to overlying sediments from the Kheis Supergroup. The Kheis Supergroup in **Figure 6C** lies within the bounds interpreted by McCarthy et al. (2018) in their sub-Karoo map (**Figure 2**), with a maximum thickness of 2.5 km. Furthermore, the 30° dip of the Trompsburg layers in the outer SW and inner NE sections of our interpretation is the same as the dip that Buchmann (1960) characterized for the NW outer Trompsburg layers based on the boreholes drilled in the 1950s. Hence, our seismic interpretation of the Trompsburg Complex is fairly well constrained by previous studies in the literature.

While multiple reflectors were identified within the Trompsburg Complex, their lack of continuity, complex layering reflection patterns, and weak reflection amplitude

prevented distinction between internal layers within the complex. The absence of strong reflections within the complex can be attributed to a general lack of seismic energy penetrating beneath the Karoo, or an insignificant acoustic impedance contrast. The densities illustrated in **Figure 4** suggest that any significant reflections originating from within the complex would be associated with zones of mineralization; it is possible that mineralization within the complex is restricted to the NW and N regions. The seismic profiles appear to traverse a break in the magnetic high along the outer rim of the complex (**Figure 1**).

The 6.6 km thickness of the Trompsburg Complex near its centre at CMP 800 (**Figure 6**) is more partial to Buchmann's (1960) 10 km thickness than to Ortlepp's (1959) 2–3 km. The 3D potential field model by Maré and Cole (2006) required a centre thickness of 16 km (6 km without the modelled feeder, which is the closest value to the seismic thickness). While the 6.6 km central depth of the complex in **Figure 6** is not tightly substantiated, a further constraint can be placed on the basal depth of the complex by extending the 30° dipping SW bound of the complex and the 45° dipping NE bound of the complex and finding their intersection. Whilst this gives a reasonable depth constraint, it is possible that reflectors with dips greater than 45° are less likely to be imaged, hence the depth obtained by this method is essentially a minimum depth. The result is marked with a green star in **Figures 6C,D** is located at CMP 800 and −9,000 msl, which corresponds to a maximum thickness of 7.5 km for the complex. At this point, no strong or continuous reflections can be associated with the base of the complex, nor with the contact between mafic rocks and the central granite.

Apart from the Trompsburg and Kheis rocks, the pre-Karoo supracrustals that were identified in the seismic profiles with a moderate degree of certainty were the Witwatersrand, Ventersdorp, and Transvaal Supergroups. The Ventersdorp Supergoup exhibits a maximum thickness of 1.1 km at the SW end of profile P1 and pinches out between the other two aforementioned units before they are intruded by the Trompsburg Complex. The Witwatersrand Supergroup is discontinuous in the SW portion of the seismic profiles due to reverse and thrust faulting, and is continuous NE of the Trompsburg intrusion with an average thickness of 2 km. The Transvaal Supergroup underlies the Kheis Supergroup in the SW before it is intruded by Trompsburg rocks. It is faulted in this region and has an average thickness of 1.5 km. NE of the Trompsburg Complex, the Transvaal Supergroup has a thickness of 1 km before pinching out further NE, where Witwatersrand Supergroup subcrops against the Karoo cover. The basement boundary is uncertain throughout much of the profiles due to the lack of reflections associated therewith, and the seismic signature at >7 km depths is chaotic and incoherent.

In summary, our interpretation of the seismic profiles P1 and P2 suggests that the Trompsburg Complex is ~6.6 km thick near its centre, has a 60 km lateral extent beneath the Karoo cover, and is overlain by Kheis Supergroup sediments in the SE. Due to weak seismic energy at depth, intra-Trompsburg layering was not resolvable but dips of various reflectors within the complex were identified to be 30° near its SW extent, and 45° near its NE extent, where the complex intruded into supracrustals comprising both Witwatersrand and Transvaal Supergroups. Lastly, the reverse fault at CMP 2400 and the broad synform structure of the Kheis and Transvaal Supergroups between CMP 3000 and CMP 1000 appear consistent with the thrusting style of deformation characteristic of the Kheis Supergroup (Van Niekerk and Beukes, 2019).

We have shown in this study that integration of seismic reflection data with geological and potential field data is useful in constraining the expanse and depth of the Trompsburg Igneous Complex. In general, the seismic method is an important tool in discovering and characterizing igneous plumbing systems and possibly unlocking the economic potential thereof. 3D seismic surveys in particular are not restricted by the challenges that come with 2D data, such as dip and thickness approximations, out-of-plane anomalies, inaccuracies in migration imaging, etc. Layered intrusions often exhibit strong acoustic impedance contrasts, both internal (due to mineralization zones as well as density contrasts between subsequent intrusion events) and external (due to strong density contrasts between igneous intrusions and sedimentary host rocks as well as metamorphism thereby) that allow for the detection and resolution of such boundaries (e.g., Deemer and Huricj, 1997; Manzi et al., 2019; Sehoole et al., 2020).

DATA AVAILABILITY STATEMENT

The original contributions presented in the study are included in the article/Supplementary Material, further inquiries can be directed to the corresponding author.

AUTHOR CONTRIBUTIONS

MW was responsible for processing and interpreting the seismic data, as well as drafting the manuscript and assembling all images. MM conceptualized the research project, facilitated the seismic data transfer and assisted with seismic interpretation and manuscript writeup. IJ assisted with seismic data processing. MA assisted with interpretation of structural geology within seismic data. RD assisted with seismic processing and interpretation.

FUNDING

This project was funded by CIMERA. The support of the DSI-NRF Centre of Excellence (CoE) for Integrated Mineral and Energy Resource Analysis (DSI-NRF CIMERA) towards this research is hereby acknowledged. Opinions expressed and conclusions arrived at are those of the authors and are not necessarily to be attributed to the CoE.

ACKNOWLEDGMENTS

In addition to the CoE who funded this project, the donation of seismic data by AngloGold Ashanti is acknowledged and greatly appreciated. HiSeis Pty. Ltd. is acknowledged for sponsoring Petrosys Globe Claritas software licenses that

enabled processing of the seismic data. The Council of Geosciences of South Africa is also acknowledged for providing geological, gravity magnetic data. The work presented here was facilitated by the Seismic Research Centre at the University of the Witwatersrand, South Africa, without which this research would not have been possible.

REFERENCES

Borchers, R. (1964). "Exploration of the Witwatersrand and its Extensions," in *The Geology of Some Ore Deposits in Southern Africa*. Editor S. H. Haughton (Johannesburg, South Africa: Geological Society of South Africa), 1–24.

Buchmann, J. P. (1960). Exploration of a Geophysical Anomaly at Trompsburg, Orange Free State, South Africa. *Trans. Geol. Soc. South Africa* 63, 1–10.

Buick, I. S., Maas, R., and Gibson, R. (2001). Precise U-Pb Titanite Age Constraints on the Emplacement of the Bushveld Complex, South Africa. *J. Geol. Soc.* 158 (1), 3–6. doi:10.1144/jgs.158.1.3

Buske, S., Bellefleur, G., and Malehmir, A. (2015). Introduction to Special Issue on "Hard Rock Seismic Imaging". *Geophys. Prospecting* 63 (4), 751–753. doi:10.1111/1365-2478.12257

Coetzee, A., and Kisters, A. (2016). The 3D Geometry of Regional-Scale Dolerite Saucer Complexes and Their Feeders in the Secunda Complex, Karoo Basin. *J. Volcanology Geothermal Res.* 317, 66–79. doi:10.1016/j.jvolgeores.2016.04.001

Deemer, S., and Hurich, C. (1997). Seismic Image of the Basal Portion of the Bjerkreim-Sokndal Layered Intrusion. *Geol* 25 (12), 1107–1110. doi:10.1130/0091-7613(1997)025<1107:siotbp>2.3.co;2

Durrheim, R. J. (2015). "Structural Seismology: Investigations of the Crust and Mantle," in *The History of Geophysics in Southern Africa*. Editor J. H. de Beer (Stellenbosch, South Africa: Sun Press), 165–189.

Eide, C. H., Schofield, N., Lecomte, I., Buckley, S. J., and Howell, J. A. (2018). Seismic Interpretation of Sill Complexes in Sedimentary Basins: Implications for the Sub-sill Imaging Problem. *J. Geol. Soc.* 175 (2), 193–209. doi:10.1144/jgs2017-096

Logan, C. T. (19792012). A Mineralogical Investigation of Borehole Cores from the Trompsburg Complex. *MINTEK. Rep. no.*, 1–16.

Maier, W. D., Peltonen, P., Grantham, G., and Mänttäri, I. (2003). A New 1.9 Ga Age for the Trompsburg Intrusion, South Africa. *Earth Planet. Sci. Lett.* 212, 351–360. doi:10.1016/s0012-821x(03)00281-4

Malehmir, A., Markovic, M., Marsden, P., Gil, A., Buske, S., Sito, L., et al. (2021). Sparse 3D Reflection Seismic Survey for Deep-Targeting Iron Oxide Deposits and Their Host Rocks, Ludvika Mines, Sweden. *Solid Earth* 12 (2), 483–502. doi:10.5194/se-12-483-2021

Manzi, M. S. D., Cooper, G. R. J., Malehmir, A., and Durrheim, R. J. (2019). Improved Structural Interpretation of Legacy 3D Seismic Data from Karee Platinum Mine (South Africa) through the Application of Novel Seismic Attributes. *Geophys. Prospecting* 68 (1), 145–163. doi:10.1111/1365-2478.12900

Maré, L. P., and Cole, J. (2006). The Trompsburg Complex, South Africa: A Preliminary Three Dimensional Model. *J. Afr. Earth Sci.* 44, 314–330. doi:10.1016/j.jafrearsci.2005.11.026

Markovic, M., Maries, G., Malehmir, A., Ketelhodt, J., Bäckström, E., Schön, M., et al. (2019). Deep Reflection Seismic Imaging of Iron-oxide Deposits in the Ludvika Mining Area of central Sweden. *Geophys. Prospecting* 68 (1), 7–23. doi:10.1111/1365-2478.12855

McCarthy, T. S., Corner, B., Lombard, H., Beukes, N. J., Armstrong, R. A., and Cawthorn, R. G. (2018). The Pre-karoo Geology of the Southern Portion of the Kaapvaal Craton, South Africa. *South. Afr. J. Geology.* 121 (1), 1–22. doi:10.25131/sajg.121.0006

Ortlepp, R. J. (1959). A Pre-karoo Igneous Complex at Trompsburg, Orange Free State, Revealed by Drilling Exploration. *Trans. Geol. Soc. South Africa* 62, 33–57.

Pretorius, C. C., Muller, M. R., Larroque, M., and Wilkins, C. (2003). "A Review of 16 Years of Hardrock Seismics on the Kaapvaal Craton," in *Hardrock Seismic Exploration*. Editors D. W. Eaton, B. Milkereit, and M. H. Salisbury (Tulsa, OK: Society of Exploration Geophysicists).

Pretorius, D. A. (1986). "The Witwatersrand Basin," in *Mineral Deposits of Southern Africa*. Editors C. R. Anhaeusser and S. Maske (Johannesburg, South Africa: Geological Society of South Africa).

Reynolds, I. M. (19792017). Vanadium-bearing Titaniferous Iron Ores from the Rooiwater, Usushwana, Mambula, Kaffirskraal, and Trompsburg Igneous Complexes. *MINTEK. Rep. no.*, 1–65.

Scheiber-Enslin, S. E., and Manzi, M. (2018). Integration of 3D Reflection Seismics and Magnetic Data for Deep Platinum Mine Planning and Risk Mitigation: a Case Study from Bushveld Complex, South Africa. *Exploration Geophys.* 49 (6), 928–939. doi:10.1071/eg17083

Scheiber-Enslin, S. E., Manzi, M., and Webb, S. J. (2021). Seismic Imaging of Dolerite Sills and Volcanic Vents in the Central Karoo, South Africa: Implications for Shale Gas Potential. *South. Afr. J. Geology.* 124 (2), 465–480. doi:10.25131/sajg.124.0043

Scheiber-Enslin, S. E., Webb, S. J., and Ebbing, J. (2014). Geophysically Plumbing the Main Karoo Basin, South Africa. *South. Afr. J. Geology.* 117 (2), 275–300. doi:10.2113/gssajg.117.2.275

Sehoole, L., Manzi, M. S. D., Zhang, S. E., and Bourdeau, J. E. (2020). An Innovative Seismic and Statistical Approach to Understand 3D Magmatic Structures and Ore Deposits in the Western Bushveld Complex, South Africa. *Ore Geology. Rev.* 126, 103784. doi:10.1016/j.oregeorev.2020.103784

Stettler, E. H., Prinsloo, J., Hauger, M. E., and du Toit, M. C. (1999). A Crustal Geophysical Model for the Kheis Tectonic Province, South Africa, Based on Magnetotelluric, Reflection Seismic, Gravity and Magnetic Data Sets. *South. Afr. Geophys. Rev.* 3, 54–68.

Stratton, T. (1970). "Sub-Karoo Geology of the Karoo Basin in South Africa," in Proceedings and Papers of the Second Gondwana Symposium (South Africa, 209–211.

Tinker, J., de Wit, M., and Grotzinger, J. (2002). Seismic Stratigraphic Constraints on Neoarchean - Paleoproterozoic Evolution of the Western Margin of the Kaapvaal Craton, South Africa. *South. Afr. J. Geology.* 105, 107–134. doi:10.2113/105.2.107

Van Niekerk, H. S., and Beukes, N. J. (2019). Revised Definition/outline of the Kheis Terrane along the Western Margin of the Kaapvaal Craton and Lithostratigraphy of the Newly Proposed Kheis Supergroup. *South. Afr. J. Geology.* 122 (2), 187–220. doi:10.25131/sajg.122.0014

Walraven, F., and Hattingh, E. (1993). Geochronology of the Nebo Granite, Bushveld Complex. *South. Afr. J. Geology.* 96, 31–41.

Westgate, M., Manzi, M. S. D., James, I., and Harrison, W. (2020). New Insights from Legacy Seismic Data: Reprocessing of Legacy 2D Seismic Data for Imaging of Iron-oxide Mineralization Near Sishen Mine, South Africa. *Geophys. Prospecting* 68 (7), 2119–2140. doi:10.1111/1365-2478.12996

Westgate, M., Manzi, M. S. D., Malehmir, A., Gibson, R. L., Andreoli, M. A. G., and Bumby, A. (2021). A Reappraisal of Legacy Reflection Seismic Data from the Western Margin of the Kaapvaal Craton, South Africa, with Implications for Mesozoic-Cenozoic Regional Tectonics. *Tectonophysics* 813, 228934. doi:10.1016/j.tecto.2021.228934

Widess, M. B. (1973). How Thin Is a Thin Bed? *Geophysics* 38 (6), 1176–1180. doi:10.1190/1.1440403

Yilmaz, O. (2001). Seismic Data Analysis: Processing, Inversion and Interpretation of Seismic Data. *Soc. Explor. Geophys.* 1, 1803–1805. doi:10.1190/1.9781560801580

Conflict of Interest: At the time of research/writing, Author IJ was employed by HighSeis Pty Ltd. They are now employed by Southern Geoscience Consultants.

The remaining authors declare that the research was conducted in the absence of any commercial or financial relationships that could be construed as a potential conflict of interest.

Publisher's Note: All claims expressed in this article are solely those of the authors and do not necessarily represent those of their affiliated organizations, or those of the publisher, the editors, and the reviewers. Any product that may be evaluated in this article, or claim that may be made by its manufacturer, is not guaranteed or endorsed by the publisher.

frontiers | Frontiers in Earth Science

ORIGINAL RESEARCH
published: 12 May 2022
doi: 10.3389/feart.2022.827011

Influence of Meteorological Processes on cGPS Measurements of Crustal Movements

Sikelela Gomo, Gordon R. J. Cooper, Raymond J. Durrheim and Musa S. D. Manzi*

School of Geosciences, University of the Witwatersrand, Johannesburg, South Africa

Surface displacement measurements collected using continuous Global Positioning System (cGPS) stations include the contribution of both endogenic processes (e.g., plate tectonics, isostasy) and exogenic processes that show seasonal variation (e.g., climate). These seasonal variations distort the tectonic signals and limit the usefulness of short-term investigations. This paper explores cGPS and meteorological time series collected in southern Africa and investigates whether the usefulness of cGPS time series can be improved by accounting for the seasonal effects of the dominant meteorological processes. The study is carried out using time, frequency, and time-frequency domain signal processing (inferential) analysis techniques. It was found that from the considered atmospheric processes, thermally-induced effects, which are not corrected for in the cGPS data, are the most prominent meteorological contributors in the vertical annual deformation component observed in cGPS time series. The effects of heave action (due to seasonal subsurface water infiltration and absorption, as well as changes in the water table) and changes of water mass distribution (caused by infiltration, transportation, extractions, and evaporation) on the displacement time series are much smaller. This suggests that correcting for thermal expansion, contraction, and thermal-induced errors could reduce the annual seasonal deformation component observed in cGPS position measurements in southern Africa and, most probably, in other parts of the world subjected to large seasonal variations in atmospheric temperatures. Reducing the magnitude of the seasonal components would increase the usefulness of short-term cGPS campaigns.

Keywords: Signal processing, meteorological, cGPS, wavelet, Fourier, semblance, southern Africa

OPEN ACCESS

Edited by:
Mourad Bezzeghoud, Universidade de Évora, Portugal

Reviewed by:
Yuanjin Pan, Wuhan University, China
Alexis Rigo, Laboratoire de géologie de l'Ecole Normale Supérieure (LG-ENS), France

****Correspondence:***
Sikelela Gomo
sikelelagomo@gmail.com

Specialty section:
This article was submitted to Solid Earth Geophysics, a section of the journal Frontiers in Earth Science

Received: *01 December 2021*
Accepted: *19 April 2022*
Published: *12 May 2022*

Citation:
Gomo S, Cooper GRJ, Durrheim RJ and Manzi MSD (2022) Influence of Meteorological Processes on cGPS Measurements of Crustal Movements. Front. Earth Sci. 10:827011. doi: 10.3389/feart.2022.827011

INTRODUCTION

The continuous Global Positioning System (cGPS) is a space geodetic technique that measures positional changes on the Earth's surface. cGPS measurements are used to study, infer, and monitor plate tectonic motion and drift rates, crustal deformation caused by earthquakes and volcanoes, and crustal motion due to geodynamic and hydrospheric processes (Rabbel and Schuh, 1986; Yan et al., 2009; Argus et al., 2014; Knowles et al., 2020). cGPS data have been used to investigate many space and Earth science research questions, for example, Cilliers et al. (2004) and Malservisi et al. (2013) used the South African cGPS TrigNet network to study the ionospheric conditions over southern Africa, and to investigate the dynamics of the South African portion of the African plate, respectively.

cGPS position measurements generally contain annual and semi-annual seasonal deformation components that are not accounted for and, thus, distort the cGPS measurements (**Figure 1**). Rabbel and Schuh (1986), van Dam and Wahr (1998), and Yan et al. (2009) attribute these deformation

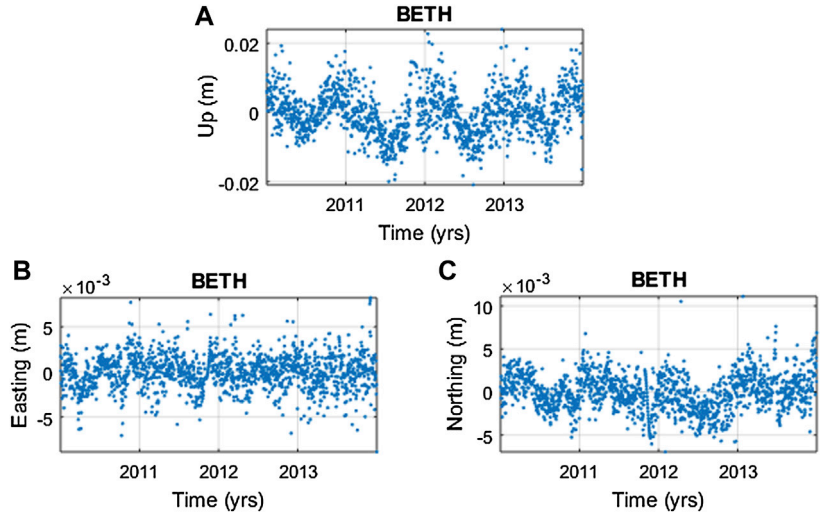

FIGURE 1 | cGPS daily position time series of station BETH located in Bethlehem, South Africa. **(A)** Detrended and interpolated vertical surface displacement time series at the station. **(B,C)** are detrended and interpolated horizontal surface displacement time series x (easting) and y (northing) directions, respectively. 27.

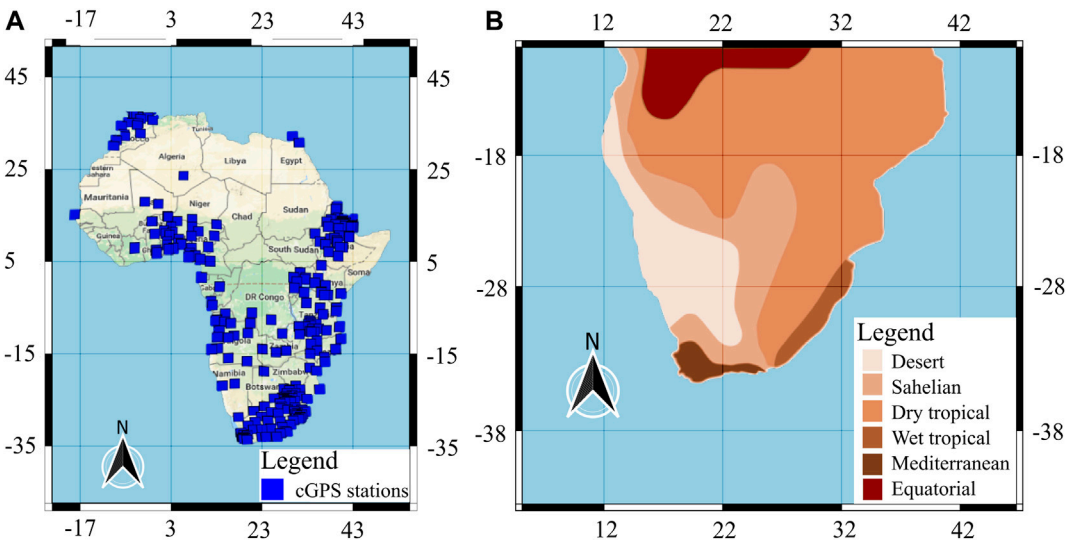

FIGURE 2 | (A) Location of cGPS station in the African continent. **(B)** Climatic zones in southern Africa (modified after Hepburn and Radloff, 1998). 27. Southern Africa is a largely semi-arid region, consisting of five different climatic zones (i.e., the Mediterranean, Desert, Sahelian, Dry tropical, and Wet tropical climatic zones). Its general climate varies from dry arid conditions in the west to humid tropical conditions in the north and east sides.

signals to seasonal and partly seasonal variations from multiple sources including surface loading owing to solid Earth tides, pole tides, oceanic tides, atmospheric mass variations, and non-tidal surface fluctuations. Moreover, processing- and equipment-induced errors contribute to the observed seasonal variations. Thermal expansion and contraction of the cGPS monument and the bedrock, along with soil consolidation and the extraction of surface and subsurface water mass near a cGPS station are also thought to be significant contributors of local surface deformation signals (van Dam et al., 2001; Romagnoli et al., 2003; Yan et al., 2009). The vertical displacement of these seasonal deformation components tends to be largest as some exogenic processes (e.g., atmospheric loading and oceanic loading) induce greater surface displacement in the vertical direction than in the horizontal direction (**Figure 1**) (Dong et al., 2002; Min et al., 2005; He et al., 2015).

This study sought to better understand cGPS and meteorological data collected in southern Africa and draw inference on the seasonal influence of meteorological processes and climatic zones on the vertical component of cGPS surface displacement measurements. This study is fitting, as in some areas (e.g., the Amazon basin) mass loading has been demonstrated to be driven by its local climatic system, and cGPS measurements have been observed to have high enough

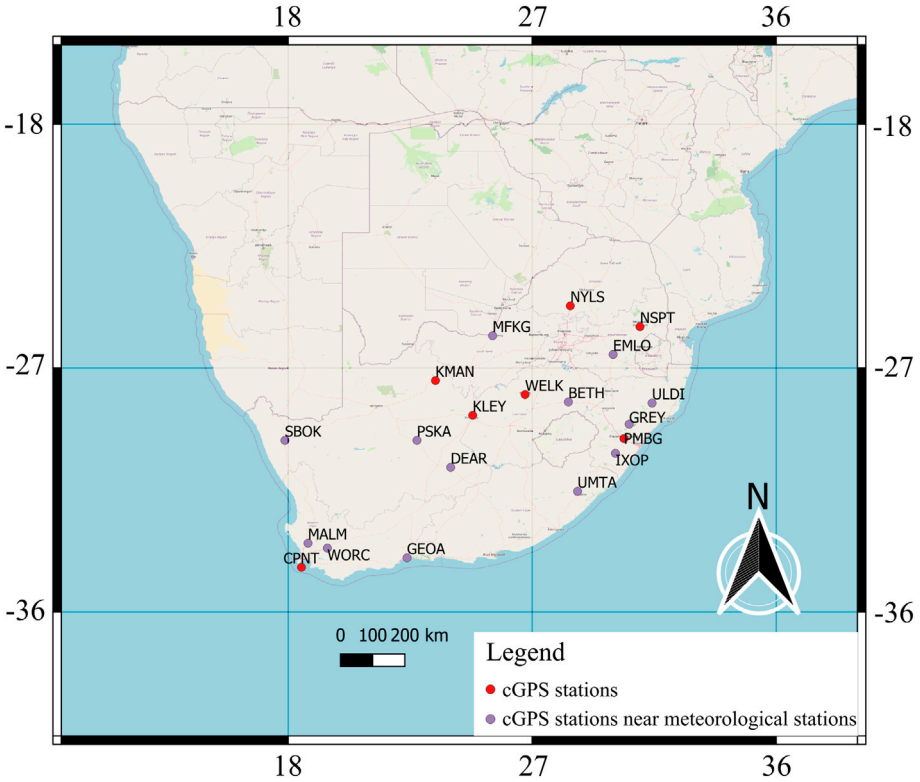

FIGURE 3 | Spatial distribution of the chosen cGPS and meteorological stations. 28.

temporal resolution to enable the correlation of cGPS measurements and that of several other environmental parameters (Romagnoli et al., 2003; Davis et al., 2004; Yan et al., 2009; Fu et al., 2013; Knowles et al., 2020). Additionally, Knowles et al. (2020) suggest that cGPS time series record displacements are driven by local- and large-scale climate oscillations. Southern Africa is an ideal place to conduct such research because it has several well-maintained cGPS (**Figure 2A**) and meteorology stations, situated in regions of varying climatic zones (**Figure 2B**), and low seismic and tectonic activity.

MATERIALS AND METHODS

Description

In this paper, we used data from the South African TrigNet geodetic network and the South African Weather Service (SAWS) to investigate the seasonal effects of changing atmospheric temperature, pressure, rainfall, and humidity processes on vertical cGPS surface displacement measurements. The cGPS data are archived and processed by the geodetic laboratory at the University of Nevada Reno (UNR) (http://geodesy.unr.edu/index.php) (Blewitt et al., 2018). The data processing is based on the International GNSS Service (IGS14) realization of the International Terrestrial Reference Frame 2014 (ITRF14) (Altamimi et al., 2016; Rebischung et al., 2016). The processing by UNR includes corrections for tropospheric effects (i.e., hydrostatic and non-hydrostatic delays), first-order ionospheric effects, solid Earth tides, pole tides, and oceanic tide loading. However, it does not include corrections for non-tidal loading effects (e.g., atmospheric pressure, ocean bottom pressure, surface hydrology), seasonal thermal expansion, and shrink-swell heave effects. The complete processing procedure of the cGPS dataset is given at http://geodesy.unr.edu/gps/ngl.acn.txt. The meteorological data used are from meteorological ground stations managed by the SAWS. To be able to analyse the data for annual and semi-annual seasonal variation, both the cGPS and meteorological data were corrected for long term tectonic and climatic variations by detrending the data. In preparing the data for spectral analysis, the data were detrended, zero centred, interpolated and windowed to minimise the occurrence of spectral distortion, leakage, shift, and the formation of false peaks.

All the data used for the study were acquired in South Africa (**Figure 3**) because 1) most of the cGPS stations in southern Africa are in South Africa; and 2) the cGPS data from other southern African countries have many gaps, which makes it difficult to apply signal processing techniques. Our results are expected to be valid in other southern African regions as the environmental setting is similar.

Analysis Techniques

Inferential signal processing techniques were used to explore the nature of the chosen cGPS and meteorological datasets and to infer their relationships. The time series were decomposed and

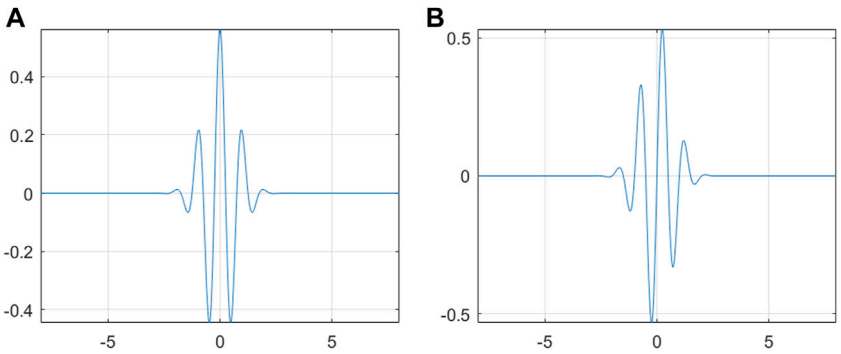

FIGURE 4 | (A) Real part of the complex Morlet wavelet and **(B)** Imaginary part of the complex Morlet wavelet. 28.

correlated in the time, frequency, and time-frequency domains. The various analysis techniques are briefly described below.

Spearman's correlation coefficient (rho) is a nonparametric (distribution free) rank correlation time domain technique defined as (Gauthier, 2001; Mukaka, 2012):

$$r_s = 1 - \frac{6\sum_{i=1}^{n} d_i^2}{n(n^2-1)} \quad (1)$$

where d_i is the difference in rank for each continuous variable pair $x(t)$ and $y(t)$, while n is the total number of continuous variable pairs (Mukaka, 2012). The technique is used because it is not affected by outliers, nor assume linearity and normality (Gauthier, 2001).

The Fourier Transform (FT) is a frequency domain decomposition technique used in this study to uncover the dominant frequency components of the cGPS and meteorological time series. The FT $X(f)$ of a time series $x(t)$ is defined as (Cooper and Cowan, 2008; Mallat, 2009):

$$X(f) = \int_{-\infty}^{\infty} x(t) e^{-2\pi i f t} dt \quad (2)$$

where f is the frequency of the time series, i is the imaginary unit, x(t) is the dataset to be analyzed, and t is the time. In this study, Fourier analysis is implemented using the Fast Fourier Transform (FFT), which is an efficient technique for implementing the discrete Fourier transform (DFT) (Cochran et al., 1967; Mallat 2009; Trauth, 2010; Ryan, 2015). The Welch periodogram was used to produce the power spectrum of the datasets and the FFT was used to compute the amplitude of the time series (Warner, 1998).

The magnitude-squared coherence (MSC) is a complex frequency domain technique used in this study to determine and quantify the relationship strength of the components of the cGPS and meteorological time series in the frequency domain (Torrence and Compo, 1998; Friston et al., 2011). The technique is mathematically defined as:

$$C_{xy} = \frac{|X_{xy}(f)|^2}{X_{xx}(f) X_{yy}(f)} \quad (3)$$

where X_{xy} is the cross-power spectral density of time series $x(t)$ and $y(t)$, $X_{xx}(f)$ and $X_{xx}(f)$ are the power spectral densities of $x(t)$ and $y(t)$, and C_{xy} is the coherence (Friston et al., 2011).

The continuous wavelet transform (CWT) is a time-frequency domain decomposition technique used in this study to decompose the cGPS and meteorological time series. The CWT is good at analyzing both continuous and discrete time series; unlike the FT, it is also good at decomposing non-stationary time series (Zhao et al., 2004; Baker, 2007; Kaiser, 2011). The CWT is mathematically defined as (Mallat, 1998, p. 5):

$$CWT(u,s) = \int_{-\infty}^{\infty} f(t) \frac{1}{|s|^{0.5}} \psi^* \left(\frac{t-u}{s} \right) dt, \quad (4)$$

where s and u are the scale and translation (position) factors, respectively, f(t) is the time domain function being decomposed, ψ is the mother wavelet and $*$ means complex conjugate (Meyers et al., 1993; Cooper and Cowan, 2008). The method decomposes a time series at multiple scales using a linear combination of translated and dilated daughter wavelets, which enable it to easily map temporal variations in the spectral characteristics of a time series over time (Graps, 1995; Torrence and Compo, 1998; Baker, 2007; Cooper and Cowan, 2008; Fletcher and Sangwine, 2017). However, it is unable to obtain precise measurements of both frequency and time, as the technique has a trade-off between the accuracy in time and frequency as dictated by the uncertainty principle (Issartel et al., 2015). The complex Morlet wavelet transform was used in this study because of its nonorthogonality, similarity to the cGPS and meteorological time series, as well as for its high degree of smoothing (Torrence and Compo, 1998; Struzik, 2001; Mallat, 2009) (**Figure 4**). The complex Morlet wavelet transform is defined as (Teolis, 1998, p. 66):

$$\psi_o(x) = \frac{1}{\pi f_b} e^{2\pi i f_c x} e^{-x^2/f_b} \quad (5)$$

where f_b is the bandwidth parameter, i is the imaginary unit and f_c is the wavelet centre frequency. A centre frequency and bandwidth value of one was used to compute the wavelet transform, so as to make the used scales equivalent to the

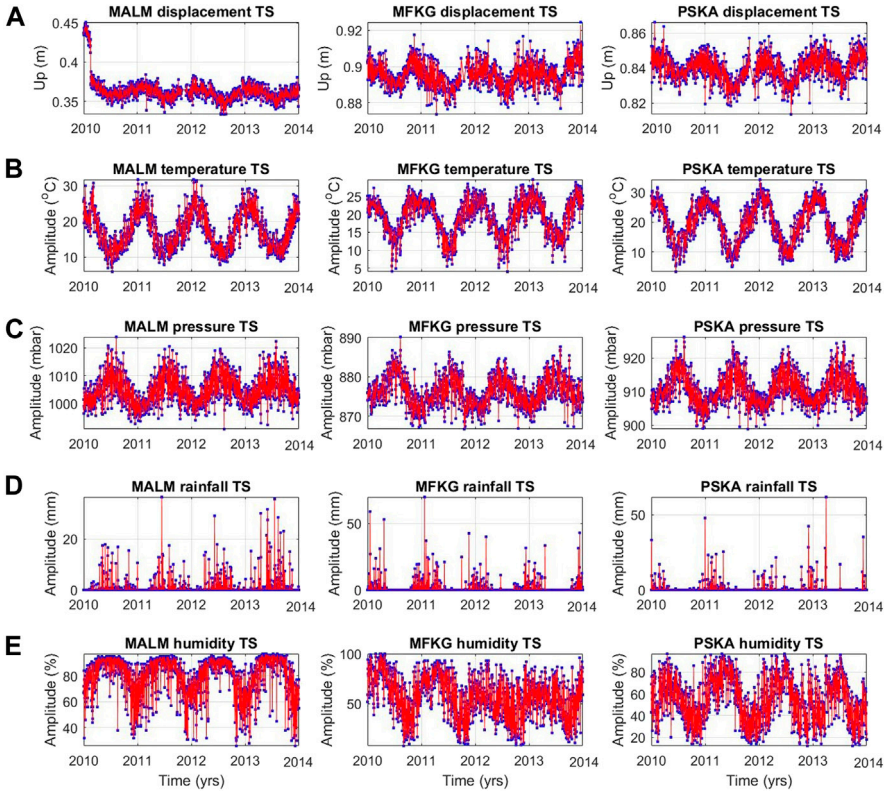

FIGURE 5 | Time domain displacement and meteorological time series at stations MALM, MFKG, and PSKA situated in the towns of Malmesbury, Mahikeng, and Prieska, respectively, the station names are the abbreviations of the town names where they are located. **(A)** cGPS surface displacement, **(B)** atmospheric temperature, **(C)** atmospheric pressure, **(D)** rainfall, and **(E)** humidity time series across stations in southern Africa. Due to a lack of space and similarity of the results, results for only three stations are shown. 29.

wavelength (Cooper and Cowan, 2008), which is also an inverse of frequency.

The wavelet-based semblance (WS) is a qualitative time-frequency domain technique used in this study to correlate the cGPS and meteorological time series in the time-frequency domain. Since the method uses phase information, it can be used to compute the correlation of time series with different units of measure and is mathematically defined as (Christensen, 2003; Cooper, 2009).

$$S = \cos^{n}(\theta) \tag{6}$$

where n is an odd integer greater than zero, that allows the response of the technique to be refined, in this paper, n = 1 was used to compute the semblance results, while θ refers to the local phase of the time series.

RESULTS AND INTERPRETATION

FFT and CWT Decomposition Analysis

Surface Displacement

Frequency and time-frequency domain decomposition results show that surface displacement time series consist of an annual and semi-annual deformation component (**Figures 5A**, **6A**, **7A**, **Supplementary Material Appendix 1, Figures 1, 2, 3**). The power of the annual displacement component is larger than that of the semi-annual component at most stations, often by one order of magnitude (**Table 1**). This is consistent with the findings in other areas of the world (Ray et al., 2008). The power of the time series varies systematically between the different climatic zones (**Table 1**). This implies that the magnitude of seasonal weather variation within a climatic zone has an influence on the magnitude of the deformation components observed in the surface displacement time series. The annual displacement components are largest in cGPS data from the Desert climatic zone and lower in time series at stations located in the Wet and Dry Tropical climatic zones (**Table 1**). The CWT spectrums show slight variation in cycle periods and frequency (non-stationarity) of the time series over time, this is characteristic of signals in the real environment (**Figure 7**).

Atmospheric Temperature

Atmospheric temperature time series are predominantly composed of an annual and semi-annual seasonal component. (**Figures 5B**, **6B**, **7B**, **Supplementary Material Appendix 2**, **Figures 4**, **5**, **6**). The semi-annual component is absent in the

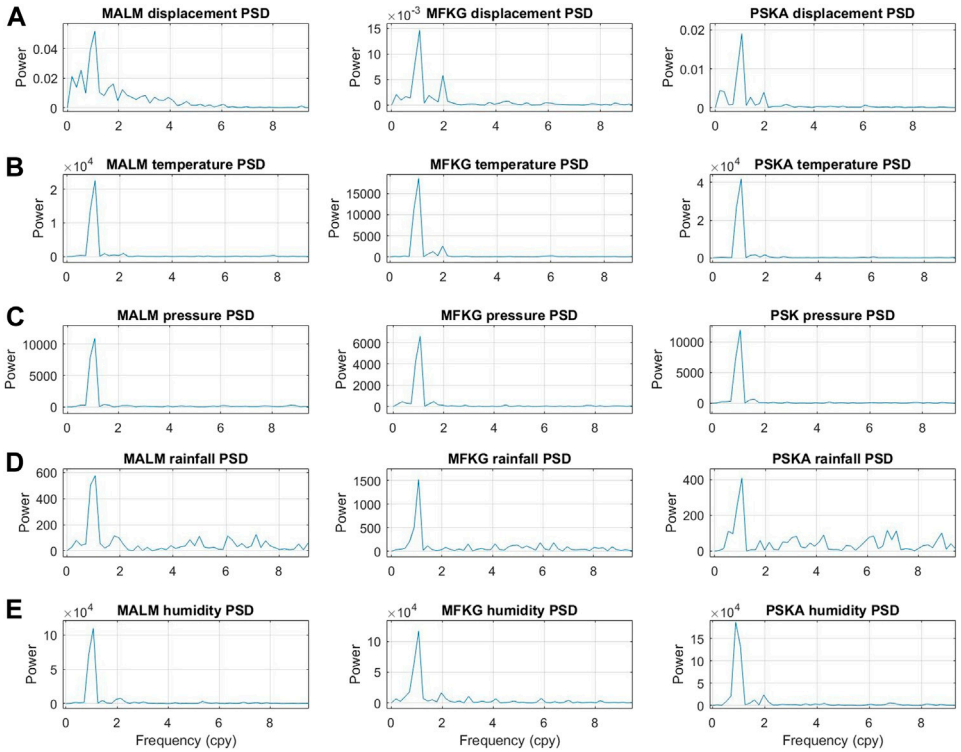

FIGURE 6 | Fourier power spectra. **(A)** cGPS surface displacement, **(B)** atmospheric temperature, **(C)** atmospheric pressure, **(D)** rainfall, and **(E)** humidity decomposition spectra. 30.

temperature time series in the Mediterranean climatic zone. The temperature time series are also characterised by a low noise level and a high degree of stationarity (**Figures 6B**, **7B**, **Supplementary Material Appendix 2, Figures 4, 5, 6**). Annual seasonal temperature fluctuations are higher in time series from the Desert and Sahelian climatic zones, regions where the Intertropical Convergence Zone (ITCZ) does not move over, and lower in time series from the Dry and Wet Tropical climatic zones - regions where the ITCZ passes over (**Table 2**). This is because areas characterised by low levels of cloudiness are characterised by high temperatures and extreme seasonal temperature fluctuation, while areas of high cloudiness are characterised by low temperatures and low-temperature fluctuation, except during tropical storms (Hobbs et al., 1998; Barry and Chorley, 2010).

Atmospheric Pressure

Atmospheric pressure time series consist only of the annual seasonal component (**Figures 5C**, **6C**, **7C**, **Supplementary Material Appendix 2, Figures 7, 8, 9**). The time series are characterised by low levels of noise, variance, spectral averaging, and a high degree of stationarity (**Figures 6C**, **7C**). Seasonal atmospheric pressure fluctuations are higher at stations from the Desert and Mediterranean climatic zones and lower at stations from the Wet and Dry Tropical climatic zones (**Table 2**). This is because subtropical deserts are high seasonal atmospheric pressure zones due to the seasonal presence of Hadley cells over them, and tropical climatic regions are low atmospheric pressure fluctuation zones (Nicholson and Flohn, 1980; Barry and Chorley, 2010; Bollasina and Nigam, 2010). Insolation differences due to the absence and presence of clouds in the Desert and Tropical climatic zones, respectively, may also play a role.

Rainfall

Rainfall time series predominantly consist of an annual seasonal component only, the phase of the annual component varies moving across the central, north-eastern, and south-western parts of southern Africa (**Figures 5D**, **6D**, **7D**, **Supplementary Material Appendix 2, Figures 10, 11, 12**). The time series are characterised by a high degree of noise and variance, which, according to Potter and Colman (2003), Jury (2013) and MacKellar et al. (2014) is caused by processes, such as the ITCZ, solar radiation, El Niño-Southern Oscillation (ENSO), and variations in atmospheric circulation. Seasonal rainfall fluctuations are higher in time series from the Wet and Dry Tropical climatic zones and low in time series from the Desert climatic zone (**Table 2**). These findings are consistent with known information, i.e., continental Dry and Wet Tropical climatic zones are characterised by well-defined alternating high

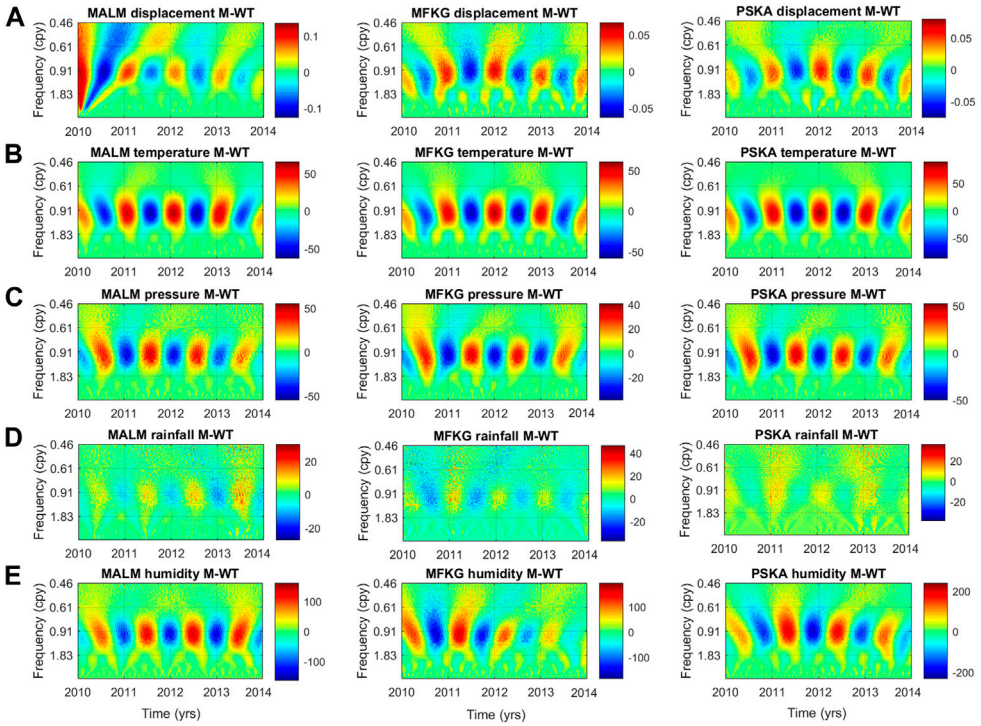

FIGURE 7 | Wavelet Transform (WT) decomposition spectra. **(A)** cGPS surface displacement, **(B)** atmospheric temperature, **(C)** atmospheric pressure, **(D)** rainfall, and **(E)** humidity decomposition spectra. Some of the characteristic CWT features observed in the plots are the exaggeration of low frequencies, suppression of high frequencies, and component frequency overlap. The spectra are also characterised by good time localisation. 31.

TABLE 1 | Climatic zone, latitude longitude, power, and amplitude of the analysed cGPS station, displacement time series.

Station name	Climatic zone	Latitude	Longitude	Percentage of at hand data points (%)	Interpolation technique (linear <95%> Cubic)	Variance (Time domain)	Power		Amplitude (m)	
							Annual component	Semi-annual component	Annual component	Semi-annual component
KMAN	Desert	−27.461	23.432	99	Cubic Hermite	0.0000594	0.0225	0.0029	0.0048	0.0010
PSKA	Desert	−29.668	22.749	93	Linear	0.0000511	0.0155	0.0031	0.0054	0.0019
SBOK	Desert	−29.669	17.879	94	Linear	0.0000504	0.0174	0.0036	0.0054	0.0022
PMBG	Wet Tropical	−29.601	30.383	95	Cubic Hermite	0.0000487	0.0109	0.0031	0.0039	0.0014
ULDI	Wet Tropical	−28.293	31.421	90	Linear	0.0000456	0.0049	0.0008	0.0027	0.0010
GREY	Wet Tropical	−29.071	30.578	92	Linear	0.0000468	0.0078	0.0014	0.0044	0.0007
IXOP	Wet Tropical	−30.146	30.069	95	Cubic Hermite	0.0000740	0.0143	0.0023	0.0054	0.0008
UMTA	Wet Tropical	−31.549	28.673	85	Linear	0.0000363	0.0025	0.0011	0.0019	0.0014
KLEY	Sahelian	−28.743	24.806	99	Cubic Hermite	0.0000564	0.0189	0.0039	0.0048	0.0016
DEAR	Sahelian	−30.665	23.993	93	Linear	0.0000457	0.0146	0.0028	0.0051	0.0019
WELK	Sahelian	−27.978	26.738	99	Cubic Hermite	0.0000398	0.0074	0.0026	0.0029	0.0008
MFKG	Sahelian	−25.805	25.540	93	Linear	0.0000457	0.0121	0.0047	0.0049	0.0026
BWES	Sahelian	−33.347	22.574	98	Cubic Hermite	0.0000539	0.0146	0.0021	0.0030	0.0010
EMLO	Dry Tropical	−26.498	29.984	93	Linear	0.0000421	0.0077	0.0018	0.0038	0.0016
BETH	Dry Tropical/ Sahelian	−28.250	28.334	96	Cubic Hermite	0.0000455	0.0119	0.0033	0.0047	0.0022
NSPT	Dry Tropical	−25.475	30.975	99	Cubic Hermite	0.0000483	0.0066	0.0031	0.0037	0.0013
NYLS	Dry Tropical	−24.703	28.406	98	Cubic Hermite	0.0000530	0.0098	0.0041	0.0038	0.0014
CPNT	Mediterranean	−34.353	18.490	97	Cubic Hermite	0.0000426	0.0035	0.0033	0.0018	0.0013
MALM	Mediterranean	−33.464	18.731	96	Cubic Hermite	0.0002089	0.0468	0.0063	0.0102	0.0026
GEOA	Mediterranean	−34.002	22.383	94	Linear	0.0000350	0.0041	0.0013	0.0029	0.0012
WORC	Mediterranean	−33.645	19.445	93	Linear	0.0000803	0.0223	0.0029	0.0064	0.0019

TABLE 2 | Quantified power of the annual and semi-annual frequency components forming the meteorological time series as obtained from FFT.

Climatic Zones	GPS Station Name	Annual and Semi-annual Power of the cGPS Vertical Component Time Series							
		Temperature		Pressure		Rainfall		Humidity	
		Annual	Semi-annual	Annual	Semi-annual	Annual	Semi-annual	Annual	Semi-annual
Desert	PSKA	36,021	1,360	10,098	101	350.7	14.2	154,380	20,240
	SBOK	17,539	993	4,560.5	29.5	58.1	22.3	29,000	5,235
	KMAN	—	—	—	—	—	—	—	—
Wet Tropical	GREY	11,577	1,174	4,281	111.3	1,052.5	47.7	13,597	1,215
	UMTA	8,794	926.4	2,740.7	629.2			9,656.3	905.3
	IXOP	19,476	1,349	4,115.8	127.2	1,169	43.3	10,573	1,131
	ULDI	7,886	768	5,645	131	1885.5	94.5	20,085	845
	PMBG	—	—	—	—	—	—	—	—
Sahelian	DEAR	26,648	1,103			735	69.8	103,010	14,440
	MFKG	15,758	2063	5,709.4	107.9	1,120	37.4	96,145	14,339
	KLEY	—	—	—	—	—	—	—	—
	WELK	—	—	—	—	—	—	—	—
Dry Tropical	EMLO	10,292	1,277	1,438.6	46.6	1921.3	22.8	-	-
	BETH	20,424	1,581	2,169.8	277.7	2,661.6	403.7	-	-
	NSPT	—	—	—	—	—	—	—	—
	NYLS	—	—	—	—	—	—	—	—
Mediterranean	MALM	19,301	390	9,728.5	61	548.5	87.67	95,412	6,597
	GEOA	6,782	40.7	3,989.7	51.4	142.7	31.3	2,930.4	4,990.3
	WORC			6,843.7	47.7	328.1	51.1	62,707	1889
	CPNT	—	—	—	—	—	—	—	—

rainfall and dry seasons (Hepburn and Radloff, 1998; Barry and Chorley, 2010).

Humidity

Humidity data consist of an annual and semi-annual seasonal component, except for stations in the Wet Tropical climatic zone (**Figures 5E**, **6E**, **7E**, **Supplementary Material Appendix 2, Figures 13, 14, 15**). The phase of the humidity time series varies as a function of time and spatial geographic location, similar to rainfall time series but less defined. In general, in the central and north-eastern parts of southern Africa, the moisture content is high during summer and low during winter; while in the south-western parts of southern Africa, humidity levels are high during winter and low during summer. It is important to note that at some stations (e.g., PSKA), a deviation is observed from this general trend. It is also observed that humidity fluctuations are greater in the semi-arid regions than in tropical regions, which could be because annual humidity fluctuation is more defined in the semi-arid region than in the tropics.

Correlation Analysis

The time, frequency, and time-frequency domain comparisons show that surface displacement is directly and inversely proportional to atmospheric temperature and pressure changes, respectively. The correlation between atmospheric temperature, pressure, and surface displacement is highest in stations in the Desert, Sahelian, and Mediterranean climatic zones (**Tables 3**, **4**), these are zones that receive the most solar radiation, heat, and least amount of water in southern Africa. The displacement-temperature correlation is observed to be smallest in the Dry and Wet Tropical climatic zones, which are climatic zones that are cooler and receive the most amounts of rainfall. In addition, the frequency and phase correlation results between surface displacement-temperature and surface displacement-pressure time series show a high and consistent frequency and phase correlation

TABLE 3 | Displacement time series correlation values with atmospheric temperature (T), atmospheric pressure (P), rainfall (R), and humidity (H) time series at the selected stations in southern Africa.

Climatic Zones	cGPS Station Name	Spearman's Correlation (Rho)			
		T	P	R	H
Desert	PSKA	0.59	–0.40	0.09	–0.35
	SBOK	0.65	–0.27	–0.16	–0.44
Sahelian	DEAR	0.61	—	0.05	–0.34
	MFKG	0.57	–0.39	0.17	–0.10
Mediterranean	MALM	0.59	–0.28	–0.42	–0.34
	GEOA	0.47	–0.22	–0.05	–0.01
	WORC	0.50	0.02	–0.21	–0.16
Dry tropical	EMLO	0.43	–0.32	0.12	—
	BETH	0.51	–0.28	0.22	—
Wet tropical	GREY	0.38	–0.19	0.11	–0.09
	UMTA	0.33	–0.31	—	–0.19
	IXOP	0.41	–0.10	–0.02	0.00
	ULDI	0.30	–0.26	0.10	–0.03

TABLE 4 | Coherence correlation strength of displacement vs. meteorological (average temperature, pressure, rainfall, and humidity) processes.

Climatic Zones	GPS Station Name	Coherence Spectral Correlation (Vertical Component of Displacement vs. Atmospheric Processes)							
		Temperature		Pressure		Rainfall		Humidity	
		Annual	Semi-annual	Annual	Semi-annual	Annual	Semi-annual	Annual	Semi-annual
Desert	PSKA	0.92	0.90	0.89	0.24	0.75	0.31	0.99	-
	SBOK	0.99	0.56	0.95	0.13	0.42	0.30	0.91	0.36
Sahelian	DEAR	0.91	0.73	—	—	0.75	0.35	0.97	0.97
	MFKG	0.92	0.96	0.87	0.42	0.73	0.97	0.78	0.86
Mediterranean	MALM	0.99	0.21	0.98	0.59	0.98	0.31	0.99	0.08
	GEOA	0.87	0.85	0.83	0.88	0.77	0.37	0.79	0.94
	WORC	0.99	0.86	0.98	0.19	0.99	0.72	1.00	0.92
Dry Tropical	EMLO	0.89	0.79	0.86	0.13	0.88	0.03	—	—
	BETH	0.90	0.84	0.87	0.28	0.77	0.81	—	—
Wet Tropical	GREY	0.75	0.58	0.70	0.11	0.60	0.24	0.44	0.41
	UMTA	0.95	0.86	0.93	0.73	—	—	0.72	0.68
	IXOP	0.84	0.73	0.80	0.39	0.78	0.18	0.59	0.52
	ULDI	0.89	0.65	0.86	0.76	0.92	0.95	0.72	0.40
Annual average		0.91	-	0.88	—	0.76	—	0.81	—
Semi-annual average		0.72	—	0.40		0.44		0.61	
STD annual		0.07		0.08		0.16		0.18	
STD semi-annual			0.20		0.27		0.32		0.31

between the time series (**Figures 8A**,**8B**, **9A**,**9B**, **Supplementary material Appendix 3: Figures 16, 17**).

Depending on the spatial location, rainfall and humidity time series are either directly or inversely correlated to surface displacement time series. The correlation of the time series is low in the time domain, that of the annual component is high to moderate in the frequency and time-frequency domains (**Tables 3**, **4**; **Figures 8C**, D, **9C**, D, **Supplementary Material Appendix 3: Figures 16, 17**). The displacement-rainfall and displacement-humidity correlation, at certain locations, is observed to be inconsistent over time (**Figure 9**).

The relation between the semi-annual component of the temperature and humidity time series with that of the cGPS surface displacement is too inconsistent to suggest that any of the considered meteorological processes have an influence, if at all, on the semi-annual deformation components (**Table 4**) (**Figure 8**).

DISCUSSION

Meteorological Time Series

The temperature, pressure, rainfall, and humidity fluctuations in southern Africa are primarily controlled by the complex interaction between midlatitude, tropical, and subtropical climate systems, together with the development, seasonal positional-shift, and interaction of atmospheric and oceanic circulation systems of the Atlantic, Indian, and Southern oceans (Chase and Meadows, 2007). This is apparent in the temperature and pressure data in southern Africa, which appear to be controlled by 1) the seasonal variation in the Sun's radiation, 2) migration of the ITCZ away from the southern hemisphere (after summer periods) to the northern hemisphere, and 3) a shift of anticyclones from the southern Atlantic and Indian oceans towards the southern Africa continent in winter (Hobbs et al., 1998; Sun et al., 2017; Byrne et al., 2018).

The ITCZ is also the primary source of rainfall activity in the central and north-eastern parts of southern Africa, thus these regions are summer rainfall regions. In the south-western parts of southern Africa, rainfall is associated with the winter inflow of low- and high-level westerlies that carry moist air (Ellis and Galvin, 1994; Barry and Chorley, 2010).

Moist air, in the central and north-eastern parts of southern Africa, is brought by inflowing easterlies that carry moist air from the southwest Indian Ocean and warm Agulhas currents (Chase and Meadows, 2007; Jury, 2013). In the south-western parts of southern Africa, moist air is brought about by westerlies as they move towards the equator during winter (Chase and Meadows, 2007).

Displacement Time Series

Similar to the studies conducted by Dong et al. (2002) and Ray et al. (2008), using a global dataset and Earth model, cGPS displacement time series in southern Africa are found to consist of two dominant seasonal components. Dong et al. (2002), Romagnoli et al. (2003) and Xu et al. (2017) link these deformation components to gravitational attraction, thermal, hydrodynamical, unmodeled, and error-related processes. The observed systematic variation of the power of the displacement

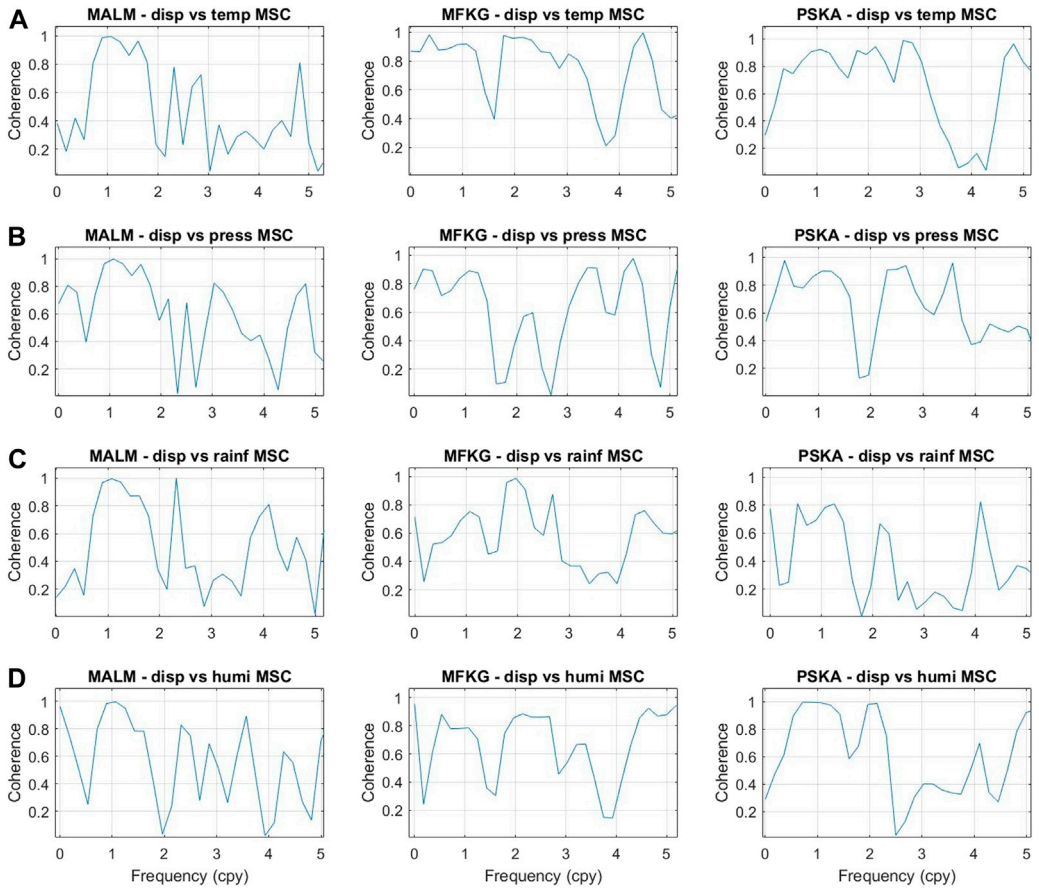

FIGURE 8 | cGPS surface displacement and meteorological time series coherence correlation spectra. **(A)** displacement-temperature (disp vs. temp), **(B)** displacement-atmospheric pressure (disp vs. pressure), **(C)** displacement-rainfall (disp vs. rainf), and **(D)** displacement-humidity (disp vs. humi). 32.

time series suggests that the magnitude of seasonal weather variation within a climatic zone has an influence on the magnitude of the deformation components observed in the cGPS surface displacement time series. It indicates that changes in atmospheric temperature, atmospheric pressure, rainfall, and humidity processes in each climatic zone do have an influence on the surface deformation recorded by cGPS station. These findings demonstrate the influence of local effects on cGPS measurements, which is consistent with what has been found in other studies (Romagnoli et al., 2003; Nahmani et al., 2012; Fu et al., 2013; Knowles et al., 2020).

Meteorological Processes and Surface Displacement Relation

Generally, high temperatures cause thermal expansion of consolidated soil particles and water molecules in the near subsurface, expansion of the concrete and metallic components of the cGPS station, and the expansion of atmospheric air mass density (which results in a reduction in atmospheric pressure); all these phenomena may affect cGPS measurements. The opposite is thought to apply in cold conditions (i.e., winter), which might explain the high correlation observed between atmospheric temperature, pressure, and vertical displacement changes.

The type of interaction (*viz*. reinforcement or opposition) between rainfall and humidity effects vs temperature and pressure effects on surface displacement is thought to vary spatially as postulated below:

1 In southern Africa's central and north-eastern parts, the rainfall-displacement and humidity-displacement time series are largely directly correlated. Thus, in summer, constructive interference may occur between rainfall and humidity surface deformation effects, with surface deformation effects induced by variations in atmospheric temperature and atmospheric pressure. Constructive interference may be occurring between surface deformation effects due to swelling on soil absorption of water and the seasonal tropospheric error introduced in the cGPS datasets due to high rainfall and humidity levels; with thermal expansion effects caused by thermal expansion of soil particles and water molecules in the near subsurface; and thermal expansion of concrete and metallic components of the cGPS stations in response to the prevalence of high temperatures and low atmospheric pressure.
2 In the south-western parts of southern Africa, the rainfall-displacement and humidity-displacements are anticorrelated.

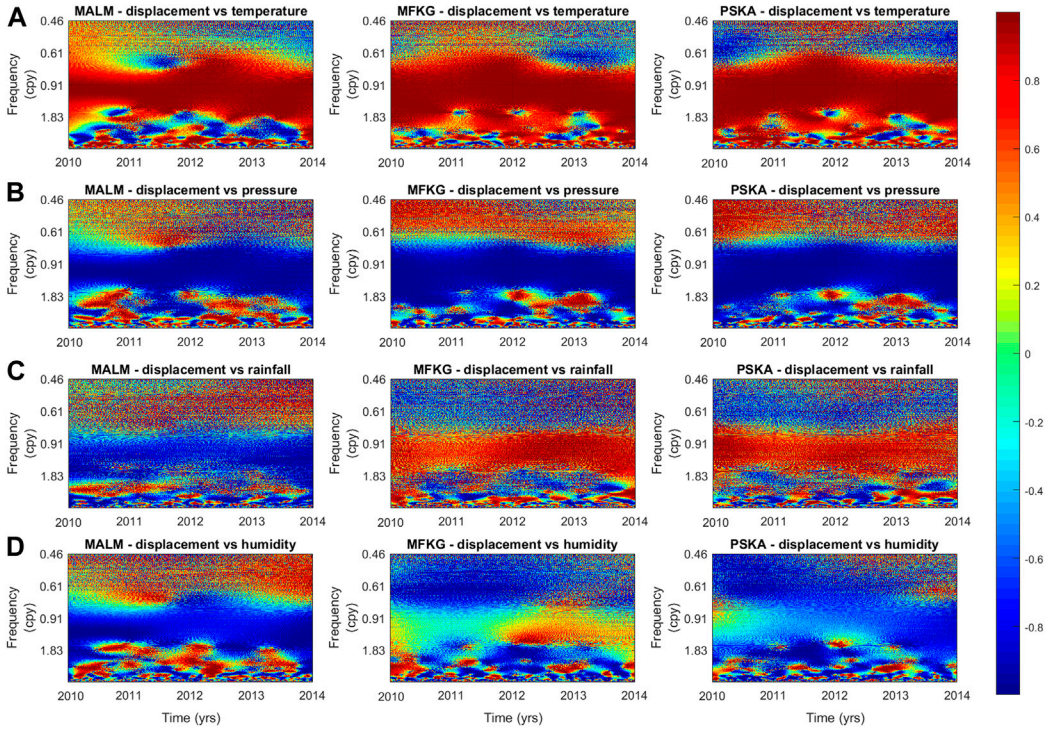

FIGURE 9 | cGPS surface displacement and meteorological time series wavelet-based semblance correlation spectra. **(A)** cGPS surface displacement-temperature spectra, **(B)** cGPS surface displacement-atmospheric spectra, **(C)** cGPS surface displacement-rainfall spectra, **(D)** cGPS surface displacement-humidity spectra. 32.

Thus, in winter, destructive interference may occur between rainfall- and humidity-induced surface deformation effects, with surface deformation effect induced by variations in atmospheric temperature and atmospheric pressure. In addition, destructive interference may occur between surface deformation effects due to soil absorption of water molecules and the seasonal tropospheric error introduced in the cGPS datasets due to high rainfall and humidity levels, with thermal contraction effects due to the contraction of soil particles and water molecules in the near subsurface, and thermal contraction of concrete and metallic components of the cGPS stations in response to the prevalence of cold temperatures and high atmospheric pressure.

The spatially inconsistent and weak relationship between surface displacement, rainfall, and humidity processes observed from time, frequency, and time-frequency correlation is interpreted to imply that rainfall and humidity processes have little influence on seasonal surface displacement variations. Thus, deformation due to surficial hydrology (i.e., gravitational loading and soil consolidation induced by changes in surface and ground water levels) is also observed to have lesser influence on the seasonal surface displacement variations, the dominant factor is temperature. These findings are different to what has been found in other research studies and highlight the importance of carrying out thermal corrections (Wahr et al., 2004; Schmidt et al., 2006; Nahmani et al., 2012).

CONCLUSION

This study examines cGPS surface displacement and meteorological time series with the aim of improving their understanding and inferring the seasonal influence that the meteorological processes considered in this study have on surface displacement measurements measured by cGPS systems in southern Africa. Atmospheric temperature variations (thermoelastic effects) are found to have higher correlation with surface displacement time series, suggesting a greater thermal influence on the surface displacement measurements than water mass changes. These findings imply that correcting for thermal expansion effects in summer, thermal contraction in winter, and thermally-induced seasonal errors (thermoelastic effects) could reduce the seasonal variations observed in cGPS displacement time series in southern Africa and increase the accuracy of the cGPS displacement measurements. In turn, this could improve the accuracy of short-term crustal deformation measurements and their usefulness, for example, in the assessment of seismic hazard.

DATA AVAILABILITY STATEMENT

The datasets presented in this study can be found in online repositories. The names of the repository/repositories and accession number(s) can be found in the article/**Supplementary Material**.

AUTHOR CONTRIBUTIONS

SG wrote the manuscript under the supervision of GC, RD, and MM. All authors reviewed the final manuscript.

FUNDING

Council for Geoscience NRF through the South African Research Chairs Initiative (SARChI).

ACKNOWLEDGMENTS

We would like to acknowledge the Council for Geoscience and CIMERA for funding this research work, the South African Weather Service (SAWS), and TrigNet for providing the meteorological and availing the cGPS displacement data used to conduct the research. Special thanks go to the Department of Geophysics at the University of the Witwatersrand for providing the platform to carry out this work and its staff for providing constructive feedback on the work. RD acknowledges support from the NRF through the South African Research Chairs Initiative (SARChI). Some of the work presented here is part of the first author's MSc thesis, titled: **Analysing ground surface position cGPS and meteorology measurements in southern Africa using signal processing techniques** (Gomo, 2019).

SUPPLEMENTARY MATERIAL

The Supplementary Material for this article can be found online at: https://www.frontiersin.org/articles/10.3389/feart.2022.827011/full#supplementary-material

REFERENCES

Altamimi, Z., Rebischung, P., Métivier, L., Collilieux, X., and Baker, J. W. (2016). ITRF2014: A New Release of the International Terrestrial Reference Frame Modeling Nonlinear Station motionsQuantitative Classification of Near-Fault Ground Motions Using Wavelet Analysis. *J. Geophys. Res. Solid EarthBulletin Seismol. Soc. Am.* 12197, 61091486–61311501. doi:10.1785/012006025510. 1002/2016jb013098

Argus, D. F., Fu, Y., and Landerer, F. W. (2014). Seasonal Variation in Total Water Storage in California Inferred from GPS Observations of Vertical Land Motion. *Geophys. Res. Lett.* 41, 1971–1980. doi:10.1002/2014gl059570

Baker, J. W. (2007). Quantitative classification of near-fault ground motions using wavelet analysis. *Bull. Seismol. Soc. Am.* 97, 1486–1501. doi:10.1785/0120060255

Barry, R. G., and Chorley, R. J. (2010). *Atmosphere, Weather and Climate*. 9th edition. London, UK: Routledge Taylor & Francis Group.

Blewitt, G., Hammond, W., and Kreemer, C. (2018). Harnessing the GPS Data Explosion for Interdisciplinary Science. *Eos* 99. doi:10.1029/2018EO104623

Bollasina, M., and Nigam, S. (2010). The Summertime "Heat" Low over Pakistan/northwestern India: Evolution and Origin. *Clim. Dyn.* 37, 957–970. doi:10.1007/s00382-010-0879-y

Byrne, M. P., Pendergrass, A. G., Rapp, A. D., and Wodzicki, K. R. (2018). Response of the Intertropical Convergence Zone to Climate Change: Location, Width, and Strength. *Curr. Clim. Change Rep.* 4, 355–370. doi:10.1007/s40641-018-0110-5

Chase, B. M., and Meadows, M. E. (2007). Late Quaternary Dynamics of Southern Africa's Winter Rainfall Zone. *Earth-Science Rev.* 84, 103–138. doi:10.1016/j.earscirev.2007.06.002

Christensen, A. N. "Semblance Filtering of Airborne Potential Field Data," in Proceedings of the Extended Abstracts, 16th ASEG Geophysical Conference and Exhibition, Adelaide, Australia, February 2003. (2003). doi:10.1071/aseg2003ab024

Cilliers, P. J., Opperman, B. D. L., Mitchell, C. N., and Spencer, P. J. (2004). Electron Density Profiles Determined from Tomographic Reconstruction of Total Electron Content Obtained from GPS Dual Frequency Data: First Results from the South African Network of Dual Frequency GPS Receiver Stations. *Adv. Space Res.* 34, 2049–2055. doi:10.1016/j.asr.2004.08.002

Cochran, W. T., Cooley, J. W., Favin, D. L., Helms, H. D., Kaenel, R. A., Lang, W. W., et al. (1967). What Is the Fast Fourier Transform? *Proc. IEEE* 55, 1664–1674. doi:10.1109/proc.1967.5957

Cooper, G. R. J., and Cowan, D. R. (2008). Comparing Time Series Using Wavelet-Based Semblance Analysis. *Comput. Geosciences* 34, 95–102. doi:10.1016/j.cageo.2007.03.009

Cooper, G. R. J. (2009). Wavelet-based Semblance Filtering. *Comput. Geosciences* 35, 1988–1991. doi:10.1016/j.cageo.2008.10.017

Davis, J. L., Elsegue, P., Mitrovica, J. X., and Tamisiea, M. E. (2004). Climate-driven Deformation of the Solid Earth from GRACE and GPS. *Geophys. Res. Lett.* 31, 1–4. doi:10.1029/2004GL021435

Dong, D., Fang, P., Bock, Y., Cheng, K. M., and Miyazaki, S. (2002). Anatomy of Apparent Seasonal Variations from GPS-Derived Site Position Time Series. *J. Geophys. Res.* 107, 1–17. doi:10.1029/2001jb000573

Ellis, J., and Galvin, K. A. (1994), Climate Patterns and Land-Use Practices in the Dry Zones of Africa, *BioScience* 44, 340–349.doi:10.2307/1312384

Fletcher, P., and Sangwine, S. J. (2017). The Development of the Quaternion Wavelet Transform. *Signal Process.* 136, 2–15. doi:10.1016/j.sigpro.2016.12.025

Friston, K. J., Bastos, A., Litvak, V., Stephan, K. E., Fries, P., and Moran, R. J. (2012), DCM for Complex-Valued Data: Cross-Spectra, Coherence and Phase-Delays, *NeuroImage* 59, 439–455. doi:10.1016/j.neuroimage.2011.07.048

Fu, Y., Argus, D. F., Freymueller, J. T., and Heflin, M. B. (2013). Horizontal Motion in Elastic Response to Seasonal Loading of Rain Water in the Amazon Basin and Monsoon Water in Southeast Asia Observed by GPS and Inferred from GRACE. *Geophys. Res. Lett.* 40, 6048–6053. doi:10.1002/2013GL058093

Gauthier, T. (2001). Detecting Trends Using Spearman's Rank Correlation Coefficient. *Environ. Forensics* 2, 359–362. doi:10.1006/enfo.2001.0061

Gomo, S. (2019). *Analysing Ground Surface Position cGPS and Meteorology Measurements in Southern Africa Using Signal Processing Techniques*. Johannesburg, Africa. University of the Witwatersrand. MSc dissertation

Graps, A. (1995). An Introduction to Wavelets. *IEEE Comput. Sci. Eng.* 2, 50–61. doi:10.1109/99.388960

He, X., Hua, X., Yu, K., Xuan, W., Lu, T., Zhang, W., et al. (2015). Accuracy Enhancement of GPS Time Series Using Principal Component Analysis and Block Spatial Filtering. *Adv. Space Res.* 55, 1316–1327. doi:10.1016/j.asr.2014.12.016

Hepburn, H. R., and Radloff, S. E. (1998). *Honeybees of Africa*. Berlin, Germany. Springer-Verlag Berlin Heidelberg GmBH, United States of America. doi:10.1007/978-3-662-03604-4

Hobbs, J. E., Lindesay, L. A., and Bridgman, H. A. (1998). *Climate of the Southern Continents: Present, Past and Future*. New York, NY, USA: John Wiley & Sons.

Issartel, J., Bardainne, T., Gaillot, P., and Marin, L. (2015). The relevance of the cross-wavelet transform in the analysis of human interaction-a tutorial. *Frontiers in Psychology* 5, 1566. doi:10.3389/fpsyg.2014.01566

Jury, M. R. (2013). Climate Trends in Southern Africa. *Sajs* 109, 1–11. doi:10.1590/sajs.2013/980

Kaiser, G. (2011). *A Friendly Guide to Wavelets*. Basel, Switzerland. Birkhuser. doi:10.1007/978-0-8176-8111-1

Knowles, L. A., Bennett, R. A., and Harig, C. (2020). Vertical Displacement of the Amazon Basin from GRACE and GPS. *J. Geophys. Res.* 125. doi:10.1029/2019JB018105

MacKellar, N., New, M., and Jack, C. (2014). Observed and Modelled Trends in Rainfall and Temperature for South Africa: 1960-2010. *Sajs* 110, 1–13. doi:10.1590/sajs.2014/20130353

Mallat, S. (1998). *A Wavelet Tour of Signal Processing*. New York: Academic Press.

Mallat, S. (2009). *A Wavelet Tour of Signal Processing*. 3rd edition. Cambridge, MA, USA: Academic Press.

Malservisi, R., Hugentobler, U., Wonnacott, R., and Hackl, M. (2013). How Rigid Is a Rigid Plate? Geodetic Constraint from the TrigNet CGPS Network, South Africa. *Geophys. J. Int.* 192, 918–928. doi:10.1093/gji/ggs081

Meyers, S. D., Kelly, B. G., and O'Brien, J. J. (1993). An Introduction to Wavelet Analysis in Oceanography and Meteorology: with Application to the Dispersion of Yanai Waves. *Mon. Wea. Rev.* 121, 2858–2866. doi:10.1175/1520-0493(1993)121<2858:aitwai>2.0.co;2

Min, W., Zheng-Kang, S., and Da-Nan, D. (2005). The Effect and Correction of Non-tectonic Crustal Deformation and Continuous GPS Position Time Series. *Chin. J. Geophys.* 48, 1121–1129. doi:10.1002/cjg2.755

Mukaka, M. M. (2012). Statistics Corner: A Guide to Appropriate Use of Correlation Coefficient in Medical Research. *Malawi Med. J.* 24, 69–71. doi:10.1016/j.cmpb.2016.01.020

Nahmani, S., Bock, O., Bouin, M.-N., Santamaría-Gómez, A., Boy, J.-P., Collilieux, X., et al. (2012). Hydrological Deformation Induced by the West African Monsoon: Comparison of GPS, GRACE and Loading Models. *J. Geophys. Res.* 117, a–n. doi:10.1029/2011JB009102

Nicholson, S. E., and Flohn, H. (1980). African Environmental and Climatic Changes and the General Atmospheric Circulation in Late Pleistocene and Holocene. *Clim. Change* 2, 313–348. doi:10.1007/bf00137203

Potter, T. R., and Colman, B. R. (2003). *Handbook of Weather, Climate, and Water: Atmospheric Chemistry, Hydrology and Social Impacts*. Hoboken, NJ, USA: John Wiley & Sons.

Rabbel, W., and Schuh, H. (1986). The Influence of Atmospheric Loading on VLBI-Experiments. *J. Geophys.* 59, 164–170.

Ray, J., Altamimi, Z., Collilieux, X., and van Dam, T. (2008). Anomalous Harmonics in the Spectra of GPS Position Estimates. *GPS Solut.* 12, 55–64. doi:10.1007/s10291-007-0067-7

Rebischung, P., Altamimi, Z., Ray, J., and Garayt, B. (2016). The IGS Contribution to ITRF2014. *J. Geod.* 90, 611–630. doi:10.1007/s00190-016-0897-6

Romagnoli, C., Zerbini, S., Lago, L., Richter, B., Simon, D., Domenichini, F., et al. (2003). Influence of Soil Consolidation and Thermal Expansion Effects on Height and Gravity Variations. *J. Geodyn.* 35, 521–539. doi:10.1016/S0264-3707(03)00012-7

Ryan, O. (2015). Linear Algebra, Signal Processing, and Wavelets: a Unified Approach-MATLAB Version. Available from: https://www.uio.no/studier/emner/matnat/math/nedlagte-emner/MAT-INF2360/v15/kompendium/applinalgmatlab.pdf.

Schmidt, R., Schwintzer, P., Flechtner, F., Reigber, C., Guntner, A., Doll, P., et al. (2006). GRACE Observations of Changes in Continental Water Storage. *Glob. Planet. Change* 50, 112–126. doi:10.1016/j.gloplacha.2004.11.018

Struzik, Z. R. (2001). Wavelet Methods in (Financial) Time-Series Processing. *Phys. A Stat. Mech. its Appl.* 296, 307–319. doi:10.1016/s0378-4371(01)00101-7

Sun, X., Cook, K. H., and Vizy, E. K. (2017). The South Atlantic Subtropical High: Climatology and Interannual Variability. *J. Clim.* 30, 3279–3296. doi:10.1175/JCLI-D-16-0705.1

Teolis, A. (1998). *Computational Signal Processing with Wavelets*. Boston, MA, USA: Birkhuser Boston Inc.

Torrence, C., and Compo, G. P. (1998). A Practical Guide to Wavelet Analysis. *Bull. Amer. Meteor. Soc.* 79, 61–78. doi:10.1175/1520-0477(1998)079<0061:apgtwa>2.0.co;2

Trauth, M. H. (2010). *MATLAB Recipes for Earth Sciences*. 3rd edition. Berlin, Germany: Springer.

van Dam, T. M., and Wahr, J. (1998). Modeling Environment Loading Effects: a Review. *Phys. Chem. Earth* 23, 1077–1087. doi:10.1016/S0079-1946(98)00147-5

van Dam, T., Wahr, J., Milly, P. C. D., Shmakin, A. B., Blewitt, G., Lavallée, D., et al. (2001). Crustal Displacements Due to Continental Water Loading. *Geophys. Res. Lett.* 28, 651–654. doi:10.1029/2000gl012120

Wahr, J., Swenson, S., Zlotnicki, V., and Velicogna, I. (2004). Time-variable Gravity from GRACE: First Results. *Geophys. Res. Lett.* 31, a–n. doi:10.1029/2004GL019779

Warner, R. M. (1998). New York, NY, USA: Guilford Press, xiv. 225.

Xu, X., Dong, D., Fang, M., Zhou, Y., Wei, N., and Zhou, F. (2017). Contributions of Thermoelastic Deformation to Seasonal Variations in GPS Station Position. *GPS Solut.* 21, 1265–1274. doi:10.1007/s10291-017-0609-6

Yan, H., Chen, W., Zhu, Y., Zhang, W., and Zhong, M. (2009). Contributions of Thermal Expansion of Monuments and Nearby Bedrock to Observed GPS Height Changes. *Geophys. Res. Lett.* 36, 1–5. doi:10.1029/2009GL038152

Zhao, G., Jiang, D., Diao, J., and Qian, L. (2004). "Application of Wavelet Time-Frequency Analysis on Fault Diagnosis for Steam Turbine," in Proceedings of the Surveillance 5 CETIM, Senlis, France, October 2004, 11–13

Conflict of Interest: The authors declare that the research was conducted in the absence of any commercial or financial relationships that could be construed as a potential conflict of interest.

frontiers | Frontiers in Earth Science

ORIGINAL RESEARCH
published: 24 June 2022
doi: 10.3389/feart.2022.840703

Crustal and Upper Mantle Imaging of Botswana Using Magnetotelluric Method

Stephen Akinremi, Islam Fadel and Mark van der Meijde*

Faculty of Geo-Information Science and Earth Observation (ITC), University of Twente, Enschede, Netherlands

We used magnetotelluric data from 352 sites in Botswana to derive a country-wide electrical conductivity model of the crust and upper mantle structure. A robust methodological scheme and 3D inversion were used to derive a 3D electrical conductivity model with unprecedented spatial coverage. The model results show interesting features, including the major cratonic blocks and the mobile belts in Botswana. A distinctive resistive structure was imaged in southwest Botswana, which suggests the existence of the Maltahohe microcraton as a separate cratonic unit as proposed by other studies. Furthermore, the model gives new insight into the extension of the East African Rift System to Botswana and the incipient rifting in the Okavango Rift Zone. In northern Botswana, the electrical conductivity model shows a highly conductive structure beneath the Okavango Rift Zone, which connects with a deeper conductive structure that we attribute to the East African Rift System due to its vicinity to Lake Kariba, the last surface expression of the rift system. We suggest that ascending fluids or melt from the East African Rift System causes the weakening of the lithosphere and plays a significant role in the incipient continental rifting in the Okavango Rift Zone.

Keywords: electrical modelling, magnetotellurics, tectonics, continental rift, rift initiation, Africa

OPEN ACCESS

Edited by:
Nibir Mandal,
Jadavpur University, India

Reviewed by:
Radhakrishna Munukutla,
Indian Institute of Technology Bombay, India
Arun Singh,
Indian Institute of Technology Dhanbad, India

****Correspondence:***
Stephen Akinremi
s.akinremi@utwente.nl

Specialty section:
This article was submitted to Solid Earth Geophysics, a section of the journal Frontiers in Earth Science

Received: *21 December 2021*
Accepted: *31 May 2022*
Published: *24 June 2022*

Citation:
Akinremi S, Fadel I and van der Meijde M (2022) Crustal and Upper Mantle Imaging of Botswana Using Magnetotelluric Method. Front. Earth Sci. 10:840703. doi: 10.3389/feart.2022.840703

1 INTRODUCTION

Our understanding of the geology and tectonics of Botswana still carry a few disputed and debated hypotheses. Botswana has a diverse geology with large cratons, in between mobile belts, and two deep sedimentary basins (Begg et al., 2009). Next to that, it is geodynamically influenced by the African Superswell, which is a large topographic anomaly in eastern and southern Africa at an average of 500 m higher than the continental height (Brandt et al., 2011; **Figure 1**). Also, the East African Rift System (EARS), an intracontinental rift zone, which supposedly has its terminus in the Okavango Rift Zone (ORZ) in northern Botswana influences its geodynamics (e.g., Fadel et al., 2020; Leseane et al., 2015; **Figure 1**). Even though in recent years different geophysical data has been collected (seismic, gravity, magnetic, magnetotelluric (MT)), there are still areas and processes that are not well understood (e.g., Hutchins and Reeves, 1980; Jones et al., 2009b; Gao et al., 2013; Fadel, 2018). Two major debates are on the existence and boundaries of Maltahohe microcraton and the extension of EARS to Botswana. This study provides additional insight into the general tectonic architecture of Botswana and specifically these two debates from the first 3D inversion of country-wide MT data for Botswana.

The Maltahohe microcraton is an enigma in Botswana geology and geodynamics. There are debates on the actual existence, location, and boundaries of Maltahohe microcraton in southwest Botswana. According to Begg et al. (2009), there may exist an ancient Maltahohe microcraton

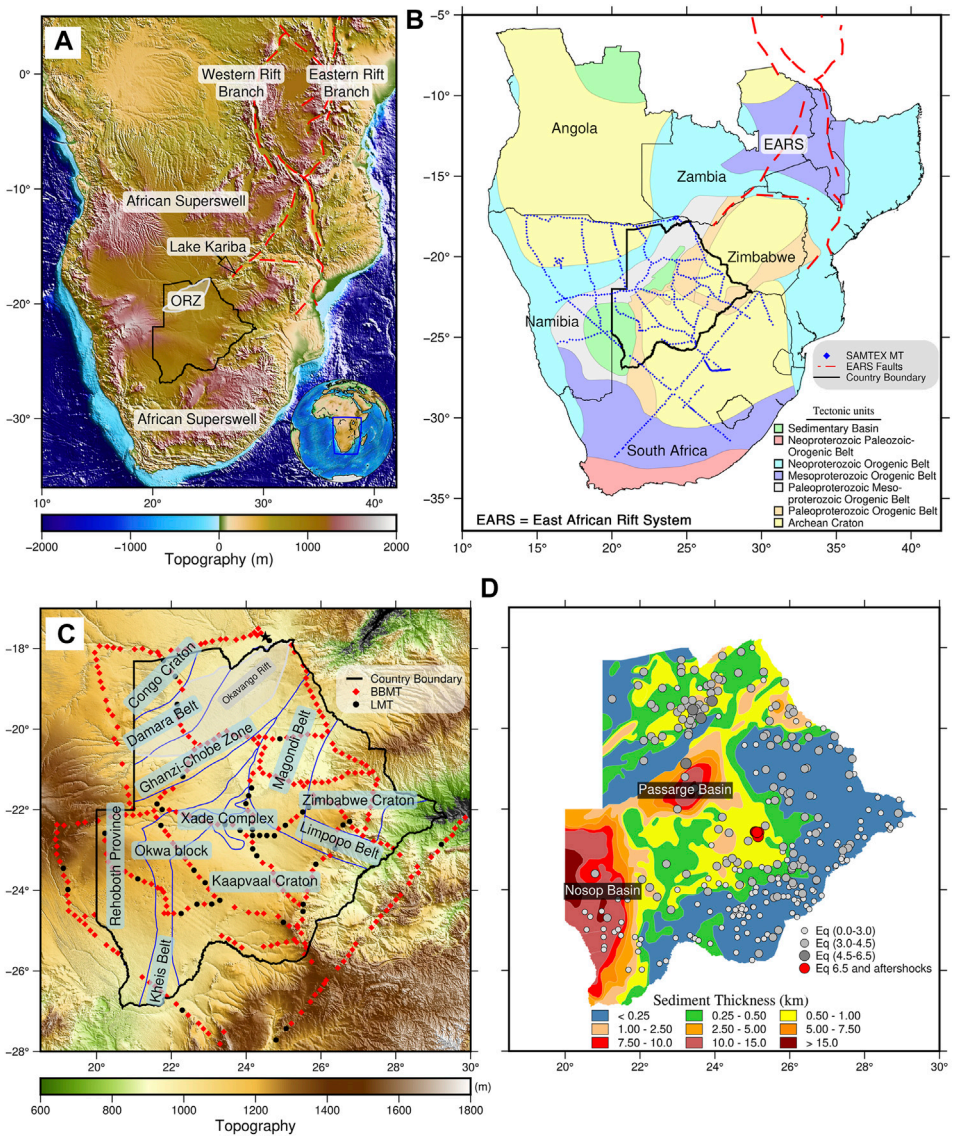

FIGURE 1 | (A) Topographic map of southern Africa, showing the branches of the EARS, the last surface expression of the western branch of EARS at Lake Kariba, the African superswell, Botswana in black outline and the ORZ in white outline (Fadel 2018). **(B)** Tectonic map of southern Africa with the distribution of the Southern Africa Magnetotelluric Experiment (SAMTEX) sites (Jones et al., 2009a). **(C)** Tectonic map of Botswana (McCourt et al., 2013) with the distribution of the SAMTEX data used. Broadband MT data (BBMT) are shown in red diamonds and long-period MT (LMT) are shown in black circles. The MT station shown in black star represents the ELZ208_94A site and the data from the site are shown in **Figure 2**. **(D)** Sedimentary thickness map derived from aeromagnetic data (Pretorius 1984) and earthquake distributions in Botswana with the range of the magnitude represented by 'Eq'.

beneath the Rehoboth Province in southwest Botswana (**Figure 1**). In an earlier active seismic study, Wright and Hall (1990) interpreted the cratonic structure beneath the Rehoboth Province as a western extension of the Kaapvaal Craton. However, more recent seismological studies in the area argue that the Maltahohe microcraton exist as a separate structure from the Kaapvaal Craton, which is evident from the observed different Vp/Vs ratios from receiver functions and 3D shear wave velocity model (Fadel et al., 2018; Fadel et al., 2020). Similarly, Chisenga et al. (2020b), in a study using gravity and aeromagnetic data supported the existence of the Maltahohe microcraton. However, the study argues that the location of the Maltahohe microcraton is likely south of the region suggested by Fadel et al. (2020), Fadel et al. (2018). Therefore, it is imperative to study this area further using other data, to confirm or reject the hypothesis on the existence of the Maltahohe microcraton, and if it does exist, understand its boundaries and relationship with the other cratonic blocks.

The extension of the EARS to Botswana is a debated phenomenon in the literature (e.g., Kinabo et al., 2007; Khoza et al., 2013b; Yu et al., 2015a; Leseane et al., 2015; Pastier et al., 2017; Fadel et al., 2020). There are still questions about the

existence of rifting in ORZ, and if it exists, its connection with the mature EARS is still debated (Kinabo et al., 2007; Pastier et al., 2017; Fadel et al., 2020; Khoza et al., 2013b). Furthermore, there are varying opinions about the possible further extension of the EARS to central Botswana. The ORZ, which consists of several normal to dextral strike-slip faults is widely interpreted to be the terminus of the western branch of the EARS by several studies (Kinabo et al., 2008; Modisi, 2000; Modisi et al., 2000; Yu et al., 2015b; Yu et al., 2015c; Fadel et al., 2020). However, Pastier et al. (2017) argue that there is no rifting in the Okavango area and proposed a model of differential movement between the Congo and Kalahari Cratons from their geodetic study. Also, from various studies that support the existence of rifting in the ORZ, there are divergent opinions on the rift mechanism and its link to the mature EARS. Kinabo et al. (2007), in a gravity and magnetic investigation argue that there is a strong correlation between the orientation of the pre-existing basement fold axes and foliation and the rift induced faults. They inferred that the pre-existing basement structures have considerable influence on the development of the rift faults in ORZ. Similarly, Khoza et al. (2013b), in a MT study argue that evidence of continental rifting such as thinned lithosphere and highly conductive mantle anomaly are not present in the ORZ. They proposed a model in which the incipient rifting in ORZ is initiated from the surface and not linked to the EARS. However, Leseane et al. (2015) in a thermal and Moho depth study suggest that the earthquakes in the ORZ are triggered by the migration of fluids from the mantle to the crust. Their results show shallow Curie Point depths, thin-crust, and high crustal heat from upward movement of mantle fluid to the lithosphere through weak zones beneath the ORZ. Similarly, results from seismic studies, for example, Fadel et al. (2020) and Yu et al. (2015a) show low-velocity anomaly and mantle seismic anisotropy in the ORZ, which connects to the EARS. Their findings provide a piece of evidence for the role of ascending fluids from the EARS in the rifting in ORZ. From the various divergent views, rifting in ORZ, the mechanism of rifting, and its link with the EARS is yet to be fully understood.

On the further southward extension of the EARS, there was a 6.5 Mw intra-plate earthquake in central Botswana and its link to the EARS is still a subject to debate (Gardonio et al., 2018; Midzi et al., 2018; **Figure 1D**). The earthquake, which occurred at an approximate depth of 29 km on 03 April 2017 was the second strongest in magnitude in the country's history and the second strongest intra-plate earthquake in the last 30 years (Gardonio et al., 2018; Midzi et al., 2018). Several studies, including the use of geophysical methods, have discussed the cause of the earthquake. Kolawole et al. (2017), in a combined magnetic, gravity, and differential interferometric synthetic aperture radar study, proposed that the 6.5 Mw earthquake in central Botswana is not linked to the EARS. From their results, the orientation of the tensional stress that caused the earthquake (northeast-southwest) is different from the northwest-southeast directed tensional stress acting on the southwestern end of the EARS. They suggest that the earthquake event was caused by extensional reactivation of a thrust play in the crust. On the contrary to Kolawole et al. (2017), some studies suggest the role of fluids or melt as the cause of the earthquake (Gardonio et al., 2018; Moorkamp et al., 2019; Fadel et al., 2020). Gardonio et al. (2018) in an interferometric synthetic aperture radar study suggest that the earthquake event was triggered by stress released from fluid migration from the mantle. Moorkamp et al. (2019) in a study using surface waves and MT data investigated the cause of the earthquake. Their results showed two displaced conductors in the crust, which they interpret to be related to graphite. Their study could neither confirm nor refute the possibility of mantle upwelling fluids as a trigger for the earthquake as suggested by Gardonio et al. (2018). Moorkamp et al. (2019) suggest that passive rifting explains the cause of the earthquake than thermal weakening from the mantle. Fadel et al. (2020) in a shear wave velocity study argue that the EAR does not only extend to northern Botswana in the ORZ, but that it does extend to central Botswana. From their model, the low-velocity anomaly of the EARS extends to the location of the 6.5 Mw earthquake in central Botswana. According to Fadel et al. (2020), the process that caused the earthquake suggests that it was associated with fluids or melt from the EARS. In a recent seismological study, Paulssen et al. (2022) also support that the EARS further continues to central Botswana based on the upward migration of the relocated aftershocks and their extensional mechanism, suggesting the earthquakes were produced by fluid intrusion from the mantle causing the eclogitization of dry metastable granulite facies rocks. These divergent views on the extension of the EARS to Botswana require further exploration and understanding from other geophysical data and models.

In the last 2 decades, different novel country-wide geophysical data have been compiled and processed in Botswana including gravity, magnetics, seismic, and MT data. Country-wide gravity and magnetic data provided some of the earliest understanding of the geological provinces and tectonics of Botswana due to the obscuring of the Precambrian geology by thick overburden formed from Kalahari group sediment (Hutchins and Reeves, 1980; Reeves and Hutchins, 1982; Chisenga et al., 2020b; **Figure 1D**). Also, several seismological studies have been done to understand the tectonics of Botswana. One of the earliest seismological studies was done by Reeves (1972), which focused on investigating seismicity in the ORZ. Wright and Hall (1990) investigated the Rehoboth Province and its relationship with the Kaapvaal Craton using active deep seismic profiling covering southwest Botswana. Many years later, several other seismological campaigns covering the eastern and southeast Botswana were done to image high resolution structure of the crust and upper mantle including the temporary network of the Southern Africa Seismic Experiment and the Africa Array Initiative (Carlson et al., 1996; Nyblade et al., 2008). Between 2013 and 2015, the Seismic Arrays for African Rift Initiation was deployed across the ORZ to further understand the incipient rifting and crustal and upper mantle structure of the region (Gao et al., 2013). More recently, a country-wide seismological project, Network of Autonomously Recording Seismographs was conducted between 2013 and 2018 to image the crustal and upper mantle structure beneath Botswana (Fadel, 2018).

Another geophysical data collection in Botswana was the MT data. In 2002, the Southern African Magnetotelluric Experiment (SAMTEX) was started with the aim to image the electrical structure of the crust and upper mantle beneath the southern

African region covering Botswana, Namibia, and South Africa (Jones et al., 2009a). The MT method gives information about the distribution of electrical conductivity in the crust and upper mantle, which is independent geophysical information that is not accessible by other methods. Out of the different geophysical properties, electrical conductivity shows the most significant contrasts in the subsurface material with variance spanning up to 14 orders of magnitude, as dry crystalline rocks can have resistivity above 10^6 Ωm, while rocks bearing graphite can have resistivity values below 0.01 Ωm (Telford et al., 2004; Simpson and Bahr, 2005). The wide variance in electrical conductivity gives a potential for producing well-constrained electrical models that can delineate variations in temperature and composition of the Earth's subsurface material.

In the context of our study, the MT method is suitable for imaging different geological terranes and their boundaries using their electrical conductivity properties. Cratonic segments can be delineated from the mobile belts based on conductivity signatures (Muller et al., 2009). Older lithospheric units (Archean Cratons) are more resistive than the younger lithospheric units (Proterozoic mobile belts) (Muller et al., 2009). Cratonic boundaries and tectonic transition zones are made of suture zones which are characterized by weakened crustal materials due to deformation processes (Khoza et al., 2013a; Muller et al., 2009). Also, the electrical conductivity model derived from MT data could give a piece of evidence about the presence of aqueous fluids and partial melts, rifting, and rift extensions. While there have been a few studies in Botswana that used the SAMTEX data, the studies so far are either focused on regional interpretations or too fragmented and hardly overlap (Muller et al., 2009; Miensopust et al., 2011; Evans et al., 2019; Jones et al., 2009b; Khoza et al., 2013a; Khoza et al., 2013b; Moorkamp et al., 2019). These hinder complete imaging and understanding of the electrical structure of the crust and upper mantle beneath Botswana, and the relationships between the cratons and the mobile belts.

In this study, we used MT data to obtain a country-wide 3D electrical model of Botswana to image the crust and upper mantle structure besides investigating the Maltahohe microcraton and the extension of the EARS in Botswana. The result of this research provides straightforward, connected, and precise geologic interpretations about the crust and upper mantle beneath Botswana and arguments raised in the literature about the Maltahohe microcraton and the extension of EARS to Botswana. Our results overcome the fragmented nature of the previous MT studies in Botswana and the different methodologies and approaches that have led to some conflicting interpretations. The new electrical model of the crust and upper beneath Botswana gives more insight into the tectonic development, current tectonic settings, cratons deformation, and rift initiation processes in the region.

2 GEOLOGY OF BOTSWANA

Botswana is in southern Africa and covers parts of the two cratons in the region and the transitions between them. In Botswana, the Congo Craton covers the northwest region and the Kalahari Craton, which comprises the Zimbabwe and Kaapvaal blocks covers the east and south, respectively (Begg et al., 2009; **Figure 1**). One of the prominent features in the Kaapvaal Craton is the Bushveld Complex, which is the most extensive layered mafic intrusion into the crust in the world (Begg et al., 2009). The emplacement of the Bushveld Complex in the north-central part of the Kaapvaal Craton (in South-Africa and the far western limb extending to south-east Botswana) took place between 2.06 and 2.05 Ga (Haddon, 2005; Begg et al., 2009). In southwest Botswana is the Rehoboth Province, which extends to eastern Namibia (**Figure 1C**). The Rehoboth Province is composed of aggregated mobile belts of Paleoproterozoic age around an Archean nucleus (van Schijndel et al., 2011; van Schijndel et al., 2014). There may exist an ancient microcraton beneath the Rehoboth Province in Botswana (Begg et al., 2009; Fadel et al., 2020).

In between the cratonic blocks, the lithosphere of Botswana is composed of mobile belts, which were formed from various rifting and accretion processes: Limpopo, Kheis-Okwa-Magondi, Damara, and Ghanzi-Chobe Belts (Begg et al., 2009; Key and Ayres, 2000; **Figure 1**). The Limpopo Belt is an Archean mobile belt formed from the collision between the Zimbabwe and Kaapvaal Cratons (Begg et al., 2009). The Kheis-Okwa-Magondi Belt composite is a Paleoproterozoic belt covering the central part of Botswana along the western boundaries of Kaapvaal and Zimbabwe Craton. The Damara Belt is a Neoproterozoic Pan-African belt that bounds the southeastern part of the Congo Craton (**Figure 1**). To the southeast of the Damara Belt is the Ghanzi-Chobe Belt, which is composed of sequences of folded meta-sediments (Wright and Hall, 1990). Across the Damara-Ghanzi-Chobe Belt is the ORZ, which is considered as an incipient continental rift zone (Kinabo et al., 2008; Modisi et al., 2000; **Figure 1**).

In central and southwest Botswana, the upper crust includes two sedimentary basins; the Passarge Basin and the Nosop Basin (**Figure 1D**). The Passarge Basin is in central Botswana and is filled with weakly folded siliciclastic and carbonates from the Ghanzi Group sediments with thickness up to 15 km, and formed during Neoproterozoic and early Paleozoic times (Pretorius, 1984; Key and Ayres, 2000). In the southwest Botswana is the Nosop Basin, which is filled with siliciclastic and marine carbonates from of the Nama Group sediments from Neoproterozoic and early Paleozoic times with thickness up to 15 km (Pretorius, 1984; Wright and Hall, 1990; Begg et al., 2009).

3 DATA AND METHODS

3.1 Data

We used data from 352 MT sites covering Botswana from the freely available Southern African Magnetotelluric Experiment (SAMTEX) data to obtain the electrical conductivity using 3D inverse modelling (Jones et al., 2009a; **Figures 1B,C**). The data used consists of broadband MT data (0.1–6,000 s) from 302 sites and long-period MT data (0.1–10,000 s) from 50 sites. The robust processing methods described in Jones et al. (1989) was used to process the electric and magnetic fields time series recordings to MT impedance (**Z**), apparent resistivities, tipper (**T**), and phase

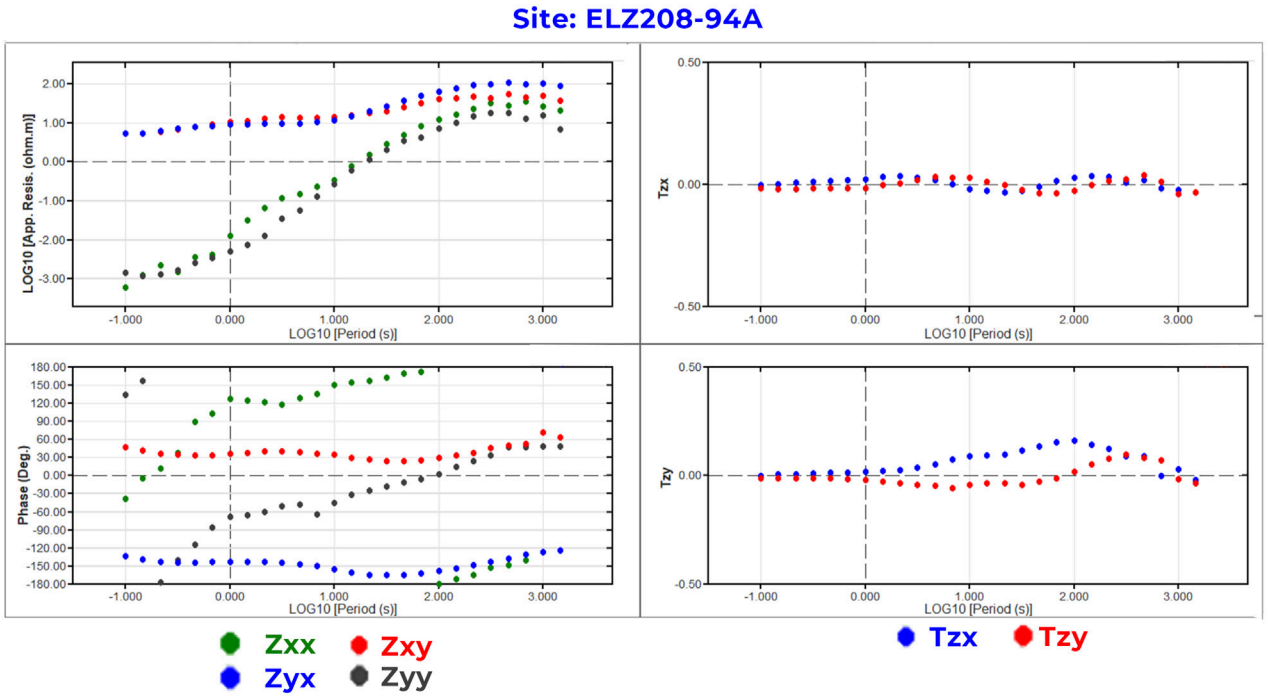

FIGURE 2 | Example of MT data from site ELZ208-94A showing the apparent resistivity and impedance phases against period (in logarithmic scale) for Zxx, Zxy, Zyx, and Zyy components and the tipper components plot against period (in logarithm scale) for Tzx and Tzy.

data by Jones et al. (2009). Preliminary regional electrical conductivity and electrical anisotropy maps from the SAMTEX data were presented by Jones et al. (2009). Moreover, a recent 3D electrical conductivity model of southern Africa using the whole SAMTEX data was developed by Özaydın et al. (2022) and compared with garnet xenocryst from kimberlites for more constrained interpretation of mantle structures. Aside from these regional interpretations of the SAMTEX data, a few other small-scale studies have used the SAMTEX data covering sections within Botswana or across its borders (Muller et al., 2009; Miensopust et al., 2011; Evans et al., 2019; Jones et al., 2009b; Khoza et al., 2013a; Khoza et al., 2013b; Moorkamp et al., 2019). For the country-wide 3D electrical modelling of Botswana, we focused on imaging the electrical structure of crustal and upper mantle in relation to the tectonic development, while providing more insights to some debated hypotheses about its tectonics. We used the full **Z** and **T** data for 31 periods from 0.1–10,000 s. Incorporating **T** into the inversion complements the model development by improving the resolution of the 3D electrical structures than inversion with **Z** only (Becken et al., 2008; Campanyà et al., 2016). **Figure 2** shows an example of the MT data from site ELZ208-94A, which is highlighted in black star in **Figure 1C**. Other MT data samples are given in **Supplementary Figures S1, S14, S15**.

3.2 Methodology

The methodology we used to derive the country-wide 3D electrical conductivity model of Botswana consists of three stages. In the first stage, we corrected the MT data for galvanic distortion and removed high error data to improve the data quality. In the second stage, we analyzed the properties and sensitivity of the MT data by performing depth resolution and dimensionality analysis. Finally, in the third stage, we inverted the MT data using 3D inversion technique. The details of the methodological steps are discussed further in the following subsections. We used the Python Toolbox for MT data processing, analysis, and visualization (MTpy; Kirkby et al., 2019; Krieger and Peacock, 2014). The 3D inversion of the MT data was done using the Modular System for Electromagnetic Inversion (ModEM) (Egbert and Kelbert, 2012; Kelbert et al., 2014).

3.2.1 MT Data Processing

We processed the MT data in two steps. First, we corrected the data for galvanic distortion and static shift error. Subsequently, the MT data that have been corrected for distortion were cleaned automatically and visually to remove data points with high errors.

The MT data is often affected by distortions (galvanic distortion) in the electromagnetic field, which are caused by the disturbance of the current that generates the electrical field. Galvanic distortions are non-inductive frequency-independent responses caused by the scattering of regional MT response by accumulated charge distribution on small-scale shallow bodies or inhomogeneity in local geologic structures (Jones, 2012). Galvanic distortion causes obscuring of the geoelectric strike, phase mixing, masking of properties of regional structures, and distortion of the magnitudes of **Z**. A subclass of the galvanic distortion of the MT data is the static shift, which is a frequency-independent shift in the apparent

resistivity curve by a factor (Simpson and Bahr, 2005; Jones, 2012). In 1D modelling, static shift causes a shift in the depth to conductive structures and error in the modelled resistivity values. In 2D and 3D cases, static shift, if not corrected, may cause artefacts in the model (Simpson and Bahr, 2005). The inherent distortions in the MT data might require corrections to extract undistorted data from the measured data for the purpose of modelling the subsurface electrical structure. According to Jones (2012) and Meqbel et al. (2014), the scattering effects of small-scale local structures with dimensions or spatial scales larger than the MT site spacing can be modelled in 3D inversion, and galvanic distortion correction is not required. However, the SAMTEX MT data has high spatial aliasing, hence galvanic distortion removal is necessary (**Figure 1D**). The galvanic distortion removal was done following Bibby et al. (2005) approach, which makes use of phase tensor parameters and implements minimum explicit assumptions about the data parameters. The phase relationship between the magnetic field and electric field remains undistorted and can be used to retrieve the regional impedance (Caldwell et al., 2004). On this basis, Bibby et al. (2005) described an approach of galvanic distortion removal in MT response using the phase tensor, which provides maximum information about the dimensionality of the regional impedance with the minimum assumptions about the data. The phase tensor approach also overcomes the challenges of other distortion removal techniques, such as preconditioned interpretation of regional structures in 2D along average or dominant strike direction (e.g., Groom and Bailey, 1991; Smith, 1995).

Static shift correction factors are undeterminable from the MT data itself (Simpson and Bahr, 2005). In this study, we used statistical averaging method to estimate the relative static shift correction factor for each MT station from other stations in the radius of 30 km (Simpson and Bahr, 2005). The outputs of the process are static shift corrected MT responses.

The MT responses were further processed by removing data points with high errors and outliers to improve the convergence of the data in the inversion process. Poor-quality data points with error bars of the **Z** and **T** data above 5% were removed automatically from the data, which is also the percentage of error floor used in the 3D inversion step that will be described later. After that, the MT curve smoothness was examined visually on the criteria that the variation in MT apparent resistivity curve from period to period should not be more than 45^{o} on a logarithm versus logarithm scale plot. From the data visual check, outlying period data points from the MT curve were removed to improve the smoothness of the MT response curve. The MT data were subsequently used in the data analyses and inversion stages.

3.2.2 MT Data Analysis

We performed two analyses to determine the sensitivity of the MT data. Depth resolution test was done to evaluate the depth in the subsurface to which the data is sensitive and can be reliably interpreted. Also, we examined the dimensionality captured in the MT data to understand the most appropriate dimension for modelling the data. To test the depth resolution of the MT dataset, we calculated the depth of penetration of the MT data per station using the Niblett-Bostick transformation (Niblett and Sayn-Wittgenstein, 1960). The Niblett-Bostick transformation accounts for variation in depth of penetration for MT sites at similar periods by comparing the MT responses than analysis based only on the period (Adetunji et al., 2015).

The dimensionality of the MT data is an important property which is required to determine the dimension of the modelling approach. The subsurface structure captured in the MT data should have the same dimensionality as the modelling approach used. Modelling MT data in dimensions higher or lower than the dimensionality captured in the data causes the propagation of the dimensionality distortion in the model, which leads to erroneous interpretation (e.g., a 1D interpretation of a 2D or 3D structure; Ledo et al., 2002; Ledo, 2005). We used phase tensor analysis to examine the dimensionality of the MT data. The phase tensor is not affected by galvanic distortion, and it holds essential information about the dimensionality of the MT data (Caldwell et al., 2004; Booker, 2014). The dimensionality analysis results showed that the MT data should be modeled in 3D and the results are further explained in **Section 4.1**. Therefore, 3D inversion was implemented to invert the MT data.

3.2.3 Three-Dimensional MT Data Inversion

We used ModEM for the inversion of the MT data (Egbert and Kelbert, 2012; Kelbert et al., 2014). The ModEM utilizes the finite difference approach for forward calculations and the non-linear conjugate gradient (NLCG) technique for solving the inverse problem. The finite difference method is a robust technique for electromagnetic response computation (Egbert and Kelbert, 2012). The NLCG method is efficient in solving large inverse problems because it requires lesser processing units (CPU and memory) as inversion model grids and data increase.

The ModEM requires constructing starting 3D mesh of the study area with initial electrical conductivity values. Once MT data and starting 3D model are prepared, the inversion process can be executed. Two main parameters govern the inversion process; model covariance and initial damping (Kelbert et al., 2014). The model covariance (value between 0 and 1) controls how the norm of the model behaves. Large model covariance values result in smoother models with poor data fit, while small model covariance values result in rough models with higher data fit (Robertson et al., 2020). On the other hand, the initial damping parameter controls how the model fits the data progressively.

The MT data over Botswana was inverted using a 3D mesh with cell dimensions of 10 km × 10 km in the horizontal plane. The choice of the horizontal griding dimensions was based on the minimum data interstation spacing of 10 km and the grid resolution test, which is described in the next paragraph. A first layer thickness of 50 m was used, and the subsequent vertical layers' thicknesses increased by a factor of 1.1 logarithmically. The mesh is composed of 137, 138, and 100 cells in the X, Y, and Z directions, and padding cells of 7, 7, and 6, respectively. A resistivity value of 100 Ωm was used for the starting model (Robertson et al., 2020). Also, an error floor of 5% of ($\sqrt{|\mathbf{Z}_{xy}\mathbf{Z}_{yx}|}$) was used for $\mathbf{Z}_{xy}$ and $\mathbf{Z}_{yx}$, an error floor of 5% of ($\sqrt{|\mathbf{Z}_{xx}\mathbf{Z}_{yy}|}$) was used for $\mathbf{Z}_{xx}$ and $\mathbf{Z}_{yy}$, and an 0.03 error floor for the **T** data (Meqbel et al., 2014). Topography data (MT station

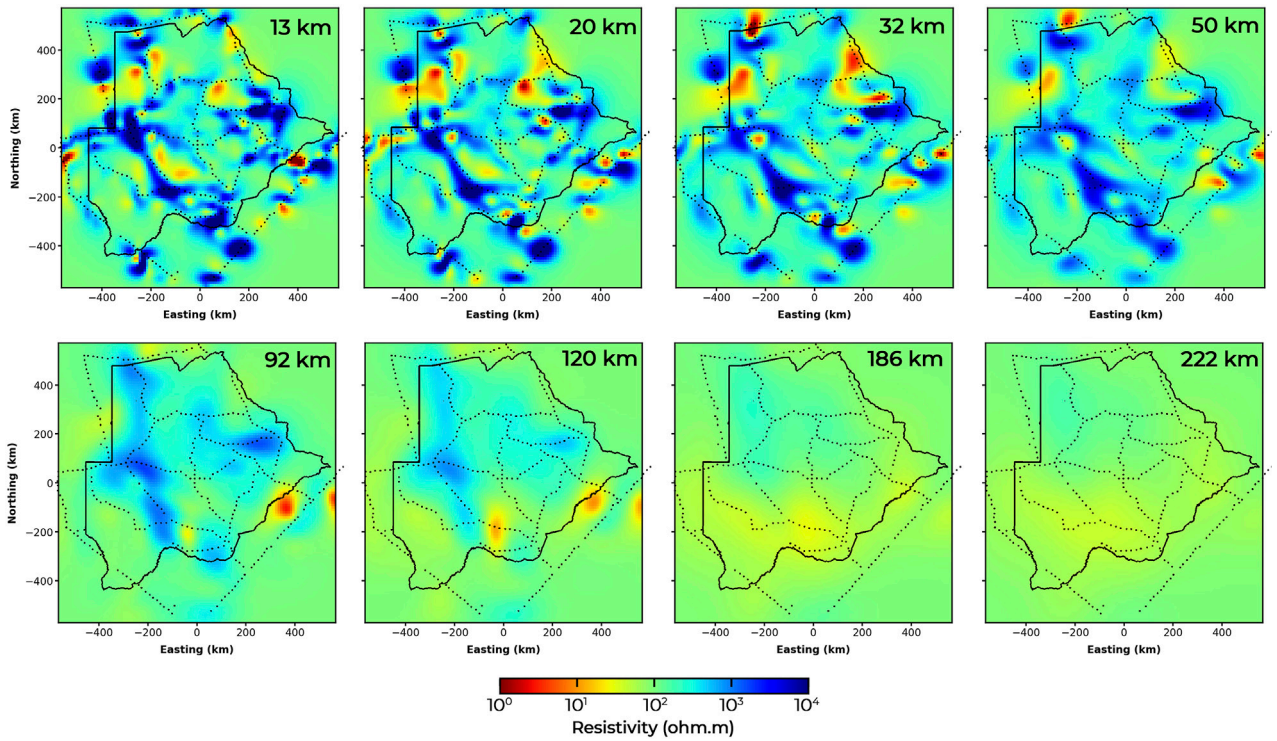

FIGURE 3 | Plan view of electrical conductivity model depth slices at 13, 20, 32, 50, 92, 120, 186, and 222 km depths. MT sites are represented in black dots.

elevation data) was incorporated into the model to compensate for site elevation difference. Ten air layers were added to the starting model to pad the Earth model. A model covariance value of 0.4 was used to resolve less smooth features and create a geologically plausible electrical model (Robertson et al., 2020). The initial damping parameter of 10 was used for the inversion to minimize required computation time and resources (Robertson et al., 2020). The final misfit for the electrical conductivity model is 3.22 after 126 iterations. Details of the model misfit are discussed in **Section 4** of the **Supplementary Figures S12–S15**.

We carried out several inversions to investigate the sensitivity of the inverted electrical model to three main parameters; the initial damping parameter, the grid resolution, and the certainty of the retrieved low conductive anomalies with values between 1–10 Ωm in the model. A model covariance value of 0.4 was fixed for all the tests, like main inversion covering Botswana described earlier. For the sensitivity tests, smaller datasets were used to ensure that the computation times required are shorter. Details about the sensitivity tests are discussed in the **Supplementary Material**. In the following, we briefly describe three sensitivity tests on the initial damping parameter, model grid resolution, and highly conductive structures.

1) We investigated how the initial damping parameter affects the resultant electrical model with varying values of 1, 10, 100, and 1,000.
2) Model grid resolution determination is a crucial step in 3D MT inversion. The decision of the size of the model grid is usually balanced between the need to recover fine model details by using a higher-resolution grid and, on the other side, minimizing the computational time and resources required by using a coarser-resolution grid. We investigated how the horizontal grid resolution affects the resultant electrical model using a coarse grid of 30 km × 30 km, an intermediate grid of 15 km × 15 km and a fine 10 km × 10 km grid resolutions.
3) A major uncertainty in our electrical modelling result was the highly conductive structures (1–10 Ωm) in the lower crust and upper mantle. A sensitivity test was carried out to verify the certainty of these highly conductive structures if they are data related. The test involved inverting the MT data for 120 iterations with misfit of 3.55 and removing the conductive structures (<100 Ωm) in the model and replacing them with the resistivity of the starting model (100 Ωm). The inversion is then restarted with the modified model and continued for another 74 iterations with misfit of 3.42. The resultant model was examined to see whether the highly conductive structures are returned in the model or not.

4 RESULTS AND DISCUSSION

4.1 Resolution Depth and Dimensionality

The results of the resolution depth and the dimensionality of the MT data are presented and discussed in detail in the **Supplementary Figures S2–S6**. Here, we discuss the main

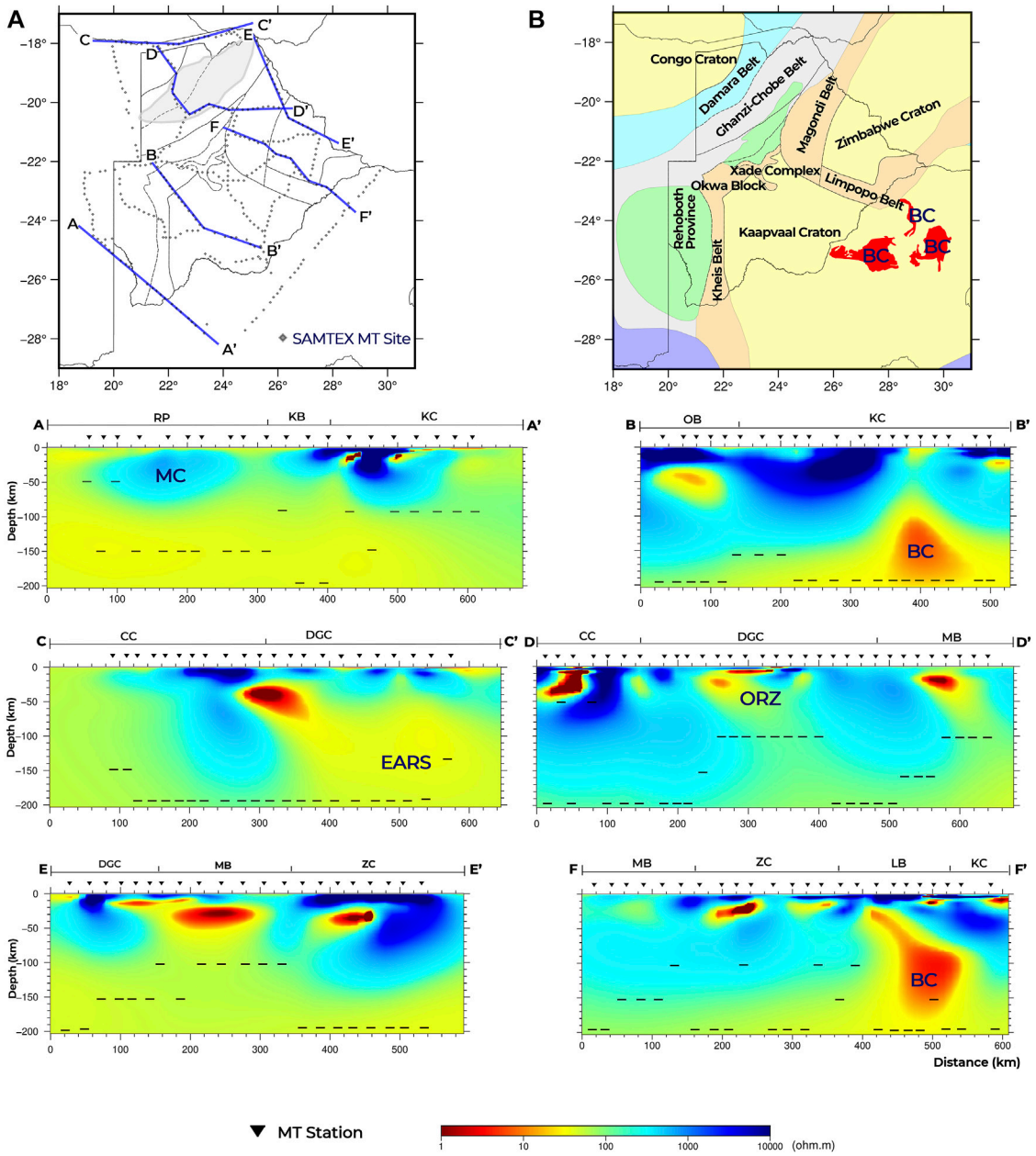

FIGURE 4 | The 3-D electrical conductivity model of Botswana along five cross sections represented with blue lines in **(A)**. **(B)** shows the tectonic map of Botswana. RP, Rehoboth Province; KB, Kheis Belt; KC, Kaapvaal Craton; OB, Okwa Block; CC, Congo Craton; DGC, Damara-Ghanzi-Chobe Belt; MB, Magondi Belt; ZC, Zimbabwe Craton; LB, Limpopo Belt; MC, Maltahohe microcraton; ORZ, Okavango Rift Zone; EARS, East African Rift System; BC, Bushveld Complex. Black dashes underneath each MT station in the electrical model = depth sensitivity per MT site.

findings. The conclusion from the depth resolution test is that the MT data used in this study can image down to 200–250 km depth (**Supplementary Figure S2**). The electrical models are presented up to depth of 200 km and sensitivity depth per MT site are also indicated (**Figures 4–6**). The MT data is not only sensitive to depths but also to the volumetric electrical conductivity of the subsurface, because electromagnetic waves have diffusive nature. The lateral distance to which the MT data is sensitive at any depth is referred to as horizontal adjustment length. At the various depths of penetration of the MT data, the horizontal adjustment length is 2–3 times the value of the penetration depth (Simpson and Bahr, 2005). However, due to high spatial aliasing between the MT sites, at shallow depths, the horizontal adjustment lengths are small (**Figure 1**). Hence, the results of the electrical model are interpreted and discussed along cross sections on top or in the near proximity of the MT stations (**Figures 3–5**) to address the shortcoming of the small horizontal adjustment length.

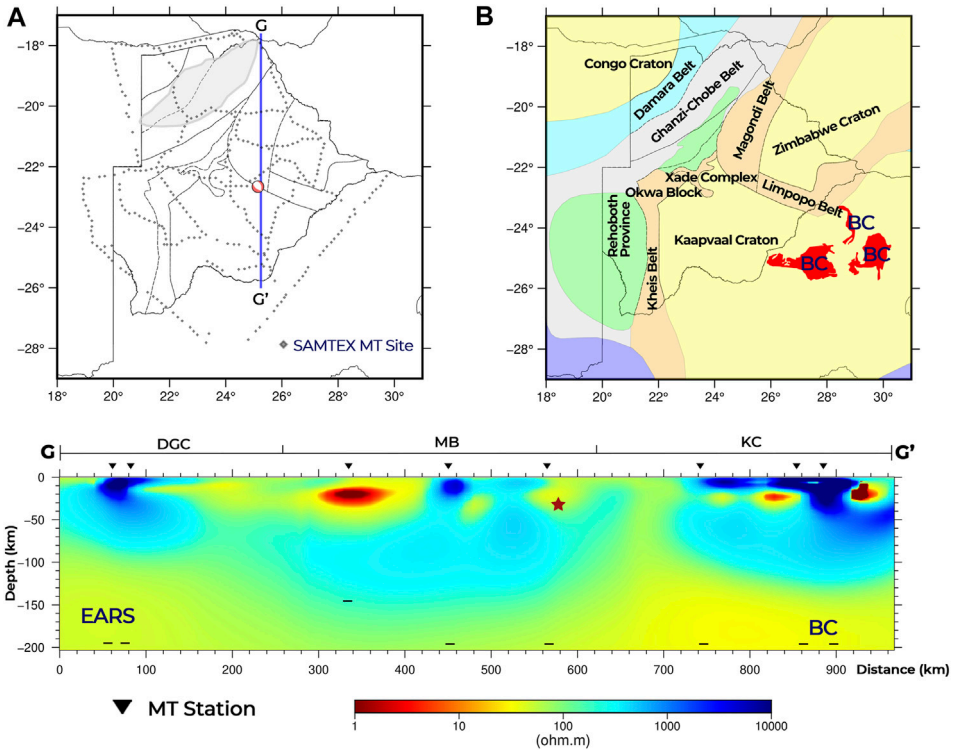

FIGURE 5 | Electrical conductivity model north-south cross section (represented with blue line in **(A)**) across the epicenter of the 03 April 2017 earthquake in central Botswana. **(B)** shows the tectonic map of Botswana. DGC, Damara-Ghanzi-Chobe Belt; MB, Magondi Belt; KC, Kaapvaal Craton; EARS, East African Rift System; BC, Bushveld Complex. Black dashes underneath each MT station in the electrical model = depth sensitivity per MT site.

The results of the dimensionality analysis (**Supplementary Figures S3–S6**) show high skew values (>6°) and high ellipticity of the phase tensor for majority of the MT sites. High skew values of the phase tensor greater than 6° indicate 3D effects, skew values of 0° indicate 2D data, and lower skew values indicate 1D subsurface structure (Cherevatova et al., 2015; Comeau et al., 2020). When the phase tensor is a circle, it indicates 1D subsurface, while the elliptical phase tensor represents 2D or 3D effects in the conductivity distribution (Becken and Burkhardt, 2004; Bibby et al., 2005). Hence, the results indicate the presence of 3D signature in the MT dataset.

The previous MT studies done in Botswana using the SAMTEX data showed the existence of multiple principal geoelectric strike directions in the data, which confirms the presence of 3D signature in the data (e.g., Miensopust et al. (2011), Muller et al. (2009), and Khoza et al. (2013a)). The result of the phase tensor analysis confirms the 3D nature of the structure beneath Botswana as reflected in the MT data. Therefore, the MT data for this study were modelled in 3D without need for assumption of geoelectric strike directions, which is required for 2D modelling approach.

4.2 Sensitivity Tests

The results of the sensitivity tests are presented and discussed in the **Supplementary Material**. Here we highlight the main findings on the inversion initial damping parameter, grid resolution, and conductive structures.

4.2.1 Initial Damping Parameter

The different initial damping parameters tested (1, 10, 100, and 1,000) did not influence the data fit nor the resolved structures in the resultant models (**Supplementary Figure S7**). However, higher initial damping parameters took more NLCG iterations and computation time to achieve convergence of the inversions. These observations are consistent with the results from model space exploration with the Australian Lithospheric Architecture Magnetotelluric Project data using ModEM done by Robertson et al. (2020). For the inversions in this study, we used an initial damping parameter of 10 to reduce the computing time.

4.2.2 Grid Resolution

We observed that increasing the grid resolution from 30 to 15 km and from 15 to 10 km led to an increase in the data fit of the resultant model (**Supplementary Figure S8**) and geologically plausible electrical structures (**Supplementary Figures S8–S10**). A choice of 10 km horizontal grid resolution, which is also the minimum interstation spacing in the data was made to recover a high-resolution model that can better fit the MT data.

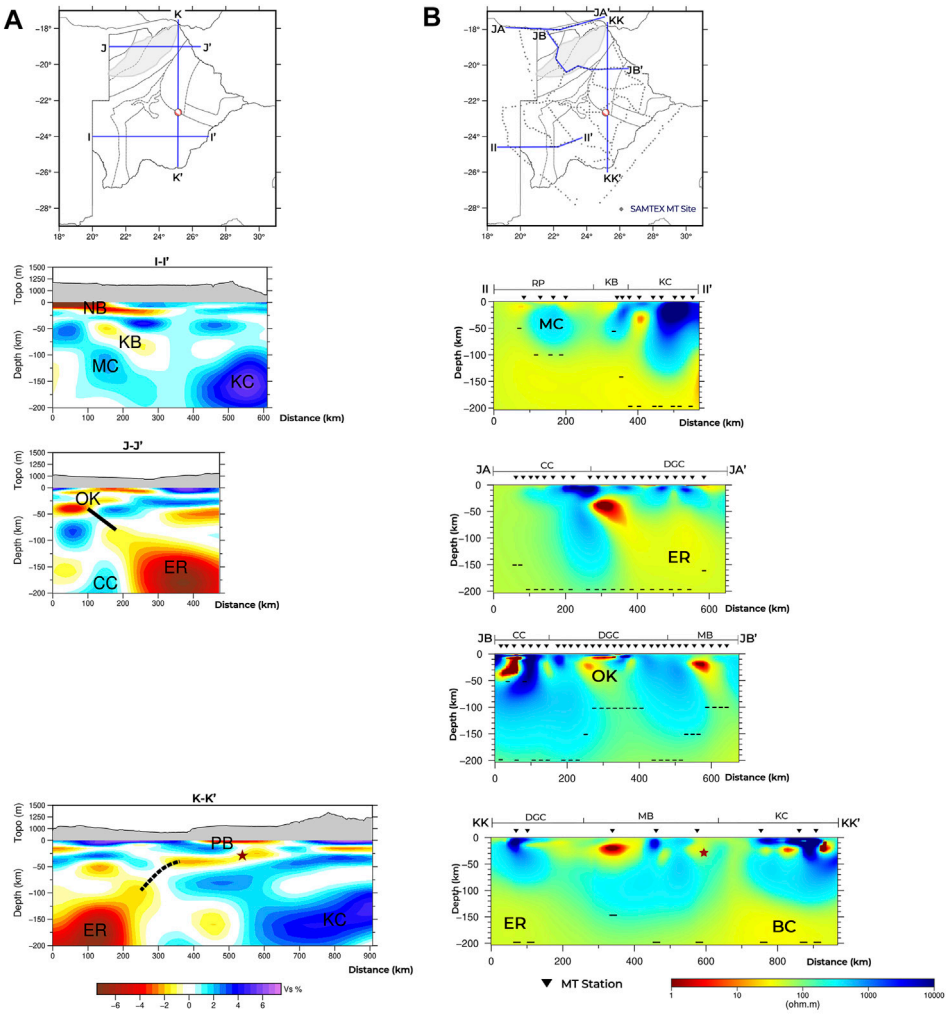

FIGURE 6 | (A) The 3-D shear wave velocity model of Botswana after Fadel et al. (2020). **(B)** Electrical conductivity model derived from MT data. The red star = location of the 6.5 Mw earthquake in 2017. The highlighted features: CC, Congo Craton; DGC, Damara-Ghanzi-Chobe Belt; ER, East African Rift System; KC, Kaapvaal Craton; KB, Kheis Belt; MB, Magondi Belt; MC, Maltahohe microcraton; NB, Nosop Basin; OK, Okavango Rift Zone; PB, Passarge Basin, and RP, Rehoboth Province; BC, Bushveld Complex. Black dashes underneath each MT station in the electrical model = depth sensitivity per MT site.

4.2.3 Conductive Structures

We observed that the highly conductive structures with resistivity values between 1–10 Ωm in the crust and upper mantle in our electrical model are required and are data related. From the test, the highly conductive features return to the model after a continued inversion of the modified model as described in **Section 3.2.3** in the **Supplementary Figure S11**.

4.3 The Electrical Conductivity Model

The final 3D electrical model of Botswana is presented as depth slices in **Figure 3** and cross sections in **Figure 4** to show the variation of the electrical conductivity of the different tectonic terranes in the study area. The cross sections were chosen along the data profiles to overcome the shortcoming of small horizontal adjustment length at shallow depth and make the results interpretable reliably.

From the results (**Figures 3, 4**), there are distinctive high conductive structures, both in the crust and upper mantle. Several factors can contribute to the high conductivity in the mid-lower crust and upper mantle. Anomalous conductive structures in the lower crust can be interpreted as the presence of graphite or aqueous fluids (Jones et al., 2005). In some areas, sulfides and other metalliferous ore deposits or partial melt contribute to high conductivity in the lower crust (Wannamaker et al., 2008). Regions that are spatially close to suture zones or fault zones also have highly conductive features due to the weakening of the crust (Jones et al., 2005). In the mantle, highly conductive anomalies can be due to high temperatures, partial melting, hydration, or mineralization of the mantle material (such as

iron enrichment) from magmatic intrusion (Jones et al., 2005; Khoza et al., 2013a; Khoza et al., 2013b; Evans et al., 2019).

In southwest Botswana (**Figure 4**; A-A′), there are distinctive electrical structures across the Rehoboth Province, Kheis Belt, and the Kaapvaal Craton. The Kheis Belt has the lowest bulk electrical resistivity, while the Kaapvaal Craton has the highest bulk electrical resistivity. The Kaapvaal craton is imaged as a highly resistive structure (approximately 10,000 Ωm). The Kheis Belt is imaged next to the Kaapvaal Craton as a less resistive lithosphere (500–1,000 Ωm). Beneath the Rehoboth Province, the result shows a separate resistive structure (with average resistivity above 1,000 Ωm) between 10 and 100 km depth. This signature is indicative of a cratonic structure. However, there is broad conductive structure from the upper mantle (100 km) downward across the profile A-A′, which could be due to high temperatures regimes in the mantle (Sobh et al., 2021). The observed lateral variation across the Rehoboth Province-Kheis Belt-Kaapvaal Craton is confirmed by the shear wave velocity model by Fadel et al. (2020).

Figure 4; B-B′ shows distinctive electrical structures across the Okwa Block and the Kaapvaal Craton. The Okwa Block is imaged as a resistive structure (~1,000–10,000 Ωm) with the presence of a conductor (~10 Ωm) at a depth of ~40 km. The Kaapvaal Craton is imaged as a resistive structure. However, from the depth of ~100 km downward, there exists a broad highly conductive structure (~5 Ωm), which may be due to iron enrichment of the mantle from the emplacement of the Bushveld Complex (Fouch et al., 2004). In the northwest margin of Botswana (**Figure 4**; C-C′), the Congo Craton is imaged as a resistive structure. In the Damara-Ghanzi Chobe Belt, there are distinctive highly conductive structures in the crust (~30 km) and at a deeper depth (~80 km downwards) around the east of profile C-C′ in **Figure 4**. The highly conductive structures may be due to fluids or melts from the EARS. Cross-section D-D′ shows the electrical conductivity model across Congo Craton, Damara-Ghanzi Chobe Belt, and the Magondi Belt. The Congo Craton is imaged in northwest Botswana as a highly resistive structure with the presence of a crustal conductor, which may be due to presence of ironstone in the metasedimentary rocks of Xaudum Group (Begg et al., 2009; Chisenga et al., 2020a). In the Damara-Ghanzi-Chobe Belt, the ORZ is imaged as a highly conductive crustal structure (~5 Ωm) that connects with mantle structure of intermediate conductivity (**Figure 4**; D-D′). Similarly, in Magondi Belt, a highly conductive crustal structure (~1 Ωm) is imaged, which seems to connect with a conductive mantle structure. These structures can be interpreted to be due to the upward movement of fluids or melt from the mantle to the crust beneath the ORZ and the Magondi Belt through zones of weakness as suggested by previous studies (e.g., Fadel et al., 2020).

Figure 4; F-F′ shows the electrical conductivity model across the Magondi Belt, Zimbabwe Craton, and the Limpopo Belt. The Zimbabwe Craton is imaged as a highly resistive structure with the presence of crustal conductive structures, which may be due to presence of graphite and/or sulfide (Khoza et al., 2013a). The observed high resistivity structure of the Zimbabwe Craton is consistent with results from velocity models, which show high-velocity anomalies beneath the Zimbabwe Craton (Ortiz et al., 2019; Fadel et al., 2020; White-Gaynor et al., 2021). Another feature of note along F-F′ is the highly conductive structure, which may be due to iron enrichment during the Bushveld Complex beneath the Kaapvaal Craton and the Limpopo Belt. This observation is consistent with a region of low velocity beneath the Limpopo belt from seismic study (Ortiz et al., 2019). The finding supports that this region of low velocity resulted from modification of the lithospheric and the mantle material by the Bushveld Complex magmatic event. **Figure 4**; E-E shows the lithosphere beneath the Magondi Belt is imaged as a conductive structure. Miensopust et al. (2011), in a previous MT study in northeast Botswana, observed crustal conductors beneath the Magondi Belt and suggest the structures to be due to the presence of graphite or sulphide. The Magondi belt was accreted to the Kheis-Okwa Belt (Thomas et al., 1993), and the Kheis-Okwa-Magondi Belt composite was modified during the Bushveld Complex emplacement (Begg et al., 2009).

4.4 Velocity-Conductivity Interpretation

Seismology and magnetotelluric methods are two primary geophysical methods for studying the structure of the crust and upper mantle because of their capacities to image deep Earth structures (Panza et al., 2007). These two methods look at different independent physical properties; velocity and conductivity, and they have different sensitivities to subsurface structures. Therefore, there is usually no complete match between the seismic velocity models and the electrical models. However, using both methods may support and complement some interpretations of subsurface structures. Here, we complement the interpretations from our new 3D electrical conductivity model with the country-wide 3D shear wave velocity model of Botswana by Fadel et al. (2020) to arrive at better interpretations (**Figure 6**). Their results included investigation of similar tectonic domains of this study; the Maltahohe microcraton and the extension of the EARS to Botswana, which are discussed in detail in coming sections.

4.5 The Maltahohe Microcraton

The resistive structure beneath the Rehoboth Province (**Figure 4**; A-A′) indicates the presence of a cratonic structure from depths of 10–100 km. This cratonic structure is clearly separated from the Kaapvaal Craton by the Kheis Belt. We interpret the cratonic structure beneath the Rehoboth Province as the Maltahohe microcraton, being distinct from the Kaapvaal Craton. This is contrary to the proposition of thinned western extension of the Kaapvaal Craton by Wright and Hall (1990). In an earlier MT study, Muller et al. (2009) carried out a 2D interpretation of the MT data across Kaapvaal Craton, Rehoboth Province and Damara-Ghanzi-Chobe Belt. According to the data decomposition study by Muller et al. (2009), multiple geoelectric strike directions are present in the data, which could be best solved using a 3D modelling approach. However, they inverted the MT data independently in two geoelectric strike directions of 25° and 45° due to computational limitations. Their electrical model showed conductive and resistive blobs beneath the Rehoboth Province, which could be due to dimensionality distortion in the 2D

interpretations. 3DThe 3D modelling methodological approach we employed helped to improve the imaging of the cratonic structure beneath Rehoboth Province, which we interpret as the Maltahohe microcraton. The 3D MT modelling does not require assumption on geoelectric strike direction, which prevents dimensionality distortion in the interpretation of the electrical model compared to the previous 2D modelling.

The finding from our 3D electrical model on the existence of the Maltahohe microcraton is consistent with some previous studies (e.g., Begg et al., 2009; Chisenga et al., 2020a; Fadel et al., 2020). Our finding also confirms the location of the Maltahohe microcraton to be similar to Fadel et al. (2020) and that is it a separate cratonic structure from the Kaapvaal Craton (**Figure 4**, A-A′ and **Figure 6**; II-II′). Fadel et al. (2020), from their 3D shear wave velocity study, observed a high shear wave velocity beneath the Rehoboth Province interpreted as the Maltahohe microcraton. In the shear wave velocity model, the high velocity structure of the Maltahohe microcraton is imaged up to 200 km depth as compared to 100 km depth in the electrical model (**Figure 6**; I-I′ and II-II′). The disparity in the imaged depth may be due to low MT site coverage along the II-II' profile. In the unresolved section along the II-II′ profile (low MT site coverage), the conductivity model could not image the possible deeper sections of the Maltahohe microcraton compared to the 3D shear wave velocity model.

4.6 The Bushveld Complex

Fouch et al. (2004), in a seismic study observed low seismic wave velocities in the Bushveld Complex around the southeastern border of Botswana. The location of the low seismic anomaly from the model of Fouch et al. (2004) coincides with the interpreted Bushveld Complex highly conductive anomaly along B-B′ and F-F′ in **Figure 4**. Their study suggests that the low seismic wave velocity anomaly is linked to compositional changes in the mantle due to iron enrichment from the formation of the Bushveld Complex. Similarly, other seismic investigations, including the P and S wave velocity study by Ortiz et al. (2019) and the shear-wave velocity study by White-Gaynor et al. (2021), show a region of low velocities beneath the Bushveld Complex in the Kaapvaal Craton. Ortiz et al. (2019), supporting Fouch et al. (2004), argue that the low velocities anomalies observed beneath the Okwa Block, Magondi Belt and Limpopo Belt, which are extensions of the Bushveld Complex, are results of the modification of the composition of the mantle material from the magmatic event. Ortiz et al. (2019) ruled out the possibilities of thermal anomalies as the cause of these low-velocity anomalies since no tectonic event affected these terranes in the Phanerozoic age.

In a previous MT study across the Kaapvaal Craton, Evans et al. (2011) found high electrical conductivity structure of ~10 Ωm in the Bushveld Complex. The interpreted MT data profile by Evans et al. (2011) intersects with the interpreted Bushveld Complex highly conductive anomaly in cross-section F-F′ in **Figure 4**. They suggest that connected metallic sulphides, iron-rich garnets, and other economic minerals form the network of conductors within the Bushveld Complex. This is like the proposition of Jones and Garcia (2006) for the highly conductive anomalies beneath the Yellowknife River Fault zone in the Slave Craton in northern Canada. Jones (1988) reported that the geotherms in the Bushveld Complex are not significantly higher compared to other parts of the Kaapvaal Craton from heat flow data. Also, the last thermal event in the emplacement of the Bushveld Complex occurred in the Archean (Begg et al., 2009; Evans et al., 2011). With these pieces of evidence, this study, supporting the interpretation of Fouch et al. (2004), attributes the iron enrichment of the mantle material from the Bushveld Complex emplacement as the cause of highly conductive structures beneath the Kaapvaal Craton (**Figure 4**; B-B′ and F-F′).

4.7 The Extension of the East African Rift System to Botswana

The southwestern branch of the EARS is often interpreted to have its terminus in northern Botswana (e.g., Modisi, 2000; Yu et al., 2015a; Leseane et al., 2015; Ortiz et al., 2019; Fadel et al., 2020). The southernmost surface expression of the EARS occurs at Lake Kariba, near the northeastern tip of Botswana (**Figure 1**). Our study investigates the possible extension of the EARS in Botswana. The electrical conductivity model across the northern border of Botswana in Namibia along the MT sites shows a distinctive highly conductive anomaly in the lower crust (~30 km), which connects with a conductive structure in the mantle (~80 km downwards; **Figure 4**; C-C′). This highly conductive mantle structure may be due to the further subsurface extension of the EARS from lake Kariba. The high conductive anomaly in the lower crust could be due to the migration of fluids or melt from the EARS into the crust through zones of weakness (**Figure 4**; C-C′). In the ORZ, we found a highly conductive crustal structure (~5 Ωm) that connects with a conductive upper mantle structure, which also supports the interpretation of ascending fluids or melt as the cause of the rifting in the ORZ (**Figure 4**; D-D′). This mechanism of ascending fluids or melt from the mantle to the crust is similar to the interpretation by Fadel et al. (2020) from shear wave velocity cross-section across the ORZ in northern Botswana. Their velocity model shows that the mantle low-velocity anomaly, which is linked to the EARS, seems to connect with the shallow low-velocity anomaly of the ORZ (Fadel et al., 2020; **Figure 6**; J-J′). Both cross-sections C-C′ and D-D′ from the electrical model are spatially displaced from the cross-section J-J′ from the shear wave velocity model. However, the mechanism of ascending fluids or melt from the mantle to the crust is similar to the proposition of Fadel et al. (2020) about the rifting in the ORZ. The interpretation of the conductive anomaly beneath the ORZ in our electrical model is supported by a high Vp/Vs ratio from the receiver function studies (Yu et al., 2015c; Fadel et al., 2018) and shallow Curie depth from aeromagnetic data (Leseane et al., 2015). According to Leseane et al. (2015) and references therein, it is suggested that the earthquakes in the ORZ are triggered by the migration of fluids from the mantle to the crust. Our interpretation also supports the proposition by Fadel et al. (2020) on the role of ascending fluids from the EARS in the weakening of the lithosphere and subsequent rifting in the ORZ. However, there exist contrary opinions on

the extension of the EARS to northern Botswana and mechanism of the incipient rifting in the ORZ (e.g., Khoza et al., 2013b; Kinabo et al., 2007; and references therein). Khoza et al. (2013b), in a previous MT study covering some parts of northwest Botswana, argue that neither a thinned lithospheric structure nor highly conductive mantle anomalies are present beneath the ORZ from their electrical model. They go further to propose a model in which the incipient rifting in ORZ is initiated from the surface. The result from our 3D electrical conductivity model provides a piece of evidence for the ascending fluids from the EARS to the crust in the northern border of Botswana with Namibia in a similar mechanism as suggested for the ORZ by Fadel et al. (2020).

Furthermore, Fadel et al. (2020) suggest that the EARS does not only extend to the ORZ, but further extends to central Botswana from their velocity model. Cross-section K-K′ in **Figure 6** shows a connection between a low-velocity anomaly beneath the epicentre of the 6.5 Mw earthquake and a deeper low-velocity anomaly, which may be due to the EARS. According to Fadel et al. (2020), the ascending fluids or melt from the EARS into the region below central Botswana may be the cause of the 6.5 Mw earthquake. Similarly, Chisenga et al. (2020b) modelled the crustal thickness of the crust beneath Botswana using gravity data. From their results, the crust beneath the epicentre of the 6.5 Mw earthquake in central Botswana is thinner with an approximate thickness of 40 km compared to 43 and 46 km thicknesses in the adjacent Kaapvaal Craton and central part of Limpopo Belt, respectively. Their result suggests that the thinning of the crust beneath the earthquake epicentre was caused by migrating thermal fluids from the EARS, eroding the lower crust structure. They propose that the combination of migrating thermal fluids from EARS, high heat flow, thin-crust and local stress in the crust contributed to the 6.5 Mw earthquake occurrence.

Our electrical conductivity model is not able to confirm or refute the proposition of EARS' extension to central Botswana because of under sampling of the MT data along the transect to investigate the phenomenon (**Figure 5**; G-G′). Hence, the electrical conductivity model is not able to provide more insight into the extension of the EARS to central Botswana. At shallow depth of penetration of the MT data, the horizontal adjustment length to which the data is sensitive is small. Due to this, shallow structures that are laterally far away from the MT sites cannot be reliably interpreted along the G-G′ transect. At large depths (greater than 100 km), the horizontal adjustment length increases and the MT response at the MT site becomes more regional. Hence, the structures in the model that are laterally displaced from the MT sites can be interpreted reliably. At the epicenter of the 6.5 Mw earthquake, the model shows a highly conductive anomaly at a depth of 30 km, which is resolved by at least one MT site. Moorkamp et al. (2019) in a study in central Botswana using surface wave and MT data found two displaced conductive structures which were interpreted as likely related to graphite. From their electrical model and seismic velocity results suggest, they suggest reactivation of the old fault zone associated with a weak mantle because of amphibole enrichment and reduced grain size in central Botswana. While they did not confirm or refute the concept of mantle upwelling fluids as a trigger for the earthquake, they attributed the earthquake and the associated weak mantle to be more likely due to passive rifting related to the ambient stress field driven from top to bottom rather than thermal weakening from below. Also, Moorkamp et al. (2019) suggest that the 6.5 Mw earthquake reactivated existing fault from the deformation process of the collision between Kaapvaal and Zimbabwe cratonic blocks. However, other studies suggest that ascending fluids or melt from the EARS extends to central Botswana through the weak lithospheric zones and played a role in triggering the earthquake (Chisenga et al., 2020b; Fadel et al., 2020; Paulssen et al., 2022).

There is also a highly conductive anomaly in the northern part of this cross section from ~100 km depth, which is resolved by at least two MT sites (**Figure 5**; G-G′). We interpreted this highly conductive structure as the possible extension of the EARS to northern Botswana. Another feature of note is the conductive structure beneath the Kaapvaal Craton from a depth of 120 km, which is resolved by at least three MT sites at that depth (**Figure 5**; G-G′). This highly conductive structure may be due high temperatures regimes in the upper mantle or from iron enrichment from the Bushveld magmatic emplacement in the Kaapvaal Craton. Additional MT measurements along this transect are required to resolve the electrical structure of the crust and upper mantle and further investigate the suggested extension of the EARS to central Botswana and its role in the 6.5 Mw earthquake in central Botswana.

5 SUMMARY AND CONCLUSION

We presented the 3D electrical conductivity model of Botswana derived from MT data. Our homogenous 3D modelling approach for interpreting the MT data covering Botswana overcame the preconditioned 2D interpretation of the electrical structure of the crust and upper mantle along geoelectric strike directions. Besides this, the country-wide electrical modelling provides a connected and precise interpretation of the electrical structure, overcoming the limitations of fragmented nature of the previous MT studies in Botswana. Our electrical model showed significant structures in the crust and upper mantle of Botswana. The model highlights the main geologic terranes in Botswana, including the very resistive structures of the cratonic terranes – Congo, Kaapvaal, Zimbabwe Cratons and Rehoboth Province; and the less resistive structures of the mobile belts – Damara-Ghanz-Chobe, Limpopo, and Kheis-Okwa-Magondi Belts. In southwest Botswana, we find a distinctive resistive structure beneath the Rehoboth Province, which suggests the existence of the Maltahohe microcraton as a separate cratonic unit as proposed by other studies. In addition to these, we imaged a highly conductive anomaly in the crust beneath the ORZ, which connects to a deeper highly conductive anomaly that may be related to the last surface expression of the EARS. We suggest that ascending fluids or melt from the EARS, which causes the weakening of the lithosphere, play a significant role in the incipient continental rifting in the ORZ. Lastly, our electrical model is not able to confirm or refute the suggested extension of the EARS to central

Botswana. Additional MT data measurements along northeast to central Botswana would solve the challenge of under sampling and help resolve the electrical structure along this transect better.

DATA AVAILABILITY STATEMENT

The data for the original contributions presented in the study are included in https://github.com/akinremisa/3D_Electrical_Model_MTBotswana, further inquiries can be directed to the corresponding author.

AUTHOR CONTRIBUTIONS

SA: conceptualization, data curation, methodology, software, writing original draft, writing, review, and editing and visualization. IF: conceptualization, software, writing, review and editing, visualization, and supervision. MM: conceptualization, review and editing, validation, and supervision. All authors contributed to the article and approved it for publication.

ACKNOWLEDGMENTS

The freely available SAMTEX data was used in this study (https://www.mtnet.info/data/samtex/samtex.html). The SAMTEX was conducted to image the electrical structure of the crust and upper mantle beneath the southern African region, covering Botswana, Namibia, and South Africa (Jones et al., 2009a) (**Figure 1**). The authors wish to acknowledge the contributions of the SAMTEX consortium comprising: The Dublin Institute for Advanced Studies, Woods Hole Oceanographic Institution, the Council for Geoscience, De Beers Group Services, The University of the Witwatersrand, Geological Survey of Namibia, Geological Survey of Botswana, Rio Tinto Mining and Exploration, BHP Billiton, Council for Scientific and Industrial Research of South Africa, and ABB Sweden for the Namibian Power Corporation. Other contributors to the SAMTEX project in terms of instruments and instrumentations are Phoenix Geophysics, the Geological Survey of Canada, and the U.S. Electromagnetic Studies of Continents consortium (EMSOC). Special thanks to the SAMTEX funding sponsors: the Continental Dynamics programme of the U.S. National Science Foundation (grant number: EAR0455242 and EAR-0309584), the South African Department of Science and Technology, and Science Foundation Ireland (Ireland, grant 05/RFP/GEO001). Also, thanks to the farmers and landowners for allowing access to their properties for MT station deployment. Special acknowledgement to the providers of the various facilities and codes used for this study. For the visualization of the results, figures, and illustrations, we used the MTPy (Krieger and Peacock, 2014; Kirkby et al., 2019) and the Generic Mapping Tools (GMT) (Wessel et al., 2019). We used the ModEM (Egbert and Kelbert, 2012; Kelbert et al., 2014) for the 3D MT inversion process. Computational resources from the Faculty of Geoinformation and Earth Observation (ITC), University of Twente and the Dutch National Supercomputing Facilities (Grant Number: EINF-1468), were used for the 3D MT inversion computations. The authors would like to thank Dr. Naser Meqbel for the support on the use of ModEM software. Special thanks to Prof. Michael Becken for fruitful discussions and suggestions. Finally, the results presented in the article first appeared in the Master's degree thesis of Akinremi S. (Akinremi, 2021) at the Department of Applied Earth Sciences, Faculty of Geo-Information Science and Earth Observation (ITC) of the University of Twente, The Netherlands. Special appreciation to the ITC Foundation Special Scholarship (ITCFSS), which funded the graduate study of Akinremi S.

SUPPLEMENTARY MATERIAL

The Supplementary Material for this article can be found online at: https://www.frontiersin.org/articles/10.3389/feart.2022.840703/full#supplementary-material

REFERENCES

Adetunji, A. Q., Ferguson, I. J., and Jones, A. G. (2015). Reexamination of Magnetotelluric Responses and Electrical Anisotropy of the Lithospheric Mantle in the Grenville Province, Canada. *J. Geophys. Res. Solid Earth* 120 (3), 1890–1908. doi:10.1002/2014JB011713

Akinremi, S. (2021). *Crustal And Upper Mantle Imaging of Botswana Using Magnetotelluric Method* (Faculty of Geoinformation Science and Earth Observation (ITC) of the University of Twente). Retrieved from https://essay.utwente.nl/88633/.

Becken, M., and Burkhardt, H. (2004). An Ellipticity Criterion in Magnetotelluric Tensor Analysis. *Geophys. J. Int.* 159 (1), 69–82. doi:10.1111/j.1365-246X.2004.02376.x

Becken, M., Ritter, O., and Burkhardt, H. (2008). Mode Separation of Magnetotelluric Responses in Three-Dimensional Environments. *Geophys. J. Int.* 172 (1), 67–86. doi:10.1111/j.1365-246X.2007.03612.x

Begg, G. C., Griffin, W. L., Natapov, L. M., O'Reilly, S. Y., Grand, S. P., O'Neill, C. J., et al. (2009). The Lithospheric Architecture of Africa: Seismic Tomography, Mantle Petrology, and Tectonic Evolution. *Geosphere* 5 (1), 23–50. doi:10.1130/GES00179.1

Bibby, H. M., Caldwell, T. G., and Brown, C. (2005). Determinable and Non-determinable Parameters of Galvanic Distortion in Magnetotellurics. *Geophys. J. Int.* 163 (3), 915–930. doi:10.1111/j.1365-246X.2005.02779.x

Booker, J. R. (2014). The Magnetotelluric Phase Tensor: a Critical Review. *Surv. Geophys* 35 (1), 7–40. doi:10.1007/s10712-013-9234-2

Brandt, M. B. C., Grand, S. P., Nyblade, A. A., and Dirks, P. H. G. M. (2011). Upper Mantle Seismic Structure beneath Southern Africa: Constraints on the Buoyancy Supporting the African Superswell. *Pure Appl. Geophys.* 169 (4), 595–614. doi:10.1007/s00024-011-0361-8

Caldwell, T. G., Bibby, H. M., and Brown, C. (2004). The Magnetotelluric Phase Tensor. *Geophys. J. Int.* 158 (2), 457–469. doi:10.1111/j.1365-246X.2004.02281.x

Campanyà, J., Ogaya, X., Jones, A. G., Rath, V., Vozar, J., and Meqbel, N. (2016). The Advantages of Complementing MT Profiles in 3-D Environments with Geomagnetic Transfer Function and Interstation Horizontal Magnetic Transfer Function Data: Results from a Synthetic Case Study. *Geophys. J. Int.* 207 (3), 1818–1836. doi:10.1093/gji/ggw357

Carlson, R. W., Grove, T. L., De Wit, M. J., and Gurney, J. J. (1996). Program to Study Crust and Mantle of the Archean Craton in Southern Africa. *Eos Trans. AGU* 77 (29), 273. doi:10.1029/96EO00194

Cherevatova, M., Smirnov, M. Y., Jones, A. G., Pedersen, L. B., Becken, M., Biolik, M., et al. (2015). Magnetotelluric Array Data Analysis from North-West Fennoscandia. *Tectonophysics* 653, 1–19. doi:10.1016/j.tecto.2014.12.023

Chisenga, C., Jianguo, Y., Fadel, I., Meijde, M. v. d., and Atekwana, E. A. (2020a). Updated Tectonic Terrane Boundaries of Botswana Determined from Gravity and Aeromagnetic Data. *Episodes* 43 (4), 919–933. doi:10.18814/epiiugs/2020/020054

Chisenga, C., Van der Meijde, M., Yan, J., Fadel, I., Atekwana, E. A., Steffen, R., et al. (2020b). Gravity Derived Crustal Thickness Model of Botswana: its Implication for the Mw 6.5 April 3, 2017, Botswana Earthquake. *Tectonophysics* 787, 228479. doi:10.1016/j.tecto.2020.228479

Comeau, M. J., Becken, M., Käufl, J. S., Grayver, A. V., Kuvshinov, A. V., Tserendug, S., et al. (2020). Evidence for Terrane Boundaries and Suture Zones across Southern Mongolia Detected with a 2-dimensional Magnetotelluric Transect. *Earth Planets Space* 72 (1), 1–13. doi:10.1186/s40623-020-1131-6

Egbert, G. D., and Kelbert, A. (2012). Computational Recipes for Electromagnetic Inverse Problems. *Geophys. J. Int.* 189 (1), 251–267. doi:10.1111/j.1365-246X.2011.05347.x

Evans, R. L., Elsenbeck, J., Zhu, J., Abdelsalam, M. G., Sarafian, E., Mutamina, D., et al. (2019). Structure of the Lithosphere beneath the Barotse Basin, Western Zambia, from Magnetotelluric Data. *Tectonics* 38 (2), 666–686. doi:10.1029/2018TC005246

Evans, R. L., Jones, A. G., Garcia, X., Muller, M., Hamilton, M., Evans, S., et al. (2011). Electrical Lithosphere beneath the Kaapvaal Craton, Southern Africa. *J. Geophys. Res.* 116 (B4), 1–16. doi:10.1029/2010JB007883

Fadel, I. E. A. M. (2018). *Crustal and Upper Mantle Structure of Botswana*. Enschede: University of Twente. doi:10.3990/1.9789036544641

Fadel, I., Paulssen, H., van der Meijde, M., Kwadiba, M., Ntibinyane, O., Nyblade, A., et al. (2020). Crustal and Upper Mantle Shear Wave Velocity Structure of Botswana: the 3 April 2017 Central Botswana Earthquake Linked to the East African Rift System. *Geophys. Res. Lett.* 47 (4), 1–12. doi:10.1029/2019GL085598

Fadel, I., van der Meijde, M., and Paulssen, H. (2018). Crustal Structure and Dynamics of Botswana. *J. Geophys. Res. Solid Earth* 123 (12), 10,659–10,671. doi:10.1029/2018JB016190

Fouch, M. J., James, D. E., VanDecar, J. C., and van der Lee, S. (2004). Mantle Seismic Structure beneath the Kaapvaal and Zimbabwe Cratons. *South Afr. J. Geol.* 107 (1–2), 33–44. doi:10.2113/107.1-2.33

Gao, S. S., Liu, K. H., Reed, C. A., Yu, Y., Massinque, B., Mdala, H., et al. (2013). Seismic Arrays to Study African Rift Initiation. *Eos Trans. AGU* 94 (24), 213–214. doi:10.1002/2013EO240002

Gardonio, B., Jolivet, R., Calais, E., and Leclère, H. (2018). The April 2017 Mw 6.5 Botswana Earthquake: An Intraplate Event Triggered by Deep Fluids. *Geophys. Res. Lett.* 45 (17), 8886–8896. doi:10.1029/2018GL078297

Groom, R. W., and Bailey, R. C. (1991). Analytic Investigations of the Effects of Near-surface Three-dimensional Galvanic Scatterers on MT Tensor Decompositions. *GEOPHYSICS* 56 (4), 496–518. doi:10.1190/1.1443066

Haddon, I. G. (2005). *The Sub-kalahari Geology and Tectonic Evolution of the Kalahari Basin, Southern Africa*. Johannesburg: University of the Witwatersrand. Retrieved from https://wiredspace.wits.ac.za/bitstream/handle/10539/193/Haddonthesistext.pdf.

Hutchins, D. G., and Reeves, C. V. (1980). Regional Geophysical Exploration of the Kalahari in Botswana. *Tectonophysics* 69 (3–4), 201–220. doi:10.1016/0040-1951(80)90211-5

Jones, A. G., Chave, A. D., Egbert, G., Auld, D., and Bahr, K. (1989). A Comparison of Techniques for Magnetotelluric Response Function Estimation. *J. Geophys. Res.* 94 (B10), 14201–14213. doi:10.1029/JB094iB10p14201

Jones, A. G., Chave, A. D., Jones, A. G., Mackie, R., and Rodi, W. (2012). "Distortion of Magnetotelluric Data: its Identification and Removal," in *The Magnetotelluric Method*. Editors A. D. Chave, and A. G. Jones, 219–302. doi:10.1017/CBO9781139020138.008

Jones, A. G., Evans, R. L., Muller, M. R., Hamilton, M. P., Miensopust, M. P., Cole, P., et al. (2009a). "The SAMTEX Experiment: Overview and Preliminary Results," in 11th SAGA Biennial Technical Meeting and Exhibition, Swaziland, South Africa, 16 Sep 2009 - 18 Sep 2009. doi:10.3997/2214-4609-pdb.241.jones_paper1

Jones, A. G., Evans, R. L., Muller, M. R., Hamilton, M. P., Miensopust, M. P., Garcia, X., et al. (2009b). Area Selection for Diamonds Using Magnetotellurics: Examples from Southern Africa. *Lithos* 112, 83–92. doi:10.1016/j.lithos.2009.06.011

Jones, A. G., and Garcia, X. (2006). "Electrical Resistivity Structure of the Yellowknife River Fault Zone and Surrounding Region," in *Gold in the Yellowknife Greenstone Belt, Northwest Territories: Results of the EXTECH III Multidisciplinary Research Project*. Editors C. D. Anglin, H. Falck, D. F. Wright, and E. J. Ambrose (Toronto: Geological Association of Canada, Mineral Deposits Division), 3, 126–141.

Jones, A. G., Ledo, J., and Ferguson, I. J. (2005). Electromagnetic Images of the Trans-Hudson Orogen: the North American Central Plains Anomaly Revealed. *Can. J. Earth Sci.* 42 (4), 457–478. doi:10.1139/e05-018

Jones, M. Q. W. (1988). Heat Flow in the Witwatersrand Basin and Environs and its Significance for the South African Shield Geotherm and Lithosphere Thickness. *J. Geophys. Res.* 93 (B4), 3243–3260. doi:10.1029/JB093iB04p03243

Kelbert, A., Meqbel, N., Egbert, G. D., and Tandon, K. (2014). ModEM: A Modular System for Inversion of Electromagnetic Geophysical Data. *Comput. Geosciences* 66, 40–53. doi:10.1016/j.cageo.2014.01.010

Key, R. M., and Ayres, N. (2000). The 1998 Edition of the National Geological Map of Botswana. *J. Afr. Earth Sci.* 30 (3), 427–451. doi:10.1016/S0899-5362(00)00030-0

Khoza, D., Jones, A. G., Muller, M. R., Evans, R. L., Webb, S. J., and Miensopust, M. (2013a). Tectonic Model of the Limpopo Belt: Constraints from Magnetotelluric Data. *Precambrian Res.* 226, 143–156. doi:10.1016/j.precamres.2012.11.016

Khoza, T. D., Jones, A. G., Muller, M. R., Evans, R. L., Miensopust, M. P., and Webb, S. J. (2013b). Lithospheric Structure of an Archean Craton and Adjacent Mobile Belt Revealed from 2-D and 3-D Inversion of Magnetotelluric Data: Example from Southern Congo Craton in Northern Namibia. *J. Geophys. Res. Solid Earth* 118 (8), 4378–4397. doi:10.1002/jgrb.50258

Kinabo, B. D., Atekwana, E. A., Hogan, J. P., Modisi, M. P., Wheaton, D. D., and Kampunzu, A. B. (2007). Early Structural Development of the Okavango Rift Zone, NW Botswana. *J. Afr. Earth Sci.* 48 (2–3), 125–136. doi:10.1016/j.jafrearsci.2007.02.005

Kinabo, B. D., Hogan, J. P., Atekwana, E. A., Abdelsalam, M. G., and Modisi, M. P. (2008). Fault Growth and Propagation during Incipient Continental Rifting: Insights from a Combined Aeromagnetic and Shuttle Radar Topography Mission Digital Elevation Model Investigation of the Okavango Rift Zone, Northwest Botswana. *Tectonics* 27 (3), a–n. doi:10.1029/2007TC002154

Kirkby, A., Zhang, F., Peacock, J., Hassan, R., and Duan, J. (2019). The MTPy Software Package for Magnetotelluric Data Analysis and Visualisation. *Joss* 4 (37), 1358–1364. doi:10.21105/joss.01358

Kolawole, F., Atekwana, E. A., Malloy, S., Stamps, D. S., Grandin, R., Abdelsalam, M. G., et al. (2017). Aeromagnetic, Gravity, and Differential Interferometric Synthetic Aperture Radar Analyses Reveal the Causative Fault of the 3 April 2017Mw6.5 Moiyabana, Botswana, Earthquake. *Geophys. Res. Lett.* 44 (17), 8837–8846. doi:10.1002/2017GL074620

Krieger, L., and Peacock, J. R. (2014). MTpy: A Python Toolbox for Magnetotellurics. *Comput. Geosciences* 72, 167–175. doi:10.1016/j.cageo.2014.07.013

Ledo, J. (2005). 2-D versus 3-D Magnetotelluric Data Interpretation. *Surv. Geophys* 26 (5), 511–543. doi:10.1007/s10712-005-1757-8

Ledo, J., Queralt, P., Martí, A., and Jones, A. G. (2002). Two-dimensional Interpretation of Three-Dimensional Magnetotelluric Data: an Example of Limitations and Resolution. *Geophys. J. Int.* 150 (1), 127–139. doi:10.1046/j.1365-246X.2002.01705.x

Leseane, K., Atekwana, E. A., Mickus, K. L., Abdelsalam, M. G., Shemang, E. M., and Atekwana, E. A. (2015). Thermal Perturbations beneath the Incipient Okavango Rift Zone, Northwest Botswana. *J. Geophys. Res. Solid Earth* 120 (2), 1210–1228. doi:10.1002/2014JB011029

McCourt, S., Armstrong, R. A., Jelsma, H., and Mapeo, R. B. M. (2013). New U–Pb SHRIMP Ages From the Lubango Region, SW Angola: Insights Into the Palaeoproterozoic Evolution of the Angolan Shield, Southern Congo Craton, Africa. *Journal of the Geological Society* 170 (2), 353–363. doi:10.1144/jgs2012-059

Midzi, V., Saunders, I., Manzunzu, B., Kwadiba, M. T., Jele, V., Mantsha, R., et al. (2018). The 03 April 2017 Botswana M6.5 Earthquake: Preliminary Results. *J. Afr. Earth Sci.* 143, 187–194. doi:10.1016/j.jafrearsci.2018.03.027

Miensopust, M. P., Jones, A. G., Muller, M. R., Garcia, X., and Evans, R. L. (2011). Lithospheric Structures and Precambrian Terrane Boundaries in Northeastern Botswana Revealed through Magnetotelluric Profiling as Part of the Southern African Magnetotelluric Experiment. *J. Geophys. Res.* 116 (B2), 1–21. doi:10.1029/2010JB007740

M. Meqbel, N., Egbert, G. D., Wannamaker, P. E., Kelbert, A., and Schultz, A. (2014). Deep Electrical Resistivity Structure of the Northwestern U.S. Derived from 3-D Inversion of USArray Magnetotelluric Data. *Earth Planet. Sci. Lett.* 402 (C), 290–304. doi:10.1016/j.epsl.2013.12.026

Modisi, M. P., Atekwana, E. A., Kampunzu, A. B., and Ngwisanyi, T. H. (2000). Rift Kinematics during the Incipient Stages of Continental Extension: Evidence from the Nascent Okavango Rift Basin, Northwest Botswana. *Geology* 28 (10), 939. doi:10.1130/0091-7613(2000)028<0939:rkdtis>2.3.co;2

Modisi, M. P. (2000). Fault System at the Southeastern Boundary of the Okavango Rift, Botswana. *J. Afr. Earth Sci.* 30 (3), 569–578. doi:10.1016/S0899-5362(00)00039-7

Moorkamp, M., Fishwick, S., Walker, R. J., and Jones, A. G. (2019). Geophysical Evidence for Crustal and Mantle Weak Zones Controlling Intra-plate Seismicity - the 2017 Botswana Earthquake Sequence. *Earth Planet. Sci. Lett.* 506, 175–183. doi:10.1016/j.epsl.2018.10.048

Muller, M. R., Jones, A. G., Evans, R. L., Grütter, H. S., Hatton, C., Garcia, X., et al. (2009). Lithospheric Structure, Evolution and Diamond Prospectivity of the Rehoboth Terrane and Western Kaapvaal Craton, Southern Africa: Constraints from Broadband Magnetotellurics. *Lithos* 112, 93–105. doi:10.1016/j.lithos.2009.06.023

Niblett, E. R., and Sayn-Wittgenstein, C. (1960). Variation of Electrical Conductivity with Depth by the Magneto-telluric Method. *GEOPHYSICS* 25 (5), 998–1008. doi:10.1190/1.1438799

Nyblade, A., Dirks, P., Durrheim, R., Webb, S., Jones, M., Cooper, G., et al. (2008). AfricaArray: Developing a Geosciences Workforce for Africa's Natural Resource Sector. *Lead. Edge* 27 (10), 1358–1361. doi:10.1190/1.2996547

Ortiz, K., Nyblade, A., Meijde, M., Paulssen, H., Kwadiba, M., Ntibinyane, O., et al. (2019). Upper Mantle P and S Wave Velocity Structure of the Kalahari Craton and Surrounding Proterozoic Terranes, Southern Africa. *Geophys. Res. Lett.* 46 (16), 9509–9518. doi:10.1029/2019GL084053

Özaydın, S., Selway, K., Griffin, W. L., and Moorkamp, M. (2022). Probing the Southern African Lithosphere with Magnetotellurics: 2. Linking Electrical Conductivity, Composition, and Tectonomagmatic Evolution. *JGR Solid Earth* 127 (3), 1–28. doi:10.1029/2021JB023105

Panza, G., Peccerillo, A., Aoudia, A., and Farina, B. (2007). Geophysical and Petrological Modelling of the Structure and Composition of the Crust and Upper Mantle in Complex Geodynamic Settings: The Tyrrhenian Sea and Surroundings. *Earth-Science Rev.* 80 (1–2), 1–46. doi:10.1016/j.earscirev.2006.08.004

Pastier, A.-M., Dauteuil, O., Murray-Hudson, M., Moreau, F., Walpersdorf, A., and Makati, K. (2017). Is the Okavango Delta the Terminus of the East African Rift System? towards a New Geodynamic Model: Geodetic Study and Geophysical Review. *Tectonophysics* 712-713, 469–481. doi:10.1016/j.tecto.2017.05.035

Paulssen, H., Micallef, T., Bouwman, D. R., Ruigrok, E., Herman, M. W., Fadel, I., et al. (2022). Rifting of the Kalahari Craton through Botswana? New Seismic Evidence. *JGR Solid Earth* 127 (4), 1–17. doi:10.1029/2021JB023524

Pretorius, D. A. (1984). *The Kalahari Foreland, its Marginal Troughs and Overthrust Belts, and the Regional Structure of Botswana*. Johannesburg, South Africa: University of Witwatersrand.

Reeves, C. V., and Hutchins, D. G. (1982). A Progress Report on the Geophysical Exploration of the Kalahari in Botswana. *Geoexploration* 20 (3–4), 209–224. doi:10.1016/0016-7142(82)90022-9

Reeves, C. V. (1972). Rifting in the Kalahari? *Nature* 237 (5350), 95–96. doi:10.1038/237095a0

Robertson, K., Thiel, S., and Meqbel, N. (2020). Quality over Quantity: on Workflow and Model Space Exploration of 3D Inversion of MT Data. *Earth Planets Space* 72 (1), 2. doi:10.1186/s40623-019-1125-4

Simpson, F., and Bahr, K. (2005). *Practical Magnetotellurics*. Cambridge, UK: Cambridge University Press.

Smith, J. T. (1995). Understanding Telluric Distortion Matrices. *Geophys. J. Int.* 122 (1), 219–226. doi:10.1111/j.1365-246X.1995.tb03549.x

Sobh, M., Gerhards, C., Fadel, I., and Götze, H. J. (2021). Mapping the Thermal Structure of Southern Africa from Curie Depth Estimates Based on Wavelet Analysis of Magnetic Data with Uncertainties. *Geochem Geophys Geosyst* 22 (11), 1–29. doi:10.1029/2021GC010041

Telford, W. M., Geldart, L. P., and Sheriff, R. E. (2004). *Applied Geophysics*. Cambridge, UK: Cambridge University Press. (Second).

Thomas, R. J., von Veh, M. W., and McCourt, S. (1993). The Tectonic Evolution of Southern Africa: an Overview. *J. Afr. Earth Sci.* 16 (1–2), 5–24. doi:10.1016/0899-5362(93)90159-N

van Schijndel, V., Cornell, D. H., Frei, D., Simonsen, S. L., and Whitehouse, M. J. (2014). Crustal Evolution of the Rehoboth Province from Archaean to Mesoproterozoic Times: Insights from the Rehoboth Basement Inlier. *Precambrian Res.* 240, 22–36. doi:10.1016/j.precamres.2013.10.014

van Schijndel, V., Cornell, D. H., Hoffmann, K.-H., and Frei, D. (2011). Three Episodes of Crustal Development in the Rehoboth Province, Namibia. *Geol. Soc. Lond. Spec. Publ.* 357 (1), 27–47. doi:10.1144/SP357.3

Wannamaker, P. E., Hasterok, D. P., Johnston, J. M., Stodt, J. A., Hall, D. B., Sodergren, T. L., et al. (2008). Lithospheric Dismemberment and Magmatic Processes of the Great Basin-Colorado Plateau Transition, Utah, Implied from Magnetotellurics. *Geochem. Geophys. Geosyst.* 9 (5), a–n. doi:10.1029/2007GC001886

Wessel, P., Luis, J. F., Uieda, L., Scharroo, R., Wobbe, F., Smith, W. H. F., et al. (2019). The Generic Mapping Tools Version 6. *Geochem. Geophys. Geosyst.* 20 (11), 5556–5564. doi:10.1029/2019GC008515

White-Gaynor, A. L., Nyblade, A. A., Durrheim, R. J., Raveloson, R., van der Meijde, M., Fadel, I., et al. (2021). Shear-Wave Velocity Structure of the Southern African Upper Mantle: Implications for Craton Structure and Plateau Uplift. *Geophys Res. Lett.* 48 (7), 1–10. doi:10.1029/2020GL091624

Wright, J. A., and Hall, J. (1990). Deep Seismic Profiling in the Nosop Basin, Botswana: Cratons, Mobile Belts and Sedimentary Basins. *Tectonophysics* 173 (1–4), 333–343. doi:10.1016/0040-1951(90)90228-Z

Yu, Y., Gao, S. S., Moidaki, M., Reed, C. A., and Liu, K. H. (2015a). Seismic Anisotropy beneath the Incipient Okavango Rift: Implications for Rifting Initiation. *Earth Planet. Sci. Lett.* 430, 1–8. doi:10.1016/j.epsl.2015.08.009

Yu, Y., Liu, K. H., Moidaki, M., Reed, C. A., and Gao, S. S. (2015b). No Thermal Anomalies in the Mantle Transition Zone beneath an Incipient Continental Rift: Evidence from the First Receiver Function Study across the Okavango Rift Zone, Botswana. *Geophys. J. Int.* 202 (2), 1407–1418. doi:10.1093/gji/ggv229

Yu, Y., Liu, K. H., Reed, C. A., Moidaki, M., Mickus, K., Atekwana, E. A., et al. (2015c). A Joint Receiver Function and Gravity Study of Crustal Structure beneath the Incipient Okavango Rift, Botswana. *Geophys. Res. Lett.* 42 (20), 8398–8405. doi:10.1002/2015GL065811

Conflict of Interest: The authors declare that the research was conducted in the absence of any commercial or financial relationships that could be construed as a potential conflict of interest.

Advantages of publishing in Frontiers

OPEN ACCESS
Articles are free to read for greatest visibility and readership

FAST PUBLICATION
Around 90 days from submission to decision

HIGH QUALITY PEER-REVIEW
Rigorous, collaborative, and constructive peer-review

TRANSPARENT PEER-REVIEW
Editors and reviewers acknowledged by name on published articles

Frontiers
Avenue du Tribunal-Fédéral 34
1005 Lausanne | Switzerland

Visit us: www.frontiersin.org
Contact us: frontiersin.org/about/contact

REPRODUCIBILITY OF RESEARCH
Support open data and methods to enhance research reproducibility

DIGITAL PUBLISHING
Articles designed for optimal readership across devices

FOLLOW US
@frontiersin

IMPACT METRICS
Advanced article metrics track visibility across digital media

EXTENSIVE PROMOTION
Marketing and promotion of impactful research

LOOP RESEARCH NETWORK
Our network increases your article's readership